water

Special Issue Reprint

Soil and Groundwater Quality and Resources Assessment

Edited by
Wanjun Jiang and Yizhi Sheng

mdpi.com/journal/water

MDPI

Soil and Groundwater Quality and Resources Assessment

Soil and Groundwater Quality and Resources Assessment

Guest Editors

Wanjun Jiang
Yizhi Sheng

MDPI

Basel • Beijing • Wuhan • Barcelona • Belgrade • Novi Sad • Cluj • Manchester

Guest Editors

Wanjun Jiang
Tianjin Center
China Geological Survey
Tianjin
China

Yizhi Sheng
State Key Laboratory of
Biogeology and
Environmental Geology
China University of
Geosciences
Beijing
China

Editorial Office
MDPI AG
Grosspeteranlage 5
4052 Basel, Switzerland

This is a reprint of the Special Issue, published open access by the journal *Water* (ISSN 2073-4441), freely accessible at: https://www.mdpi.com/journal/water/special_issues/6R48D4KCL5.

For citation purposes, cite each article independently as indicated on the article page online and as indicated below:

Lastname, A.A.; Lastname, B.B. Article Title. *Journal Name* **Year**, *Volume Number*, Page Range.

ISBN 978-3-7258-4345-9 (Hbk)
ISBN 978-3-7258-4346-6 (PDF)
https://doi.org/10.3390/books978-3-7258-4346-6

© 2025 by the authors. Articles in this book are Open Access and distributed under the Creative Commons Attribution (CC BY) license. The book as a whole is distributed by MDPI under the terms and conditions of the Creative Commons Attribution-NonCommercial-NoDerivs (CC BY-NC-ND) license (https://creativecommons.org/licenses/by-nc-nd/4.0/).

Contents

About the Editors . . . . . **vii**

Wanjun Jiang and Yizhi Sheng
Soil–Groundwater Environmental Quality and Water Resource: Assessment of Contaminant Sources, Species, and Transformations
Reprinted from: *Water* **2025**, *17*, 1493, https://doi.org/10.3390/w17101493 . . . . . **1**

Sheming Chen, Wanjun Jiang, Zhuo Zhang, Futian Liu, Jing Zhang and Hang Ning
Analysis of Runoff Variation Characteristics and Influencing Factors in the Typical Watershed of Miyun Reservoir, China
Reprinted from: *Water* **2025**, *17*, 442, https://doi.org/10.3390/w17030442 . . . . . **8**

Lishan Meng, Hang Ning, Wanjun Jiang, Yizhi Sheng, Wei Wang and Chao Tang
Comprehensive Study on Hydrogeological Conditions and Suitability Evaluation of In Situ Leaching for Sandstone-Hosted Uranium Deposit in Erlian Basin
Reprinted from: *Water* **2024**, *16*, 2785, https://doi.org/10.3390/w16192785 . . . . . **27**

Xiufang Yang, Muhammad Uris Mirjat, Abdullah Baloch, Mashooque Ali Talpur, Shafi Muhammad Kori, Rajesh Kumar Soothar, et al.
The Characterization of Aquifer Parameters in Using Skimming Tubewells Through the Pumping Test Method: A Case Study of Tando Allahyar
Reprinted from: *Water* **2024**, *16*, 3180, https://doi.org/10.3390/w16223180 . . . . . **46**

Bing Wang, Yanting Zhao, Yun Cai, Sen Zhang, Baomei Yang and Fei Liu
Feasibility Research on Surface Water Reinjection into the Sandstone Geothermal Reservoir of the Guantao Formation in Tianjin Based on Laboratory Experiments
Reprinted from: *Water* **2024**, *16*, 2475, https://doi.org/10.3390/w16172475 . . . . . **60**

Jun He, Pan Wu, Yiyong Li, Min Zeng, Chen Chen, Hamza Jakada and Xinwen Zhao
Comprehending Spatial Distribution and Controlling Mechanisms of Groundwater in Topical Coastal Aquifers of Southern China Based on Hydrochemical Evaluations
Reprinted from: *Water* **2024**, *16*, 2502, https://doi.org/10.3390/w16172502 . . . . . **76**

Yubo Xia, Guangfang Chen, Futian Liu, Jing Zhang and Hang Ning
Hydrogeochemical Characteristics and Health Risk Assessment of Groundwater in Grassland Watersheds of Cold and Arid Regions in Xilinhot, China
Reprinted from: *Water* **2024**, *16*, 2488, https://doi.org/10.3390/w16172488 . . . . . **93**

Letian Si, Bing Zhang, Ruiqing Zhou, Ruirui Jiang, Wanggang Dong, Rong Ma and Sihang Liu
Study on the Evolution Mechanism of Temporal Variability of Chloride Ions in Typical Districts of Ordos City
Reprinted from: *Water* **2024**, *16*, 2935, https://doi.org/10.3390/w16202935 . . . . . **114**

Yuanyuan Ji, Yinzhu Zhou, Xiaoyu Zhao, Jinlong Zhou, Ying Sun and Mi Lei
Distribution and Co-Enrichment Factors of Arsenic and Fluoride in the Groundwater of the Plain Area of the Aksu River Basin, Xinjiang, PR China
Reprinted from: *Water* **2024**, *16*, 3201, https://doi.org/10.3390/w16223201 . . . . . **132**

Mingxia Zhu, Zhen Yao, Xianhong Xu, Youning Wei, Xufa Yan and Ming Xiao
Accumulation, Source Apportionment, and Ecological-Health Risks Assessment of Topsoil Heavy Metals in Agricultural and Pastoral Areas in the Eastern Qaidam Basin, China
Reprinted from: *Water* **2024**, *16*, 3719, https://doi.org/10.3390/w16243719 . . . . . **156**

Hongwei Liu, Yaonan Bai, Yihang Gao, Bo Han, Jinjie Miao, Yanchao Shi and Fengtian Yang
Status, Sources, and Risks of Heavy Metals in Surface Sediments of Baiyangdian Lake and Inflow Rivers, North China
Reprinted from: *Water* **2024**, *16*, 2723, https://doi.org/10.3390/w16192723 . . . . . **174**

Yifan Zeng, Zuxin Xu and Bin Dong
Spatial Distribution, Leaching Characteristics, and Ecological and Health Risk Assessment of Potential Toxic Elements in a Typical Open-Pit Iron Mine Along the Yangzi River
Reprinted from: *Water* **2024**, *16*, 3017, https://doi.org/10.3390/w16213017 . . . . . **193**

Mingxing Yang, Bing Wang, Yubo Xia, Yan Qiu, Chunling Li and Zhendong Cao
Changing Soil Water Content: Main Trigger of the Multi-Phase Mobilization and Transformation of Petroleum Pollution Components—Insights from the Batch Experiments
Reprinted from: *Water* **2024**, *16*, 1775, https://doi.org/10.3390/w16131775 . . . . . **208**

Weichao Sun, Shuaiwei Wang, Jianzhou Yu, Huimin Lin and Lin Sun
Mechanisms of Non-Aqueous Phase Liquid Retention in Low-Permeability Aquifer Lenses: Effects on Contaminant Remediation
Reprinted from: *Water* **2024**, *17*, 573, https://doi.org/10.3390/w17040573 . . . . . **228**

Shuai Yang, Shucai Zhang, Shici Ma, Sheng Zhao and Zhengwei Liu
Field Demonstration of In Situ Slow-Release Oxygen Chemicals Coupled with Microbial Agents for Injection to Remediate BTEX Contamination
Reprinted from: *Water* **2024**, *16*, 2815, https://doi.org/10.3390/w16192815 . . . . . **247**

Peng Chen, Rong Ma, Letian Si, Lefan Zhao, Ruirui Jiang and Wanggang Dong
A Risk Assessment of the Vegetation Ecological Degradation in Hunshandake Sandy Land, China: A Case Study of Dabusennur Watershed
Reprinted from: *Water* **2024**, *16*, 2258, https://doi.org/10.3390/w16162258 . . . . . **263**

Feicui Wang, Fu Wang, Ke Zhu, Peng Yang, Tiejun Wang, Yunzhuang Hu and Lijuan Ye
Spatiotemporal Dynamics and Drivers of Coastal Wetlands in Tianjin–Hebei over the Past 80 Years
Reprinted from: *Water* **2024**, *16*, 2612, https://doi.org/10.3390/w16182612 . . . . . **280**

Di Zhan, Qingyin Xia, Gaoyuan Li, Xinyu Li, Yang Li, Dafu Hu, et al.
Biogeochemical Fe-Redox Cycling in Oligotrophic Deep-Sea Sediment
Reprinted from: *Water* **2024**, *16*, 2740, https://doi.org/10.3390/w16192740 . . . . . **297**

About the Editors

Wanjun Jiang

Wanjun Jiang is an Associate Researcher at the Tianjin Center of China Geological Survey and holds a Ph.D. in Hydrogeology from the China University of Geosciences (Beijing). His main research interests include the application of isotope hydrogeochemistry to identifying the groundwater environment, regional groundwater circulation and evolution, the genetic mechanism of deep formation water, and paleoclimate change and paleocgroundwater recharge. Wanjun Jiang currently serves as a Youth Editorial Board Member for *Hydrology* and a Guest Editor for multiple SCI-indexed journals (e.g., *Water*, *Applied Sciences*, *Sustainability*, and *Atmosphere*), driving interdisciplinary research on groundwater sustainability. He has published 20+ papers in leading journals such as *Science of the Total Environment*, *Journal of Hydrology*, and *Environmental Chemistry Letters*, advancing insights into decoding groundwater evolution, environmental tracers, and ancient recharge processes.

Yizhi Sheng

Yizhi Sheng is a Professor and Doctoral Supervisor at the China University of Geosciences (Beijing). He earned his Ph.D. through a joint program between China University of Geosciences (Beijing) and Pennsylvania State University (USA). From 2016 to 2022, he conducted postdoctoral research and taught as an instructor/lecturer at Tsinghua University and the University of Miami (USA). Prof. Sheng currently serves as Associate Editor for *Geo-Bio Interfaces* and *Frontiers in Microbiology*, and as Editorial Board Member for six journals, including *Earth Science Frontiers* and *PLOS ONE*. His research focuses on biogeochemical cycles and soil/groundwater pollution remediation. He has published 60+ papers in leading journals such as *Nature Reviews Earth & Environment*, *Environmental Science & Technology*, *Geochimica et Cosmochimica Acta*, and *Water Research*, advancing insights into microbial–environment interactions and sustainable remediation strategies.

water

MDPI

Editorial

Soil–Groundwater Environmental Quality and Water Resource: Assessment of Contaminant Sources, Species, and Transformations

Wanjun Jiang [1,2] and Yizhi Sheng [3,*]

[1] Tianjin Center, China Geological Survey, Tianjin 300170, China; jiangwanjun0718@163.com
[2] Tianjin Key Laboratory of Coast Geological Processes and Environmental Safety, Tianjin 300170, China
[3] State Key Laboratory of Biogeology and Environmental Geology, China University of Geosciences, Beijing 100083, China
* Correspondence: shengyz@cugb.edu.cn

1. Introduction

Globally, 80% of the world's population are at high risk of water scarcity, with global water scarcity increasing due to climate change, population growth, and economic development [1–4]. As the largest available fresh water and key component of the global water cycle, groundwater provides a valuable water resource for the vast majority of the population, supplying river flow, lakes or wetlands, industrial–agricultural activities, ecosystem health, and sustainable development [5–8]. However, under the influence of climate change and high-intensity human activities, groundwater resources and security have suffered a serious crisis [7,9,10]. This problem has attracted the attention of many countries, and it is also a hotspot and crucial problem in hydrogeology and hydrology [1,8,11]. Therefore, a comprehensive understanding of the changes in groundwater resources and quality, along with the factors influencing them, is essential to ensure sustainable groundwater resources for humans and ecosystems.

Human activities, particularly in regions experiencing the development of industry and agriculture and exploitation of mineral resources, pose increasing threats to terrestrial ecosystems and groundwater environments [1,8]. This situation is critical in areas facing water scarcity, where groundwater serves as the primary source of drinking water. Such concerns center around water depletion, soil–groundwater environment deterioration, and ecological–health risks associated with various contaminants [1,12]. The concentrations of contaminants in these ecosystems are complex due to complex hydrogeological conditions, long-term water–rock interactions, diverse groundwater recharge patterns, hydrologic–biogeochemical processes, and intensive human exploitation [7,13,14]. Notably, the threat extends to both traditional and emerging inorganic and organic pollutants, which find their way into human bodies via bioaccumulation, food chains, and drinking water, thus leading to health risks such as chemical toxicity, radiation exposure, and carcinogenic effects. Thus, the synergetic effects of natural and anthropogenic drivers further complicate conventional groundwater quality and resource problems.

Faced with increasingly severe water scarcity and ecological environment deterioration, there is an urgent need to carry out in-depth and detailed research on groundwater quality and resource management, as well as the type, sources, and mobilization and transformation of various contaminants. Meanwhile, on the basis of traditional methods such as numerical simulation, hydrogeochemistry, and environmental isotopic tracer (C, N, S, H, O, etc.), it is imperative to explore advances in technologies or methods such as remote sensing techniques, emerging datasets, machine learning, earth system models, and non-traditional stable isotopes (Fe, Ca, Mg, B, Li, Br, Cl, etc.). Leveraging these innovations

is essential for scientifically managing groundwater resources and uncovering the sources, mobilization, and transformation of contaminants [1,4,6,7,15–20].

This Special Issue, entitled "Soil and Groundwater Quality and Resources Assessment", synthesizes interdisciplinary investigations into hydrological mechanisms, contaminant transport processes, and sustainable resource management strategies. Through systematic analysis of 17 peer-reviewed studies, this collection elucidates critical advancements and persistent barriers in groundwater quality preservation and resource governance. Crucially, the compiled works collectively advance methodological frameworks for quantifying climate change or anthropogenic impacts on contaminant fate and aquifer systems and optimize remediation protocols through coupled experimental–numerical approaches. By elucidating contamination pathways, remediation strategies, and resource allocation models, these studies reinforce the scientific foundation for ecosystem preservation while addressing technical and policy implementation gaps.

2. Hydrological Processes and Water Resources

Emerging research highlights the intensification of hydrological stress and water resource instability under combined climatic change and anthropogenic perturbations, critically constraining water accessibility for both societal and ecological systems across multiple regions [1,8,21]. Chen's predictive modeling (contribution 1), integrating remote sensing datasets with statistical methods, has demonstrated significant runoff reductions in the Miyun Reservoir Basin, primarily attributed to shifting precipitation regimes and urban expansion. Concurrently, the hydrogeological suitability evaluated by Meng et al. (contribution 2) in the Erlian Basin has optimized in situ uranium leaching (ISL) operations through geochemical and permeability analyses, achieving equilibrium between mineral exploitation and aquifer preservation. Yang and Mirjat (contribution 3) determined the hydrogeological characterization of the Tando Allahyar aquifer through coupled pumping tests and numerical simulations to quantify aquifer parameters and evaluate the risks of saline intrusion during prolonged extraction. The innovative field experiments carried out by Wang et al. (contribution 4) further demonstrate the technical viability of sandstone reservoir reinjection in Tianjin's geothermal systems, presenting dual solutions for energy production and aquifer conservation. These investigations collectively highlight the compounding impacts of precipitation variability and human interventions on water resource sustainability.

Concurrently, coastal and arid zone aquifers face escalating challenges regarding both water quality and quantity. For example, through a comprehensive analysis of Southern China's coastal groundwater systems, He et al. (contribution 5) identified four dominant controls on hydrochemistry, including mineral weathering, evaporative concentration, seawater intrusion, and anthropogenic inputs. Also, it was found that the sources of nitrate present distinct spatial heterogeneity, which provides new insights into groundwater pollution in the coastal zone. The complementary studies in Xilinhot's grassland aquifers by Xia et al. (contribution 6) establish that livestock operations and mineral dissolution jointly govern groundwater quality patterns, exposing the vulnerability of the ecological environment and water resources in cold arid regions under intensified human pressures. Si's critical investigations (contribution 7) in typical districts of Ordos city elucidate the cyclical changes in chloride ions in groundwater systems, quantitatively differentiating contamination contributions from natural geochemical processes versus human pollution sources in arid environments.

These findings underscore the need to prioritize groundwater quality research, given its equivalent significance to water security compared to quantity concerns, particularly

as groundwater sustains potable water supplies for approximately 50% of the global population [6,7].

3. Contaminant Assessment and Sources

Soil–groundwater contamination assessment and the sources controlled by intense climate change and intensified human activities are long-term global challenges [21–23]. Under the combined influence of multiple factors, physical–chemical–biological processes such as the leaching, dissolution, desorption, enrichment, degradation, and transformation of various contaminants occur and migrate underground through surface water–soil–groundwater interactions [12]. Additionally, the extraction of groundwater, hydrogeological features, geogenic hazardous substances, dominant hydrogeochemical processes, and key factors have been verified to control the occurrence of geogenic contaminated groundwater [21,24–29].

For instance, the co-enrichment mechanism of arsenic and fluorine in the Aksu River Basin uncovered by Ji et al. (contribution 8), posing significant health risks, is attributed to the synergistic effect of a weak reducing alkaline groundwater environment and strong evaporative concentration, and this phenomenon is increasingly observed in arid areas. Notably, Zhu's research (contribution 9) and Liu's study (contribution 10) confirmed that heavy metal contamination caused by human activities, particularly in mining-affected regions and intensive agricultural zones, remains an urgent problem, as evidenced by topsoil in the Qaidam Basin and water sediments in the Baiyangdian Lake. Advanced source apportionment methodologies, integrating positive matrix factorization (PMF) with principal component analysis (PCA), successfully discriminate between geogenic weathering signatures and anthropogenic emission fingerprints, enabling targeted risk mitigation strategies.

4. Mobilization and Transformation

Contaminants, both geogenic (arsenic, fluoride, uranium) and anthropogenic (heavy metal, pesticides, PAHs, microplastics, emerging pollutants), exhibit complex speciation, mobility, and toxicity [12,21,22,24–26,30–35]. Their distribution and transformations are governed by hydrogeological heterogeneity, biogeochemical cycling, and land-use interactions. Notably, emerging contaminants such as endocrine disruptors, antibiotic resistance genes, PFASs, rare earth elements, etc., have gradually attracted worldwide attention. Their occurrence form, mobilization and transformation, biotoxicity, and treatment technology in groundwater systems have become research hotspots in recent years [34,36–41]. Recent work has advanced our understanding of the contaminants that migrate and transform through soil–groundwater systems via leaching, sorption, redox shifts, and biological mediation.

Some case studies have advanced our understanding of contaminant transport mechanisms and remediation strategies across diverse environmental systems. In the Yangtze River iron mining district, Zeng et al. (contribution 11) adopted sequential chemical extraction protocols combined with leaching simulations under rainfall conditions to clarify the migration dynamics of potentially toxic elements (PTEs). They demonstrated critical associations between spatial distribution patterns, weathering processes, and resultant ecological risks. Furthermore, batch experiments, explored by Yang and Wang (contribution 12), have quantified petroleum pollutants' transport mechanisms and differentiation processes in vadose zones, revealing that medium–low-permeability strata combined with elevated moisture content effectively suppress nonaqueous-phase liquid (NAPL) migration and volatilization. Meanwhile, recent pore-scale investigations in low-permeability aquifers conducted by Sun et al. (contribution 13) have identified capillary heterogeneity as a pri-

mary control on NAPL retention. Their experiments reveal the hindrance of capillary action to remediation work and challenge conventional remediation approaches. The concurrent technological innovations by Yang and Zhang (contribution 14) demonstrate synergistic effects when combining slow-release oxygen materials with specialized microbial consortia. The 98% BTEX degradation efficiency on the field scale marks a breakthrough in the in situ repair progress of bioenhancement technology.

These findings collectively underscore the necessity for characterizing and simulating the mobilization and transformation of contaminants across surface–subsurface hydrological continua to inform sustainable groundwater management. To confront this challenge effectively, in-depth and comprehensive research is imperative to uncover the sources of these pollutants and assess their potential impacts on human health and ecosystems [40,42,43].

5. Challenges and New Techniques

Emerging as a critical priority in global water security, comprehensive groundwater resource evaluation requires the systematic integration of quantity and quality assessments to address escalating ecological degradation. Sustaining aquifer ecosystem integrity constitutes a complex challenge necessitating interdisciplinary solutions, where pollutant dynamics (sources, species, mobilization, transformation, and fate) exhibit significant complexity due to synergistic interactions between natural and anthropogenic drivers. These include climate change, land-use practices, groundwater extraction intensity, the heterogeneity of water-bearing media, the complexity of hydrogeological structures, hydrodynamic conditions, and their coupling with geochemical or biogeochemical processes. Such multifaceted interactions fundamentally govern contaminant migration pathways while posing substantial challenges to predictive modeling and sustainable management frameworks.

In response, there is an urgent need to develop and adopt innovative methods and technologies for effectively identifying and managing groundwater resources and quality. Since the late 20th century, advancements in satellite technology, data science, information systems, and experimental testing have enabled the exploration of cutting-edge approaches. These include remote sensing techniques [18,19,44], emerging datasets [45,46], machine learning [34,35,47], advanced geological and hydrological models [8,48], contaminant migration modeling [49,50], and non-traditional stable isotopes [16,51]. Such innovations are crucial for achieving the scientific and sustainable management of groundwater resources and ensuring water quality.

Author Contributions: Conceptualization, W.J. and Y.S.; writing—original draft preparation, W.J. writing—review and editing, Y.S. All authors have read and agreed to the published version of the manuscript.

Funding: This research was funded by the National Natural Science Foundation of China (42302299).

Acknowledgments: We would like to thank all the authors who contributed and will contribute to this Special Issue. We would also like to thank all the reviewers for providing their valuable comments, which have greatly improved the quality of the published papers.

Conflicts of Interest: The authors declare no conflicts of interest.

List of Contributions:

1. Chen, S.; Jiang, W.; Zhang, Z.; Liu, F.; Zhang, J.; Ning, H. Analysis of Runoff Variation Characteristics and Influencing Factors in the Typical Watershed of Miyun Reservoir, China. *Water* **2025**, *17*, 442.
2. Meng, L.; Ning, H.; Jiang, W.; Sheng, Y.; Wang, W.; Tang, C. Comprehensive Study on Hydrogeological Conditions and Suitability Evaluation of In Situ Leaching for Sandstone-Hosted Uranium Deposit in Erlian Basin. *Water* **2024**, *16*, 2785.

3. Yang, X.; Mirjat, M.U.; Baloch, A.; Talpur, M.A.; Kori, S.M.; Soothar, R.K.; Shaikh, S.A.; Mari, I.A.; Chandio, F.A. The Characterization of Aquifer Parameters in Using Skimming Tubewells Through the Pumping Test Method: A Case Study of Tando Allahyar. *Water* **2024**, *16*, 3180.
4. Wang, B.; Zhao, Y.; Cai, Y.; Zhang, S.; Yang, B.; Liu, F. Feasibility Research on Surface Water Reinjection into the Sandstone Geothermal Reservoir of the Guantao Formation in Tianjin Based on Laboratory Experiments. *Water* **2024**, *16*, 2475.
5. He, J.; Wu, P.; Li, Y.; Zeng, M.; Chen, C.; Jakada, H.; Zhao, X. Comprehending Spatial Distribution and Controlling Mechanisms of Groundwater in Topical Coastal Aquifers of Southern China Based on Hydrochemical Evaluations. *Water* **2024**, *16*, 2502.
6. Xia, Y.; Chen, G.; Liu, F.; Zhang, J.; Ning, H. Hydrogeochemical Characteristics and Health Risk Assessment of Groundwater in Grassland Watersheds of Cold and Arid Regions in Xilinhot, China. *Water* **2024**, *16*, 2488.
7. Si, L.; Zhang, B.; Zhou, R.; Jiang, R.; Dong, W.; Ma, R.; Liu, S. Study on the Evolution Mechanism of Temporal Variability of Chloride Ions in Typical Districts of Ordos City. *Water* **2024**, *16*, 2935.
8. Ji, Y.; Zhou, Y.; Zhao, X.; Zhou, J.; Sun, Y.; Lei, M. Distribution and Co-Enrichment Factors of Arsenic and Fluoride in the Groundwater of the Plain Area of the Aksu River Basin, Xinjiang, PR China. *Water* **2024**, *16*, 3201.
9. Zhu, M.; Yao, Z.; Xu, X.; Wei, Y.; Yan, X.; Xiao, M. Accumulation, Source Apportionment, and Ecological-Health Risks Assessment of Topsoil Heavy Metals in Agricultural and Pastoral Areas in the Eastern Qaidam Basin, China. *Water* **2024**, *16*, 3719.
10. Liu, H.; Bai, Y.; Gao, Y.; Han, B.; Miao, J.; Shi, Y.; Yang, F. Status, Sources, and Risks of Heavy Metals in Surface Sediments of Baiyangdian Lake and Inflow Rivers, North China. *Water* **2024**, *16*, 2723.
11. Zeng, Y.; Xu, Z.; Dong, B. Spatial Distribution, Leaching Characteristics, and Ecological and Health Risk Assessment of Potential Toxic Elements in a Typical Open-Pit Iron Mine Along the Yangzi River. *Water* **2024**, *16*, 3017.
12. Yang, M.; Wang, B.; Xia, Y.; Qiu, Y.; Li, C.; Cao, Z. Changing Soil Water Content: Main Trigger of the Multi-Phase Mobilization and Transformation of Petroleum Pollution Components—Insights from the Batch Experiments. *Water* **2024**, *16*, 1775.
13. Sun, W.; Wang, S.; Yu, J.; Lin, H.; Sun, L. Mechanisms of Non-Aqueous Phase Liquid Retention in Low-Permeability Aquifer Lenses: Effects on Contaminant Remediation. *Water* **2025**, *17*, 573.
14. Yang, S.; Zhang, S.; Ma, S.; Zhao, S.; Liu, Z. Field Demonstration of In Situ Slow-Release Oxygen Chemicals Coupled with Microbial Agents for Injection to Remediate BTEX Contamination. *Water* **2024**, *16*, 2815.

References

1. Scanlon, B.R.; Fakhreddine, S.; Rateb, A.; de Graa, I.; Famiglietti, J.; Gleeson, T.; Grafton, R.Q.; Jobbagy, E.; Kebede, S.; Kolusu, S.R.; et al. Global water resources and the role of groundwater in a resilient water future. *Nat. Rev. Earth Environ.* **2023**, *4*, 87–101. [CrossRef]
2. Srivastava, S.; Mehta, L.; Naess, L.O. Increased attention to water is key to adaptation. *Nat. Clim. Chang.* **2022**, *12*, 113–114. [CrossRef]
3. Xiao, Y.; Zhang, Y.; Yang, H.; Wang, L.W.; Han, J.B.; Hao, Q.C.; Wang, J.; Zhao, Z.; Hu, W.X.; Wang, S.B.; et al. Interaction regimes of surface waterand groundwater in a hyper-aridendorheic watershed on TibetanPlateau: Insights from multi-proxydata. *J. Hydrol.* **2024**, *644*, 132020. [CrossRef]
4. Xie, J.; Liu, X.; Jasechko, S.; Berghuijs, W.; Wang, K.; Liu, C.; Reichstein, M.; Jung, M.; Koirala, S. Majority of global river flow sustained by groundwater. *Nat. Geosci.* **2024**, *2024. 17*, 770–777. [CrossRef]
5. Cuthbert, M.O.; Gleeson, T.; Moosdorf, N.; Befus, K.M.; Schneider, A.; Hartmann, J.; Lehner, B. Global patterns and dynamics of climate-groundwater interactions. *Nat. Clim. Change* **2019**, *9*, 137–141. [CrossRef]
6. Rohde, M.M.; Albano, C.M.; Huggins, X.; Klausmeyer, K.R.; Morton, C.; Sharman, A.; Zaveri, E.; Saito, L.; Freed, Z.; Howard, J.K.; et al. Groundwater-dependent ecosystem map exposes global dryland protection needs. *Nature* **2024**, *632*, 101–107. [CrossRef]
7. Jasechko, S.; Seybold, H.; Perrone, D.; Fan, Y.; Shamsudduha, M.; Taylor, R.G.; Fallatah, O.; Kirchner, J.W. Rapid groundwater decline and some cases of recovery in aquifers globally. *Nature* **2024**, *625*, 715–721.
8. Kuang, X.X.; Liu, J.G.; Scanlon, B.R.; Jiao, J.J.; Jasechko, S.; Lancia, M.; Biskaborn, B.K.; Wada, Y.; Li, H.L.; Zeng, Z.Z.; et al. The changing nature of groundwater in the global water cycle. *Science* **2024**, *383*, eadf0630. [CrossRef]

9. Niazi, H.; Wild, T.B.; Turner, S.W.D.; Graham, N.T.; Hejazi, M.; Msangi, S.; Kim, S.; Lamontagne, J.R.; Mengqi Zhao, M.Q. Global peak water limit of future groundwater withdrawals. *Nat. Sustain.* **2024**, *7*, 413–422. [CrossRef]
10. Long, D.; Yang, W.; Scanlon, B.R.; Zhao, J.S.; Liu, D.; Burek, P.; Pan, Y.; You, L.Z.; Wada, Y. South-to-North Water Diversion stabilizing Beijing's groundwater levels. *Nat. Commun.* **2020**, *11*, 3665. [CrossRef]
11. Thaw, M.; GebreEgziabher, M.; Villafañe-Pagán, J.Y.; Jasechko, S. Modern groundwater reaches deeper depths in heavily pumped aquifer systems. *Nat. Commun.* **2022**, *13*, 5263. [CrossRef] [PubMed]
12. Sheng, Y.Z.; Jiang, J.W.; Zhang, M. Mobilization, Speciation, and Transformation of Organic and Inorganic Contaminants in Soil-Groundwater Ecosystems. *Appl. Sci.* **2023**, *13*, 11454. [CrossRef]
13. Sheng, Y.; Baars, O.; Guo, D.; Whitham, J.; Srivastava, S.; Dong, H.L. Mineral-bound trace metals as cofactors for anaerobic biological nitrogen fixation. *Environ. Sci. Technol.* **2023**, *57*, 7206–7216. [CrossRef]
14. Rohde, M.M.; Stella, J.C.; Singer, M.B.; Roberts, D.A.; Caylor, K.K.; Albano, C.M. Establishing ecological thresholds and targets for groundwater management. *Nat. Water.* **2024**, *2*, 312–323. [CrossRef]
15. Jiang, W.J.; Wang, G.C.; Sheng, Y.Z.; Shi, X.M.; Zhang, H. Isotopes in groundwater (^{2}H, ^{18}O, ^{14}C) revealed the climate and groundwater re-charge in the Northern China. *Sci. Total Environ.* **2019**, *666*, 298–307. [CrossRef] [PubMed]
16. Jiang, W.J.; Sheng, Y.Z.; Wang, G.C.; Shi, Z.M.; Liu, F.T.; Zhang, J.; Chen, D.L. Cl, Br, B, Li, and noble gases isotopes to study the origin and evolution of deep groundwater in sedimentary basins, a review. *Environ. Chem. Lett.* **2022**, *20*, 1497–1528. [CrossRef]
17. Cao, W.G.; Zhang, Z.; Fu, Y.; Zhao, L.H.; Ren, Y.; Nan, T.; Guo, H.M. Prediction of arsenic and fluoride in groundwater of the North China Plain using enhanced stacking ensemble learning. *Water Res.* **2024**, *259*, 121848. [CrossRef] [PubMed]
18. Rateb, A.; Scanlon, B.R.; Pool, D.R.; Sun, A.; Zhang, Z.Z.; Chen, J.L.; Clark, B.; Faunt, C.C.; Haugh, C.J.; Hill, M.; et al. Comparison of Groundwater Storage Changes From GRACE Satellites With Monitoring and Modeling of Major U.S. Aquifers. *Water Resour. Res.* **2020**, *56*, e2020WR027556. [CrossRef]
19. Yang, J.; Pan, Y.; Zhang, C.; Gong, H.; Xu, L.; Huang, Z.; Lu, S. Comparison of groundwater storage changes over losing and gaining aquifers of China using GRACE satellites, modeling and in-situ observations. *Sci. Total Environ.* **2024**, *938*, 173514. [CrossRef]
20. Jiang, W.J.; Sheng, Y.Z.; Shi, Z.M.; Guo, H.M.; Chen, X.L.; Mao, H.R.; Liu, F.T.; Ning, H.; Liu, N.N.; Wang, G.C. 2024 Hydrogeochemical characteristics and evolution of formation water in the continental sedimentary basin: A case study in the Qaidam Basin, China. *Sci. Total Environ.* **2024**, *957*, 177672. [CrossRef]
21. Mukherjee, A.; Coomar, P.; Sarkar, S.; Johannesson, K.H.; Fryar, A.E.; Schreiber, M.E.; Ahmed, K.M.; Alam, M.A.; Bhattacharya, P.; Bundschuh, J.; et al. Arsenic and other geogenic contaminants in global groundwater. *Nat. Rev. Earth Environ.* **2024**, *5*, 312–328. [CrossRef]
22. Abascal, E.; Gómez-Coma, L.; Ortiz, I.; Ortiz, A. Global diagnosis of nitrate pollution in groundwater and review of removal technologies. *Sci. Total Environ.* **2022**, *810*, 152233. [CrossRef]
23. Gandhi, T.P.; Sampath, P.V.; Maliyekkal, S.M. A critical review of uranium contamination in groundwater: Treatment and sludge disposal. *Sci. Total Environ.* **2022**, *825*, 153947. [CrossRef]
24. Wang, Y.X.; Li, J.X.; Ma, T.; Xie, X.J.; Deng, Y.M.; Gan, Y.Q. Genesis of geogenic contaminated groundwater: As, F and I. *Crit. Crit. Rev. Environ. Sci. Technol.* **2020**, *51*, 2895–2933. [CrossRef]
25. Zhao, B.; Sun, Z.X.; Guo, Y.D.; Zhou, Z.K.; Wang, X.G.; Ke, P.C. Occurrence characteristics of uranium mineral-related substances in various environmental media in China: A critical review. *J. Hazard. Mater.* **2023**, *441*, 129856. [CrossRef] [PubMed]
26. Liu, X.; Beusen, A.H.W.; van Grinsven, H.J.M.; Wang, J.J.; van Hoek, W.J.; Ran, X.B.; José, M.; Mogollón, J.M.; Bouwman, A.F. Impact of groundwater nitrogen legacy on water quality. *Nat. Sustain.* **2024**, *7*, 891–900. [CrossRef]
27. Podgorski, J.; Berg, M. Global analysis and prediction of fluoride in groundwater. *Nat. Commun.* **2022**, *13*, 4232. [CrossRef] [PubMed]
28. Podgorski, J.; Berg, M. Global threat of arsenic in groundwater. *Science* **2020**, *368*, 845–850. [CrossRef]
29. Aullón, A.A.; Schulz, C.; Bundschuh, J.; Jacks, G.; Thunvik, R.; Gustafsson, J.P.; Mörth, C.M.; Sraceke, O.; Ahmad, A.; Bhattacharya, P. Hydrogeochemical controls on the mobility of arsenic, fluoride and other geogenic co-contaminants in the shallow aquifers of northeastern LaPampa Province in Argentina. *Sci. Total Environ.* **2020**, *715*, 136671. [CrossRef]
30. Zhou, X.; Sheng, Y.; Zheng, Y.; Jiang, M.Y.; Wang, M.M.; Zhu, Z.H.; Li, G.Y.; Baars, O.; Dong, H.L. Bioavailability of molybdenite to support nitrogen fixation on early Earth by an anoxygenic phototroph. *Earth Planet Sci. Lett.* **2024**, *647*, 119056. [CrossRef]
31. Nghiem, A.A.; Prommer, H.; Mozumder, M.R.H.; Siade, A.; Jamieson, J.; Ahmed, K.M.; van Geen, A.; Bostick, B.C. Sulfate reduction accelerates groundwater arsenic contamination even in aquifers with abundant iron oxides. *Nat. Water* **2023**, *1*, 151–165. [CrossRef] [PubMed]
32. Ning, H.; Jiang, W.J.; Sheng, Y.Z.; Wang, K.L.; Chen, S.M.; Zhang, Z.; Liu, F.T. Comprehensive evaluation of nitrogen contamination in water ecosystems of the Miyun reservoir watershed, northern China: Distribution, source apportionment and risk assessment. *Environ. Geochem. Health* **2024**, *46*, 278. [CrossRef] [PubMed]

33. Vengosh, A.; Coyte, R.M.; Podgorski, J.; Johnson, T.M. A critical review on the occurrence and distribution of the uranium- and tho-rium-decay nuclides and their effect on the quality of groundwater. *Sci. Total Environ.* **2022**, *808*, 151914. [CrossRef]
34. Zainab, S.M.; Junaid, M.; Xu, N.; Malik, R.N. Antibiotics and antibiotic resistant genes (ARGs) in ground Water. A global review on dissemination, sources, interactions, environmental and human health risks. *Water Res.* **2020**, *187*, 116455. [CrossRef] [PubMed]
35. Fernández-Fernández, V.; Ramil, M.; Cela, R.; Rodríguez, I. Occurrence and risk assessment of pesticides and pharmaceuticals in viticulture impacted watersheds from Northwest Spain. *Chemosphere* **2023**, *341*, 140098. [CrossRef]
36. Yun, J.; Yang, Q.; Zhao, C.; Chen, C.Z.; Liu, G.R. Atmospheric emissions of fine particle matter bound rare earth elements from industry. *Nat. Commun.* **2024**, *15*, 9338. [CrossRef]
37. Zhou, J.; Yang, Z.S.; Liu, Q.; Liu, Y.M.; Liu, M.L.; Wang, T.C.; Zhu, L.Y. Insights into Uptake, Translocation, and Transformation Mechanisms of Perfluorophosphinates and Perfluorophosphonates in Wheat (*Triticum aestivum* L.). *Environ. Sci. Technol.* **2020**, *54*, 276–285. [CrossRef]
38. MacLeod, M.; Arp, H.P.H.; Tekman, M.B.; Jahnke, A. The global threat from plastic pollution. *Science* **2021**, *373*, 61–65. [CrossRef]
39. Tang, K.H.D.; Li, R.; Li, Z.; Wang, D. Health risk of human exposure to microplastics: A review. *Environ. Chem. Lett.* **2024**, *22*, 1155–1183. [CrossRef]
40. Grunfeld, D.A.; Gilbert, D.; Hou, J.; Jones, A.M.; Lee, M.J.; Kibbey, T.C.G.; O'Carroll1, D.M. Underestimated burden of per- and polyfluoroalkyl substances in global surface waters and groundwaters. *Nat. Geosci.* **2024**, *17*, 340–346. [CrossRef]
41. Lyu, X.Y.; Xiao, F.; Shen, C.Y.; Chen, J.J.; Park, C.M.; Sun, Y.Y.; Flury, M.; Wang, D.J. Per- and Polyfluoroalkyl Substances (PFAS) in Subsurface Environments: Occurrence, Fate, Transport, and Research Prospect. *Rev. Geophys.* **2022**, *60*, e2021RG000765. [CrossRef]
42. Wang, F.; Xiang, L.; Leung, K.; Elsner, M.; Zhang, Y.; Guo, Y.; Pan, B.; Sun, H.; An, T.; Ying, G.; et al. Emerging contaminants: A One Health perspective. *Innovation* **2024**, *5*, 100612. [CrossRef]
43. Kozlov, M. Landmark study links microplastics to serious health problems. *Nature* **2024**. [CrossRef] [PubMed]
44. Huang, Z.; Yeh, P.J.F.; Jiao, J.J.; Luo, X.; Pan, Y.; Long, Y.; Pan, Y.; Long, Y.N.; Zhang, C.; Zheng, L.Q. A new approach for assessing groundwater recharge by combining GRACE and baseflow with case studies in karst areas of southwest China. *Water Resour. Res.* **2023**, *59*, e2022WR032091. [CrossRef]
45. He, Y.Q.; McDonough, L.K.; Zainab, S.M.; Guo, Z.F.; Chen, C.; Xu, Y.Y. Microplastic accumulation in groundwater: Data-scaled insights and future research. *Water Res.* **2024**, *258*, 121808. [CrossRef]
46. Reichstein, M.; Camps-valls, G.; Stevens, B.; Jung, M.; Denzler, J.; Carvalhais, N.; Prabhat. Deep learning and process understanding for data-driven Earth system science. *Nature* **2019**, *566*, 196–204. [CrossRef]
47. Jiang, W.J.; Meng, L.S.; Liu, F.T.; Sheng, Y.Z.; Chen, S.M.; Yang, J.L.; Mao, H.R.; Zhang, J.; Zhang, Z.; Ning, H. Distribution, source investigation, and risk assessment of topsoil heavy metals in areas with intensive anthropogenic activities using the positive matrix factorization (PMF) model coupled with self-organizing map (SOM). Environ. *Geochem. Health* **2023**, *45*, 6353–6370. [CrossRef] [PubMed]
48. Zang, Y.G.; Hou, X.S.; Li, Z.P.; Li, P.; Sun, Y.; Yu, B.W.; Li, M. Quantify the effects of groundwater level recovery on groundwater nitrate dynamics through a quasi-3D integrated model for the vadose zone-groundwater coupled system. *Water Res.* **2022**, *226*, 119213. [CrossRef]
49. Wei, Y.Q.; Chen, Y.L.; Cao, X.D.; Yeh, T.C.J.; Zhang, J.; Zhan, Z.; Cui, Y.D.; Li, H. Modeling of Microplastics Migration in Soil and Groundwater: Insights into Dispersion and Particle Property Effects. *Environ. Sci. Technol.* **2024**, *58*, 15224–15235. [CrossRef]
50. Pang, M.; Du, E.H.; Zheng, C.M. Contaminant Transport Modeling and Source Attribution with Attention-Based Graph Neural Network. *Water Resour. Res.* **2024**, *60*, e2023WR035278. [CrossRef]
51. Mao, H.R.; Wang, G.C.; Liao, F.; Shi, Z.; Rao, Z.; Zhang, H.Y.; Qiao, Z.Y.; Bai, Y.F.; Chen, X.L.; Yan, X.; et al. Spatiotemporal Variation of Groundwater Nitrate Concentration Controlled by Groundwater Flow in a Large Basin: Evidence From Multi-Isotopes (^{15}N, ^{11}B, ^{18}O, and ^{2}H). *Water Resour. Res.* **2024**, *60*, e2023WR035299. [CrossRef]

Disclaimer/Publisher's Note: The statements, opinions and data contained in all publications are solely those of the individual author(s) and contributor(s) and not of MDPI and/or the editor(s). MDPI and/or the editor(s) disclaim responsibility for any injury to people or property resulting from any ideas, methods, instructions or products referred to in the content.

water

MDPI

Article

Analysis of Runoff Variation Characteristics and Influencing Factors in the Typical Watershed of Miyun Reservoir, China

Sheming Chen [1,2,3], Wanjun Jiang [1,2,3,*], Zhuo Zhang [1,2,3,*], Futian Liu [1,2,3], Jing Zhang [1,2,3] and Hang Ning [1,2,3]

[1] Tianjin Center (North China Center for Geoscience Innovation), China Geological Survey, Tianjin 300170, China; tjdzdczx2013@126.com (S.C.)
[2] Tianjin Key Laboratory of Coast Geological Processes and Environmental Safety, Tianjin 300170, China
[3] Xiong'an Urban Geological Research Center, China Geological Survey, Tianjin 300170, China
* Correspondence: jiangwanjun0718@163.com (W.J.); hydro_zhangzhuo@163.com (Z.Z.)

Abstract: As an important drinking water source for Beijing, the capital of China, the water inflow of Miyun Reservoir has been decreasing year by year, which has affected the urban water supply security. To understand the variation trend of the inflow and analyze the main factors influencing the runoff change, this research focused on the watershed of Miyun Reservoir as the target. Based on the runoff data from 1984 to 2020 at the outlet of the basin, as well as the precipitation, potential evaporation intensity, NDVI (normalized difference vegetation index), population, and GDP (Gross Domestic Product) data, combined with correlation analysis methods, empirical statistical methods, the SCRCQ (Slope Change Ratio of Cumulative Quantity) method, and the GIS, the interannual variation characteristics of various elements in the basin were analyzed, the correlation between runoff and other factors was studied, and the influencing degrees of precipitation, water surface evaporation intensity, human activities, and other factors on the runoff change in the basin were quantitatively separated. The research results showed that the runoff exhibited a distinct decreasing trend, and there were two mutation points in the basin runoff from 1984 to 2020, which were 1995 and 2014, respectively. The runoff change was divided into three stages: 1984–1995 (upward trend in T1), 1995–2014 (downward trend in T2), and 2014–2020 (stable trend in T3). Runoff was significantly correlated with four indicators: the summer leaf area index of the Chaohe River and Baihe River, the regional GDP and population, among which the correlation of the summer leaf area index was the largest. Compared with the period T1, the contribution rates of climate change to the runoff reduction in T2 and T3 were 6.38% and 5.73%, and the contribution rates of human activities to the runoff reduction were 93.62% and 94.27%, respectively. Therefore, the change in annual runoff in the Miyun Reservoir watershed is mainly affected by human activities, and the contribution of climate change to the runoff attenuation is weak. This study is significant in the maintenance and enhancement of runoff in typical watershed.

Keywords: contribution rate; Miyun Reservoir watershed; Pearson correlation analysis; runoff variation characteristics

1. Introduction

Water resources are an important ecological factor in the global ecosystem and a basic condition for human survival. In recent years, under the background of global change and rapid economic development, human demand for water resources has been increasing, resulting in frequent water shortages, water quality pollution, water environment

degradation, and other problems. The sustainable use of water resources has become a key part of the global sustainable development strategy [1–6]. Changes in precipitation and evapotranspiration intensity caused by climate change and changes in land use caused by human activities (mainly manifested as changes in vegetation cover), and excessive development of water resources are the two major factors affecting surface runoff, which have been the focus of researchers at home and abroad for many years [7–10]. As the most important surface water source in Beijing, the capital city of China, Miyun Reservoir is of strategic importance for the water security and sustainable development of the capital city [11]. In recent decades, the amount of water entering the Miyun Reservoir has decreased significantly, at a rate of about 0.3 billion m^3/year from 1956 to 2008, which has a significant impact on realizing the sustainable use of water resources in Beijing [12], and is also known as a risk factor that restricts the future development of the city. In response to similar problems around the globe, scholars have conducted numerous studies using different methods.

Regional climate change, as a recognized influence on runoff, was studied by Berezovskaya et al. [13], Donohue et al. [14], and Milly et al. [15], respectively, in terms of the compatibility of precipitation and runoff trends, the sensitivity of runoff from large watersheds to changes in climatic conditions, and quantifying the impact of hydrological adjustments on the prediction of runoff changes associated with climate change. The results showed that the trend of precipitation and runoff changes in different basins are not consistent. Some other scholars had focused on the use of statistical analysis methods and hydrological models to reveal the interactions among precipitation, land cover, climate change, human activities and hydrological production and sink processes, and to explore the influence of different factors on hydrological processes and runoff volume. Wang et al. [16], Xu et al. [17], and Wu et al. [18] analyzed meteorological runoff data from the Yellow and Yangtze River Basins in China, the Hai River Basin, and the Loess Plateau in China, respectively, to investigate the contribution of long-term changes in seasonal runoff, and attributional analyses based on Budyko's hypothesis to find out the main reasons for the decline of runoff in recent years. Ayalew et al. (2021) sought to understand the pattern change in a watershed in runoff; the hydrological model SWAT was applied to five selected watersheds in Ethiopia to study the hydrological cycle processes and runoff in the watersheds due to rapid population growth and climate change [19].

Although there are more research results on the effects of precipitation changes due to climate change or vegetation changes due to human activities on runoff, the research on the importance and contribution of both to runoff effects started late and did not become a key point of research until the 21st century. In 2014, Ahn et al. [20] quantitatively analyzed the impacts of climate and humans by using historical stream flow records in combination with trend analyses and hydrologic modeling impacts on stream flow conditions in four states in the U.S. In 2014, Huang et al. calculated the relative contributions of human activities and climate change to basin-wide runoff reductions in the Weihe River Basin using the cumulative slope rate of change of accumulation (SCRAQ) methodology [21]. In 2024, Xia et al. quantified the individual contributions of climate change and human activities to these changes by using the example of four major tributaries upstream of the Shiyang River in China as an example to support the sustainable utilization of water resources [22]. The study above proved that an in-depth understanding of the contribution of climate change and human activities to runoff impacts not only helps the government to formulate targeted measures to cope with climate change but also better facilitates the development and effective implementation of sustainable water resource management strategies at regional and local levels, which can reduce the loss of water in the process of the water cycle in river basin ecosystems.

In response to the above mentioned causes of runoff decay and the unique geographical location and strategic importance of Miyun Reservoir, this study focusing on the combined impacts of climate change, including precipitation and water surface evaporation intensity, and human activities, including land use, vegetation cover, and water resource development, is based on the analysis of the interannual evolution pattern of runoff. Additionally, the Pearson correlation analysis method was used to identify the main controlling factors. Based on the cumulative Pearson correlation analysis, the main controlling factors were identified, and, based on the cumulative slope rate of change method, the contribution rate of each influencing factor was quantified. The recommendations and restoration measures for the maintenance and enhancement of runoff in the watershed were finally put forward to provide an important reference, to guarantee the security of regional water supply.

2. Research Data and Methods

2.1. Overview of the Study Area

Miyun Reservoir is located in the northeastern part of Beijing, China, with an area of approximately 188 km^2 and a total storage capacity of about 4.41×10^9 m^3 (Figure 1). It was built in 1960 and is the main surface water source for Beijing. The Miyun Reservoir watershed is located in the transition zone between the North China Plain and the Inner Mongolia Plateau and belongs to the Yanshan Mountains. There are undulating mountains, crisscrossing gullies, and the ground is fragmented by cutting. The watershed area of Miyun Reservoir is 15,788 km^2, including two major tributaries, the Chaohe river and the Baihe river, as well as small tributaries such as the Sheyu river, the Baimaguan river, and the Qingshui river [23]. Among them, the drainage area of the Chaohe river sub-basin is 6277.50 km^2, and that of the Baihe river sub-basin is 9227.50 km^2. The distribution of rainfall is decreasing from the southeast to the northwest, with the annual average precipitation ranging from 300 to 700 mm. The wet season is from June to October, the dry season is from December to April of the following year, and the normal-flow season is in May and November. The precipitation from June to August in the region accounts for about 65–75% of the total annual precipitation. The average annual precipitation in the catchment area is 660 mm. The average daily domestic water consumption per inhabitant within the catchment area ranges from 40 to 60 L.

2.2. Data Sources

This paper collected the conventional surface meteorological data (including rainfall and potential evaporation intensity) from 1984 to 2020 of three national basic meteorological stations (Chicheng Station, Fengning Station, and Miyun Station), which were provided by the National Meteorological Science Data Center (http://data.cma.cn/), accessed on 15 July 2024. The surface runoff data mainly utilized the natural annual runoff data from 1951 to 2020 of the hydrological stations at the basin outlet sections (Zhangjiafen Station and Xiahui Station), and the sum of the two was regarded as the total flow at the basin outlet. The locations of the stations are shown in Table 1. The human activity data mainly took into account the population and GDP data in the basin from 2000 to 2020. The population data were sourced from the raster data shared by the University of Southampton on the WorldPop platform (https://hub.worldpop.org/), with a data accuracy of 1 km, accessed on 20 December 2024.; the GDP data were summarized from the statistical yearbook data of the counties within the basin.

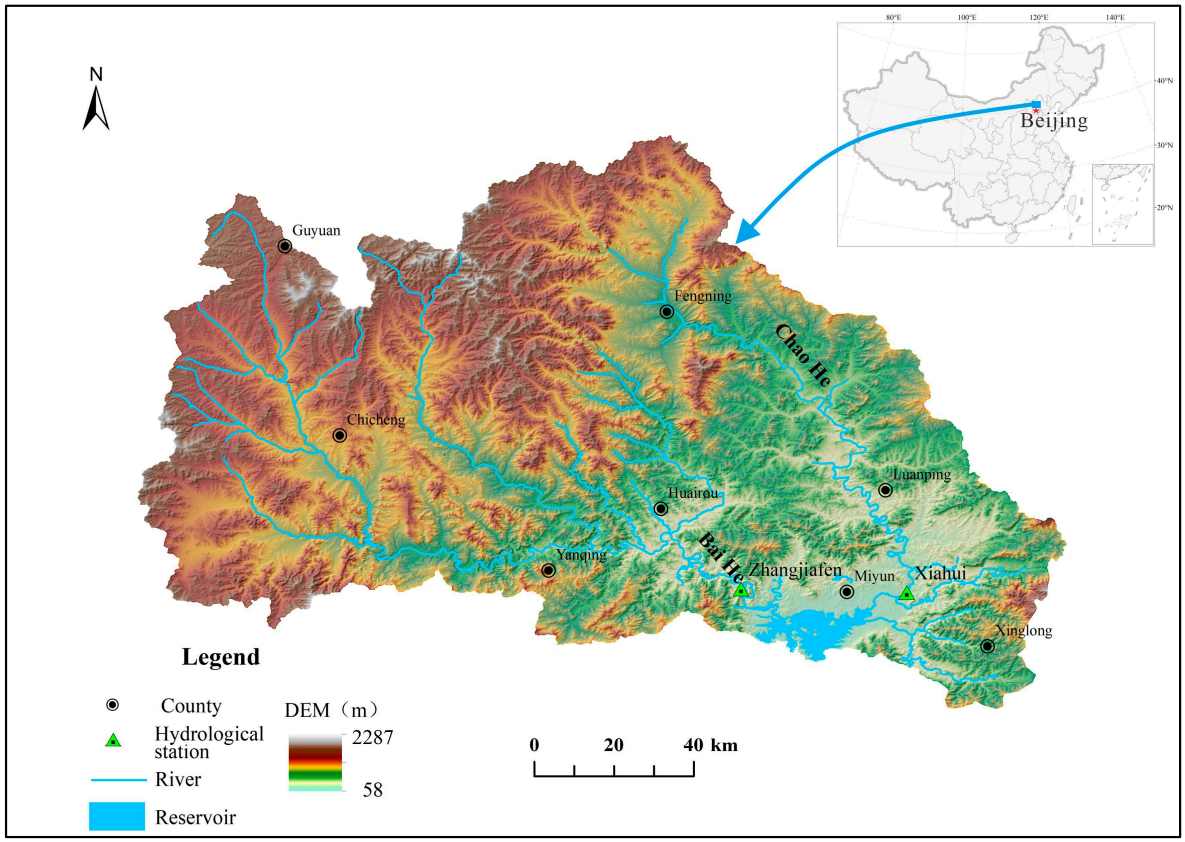

Figure 1. Location map of the Miyun Reservoir watershed.

Table 1. Location of hydrological stations and meteorological stations.

Station Type	Station Name	Administrative Region	Longitude/°	Latitude/°	Elevation/m	Location in the Watershed
Meteorological stations	Chicheng	Chicheng County, Hebei Province	115.083	40.883	868.71	located on the tributary of the Baihe River
	Fengning	Fengning County, Hebei Province	116.633	41.2000	736.30	located on the tributary of the Chaohe River
	Miyun	Miyun District, Beijing City	116.867	40.383	71.82	located downstream of the Miyun Reservoir
Hydrological Stations	Xiahui	Miyun District, Beijing City	117.167	40.617	185.63	located on the tributary of the Chaohe River
	Zhangjiafen	Miyun District, Beijing City	116.783	40.617	179.55	located on the tributary of the Baihe River

2.3. Research Methods

2.3.1. Selection of Influencing Factors

There are numerous factors that affect the runoff in a basin, mainly including the impacts of climatic factors and human activities [21]. In the impacts of human activities, the changes in underlying surface (land use types, planting structures) and the development and use of water resources are mainly taken into consideration.

Climatic Factors

Among the climate indicators, precipitation and potential evaporation intensity are important indicators that affect the runoff in the basin. An increase in precipitation will replenish the water source and increase the runoff generated in the basin. The greater the potential evaporation intensity, the stronger the ability of the atmosphere in the basin to demand water, resulting in a reduction in the runoff converted from rainfall to the basin outlet.

Human Activity Factors

Firstly, the underlying surface conditions affected by human activities influence the runoff generation and concentration processes in the basin. Among the changes in the underlying surface, the adjustment of land use types leads to changes in the vegetation coverage degree, which has the greatest impact on the hydrological process, mainly manifested in aspects such as the impacts on hydrothermal conditions and the water cycle. Vegetation evapotranspiration participates in the redistribution process of precipitation, making each subsequent link affected to a considerable extent, changing the hydrological characteristics and effects, and ultimately changing the water balance and cycle process in the basin. In this study, the normalized difference vegetation index (NDVI), which represents the vegetation coverage degree, was selected to analyze the impact of changes in the underlying surface on the runoff.

Secondly, the development and utilization of water resources in the basin by human activities affect the water balance in the basin and will cause additional water resource losses. On the one hand, in industrial and agricultural production activities, humans need to directly develop and utilize water resources from the basin for production and living. Water intake and utilization projects, due to their direct consumption of water volume, weaken the actual regional water resources to a certain extent. With the increase in population and economic development, the amount of development and utilization will increase year by year, but, with the influence of the scientific and technological level and environmental protection policies, the amount of development and utilization will tend to be stable. On the other hand, human activities have a direct impact on the microclimate, such as the construction of reservoirs and changes in the planting structure, which indirectly affect the runoff in the basin. Since the amount of development and utilization of water resources includes surface water and groundwater, it is difficult to directly count its utilization amount. In this correlation analysis, the indicators of human activities mainly select the population quantity and GDP in the basin.

Finally, human activities such as soil and water conservation management, the construction of water conservancy projects, urbanization construction, and mining and sand extraction in the basin will also have an impact on various aspects such as topography, type of soil, and the areas of lakes and reservoirs, changing the regulation and storage capacity of the basin and then indirectly affecting the runoff. Considering that the influence ranges of the above activities are relatively small and their impacts on the runoff are relatively weak, impact analysis will not be carried out separately during the research process.

2.3.2. Analytical Methods

Pearson Correlation Analysis

In order to study the impacts of different factors on the runoff in the catchment area of Miyun Reservoir, the Pearson correlation analysis method is utilized in this calculation process [24]. Different indicators of three types of influencing factors are selected to conduct a correlation analysis on the influence degrees of climatic factors, changes in the underlying surface, and human activities, interpret the correlation strength between different indicators and the runoff, and analyze the main controlling factors that affect the water conservation capacity. Pearson correlation analysis is a common method for studying the relationship among quantitative data, determining whether there is a relationship and assessing the strength of the relationship. The strength of the correlation relationship is measured by the Pearson correlation coefficient, which is between 1 and -1. The larger the absolute value of the coefficient, the greater the degree of correlation. When $|r|$ is close to 1, it indicates a perfect correlation between the two; when $|r|$ is close to 0, it indicates that

there is no linear correlation between the two (there may also be a nonlinear correlation). The calculation method of the Pearson correlation coefficient is as follows [25–27]:

$$\mathrm{r} = \frac{Cov(X, Y)}{\sigma X * \sigma Y} \tag{1}$$

where $Cov(X, Y)$ represents the covariance of variables X and Y, and σX and σY, respectively, represent the standard deviations of variables X and Y. For two variables X and Y, the calculation formula of the covariance is as follows:

$$Cov(X, Y) = \frac{1}{n-1}\sum_{i=1}^{n}(X_i - \bar{X})(Y_i - \bar{Y}) \tag{2}$$

where $\bar{X}$ and $\bar{Y}$ are the means of X and Y, respectively, and n is the number of samples. By calculating the covariance and standard deviation, the correlation coefficient between the two variables can be obtained.

Cumulative Anomaly Analysis

The cumulative anomaly method is a nonlinear statistical method that can effectively and intuitively reflect the mutation points and change trends of discrete data in long time series. It is widely used in hydrological studies such as the analysis of precipitation and runoff change trends [28]. For a hydrological sequence, the cumulative anomaly value at a certain time point t can be expressed as follows:

$$\check{X} = \sum_{i=1}^{t}(X_i - \bar{X}),\ t = 1, 2, 3 \ldots n \tag{3}$$

where $\bar{X}$ represents the average value of the discrete data in the hydrological time series. The main basis for this method to judge the mutation points of data is to judge the relationship between the discrete data and its average value. If the cumulative anomaly value at a certain moment is positive, it indicates that the discrete data at this time are greater than its average value, and vice versa. If the cumulative anomaly shows significant increasing and decreasing trends before and after a certain time point, then the time point corresponding to the cumulative anomaly value at this time is the mutation point of the hydrological sequence, also known as the inflection point. Taking the inflection point year as the boundary, the periods before and after the change in runoff can be obtained, and the periods before and after the mutation year can be divided into the reference period and the verification period, laying a foundation for the quantitative analysis of the contribution rates of other factors such as precipitation and evapotranspiration to the impact on runoff.

Contribution Rate Analysis

On the basis of using the cumulative anomaly method to a conduct trend analysis on runoff and test the mutation years, the changes in the basin runoff were divided into multiple different periods according to the mutation years. Taking the first period as the reference period and the subsequent periods as the verification period, the Slope Change Ratio of Cumulative Quantity Comparison Method (SCRCQ) [29] was used to obtain the relationship equations among the cumulative precipitation, cumulative runoff, and cumulative potential evaporation intensity and the years in each period. The principle of the Slope Change Ratio of Cumulative Quantity Comparison Method is as follows: According to the water balance equation of the entire basin $P = R + ET + \Delta W$, where P is the multi-year average precipitation in the basin, R is the multi-year average river runoff in the basin, ET is the multi-year average evapotranspiration in the basin, and ΔW is the change

in the water storage volume in the basin. For a closed basin, the sum of the changes in the annual water storage volume in the basin is approximately 0 under a long time series. The actual evaporation in the basin is mainly composed of the evaporation of surface water bodies, soil evaporation, and plant transpiration, which can be characterized by the water surface evapotranspiration intensity index. In this study, the sum of the impacts of factors such as precipitation, evaporation intensity, and human activities (changes in vegetation coverage and the development and utilization of water resources) on runoff is regarded as 100%. The influence degree of each influencing factor on runoff can be expressed as the ratio of the slope change rate of the relationship curve between its cumulative quantity and the year to the slope change rate of the cumulative runoff. Based on the precipitation and potential evaporation intensity, the contribution rates of them to the basin runoff can be obtained, and the remaining contribution rate is the contribution rate of human activities to the runoff change, thus quantitatively separating the influence degrees of various factors on runoff.

Suppose the slopes of the linear relationship between the cumulative runoff and the year in the reference period (A) and the verification period (B) are K_{RA} and K_{RB}, respectively; then, the expression of the slope change rate of the cumulative precipitation (ΔK_R) is as follows:

$$\Delta K_R = 100\% \times \frac{K_{RB} - K_{RA}}{K_{RA}} \tag{4}$$

Similarly, the slope change rate expressions of the cumulative quantities of precipitation (ΔK_P) and potential evaporation intensity (ΔK_{ET}) are, respectively, and the slope change rate expressions are as follows:

$$\Delta K_P = 100\% \times \frac{K_{PB} - K_{PA}}{K_{PA}} \tag{5}$$

$$\Delta K_{ET} = -100\% \times \frac{K_{ETB} - K_{ETA}}{K_{ETA}} \tag{6}$$

Therefore, the contribution rates of precipitation (C_P) and potential evaporation intensity (C_{ET}) to the change in runoff are calculated by the following formulas, and the sum of them represents the contribution rate of climate change:

$$C_P = 100\% \times \frac{\Delta K_p}{\Delta K_R} \tag{7}$$

$$C_{ET} = 100\% \times \frac{\Delta K_{ET}}{\Delta K_R} \tag{8}$$

Therefore, the contribution rate of human activities (changes in vegetation coverage and the development and utilization of water resources) to the impact on runoff C_v is as follows:

$$C_\mathrm{v} = 100 - C_P - C_{ET} \tag{9}$$

3. Results

3.1. Variation Characteristics of Runoff

The monthly average flow of the runoff in the catchment area of Miyun Reservoir from 1951 to 2020 is shown in Table 2. The seasonal differences in runoff are obvious, and the intra-annual distribution of runoff is relatively uneven. The wet season is from July to September, during which the runoff accounts for 60.94% of the total annual runoff; the runoff in other months does not differ much. The runoff in January is the smallest, with 26.10×10^6 m^3, accounting for 3.01% of the annual runoff. The trend of runoff changes

from 1951 to 2020, as shown in Figure 2. The interannual variation in runoff in this region is relatively large, with the runoff varying between 185 and 3740 $\times$ 10^6 m^3. The maximum value appeared in 1956, which was 3740 $\times$ 10^6 m^3, and the minimum value appeared in 2000, which was 185 $\times$ 10^6 m^3. The multi-year average runoff is 1026.70 $\times$ 10^6 m^3. Among them, the fluctuations were the most obvious from 1973 to 1984. Judging from the trend line, the runoff generally showed a significant downward trend, with a linear reduction rate of 22.70 $\times$ 10^6 m^3/a. Especially after 1999, the runoff showed a continuous downward trend. According to the 5-year moving average curve, it can be found that the runoff showed a fluctuating downward trend. The runoff showed an increasing trend from 1951 to 1959, 1973 to 1977, 1984 to 1998, and 2003 to 2020, while it showed a decreasing trend from 1960 to 1972, 1978 to 1983, and 1999 to 2002.

Table 2. Monthly average runoff in watershed of Miyun reservoir from 1951 to 2020.

Month	Average Runoff/10^6 m^3	Percentage/%	Month	Average Runoff/10^6 m^3	Percentage/%
1	26.10	3	7	184.30	21
2	28.00	3	8	243.40	28
3	40.80	5	9	102.50	18
4	33.50	4	10	64.90	7
5	27.10	3	11	44.20	5
6	46.10	5	12	29.20	3

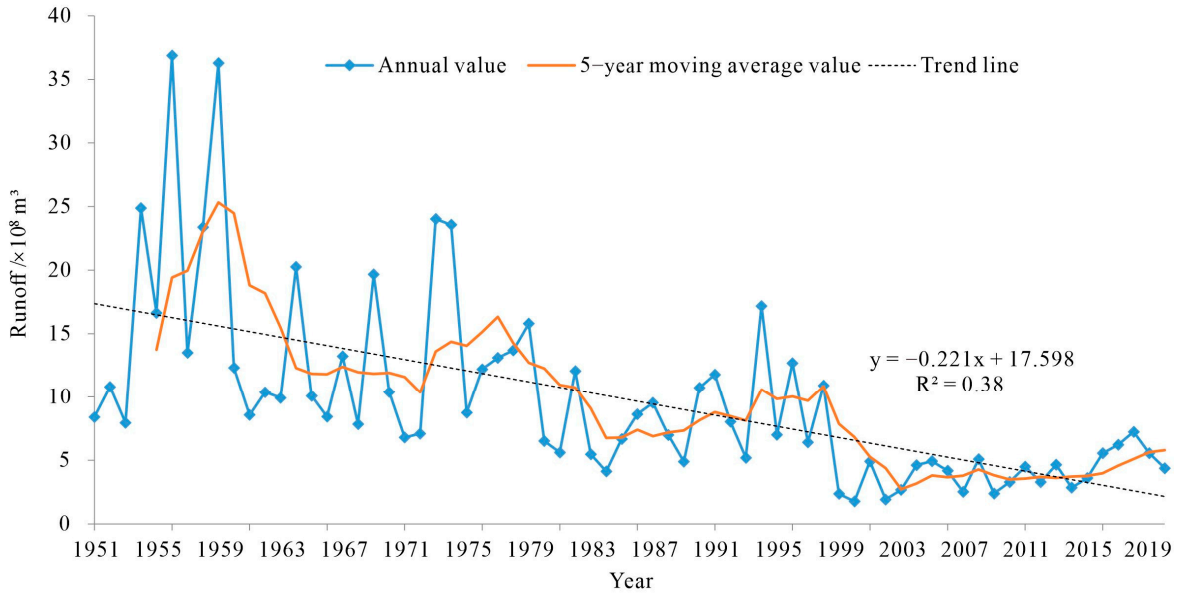

Figure 2. Variation curves of annual runoff during 1951–2020 in watershed of Miyun reservoir.

The cumulative anomaly method was used to determine the mutation years of the runoff. The cumulative anomaly curves of the runoff are shown in Figure 3. From 1951 to 1959, the interannual changes in the runoff were relatively significant, all showing a rapid upward trend. From 1959 to 1979, the interannual changes showed a slow fluctuating upward trend. A mutation point appeared in 1979, and the cumulative anomaly value gradually decreased in the later period. From 1979 to 1998, it showed a slow downward trend, and the downward trend intensified after 1998. To ensure the consistency of the data, the time period selected for the contribution rate analysis in this study is from 1984 to 2020. According to the cumulative anomaly curve, the mutation points are 1995 and 2013. The research period is divided into three stages: 1984–1995 (T1), 1995–2014 (T2), and 2014–2020 (T3). In the T1 period, the runoff showed an upward trend, and no obvious attenuation of the runoff occurred, so it can be used as the reference period. While the runoff in the T2 period showed a downward trend, and the runoff in the T3 period showed a stable trend, and both can be used as the change periods for analysis.

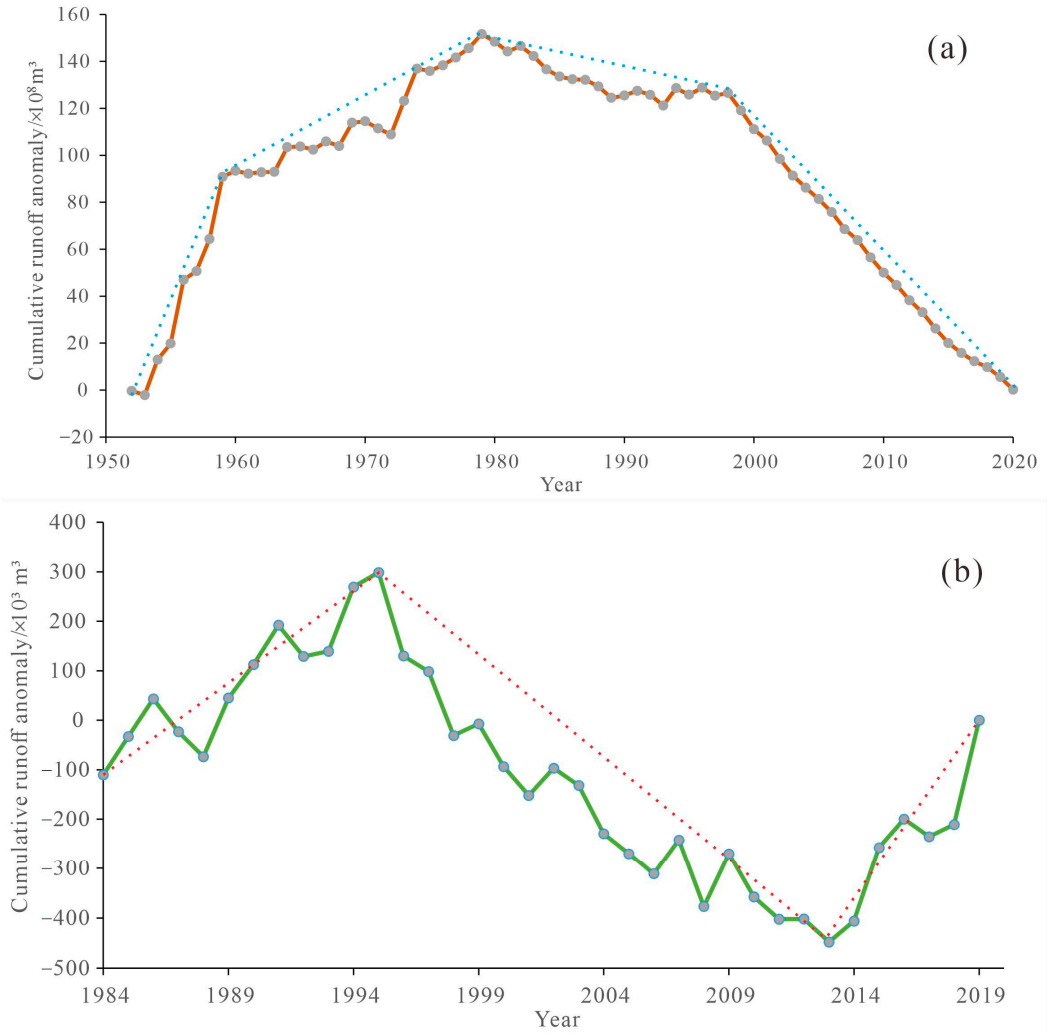

Figure 3. Cumulative runoff anomaly in 1951–2020 (**a**) and 1984–2020 (**b**).

3.2. Variation Characteristics of the Influencing Factors of Runoff

3.2.1. Precipitation and Evaporation

For the climatic factors in the catchment area of Miyun Reservoir, precipitation and evaporation intensity indicators are selected. Based on the analysis of the variation characteristics of precipitation from 1984 to 2020 (Figure 4), the precipitation in the Baihe river sub-basin varies from 260 to 640 mm, and the precipitation in the Chaohe river sub-basin ranges from 288 to 696 mm. The interannual variation in precipitation is relatively large, and the ratio of the maximum value to the minimum value reaches 2.4. The multi-year average precipitation in the two regions is 431 mm and 463 mm, respectively, and their fluctuation characteristics are basically the same. Through trend analysis, the rainfall in both basins showed an apparent increasing trend from 1984 to 2020, with an annual growth rate of 1.2 mm in the Baihe river sub-basin and 1.4 mm in the Chaohe river sub-basin.

The potential evaporation intensity data come from the data of Chicheng County Station on the Meteorological Data Sharing Network. The multi-year average value of the potential evaporation intensity in the catchment area is 1877.3 mm, the maximum value is 2421.5 mm, and the minimum value is 1442.4 mm. The potential evaporation intensity generally shows an increasing trend, with an average annual growth rate of 20.7 mm.

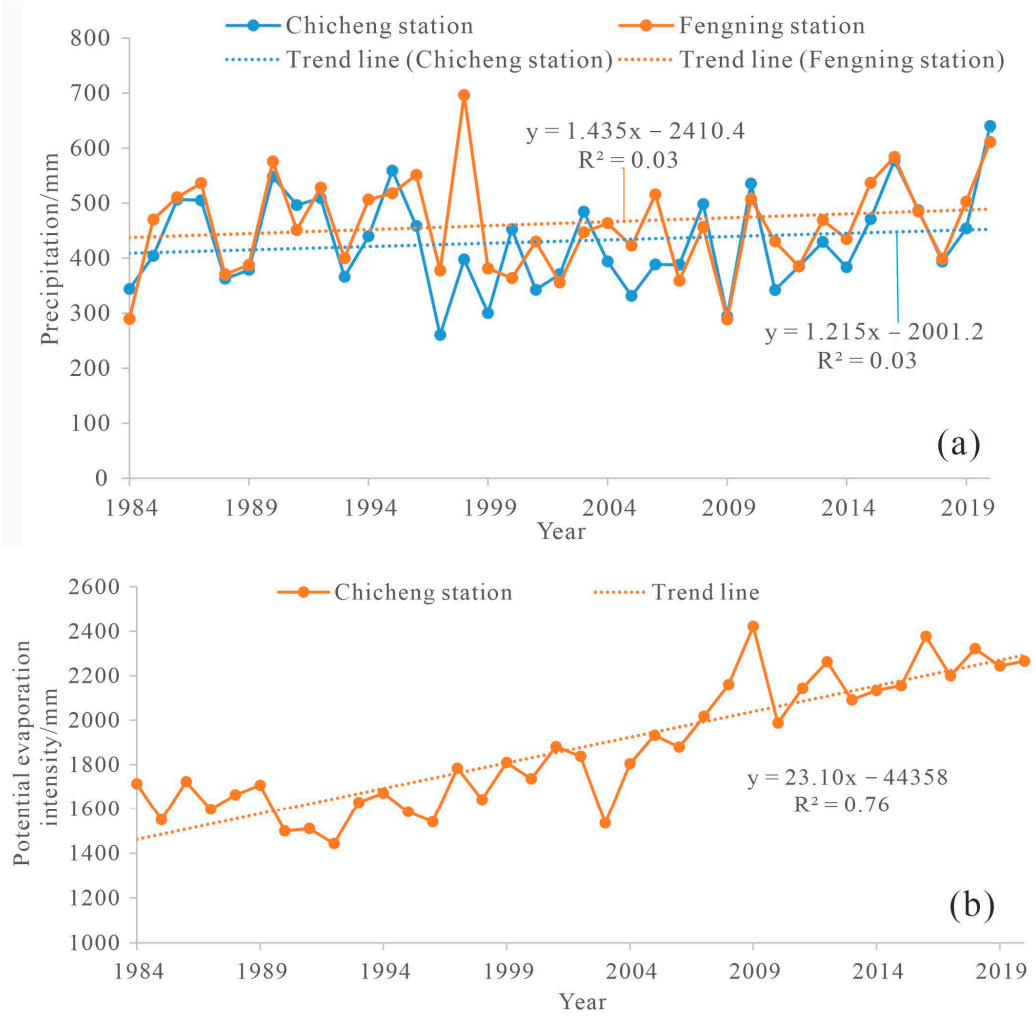

Figure 4. Annual precipitation (**a**) and potential evaporation intensity (**b**) during 1984–2020.

3.2.2. Changes in Land Use Types

Changes in land use patterns have the greatest impact on the water conservation capacity. This study conducted statistics on the changes in land use types from 1980 to 2020 (Figure 5 and Table 3). In the catchment area of Miyun Reservoir, the areas of forest land and construction land have increased, while the areas of cultivated land and grassland have decreased. Among them, from 1980 to 2020, the forest land area increased by 109.41 km^2, accounting for 1.45% of the total forest land area, and the construction land area increased by 179.62 km^2, which increased by 2.35 times. The sharp increase in the area of construction land reflects the expansion of the scale of human activities. The cultivated land area decreased by 130.72 km^2, accounting for 4.13% of the total cultivated land area. The bare land area decreased by 6.68 km^2, accounting for 28.96% of the total bare land area. The direct remote sensing area cannot fully represent the development degree and change status of the surface vegetation on the underlying surface, and it needs to be determined in combination with the degree of vegetation development.

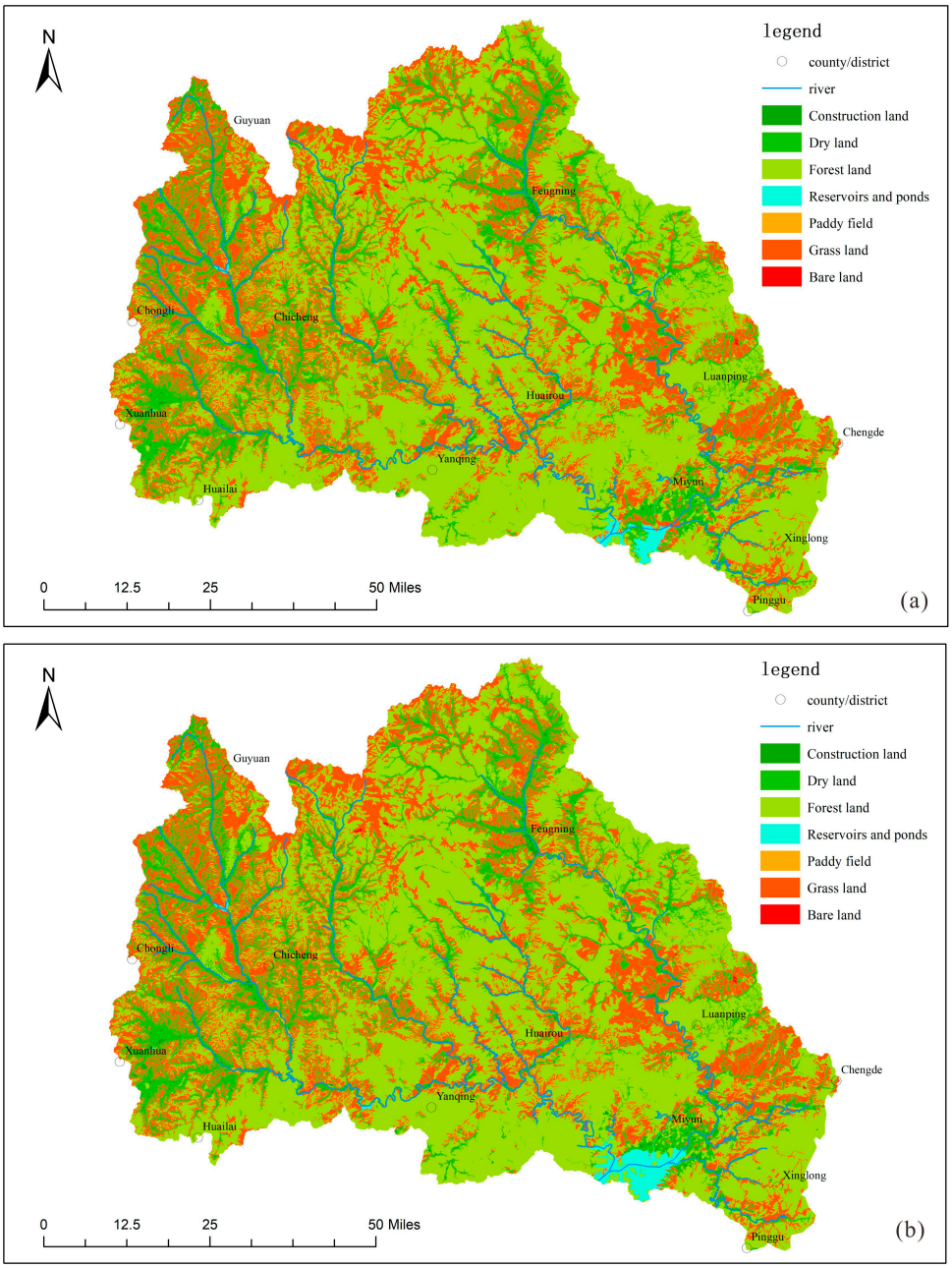

Figure 5. Land use type maps of the watershed Miyun reservoir in 1980 (**a**) and 2020 (**b**).

Table 3. Statistical table on the area changes in land use types from 1980 to 2020.

Land Type		In 1980		In 2020	
		Area (km^2)	Percentage (%)	Area (km^2)	Percentage (%)
Cultivated land	Paddy field	3168.66	21.0	3037.94 ↓	20.1 ↓
	Dry land	24.59 3144.07	0.2 20.8	59.56 ↑ 2978.38 ↓	0.4 ↑ 19.7 ↓
Forest land		7521.08	49.9	7630.49 ↑	50.6 ↑
Grass land		4050.09	26.9	3886 ↓	25.8 ↓
Reservoirs and ponds		245.38	1.6	257.84 ↑	1.7 ↑
Construction land		76.23	0.5	255.85 ↑	1.7 ↑
Bare land		23.07	0.2	16.39 ↓	0.1 ↓
Total		15,084.51	100.0	15,084.51	100.0

3.2.3. Normalized Difference Vegetation Index (NDVI)

Considering that the development and structure of the underlying surface vegetation have an impact on the water conservation capacity, the NDVI is selected in this study to represent the changes in the underlying surface. In this work, the monthly NDVI data of the catchment area of Miyun Reservoir from 2000 to 2020 were collected, with a spatial resolution of 250 m. According to the spatial range of the research area, the corresponding grid unit monthly NDVI data were extracted, the average NDVI values in summer and winter in the Chaohe river and Baihe river basins were obtained (Figure 6). According to the monthly data analysis of the NDVI, the value in the catchment area fluctuated and increased in summer (August), with an average value of 0.72 and an average annual growth of 0.51×10^{-2}. During the period from 2000 to 2020, in summer, the average NDVI values in the Baihe River rose from 0.65 to 0.77, while those in the Chaohe River increased from 0.61 to 0.78; the NDVI also fluctuated and increased in winter (February), with an average value of 0.22 and an average annual growth of 0.24×10^{-2}. During the period from 2000 to 2020, in winter, the average NDVI values in the Baihe River rose from 0.20 to 0.25, while those in the Chaohe River increased from 0.19 to 0.23; the increase in the NDVI reflects the continuous improvement of the vegetation conditions in the catchment area.

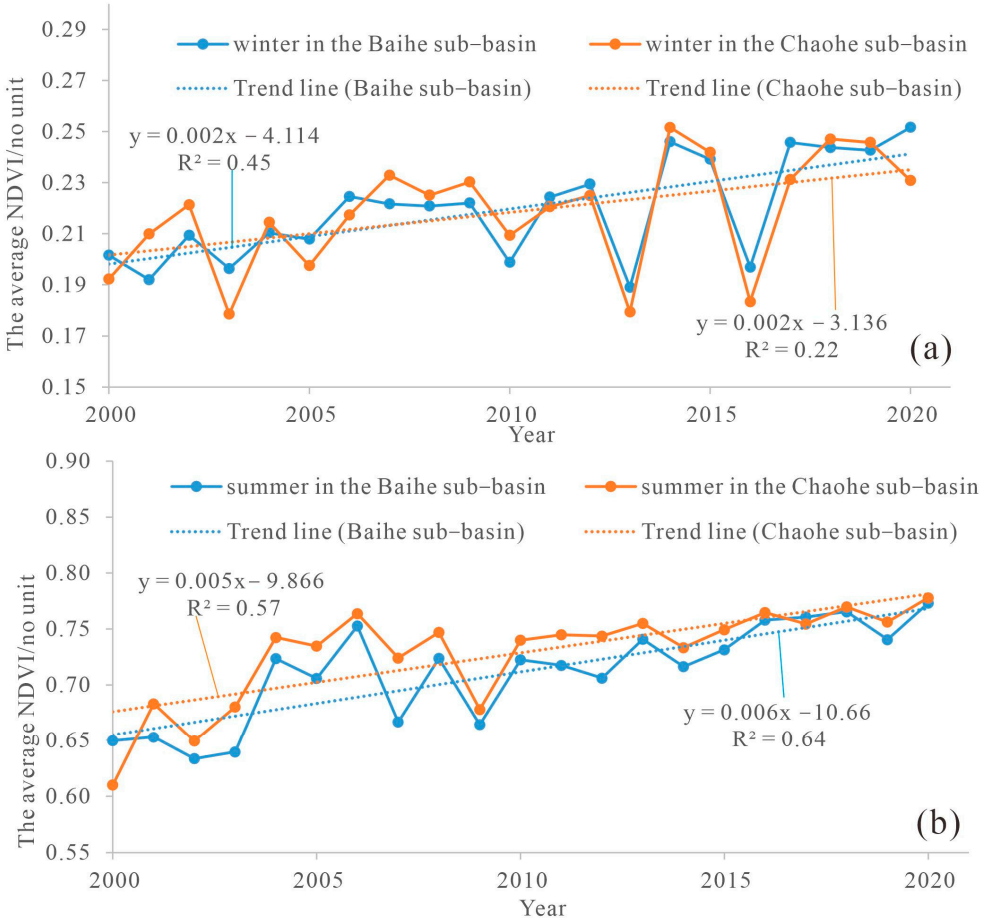

Figure 6. Diagram of variation in average NDVI in different seasons during 2000–2020 in sub-watershed of Miyun reservoir in (**a**) winter and (**b**) summer.

3.2.4. Population and GDP

The data of human activities mainly consider the impact of population and the GDP on the water conservation capacity. The population in the catchment area of Miyun reservoir is counted using raster data. Judging from the raster density, the population in the area is mainly concentrated in Chicheng, Fengning county towns, and major townships. The

overall population quantity shows a continuous growth trend, and the average annual growth is 7500 people calculated according to the trend line (Figure 7a). Correspondingly, the GDP also shows an annual growth trend, with an average annual growth amount of CNY 68.9 billion (Figure 7b). The ongoing growth of the population remains a pivotal influencing factor for the aforementioned changes in land-use types. In a reciprocal relationship, land-use change serves as a critically important determinant of global change. It modifies the exchange of energy and materials between the terrestrial surface and the atmosphere, thereby bringing about alterations to the global climate.

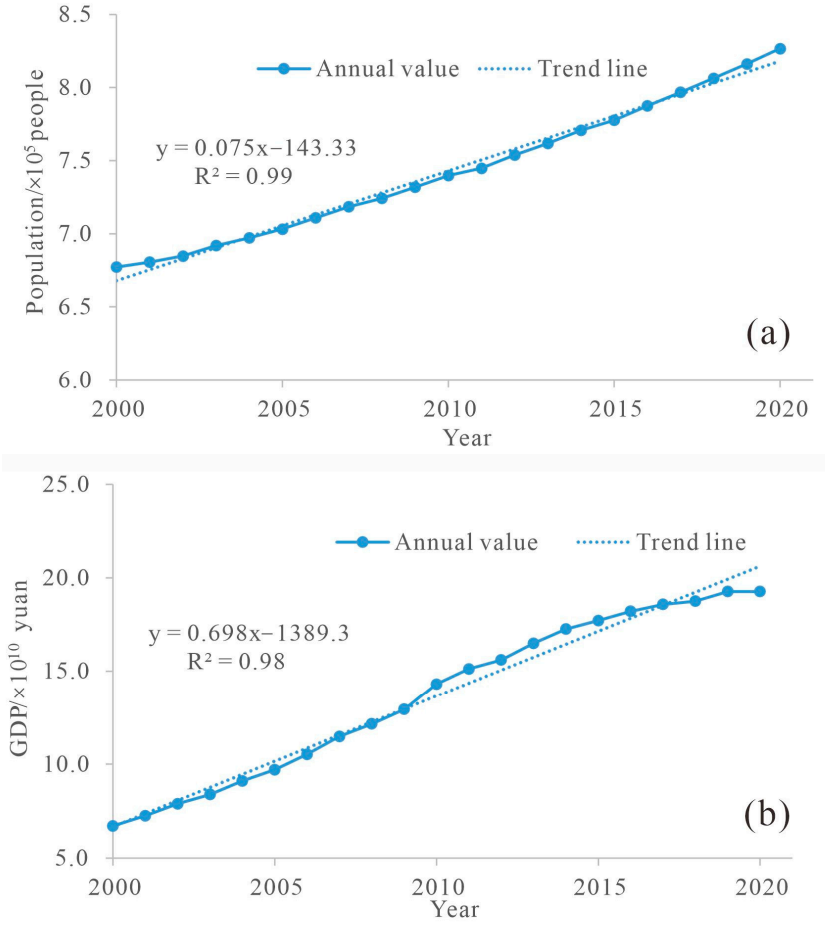

Figure 7. Annual population (**a**) and GDP (**b**) during 2000–2020.

3.3. Correlations Between Runoff and Various Variables

Based on the correlation analysis between the runoff in the catchment area and population, GDP, potential evaporation intensity, precipitation, the summer NDVI of the Baihe and Chaohe rivers from 2000 to 2020, the four indicators of the summer NDVI of the Baihe river and the Chaohe river, regional GDP, and population are significantly correlated with the runoff (Table 4). Among them, the correlation between the summer NDVI of the Baihe river and the runoff is the best, reaching 0.71, followed by the summer NDVI of the Chaohe river, reaching 0.68, and, finally, between the population and GDP, with the correlation coefficients being 0.50 and 0.48, which are significantly correlated at the 0.05 level. The above analysis results show that the change in the runoff in the catchment area is most affected by the NDVI, which is the degree of vegetation development. The natural runoff is highly sensitive to vegetation changes. Furthermore, it also indicates that the continuous increase in the normalized difference vegetation index from 2000 to 2020, and the changes in the underlying surface characterized by vegetation changes play a dominant role in the attenuation of the natural runoff in the catchment area of Miyun Reservoir. Secondly, the

continuous strengthening of human activities (reflected in the continuous increase in GDP and population) and the increase in water consumption also play a secondary role in the attenuation of the natural runoff in the catchment area.

Table 4. Calculation results of Pearson correlation coefficients.

Influencing Indicators		Population	GDP	Potential Evaporation Intensity	Runoff	Precipitation	NDVI in Summer of the Baihe River Sub-Basin	NDVI in Summer of the Chaohe River Sub-Basin
Runoff	Pearson Correlation	0.50 *	0.48 *	0.38	1	0.19	0.71 **	0.68 **
	Significance (Two-tailed)	0.02	0.03	0.09	-	0.40	0.00	0.00
	Number of Cases	21	21	21	21	21	21	21

Note: **. Significantly correlated at the 0.01 level (two-tailed). *. Significantly correlated at the 0.05 level (two-tailed).

3.4. Contribution Rates of Climatic Factors and Human Activities to Runoff

According to the mutation test results of the cumulative anomaly method, linear equations among runoff, precipitation, and potential evaporation intensity and years in T1 (1984–1995), T2 (1995–2014), and T3 (2014–2020) are established, respectively, and the corresponding regression curves are obtained. Their determination coefficients are all greater than 0.99 (Figure 8).

It can be seen from Tables 5 and 6 that, compared with the T1 period, the slope of the linear equation between the cumulative runoff and the year in the T2 period decreased by 529.30 million m^3 per year, with a reduction rate of 58.81%. In the same period comparison, the slope of the linear equation between the cumulative precipitation and the year decreased by 54.7 mm per year, a 11.70% decrease compared with the T1 period. The slope of the linear equation between the cumulative potential evaporation intensity and the year decreased by 249.5 mm per year, a 15.50% decrease compared with the T1 period. Obviously, the change rate of precipitation is less than that of runoff, and the decrease in potential evaporation intensity is conducive to the increase in runoff. There must be other factors that cause the runoff to decrease, that is, the impact of vegetation changes and water resource development and utilization caused by human activities. According to the cumulative slope method formula, compared with the T1 period, the contribution rate of precipitation change to the decrease in runoff in the T2 period is 19.96%, and the contribution rate of water surface evapotranspiration intensity to the decrease in runoff is −26.34%. Compared with the T1 period, the contribution rate of human activities to the increase in runoff depth in the T2 period is 93.62%. It can be seen that, compared with the T1 stage, after the increase in the vegetation coverage and the improvement in the amount of water resource development and utilization in the catchment area in the T2 period, the runoff in the basin is reduced by affecting the water resource change processes such as evapotranspiration, interception, and infiltration. Compared with the T1 period, the slope of the linear equation between the cumulative runoff and the year in the T2 period decreased by 304.00 million m^3 per year, a decrease of 33.76%. In the same period comparison, the slope of the linear equation between the cumulative precipitation and the year increased by 28.1 mm per year, a 6.03% increase compared with the T1 period. The slope of the linear equation between the cumulative potential evaporation intensity and the year increased by 66.0 mm per year, a 4.09% increase compared with the T1 period. Therefore, the contribution rate of precipitation to the decrease in runoff is −17.87%. The contribution rate of water surface evapotranspiration intensity to the decrease in runoff is 12.14%, and the contribution rate of human activities to the decrease in runoff is 94.27%.

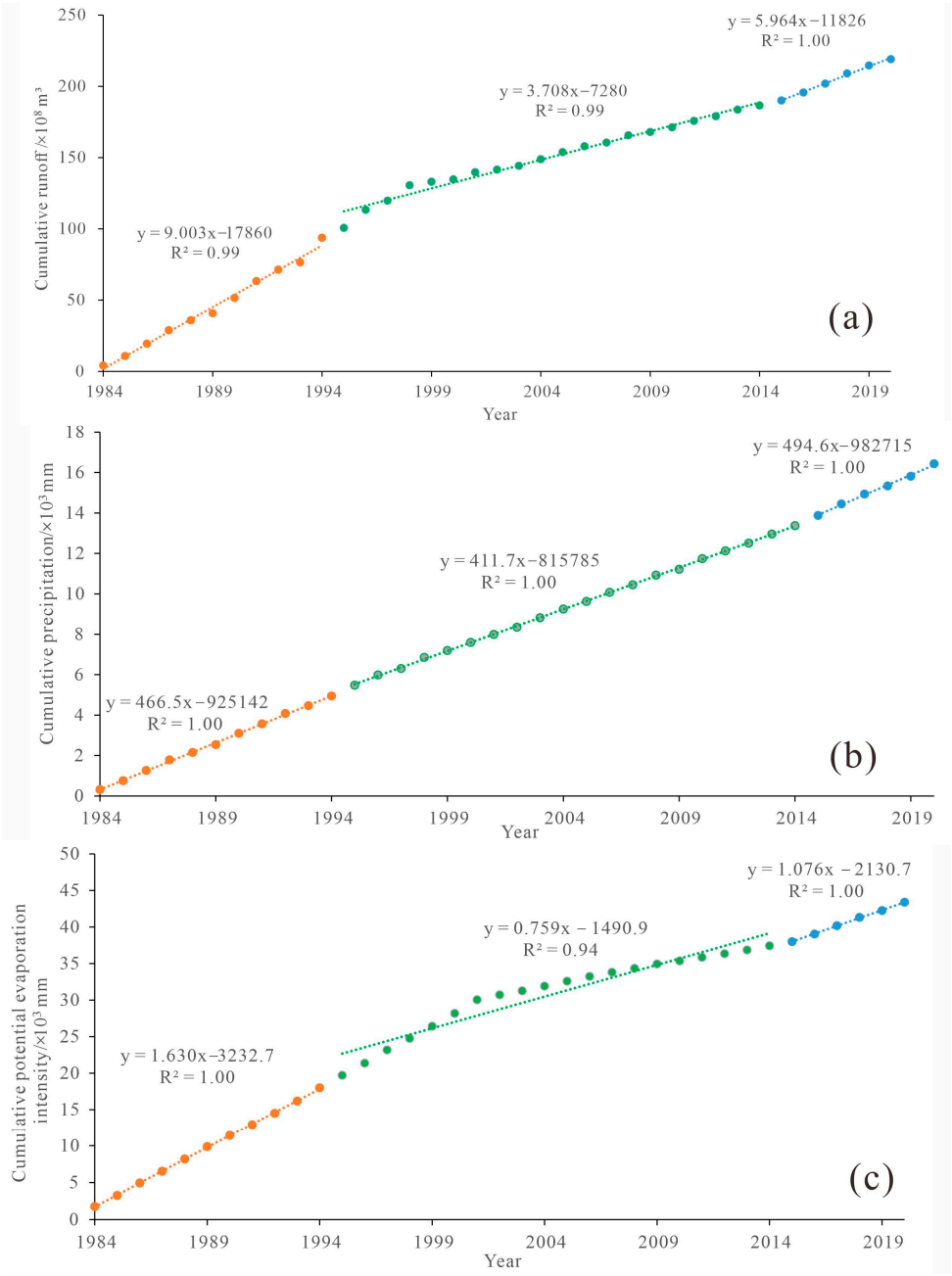

Figure 8. Relationships between year and cumulative runoff (**a**), precipitation (**b**), and potential evaporation intensity (**c**).

Table 5. Slope change ratios of annual cumulative quantities during three periods.

Period	S_R/10^8 $m^3 \cdot a^{-1}$	Change Rate/%	S_P/mm·a^{-1}	Change Rate/%	S_{ET}/mm·a^{-1}	Change Rate/%
T1	9.00	--	466.5	--	1610.3	--
T2:T1	3.71	−58.81	411.7	−11.74	1360.8	−15.49
T3:T1	5.96	−33.76	494.6	6.03	1676.3	4.10

Note: S_R, S_P, and S_{ET} are the slopes of the relational expressions between the cumulative amounts of runoff, precipitation, potential evaporation intensity, and the year, respectively.

Table 6. Contribution rates of all factors on annual runoff in watershed of Miyun reservoir.

Period	C_P/%	C_{ET}/%	(C_P + C_{ET})/%	C_V/%
T2:T1	19.96	−26.34	−6.38	−93.62
T3:T1	−17.87	12.14	−5.73	−94.27

Note: C_P + C_{ET} represents the contribution rate of climatic factors to runoff, and C_V represents the contribution rate of human activities to runoff. A negative value of the contribution rate indicates a reduction in runoff, while a positive value indicates an increase in runoff.

4. Discussion

4.1. Impact of Climatic Factors on the Change in Runoff

Precipitation, as a direct source of water resources in the basin among climatic factors, has a direct impact on the runoff during its changing process [30]. Analyzing the mutation years determined by the cumulative anomaly curves of precipitation and runoff (Figures 3b and 9), the mutation point where precipitation changes from increasing to decreasing is in 1995, and the mutation point where it changes from decreasing to increasing is in 2013, which are relatively close to the mutation points of runoff in 1998 and 2015, and the relevant change trends are basically the same. Analyzing from the dynamic characteristics within the year, the rainfall from June to September in the wet season accounts for 64% of the annual rainfall, which is consistent with the proportion of runoff in the same months. Analyzing from the contribution rate, the contribution rates of precipitation to the change in runoff in the T1:T2 period and the T2:T3 period are both positive, being 19.96% and 33.11%, respectively. The increase and decrease trends of precipitation are consistent with those of runoff, and the contribution degree increases. From the results of the Pearson correlation analysis, it can be found that the correlation between precipitation and runoff in the interannual variation sequence from 2000 to 2020 is not strong. The above analysis indicates that the interannual abundance and scarcity changes in precipitation have an obvious impact on the runoff, but the contribution rate to the runoff attenuation problem shown in the basin over the years is relatively small, with an average contribution degree of 11.73%.

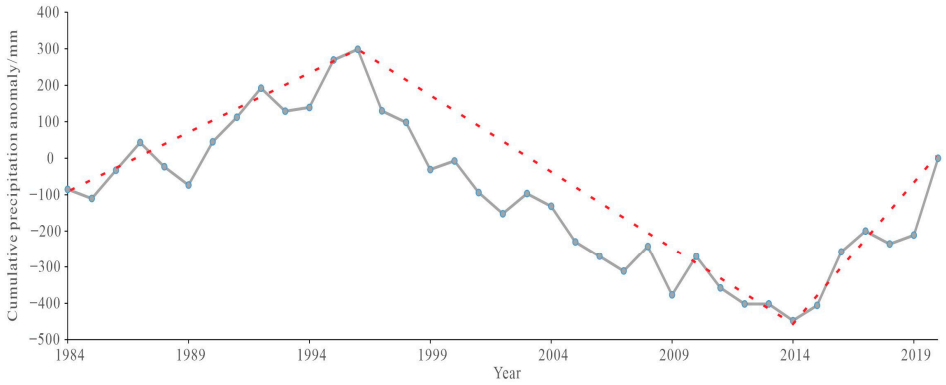

Figure 9. Cumulative precipitation anomaly in 1984–2020 in watershed of Miyun reservoir.

The potential evaporation intensity is controlled by local meteorological conditions such as temperature, wind, and humidity, and it is an important indicator of evaporation capacity. The greater the potential evaporation intensity, the smaller the runoff formed by rainfall under the same conditions. The catchment area of Miyun Reservoir belongs to a semi-humid and semi-arid region, and the potential evaporation intensity is relatively large. Judging from the Pearson correlation analysis between the potential evaporation intensity and the runoff, the correlation coefficient is 0.38, indicating a certain correlation. In the contribution rate analysis, the average contribution rate of the potential evaporation intensity to the runoff is −7.10, indicating that the increase or decrease in the potential evaporation intensity has not caused the runoff to decrease or increase. The above analysis shows that the interannual change in the potential evaporation intensity has a relatively small impact on the runoff.

4.2. Impact of Human Activities on the Change in Runoff

According to the research results mentioned above, the impact of human activities on the runoff is mainly manifested in two aspects. On the one hand, human activities

change the underlying surface conditions of the basin, including the change in vegetation coverage caused by the change in land use types. On the other hand, there is the change in the amount of water resource development and utilization caused by economic and social development and population increase. According to the Pearson correlation analysis, the summer NDVI, GDP, and population quantity in the sub-basins of the Chaohe river and Baihe river are significantly correlated with the runoff. The change in the underlying surface characterized by vegetation change plays a dominant role in the change in the natural runoff in the catchment area of Miyun Reservoir. Secondly, economic and social development and a population increase lead to an increase in water consumption, an increase in the loss of water resources in the basin, and a change in the runoff. In the contribution rate analysis, the contribution rate of human activities is more than 90%, and, with the passage of time, the contribution rate gradually increases.

5. Conclusions

(1) The seasonal differences in the runoff in the catchment area of Miyun Reservoir are obvious, and the intra-annual distribution of the runoff is uneven. The wet season is from July to September, during which the runoff accounts for 60.94% of the total annual runoff. The interannual variation range of the runoff is relatively large, ranging from 185 million to 3740 million m^3 per year. Judging from the trend line, the runoff generally shows a significant decreasing trend, with a linear reduction rate of 22.70 million m^3 per year. Especially after 1999, the runoff shows a continuous downward trend. According to the cumulative anomaly curve of the runoff, there are two mutation points in the runoff from 1984 to 2020, which are 1995 and 2014, respectively. The change in the runoff can be divided into three stages: 1984–1995 (T1), 1995–2014 (T2), and 2014–2020 (T3). In the T1 period, the runoff shows an upward trend, in the T2 period, the runoff shows a downward trend, and, in the T3 period, the runoff tends to be stable.

(2) Through the Pearson correlation analysis, it is found that the runoff in the catchment area is significantly correlated with the summer NDVI of the Chaohe river and Baihe river in the sub-basin, regional GDP, and population quantity, among which the correlation with the summer NDVI is the strongest. The analysis results show that the watershed runoff is highly sensitive to vegetation changes. The continuous increase in the NDVI from 2000 to 2020 has strengthened the interception of rainfall by the underlying surface and the effect of vegetation evapotranspiration, thus affecting the natural runoff in the catchment area of Miyun Reservoir. Secondly, the continuous strengthening of human activities (reflected in the continuous increase in GDP and population) also leads to an increase in water consumption and plays a secondary role in the attenuation of the natural runoff in the catchment area.

(3) When quantitatively analyzing the contribution rates of various factors to the impact on runoff, the research period is divided into the reference period T1 (1984–1995), which is mainly affected by climate change, and the change periods T2 (1995–2014) and T3 (2014–2020), which are affected by climate change and human activities. Based on the modified Slope Change Ratio of Cumulative Quantity Comparison Method, the contribution rates of various factors in the change periods are quantitatively analyzed. Compared with the reference period, the contribution rates of climate change to the reduction in runoff in the T2 and T3 periods are 6.38% and 5.73%, respectively, and the contribution rates of human activities (vegetation change, water resource development and utilization) to the reduction in runoff are 93.62% and 94.27%, respectively. The analysis results show that, in recent years, the change in the annual runoff in the catchment area of Miyun Reservoir is mainly affected by human activities, and the contribution of climate change to the attenuation of the runoff is relatively weak. Therefore, in the process of maintaining and increasing

the runoff of Miyun Reservoir, it is necessary to focus on carrying out comprehensive treatment projects from aspects such as adjusting vegetation types, reducing excessive water consumption by humans, and increasing groundwater regulation and storage.

Author Contributions: Data curation, J.Z.; investigation, F.L.; validation, Z.Z.; visualization, H.N.; writing—original draft, S.C.; writing—review and editing, W.J. All authors have read and agreed to the published version of the manuscript.

Funding: This study was funded by the National Natural Science Foundation of China (NO. 42102298 and NO. 42302299), and multiple geological survey projects from the China Geological Survey (NO. DD20230426 and NO. DD20230431).

Data Availability Statement: The original contributions presented in this study are included in the article. Further inquiries can be directed to the corresponding authors.

Conflicts of Interest: The authors declare no conflicts of interest.

References

1. Deng, W.; Bai, J.H.; Yan, M. hua Problems and Countermeasures of Water Resources for Sustainable Utilization in China. *Chin. Geogr. Sci.* **2002**, *12*, 289–293. [CrossRef]
2. Jiang, W.J.; Wang, G.C.; Sheng, Y.Z.; Shi, Z.M.; Zhang, H. Isotopes in groundwater (2H, 18O, 14C) revealed the climate and groundwater recharge in the Northern China. *Sci. Total Environ.* **2019**, *666*, 298–307. [CrossRef] [PubMed]
3. Chen, S.; Liu, F.; Zhang, Z.; Zhang, Q. Changes of Groundwater Flow Field and Its Impact on the Ecological Environment in Luanhe River Delta under the Influence of Human Activities in the Past 30 Years. *China Geol.* **2021**, *4*, 455–462. [CrossRef]
4. Jiang, W.J.; Sheng, Y.Z.; Shi, Z.M.; Guo, H.M.; Chen, X.L.; Mao, H.R.; Liu, F.T.; Ning, H.; Liu, N.N.; Wang, G.C. Hydrogeochemical characteristics and evolution of formation water in the continental sedimentary basin: A case study in the Qaidam Basin, China. *Sci. Total Environ.* **2024**, *957*, 177672. [CrossRef]
5. Zhang, Z.; Liu, F.; Chen, S.; Jiang, W.; Zhang, H.; Gao, Z.; Zhang, J.; Xie, H.; Meng, Q.; Xia, Y.; et al. Hydrogeochemical and Isotopic Insights into Groundwater Evolution in the Agricultural Area of the Luanhe Plain. *Environ. Earth Sci.* **2024**, *83*, 593. [CrossRef]
6. Zhang, Z.; Liu, F.; Jiang, W.; Chen, S.; Zhang, H.; Gao, Z.; Zhang, J.; Niu, X.; Cao, W.; Shan, Q. Quantifying the Factors Controlling Groundwater Fluoride and Associated Health Risks in the Coastal River Delta, Northern China. *J. Asian Earth Sci.* **2024**, *259*, 105929. [CrossRef]
7. Milly, P.C.D.; Dunne, K.A.; Vecchia, A.V. Global Pattern of Trends in Streamflow and Water Availability in a Changing Climate. *Nature* **2005**, *438*, 347–350. [CrossRef]
8. Zhang, A.; Zhang, C.; Fu, G.; Wang, B.; Bao, Z.; Zheng, H. Assessments of Impacts of Climate Change and Human Activities on Runoff with SWAT for the Huifa River Basin, Northeast China. *Water Resour. Manag.* **2012**, *26*, 2199–2217. [CrossRef]
9. Wu, J.; Miao, C.; Wang, Y.; Duan, Q.; Zhang, X. Contribution Analysis of the Long-Term Changes in Seasonal Runoff on the Loess Plateau, China, Using Eight Budyko-Based Methods. *J. Hydrol.* **2017**, *545*, 263–275. [CrossRef]
10. Jiang, S.; Ren, L.; Gourley, J.J.; Singh, V.; Yang, X.; Yuan, F. Quantifying the Effects of Climate Variability and Human Activities on Runoff from the Laohahe Basin in Northern China Using Three Different Methods. *Hydrol. Process.* **2011**, *25*, 2492–2505. [CrossRef]
11. Ning, H.; Jiang, W.; Sheng, Y.; Wang, K.; Chen, S.; Zhang, Z.; Liu, F. Comprehensive Evaluation of Nitrogen Contamination in Water Ecosystems of the Miyun Reservoir Watershed, Northern China: Distribution, Source Apportionment and Risk Assessment. *Environ. Geochem. Health* **2024**, *46*, 278. [CrossRef] [PubMed]
12. Zhang, N.N. Analysis on Runoff Changes and Their Attributions in the Miyun Reservoir Basin over the Past Three Decades. Master's Thesis, Tsinghua University, Beijing, China, 2014.
13. Berezovskaya, S.; Yang, D.; Kane, D.L. Compatibility Analysis of Precipitation and Runoff Trends over the Large Siberian Watersheds. *Geophys. Res. Lett.* **2004**, *31*, L21502. [CrossRef]
14. Donohue, R.J.; Roderick, M.L.; McVicar, T.R. Assessing the Differences in Sensitivities of Runoff to Changes in Climatic Conditions across a Large Basin. *J. Hydrol.* **2011**, *406*, 234–244. [CrossRef]
15. Milly, P.C.D.; Dunne, K.A. On the Hydrologic Adjustment of Climate-Model Projections: The Potential Pitfall of Potential Evapotranspiration. *Earth Interact.* **2011**, *15*, 1–14. [CrossRef]
16. Wang, Y.; Ding, Y.; Ye, B.; Liu, F.; Wang, J.; Wang, J. Contributions of Climate and Human Activities to Changes in Runoff of the Yellow and Yangtze Rivers from 1950 to 2008. *Sci. China Earth Sci.* **2012**, *56*, 1398–1412. [CrossRef]

17. Xu, X.; Yang, D.; Yang, H.; Lei, H. Attribution Analysis Based on the Budyko Hypothesis for Detecting the Dominant Cause of Runoff Decline in Haihe Basin. *J. Hydrol.* **2014**, *510*, 530–540. [CrossRef]
18. Wu, L.; Wang, S.; Bai, X.; Luo, W.; Tian, Y.; Zeng, C.; Luo, G.; He, S. Quantitative Assessment of the Impacts of Climate Change and Human Activities on Runoff Change in a Typical Karst Watershed, SW China. *Sci. Total Environ.* **2017**, *601–602*, 1449–1465. [CrossRef]
19. Ayalew, A.D.; Wagner, P.D.; Tigabu, T.B.; Sahlu, D.; Fohrer, N. Hydrological Responses to Land Use and Land Cover Change and Climate Dynamics in the Rift Valley Lakes Basin, Ethiopia. *J. Water Clim. Change* **2023**, *14*, 2788–2807. [CrossRef]
20. Ahn, K.-H.; Merwade, V. Quantifying the Relative Impact of Climate and Human Activities on Streamflow. *J. Hydrol.* **2014**, *515*, 257–266. [CrossRef]
21. Huang, S.; Liu, D.; Huang, Q.; Chen, Y. Contributions of Climate Variability and Human Activities to the Variation of Runoff in the Wei River Basin, China. *Hydrol. Sci. J.* **2014**, *61*, 1026–1039. [CrossRef]
22. Xia, H.; Su, Y.; Yang, L.; Feng, Q.; Liu, W.; Ma, J. Effects of Climate Change and Human Activities on Streamflow in Arid Alpine Water Source Regions: A Case Study of the Shiyang River, China. *Land* **2024**, *13*, 1961. [CrossRef]
23. Li, Y.; Luo, Y.; Liu, G.; Ouyang, Z.; Zheng, H. Effects of Land Use Change on Ecosystem Services: A Case Study in Miyun Reservoir Watershed. *Acta Ecol. Sin.* **2013**, *33*, 726–736. [CrossRef]
24. Zhu, B.; Yuan, J. Pressure transfer modeling for an urban water supply system based on Pearson correlation analysis. *J. Hydroinform.* **2015**, *17*, 90–98. [CrossRef]
25. Dou, P.; Tian, Y.; Zhang, J.; Fan, Y. Multi-Scale Spatial Relationship Between Runoff and Landscape Pattern in the Poyang Lake Basin of China. *Water* **2024**, *16*, 3501. [CrossRef]
26. Niu, Y.; Jiao, S.; Tang, S.; Tang, X.; Yin, J. Evolution Pattern of Blue–Green Space in New Urban Districts and Its Driving Factors: A Case Study of Zhengdong New District in China. *Water* **2023**, *15*, 2417. [CrossRef]
27. Oke, S.A. Contaminant of Emerging Concerns in Modder River Catchment of Free State: Implication for Environmental Risk and Water Sources Protection. *Water* **2024**, *16*, 2494. [CrossRef]
28. Ouyang, L. Analysis on the Runoff Changes in the Dakeng Small Watershed and the Contribution Rate of Its Influencing Factors. Master's Thesis, Jiangxi Agricultural University, Nanchang, China, 2018.
29. Wang, S.; Wang, Y.; Ran, L.; Su, T. Climatic and Anthropogenic Impacts on Runoff Changes in the Songhua River Basin over the Last 56 years (1955–2010), Northeastern China. *CATENA* **2015**, *127*, 258–269. [CrossRef]
30. Montes-Pajuelo, R.; Rodríguez-Pérez, Á.M.; López, R.; Rodríguez, C.A. Analysis of Probability Distributions for Modelling Extreme Rainfall Events and Detecting Climate Change: Insights from Mathematical and Statistical Methods. *Mathematics* **2024**, *12*, 1093. [CrossRef]

Disclaimer/Publisher's Note: The statements, opinions and data contained in all publications are solely those of the individual author(s) and contributor(s) and not of MDPI and/or the editor(s). MDPI and/or the editor(s) disclaim responsibility for any injury to people or property resulting from any ideas, methods, instructions or products referred to in the content.

water

MDPI

Article

Comprehensive Study on Hydrogeological Conditions and Suitability Evaluation of In Situ Leaching for Sandstone-Hosted Uranium Deposit in Erlian Basin

Lishan Meng [1,2,3,†], Hang Ning [1,2,3,†], Wanjun Jiang [1,2,3,*], Yizhi Sheng [4], Wei Wang [1,2,3] and Chao Tang [1,2,3]

[1] Tianjin Center, China Geological Survey, Tianjin 300170, China; mls_316@126.com (L.M.); ninghang1123@163.com (H.N.); wangwei_wangwei@126.com (W.W.); tjtangchao@163.com (C.T.)
[2] Tianjin Key Laboratory of Coast Geological Processes and Environmental Safety, Tianjin 300170, China
[3] North China Center for Geoscience Innovation, China Geological Survey, Tianjin 300170, China
[4] State Key Laboratory of Biogeology and Environmental Geology, China University of Geosciences, Beijing 100190, China; shengyz0330@163.com
* Correspondence: jiangwanjun0718@163.com
† These authors contributed equally to this work.

Abstract: As a strategic mineral and energy resource, the enrichment and metallogenic mechanism of sandstone-hosted uranium deposits are highly dependent on hydrogeological conditions. However, the relationship between sandstone uranium mineralization and hydrogeological conditions has not received sufficient attention yet. The pumping test, hydrogeological parameters and hydrochemical characteristics were employed to analyze the change characteristics of hydrogeological conditions and evaluate the suitability of in situ leaching (ISL). The results showed that the study area in the Inner Mongolia Autonomous Region could be divided into two groundwater subsystems, namely Quanzha-Engeriyin and Luhai-Zhendai. The latter with relatively high water richness is confined and a main ore-bearing aquifer, which consists of four orebodies. The well discharge (Q) and hydraulic conductivity (*K*) of Orebody II ranged from 98.40 to 867.36 m^3/d and 0.25 to 5.64 m/d, respectively, indicating the aquifer is suitable for the migration, enrichment and mineralization of uranium due to relatively high permeability and fast flow rate. The water storage of Orebodies III-IV gradually deteriorated from east to west in a stepped pattern. And the highest values of Q and *K* in Orebodies III-IV decreased from 1200 m^3/d to 120 m^3/d and 1.75 m/d to 0.035 m/d, respectively, suggesting these were conducive to a reduction in and accumulation of uranium under poor hydrodynamic conditions. Additionally, the study area would be defined as three grades, including favorable, relatively favorable and unfavorable areas of ISL according to a comprehensive evaluation. This study provided a scientific basis for evaluating the possibility of in situ leaching for sandstone-hosted uranium deposit.

Keywords: hydrogeological and hydrodynamic conditions; migration and transformation; sandstone-hosted uranium deposit; in situ leaching; Erlian Basin

1. Introduction

As an important clean energy source with low carbon and high efficiency, nuclear energy has the potential to replace fossil fuels and meet the needs of large-scale industrial development [1–4]. Additionally, the development of nuclear energy can effectively mitigate the reliance on fossil fuels (such as petroleum, natural gas, and coal), thereby assuming an increasingly pivotal role in addressing environmental pollution issues [5–7]. Natural uranium (U), as a primary raw material for nuclear energy, is a crucial strategic mineral and energy resource globally. U holds significant importance for societal production and economic development [8–10]. The primary terrestrial uranium resources consist of sandstone-type, unconformity-type, and iron oxide-type deposits. Uranium ore deposits

have been identified within sandstone, breccia, organic matter (OM)-rich sediments, unconformities, roll-front formations, and granitic plutons across all continents [9,11–15]. The sandstone-type uranium deposits are among the main types of uranium deposits in the United States, Australia, Niger, South Africa, and Central Asia [16,17]. Similarly, China primarily focuses on exploring and developing sandstone uranium deposits [10,17]. The sandstone-type uranium deposits make up 45.51% of the known resources and are widely recognized as the predominant forms of uranium deposits [18]. Therefore, sandstone uranium resources are an important material basis for the nation's economic development. It is imperative to study sandstone uranium deposits' enrichment laws and mineralization mechanisms to ensure their effective exploitation and sustainable utilization.

Numerous perspectives exist regarding the genetic classifications of sandstone-type uranium deposits. Nevertheless, the majority of investigations are grounded in mineralogy, geochemistry, and sedimentology [10,17,19–21]. In recent years, numerous studies have shown that the formation of sandstone-type uranium ore rolls is closely related to hydrogeological conditions. Uranium ore rolls, in particular, are prone to form in the front of the oxidation–reduction zone of the confined aquifer [9,16,19,22]. Typical sandstone-hosted U roll-front deposits are formed in confined aquifers at a redox front of oxidized groundwater reacting with unaltered reduced aquifer materials, often associated with organic detritus. During the migration process to the deep basin, groundwater undergoes hydrogeochemical processes primarily governed by redox reactions, resulting in the transformation of uranium into different valence states and its adsorption onto the surface of porous media solid particles, thereby facilitating mineral enrichment [15,22–25]. Consequently, the hydrogeological conditions are pivotal in elucidating the formation processes and mechanisms of sandstone-type uranium deposits, and in forecasting uranium mineralization targets [26–30]. However, the relationship between sandstone uranium mineralization and hydrogeological conditions (including hydrodynamics, hydrochemistry, and paleohydrogeology) has not yet received sufficient attention, necessitating further research.

In recent years, extensive coal and oil exploration efforts have confirmed the significance of uranium-bearing rocks in the sandstone strata of the late Cretaceous Saihan Formation in the Luhai area of the Erlian Basin, Inner Mongolia. The sandstone strata in this formation have the characteristics of shallow burial depth, good continuity, and high ratio of adsorbed uranium. However, the source and enrichment mechanisms of uranium deposits are not yet clear, and the key factors that influence the "hydrothermal uranium deposit genesis theory" are not yet understood. This paper systematically analyzes the geological characteristics of uranium deposits in the Luhai area, combining hydrogeological surveys and hydrogeological drilling, conducting field pumping tests, calculating hydrogeological parameters, and studying the hydrochemical characteristics. From the perspectives of groundwater flow field and hydrochemical characteristics, this study explores the hydrogeological and hydrodynamic conditions for uranium mineralization in sandstone. It reveals the differences and changes in features between uranium migration and the conditions. At the same time, this paper conducts a suitability evaluation of hydrogeological conditions for in situ leaching of uranium ore, providing a new perspective for studying uranium mineralization conditions. This study contributes to a deeper understanding of the relationship between basin sandstone uranium mineralization and hydrogeological conditions. It has significant scientific implications for the rational exploitation and utilization of sandstone uranium resources.

2. Study Area

2.1. Physical Geography

The Erlian Basin is located in the central–northern part of Inner Mongolia Autonomous Region, China, with a geographical range of 107°30′–119°10′ E and 40°40′–45°45′ N. It stretches from the east to the Greater Khingan Range, west to the Baoyintu Uplift, south to the northern foot of Yin Mountains, and north to the Sino-Mongolian border. The basin is oriented in a northeast direction and encompasses an area of approximately 110,000 km^2.

The Luhai mining area, located in the north–central Erlian Basin, falls under the jurisdiction of Sunite Left Banner in the Xilingol League of Inner Mongolia Autonomous Region. It is situated approximately 40 km away from Mandu Latuo Town, which serves as the administrative center for Sunite Left Banner (Figure 1). The study area is situated in the hinterland of Sunit Grassland, presenting a landform characterized by hills. The terrain exhibits a northeast high and southwest low trend, with an elevation ranging from 909 m to 945 m. Although the relative height difference is minimal, the surface water system is underdeveloped, resulting in only temporary gully floods during the rainy season. In other seasons, riverbeds and dish depressions remain dry without any water presence. The climatic conditions correspond to the typical temperate semi-arid continental monsoon climate type. The average annual precipitation is 300 mm, the evaporation is 2580.56 mm, and the precipitation is mostly concentrated in July and August, often appearing as showers and heavy rainstorms.

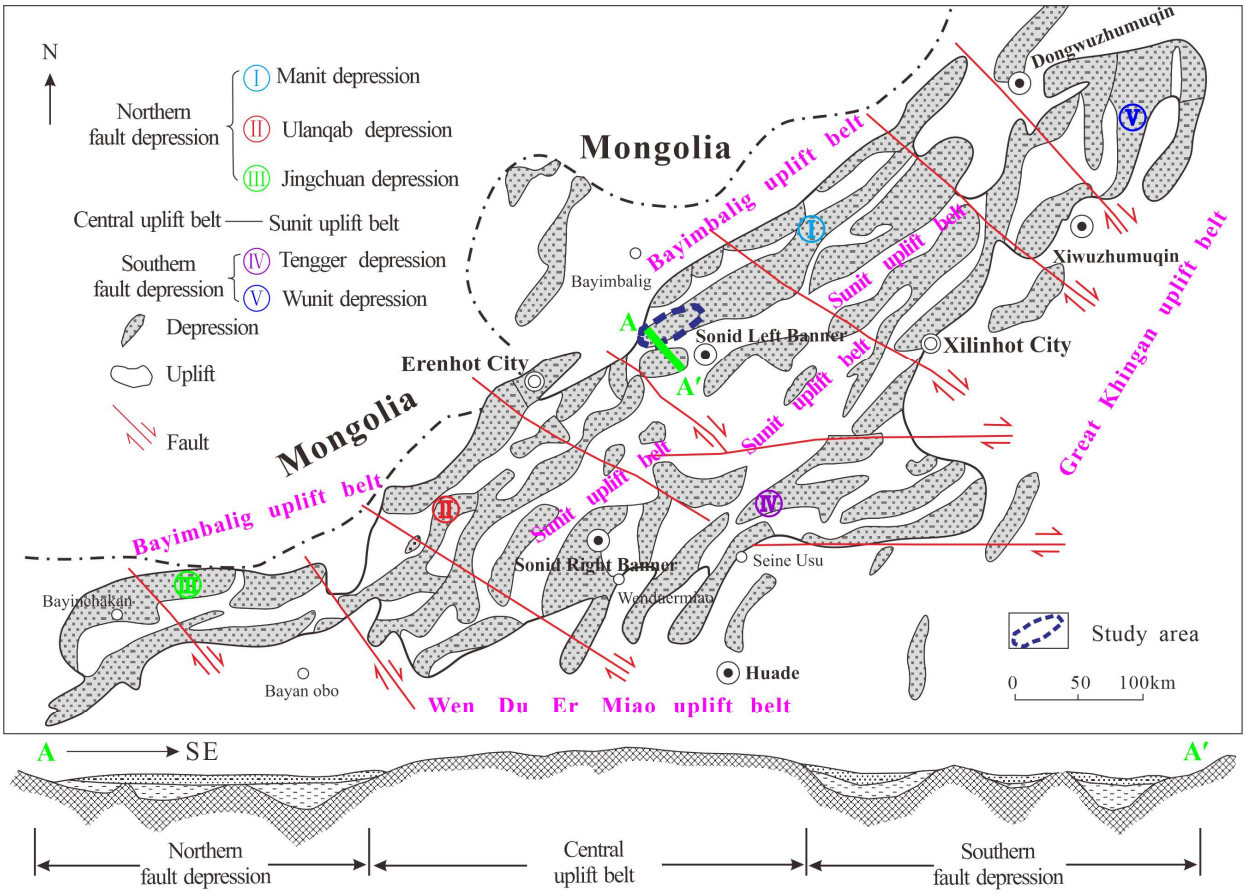

Figure 1. Study area and structural division of Erlian Basin (the third-level tectonic units: 43 sags and 22 uplifts in the basin; 10 sags in the basin margin).

2.2. Regional Geological Structure

Erlian Basin is situated in the central and northern region of Inner Mongolia, occupying a tectonic position along the suture line between the Asian Plate and the Siberian Plate. This basin represents a vast Mesozoic and Cenozoic fault-depression sedimentary basin that developed on the folded basement of Inner Mongolia–Daxing'anling due to extensional–occlusive tectonic stress during the Yanshan period. The eastern boundary of the basin is situated in the northeastern region of the Great Xing'an Mountains, while its northern boundary extends towards Bayanbulak in a similar direction. The southern boundary runs from east to west and terminates at Wendul Temple, whereas the western boundary stretches northeastwards towards Solon Mountain (Figure 1). The basin is char-

acterized by three levels of positive and negative tectonic units: the first level comprises faulted and uplifted zones, the second level consists of uplifted areas and depressions, and the third level exhibits both uplifts and depressions. Specifically, the first level tectonic unit has distinct divisions, including a northern fault zone, a central uplift zone, and a southern fault zone. Moreover, the second level tectonic unit can be further subdivided into six units comprising five depressions and one uplift. These structural units consist of multiple secondary depressions and uplifts, among which the Manit depression is most relevant to this study.

The Maniet depression is a significant secondary depression located in the northeastern region of the Erlian Basin. It exhibits a northeastward distribution, spanning approximately 300 km from east to west and measuring 20–80 km in width from north to south. The total area covered by this depression amounts to about 1.4×10^4 km^2. Its southeastern boundary lies adjacent to the Sunit uplift, while its northwestern boundary is in close proximity to the Bayanbulak uplift. The basement structure of this depression is highly complex, characterized by distinct convex and concave patterns. Generally, the depth of each depression's basement ranges between 800 and 2800 m, with a maximum depth reaching up to 4500 m, whereas for the uplifted areas, basement depths range from 200 to 800 m. The study area is located within the sub-tectonic basin of Tabie Sag in Manite Sag, Erlian Basin. The Lower Cretaceous represents the primary sedimentary fill within this basin, while distinct basin types can be identified during different periods of the Early Cretaceous: fault depression type in the early Early Cretaceous, fault depression type in the late Early Cretaceous, and depression type following the Late Cretaceous.

2.3. Regional Stratigraphy

The Erlian Basin is a Mesozoic sedimentary basin developed on the Hercynian basement. The basement of the basin consists of Meso-Neoproterozoic and Paleozoic strata, which are extensively exposed in the bedrock mountains on both sides of the basin. The lithology primarily comprises granite, volcanic rock, and volcanic clastic rock. These rocks exhibit high uranium content that readily precipitates, thereby providing an abundant source for sandstone-type uranium deposit formation. The basin cover includes Mesozoic and Cenozoic continental clastic sedimentary strata such as Triassic, Jurassic, Cretaceous, Paleogene, Neogene, and Quaternary formations that can be categorized into three filling sequences (Figure 2).

The Luhai mining area is located in the southwestern margin of the Tabei Sag in the Manite Depression of the Ertan Basin (Figure 1). Most parts of the area are covered by Neogene Paleocene and Quaternary deposits, rich in coal, uranium, and other sedimentary minerals. Currently, a preliminary control has been established over a mineral belt with a length of 15 km. The extension of orebodies is controlled by ancient river valleys, which favor mineralization. The orebodies generally have a tabular shape and are buried at depths ranging from 70 to 150 m. Four main orebodies have been identified so far, occurring in sandstones above angular unconformities between the mudstones of the Upper Cretaceous Tenggeer Formation and sandstones of the Saihan Formation. The top part of these sandstone bodies consists of mudstones from the Saihan Formation, with an ore-body-thickness-to-sandstone-thickness ratio greater than 0.1. Furthermore, this mining area is adjacent to the already underground leached Bayanwula uranium deposit. It shares similar geological conditions for mineralization as well as similarities in terms of ore material composition and structural characteristics with that deposit. It possesses excellent resource endowment characterized by shallow burial depth, large-scale reserves with good continuity, high permeability, and adsorption capacity for hexavalent uranium ions, making it suitable for underground leaching development.

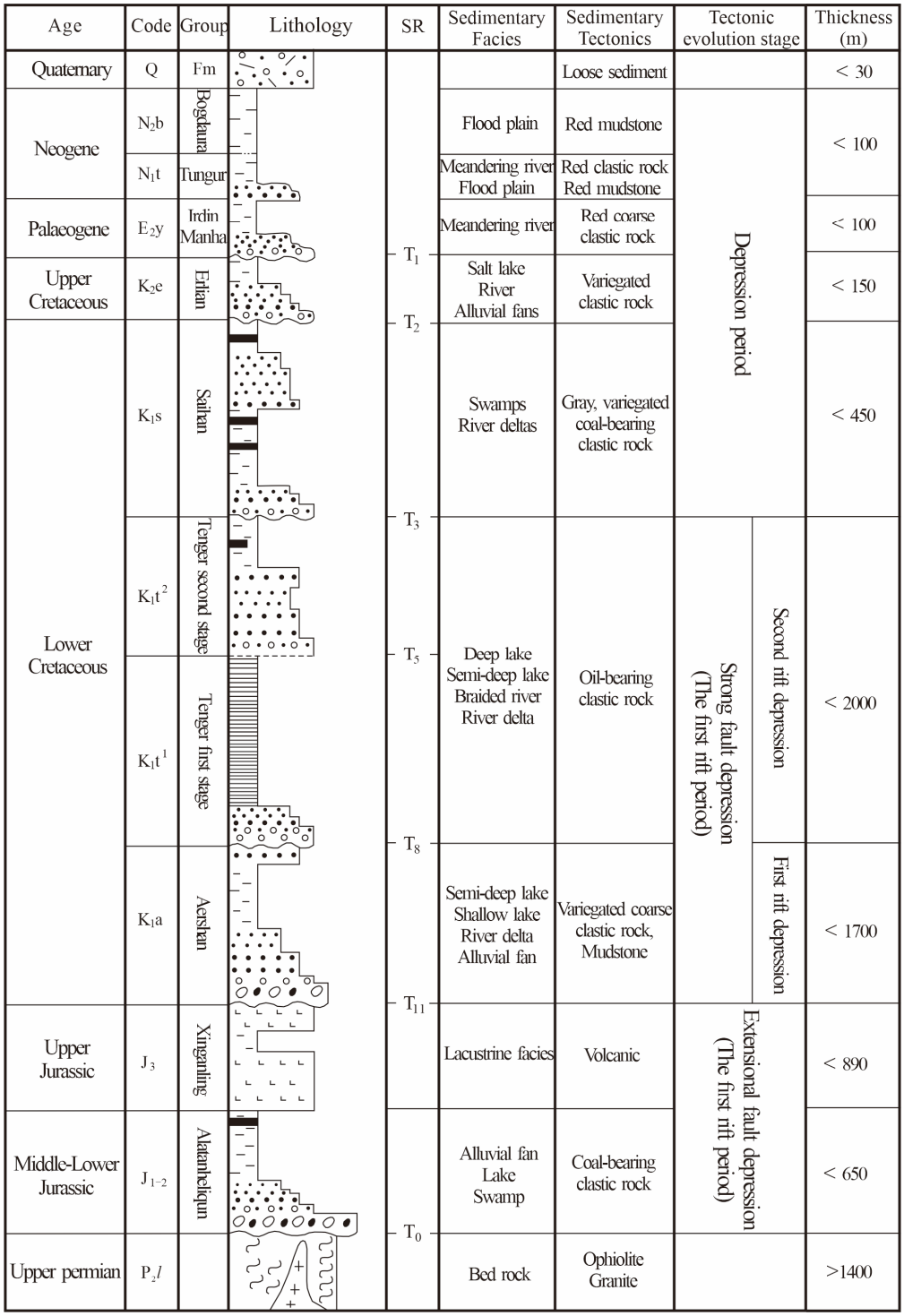

Figure 2. Comprehensive columnar and tectonic evolution map of the middle Erlian Basin.

3. Materials and Methods

The in situ leaching uranium mining technique is an innovative and non-conventional method primarily utilized in sandstone uranium deposits [31,32]. In situ uranium mining technology utilizes the high water content of sandstone to introduce chemical reagents into the ore seam, facilitating a reaction between the reagent and uranium within the ore, resulting in the dissolution of uranium and the formation of leaching liquid. This liquid is subsequently extracted from the leaching hole and purified in a water refinery. Therefore,

successful implementation of in situ uranium mining relies on both the distribution of ore deposits and hydrological conditions associated with the ore-bearing seam.

In the study area, a total of 20 geological drillings and 2 hydrogeological drillings datasets were collected, resulting in an overall penetration depth of 3457.89 m. Among them, the shallowest drilling depth was 85.11 m, while the deepest drilling depth reached 281.34 m. The depth of the hydrogeological drilling SZK01 was 160.86 m, and the depth of SZK02 was 253.62 m.

The pumping test method consists of stable flow pumping and unstable flow observation, which can be divided into two types. For machine-drilled wells, a simplified pumping test is employed, while hydrogeological exploration boreholes adopt stable flow pumping tests with no less than one set of pumping cycles [33]. The calculation of K, R, and T is carried out iteratively using the Dupuit Formula (1) and the Siechardt Formula (2) for confined aquifer single-well steady-state flow. The calculation formulas are as follows:

$$K = \frac{0.366Q}{M \times s} lg\frac{R}{r} \quad (1)$$

$$R = 10s\sqrt{K} \quad (2)$$

$$T = KM \quad (3)$$

K represents the hydraulic conductivity (m/d), R represents the influence radius (m), T represents the coefficient of transmissivity (m/d), Q represents the well discharge (m^3/d), r represents the well radius (m), s represents the drawdown value (m), and M represents the thickness of confined water aquifer (m).

The classification and evaluation indexes for in situ sandstone uranium deposits have been refined according to the nuclear industry standard of the People's Republic of China, with a focus on assessing hydrogeological conditions in the Luhai area. The hydrogeological classification takes into account five key aspects: permeability, pressure-bearing capacity, unit water inflow, groundwater depth, and hydrogeological complexity (Table 1). Additionally, based on complexity levels, these deposits are categorized into three types.

Table 1. Hydrogeological classification indexes of in situ leaching sandstone-type uranium deposits.

Permeability of Ore-Bearing Aquifer		**Bearing Capacity of Ore-Bearing Aquifer**	
Classification of deposit	K (m/d)	Classification of deposit	Groundwater depth (m)
High permeability	$K \geq 10$	High confined water	$H \geq 100$
Relatively high permeability	$1 < K \leq 10$	Relatively high confined water	$20 < H \leq 100$
General permeability	$0.1 < K \leq 1$	Low confined water	$H \leq 20$
Limited permeability	$K \leq 0.1$	Non- confined water	Missing bulkhead
Inflow rate of water in the ore-bearing aquifer		Groundwater table in the ore-bearing aquifer	
Classification of deposit	Inflow rate of water (L/s·m)	Classification of deposit	Groundwater Table (m)
Huge water yield	$Q \geq 0.10$	Large depth of groundwater level	$h \geq 150$
Large water yield	$0.05 < Q \leq 0.10$	Medium depth of groundwater level	$50 < h \leq 150$
Small water yield	$0.01 < Q \leq 0.05$	Little depth of groundwater level	$h \leq 50$
Little water yield	$Q \leq 0.01$		

(1) Type I: mineral deposits with simple hydrogeological conditions. The ore-bearing aquifer is buried at a depth of less than 350 m, exhibiting stable distribution and thickness of less than 30 m. It possesses stable rock strata acting as an impermeable roof and floor, lacking a hydraulic connection with other aquifers and surface water bodies. Additionally, it demonstrates strong confinement of water within the aquifer, while the burial depth of

groundwater static water level remains below 50 m. The permeability of ore-bearing rocks in this aquifer surpasses that of non-ore-bearing rocks, displaying both high and moderate permeability levels.

(2) Type II: Mineral deposits under moderate hydrogeological conditions are characterized by an ore-bearing aquifer buried at depths of less than 350 m, showing a stable distribution with a thickness ranging from 30 to 50 m. The rock layers forming the impermeable roof and floor remain relatively stable and have limited hydraulic connections with other aquifers and surface water bodies. These deposits exhibit either strong confinement or weak confinement of water flow. The static groundwater level is typically found between depths of 50 and 150 m. Regarding permeability, the ore-bearing rocks within this aquifer demonstrate equal or higher permeability compared to non-ore-bearing rocks while also displaying more uniform patterns of permeability distribution. As such, these mineral deposits can be categorized as having strong or similar levels of permeability characteristics in accordance with scientific literature standards.

(3) Type III: mineral deposits characterized by intricate hydrogeological conditions. The underlying aquifer containing ores lies at depths shallower than 350 m but exhibits an unstable distribution pattern. It has an approximate thickness of around 50 m, with precarious rock formations serving as both impermeable roofs and floors. This type of deposit demonstrates a robust hydraulic connection with adjacent aquifers and surface waters; however, confined water may be scarce or absent altogether. Groundwater's static level resides below depths exceeding 150 m in this context. The permeability of these ore-containing rocks within the aforementioned aquifer tends to be lower when compared to non-ore-bearing rocks, displaying irregular permeability traits that can generally be categorized as moderate or weak for mineral deposits.

Additionally, the TDS was measured by a gravimetric method. Major cations (K^+, Na^+, Ca^{2+}, Mg^{2+}) were measured with an Inductively Coupled Atomic Emission Spectrometer (ICP-AES, iCAP6300, Thermo, Waltham, MA, USA). ${SO_4}^{2-}$ and Cl^- were measured by ion chromatography (DX-120 IC, Dionex, Sunnyvale, CA, USA). ${HCO_3}^-$ and ${CO_3}^{2-}$ were measured by the volumetric method.

4. Results

4.1. Hydrogeological Characteristics of Uranium Ore Beds in the Luhai Mining Area

4.1.1. Hydrodynamic Characteristics of Groundwater

The Erlian Basin belongs to a first-level hydrogeological unit. Based on the structural division of the basement and the modern characteristics of groundwater recharge, flow, and discharge, the Erlian Basin is further divided into five sub-level hydrogeological units: Chuanjing autochthonous basin, Wulanchabu autochthonous basin, Manit autochthonous basin, Uinit autochthonous basin, and Tengger autochthonous basin (Figure 3). The area under study is situated within the hydrogeological unit of Manit Depression, which serves as the runoff-discharge region for Manit Depression. The paleohydrogeological conditions in Manit Depression exhibit distinct segmentation and differential development, lacking a unified lake presence. Instead, it predominantly consists of various depressions that form an independent hydrogeological system.

According to variations in groundwater aquifer lithology, occurrence conditions, and hydraulic characteristics, the groundwater in the Luhai region can be classified into three primary types: bedrock fracture water, clastic rock fracture porosity water, and loose rock pore water. Bedrock fracture water is predominantly found in the erosion source areas of northwestern and southeastern regions where the aquifer lithology consists of Permian–Jurassic medium-acid intrusive rock, Permian clastic rock with limestone, and Carboniferous medium-acid volcanic rock with clastic rock that contains weathered fracture water. Groundwater distribution exhibits significant heterogeneity with low water content. However, well-developed structural fractures within fault zones contribute to a higher water content.

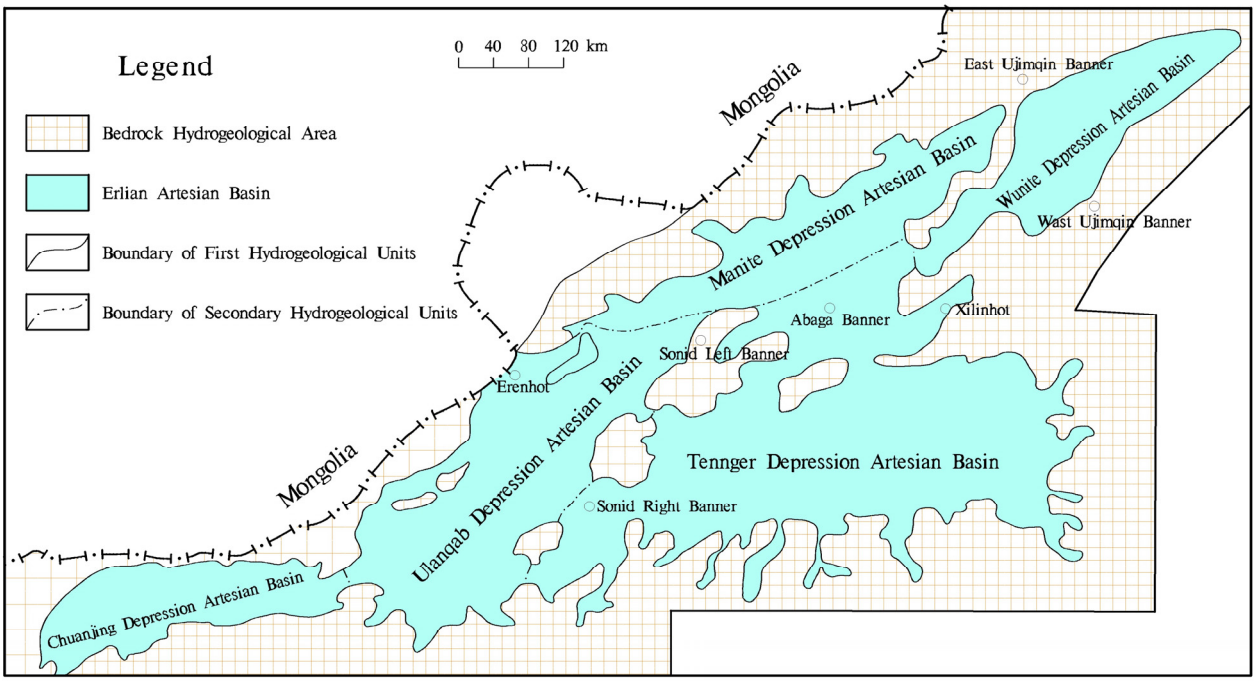

Figure 3. Hydrogeological unit division map of Erlian Basin.

The clastic rock fissure porosity water is the predominant groundwater type in the region, widely distributed, and its water content is controlled by the sedimentary environment. Aquifers are poorly developed and have limited groundwater storage in areas such as alluvial fans, flood plains, and lacustrine sedimentary regions. Conversely, in river facies areas, the aquifer thickness increases, resulting in substantial subterranean groundwater storage. This groundwater type primarily occurs within the clastic rock pore-fissure water-bearing rock group of both Lower Cretaceous Saihan Formation and Paleogene formations. The Cretaceous aquifer is predominantly influenced by ancient riverbeds trending northeast and are extensively distributed across the central region of the terrace-like high plain. This aquifer demonstrates a stable and continuous belt-like distribution characteristic, oriented northeast, with a significant water-bearing capacity. The lithology of this aquifer consists predominantly of sandstone with occasional interlayers of mudstone and argillaceous siltstone in localized areas. On the other hand, the Paleogene aquifer occurs extensively across a vast area on a stepped-high plain but exhibits unstable distribution patterns with significant variations in thickness. The primary lithologies within this water-bearing rock group include coarse sandstone and gravel-bearing coarse sandstone, along with some occurrences of sandstone. Loose rock pore water mainly exists within intermountain alluvial plains (branched gullies), piedmont alluvial plains, and lake lowlands, where it forms quaternary sand gravel aquifers consisting of medium-coarse sands mixed with argillaceous silt layers ranging from 0.5 to 20 m thick; their average groundwater level remains below 3 m while inflow rates generally do not exceed 30 m^3/d but can locally reach up to 100 m^3/d mostly through diving flow mechanisms that exhibit pronounced seasonal dynamics.

The bedrock fractures in the Luhai region are predominantly recharged through vertical precipitation with pronounced seasonal variations in their dynamic behavior. They serve as crucial sources for replenishing both porous waters within loose rocks and fractured porous waters within clastic rocks. The peripheral and central uplift influences result in lateral recharge from bedrock fractures located in elevated regions, which contribute significantly to the recharge of porous waters within basins along with vertical infiltration from atmospheric sources. Moreover, runoff occurs at the edges of these basins, while discharge happens towards their interiors. Consequently, an autonomous yet compre-

hensive system encompassing replenishment–runoff–discharge is established within each depression's self-flowing zone that exhibits distinctive hydrodynamic features.

The Luhai region is situated within the Manit depression, with the Bayanbaoligge uplift as the primary groundwater recharge zone and the Sunite uplift as a secondary recharge area. In terms of Mesoproterozoic pore fracture groundwater, it primarily undergoes vertical infiltration recharge from atmospheric precipitation and lateral recharge from upstream Cenozoic clastic rocks and bedrock characterized by hills on both sides. Under the control of bedrock and faults, groundwater flows southwestward, and it is mainly discharged through artificial extraction and lateral seepage. Mesoproterozoic pore fracture groundwater primarily undergoes vertical infiltration recharge from atmospheric precipitation and lateral recharge from upstream Cenozoic clastic rocks and bedrock characterized by hills on both sides. Due to geological formations and fault controls, the groundwater in this aquifer system flows from northeast to southwest within the basin, with artificial extraction and lateral flow being the main discharge modes.

4.1.2. Hydrogeological Study of Uranium Deposit

Uranium orebodies in the Luhai region are primarily distributed within the upper section of the Cretaceous Seihantala Formation (K_1bs^3) of the Bayanhua Group, with sporadic occurrences in the Paleogene Ildingmanha Formation (E_2y). However, these orebodies are characterized by their thinness, small-scale nature, and lack of industrial value. Consequently, this study predominantly focuses on elucidating the hydrogeological characteristics specific to the upper section of the Cretaceous Seihantala Formation (K_1bs^3) within the Bayanhua Group. Based on existing exploration data, four main orebodies have been identified in this uranium mine: Orebody II, Orebody I, and Orebodies III-IV from northeast to southwest (Figure 4). Generally, there is an inherent instability observed in terms of roof distribution within the U-hosting aquifer, along with significant variations in thickness. However, its base corresponds to a relatively stable distribution consisting mainly of mudstone belonging to the middle section of the Cretaceous Seihantala Formation (K_1bs^2) within the Bayanhua Group.

(1) Hydrogeological Characteristics of U-hosting Aquifer in Orebody II

The upper section of the Cretaceous Bayanhua Group Saihanbatala Formation (K_1bs^3) in the Orebody II area is thick, which is generally thick in the middle and thin around, and oval in shape. The middle part is the sedimentary center of the stratum, the thickness can reach 131.60 m, and the thickness in the northeast is of less than 40 m. From the southwest area to the boundary area of I and II orebodies there is an uplift area with a northwestern trend, and the upper section of the Saihanbatala Formation is missing in some drillings in the uplift area. In addition, the thickness change in the U-hosting aquifer in the Orebody II area is basically consistent with the upper section of the Saihanbatala Formation, which is thick in the middle, thin around, and oval in shape (Figure 4). The thickness of the central area can reach 108.00 m. The ore-bearing aquifer is mainly pebbly coarse sandstone, coarse sandstone, and conglomerate, and the thickness of the aquifer above the coarse sandstone accounts for more than 75% of the thickness of the whole orebody. For example, the thickness of the aquifer above the coarse sandstone is 89.10 m. The sorting and grinding of the ore-bearing aquifer are poor, which is angular–subangular, with different particle sizes and a high content of muddy material, about 5~10%. The cementation degree of the ore-bearing sand layer is relatively loose–dense.

The roof distribution of the Orebody II aquifer exhibits instability and significant thickness variations. Overall, the northern part is characterized by thinness, while the southern part displays greater thickness. Some areas are either absent or gradually transition into weak permeable layers with a high mud content, primarily composed of argillaceous siltstone and silty mudstone. The aquifer's roof thickness in the northern section ranges from 0.85 to 4.54 m, and it gradually increases to 5–7 m in the central part, reaching a maximum thickness of 11.33–13.13 m. Generally, the thickness of aquifer roof exceeds 10 m in the southern portion, with a maximum thickness of 15.86 m. The bottom layer of this ore-

body's aquifer corresponds to the middle section of the Cretaceous Bayanhua Group's Seihantala Formation (K_1bs^2), mainly consisting of stable mudstone distribution. In this study, four mechanical wells surrounding the orebody were selected for simple pumping tests, yielding hydrogeological parameters as presented in Table 2. It can be observed that individual well water inflow within Orebody II's vicinity ranges from 98.40 to 867.36 m^3/d, and unit water inflow varies between 0.077 and 2.833 L/s·m, while hydraulic conductivity ranges from 0.25 to 5.64 m/d, indicating high permeability within the Orebody II area.

Table 2. Hydrogeological parameters for pumping test in the Luhai mining area II and surrounding area.

Number	Depth of Well (m)	Well Discharge (m^3/d)	Specific Discharge of a Well (L/S·m)	Drawdown (m)	Hydraulic Conductivity (m/d)	Transmissivity (m^2/d)
SDS05	76	809.28	2.019	4.64	4.15	178.71
SDS21-1	120	98.40	0.077	14.7	0.25	7.50
SDS87	90	682.80	2.833	2.79	5.64	225.75
SDS90	110	867.36	1.227	8.18	2.24	108.17

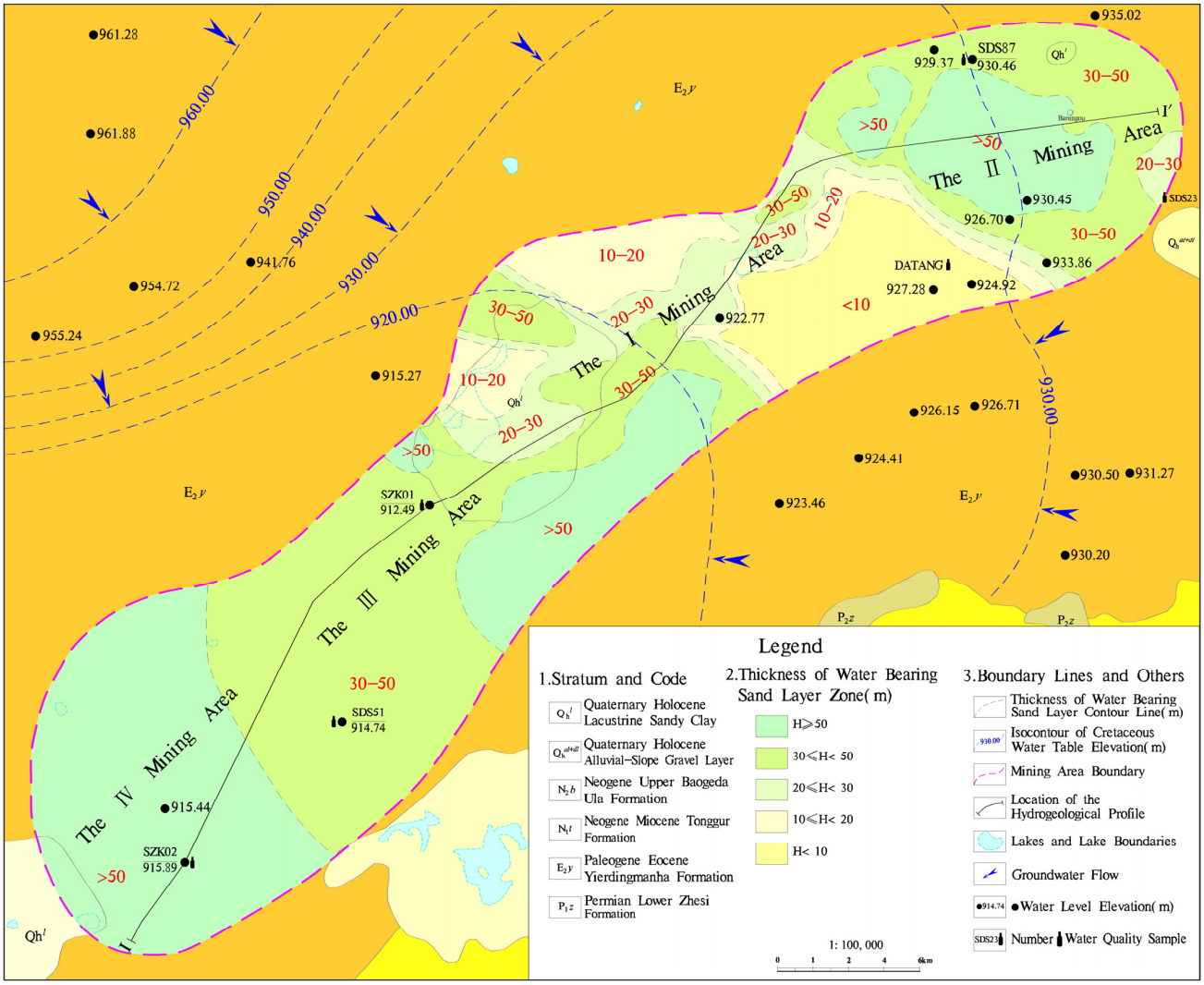

Figure 4. *Cont.*

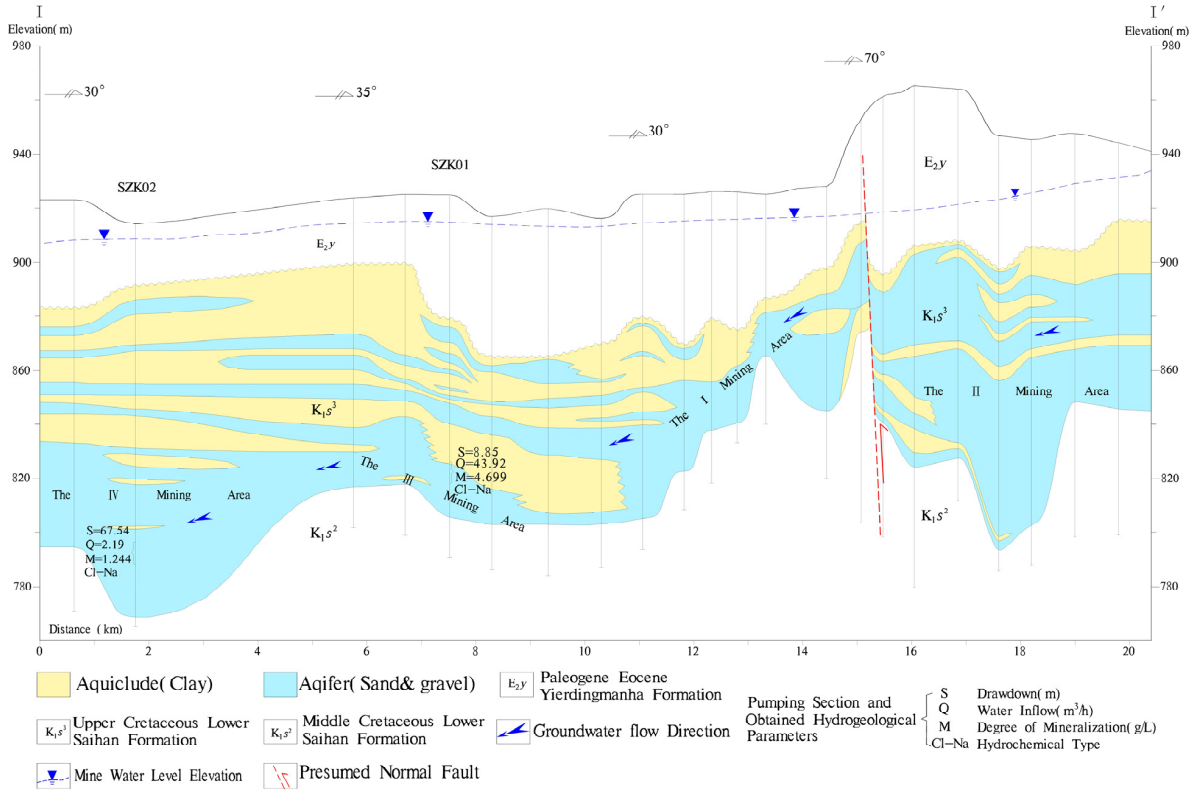

Figure 4. Contour map illustrating the thickness of the aquifer sand layer in a uranium mine situated within the Luhai mining region.

In addition, the TDS content of the groundwater in the ore-bearing aquifer of Orebody II ranges from 1143 to 1425 mg/L, with an average of 1262.3 mg/L. All samples exhibit brackish characteristics, which generally have lower TDS levels compared to the groundwater in the overlying aquifer and that of the surrounding area's same layer and other orebodies (Figure 5). The hydrochemical composition of the water primarily consists of HCO_3·Cl-Na or Cl·SO_4-Na, indicating that the groundwater in this layer is deeply buried and lacks a direct connection with contemporary atmospheric precipitation or surface water sources. Consequently, the circulation and renewal rate of groundwater are slow. Notably, the main source of HCO_3^- in groundwater is the weathering hydrolysis of silicate minerals in sandstone, revealing the occurrence of water–rock interactions. Therefore, compared to other orebodies, Orebody II exhibits a relatively faster groundwater circulation and more substantial water–rock interaction. Considering the aquifer thickness and hydrogeological parameters obtained from pumping tests, the aquifer has relatively high permeability and a relatively fast flow rate, which is conducive to the migration, transformation, and enrichment of uranium ions in the groundwater within the aquifer.

(2) Hydrogeological Characteristics of U-hosting Aquifer in Orebody I

The lithology of the ore-bearing strata primarily consists of coarse sandstone, with some occurrences of conglomerate. The water-bearing layer above the coarse sandstone makes up over 75% of the total thickness of the ore-bearing layer, while the clay content in the sand layer is relatively high, at approximately 10%. In the Orebody I area, within the upper section of the Seihantala Formation (K_1bs^3) in the Bayanhua Group Cretaceous, there are three sedimentary centers with varying thicknesses. Most areas have a thickness below 40 m, whereas the northeastern center ranges from 67.10 to 98.14 m, the western center from 56.17 to 69.96 m, and the southwestern center from 86.36 to 100.06 m (Figure 6). The variation in ore-bearing layer thickness corresponds closely to that of strata. It measures

between 41.50 and 41.89 m in the northeast region, between 40.39 and 41.28 m in the west region, and between 59.74 and 62.76 m in the southwest region.

The roof distribution of the Orebody I aquifer exhibits instability, with significant variations in thickness. Specifically, the southeastern and western regions are characterized by thin layers, generally less than 5 m thick. In some areas, there are even missing sections or a gradual transition into weak permeable layers with a high mud content, primarily composed of argillaceous siltstone and silty mudstone. Conversely, the middle and southern areas gradually thicken, reaching their maximum thickness at approximately 23.72~26.74 m. The bottom of the Orebody I aquifer corresponds to the middle section of the Seihantala Formation (K_1bs^2) within the Cretaceous Bayanhua Group. This stratum predominantly consists of mudstone and displays relatively stable distribution patterns. Based on an analysis of aquifer distribution in this region, it is observed that single-well water inflow for uranium groundwater within this area does not exceed 120 m^3/d, and in certain locations, it may be as low as 24 m^3/d or below. To further investigate these characteristics, a simple pumping test was conducted on the SDS14 mechanical well located south of Orebody I. Table 3 presents the hydrogeological parameters obtained from this pumping test. Due to mixed mining activities involving both Paleogene and Cretaceous formations at this well site, both water inflow rates and hydraulic conductivity are substantial.

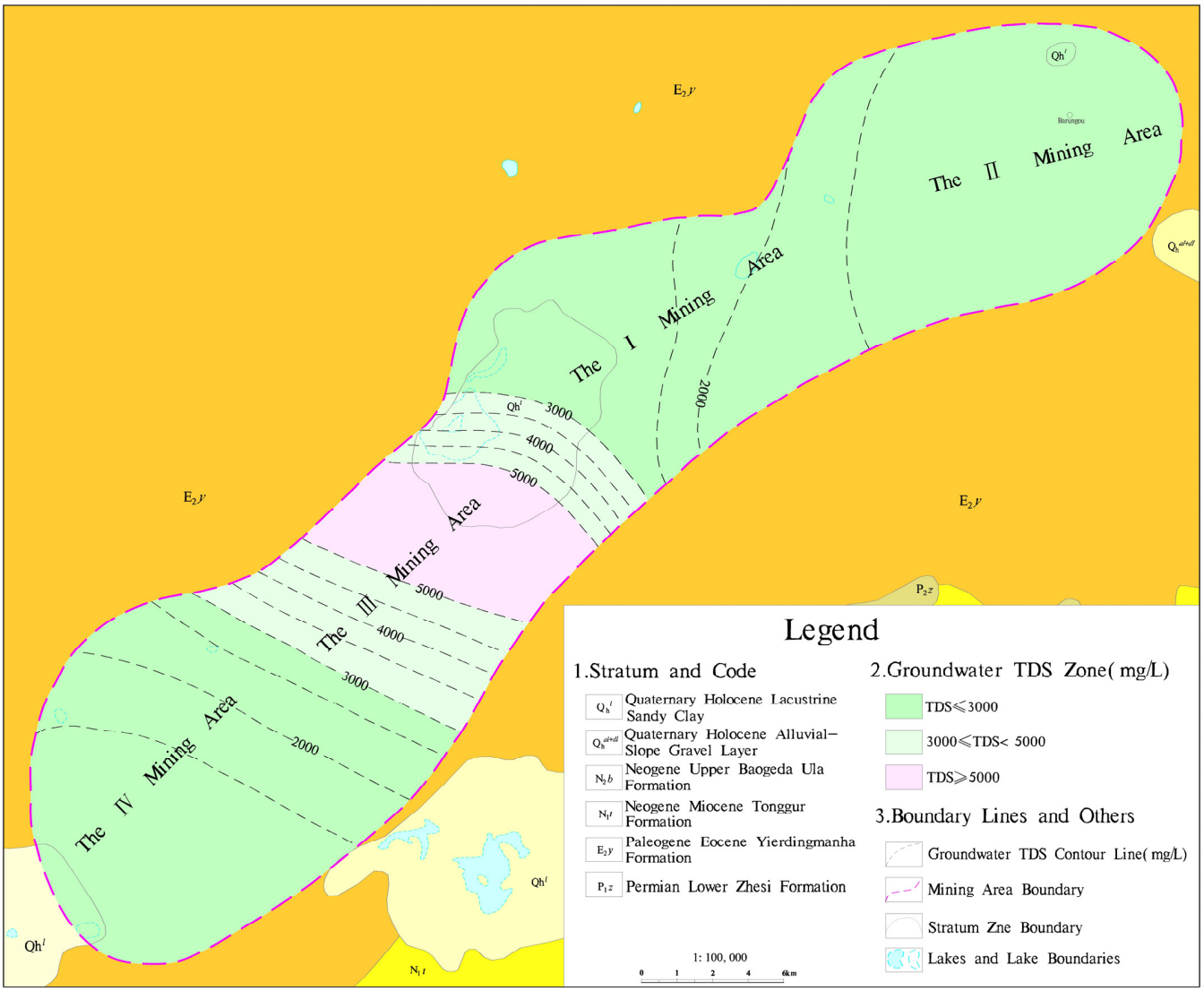

Figure 5. TDS contour map of groundwater of U-hosting aquifer in Luhai area.

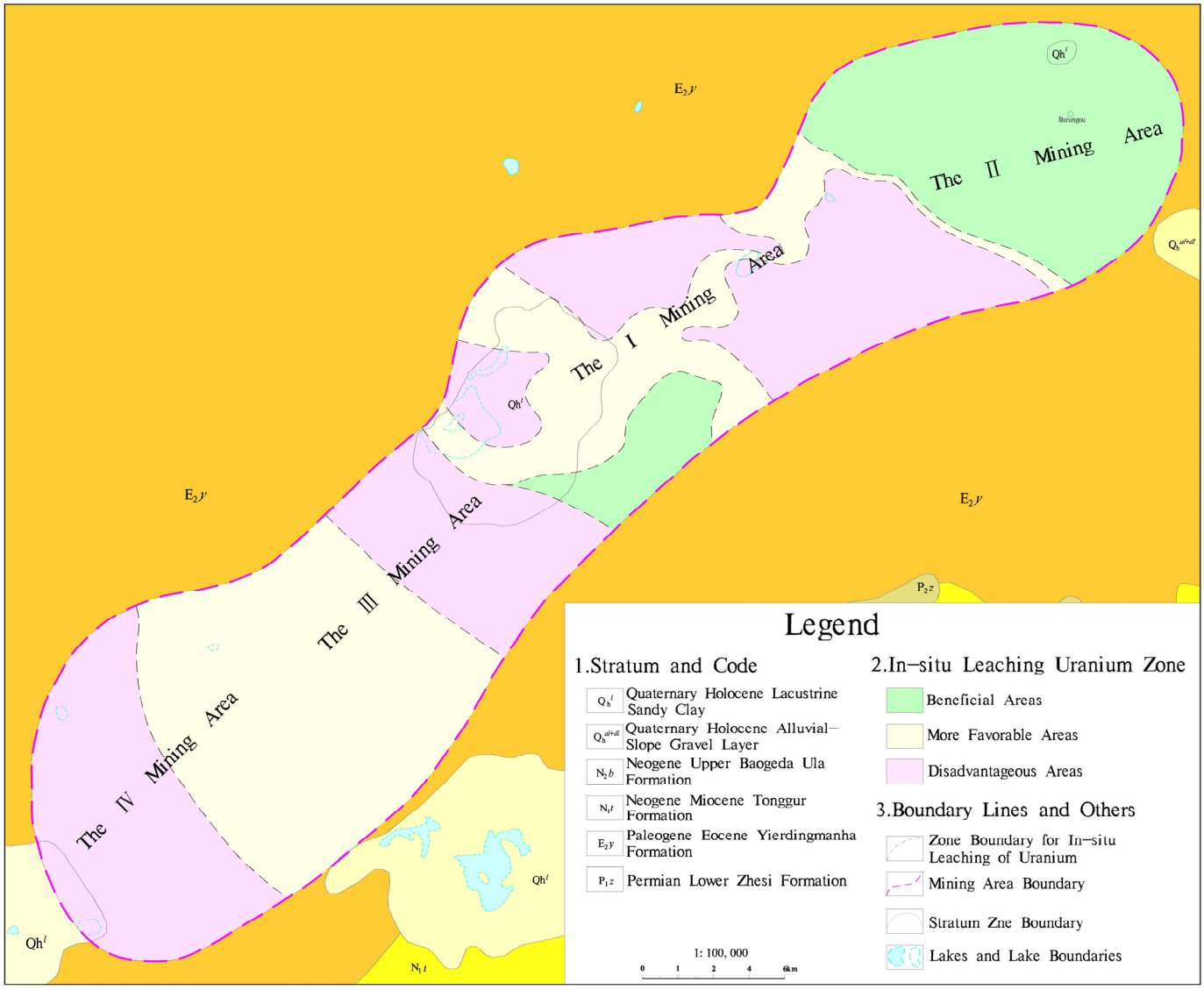

Figure 6. Comprehensive evaluation map of hydrogeological conditions for in situ leaching of sandstone type uranium ore in Luhai mining area.

Table 3. Hydrogeological parameters for pumping test in the Luhai mining area I and surrounding area.

Number	Depth of Well (m)	Well Discharge (m^3/d)	Specific Discharge of a Well (L/S·m)	Drawdown (m)	Hydraulic Conductivity (m/d)	Transmissivity (m^2/d)
SDS14	59	443.28	5.765	0.89	11.01	418.2

(3) Hydrogeological Characteristics of U-hosting Aquifer in Orebodies III-IV

The upper section of the Cretaceous Bayanhua Group Seihantala Formation (K_1bs^3) in the Orebody III–IV area exhibits a gradual thickening trend from southeast to northwest and west, forming a stepped shape. In the southeastern part, the thickness of the Orebody II is only 49.09 m, while in the western region, which serves as the sedimentary center of this stratum, the Orebody IV reaches its maximum thickness with a sedimentary depth exceeding 100 m and reaching up to 124.15~136.19 m.

The thickness of the U-hosting aquifer in the Orebody III-IV area exhibits a consistent pattern with the stratigraphic variation in the upper section of the Saihanbatala Formation, gradually increasing from east to west in a stepped manner (Figure 6). The aquifer

thickness ranges from 32.70 to 48.21 m in the Orebody II area, while exceeding 50 m in the Orebody IV area. The thickness of the aquifer containing water with a grain size greater than coarse sand makes up more than 75% of the total thickness of the aquifer in the deposit. However, this section displays poor sorting and grinding characteristics with angular–subangular particles of varying sizes, accompanied by approximately 10% muddy content which reaches up to around 10–15% in some parts of the Orebody IV area. Moreover, there is relatively loose–dense cementation within the sand layer hosting mineralization. The bottom of the Orebody III-IV aquifer is situated in the middle section of the Cretaceous Sayhantala Formation within the Bayanhua Group (K_1bs^2), primarily composed of mudstone and exhibiting a relatively consistent distribution.

The water yield property of the Orebody III-IV area is generally consistent with the trend of aquifer thickness, gradually deteriorating in a stepped manner from east to west. The eastern part of the Orebody II area exhibits the highest water inflow, ranging from 240 to 1200 m^3/d per well, while the western part of the Orebody IV area experiences a lower water inflow, ranging from 24 to 120 m^3/d per well. In this study, two hydrogeological exploration boreholes were drilled within the Orebody III-IV area and subjected to non-complete well stable flow pumping tests. The results of these tests are presented in Table 4.

Table 4. Hydrogeological parameters of pumping test for Orebody III-IV and surrounding areas in the land–sea mining area.

Number	Depth of well (m)	Location	Aquifer Thickness (m)	Well Discharge (m^3/d)	Specific Discharge of a Well (L/S·m)	Drawdown (m)	Hydraulic Conductivity (m/d)	Transmissivity m^2/d
SZK01	126	Orebody III	78.35	1054.08	1.379	8.85	1.75	137.06
				780.24	1.552	5.82	1.86	146.01
				485.52	2.073	2.71	2.25	176.01
SZK02	158	Orebody IV	27.45	52.70	0.009	67.54	0.035	0.91

The results of the pumping test indicate that the water inflow of a single well in the upper section of the Cretaceous Seihantala Formation, Bayanhua Group, located in the eastern area of Orebody II, is 1054.08 m^3/d with a hydraulic conductivity of 1.75 m/d, demonstrating high-water-yield properties and permeability. Conversely, in the southern area of Orebody IV, the water inflow from a single well in the upper section of the Cretaceous Seihantala Formation is only 52.70 m^3/d with a hydraulic conductivity as low as 0.035 m/d, indicating low-water-yield properties and permeability. The variation in groundwater richness within the Orebody III-IV area can be attributed to an uneven distribution of aquifers.

The TDS of the ore-bearing aquifer in Orebody III-IV, as depicted in Figure 5, ranges from 1243 to 11,757 mg/L, with an average value of 5064 mg/L. This value is generally higher compared to the aquifer groundwater found in the surrounding areas of the mine and other orebodies. The hydrochemical types primarily consist of HCO_3·Cl-Na type and Cl-Na type. The presence of numerous chloride ions (Cl^-) as anions and predominantly sodium ions (Na^+) as cations within the aquifer groundwater indicates a slow water circulation rate, long retention time, and weak regeneration capacity for this particular group. These conditions are conducive to uranium accumulation and mineralization within the aquifer.

4.1.3. Genetic Analysis of Sandstone-Type Uranium Deposits in the Luhai Area

As universally acknowledged, uranium primarily originates from the deep earth crust, with a relatively high concentration in bedrock during the orogenic period. Consequently, the mountainous region at the basin edge serves as an abundant source of uranium and sediment within the basin. Governed by sedimentation processes and influenced by groundwater in ore-bearing aquifers, uranium undergoes a continuous cycle of dissolution,

filtration, migration, precipitation, and enrichment from its source area to form metallogenic belts. This complete oxidation–reduction evolution sequence ultimately leads to the enrichment of uranium into ore [20,26,27,34].

The groundwater in the bedrock fractures at the edge of the Erlian Basin is primarily vertically replenished by atmospheric precipitation, establishing a close hydraulic connection with both precipitation and surface water. This region exhibits a robust and cyclic groundwater circulation, characterized by abundant O_2 and CO_2 content, making it an important zone for the oxidation and dissolution of uranium elements. Subsequently, lateral runoff supplies the basin's loose rock pore water as well as clastic rock fracture pore water. The migration of groundwater runoff leads to changes in the hydrogeological conditions of uranium-rich aquifers, increasing the lithologic detritus composition and enhanced cementation, gradually reducing permeability. Consequently, there is a decrease in groundwater flow rate with slow alternation. Continuous increases in TDS cause water chemical components to gradually reach saturation state. Groundwater transitions from an oxidation environment to a reduction environment as organic matter content increases, accompanied by high concentrations of H_2S and CH_4. This shift slows down the migration rate of uranium ions in groundwater, leading to continuous reduction and precipitation for mineralization formation [22,31,35–38].

From the regional hydrogeological perspective, Orebody I–IV are located in groundwater discharge areas (Figure 4). The migration rate of groundwater in the U-hosting aquifer is slow in the orebodies due to the poor permeability. The lack of hydraulic connection with external water bodies, such as meteoric water or surface water, is conducive to the reduction, enrichment and mineralization of uranium. Notably, according to the thickness of the U-hosting aquifer and the hydrogeological parameters (Figure 4, Tables 1–4), the permeability and alternation of circulation of the aquifer in Orebody II are relatively best and fastest compared with other U-hosting aquifers. Furthermore, the content of uranium and radioactive element in the U-hosting aquifer is also an important indicator for evaluating the scale of uranium mineralization. The ranges of uranium and ^{238}U concentration in groundwater samples in Orebody II (DATANG, SDS87, SDS23, Figure 4) are from 3.82 to 52.3 μg/L and from 48.1 to 659 mBq/L, respectively, higher than those in Orebody III-IV (SDS51, SZK01, SZK02, Figure 4), with uranium and ^{238}U concentrations from 0.34 to 19.4 μg/L and from 4.28 to 244 mBq/L, respectively. This indicates that the U-hosting aquifer of Orebody II is able to receive more recharge of U-rich groundwater from upstream aquifers, resulting in a better metallogenic effect.

4.2. Evaluation of Suitability for Leaching and Mining of Sandstone-Type Uranium Ore

Based on the analysis of hydrogeological conditions for each orebody in both the onshore and offshore mining areas, and by referring to the hydrogeological classification method used for in situ sandstone-type uranium deposits, a hydrogeological classification was conducted for each orebody within these areas. The results of this classification are presented in Table 5.

Table 5. Classification of hydrogeological conditions of each orebody in the Luhai area.

Number / Classification Index	Orebody II	Orebody I	Orebody III	Orebody IV
Permeability	Relatively Strong	Medium	Relatively Strong	Medium
Confined	Strong	Strong	Strong	Strong
Water yield	Large	Relatively Small	Large	Relatively Small
Underground water level	Medium	Medium	Medium	Medium
Hydrogeological complexity	Medium	Medium	Medium	Medium

The in situ hydrogeological conditions of sandstone-type uranium deposits are comprehensively evaluated based on a comprehensive reference to five major categories of indexes, including permeability, pressure-bearing capacity, unit water inflow, groundwater depth, and hydrogeological complexity. This evaluation encompasses 14 aspects:

single-well water inflow, hydraulic conductivity, stability of the deposit's roof and floor (hydrogeological structure), thickness of the ore-bearing aquifer, rock particle size, clay content, sorting characteristics, cementation degree, water depth and head height (water level), ratio of hydraulic conductivity between ore-bearing and non-ore-bearing layers, groundwater mineralization level and carbonate content. The evaluation parameters and grades can be found in Table 6.

Table 6. Evaluation grade of hydrogeological conditions of ground immersion.

Evaluation Parameter	Evaluation Grade of Hydrogeological Conditions of Ground Immersion			
	Most Advantageous	**Advantageous**	**Generally Favorable**	**Unfavorable**
Water yield (m^3/d)	1200–240	240–120	120–24	≥1200 or <24
Hydraulic conductivity (m/d)	10–1	1–0.5	0.5–0.1	≥10 or <0.1
Hydrogeological structure	Stable watertight top and bottom anchor		Poor stable watertight top and bottom anchor	Missing watertight top and bottom anchor
Thickness of ore-bearing aquifer (m)	20–30	30–50, 10–20	50–100	<10 or ≥100
Rock granularity	Coarse sand	Medium sand	Fine sand	Silty sand
Clay content (%)	<10	10–20	20–30	≥30
Sorting	Good	Preferably	Medium	Poor
Cementation degree	Loose	Relatively loose	Relatively compact	Compact
Underground water level (m)	<50	50–100	100–150	≥150
Head (m)	≥100	≥50	≥20	<20
Ratio of hydraulic conductivity between ore-bearing and non-ore-bearing layers	≥1	1–0.75	0.75–0.5	<0.5
Ratio of thickness of ore-bearing aquifer to ore layer	1–5		5–10	≥10
TDS (g/L)	<1	1–3	3–5	≥5
Carbonate content (%)	<1	1–2	2–3	≥3

According to the hydrogeological analysis of both onshore and offshore mining areas, significant changes in hydrogeological conditions can be observed. These changes primarily include water inflow, hydraulic conductivity, roof structure of the deposit, thickness of the ore-bearing aquifer, and salinity of groundwater. Evaluation indexes affecting in situ leaching of sandstone uranium deposits in these areas consist of water inflow from a single well, hydraulic conductivity, hydrogeological structure of the deposit, thickness ratio between the ore-bearing aquifer and uranium ore bed, and salinity of groundwater (Table 6). Comprehensive evaluation results indicate that most parts of the Orebody II area as well as the southwest region of the Orebody I are favorable for in situ leaching mining. Additionally, certain regions, including part of northwest area in Orebody II, central area in Orebody I, western area in Orebody II and eastern area in IV, are more suitable for this type of mining method, whereas other areas are deemed unfavorable for implementing an in situ leaching approach (Figure 6).

The presence of a continuous and stable impermeable roof and floor (such as mudstone, argillaceous siltstone, etc.) in the ore-bearing aquifer plays a crucial role in influencing in situ leaching mining operations. This factor significantly reduces the seepage range of the leaching solution within the aquifer, minimizes the dilution of the leaching solution, and decreases raw material consumption during production processes. Moreover, it effectively prevents contamination of adjacent upper and lower aquifers by preventing the flow of leaching solution into these areas. Additionally, considering gravity differentiation during the seepage process from injection to pumping holes is essential for successful in situ mining operations.

The main uranium ore layers with industrial value are predominantly located at the bottom of the aquifer in the Luhai area. The underlying water-proof roof, primarily composed of thick mudstone, exhibits a stable distribution pattern that effectively prevents pollution of the underlying aquifer caused by downward seepage of solution immersion liquid due to gravity differentiation. However, there is poor continuity in the water-proof roof within the land and sea area, particularly in the northern region of Orebody II and eastern/western regions of Orebody I, where the distribution becomes unstable. In these areas, the thickness gradually decreases or transitions into a weak permeable layer

characterized by a high mud content mainly consisting of argillaceous siltstone and silty mudstone. Therefore, an important hydrological factor influencing in situ mining is the thickness of this water-proof roof. During in situ uranium mining operations within these two orebodies, it is crucial to properly control water pressure to prevent excessive passage over weak permeable layers and subsequent contamination of upper groundwater.

5. Conclusions

By conducting hydrogeological surveys, drilling, field pumping tests, and a comprehensive analysis of regional water chemical characteristics, we have obtained a thorough understanding of the current state and temporal variations in hydrogeological conditions within onshore–offshore sandstone-type uranium deposits. This has enabled us to assess the mining technical conditions of these deposits and evaluate the feasibility of in situ uranium mining in the study area.

(1) The distribution of Neogene clastic pore fracture water-bearing rocks exhibits instability, significant thickness variation, and poor continuity. Besides a small proportion of thick sandstone and conglomerate, the predominant lithology is muddy with limited water saturation. As one of the primary aquifers in the study area, the Paleogene clastic pore fracture water-bearing rocks demonstrate a gradual decline in water saturation from northeast to southwest. The upper section of the Cretaceous Bayanhua Group Saihanbatala Formation comprises the principal mineral aquifer layer characterized by coarse particles primarily composed of coarse sandstone and conglomerate. These layers exhibit a high mud content and varying degrees of cementation ranging from loose to dense, generally resulting in good-to-excellent water saturation levels with consistent layer thickness.

(2) From the regional hydrogeological perspective, the hydrodynamic conditions of groundwater in the study area are generally unfavorable, characterized by slow groundwater flow resulting from low permeability. These are conducive to the reduction, enrichment and mineralization of uranium. Nonetheless, distinct hydrogeological conditions, particularly variations in hydrodynamic changes in groundwater, ultimately determine the observed scale of mineralization across different orebodies. Therefore, compared to the other orebodies, the metallogenic effect of the U-hosting aquifer in II is better according to the hydrogeological conditions and the content of uranium and radioactive element.

(3) The comprehensive assessment of hydrogeological conditions for in situ mining indicates that the key evaluation factors influencing this method include single-well water inflow, hydraulic conductivity, hydrogeological structure of the deposit, thickness of the ore-bearing aquifer, ratio of ore-bearing aquifer to uranium ore bed thickness, and groundwater mineralization. Based on these factors, the onshore and offshore mining areas can be classified into three categories: favorable area, more favorable area, and unfavorable area for in situ mining. Specifically, most parts of Orebody II and the southwest region of Orebody I are considered favorable areas for in situ mining. The northwest section of Orebody II, middle part of Orebody I, west side of Orebody II and east side of Orebody IV are categorized as more favorable areas for in situ mining. Conversely, other regions are deemed unfavorable areas for in situ mining.

Author Contributions: Conceptualization, L.M. and W.J.; methodology, L.M.; software, H.N. and W.J.; validation, L.M., H.N. and Y.S.; formal analysis, Y.S.; investigation, L.M., W.W. and C.T.; resources, W.W. and C.T.; data curation, L.M. and H.N.; writing—original draft preparation, L.M. and H.N.; writing—review and editing, W.J. All authors have read and agreed to the published version of the manuscript.

Funding: This research was funded by the National Key Research and Development Program of China (2023YFC2906700); the National Natural Science Foundation of China (42302299); the program of China Geological Survey (DD20230426).

Data Availability Statement: Data available in a publicly accessible repository.

Conflicts of Interest: The authors declare no conflicts of interest.

References

1. Cobb, J. World Nuclear Performance Report 2017. *VGB PowerTech* **2017**, *12*, 97.
2. Tsouris, C. Uranium extraction: Fuel from seawater. *Nat. Energy* **2017**, *4*, 17022. [CrossRef]
3. Wu, Y.; Cui, W.; Zhang, C.; Liang, R.; Qiu, J. Regenerable, anti-biofouling covalent organic frameworks for monitoring and extraction of uranium from seawater. *Environ. Chem. Lett.* **2021**, *19*, 1847–1856. [CrossRef]
4. Ma, C.; Gao, J.; Wang, D.; Yuan, Y.; Wen, J.; Yan, B.; Zhao, S.; Zhao, X.; Sun, Y.; Wang, X. Sunlight Polymerization of Poly(amidoxime) Hydrogel Membrane for Enhanced Uranium Extraction from Seawater. *Adv. Sci.* **2019**, *13*, 1900085. [CrossRef]
5. Yuan, Y.; Yu, Q.; Cao, M.; Feng, L.; Feng, S.; Liu, T.; Feng, T.; Yan, B.; Wang, Z.; Guo, N. Selective extraction of uranium from seawater with biofouling-resistant polymeric peptide. *Nat. Sustain.* **2021**, *8*, 708–714. [CrossRef]
6. Wang, Y.; Lin, Z.; Liu, Q.; Zhu, J.; Liu, J.; Yu, J.; Chen, R.; Liu, P.; Wang, J. Simple one-step synthesis of woven amidoximated natural material bamboo strips for uranium extraction from seawater. *Chem. Eng. J.* **2021**, *425*, 131538. [CrossRef]
7. Liu, Z.; Lan, Y.; Jia, J.; Geng, Y.; Dai, X.; Yan, L.; Hu, T.; Chen, J.; Matyjaszewski, K.; Ye, G. Multi-scale computer-aided design and photo-controlled macromolecular synthesis boosting uranium harvesting from seawater. *Nat. Commun.* **2022**, *1*, 3918. [CrossRef] [PubMed]
8. Chen, J.; Zeng, W.; Wang, J.; Ma, L.; Yang, J. Analysis of supply and demand situation of uranium resourcesin the world and China. *N. China Geol.* **2021**, *44*, 25–34. (In Chinese)
9. Cumberland, S.; Douglas, G.; Grice, K.; Moreau, J. Uranium mobility in organic matter-rich sediments: A review of geological and geochemical processes. *Earth Sci. Rev.* **2016**, *1*, 160–185. [CrossRef]
10. Chen, L.; Chen, Y.; Feng, X.; Li, J.; Guo, H.; Miao, P.; Jin, R.; Tang, C.; Zhao, H.; Wang, G.; et al. Uranium occurrence state in the Tarangaole area of the Ordos Basin, China: Implications for enrichment and mineralization. *Ore Geol. Rev.* **2019**, *115*, 103034. [CrossRef]
11. Bali, E. Economic geology: Uranium-ore giants. *Nat. Geosci.* **2012**, *2*, 96–97. [CrossRef]
12. Cuney, M. The extreme diversity of uranium deposits. *Miner. Deposita* **2009**, *1*, 3–9. [CrossRef]
13. Cuney, M. Evolution of Uranium Fractionation Processes through Time: Driving the Secular Variation of Uranium Deposit Types. *Econ. Geol.* **2010**, *3*, 553–569. [CrossRef]
14. Mills, S.; Birch, W.; Maas, R.; Phillips, D.; Plimer, I. Lake Boga Granite, northwestern Victoria: Mineralogy, geochemistry and geochronology. *J. Geol. Soc. Aust.* **2008**, *55*, 281–299. [CrossRef]
15. Bargar, J.; Williams, K.; Campbell, K.; Long, P.; Stubbs, J.; Suvorova, E.; Lezama-Pacheco, J.; Alessi, D.; Stylo, M.; Webb, S. Uranium redox transition pathways in acetate-amended sediments. *Proc. Natl. Acad. Sci. USA* **2013**, *12*, 4506–4511. [CrossRef]
16. Yue, S.; Wang, G. Relationship between the hydrogeochemical environment and sandstone-type uranium mineralization in the Ili basin, China. *Appl. Geochem.* **2011**, *26*, 133–139. [CrossRef]
17. Zhao, H.; Ao, C.; Li, J.; Chen, L.; Zhang, B.; Miao, P.; Si, Q.; Zhu, Q.; Yu, R.; Chen, Y. Occurrence and mechanism of uranium enrichment with a unique eolian sedimental environment in the Pengyang uranium deposit, Ordos Basin. *Ore geol. Rev.* **2022**, *141*, 104641. [CrossRef]
18. Zhang, J.; Li, Z.; Su, X.; Tan, Y.; Li, S.; Su, Y.; Li, J.; Deng, P.; Xu, L.; Pan, Z. Development Strategy of Nuclear Energy Mineral Resources. *Strateg. Study CAE* **2019**, *1*, 113–118. (In Chinese) [CrossRef]
19. Jin, R.; Yu, R.; Yang, J.; Zhou, X.; Teng, X.; Wang, S.; Si, Q.; Zhu, Q.; Zhang, T. Paleo-environmental constraints on uranium mineralization in the Ordos Basin: Evidence from the color zoning of U-bearing rock series. *Ore Geol. Rev. J. Compr. Stud. Ore Genes. Ore Explor.* **2019**, *104*, 175–189. [CrossRef]
20. Chen, G.; Sun, Z.; Nie, F.; Li, C.; Zhen, Y.; Zhou, Z. Hydrogeochemical characteristics of the sandstone-hosted uranium mineralization in northern Ordos Basin, China. *Ore Geol. Rev.* **2020**, *126*, 103769. [CrossRef]
21. Tao, Z.; Jiao, Y.; Wu, L.; Rong, H.; Zhang, F.; Yue, L. Architecture of a sandstone uranium reservoir and the spatial distribution of its internal carbonaceous debris: A case study of the Zhiluo Formation, eastern Ordos Basin, northern China. *J. Asian Earth Sci.* **2020**, *191*, 104219. [CrossRef]
22. Bhattacharyya, A.; Campbell, K.; Kelly, S.; Roebbert, Y.; Weyer, S.; Bernier-Latmani, R.; Borch, T. Biogenic non-crystalline U(IV) revealed as major component in uranium ore deposits. *Nat. Commun.* **2017**, *8*, 15538. [CrossRef]
23. Dai, S.; Yang, J.; Ward, C.; Hower, J.; Liu, H.; Garrison, T. Geochemical and mineralogical evidence for a coal-hosted uranium deposit in the Yili Basin, Xinjiang, northwestern China. *Ore Geol. Rev.* **2015**, *70*, 1–30. [CrossRef]
24. Campbell, K.; Kukkadapu, R.; Qafoku, N.; Peacock, A.; Lesher, E.; Williams, K.; Bargar, J.; Wilkins, M.; Figueroa, L.; Ranville, J. Geochemical, mineralogical and microbiological characteristics of sediment from a naturally reduced zone in a uranium-contaminated aquifer. *Appl. Geochem.* **2012**, *27*, 8. [CrossRef]
25. Miller, A.; Rodriguez, D.; Honeyman, B. Upscaling Sorption/Desorption Processes in Reactive Transport Models to Describe Metal/Radionuclide Transport: A Critical Review. *Environ. Sci. Technol.* **2010**, *44*, 7996–8007. [CrossRef]
26. He, Y.; Rong, H.; Huang, K.; Peng, H.; Wan, J. Hydrogeochemistry Characteristics and Uranium Metallogenic Conditions of the Groundwater in Yili Basin. *Saf. Environ. Eng.* **2019**, *1*, 7–13. (In Chinese)
27. He, Y.; Rong, H.; Huang, K.; Wang, Z.; Wan, J. Relationship between uranium mineralization and hydrologic condition in Yili Basin. *Bullet Geol. Sci. Technol.* **2020**, *5*, 139–147. (In Chinese)
28. Yang, J.; Ao, C.; Meng, L.; Teng, X.; Wei, X.; Wang, D.; Feng, P.; Yu, H. Analysis of neogeneuranium reservoir development and uranium mineralization hydrogeological conditions in southwest Qaidam basin. *Sci. Technol. Eng.* **2022**, *22*, 931–938. (In Chinese)

29. Hou, B.; Keeling, J.; Li, Z. Paleovalley-related uranium deposits in Australia and China: A review of geological and exploration models and methods. *Ore Geol. Rev.* **2017**, *88*, 201–234. [CrossRef]
30. Liu, C.; Shi, Z.; Zachara, J. Kinetics of Uranium(VI) Desorption from Contaminated Sediments: Effect of Geochemical Conditions and Model Evaluation. *Environ. Sci. Technol.* **2009**, *43*, 6560–6566. [CrossRef]
31. Lu, C.; Xiu, W.; Guo, H.; Lian, G.; Yang, B.; Zhang, T.; Bi, E.; Shi, Z. Multi-Isotope Based Identification and Quantification of Oxygen Consuming Processes in Uranium Hosting Aquifers with CO_2 + O_2 In Situ Leaching. *Water Resour. Res.* **2023**, *3*, e2022WR033980. [CrossRef]
32. Su, X.; Liu, Z.; Yao, Y.; Du, Z. Petrology, mineralogy, and ore leaching of sandstone-hosted uranium deposits in the Ordos Basin, North China. *Ore Geol. Rev. J. Compr. Stud. Ore Genes. Ore Explor.* **2020**, *127*, 103768. [CrossRef]
33. Liu, B.; Yan, G.; Ma, Y.; Scheuermann, A. Measurement of In-Situ Flow Rate in Borehole by Heat Pulse Flowmeter: Field-Case Study and Reflection. *Geosciences* **2023**, *13*, 146. [CrossRef]
34. Zhang, Z.; Fan, H.; He, F.; Liu, H.; Jia, L.; Yi, L.; Yang, M. Features of hydrogeochemistry and uranium metallogenesis in Binxian County area on the southern margin of Ordos Basin. *Geol. Bull. China* **2017**, *36*, 503–510. (In Chinese)
35. Chen, Z.; Man, A.; Chen, X.; Xiong, Y.; Shao, J.; Wang, L.; Sun, P. Relationship Between Hydrogeology and Sandstone Uranium Mineralization in Sedimentary Basin: A Case Study of Sandstone Uranium Survey in the Kailu Depression of the Songliao Basin. *Geotecton. Et Metallog.* **2021**, *6*, 1174–1184.
36. Brown, S.; Basu, A.; Christensen, J.; Reimus, P.; Heikoop, J.; Simmons, A.; Woldegabriel, G.; Maher, K.; Weaver, K.; Clay, J. Isotopic Evidence for Reductive Immobilization of Uranium Across a Roll-Front Mineral Deposit. *Environ. Sci. Technol.* **2016**, *50*, 6189–6198. [CrossRef] [PubMed]
37. Cheng, Y.; Jin, R.; Cuney, M.; Petrov, V.; Miao, P. The strata constraint on large scale sandstone-type uranium mineralization in Meso-Cenozoic basins, northern China. *Acta Geol. Sin.* **2024**, *98*, 1953–1976. (In Chinese)
38. Sheng, Y.; Baars, O.; Guo, D.; Whitham, J.; Srivastava, S.; Dong, H. Mineral-bound trace metals as cofactors for anaerobic biological nitrogen fixation. *Environ. Sci. Technol.* **2023**, *57*, 7206–7216. [CrossRef]

Disclaimer/Publisher's Note: The statements, opinions and data contained in all publications are solely those of the individual author(s) and contributor(s) and not of MDPI and/or the editor(s). MDPI and/or the editor(s) disclaim responsibility for any injury to people or property resulting from any ideas, methods, instructions or products referred to in the content.

water

MDPI

Article

The Characterization of Aquifer Parameters in Using Skimming Tubewells Through the Pumping Test Method: A Case Study of Tando Allahyar

Xiufang Yang [1], Muhammad Uris Mirjat [2], Abdullah Baloch [2], Mashooque Ali Talpur [2], Shafi Muhammad Kori [3], Rajesh Kumar Soothar [2], Sher Ali Shaikh [2], Irshad Ali Mari [2] and Farman Ali Chandio [2,*]

[1] School of Transportation Engineering, Yangzhou Polytechnic Institute, Yangzhou 225127, China; xiufanghappygirl@163.com
[2] Faculty of Agricultural Engineering and Technology, Sindh Agriculture University, Tandojam 70050, Pakistan; mumirjat@sau.edu.pk (M.U.M.); abdullahsau@gmail.com (A.B.); matalpur@sau.edu.pk (M.A.T.); rk_engr195@yahoo.com (R.K.S.); sashaikh@sau.edu.pk (S.A.S.); irshad_mari@hotmail.com (I.A.M.)
[3] USPCAS-W, Mehran University of Engineering and Technology, Jamshoro 76060, Pakistan; shafikori@yahoo.com
* Correspondence: farman_chandio@hotmail.com

Abstract: Sindh is in the lower reaches of the Indus River; it is most vulnerable to a variety of upstream water development challenges. The aim of this research was to determine aquifer characteristics in the command area of Tando Allahyar-II distributary within the culmination of underground water potential. The hydraulic properties of the aquifer as well as the susceptibility of the formation to tedious extraction and saltwater upcoming were recognized. Three pumping tests were performed at head, middle, and tail reaches along the selected distributary. The drawdowns were measured at head reach (5.1667 h), at middle reach (6.0 h), and at tail reach (19.667 h) of the selected distributary by performing the pumping tests. Groundwater levels were lower at the tail reach compared to those at the head and middle reaches, likely due to a higher concentration of tubewells in the lower reach. The head and middle reaches showed higher groundwater levels, possibly due to constant head conditions promoting infiltration and recharge. The pumping test versus drawdown analysis revealed that the tubewells should be run with 7-h (on) and 4-h (off) operation. Further, the tubewells at all reaches (head, middle, and tail) should be closed for a minimum of 4 h between operations. This strategy would allow safe groundwater extraction, maintain water quality, and prevent water table depletion in the study area. The hydrodynamic and hydro-salinity behaviors were scrutinized in PWMIN 5.3 (version) by means of the MODFLOW mode. The results were estimated to compare the calibration and validation simulation outcomes using measured data. The model was successfully calibrated, and the root mean square (RMS) value of the head tubewell varied between 0.024 and 0.108, whereas it speckled between 0.0166 and 0.0349 for the middle tubewell and between 0.0659 and 0.0069 for the tail tubewell. The RMS values for hydrodynamic behavior for the head, middle, and tail reaches were less than 10%. These values represent a suitable match between the observed and simulated heads when a water table depletion of 1 to 2 m was observed due to extreme pumping. However, the average relative error values, for all validated procedures, were less than 10%.

Keywords: aquifer characterization; skimming tubewells; pumping test analysis; groundwater extraction; MODFLOW

1. Introduction

Groundwater plays a crucial role in sustaining human life and agriculture worldwide. It is a vital resource for meeting daily needs and irrigation requirements, especially in emerging nations [1,2]. Large quantities of groundwater are present beneath the Earth's surface, and groundwater often requires minimal treatment, making it a cost-effective

option for agriculture and domestic water supplies. The prompt growth in groundwater supplies had led to the swift falling of water heights in various portions of the Afro-Asian nations, triggering surface pits to be dried up, and through a specific influence, poor growers are unable to excavate their bores due to the falling water table heights. In sea-side ranges, falling water table heights are correspondingly related with the brackish water, leading to lower crop returns, and with passage of time, they lose both abundant land and water source bores. These complications remain awfully serious in the zones triggered through solid rocks. In the meantime, the solid rock aquifers have inadequate storing volume in addition to the stores' solitary inadequate quantity. Additionally, the climatic situations in the semi-arid areas, with little or inconstant precipitation, limit the recharges and promote the formations that become vulnerable to scarcity [3].

As cultivation is the prime user of water and the need for water will rise quicker due to agriculture on both industrial and domestic sides; thus, the developing countries will be at risk. Climate change is the biggest problem, with wetter zones typically changing into even wetter and drier zones changing into even drier zones. However, the increasing global demand for water, particularly in agriculture, has led to significant challenges. The World Water Development Report indicates that water demand is growing at approximately 1% annually due to economic development and population growth. This trend is expected to continue over the next decades, with developing countries facing the highest risk. Currently, an estimated 3.6 billion people live in water-scarce regions, a number that could increase to 4.8–5.7 billion by 2050 [4]. Climate change further exacerbates this situation, with wet regions generally becoming wetter and dry regions becoming drier. This shift in precipitation patterns affects groundwater recharge, especially in semi-arid regions with already limited and variable rainfall. The intensification of groundwater usage has been particularly notable in South Asia since the 1970s, contributing significantly to the region's agricultural productivity. However, this has also led to overexploitation in many areas, resulting in aquifer depletion and groundwater contamination [5,6]. A 2012 report by the National Academy of Sciences revealed that groundwater overuse, primarily driven by irrigated agriculture, is causing water table declines at rates that surpass the impacts of glacial melt due to climate change [7,8].

Pakistan, as an arid country, heavily relies on groundwater for irrigated agriculture [9–11]. The development of groundwater resources in Pakistan began in the 1960s with the installation of large-capacity tubewells under the Salinity Control and Reclamation Project (SCARP). Since then, the number of small-capacity private tubewells has grown exponentially, reaching approximately 1.2 million, with 800,000 located in Punjab alone [12]. In the Indus Basin, where most of Pakistan's agriculture is concentrated, there are significant spatial and temporal variations in groundwater quality [13]. The continuous and intensive use of groundwater for irrigation is leading to soil salinization, as groundwater typically contains higher salt concentrations than canal water. This situation is further complicated by the practice of mixing saline and non-saline water, which is common in Pakistan but may have long-term impacts on soil salinity. Since the 1960s, groundwater usage and large-scale extraction was started when sixteen thousand seven hundred tubewells were installed by SCARP for addressing the issues of waterlogging and salinity with a median capability of 0.080 m s^{-1} [14].

In the Indus basin, there are extensive three-dimensional and time-based differences in underground water superiority, and this is because of the underground water sample interchange within the formation. The lenses of unpolluted groundwater rarely exist adjacent to the main waterways and channels, with a huge amount of restoration of unpolluted leakage water. Nonetheless, the class of groundwater variations is useless when horizontally far from the waterways. The continuous and exhaustive usage of groundwater for cultivation is accumulating plenty of salts, thereby causing salinization as groundwater contains more salts than water from canals. It has been noted that, until a soil depth of 370 mm, the total dissolved solids (TDSs) of groundwater were 1000 mg L^{-1}, which

changed the maximum depth of 300 mm into saline soil due to the infiltration of alkali, thereby reducing crop yield.

Pakistan is one of the Asian countries where 70% of privately operated tubewells are installed in the commands of canals and using groundwater conjunctively with canal water. The challenges facing groundwater management in Pakistan are multifaceted. The aquifers are recharged naturally from precipitations, canal movements, earthen channels, minors, water courses, and losses caused by the application of water to the cultivated fields. Consequently, in order to use these resources in a safe and sustainable manner, it is important to evaluate the quality of groundwater by modeling. In the Lower Indus Basin, groundwater modeling studies have been conducted at small spatial scales to study groundwater hydraulics and hydro-salinity behavior [15–17]. These studies were conducted mostly in the Sindh province as the fresh groundwater of this region is available in the upper shallow layer, which varies from place to place. Qureshi et al. [10] clearly demonstrated that the upper shallow fresh layer rests mostly over a deep saline groundwater layer, which could be mixed with fresh water through due to the continuous pumping of water by the farmers of this region. Hence, in several farming areas of the Rohri canal, the poor-quality tubewell water has been observed. Hence, the main reason for subsequent salinization and reduction in food production is the use of marginal quality of groundwater [1,18]. If unexamined groundwater pumping waters were continued in such areas, irrigation tubewells will not be able to pump with the current water quality. Current research is aimed to address such scenarios and to develop regional hydrogeological groundwater flow models. Prediction trends have been made through the application of MODFLOW for various scenarios/stress periods. The model has been calibrated and validated against observed real data from the installed piezometers. The groundwater management strategies have been developed for effective use in future.

2. Materials and Methods

2.1. Study Area

The Tando Allahyar-II distributary command area, located in the Tando Allahyar district, was selected as the study area (Figure 1). The command area of Tando Allahyar-II distributary covers 5486 hectares. Most of this area is situated in the serpentine flood plain of the Indus River and is characterized by abandoned waterways, old meandering scars, embankments, dams, and bars. The geological profile of the pumping sites reveals that the upper layers consist of predominantly clay soil, ranging in thickness from 0.5 m to 25.91 m. Below these clay layers, the aquifer is primarily composed of sandy textures. The distributary's head works are situated at coordinates 25°33′35″ N, 68°38′59″ E, with an elevation of 26 m, while the tail of the distributary is positioned at coordinates 25°27′13.74″ N, 68°41′56.08″ E, with an elevation of 20 m.

Three tubewells operational within the command area of the distributary were chosen to assess the hydrodynamic performance and salinity of the groundwater. The selected tubewells are located on the right bank of the Naseer canal and symbolize within the administrative boundary of the Tando Allahyar district. These tubewells were strategically selected to represent the head, middle, and tail reaches of the distributary. The key features of selected tubewells are listed in Table 1.

At one of the three tubewell sites, specifically at the tail reach, two types (single and nested) piezometers/observation wells were installed. These installations were designed to evaluate water level variations and vertical changes in water status over time during the pumping test. The hydrodynamic data, which include fluctuations in water level with respect to time, were used to determine aquifer properties. Concurrently, hydro-salinity and solute-transport data, particularly variations in water quality, were utilized to estimate saline-water upcoming beneath the pumping well during the test. For the remaining two tubewell sites, individual piezometers were installed at each location. Two piezometers were placed at each of these sites to collect water fluctuation data, which were essential for estimating aquifer property parameters.

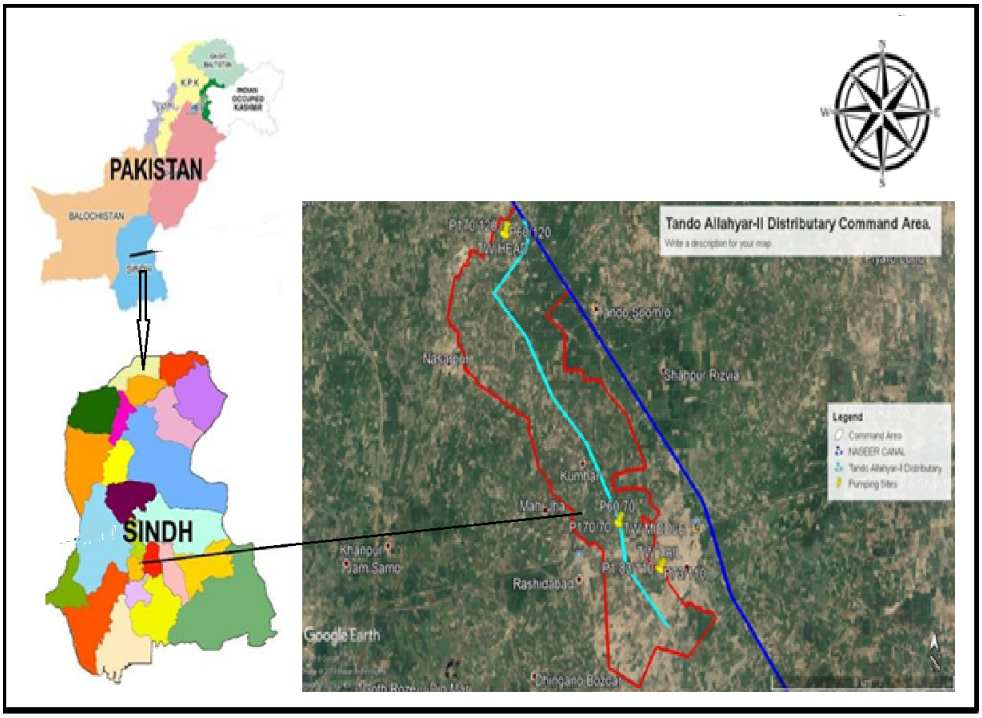

Figure 1. The red color line shows the command area map of Tando Allahyar-II distributary (blue line shows Naseer canal and light blue shows the Tando Allahyar-II distributary).

Table 1. Salient features of selected tubewells.

Description	Head	Middle	Tail
Name of watercourse	3R	11R	13L
Total depth of bore drilled (m)	76.2	59.436	67.056
Length of strainer (m)	33.538	30.48	33.538
Diameter of strainer pipe (cm)	30.48	30.48	30.48
Length of delivery pipe (m)	3.048	1.528	1.528
Diameter of delivery pipe (cm)	15.24	15.24	15.24
Motor horsepower (H.P)	25	50	25
EC of pumped water (ppm)	647	810	1500
Static water level (m)	5.7912	6.2484	8.001
Capacity (cumec)	0.03341	0.02945	0.031998
Distance from T.A. distry (m)	3289	684	2668
Distance from Naseer canal (m)	1253.0328	3591.7632	2735.8848

2.2. Geology of the Study Area

The geological map of the Tando Allahyar district is shown in Figure 2. The district Tando Allahyar is located on the left bank of the Indus River. Geologically, it mostly contains alluvium, sand, silt, and gravel. The predominantly southern-based lithology of the Indus Basin can be divided into five sedimentary units: basal sand unit, lower shale, middle sand unit, upper shale, and upper sand. The Upper Goru sequence of Middle to Late Cretaceous conformably overlies the Lower Goru formation that consists of mainly marl and calcareous sandy clay occasionally interblended with silt and limestone. The main recharging source of aquifer recharging in the study area is the Naseer Branch canal. This canal water seeps into sediments and recharges groundwater aquifers. This area is rich in fresh groundwater up to 100 m; this is due to the historical Indus courses of fresh water for many centuries before the 1890s. The groundwater quality at deeper depths is highly saline. However, a layer of fresh water of varying quality is present with varying

thickness of 75 to 125 m of the aquifer in the areas of favorable lithologies where sources of groundwater recharge are available.

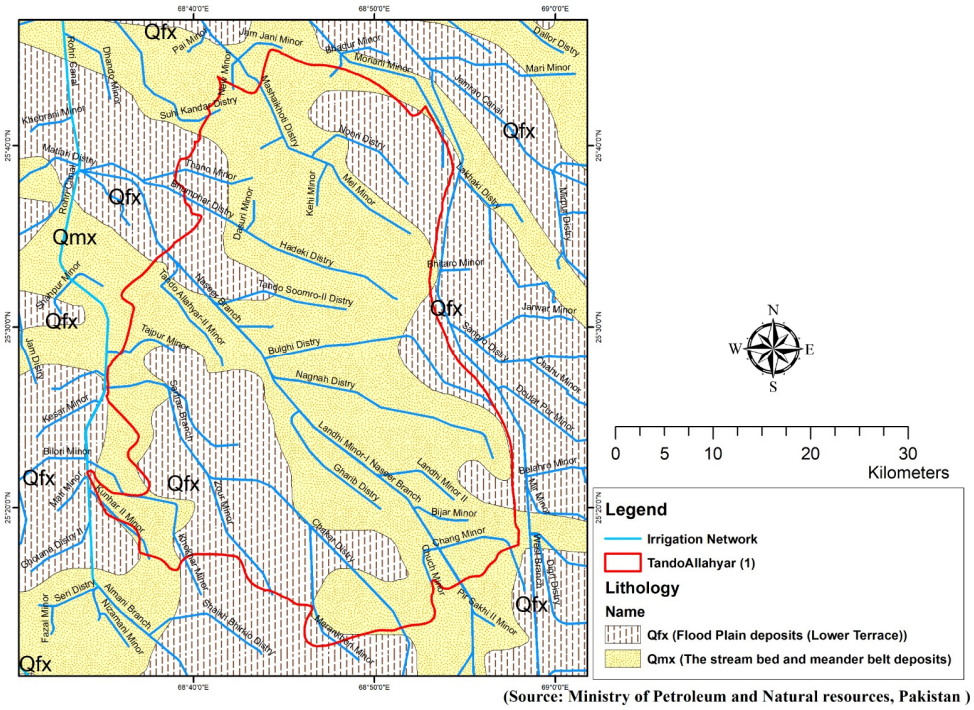

Figure 2. Geological map of Tando Allahyar district.

2.3. Piezometer Installation

The literature was reviewed to decide the number of piezometers required to determine the aquifer properties. This review suggests, i.e., T and S [19], that a single piezometer is enough to characterize the aquifer-related properties. As per British standards, only one observation well is enough for the satisfactory determination of aquifer properties. Thus, two piezometers were installed near each selected pumping site. The distance from the tube to the piezometer depends on many factors, such as soil lithology, tubewell performance, and emissions.

2.3.1. Nested Piezometers

A bunch of 5 piezometers, each having PVC pipes of a 1.27 cm diameter, were installed in the vicinity of pumping wells and placed at various depths of the corresponding point. These piezometers were used to obtain hydro-salinity data. Four special piezometers/observation wells were made of PVC pipes, having a 3.175 cm diameter. The PVC pipes, at their lower end, were connected with a 3.048 m long strainer. These piezometers were established at suitable intervals (i.e., 1.83 m, 14.02 m, 43.89 m, and 70.1 m). They also served as observation wells to assess the hydrodynamic data within the scope of the cone of depression for a given tubewell where these nested piezometers were installed. The details of the piezometer/observation well installations are described in Tables 2 and 3.

Table 2. Details of individual piezometers at the head and middle reaches.

Site	Piezometer Distance (m)	Piezometer Depth (m)	Strainer at the Bottom (m)
Head	18.288	51.816	3.048
Middle	18.288	51.816	3.048

Table 3. Installation of individual piezometers at the tail reach.

Sr. No	No. of Piezometers	Distance of Piezometers from Tubewell (m)	Bore Depth (m)
01	P1	1.8288	50.292
02	P2	14.0208	50.292
03	P3	43.8912	50.292
04	P4	70.104	50.292

2.3.2. Pumping Test

The pumping test was conducted using three tubewells that were installed at the research field. The test readings were taken when the steady pumping flow was attained. Throughout the test, the hydrodynamic data, i.e., hydraulic heads/drawdown(s), were measured from the single piezometer(s). A water-level pointer was used to record changes in the water level at different time intervals (t). The hydro-salinity data, i.e., the variation in the water state in the perpendicular path below the tubewell sieve, were estimated. For this purpose, the water specimens from the nested piezometers, drilled at various depths beneath the ground surface in the vicinity of the tubewells, were collected. The specimens of water were taken with a solar-operated 12-volt router. The router was fully assembled with the required accessories, and these accessories included the following: a hose pipe, an elbow, and pipe clips. The outflow of all tubewells was measured by volumetric technique utilizing a well-known 50 L container.

2.4. Determination of Aquifer Parameters

Aquifer limitations such as coefficient of transmissibility (T) and storage coefficient (S) are two important parameters in groundwater hydrodynamics. For the determination of T and S, the pumping tests were conducted at three tubewells installed at the study site. The average value of each determination was considered as a representative value for the entire study area. The time-drawdown data were simulated using the AQTESOLV version 4.5 software for the determination of aquifer limitations. The time-drawdown data were first tabulated in an Excel sheet, and then, values were imported for simulation into the software. The choice of method depends on the parameters to be determined. For example, Theis [20] and Cooper–Jacob [21] determined the specific gravity (S) and transmittance (T). The water-powered drawdown and time data and the tubewell outflow obtained through the pumping test have been used to restrict the aforementioned aquifer properties such as transmissivity (T), storativity (S), specific yield (Sy), and soil porosity (n) by applying the AQTESOLV software.

2.5. Selection of Model for Groundwater Simulation

The study focused on developing and implementing a numerical groundwater model to predict water levels under various scenarios. MODFLOW was chosen as the simulation model due to its versatility and ease of use [22]. This model allows for the easy modification of key parameters such as hydraulic permeability and recharge rates. It can assess the impact of different pumping conditions on hydrodynamics and saltwater intrusion. The model aids in well site design and the effective management of limited groundwater resources. Additionally, it can evaluate various scenarios to control groundwater rise and saline formations simultaneously.

2.5.1. MODFLOW Model

A linked 3D finite-difference groundwater flow model (MODFLOW-2000) was first publicized by the US Geological Survey in 1984 and has come to be the most extensively utilized simulation model for groundwater [8,23]. Representing this review, MODFLOW-96 [24] editions were run down. It is a numerical model that simulates groundwater flow

within regular and dissimilar spongy media. Inside the MODFLOW, 3D underground water flow is defined by means of partial differential equations (Equation (1)).

$$\frac{\partial}{\partial x}\left(K_{xx}\frac{\partial h}{\partial x}\right)+\frac{\partial}{\partial y}\left(K_{yy}\frac{\partial h}{\partial y}\right)+\frac{\partial}{\partial z}\left(K_{zz}\frac{\partial h}{\partial z}\right)-W=Ss\frac{\partial h}{\partial t} \quad (1)$$

where Kxx, Kyy, and Kzz were considered as permeability along the x, y, and z coordinate axes, assuming that they are parallel to the main axis of permeability, and where h stands for the potential head, and W stands for the per unit volume. The volume flux characterizes the source and/or sink of water, Ss stands for the specific storage of the spongy media, and t stands for time.

2.5.2. MODFLOW Data Requirements

The groundwater flow simulation model requires two types of data: time-constant and time-varying. Time-constant data include underground lithology settings and aquifer limitations, while time-varying data include tubewell discharge, groundwater recharge, and groundwater heads. For the head, middle, and tail reach tubewells, key time-constant information like lateral permeability and specific storage was obtained from pumping tests. Other data were collected from relevant departments. Time series data and recharge were assessed through model calibration. The model uses specified parameters to calculate transmissibility and storage coefficient values for each layer. Lateral aquifer boundaries were set as no-flow boundaries. The model was simulated for 24 h at the head and middle reach aquifer systems, with 2 stress periods. For the tail reach aquifer system, the simulation ran for 72 h and was also split into 2 stress periods. Stress periods represent the time between interruption and the continuous start of the pumping test.

Initial hydraulic heads for each domain were determined by averaging observed heads from open piezometers around each tubewell. These initial heads were assigned to all active cells in the model domain, except for constant head boundary cells. Specifically, the head reach tubewell used 70.04 m, the middle reach 53.43 m, and the tail reach 55.118 m as the starting water heads. The lowest ends of tubewell screens were considered as the baseline. The simulation used a transient type of flow model. Time discretization details are provided in Table 4, while Table 5 lists the ranges of aquifer hydraulic parameters used in various model simulations for the calibration process. These parameters were collected from different sources.

Table 4. Stress period division for the total simulation periods.

Tubewell	Stress Periods (h)	Total Stress Length (h)	Data Availability
Head	5.1667	5.1667	Data available
	6.8333	12	Simulated
	12	24	Simulated
Middle	6	6	Data available
	6	12	Simulated
	12	24	Simulated
Tail	19.667	19.667	Data available
	28.333	48	Simulated
	24	72	Simulated

Table 5. Ranges of inputs for aquifer hydraulic parameters.

Tubewell	Horizontal Permeability (m/h)	Vertical Permeability (m/h)	Porosity (Dimensionless)	Specific Yield (Fraction)	Data Source
			Aquifer		
Head	0.92172–1.3387	0.00275–0.26335	0.002853–0.26335	0.0000249–0.001206	Present study calculated
Middle	1.3519–2.739	0.00275–0.26335	0.002853–0.26335	0.0000249–0.001206	
Tail	0.92172–1.3387	0.00275–0.26335	0.002853–0.26335	0.0000249–0.001206	
			Semi-confining layer		
-	0.08333	0.002853–0.26335	0.3	0.2–0.25	GDC/BGS, 1990

2.5.3. Solver Selection

MODFLOW-2000, a groundwater modeling software, uses various solvers to solve groundwater governing equations. These solvers include Successive Over Relaxation (SSOR), Strongly Implicit Procedure (SIP), Direct Solution (DE45), and Preconditioned Conjugate Gradient Method (PCG2). The choice of solver is based on vibration control, and the convergence efficiency depends on the input parameters for each solver. In this research, the PCG2 solver was selected for model execution due to its advantages: shorter run time, higher accuracy, and a dual iterative method that helps control cell oscillations between wet and dry conditions

3. Results and Discussion

3.1. Transmissibility and Coefficient of Storage at Head Reach

Transmissibility and coefficient of storage were determined using the AQTESOLV software by Theis and Cooper–Jacob [20,21], and their approaches and results are shown in Figure 3. The transmissivity (T) values of observation wells were 0.9717 m^2/min and 2.125 m^2/min, which were obtained by using Theis's approach, whereas the storativity (S) values of observation wells were 0.002035 and 0.01466 using a similar approach at the head of the distributary for P 18.3 m and P 51.8 m, respectively. Here, the transmissivity was 0.9858 m^2/min and 1.033 m^2/min and the storativity was 0.0005655 and 0.002661, respectively, for P 18.3 m and P 51.8 m. Since the difference between the estimated parameters for both approaches is very small, thus, the average of the two approaches is considered as a representative. Consequently, at the head of the research area, the average transmissivity (T) calculated was 0.97875 m^2/min and 1.579 m^2/min, and the average storativity obtained was 0.0013 and 0.00866 for P 18.3 m and P 51.8 m, respectively.

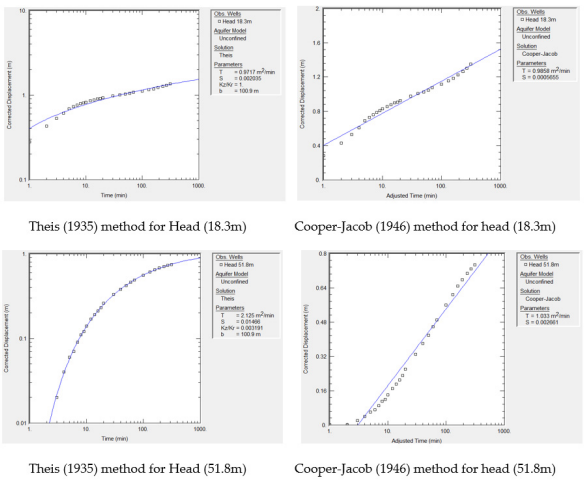

Figure 3. AQTESOLV results calculated by different testing methods at head reach.

3.2. Transmissibility and Coefficient of Storage at Middle Reach

Figure 4 presents the outcomes for the transmissivity at the middle reach as 1.173 m^2/min and 0.7497 m^2/min; however, the storativity values were 0.006484 and 0.009432 for P 18.3 m and P 51.8 m, respectively. However, by means of the Cooper–Jacob (1946) method, the similar limits for transmissivity and storativity were 1.063 m^2/min and 1.118 m^2/min and 0.007179 and 0.003761, respectively, for P 18.3 m and P 51.8 m at the middle reach of the distributary. Therefore, the average storativity value obtained at the middle reach were 0.0068315 and 0.0065965, respectively, for P 18.3 m and P 51.8 m. Similarly, the average transmissivity for the middle reach for P 18.3 and P 51.8 m were 1.118 m^2/min and 0.93385 m^2/min.

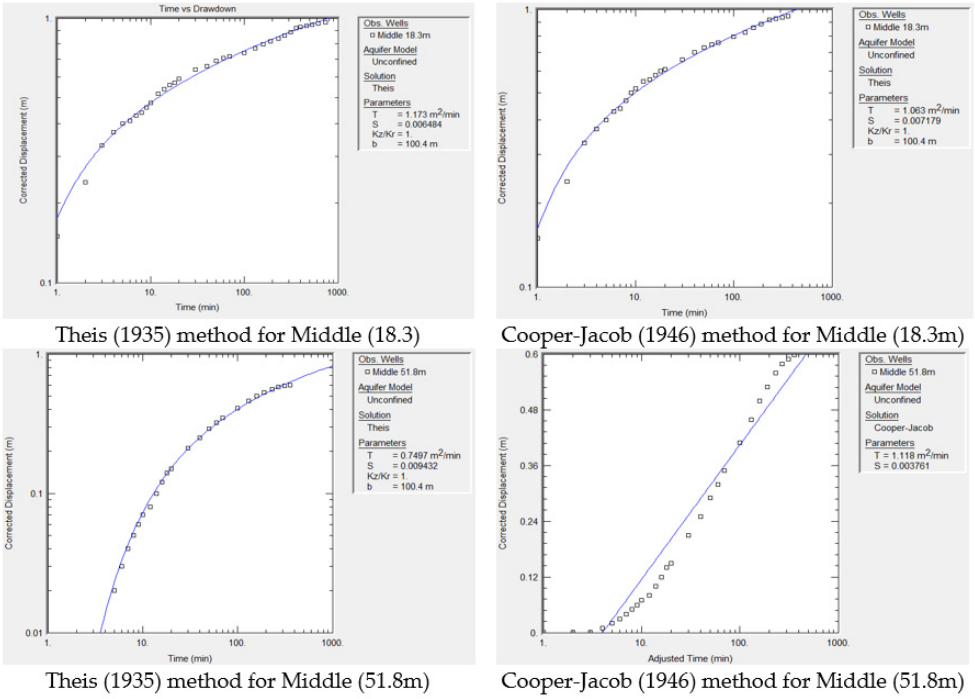

Figure 4. AQTESOLV results calculated by different testing methods at middle reach.

3.3. Transmissibility and Coefficient of Storage at Tail Reach

The transmissibility results at the tail reach are shown in Table 6. The results of transmissibility were 0.8414 m^2/min, 1.075 m^2/min, 1.389 m^2/min, and 2.243 m^2/min; however, the storativity values were 0.000768, 0.00128, 0.001963, and 0.001645 for P 1.83 m, P 14.02 m, P 43.89 m, and P 70.1 m, respectively. Similar factors for transmissivity and storativity were 0.8468 m^2/min, 1.073 m^2/min, 1.051 m^2/min, and 1.356 m^2/min and 0.0003406, 0.0002923, 0.002545, and 0.002258, respectively, for P 1.83 m, P 14.02 m, P 43.89 m, and P 70.1 m at the tail reach of the distributary. Therefore, the average storativity value obtained at the tail reach was 0.0005322, 0.00301, 0.003471, and 0.003724, respectively, for P 1.83 m, P 14.02 m, P 43.89 m, and P 70.1 m. Similarly, the average transmissivity for the tail reach for P 1.83 m, P 14.02 m, P 43.89 m, and P 70.1 m was 0.84685 m^2/min, 1.3345 m^2/min, 0.9768 m^2/min, and 1.1692 m^2/min. From the above results, it was observed that the Theis (1935) method calculated higher transmission values than the Cooper–Jacob method at the head, middle, and tail reaches of the research area except in P 18.3 m at the head, P 51.8 m at the middle and P 1.83 m at the tail reach.

Table 6. Transmissibility and coefficient of storage.

Sites	Piezometric Distance (m)	Theis	Jacob	Average
Head	P 18.3	0.9717 0.002035	0.9858 0.0005655	0.97875 0.0013
	P 51.8	2.125 0.01466	1.033 0.002661	1.579 0.00866
Middle	P 18.3	1.173 0.006484	1.063 0.007179	1.118 0.006832
	P 51.8	0.7497 0.009432	1.118 0.003761	0.93385 0.006597
Tail	P 1.83	0.8414 0.000768	0.8468 0.0003406	0.84685 0.0005322
	P 14.02	1.075 0.00128	1.073 0.0002923	1.3345 0.00301
	P 43.89	1.389 0.001963	1.051 0.002545	0.9768 0.003471
	P 70.1	2.243 0.001645	1.356 0.002258	1.1692 0.003724

3.4. Specific Yield of the Tubewell

The specific yield (Sy) of the tubewell was determined by the means of Neuman and Tartakovsky–Neuman methods [25]. The head reach specific yield (Sy) values of P 18.3 m and P 51.8 m analyzed by the means of Neuman were 0.5 and 0.001, respectively. However, Tartakovsky–Neuman computed it to be 0.5 and 0.001 for P 18.3 m and P 51.8 m, respectively. In the same way, Neuman approach at the middle reach of the distributary determined the specific yield to be 0.001 and 0.001 for P 18.3 m and P 51.8 m, respectively. The Tartakavosky–Neuman approach determined it to be 0.001 and 0.001 for P (18.3 m) and P (51.8 m), respectively. Table 7 shows the results of these parameters and their average values. However, the specific yield values obtained using the Neuman approach for the tail reach of the distributary were 0.001, 0.001, 0.001, and 0.0.001 for P 1.83 m, P 14.02 m, P 43.89 m, and P 70.1 m, respectively. However, using the Tartakavosky–Neuman approach, they were 0.001, 0.001, 0.001, and 0.001 for P 1.83 m, P 14.02 m, P 43.89 m, and P 70.1 m, respectively.

Table 7. Specific yield of tubewells.

Reaches	Piezometric Distance (m)	Neuman	Tartakovsky–Neuman	Average
Head	P 18.3	0.5	0.001	0.2505
	P 51.8	0.5	0.001	0.2505
Middle	P 18.3	0.001	0.001	0.001
	P 51.8	0.001	0.001	0.001
Tail	P 1.83	0.001	0.001	0.001
	P 14.02	0.001	0.001	0.001
	P 43.89	0.001	0.001	0.001
	P 70.1	0.001	0.001	0.001

3.5. Calibration and Validation of MODFLOW

The process of calibration [26–28] is a workout that uses a sensitivity approach to modify geological formation properties, time stresses, and boundary circumstances until the historical situations of geological formation flow and head are reproduced with appropriate precision. The initially recorded data assigned to the model were aquifer parameters such as topographical view, shape, altitude, and soil characteristics for all soil strata in geological

formation. Throughout pumping tests, values assigned to the model for recharge were taken into consideration as seepage and infiltration from irrigation canals and irrigation applications. Water drained from the system is only considered to be pumped from the well, while the evapotranspiration is insignificant. By means of a trial-and-error approach, the final choice of model factors was achieved. Throughout the process of calibration, the hydraulic properties of the model lenses varied amongst the simulation outcomes of the model and the measured data until there was sufficient correspondence for transient's groundwater flow. Quite a lot of simulations were performed during the calibration process, and the hydraulic factors of aquifers were changed until the simulated head was attained very near to the measured data as shown in Figure 5Figure 6andFigure 7.

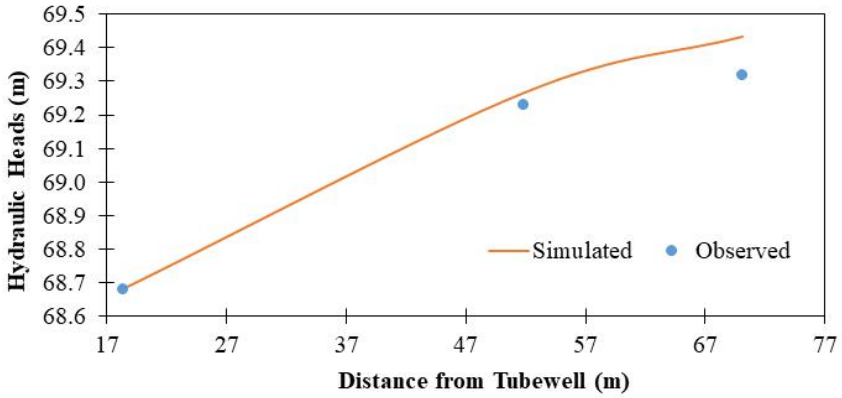

Figure 5. Comparison of simulated and observed hydraulic heads at head reach tubewell.

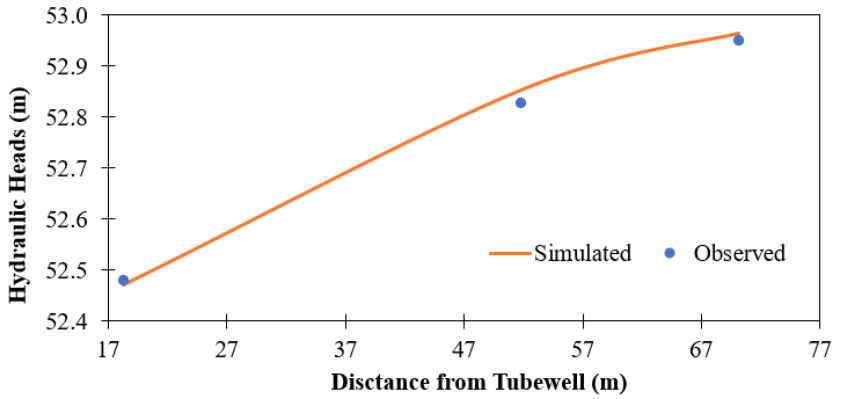

Figure 6. Comparison of simulated and observed hydraulic heads at middle reach tubewell.

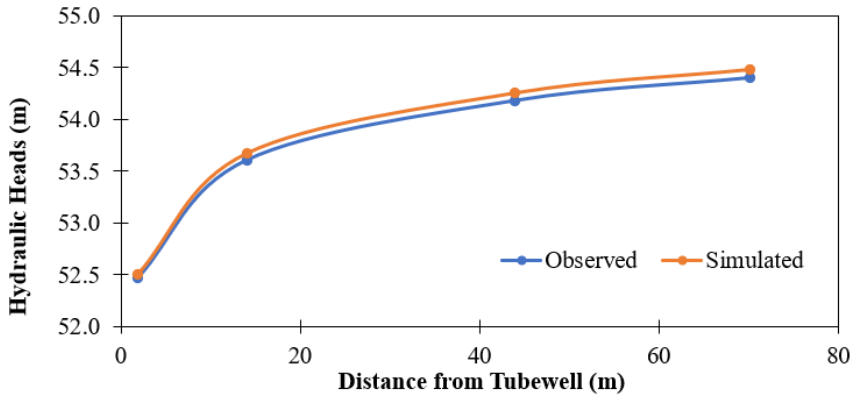

Figure 7. Comparison of simulated and observed hydraulic heads at tail reach tubewell.

In each case, the MODFLOW model is calibrated by means of data from the first stress period only, and additional data collections were used for the validation of the model. To test the precision of MODFLOW, a statistical measure of the goodness of fit was applied to evaluate the performance of the model during simulation. Accordingly, a root mean square (RMS) value was estimated to compare the calibration and validation simulation outcomes through measured data as shown in Table 8. The RMS value of head tubewell varied between 0.024 and 0.108. The model was successfully calibrated, as 0.0166 to 0.0349 for the middle tubewells and 0.0659 to 0.0069 for the tail tubewell were all less than 10%, representing a suitable match between the observed heads and the simulated heads, and Table 9 summarizes the three tubewells.

Table 8. Statistical comparison of observed heads and simulated heads based on root mean square (rms) values.

Tubewell	Calibration Runs	Validation Runs	
		01	02
Head	0.06874	0.0323	0.0873
Middle	0.0166	0.0141	0.0349
Tail	0.0659	0.0199	0.0069

Table 9. Calibrated hydraulic parameters of material properties of the layered aquifer systems.

Tubewell	Layer No	Horizontal Permeability, KH (m/hr)	Vertical Permeability, KV (m/hr)	Specific Storage, Ss (1/m)	Effective Porosity, n	Specific Yield, Sy
Head	1	0.0833	0.09	0.00003	0.25	0.25
	2	0.995	0.018	0.0001	0.25	0.25
	3	0.995	0.018	0.0001	0.25	0.25
	4	0.995	0.018	0.0001	0.25	0.25
Middle	1	0.0833	0.00833	0.00003	0.25	0.25
	2	1.53	0.246	0.0001	0.25	0.25
	3	1.53	0.246	0.0001	0.25	0.25
	4	1.53	0.246	0.0001	0.25	0.25
Tail	1	0.0833	0.00833	0.00003	0.25	0.25
	2	1.996	0.019	0.0001	0.25	0.25
	3	0.0833	0.00833	0.00003	0.25	0.25
	4	1.996	0.019	0.0001	0.25	0.25

4. Conclusions

This study characterized aquifer parameters in Tando Allahyar district using skimming tubewells and pumping test methods. The results indicated that average transmissibility (T) across the study area was 1.12888 m^2/min, mean storage coefficient (S) was 0.00479, and average specific yield (Sy) was 0.0634. Groundwater levels were lower at the tail reach compared to those at the head and middle reaches, likely due to a higher concentration of tubewells in the lower reach. The head and middle reaches showed higher groundwater levels, possibly due to constant head conditions promoting infiltration and recharge. Horizontal conductivity values ranged from 0.92172 to 2.739 m/hr across all reaches, while specific storage varied from 0.0000249 to 0.001206 per meter. Based on these findings, it is recommended that tubewells at all reaches (head, middle, and tail) should be closed for a minimum of 4 h between operations. This strategy allows for safe groundwater extraction while maintaining water quality and preventing water table depletion in the study area.

Author Contributions: Conceptualization, X.Y. and M.U.M.; methodology, M.U.M. and A.B.; software, S.A.S.; validation, R.K.S., S.M.K. and M.A.T.; formal analysis, I.A.M.; investigation, F.A.C.; resources, S.A.S.; data curation, A.B.; writing—original draft preparation, A.B. and M.U.M.; writing—review and editing, M.A.T. and F.A.C.; visualization, I.A.M.; supervision, S.M.K. and R.K.S.; project administration, F.A.C.; funding acquisition, X.Y. All authors have read and agreed to the published version of the manuscript.

Funding: This research was funded by the Jiangsu Province Industry-University-Research Cooperation Project—Key Technology Research of Intelligent Micro-tillage Machine (BY20221125), Jiangsu Province Blue Project Outstanding Young Backbone Teachers Project, and Jiangsu Province Higher Vocational College Teachers Professional Leaders High-end Training Project (2022GRFX067).

Data Availability Statement: Data will be available on request.

Conflicts of Interest: The authors declare no conflicts of interest.

References

1. Dars, R.; Qureshi, A.L.; Jamali, M.A.; Memon, H.A.S.; Kori, S.M.; Oad, S. Subsurface Groundwater Aquifer Mapping and Quality Characterization in Matiari District, Sindh, Pakistan. *Environ. Monit. Assess.* **2024**, *195*, 22. [CrossRef] [PubMed]
2. Kumar, N.; Mahessar, A.A.; Memon, S.A.; Ansari, K.; Qureshi, A.L. Impact Assessment of Groundwater Quality using WQI and Geospatial Tools: A Case Study of Islamkot, Tharparkar, Pakistan. *Eng. Technol. Appl. Sci. Res.* **2020**, *10*, 5288–5294. [CrossRef]
3. Moursi, H.; Kim, D.; Kaluarachchi, J. A Probabilistic Assessment Of Agricultural Water Scarcity In A Semi-Arid And Snowmelt-Dominated River Basin Under Climate Change. *Agric. Water Manag.* **2017**, *193*, 142–152. [CrossRef]
4. *Nature-Based Solutions for Water*; UNESCO, Ed.; The United Nations World Water Development Report; UNESCO: Paris, France, 2018; ISBN 978-92-3-100264-9.
5. Kulkarni, H.; Shah, M.; Shankar, P.V. Shaping the Contours of Groundwater Governance in India. *J. Hydrol. Reg. Stud.* **2015**, *4*, 172–192. [CrossRef]
6. Qureshi, A.S. Groundwater Governance in Pakistan: From Colossal Development to Neglected Management. *Water* **2020**, *12*, 3017. [CrossRef]
7. Basharat, M.; Hassan, D.; Bajkani, A.; Sultan, S.J. Surface Water and Groundwater Nexus: Groundwater Management Options for Indus Basin Irrigation System. *Int. Waterlogging Salin. Res. Inst. IWASRI Lahore Pak. Water Power Dev. Auth. Publ.* **2014**, *299*, 155.
8. Ahmed, W.; Ahmed, S.; Punthakey, J.F.; Dars, G.H.; Ejaz, M.S.; Qureshi, A.L.; Mitchell, M. Statistical Analysis of Climate Trends and Impacts on Groundwater Sustainability in the Lower Indus Basin. *Sustainability* **2024**, *16*, 441. [CrossRef]
9. Qazi, M.A.; Khattak, M.A.; Khan, M.S.A.; Chaudhry, M.N.; Mahmood, K.; Akhter, B.; Iqbal, N.; Ilyas, S.; Ali, U.A. Spatial Distribution of Heavy Metals in Ground Water of Sheikhupura District Punjab, Pakistan. *J. Agric. Res.* **2014**, *52*, 99–110.
10. Qureshi, A.S.; Gill, M.A.; Sarwar, A. Sustainable Groundwater Management in Pakistan: Challenges and opportunities. *Irrig. Drain.* **2010**, *59*, 107–116. [CrossRef]
11. Qureshi, A.L.; Jamali, M.A.; Hussain, S.; Memon, F.A.; Zaidi, A.Z.; Zafar, S.; Ahmed, W. Subsurface Depleting Aquifers in the Sedimentary Terrain of Quetta Valley in Balochistan: A review. *Arabian J. Geosci.* **2022**, *15*, 1648. [CrossRef]
12. Qureshi, A.S.; McCornick, P.G.; Qadir, M.; Aslam, Z. Managing Salinity and Waterlogging in the Indus Basin of Pakistan. *Agric. Water Manag.* **2008**, *95*, 1–10. [CrossRef]
13. Qureshi, A.L.; Khero, Z.I.; Lashari, B.K. Optimization of Irrigation Water Management: A Case Study of Secondary Canal, Sindh, Pakistan. In Proceedings of the Sixteenth International Water Technology Conference (IWTC16), Istanbul, Turkey, 7–10 May 2012; p. 16.
14. Bhutta, M.N.; Smedema, L.K. One Hundred Years of Waterlogging and Salinity Control in the Indus Valley, Pakistan: A Historical Review. *Irrig. Drain.* **2007**, *56*, S81–S90. [CrossRef]
15. Ahmed, W.; Rahimoon, Z.A.; Oroza, C.A.; Sarwar, S.; Qureshi, A.L.; Punthakey, J.F.; Arfan, M. Modelling Groundwater Hydraulics To Design A Groundwater Level Monitoring Network for Sustainable Management of Fresh Groundwater Lens in Lower Indus Basin, Pakistan. *Appl. Sci.* **2020**, *10*, 5200. [CrossRef]
16. Chandio, A.S.; Lee, T.S.; Mirjat, M.S. The Extent of Waterlogging in the Lower Indus Basin (Pakistan): A modeling study of groundwater levels. *J. Hydrol.* **2012**, *426–427*, 103–111. [CrossRef]
17. Kori, S.M.; Qureshi, A.L.; Lashari, B.K.; Memon, N.A. Optimum Strategies of Groundwater Pumping Regime Under Scavenger Tubewells in Lower Indus Basin, Sindh, Pakistan. *Int. Water Technol. J.* **2013**, *3*, 138–145.
18. Irfan, M.; Arshad, M.; Shakoor, A.; Anjum, L. Impact of Irrigation Management Practices and Water Quality on Maize Production and Water Use Efficiency. *JAPS J. Anim. Plant Sci.* **2014**, *24*, 1518–1524.
19. Vann, R.D.; Denoble, P.J.; Howle, L.E.; Weber, P.W.; Freiberger, J.J.; Pieper, C.F. Resolution and Severity in Decompression Illness. *Aviat. Space Environ. Med.* **2009**, *80*, 466–471. [CrossRef]
20. Theis, C.V. The Relation between the Lowering of the Piezometric Surface and the Rate and Duration of Discharge of a Well Using Ground-Water Storage. *Eos Trans. AGU* **1935**, *16*, 519–524. [CrossRef]

21. Cooper, H., Jr.; Jacob, C.E. A Generalized Graphical Method for Evaluating Formation Constants and Summarizing Well-Field History. *Eos Trans. Am. Geophys. Union.* **1946**, *27*, 526–534. [CrossRef]
22. Harbaugh, A.W. *MODFLOW-2005, the U.S. Geological Survey Modular Ground-Water Model—The Ground-Water Flow Process*; US Department of the Interior, US Geological Survey: Reston, VA, USA, 2005. [CrossRef]
23. McDonald, M.G.; Harbaugh, A.W. *A Modular Three-Dimensional Finite-Difference Ground-Water Flow Model*; US Geological Survey: Reston, VA, USA, 1988.
24. Harbaugh, A.W.; McDonald, M.G. *Programmer's Documentation for MODFLOW-96, an Update to the US Geological Survey Modular Finite-Difference Ground-Water Flow Model*; Branch of Information Services [Distributor]; US Geological Survey: Reston, VA, USA, 1996.
25. Tartakovsky, G.D.; Neuman, S.P. Three-Dimensional Saturated-Unsaturated Flow with Axial Symmetry to a Partially Penetrating Well in a Compressible Unconfined Aquifer. *Water Resour. Res.* **2007**, *43*, W01410. [CrossRef]
26. Elango, L. *Numerical Simulation of Groundwater Flow and Solute Transport*; Allied Publishers: Chennai, India, 2005.
27. Zhang, S.; Zhang, D.; Feng, G.; Chi, M. Modelling method of heterogeneous rock mass and DEM investigation of seepage characteristics. *Geomech. Geophys. Geo-Energy Geo-Resour.* **2024**, *10*, 46. [CrossRef]
28. Wu, W.; Wang, T.; Bai, J.; Liu, J.; Wand, X.; Xu, H.; Feng, G. Failure Characteristics and Cooperative Control Strategies for Gob-Side Entry Driving near an Advancing Working Face: A Case Study. *Processes* **2024**, *12*, 1398. [CrossRef]

Disclaimer/Publisher's Note: The statements, opinions and data contained in all publications are solely those of the individual author(s) and contributor(s) and not of MDPI and/or the editor(s). MDPI and/or the editor(s) disclaim responsibility for any injury to people or property resulting from any ideas, methods, instructions or products referred to in the content.

water

MDPI

Article

Feasibility Research on Surface Water Reinjection into the Sandstone Geothermal Reservoir of the Guantao Formation in Tianjin Based on Laboratory Experiments

Bing Wang [1,2], Yanting Zhao [1,2], Yun Cai [1,2,*], Sen Zhang [1,2], Baomei Yang [1,2] and Fei Liu [1,2]

[1] Tianjin Geothermal Exploration and Development Design Institute, Tianjin 300250, China; wangbingdry@126.com (B.W.); zhao_yan_ting@126.com (Y.Z.); dryzs420357810@163.com (S.Z.); ruby205tjdr@163.com (B.Y.); liufei587@126.com (F.L.)

[2] Observation and Research Station of Tianjin Low—Medium Temperature Geothermal Resources, Ministry of Natural Resources, Tianjin 300250, China

* Correspondence: caiyunjiayou@126.com

Abstract: Tianjin possesses abundant geothermal resources, and geothermal reinjection is an effective strategy for maintaining the sustainable development and utilization of these resources. However, several issues have arisen in the reinjection of sandstone geothermal reservoirs in the Tianjin area, including a mismatch between the reinjection capacity and effluent capacity, as well as challenges related to continuous reinjection. Therefore, it is crucial to investigate the reinjection of exogenous water into sandstone pore-type geothermal reservoirs. This study focuses on the geothermal reservoir of the Guantao Formation in the Binhai New Area. The surface water treatment process for reinjection into sandstone geothermal reservoirs was determined through water treatment simulation experiments. Additionally, experiments examining the interaction between the reinjected water and reservoir rock were conducted to assess the feasibility of using treated surface water for reinjection into sandstone geothermal reservoirs. The hydrogeochemical response mechanisms and the impact on the reservoir under reinjection conditions were also investigated. The results indicate that a nanofiltration module and tubular microfiltration membrane are essential to ensure the stability of the system. The pH and TDS of water samples decreased after reinjecting mixed water (HHS) into the sandstone reservoir. The hydrochemical type consistently remained Cl-Na. The conventional water chemistry components and trace elements were influenced by the corresponding water–rock reactions. The reservoir minerals exhibited minimal precipitation, primarily consisting of K-feldspar and Fe-dolomite. The minerals produced during the experiment accounted for only 0.08% of the total cuttings' mass, indicating a negligible impact on the reservoir structure. PHREEQC was employed to simulate the changes in mineral saturation index before and after the reinjection of mixed water and geothermal water, respectively. Notably, similar hydrogeochemical changes were observed in the geothermal fluids. Thus, this study demonstrates the feasibility of reinjecting treated surface water into sandstone geothermal reservoirs from a hydrogeochemical perspective. This research provides valuable insights for the development of external water reinjection projects in hot spring health care units, contributing effectively to the achievement of carbon peaking and carbon neutrality goals.

Keywords: Tianjin; surface water; reinjection; Guantao formation; sandstone geothermal reservoir

1. Introduction

Tianjin is endowed with abundant low–medium temperature geothermal resources, making it a representative area for the early development and utilization of geothermal energy in China. The geothermal resources in Tianjin are primarily distributed in sandstone pore reservoirs and carbonate fissure reservoirs [1–4]. Geothermal reinjection is an effective strategy for ensuring the sustainable development and utilization of these resources. This process is essential for maintaining pressure within geothermal reservoirs, maximizing

the use of geothermal energy, and mitigating environmental pollution associated with the direct discharge of geothermal fluids. Geothermal reinjection involves the reinjection of geothermal fluids or other utilized (cooled) water sources back into the thermal reservoir through reinjection wells. In Tianjin, the utilization model for geothermal resources is characterized by an exploitation–reinjection system. Typically, geothermal reinjection is required to occur within the same geological layer. However, the annual volume of geothermal exploitation often exceeds the reinjection volume, remaining below 100%. This discrepancy can be attributed to site-specific conditions, reinjection blockages, and the inability to reinject certain geothermal return waters [5]. In light of this, the Tianjin Municipal Bureau of Planning and Natural Resources in China issued a notice titled "Implementation Measures for Geothermal Resource Management in Tianjin" (Jin PRB Documents [2019] No. 4), which encourages eligible enterprises to conduct geothermal reinjection during non-heating periods by constructing surface water reinjection systems into geothermal reservoirs. Consequently, it is essential to investigate the reinjection of exogenous water in conjunction with the reinjection of geothermal return water. The reinjection of water into sandstone porous geothermal reservoirs has consistently posed significant challenges [6]. Therefore, examining the feasibility and impact of exogenous water reinjection into sandstone geothermal reservoirs is crucial for maintaining reservoir pressure, restoring geothermal water levels, prolonging the service life of geothermal fields, preventing land subsidence, and addressing the issue of geothermal return water.

Geothermal reinjection commenced in the 1960s and has since been widely implemented in countries such as France, Germany, Iceland, Italy, Japan, New Zealand, the Philippines, and the United States. In 1969, the first high-temperature geothermal field reinjection project was initiated in the Ahuachapan geothermal field in El Salvador, while the first low–medium temperature geothermal field reinjection project was launched in the Paris Basin in France during the same year. Following 1970, there was a notable increase in global geothermal reinjection projects [7]. The world's first geothermal power station, the Larderello geothermal power station in Italy, began reinjection in 1974. This long-term reinjection helped alleviate reservoir pressure, resulting in a significant increase in power station production. The Geysers geothermal field in California, USA, represents the most notable high-temperature geothermal reinjection project globally, where the world's first geothermal reinjection project was also initiated in 1969. By 1980, the project had commenced reinjecting surface water, including lake water and urban sewage, into the geothermal reservoir to maintain reservoir pressure. The Geysers geothermal field is recognized as the first geothermal field in the world to enhance power generation capacity through the reinjection of exogenous water [8,9]. The geothermal reinjection in the Paris Basin of France represents the most effective area for low-temperature geothermal reinjection. The world's first well-to-well system was established in 1969, followed by the construction of a geothermal well in 1995, which created a system comprising two exploitation wells and one reinjection well. To date, more than 70 mining–reinjection systems have been developed, alongside advancements in the mining–reinjection system processes and technologies [10]. Bodvarsson G., S. Stefansson V., and colleagues investigated the effects of pressure, chemistry, and temperature on reinjection through various geothermal field projects [11,12]. Additionally, Darwis R. S. and other researchers studied the impact of reinjection on geothermal fields by conducting reservoir model simulations [13]. Furthermore, Diazr (2016) and Kamila (2021) provided summaries of the global development status of geothermal reinjection [14,15].

Geothermal reinjection in China began in the 1970s, and significant advancements in the reinjection process and key technologies have been made over the years, particularly in the Beijing, Tianjin, and Shandong provinces. Recently, research on sandstone geothermal reservoir reinjection in China has progressed rapidly. Studies conducted by the Tianjin Geothermal Exploration and Development Design Institute (1990), Liancheng Wang (2014), and Xuepeng Wang (2020) have explored the effects of reinjection and the factors influencing sandstone geothermal reservoirs through various reinjection experiments [16–18].

Additionally, Xin Zhou (2013), Qun Dai (2017), and Dongxin Wu (2022) examined the blocking mechanisms and treatment measures for sandstone geothermal reservoir reinjection [19–21]. Guosheng Jiang (2014) and Yanting Zhao (2023) analyzed the well completion technologies and the application effects of sandstone reinjection wells [22,23]. Moreover, Shoutao Feng (2019), Huajun Wang (2019), and Shan Li (2023) evaluated the impact of sandstone reinjection on reservoir permeability [24–26]. Lastly, Zongyu Chen (1998), Xufei Shi (2013), and Kunyu Wu (2022) investigated the water–rock reactions occurring during sandstone reservoir reinjection from hydrogeochemical and dynamic perspectives [27–29]. Su (2018) summarized the research progress on sandstone geothermal reservoir reinjection in China, highlighting the causes of low reinjection rates, potential solutions, and future research directions. The research has addressed the primary mechanisms affecting well injectivity, the reinjection scheme, the hydrological characteristics of the reservoir, the quality of reinjected water, well completion methods, and the water–rock interactions between the reinjected water and the reservoir. For instance, the "Gravel-packed Completion Technique" was employed in reinjection experiments conducted in Donggu and Binhai in Tianjin, where the injection rates reached up to 64 m^3/d and 102 m^3/d, respectively. Additionally, the injection rate at T38-1 in Tianjin reached 51 m^3/h, with reinjected water accounting for 98% of the water exploited [30].

There are few studies on the reinjection of surface water into sandstone reservoirs, particularly concerning the hydrogeochemistry during the reinjection process. Some researchers have investigated the feasibility, geochemical reaction simulations, and reinjection processes of carbonate reservoirs in the Wumishan Formation that utilize exogenous water [31–34], providing valuable insights for this study. In response to the request for "Implementation Measures for Geothermal Resource Management in Tianjin" (Jin PRB Documents [2019] No. 4), issued by The Tianjin Municipal Bureau of Planning and Natural Resources in China, this paper draws upon the experience of a similar engineering project, the "Project for Reinjection of the Geothermal Reservoir of the Wumishan Formation in the Jixian System Using Surface Water from Dongli Lake", which commenced operations in 2021 and has a reinjection water quality treatment capacity of 450 m^3/h.

This paper focuses on the geothermal reservoir of the Guantao Formation in the Binhai New Area as its primary research subject. It presents the results of water treatment simulation experiments and explores the interactions between reinjected water and reservoir rock. The study investigates the feasibility of reinjecting treated surface water into sandstone geothermal reservoirs and examines the impacts of this reinjection on the reservoirs. The findings provide a foundation for the reinjection of surface water into sandstone geothermal reservoirs based on laboratory experiments. Furthermore, this research lays the groundwork for exploring the reinjection of exogenous water into geothermal reservoirs, thereby enhancing the replenishment of geothermal resources and maintaining reservoir pressure. Ultimately, the study aims to offer technical insights for the development of external water reinjection engineering in hot spring health care units, contributing to the achievement of carbon peaking and carbon neutrality goals.

2. Materials and Methods

2.1. Project Overview

2.1.1. Geothermal Wells

Geothermal wells A and B are located within the Neogene Guantao Formation in the Binhai New Area of Tianjin. Well A, positioned 645 m away from Well B, was originally drilled in 1996 as an exploitation well and was later converted into a geothermal exploitation well by perforating the geothermal reservoir section of the Guantao Formation. The water layer in both wells is part of this formation. Well A has a water output of 60 m^3/h and a temperature of 64 °C. In contrast, Well B, which was drilled in 2015 as a reinjection well, has a depth of 1980.81 m, exhibiting a water output of 106.48 m^3/h and a temperature of 58 °C. The total thickness of the water intake layer in Well B is 128 m, with porosity ranging from 16.05% to 30.06%, permeability between 51.61 and 732.46 $\times 10^{-3}$ μm^2, and shale content

varying from 9.37% to 31.76%. Well A primarily serves heating and hot spring bathing purposes. Since 2016, the return water from Well A has been reinjected into Well B, with an annual reinjection volume of approximately 50,000 m^3. Years of dynamic monitoring data indicate that both the water output capacity and wellhead flow temperature have remained relatively stable. The annual volume of hot spring bathing water from Well A is also approximately 50,000 m^3. The wastewater generated from bathing is treated via aeration, phosphorus removal, and nitrogen removal processes before being discharged into Yingyue Lake.

Geothermal Wells A and B are located at the northeastern edge of the Banqiao sag, which is classified as a grade IV structural unit within the Huanghua depression. The primary nearby fault is the Hai River Fault (see Figure 1). The regional stratigraphy is characterized by several layers: the Cenozoic Quaternary, with a thickness ranging from 300 to 400 m; the Neogene Minghuazhen Formation, with a baseplate depth between 1350 and 1690 m and a thickness ranging from 1130 to 1290 m; the Guantao Formation, with a baseplate depth ranging from 1710 to 2000 m and a thickness ranging from 350 to 550 m; and the Paleogene Dongying Formation, with a baseplate depth between 2250 and 2400 m.

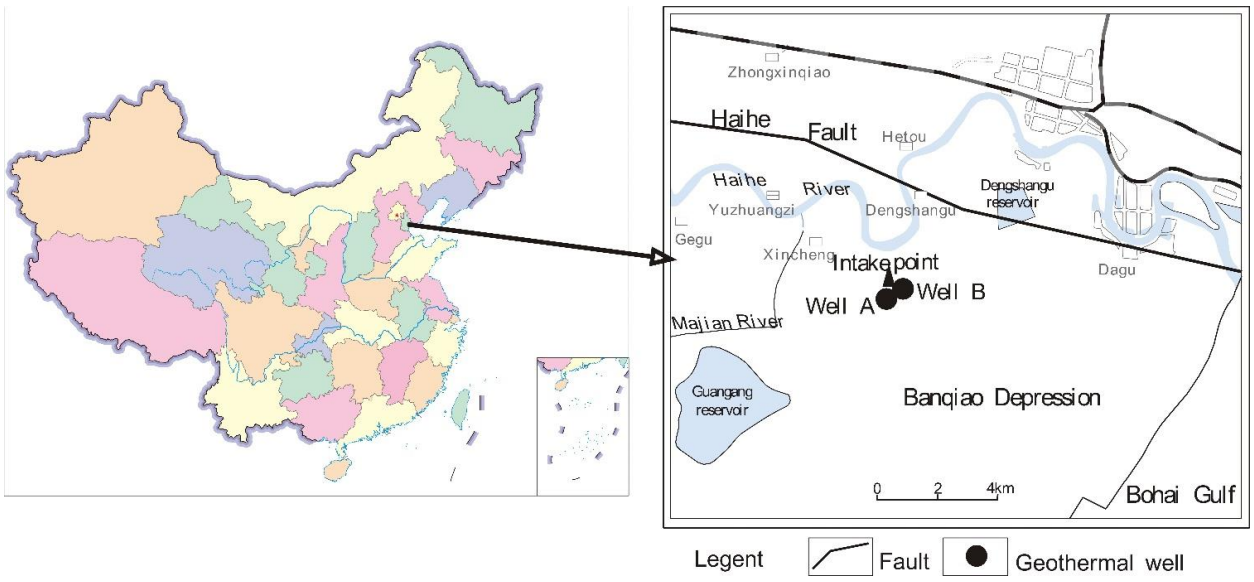

Figure 1. Location of the project.

The hydrochemical composition of the geothermal fluid in Well A is classified as $Cl{\cdot}HCO_3$-Na, exhibiting a pH of 8.25 and total dissolved solids (TDS) of 1408.4 mg/L. In contrast, the geothermal fluid in Well B is characterized as $Cl{\cdot}HCO_3{\cdot}SO_4$-Na, with a pH of 8.44 and TDS of 1577.9 mg/L (see Table 1).

Table 1. Table of the chemical composition (unit: mg/L).

Name	Na^+	K^+	Ca^{2+}	Mg^{2+}	Cl^-	NO_3^-	SO_4^{2-}	HCO_3^-	CO_3^{2-}	SiO_2	F^-	TDS	pH
A	490	3.6	10.5	0.9	363	22.4	231	510	6	27.7	4.7	1408.4	8.25
B	503.6	3.4	9.5	0.6	361.6	0.25	266	393.6	6	33.6	5.46	1577.9	8.44
Lake	787.07	25.69	31.64	51.69	1072.4	2657.3	306.03	361.2	19.8	1.78	-	2657.3	8.67

2.1.2. Surface Water

The reinjection water is sourced from Yingyue Lake, a natural lake located approximately 300 m east of Well B. The lake spans an area of about 50,000 square meters, with a water depth varying from 0 to 6 m. Its total water storage capacity is approximately 200,000 cubic meters, and the annual variation in water quantity is minimal. The eastern edge of Yingyue Lake is situated about 200 m from the Dagu Sewage River, while several

unnamed natural lakes, each ranging from 10,000 to 20,000 square meters in area, are located to the north. The lake is replenished by precipitation, river inflow, groundwater, and the discharge from bathing facilities, which undergo harmless treatment. Comprehensive analyses conducted over various periods indicate that the water exhibits characteristics of both surface water and geothermal water, with minimal seasonal variation. The chemical composition of the water is presented in Table 1.

2.2. Surface Water Reinjection Experiment

2.2.1. Experimental Platform

The laboratory water treatment experiment was conducted on a surface water reinjection platform established by the Tianjin Geothermal Exploration and Development Design Institute. This experimental platform consists of two primary components: a water treatment system and a chemical composition monitoring system.

The water treatment system has a capacity ranging from 0.5 to 1 ton per hour, while the surface water consumption for each group is approximately from 2 to 4 tons. In accordance with current mainstream water treatment technologies, the system is equipped with several standard water treatment modules. These include the raw water module, coagulation module, sterilization module, dosing system, sedimentation module, sand filtration module, deoxidization module, precision filtration module, tubular membrane module, BAF reactor module, nanofiltration membrane module, and a reducing agent scale inhibitor dosing system, along with other supporting equipment (Figure 2).

Figure 2. The experimental platform of the surface water treatment.

The chemical composition monitoring system includes a mixer, pH meter, conductivity meter, turbidity meter, and multifunctional comprehensive chemical composition analyzers. These analyzers measure the chemical oxygen demand (COD), ammonia nitrogen, total phosphorus, and suspended solids (SS), along with the necessary supporting reagents.

These components are employed to design experimental schemes and to facilitate the timely detection of the chemical composition at each stage of the process.

2.2.2. Simulation Experiment

After years of practice, a standardized geothermal water treatment process for the reinjection of sandstone geothermal reservoirs has been established in Tianjin. This process comprises the following steps: raw water collection, coagulation, sedimentation, intermediate tank storage, sand filtration, deoxygenation, precision filtration, and water production. Based on the water quality analysis of the lake and the reservoir water quality requirements for the Guantao Formation, and informed by actual operational experiences from previous surface water reinjection, three sets of water treatment technologies were designed utilizing an experimental platform module. The water production outputs from these three treatment processes were tested and analyzed, with the results being presented in Table 2. Due to the open environment, the dissolved oxygen content of the test water is elevated; however, all other analytical results meet the reinjection requirements. These requirements align with the "Reuse of Urban Recycling Water: Water Quality Standard for Groundwater Recharge" (GB/T 19772-2005, Standardization Administration of China) [35], the "Water Quality Standard and Practice for Analysis of Oilfield Injecting Waters in Clastic Reservoirs" (SY/T 5329-2012, National Energy Administration of China) [36], and the "Technical Regulation for Geothermal Return Water Reinjection of Sandstone Reservoir" (DZ/T 0330-2019, Ministry of Natural Resources of the People's Republic of China) [37].

Table 2. The analysis results of the water treatment processes and their water production outputs (unit: mg/L).

Name	Process Flow	TDS	SS	DO	PO_4^{3-}	pH
Process 1	raw water–coagulation–sedimentation–intermediate tank–sand filtration–deoxygenation–precision filter–water production	575	2.54	6	<0.02	7.83
Process 2	raw water–coagulation–sedimentation–intermediate tank–tubular microfiltration membrane–nanofiltration–produced water	620	1	8	<0.02	7.8
Process 3	Raw water–coagulation–sedimentation–BAF–intermediate tank–tubular microfiltration membrane–produced water	3050	0.98	8.25	<0.02	8.1

Note: TDS: Total dissolved solids. SS: Suspended solids. DO: Dissolved oxygen.

2.2.3. Determination of Water Treatment Process

By comparing and analyzing the chemical composition test results from the simulation experiment, along with the operational experience of the existing surface water reinjection station, the principles for determining the treatment process are outlined as follows:

(1) The inclusion of a nanofiltration module is essential in the water treatment process of the experiment to effectively reduce the total dissolved solids (TDS).
(2) Sand filtration and precision filtration processes demonstrate a relatively low filtration accuracy for suspended solids (SS) and other impurities in water, necessitating higher raw water quality standards. Additionally, the sand filter tank occupies a significant area, making it less feasible to prioritize when spatial constraints at the station are inadequate.
(3) During actual operations, the sponge iron in the deaeration tank is susceptible to contamination by microorganisms present in the water, which leads to a diminished deaeration capacity and ineffective backwashing. Consequently, the deaerator tanks frequently fail to fulfill their designed functions. Furthermore, the deaerator tank poses a challenge due to its large footprint, which limits its prioritization.

(4) The biological aerated filter (BAF) requires the pretreatment of the influent water; otherwise, the presence of numerous impurities and suspended solids (SS) can obstruct the aeration and water distribution system, adversely affecting system operation. As BAF is inherently a biochemical system, its effluent contains microorganisms and their metabolites, necessitating the addition of fungicides and deoxidants in subsequent processes. This introduces uncertainty in water quality and increases the operational load.

(5) As a membrane separation technology, tubular membranes offer several advantages, including a large diameter, low flow resistance, high surface flow velocity, reduced retention of pollutants on the membrane surface, ease of cleaning, enhanced pollution resistance, and lower requirements for water inflow. Consequently, tubular membranes are well-suited for treating lake water with fluctuating quality and demonstrate stability during laboratory experiments.

(6) In designing the reinjection process, it is essential to establish independent dosing tanks for the fungicide, coagulant, and pH regulator, while also considering the sequence of delivery.

Based on the results of preliminary investigations and laboratory simulation experiments, and taking into account operational effectiveness and cost, the surface water treatment process was identified as Process 2: "raw water–coagulation–sedimentation–intermediate tank–tubular microfiltration membrane–nanofiltration–produced water" (see Figure 3).

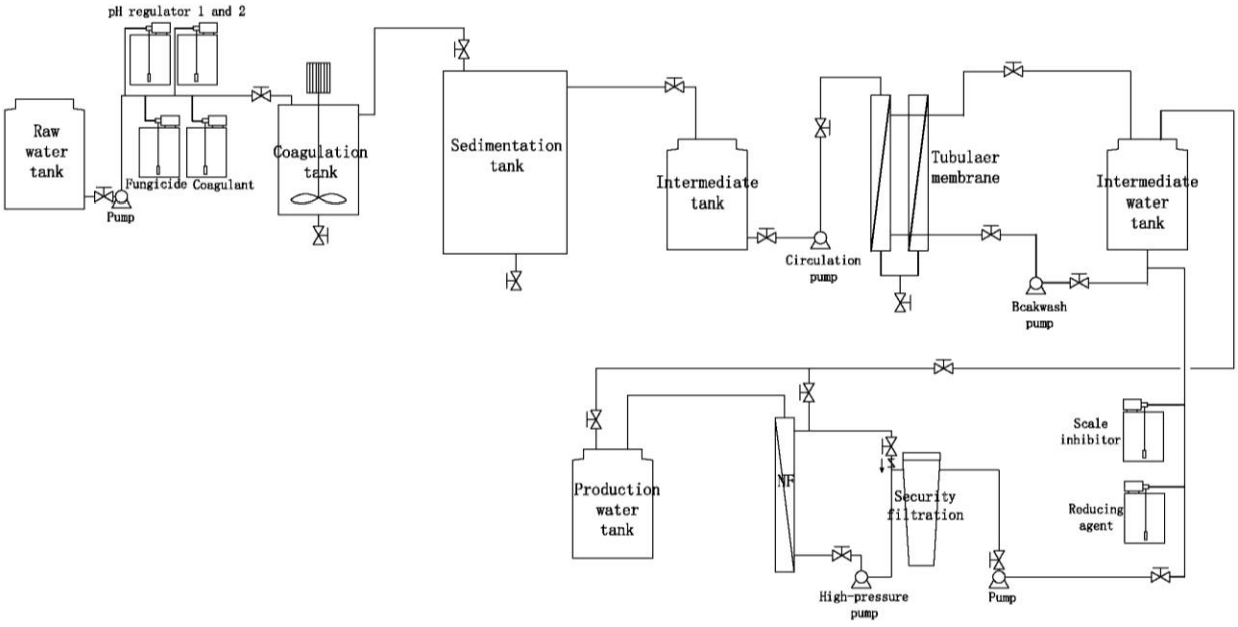

Figure 3. Water treatment process flow.

Considering the high operational costs associated with the nanofiltration process and the necessity for the reinjection water quality to match the total dissolved solids (TDS) of the geothermal raw water, a mixed proportion of nanofiltration water and intermediate water was established at a ratio of 3:1 under normal temperature and pressure conditions. The TDS of the mixed water was comparable to that of the geothermal raw water. Raw water (RW), nanofiltration water (NF), and mixed water (HHS) were subjected to chemical composition analysis, with the results being presented in Table 3. Following treatment, the chemical composition of both NF and HHS meets the requirements for reinjection.

Table 3. Chemical composition test results of the treated water (Unit: mg/L).

Name	Na^+	K^+	Ca^{2+}	Mg^{2+}	Cl^-	NH_4^+	SO_4^{2-}	HCO_3^-	SiO_2	F^-	CO_2	TDS	COD	pH
RW	787.07	25.69	31.64	51.69	1072.4	0.28	306.03	361.2	1.78	2.358	0	2657.3	20.69	8.67
NF	201.49	4.18	25.09	3.1	264.1	0.05	45.48	137.3	1.12	0.155	16.3	681.9	4	7.77
HHS	406	7.5	22.1	11.2	529.6	0.23	106.1	110	1	0.3	11.9	1142	4	8.25

2.3. Water–Rock Reaction Experiment

An experiment was conducted to investigate the effects of reinjection on the chemical dynamics within a geothermal reservoir, focusing on water–rock interactions. This study took place at the Institute of Geology and Geophysics, part of the Chinese Academy of Sciences in China. The equipment utilized was an upgraded 4575A high-temperature and high-pressure reactor manufactured by PARR Corp. in the USA. Sandstone samples were obtained from Well B of the Neogene Guantao Formation in Tianjin, China, collected from a depth ranging from 1770 to 1900 m. For the experiment, a water sample designated as HHS was used, with 300 g of the water sample combined with 33.3 g of sandstone, resulting in a water–rock mass ratio of 9:1. Reaction periods were established at 0, 5, 10, and 15 days. Temperature and pressure were monitored to replicate the conditions of the geothermal reservoir at the sandstone sampling depth, with a temperature of 60 °C and a pressure of 15 MPa maintained. Throughout the experiment, a stirring speed of 100 r/s was consistently upheld, while the temperature and pressure were continuously tracked.

The procedures for the experiment were outlined as follows: (1) cleaned sandstone samples, along with reinjection water, were introduced into the reaction chamber, which was subsequently sealed; (2) the valve controlling the cooling water was opened, and the parameters for the reaction were established; (3) the control system was initiated, allowing for the setting of reaction temperature, pressure, and stirring speed; (4) after the water–rock reaction was completed and the reaction chamber had returned to room temperature, the samples were extracted and filtered; (5) water samples were collected in bottles for hydrochemical analysis; (6) sandstone samples were dried in an oven set at 40 °C for 24 h, allowed to cool to room temperature, and then ground to 200 mesh for mineral composition analysis [38].

The hydrochemical analysis of the water samples, encompassing both major and trace elements, was performed using inductively coupled plasma optical emission spectrometry (ICP-OES) and inductively coupled plasma mass spectrometry (ICP-MS), achieving a measurement accuracy of 0.001 μg/L. The hydrogen and oxygen isotopes of fluid samples were measured using Off-axis Integrated Cavity Output Spectrometry (OA-ICOS), with measurement accuracies of 0.2‰ for 2H and 0.03‰ for 18O. The mineral compositions of the sandstone samples were analyzed using an X-ray diffraction analyzer (XRD). A Dmax2500Pc type X-ray diffractometer (Rigaku, Japan) operated at 40 kV and 100 mA with CuKα radiation. Diffractograms were recorded from 5° to 90°, with a scanning increment of 4° per minute. All tests conducted adhered to the requirements of the relevant standards or specifications.

3. Results and Discussion

3.1. Reservoir Fluid Response

The results indicate that the total dissolved solids (TDS) initially increased and subsequently decreased during the reaction, ultimately falling below the initial value (Figure 4). The pH exhibited a decreasing trend, suggesting the production of acidic substances throughout the reaction. As the reaction progressed, the fluoride (F^-) content experienced a slight increase. The concentrations of chloride (Cl^-), nitrate (NO_3^-), sulfate (SO_4^{2-}), sodium (Na^+), potassium (K^+), and calcium (Ca^{2+}) initially rose (at t = 5 d) before decreasing; however, only the concentrations of Na^+ and Cl^- fell below their initial values. The magnesium (Mg^{2+}) content decreased, while the silica (SiO_2) content continuously increased. The bicarbonate (HCO_3^-) content also increased initially before returning to the

initial value. The hydrochemical type remained consistently Cl-Na (Table 4 and Figure 5a,b). During the reaction, TDS decreased by 94.2 mg/L, indicating that precipitation was the dominant process. This reduction in TDS was equivalent to the production of 28.3 mg of debris in this experiment, representing 0.08% of the debris involved in the reaction.

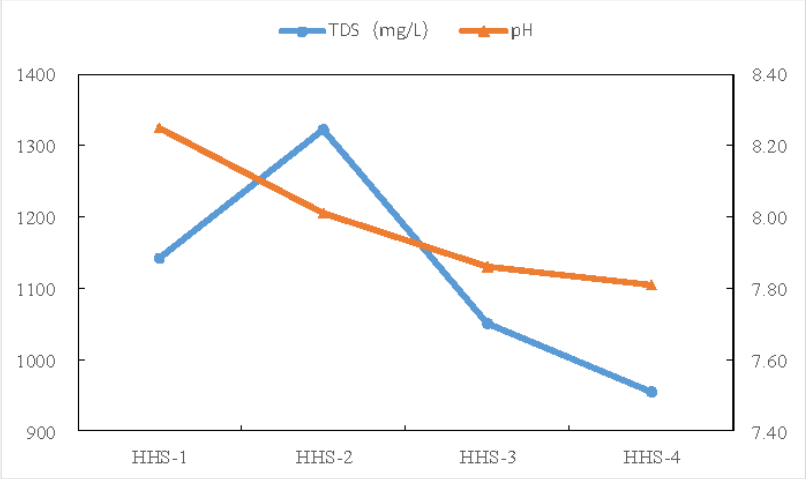

Figure 4. The variations in TDS and pH via the tests.

Table 4. Analysis results of the chemical composition of the mixed water (HHS) (unit: mg/L).

Time/d	Na^+	K^+	Ca^{2+}	Mg^{2+}	Cl^-	$SO_4{}^{2-}$	$HCO_3{}^-$	$NO_3{}^-$	SiO_2	F^-	TDS	pH
0	406	7.5	22.1	11.2	529.6	106.1	110.0	4.3	1	0.3	1142	8.25
5	418	7.9	44.6	6.1	577.7	156.1	142.0	40	12.7	0.7	1322	8.01
10	351	7.4	40	5.4	416.3	144.7	104.1	32.7	12.7	0.7	1050	7.86
15	325	7.2	38.3	5.7	355.2	130.8	112.4	36.4	12.7	0.6	956	7.81

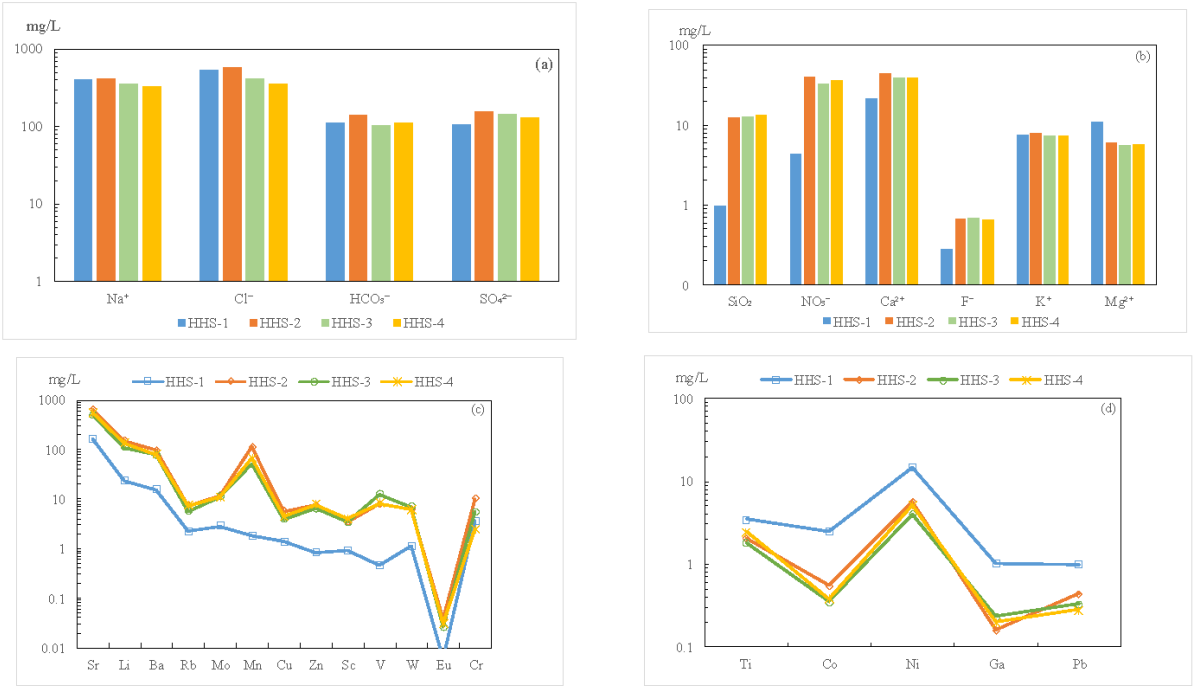

Figure 5. The variations in chemistry analyses via reinjection. (HHS−1, HHS−2, HHS−3, and HHS−4 were samples of reactions lasting for 0, 5, 10, and 15 days, respectively.) (**a**,**b**) were variations of the chemical composition via reinjection; (**c**,**d**) were variations of the trace elements variations via reinjection.

The changes in trace elements were complex. Overall, the concentrations of Sr, Li, Ba, Rb, Mo, Mn, Cu, Zn, Sc, V, W, Eu, and Cr exhibited an increase, although a decrease was observed during the intermediate process. Nevertheless, these levels remained significantly higher than the initial values (see Table 5; Figure 5c,d). In contrast, the concentrations of Ti, Co, Ni, Ga, and Pb displayed a decreasing trend. The variation in trace elements paralleled that of the conventional components of hydrochemistry, indicating that they were influenced by related water–rock reactions.

Table 5. The analysis results of the trace elements of the mixed water (HHS) (unit: mg/L).

Time/d	Sr	Li	Ba	Rb	Mo	Mn	Cu	Zn	Sc	V	W	Eu	Cr	Ti	Co	Ni	Ga	Pb
0	161.0	23.3	15.3	2.2	2.8	1.8	1.4	0.8	0.9	0.5	1.1	0.006	3.5	3.5	2.5	14.9	1.0	1.0
5	650.0	151.0	95.1	7.4	11.7	113.0	5.7	7.4	3.4	7.9	6.2	0.037	10.2	2.1	0.5	5.7	0.2	0.4
10	496.0	110.0	78.0	5.7	11.1	51.2	3.8	6.4	3.4	12.3	6.9	0.026	5.4	1.8	0.4	4.0	0.2	0.3
15	551.0	137.0	80.0	7.4	10.8	66.0	4.5	7.8	4.0	8.2	6.0	0.030	2.5	2.5	0.4	5.2	0.2	0.3

PHREEQC was utilized to calculate the ionic saturation index (Si) of the water samples during the reaction. The SOLUTION, EQUILIBRIUM, and REACTION TEMPERATURE modules of the PHREEQC program were employed to simulate the process. In the SOLUTION module, mixed water (HHS) was used to define the chemical composition of the reservoir. The EQUILIBRIUM module included dolomite, quartz, and calcite as potential minerals. The REACTION TEMPERATURE module was configured for a reservoir temperature of 60 °C. The results indicate that quartz transitioned from an unsaturated state (Si < 0) to a supersaturated state (Si > 0) during the reaction, suggesting a trend toward precipitation. Conversely, dolomite and calcite shifted from an initial supersaturated state to an unsaturated state, indicating a trend of dissolution. Aragonite and talc exhibited a pattern of initial precipitation followed by dissolution (see Figure 6).

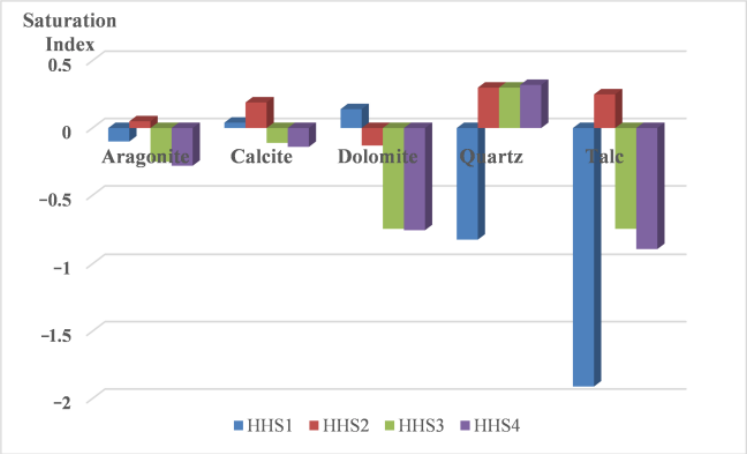

Figure 6. Saturation indices of some minerals via the tests.

As illustrated in Figure 7, the hydrogen and oxygen isotopes exhibited an enrichment trend that peaked at the initial time point (t = 5 d). This observation indicates the dissolution of minerals with relatively enriched oxygen isotopes and the exchange of these isotopes with geothermal water, resulting in a higher enrichment of oxygen isotopes in the geothermal water compared to earlier measurements. Subsequently, a reversal in this trend occurred at t = 10 d and t = 15 d, suggesting that the oxygen isotope-enriched rock minerals precipitated from the solution, albeit in lesser quantities than those that had previously dissolved. This phenomenon was primarily governed by the combined processes of dissolution and precipitation of silicate and carbonate minerals, including quartz, plagioclase feldspar, and calcite. The reaction equations are detailed in Formulations 1 to 20 [39–41]. See Table 6.

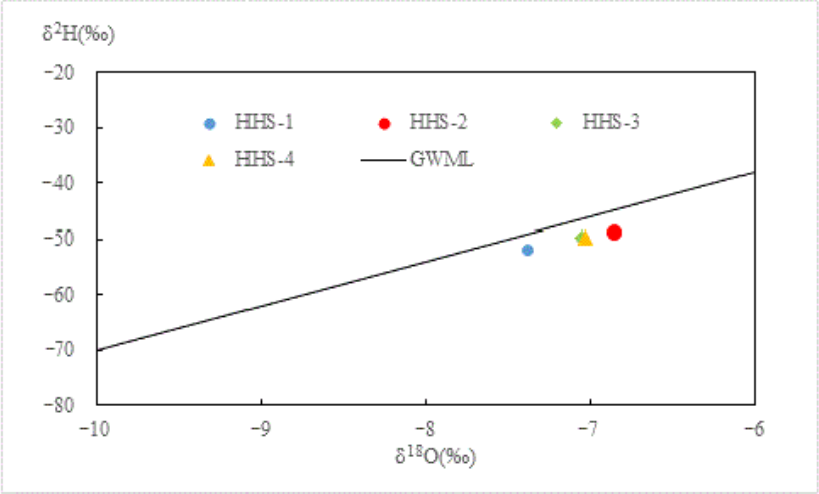

Figure 7. The behavior of $\delta^{18}O$ (‰) and $\delta^{2}H$ (‰) via reinjection.

Table 6. The isotope analysis results of the mixed water (HHS).

Time/d	$\delta^{18}O$ (‰)	$\delta^{2}H$ (‰)
0	−7.4	−52.0
5	−6.8	−49.2
10	−7.1	−49.8
15	−7.0	−49.6

3.2. Reservoir Lithology Response

The mineral compositions of sandstone samples were analyzed using an X-ray diffraction analyzer (XRD). The analysis revealed that the quartz content in the rock debris samples initially decreased (t = 5 d), followed by an increase (t = 10 d), and then a further decrease (t = 15 d). This pattern indicates that quartz and SiO_2 were converted into each other during the reaction (Formula (4)). Plagioclase feldspar exhibited a consistent downward trend, likely due to dissolution processes (Formulas (16)–(19)). In contrast, potassium feldspar, calcite, iron dolomite, and clay minerals generally showed an increasing trend, primarily driven by sedimentation (Formulas (5), (6), (11)–(15) and (20)); however, calcite and clay minerals experienced slight decreases on the 5th and 10th days of the reaction time, respectively. Notably, pyrite precipitation was observed on the 5th day of the reaction period, followed by its dissolution as the reaction progressed (Figure 8). The chemical composition of clay minerals mainly consists of silicon dioxide, alumina, and water, thus reducing its reaction equation to Formula (20). The chemical reaction equations governing the water–rock interactions occurring during the reinjection process are as follows [42]:

$$CO_2\ (g) + H_2O \Leftrightarrow H_2CO_3\ (aq) \quad (1)$$

$$H_2CO_3 \Leftrightarrow H^+ + HCO_3^- \quad (2)$$

$$HCO_3^- \Leftrightarrow H^+ + CO_3^{2-} \quad (3)$$

$$\text{Quartz (Talc)} \Leftrightarrow SiO_2\ (aq) \quad (4)$$

Calcite:

$$CaCO_3 + H^+ \Leftrightarrow Ca^{2+} + HCO_3^- \quad (5)$$

$$Ca^{2+} + CO_3^{2-} \Leftrightarrow CaCO_3 \quad (6)$$

Iron dolomite:

$$CaMg_3(CO_3) \Leftrightarrow CaMg(CO_3)_2 + 2Mg^{2+} + 2CO_3^{2-} \quad (7)$$

$$CaMg_3(CO_3) + 2H^+ \Leftrightarrow CaMg(CO_3)_2 + 2Mg^{2+} + 2HCO_3^- \quad (8)$$

$$CaMg_3(CO_3) + 4H^+ \Leftrightarrow CaMg(CO_3)_2 + 2Mg^{2+} + 2H_2O + 2CO_2\ (g) \quad (9)$$

$$CaMg_3(CO_3) + 2Ca^{2+} + 2CO_3^{2-} \Leftrightarrow 3CaMg(CO_3)_2 \quad (10)$$

Potassium feldspar:

$$3KAlSi_3O_8 + 2H^+ + 12H_2O \Leftrightarrow KAl_3Si_3O_{10}(OH)_2 + 6H_4SiO_4\ (aq) + 2K^+ \quad (11)$$

$$2KAlSi_3O_8 + 2H^+ + 9H_2O \Leftrightarrow H_4Al_2Si_2O_9 + 4H_4SiO_4\ (aq) + 2K^+ \quad (12)$$

$$2KAl_3Si_3O_{10}(OH)_2 + 2H^+ + 3H_2O \Leftrightarrow 3H_4Al_2Si_2O_9 + 2K^+ \quad (13)$$

$$2KAl_3Si_3O_{10}(OH)_2 + 2H^+ + 18H_2O \Leftrightarrow 3Al_2O_3{\cdot}3H_2O + 2K^+ + 6H_4SiO_4\ (aq) \quad (14)$$

$$3H_4Al_2Si_2O_9 + 5H_2O \Leftrightarrow Al_2O_3{\cdot}3H_2O + 2H_4SiO_4\ (aq) \quad (15)$$

Plagioclase feldspar:

$$3NaAlSi_3O_8 + 2H^+ \Leftrightarrow NaAl_3Si_3O_{10}(OH)_2 + 2Na^+ + 6SiO_2\ (aq) \quad (16)$$

$$2NaAl_3Si_3O_{10}(OH)_2 + 2H^+ + 3H_2O \Leftrightarrow 3H_4Al_2Si_2O_9 + 2Na^+ \quad (17)$$

$$KAlSi_3O_8 + NaCl \Leftrightarrow NaAlSi_3O_8 + KCl \quad (18)$$

$$2(Na,Ca)(Al,Si)_4O_8 + H_2O + 2CO_2 \Leftrightarrow 2KAlSi_3O_8 + 2Na^+ + 2HCO_3^- + Ca^{2+} \quad (19)$$

$$Clay\ mineral + 10H^+ \Leftrightarrow 2K^+ + 2Al^{3+} + SiO_2\ (aq) + 5H_2O \quad (20)$$

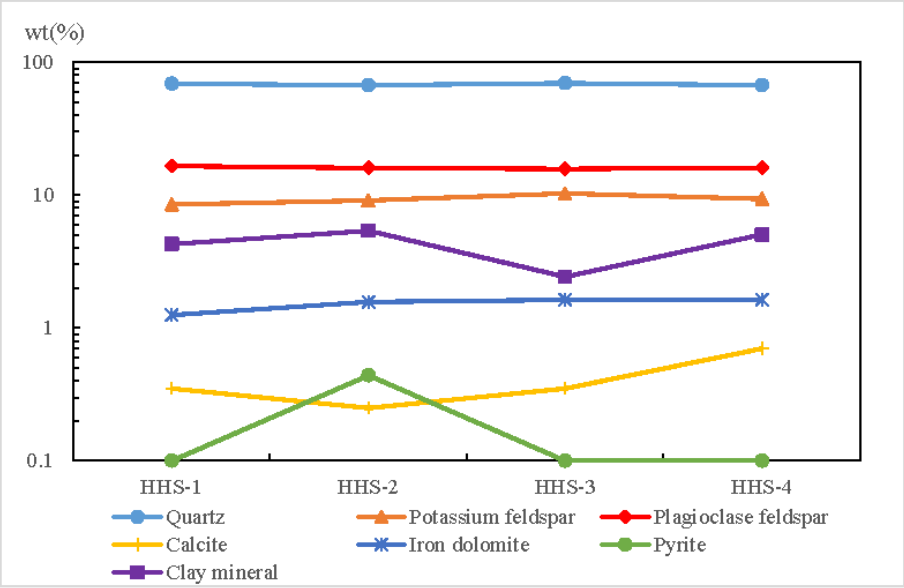

Figure 8. Contents of the mineral compositions via reinjection.

3.3. Geochemical Analysis

In the context of mixed water reinjection, along with changes in hydrochemistry and the isotopes of hydrogen and oxygen, it was observed that, during the initial stage of the reaction, quartz and plagioclase feldspar decreased, while potassium feldspar, calcite, iron dolomite, and clay minerals were formed. HCO_3^- was continuously consumed, and the reservoir rock minerals primarily precipitated throughout the entire process. The reduction in total dissolved solids (TDS) of 94.2 mg/L corresponded to 0.08% of the debris involved in the reaction. Some studies have indicated that thermal cycling-induced microcracks can alter the physical and mechanical properties of geothermal energy reservoirs, potentially affecting heat and mass transfer performance as well as the stability of the reservoir. However, changes in mineral composition do not necessarily have a significant impact on the initiation and propagation of cracks. Based on these findings, it can be concluded that mixed water reinjection has a minimal effect on the reservoir [43–45]. The content of clay minerals initially increased before subsequently decreasing. Overall, the clay mineral content increased, as evidenced by the reduction in TDS in the reinjection water.

PHREEQC was employed to simulate the variations in silicon concentration before and after the reinjection of mixed water (HHS) and geothermal water from Well A into Well B. The simulation utilized the SOLUTION, MIX, EQUILIBRIUM, and REACTION TEMPERATURE modules within the PHREEQC program. In the SOLUTION module, the geothermal fluid from Well B was used to define the chemical composition of the reservoir, while the geothermal fluid from Well A and HHS characterized the reinjection water. The MIX module established a mixing ratio of 1:1 for the reinjection water to the geothermal fluid. The EQUILIBRIUM module considered dolomite, quartz, and calcite as potential minerals. The REACTION TEMPERATURE module was adjusted to a reservoir temperature of 60 °C.

Figure 9 illustrates that, following the reinjection of the two water sources, the trends in the saturation index of minerals displayed similar patterns. Upon reaching equilibrium, carbonate minerals (aragonite, calcite, and dolomite), along with quartz, goethite, and hematite, became supersaturated, indicating a propensity for precipitation. The simulation results demonstrate that comparable hydrogeochemical changes occurred in the geothermal fluid after the reinjection of both types of water sources, thereby confirming the feasibility of reinjecting mixed water from sandstone geothermal reservoirs from a hydrogeochemical perspective.

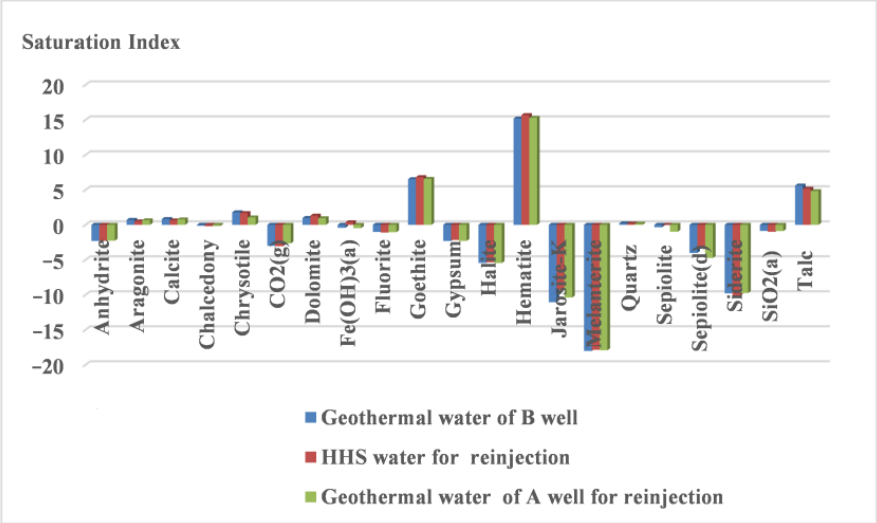

Figure 9. The variations in the saturation index before and after the reinjection into Well B from different water sources.

4. Conclusions

(1) The surface water treatment process for reinjection into sandstone geothermal reservoirs was established through water treatment simulation experiments. It is feasible to utilize the mixed water (HHS) produced from nanofiltration and intermediate water as a source for reinjection.

(2) Following the reinjection of mixed water (HHS) into the sandstone reservoir, the pH of the water exhibited a downward trend, while the total dissolved solids (TDS) content decreased by 94.2 mg/L, indicating the production of acidic substances and precipitates. The hydrochemical type consistently remained Cl-Na. The variation in trace elements paralleled that of conventional hydrochemical components, suggesting that they are influenced by related water–rock reactions. The rock minerals enriched in oxygen isotopes precipitated from the solution, with the amount of precipitation being lower than that of dissolution.

(3) Following the reinjection of mixed water (HHS) into the sandstone reservoir, the minerals within the reservoir exhibited minimal precipitation, primarily consisting of potassium feldspar and iron dolomite. During the experiment, a total of 28.3 mg of rock minerals was produced, accounting for only 0.08% of the debris involved in the reaction. This precipitation had a negligible impact on the reservoir.

(4) Similar hydrogeochemical changes were observed in the geothermal fluid after the reinjection of mixed water (HHS) and geothermal water. From the perspective of laboratory experiments, the reinjection of treated surface water into the sandstone geothermal reservoir is feasible. Future efforts should concentrate on conducting field tests to validate these findings, establishing a long-term geothermal fluid dynamic monitoring network, and utilizing numerical simulations to evaluate the application effects.

Author Contributions: Conceptualization, B.W. and Y.C.; methodology, B.W. and S.Z.; investigation, Y.Z.; resources, B.Y.; data curation, F.L.; writing—original draft preparation, B.W.; writing—review and editing, Y.Z. and Y.C.; supervision, S.Z.; project administration, Y.C.; resources, B.W., Y.Z., Y.C., S.Z., B.Y., and F.L. All authors have read and agreed to the published version of the manuscript.

Funding: This research was funded by Tianjin Bureau of Geology and Minerals Exploration, grant number Bureau of Mines Science Mission [2024] No. 4.

Institutional Review Board Statement: Not applicable.

Informed Consent Statement: Not applicable.

Data Availability Statement: Data is contained within the article.

Conflicts of Interest: The authors declare no conflicts of interest.

References

1. Wang, G.L.; Liu, Y.G.; Zhu, X.; Zhang, W. The status and development trend of geothermal resources in China. *Earth Sci. Front.* **2020**, *27*, 1–9.
2. Liu, J.; Song, M.Y.; Tian, G.H. Development situation of the geothermal resources and suggestion on sustainable development utilization in Tianjin. *Geol. Surv. Res.* **2012**, *35*, 67–73.
3. Cao, Q.; Fang, C.H.; Li, Y.; Wang, H.X.; Fang, Q.; Shi, X.Y. Development status of geothermal reinjection at home and abroad and its enlightenment. *Oil Drill. Prod. Technol.* **2021**, *43*, 203–211.
4. Yang, J.L.; Wang, D.M.; Niu, W.C.; Xiang, Z.Q.; Liu, Y.; Zhao, Z.L.; Cheng, X.Y. Prospects and problems of geothermal resources exploitation and utilization in Tianjin. *North China Geol.* **2022**, *45*, 1–6.
5. Yin, X.X.; Zao, S.M.; Cai, Y.; Yan, J.X.; Xu, L. Dynamic evolution of geothermal reservoir characteristics in Tianjin in the last three decades of large—Scale development. *Acia Geothermal Sin.* **2024**, *98*, 297–313.
6. Zhao, S.M.; Cheng, W.Q.; Zhang, W. Analysis of the geothermal reinjection blockage problem in Neogene sandstone thermal reservoir. *Geothermal Energy* **2013**, 7–12.
7. Axelsson, G. Importance of Geothermal Reinjection. In Proceedings of the Workshop for Decision Makers on Direct Heating Use of Geothermal Resources in Asia, Tinjin, China, 11–18 May 2008.
8. Capetti, G.; Parisi, L.; Ridolfi, A.; Stefani, G. Fifteen years of Reinjection in the Larderello-Valle Secolo Area: Analysis of the Production Data. In Proceedings of the World Geothermal Congress 1995, Florence, Italy, 18–31 May 1995.

9. Stark, M.A.; Tom, W.; Beall, J.J.; Goyal, K.P.; Pingol, A.S. The Santa Rosa—Geysers Recharge Project, Geysers Geothermal Field, California, USA. In Proceedings of the Transactions Geothermal Resources Council 2005, Antalya, Turkey, 14–29 April 2005.
10. Ungemach, P.; Antics, M. Sustainable Geothermal Reservoir Management Practice. In Proceedings of the International Course and EGEC Business Seminar on Organization of Successful Development of a Geothermal Project, Casta Papiernicka, Slovakia, 26–29 May 2009.
11. Allen, A.; Milenic, D. Low-enthalpy geothermal energy resources from groundwater in fluvioglacial gravels of buried valleys. *Appl. Energy* **2003**, *74*, 9–19. [CrossRef]
12. Bodvarsson, G.S.S.; Tefansson, V. Some theoretical and field aspects of reinjection in geothermal reservoirs. *Water Resour. Res.* **1989**, *25*, 1235–1248. [CrossRef]
13. Darwis, R.S.; Tampubolon, T.; Simatupang, R.; Asdassah, D. Study of Water Reinjection on the Kamojang Geothermal Reservoir Performance, Indonesia. In Proceedings of the 17th NZ Geothermal Workshop 1995, Auckland, New Zealand, 1 January 1995.
14. Diazr, A.R.; Kaya, E.; Zarrouk, S.J. Reinjection in geothermal fields—A worldwide review update. *Renew. Sustain. Energy Rev.* **2016**, *53*, 105–162.
15. Kamila, Z.; Kaya, E.; Zarrouk, S.J. Reinjection in geothermal fields: An updated worldwide review 2020. *Geothermics* **2021**, *89*, 101970. [CrossRef]
16. Zhao, S.M. *Development and Utilization of Geothermal Field in Sedimentary Basin*; Geology Press: Beijing, China, 2013.
17. Wang, L.C. *A Study of Geothermal Reinjection in the Guantao Reservoir in Tianjin*; China University of Geosciences: Beijing, China, 2015.
18. Wang, X.P.; Liu, H.; Jiang, S.J.; Deng, R.Q. Reinjection experimental research on sedimentary basin sandstone reservoir—A case study of Yucheng City' Shandong. *Geol. Rev.* **2020**, *66*, 485–492.
19. Zhou, X. *Reinjection Plugging Mechanism Researching of Sedimentary Basin Type Porous Geothermal Water—As the Reinjection Well in Sanqiao of Xi'an for an Example*; Chang'an University: Xi'an, China, 2013.
20. Dai, Q.; Wang, C.; Luo, Y.; Xu, B.B.; Yin, W.T.; Wang, P.F. Research on sandstone geothermal reservoir reinjection plugging mechanism and measures against it. *Adv. Fine Petrochem.* **2017**, *18*, 10–13.
21. Wu, D.D. Discussion on the countermeasures for blockage control of sandstone geothermal reinjection wells. *Explor. Dev.* **2022**, *18*, 166–167.
22. Jiang, G.S.; Wang, G.H.; Zhao, N.; Huang, X.L.; Shen, J. Application of gravel-packed completion technology of Guantao geothermal reinjection well in the Western Binhai New Area. *Geol. Surv. Res.* **2014**, *37*, 149–154.
23. Zhao, Y.T.; Shen, J.; Zhao, S.M.; Wen, S.; Zhang, S. Well completion technology optimization and application effect analysis of medium –deep sandstone reinjection wells: A case study of Minghuazhen Formation in Tianjin. *Pet. Reserv. Eval. Dev.* **2023**, *13*, 765–772.
24. Feng, S.T.; Wang, C.M.; Yang, Y.B.; Song, W.H.; Liu, S.; Zhao, J.C. Evaluation of the impact of sandstone thermal reservoir recharge on reservoirs: Taking the geothermal region of the northwest Shandong Depression as an example. *J. Geol.* **2019**, *93*, 158–167.
25. Wang, H.J.; Yu, M.; Zhao, S.M.; Gao, X.Z.; Liu, F. Microscopic analysis of pore characteristics and comparison of permeability of sandstone in geothermal wells of Neogene. *Acta Energiae Solaris Sin.* **2019**, *40*, 1790–1796.
26. Li, S.; Sun, X.L.; Yang, B.M.; Gao, X.Z. Evaluation and analysis of heat reservoir reinjection ability of Neogene Guantao Formation in Tianjin. *North China Geol.* **2023**, *46*, 31–44.
27. Chen, Z.Y. Modeling water-rock interaction of geothermal reinjection in the Tanggu low-temperature field, Tianjin. *Earth Sci. J. China Univ. Geosci.* **1998**, *23*, 513–518.
28. Shi, X.F.; Zhang, W.J.; Wang, H.M.; Jiao, X.; He, H.Y. Modeling of water-rock interaction during the artificial recharge. *J. Jilin Univ. Earth Sci. Ed.* **2013**, *43*, 220–227.
29. Wu, K.Y.; Xiong, Y.; Tan, X.C.; Liu, X.J.; Zhang, Y.F.; Chen, X.D.; Li, Y.F. Study of the crystallization kinetics for "water-rock" interactions in the reservoir pore-system: An overview. *Acta Sedimentol. Sin.* **2022**, *40*, 996–1009.
30. Su, Y.J.; Yang, F.T.; Wang, B.; Jia, Z.; Duan, Z.F. Reinjection of cooled water into sandstone geothermal reservoirs in China: A review. *Geosci. J.* **2018**, *22*, 199–207. [CrossRef]
31. Wang, B.; Xia, Y.B.; Liu, D.L.; Tian, G.H.; Cai, Y.; Zong, Z.H. Analysis on PHREEQC simulation surface water reinjection of Jxw geothermal wells in Baodi District, Tianjin. *Geol. Prospect.* **2015**, *38*, 317–320.
32. Liu, D.L.; Li, Y.M.; Pang, Z.H.; Zhao, S.M.; Fan, Y.F. Geochemical responses of carbonate reservoir to untreated lake water reinjection. *J. Eng. Geol.* **2019**, *27*, 178–183.
33. Li, Y.M.; Shen, J.; Zhao, S.M.; Pang, Z.H.; Liu, D.L. Feasibility study on high-effective co-reinjection of waste geothermal water and water from other sources into carbonate reservoir. *Sci. Technol. Dev.* **2020**, *16*, 332–337.
34. Xia, Y.B.; Wang, B.; Zhang, F.N.; Jia, Z. Optimization and transformation of water treatment technology for surface water reinjection into geothermal reservoir in Dongli Lake area of Tianjin. *Energy Rep.* **2023**, *9*, 25–29. [CrossRef]
35. Standardization Administration of China. GB/T 19772-2005. Available online: https://www.chinesestandard.net/PDF/English.aspx/GBT19772-2005 (accessed on 25 June 2024).
36. National Energy Administration of China. SY/T 5329-2012. Available online: https://www.chinesestandard.net/PDF/English.aspx/SYT5329-2012 (accessed on 25 June 2024).
37. Ministry of Natural Resources of the People's Republic of China. DZ/T 0330-2019. Available online: https://www.chinesestandard.net/PDF/English.aspx/DZT0330-2019 (accessed on 25 June 2024).

38. Guo, Y.L.; Xu, Y.H.; Wang, H.J.; Shen, J.; Zhao, S.M. Experimental investigation of water-rock reaction for the reinjection of sandstone geothermal reservoirs: A case from Neogene Guantao Formation in Tianjin. *Renew. Energy* **2023**, *210*, 203–214. [CrossRef]
39. Jiang, W.J.; Wang, G.C.; Sheng, Y.Z.; Shi, Z.M.; Zhang, H. Isotopes in groundwater (^{2}H, ^{18}O, ^{14}C) revealed the climate and groundwater recharge in the Northern China. *Sci. Total Environ.* **2019**, *666*, 298–307. [CrossRef]
40. Jiang, W.J.; Meng, L.S.; Liu, F.T.; Sheng, Y.Z.; Chen, S.M.; Yang, J.L.; Mao, H.R.; Zhang, J.; Zhang, Z.; Ning, H. Distribution, source investigation, and risk assessment of topsoil heavy metals in areas with intensive anthropogenic activities using the positive matrix factorization (PMF) model coupled with self-organizing map (SOM). Environ. *Geochem. Health* **2023**, *45*, 6353–6370. [CrossRef] [PubMed]
41. Ning, H.; Jiang, W.J.; Sheng, Y.Z.; Wang, K.L.; Chen, S.M.; Zhang, Z.; Liu, F.T. Comprehensive evaluation of nitrogen contamination in water ecosystems of the Miyun reservoir watershed, northern China: Distribution, source apportionment and risk assessment. *Environ. Geochem. Health* **2024**, *46*, 278. [CrossRef]
42. Garrels, R.M.; Christ, C.L. *Solutions, Minerals, and Equilibria*; Jones and Bartlett Publishiers: Boston, MA, USA, 1965.
43. Feng, G.; Wang, X.C.; Kang, Y.; Zhang, Z.T. Effect of thermal cycling-dependent cracks on physical and mechanical properties of granite for enhanced geothermal system. *Int. J. Rock Mech. Min. Sci.* **2020**, *134*, 104476. [CrossRef]
44. Feng, G.; Zhu, C.; Wang, X.; Tang, S. Thermal effects on prediction accuracy of dense granite mechanical behaviors using modified maximum tangential stress criterion. *J. Rock Mech. Geotech. Eng.* **2023**, *15*, 1734–1748. [CrossRef]
45. Zhu, D.F.; Yu, B.B.; Wang, D.Y.; Zhang, Y.J. Fusion of finite element and machine learning methods to predict rock shear strength parameters. *J. Geophys. Eng.* **2024**, *21*, 1183–1193. [CrossRef]

Disclaimer/Publisher's Note: The statements, opinions and data contained in all publications are solely those of the individual author(s) and contributor(s) and not of MDPI and/or the editor(s). MDPI and/or the editor(s) disclaim responsibility for any injury to people or property resulting from any ideas, methods, instructions or products referred to in the content.

water

MDPI

Article

Comprehending Spatial Distribution and Controlling Mechanisms of Groundwater in Topical Coastal Aquifers of Southern China Based on Hydrochemical Evaluations

Jun He [1,2], Pan Wu [1,2], Yiyong Li [1,2], Min Zeng [1,2], Chen Chen [1,2], Hamza Jakada [3,*] and Xinwen Zhao [1,2]

[1] Wuhan Center, China Geological Survey, Wuhan 430205, China; hejun@mail.cgs.gov.cn (J.H.); wupan@mail.cgs.gov.cn (P.W.); liyiyong@mail.cgs.gov.cn (Y.L.); cengmin@mail.cgs.gov.cn (M.Z.); chenchen002@mail.cgs.gov.cn (C.C.); zhaoxinwen@mail.cgs.gov.cn (X.Z.)
[2] Key Laboratory of Eco-Hydrogeological Process of River and Lake Wetlands in Changjiang Reaches, China Geological Survey, Wuhan 430205, China
[3] Department of Civil Engineering, Baze University, Abuja 900211, Nigeria
* Correspondence: jakadahamza@gmail.com

Abstract: Groundwater quality and availability in coastal aquifers have become a serious concern in recent times due to increased abstraction for domestic, agricultural and industrial purposes. (1) Background: Zhuhai city is selected as a representative coastal aquifer in Southern China to comprehensively evaluate the hydrochemical characteristics, spatial distribution and controlling mechanisms of groundwater. (2) Methods: A detailed study utilizing statistical analyses, a Piper diagram, Gibbs plots, and ion ratios was conducted on 114 surface water samples and 211 groundwater samples. (3) Results: The findings indicate that the pH of most groundwater is from 6.06 to 6.52, indicating a weakly acidic environment. The pH of surface water ranges from 5.35 to 9.86, with most values being weakly alkaline. The acidity in the groundwater may be related to the acidic atmospheric precipitation, an acidic unsaturated zone, oxidation of sulphide minerals and tidal action. The groundwater chemical types are predominantly mixed, followed by Ca-Mg-HCO_3 type. Surface water samples are predominantly Na-Cl-SO_4 type. The NO_3^- concentration in groundwater is relatively high, with a mean value of 17.46 mg/L. The NO_2^- and NH_4^+ concentrations in groundwater are relatively low, with mean values of 0.46 mg/L and 7.58 mg/L. (4) Conclusions: The spatial distribution of the principal chemical constituents in the groundwater is related to the landform. The chemical characteristics of groundwater in the study area are mainly controlled by the weathering and dissolution of silicate and sulfate minerals, evaporation, seawater mixing and cation exchange. Nitrate in clastic fissure groundwater, granite fissure groundwater and unconfined pore groundwater primarily originates from atmospheric precipitation, agricultural activities of slope farmland and forest land. Nitrate in confined pore groundwater and karst groundwater primarily originates from domestic sewage and mariculture wastewater. Our findings elucidate the processes characterizing the hydrogeology and surface water interactions in Zhuhai City's coastal system, which are relevant to other catchments with similar geological characteristics.

Keywords: coastal groundwater; southern China; hydrochemical characteristics; driving forces

1. Introduction

Groundwater has become an indispensable freshwater resource to meet the increasing domestic, agricultural and industrial demands of the growing global population [1]. Of the total amount of groundwater extracted globally, about 65% is used for drinking, 20% for irrigation and livestock rearing, and the remaining 15% is used for industrial and mining activities [2,3]. Coastal areas serve as transition zones between terrestrial and marine ecosystems, which are influenced by land and sea changes [4]. These changes are sometimes driven by anthropogenic activities along the coast, including groundwater abstraction.

Generally, coastal aquifers are in close proximity to the ocean, and a variety of complex hydrogeological and geochemical processes, such as evaporation, mineral dissolution and mixing of saline and fresh water, define the water chemistry characteristics [5]. Soil properties strongly influence groundwater chemical composition after leaching, through the soil, due to their significant role in nutrient leaching provision water supply to crops [6].

Therefore, characterizing the chemicals in groundwater is crucial for providing reliable hydrogeological descriptions and diagnosing freshwater and saltwater mixing systems [7]. Proper understanding of groundwater's hydrochemical characteristics is invaluable for assessing water quality suitability for drinking and irrigation [8], and the concentration of certain inorganic and organic substances can adversely affect human health and agricultural production. The main analysis methods for water chemistry include statistical analysis, hydrogeochemistry and isotope hydrology [9–16].

Zhuhai City is located in the coastal area of Southern China, characterized by a dense river network and a close relationship with seawater. The interaction between groundwater and seawater is frequent and significant. A series of groundwater environmental problems has arisen due to unique geological conditions and human engineering activities such as sea reclamation and mariculture [17–22]. Numerous research results have been obtained, and the origins and mechanisms of the pollution components have been analyzed. However, there is a relative dearth of research concerning the groundwater's hydrochemical characteristics, spatial patterns and driving mechanisms beyond seawater intrusion. This paper will analyze the hydrochemical composition using statistical analyses, a Piper diagram, Gibbs plots, and ion ratio methods [23,24], study the formation control mechanism of groundwater in coastal areas [10], identify the ionic sources [25] and examine major hydrogeochemical effects [26], based on the concentration data of chemical components forming a large number of surface water and groundwater samples. The study is focused on the unique geologic environment of coastal zones, including the factors of topography, hydrology and meteorology, filling the current research gaps of Southern China. The research can provide a scientific basis for the utilization and protection of groundwater resources.

2. Materials and Methods

2.1. Study Area

Zhuhai is a coastal city in Southern China with a transitional oceanic climate between the southern subtropics and the tropics. The average annual rainfall is 2472.1 mm. The terrain slopes from northwest to southeast, and there are numerous waterways from the Xijiang River dividing into the South China Sea, intertwined with local rivers and tidal surges. The distribution of groundwater in the region is mainly controlled by a combination of factors, including geological structure, stratigraphic lithology, topography, meteorology and hydrology [22]. Groundwater is categorized into four types: pore groundwater, clastic fissure groundwater, granite fissure groundwater and karst groundwater (Figure 1). Pore groundwater is primarily distributed in the coastal plain area with a well-developed river network, and the aquifer lithology is dominated by coarse and medium sand and gravel (Figure 2). The aquifer thickness ranges from 1 to 10 m, and the groundwater is mostly slightly brackish or brackish. Clastic fissure groundwater is sporadically distributed in Pingsha, Nanshui and Sanzao. The aquifer lithology is dominated by conglomerate, siltstone and quartz sandstone, and the quantity of water is low. Granite fissure groundwater is widely distributed in the hilly and terrace areas, and the aquifer lithology is primarily granite, with low to moderate quantity [19]. Karst groundwater was found in three drill holes sporadically covered by the Quaternary System, which had not been previously identified, and its distribution range remains unclear. Groundwater is primarily recharged through infiltration from rainfall and surface water. Fissure groundwater in the hilly mountainous areas is discharged into the neighboring gullies via spring seepage, or laterally recharged to the pore groundwater of the Quaternary System via a sub-surface flow. The level of pore groundwater in the valleys and flood plains is shallow, and it is locally slightly

confined. Groundwater is primarily drained through evaporation, discharged into the rivers and sea, and artificially extracted.

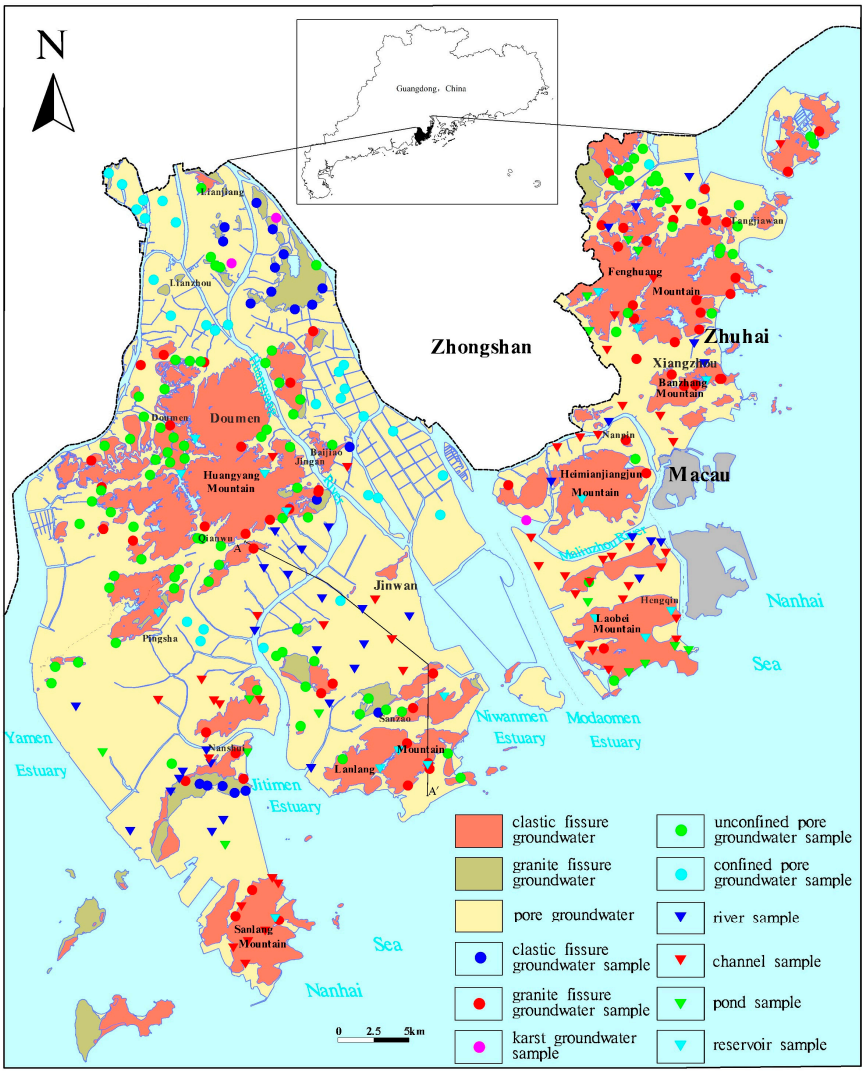

Figure 1. Simple hydrogeological map of study area and location of samples.

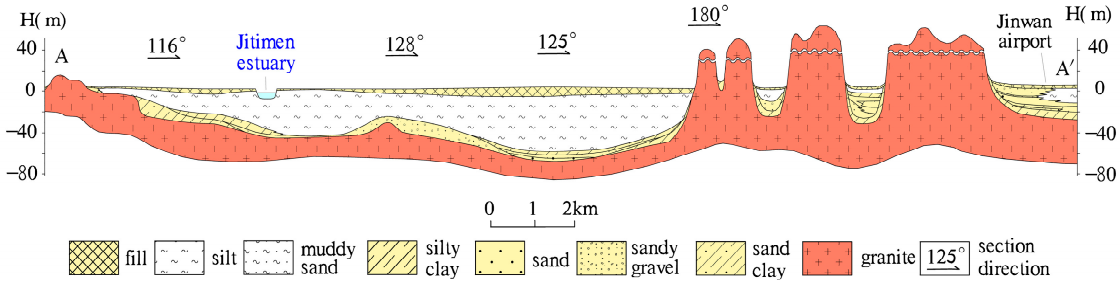

Figure 2. Section map of study area (location of the section is in Figure 1).

2.2. Sampling and Testing

From April to May 2023, 325 water samples were collected (Figure 1), including 114 surface water samples and 211 groundwater samples. Surface water samples were collected from depths of 30 to 50 cm below the water surface at 34 rivers, 49 channels, 14 ponds and 17 reservoirs. Groundwater samples included 19 clastic fissure groundwater, 63 granitic fissure groundwater, 3 karst groundwater, 97 unconfined pore groundwater and 29 confined pore groundwater samples, which were collected from 28 springs,

52 boreholes and 131 wells. The depth of the groundwater sample is from 0.1 to 58.1 m. pH, electrical conductivity (EC) and total dissolved solids (TDS) were measured on-site using a portable water quality analyzer (Manta2). The collected water samples were filtered through a 0.45 μm membrane for anion analysis. Samples for cation analysis were acidified to a pH below 2 with ultrapure concentrated nitric acid after filtering. All samples were collected in polyethylene sampling bottles and stored in a refrigerated sample preservation box at 4 °C. They were delivered to the laboratory for analysis within one week, and the analysis was performed at the South-Central Mineral Resources Testing Center of the Ministry of Natural Resources. The major cations (K^+, Na^+, Ca^{2+} and Mg^{2+}) were determined by ICP-AES (ICAP 6000 Series, Thermo Fisher Scientific, Waltham, MA, USA). The major anions (Cl^-, $SO_4{}^{2-}$, $NO_3{}^-$) were determined by ion chromatography (ICS 5000+, Thermo Fisher Scientific, Waltham, MA, USA). Bromides and iodides were determined by ICP-MS (X Series II, Thermo Fisher Scientific, Waltham, MA, USA), and bicarbonate was determined by titration. The accuracy of the test was controlled by certified reference materials or standard addition recovery methods, and the precision was controlled by sample repeatability analysis. The spiked recovery samples were inserted in each of the batch samples for accuracy control. The qualified rate of each index was 100%. More than 20% of the samples were randomly selected for repeatability analysis, and the qualified rate of relative deviation of each batch of repeated analysis results was more than 90%. The charge balance errors (CBEs) of the main cations and anions were calculated to confirm the reliability of the water quality data. The CBEs of the data were within the range of ±5%, indicating reliable water quality data.

3. Results

3.1. Hydrochemical Characteristics

The pH of groundwater in the study area ranges from 3.24 to 8.23 (Table 1), with most samples falling between 6.06 and 6.52, indicating a weakly acidic environment. The pH of surface water ranges from 5.35 to 9.86 (Table 2), with most values being weakly alkaline, typically above 7.

Table 1. Statistical eigenvalues of major macronutrient components of groundwater.

Groundwater Type		pH	EC μs/cm	K^+ mg/L	Na^+ mg/L	Ca^{2+} mg/L	Mg^{2+} mg/L	Cl^- mg/L	$SO_4{}^{2-}$ mg/L	$HCO_3{}^-$ mg/L	TDS mg/L
Clastic fissure groundwater	max	6.86	726.7	14.60	61.80	66.70	13.00	92.90	83.30	219.0	190.0
	min	4.54	31.1	0.65	3.92	0.46	0.58	2.36	1.76	6.30	3.78
	avg	5.86	178.2	4.62	12.94	16.33	3.32	14.77	13.84	61.30	54.46
	std	0.70	203.5	3.93	14.19	21.24	3.07	23.45	19.93	67.85	63.23
	cv	0.12	1.14	0.85	1.10	1.30	0.92	1.59	1.44	1.11	1.16
Granite fissure groundwater	max	8.00	3135	55.60	463.0	96.20	8.14	745.0	60.30	291.0	1480
	min	4.53	29.7	<0.07	3.80	<0.02	0.21	<0.06	<0.1	<0.5	32.20
	avg	6.29	231.9	5.98	23.20	14.68	1.93	24.26	11.31	75.15	158.9
	std	0.79	409.0	7.38	58.23	19.87	1.66	93.50	13.93	74.06	194.0
	cv	0.13	1.76	1.24	2.51	1.35	0.86	3.85	1.23	0.99	1.22
Karst groundwater	max	7.04	22,550	97.20	3670	1580	495.0	7240	420.0	339.0	12,500
	min	5.88	2632	22.80	494	18.50	32.20	500.0	150.0	25.30	1400
	avg	6.29	14,067	57.53	1795	714.2	318.4	4500	283.7	177.43	7860
	std	0.65	10,282	37.44	1664	794.5	250.1	3542	135.0	157.06	5769
	cv	0.10	0.73	0.65	0.93	1.11	0.79	0.79	0.48	0.89	0.73
Unconfined pore groundwater	max	7.79	3928	66.40	658.0	119.0	198.0	1070	172.0	973.0	2140
	min	3.24	39.8	1.38	3.98	0.45	0.29	3.16	1.89	4.76	47.30
	avg	6.18	486.7	13.97	33.48	35.37	7.42	52.13	30.15	125.05	289.0
	std	0.71	501.0	11.63	70.95	23.99	20.48	121.26	23.58	132.66	267.2
	cv	0.11	1.03	0.83	2.12	0.68	2.76	2.33	0.78	1.06	0.92
Confined pore groundwater	max	8.23	40,450	294.0	7920	814.0	1020	13,800	1380	1580	22,500
	min	4.64	454.5	8.16	15.30	10.70	3.91	41.20	3.92	<0.5	224.0
	avg	6.86	18,475	117.06	2974	259.5	381.9	5918	310.8	486.6	9801
	std	0.90	12,983	80.81	2330	194.6	320.3	4344	407.0	478.9	6799
	cv	0.13	0.70	0.69	0.78	0.75	0.84	0.73	1.31	0.98	0.69

Table 2. Statistical eigenvalues of major macronutrient components of surface water.

Surface Water Type		pH	EC μs/cm	K^+ mg/L	Na^+ mg/L	Ca^{2+} mg/L	Mg^{2+} mg/L	Cl^- mg/L	SO_4^{2-} mg/L	HCO_3^- mg/L	TDS mg/L
River	max	9.86	40,070	306.00	7700	316.0	1130	13,700	2020	267.0	25,300
	min	6.02	2.50	2.23	10.60	0.76	0.68	10.70	12.40	31.70	131.0
	avg	7.12	10,234	89.46	1803	104.92	233.8	3082	511.9	162.8	5925
	std	0.76	11,551	89.55	2135	77.77	290.8	3690	543.1	48.86	6810
	cv	0.11	1.13	1.00	1.18	0.74	1.24	1.20	1.06	0.30	1.15
Channel	max	9.42	34,640	273.00	6980	263.0	900	10,100	1750	304.0	20,400
	min	5.35	5.30	2.63	8.73	0.75	0.67	4.72	3.54	<0.5	56.70
	avg	6.67	7847	76.50	1498	85.60	189.7	2457	396.2	135.7	4472
	std	0.67	10,004	86.39	2045	77.60	261.0	3239	513.9	70.62	5859
	cv	0.10	1.27	1.13	1.37	0.91	1.38	1.32	1.30	0.52	1.31
Pond	max	8.01	37,850	305.00	7650	565.0	1010	11,900	1920	214.0	23,200
	min	6.24	53.2	5.54	8.25	0.99	0.33	5.53	3.86	23.80	48.90
	avg	6.95	10,967	88.93	1820	123.54	228.0	3167	453.7	126.9	5961
	std	0.49	13,385	104.13	2489	160.84	328.6	4244	605.5	68.96	7887
	cv	0.07	1.22	1.17	1.37	1.30	1.44	1.34	1.33	0.54	1.32
Reservoir	max	8.61	823.6	32.60	46.60	42.00	12.70	83.90	38.80	153.0	316.0
	min	5.63	29.9	2.04	4.50	0.78	0.35	3.08	2.17	14.20	12.60
	avg	6.92	140.3	10.64	15.91	7.39	2.23	14.53	8.20	39.83	89.38
	std	0.74	202.8	9.17	10.00	11.73	3.19	20.38	10.07	37.66	70.83
	cv	0.11	1.45	0.86	0.63	1.59	1.43	1.40	1.23	0.95	0.79

The EC of groundwater ranges from 29.7 to 40,450 μs/cm (Table 1), with the deep confined groundwater generally having higher EC than shallow aquifer. This may be related to recharged by seawater. The EC of the confined pore groundwater ranges from 454.5 and 40,450 μs/cm, with an average of 18,475 μs/cm. The EC of the three karst groundwater samples ranges from 2632 to 22,550 μs/cm, with an average of 14,067 μs/cm. Most of these two types of groundwater are saline. A small number of other types of groundwater with high conductivity are individually influenced by seawater. The conductivity of surface water ranges from 2.5 to 40,070 μs/cm (Table 2), and most of the surface water showing high conductivity is closely related to seawater, except for the reservoir freshwater with EC ranging from 29.9 to 823.6 μs/cm.

The cations in the groundwater are dominated by Na^+ and Ca^{2+}, with the overall trend being $Na^+ > Ca^{2+} > Mg^{2+} > K^+$, and the average concentrations are 457.7 mg/L, 67.93 mg/L, 61.30 mg/L and 25.53 mg/L, respectively. The anions are dominated by Cl^- and HCO_3^-, with the overall trend being $Cl^- > HCO_3^- > SO_4^{2-}$, and the average concentrations are 909.9 mg/L, 154.84 mg/L and 65.23 mg/L, respectively. The coefficient variations of the major anions and cations in groundwater is between 1.57 and 2.94, indicating that the chemical characteristics, source of groundwater and the water–rock interactions during transport are relatively complex.

The distribution characteristics of major anions and cations in groundwater are generally consistent across different types, except that the concentrations of various ions in confined pore groundwater and karst groundwater are significantly higher compared to other types. The average concentrations of the two types are 117.06 mg/L and 57.53 mg/L for K^+, 2974 mg/L and 1795 mg/L for Na^+, 259.5 mg/L and 714.2 mg/L for Ca^{2+}, 381.9 mg/L and 318.4 mg/L for Mg^{2+}, 5918 mg/L and 4500 mg/L for Cl^-, 310.8 mg/L and 283.7 mg/L for SO_4^{2-}, 486.6 mg/L and 117.43 mg/L for HCO_3^-.

The main cations in surface water are dominated by Na^+ and Mg^{2+}, with the overall trend being $Na^+ > Mg^{2+} > Ca^{2+} > K^+$, and the average concentrations are 1360 mg/L, 173.4 mg/L, 82.80 mg/L and 70.35 mg/L, respectively. The anions are dominated by Cl^- and SO_4^{2-}, with the overall trend being $Cl^- > SO_4^{2-} > HCO_3^-$, and the average concentrations are 2299 mg/L, 368.03 mg/L and 128.12 mg/L, respectively. The chemical composition of water in canals and ponds is broadly similar to that of rivers. The concentrations of major anions and cations in reservoir water are much lower compared to other types of surface water. Reservoir water is primarily recharged by atmospheric

precipitation and groundwater from surrounding mountains. Rivers, canals and ponds are interconnected with seawater through the water system, and their quality is significantly influenced by seawater.

The TDS of groundwater ranges from 32.2 to 22,500 mg/L, with an average of 1650 mg/L. The TDS of surface water ranges from 12.6 to 25,300 mg/L, with an average of 4435 mg/L. The variation characteristics of TDS are consistent with those of conductivity. The TDS of confined pore groundwater and karst groundwater are higher compared to other types of groundwater. The maximum TDS of the samples from rivers, canals and ponds exceeded 20 g/L, except for reservoir water, which has a maximum TDS of 316 mg/L.

The detection rates of nitrate, nitrite and ammonia nitrogen in the 211 groundwater samples collected in this survey are 97.15%, 68.72% and 75.83%, respectively. The dissolved inorganic nitrogen in groundwater is predominantly nitrate, except in confined pore water where ammonia nitrogen predominates.

The concentration of nitrate in groundwater ranges from 0.02 to 162 mg/L, with an average of 17.46 mg/L. The concentration of nitrite in groundwater ranges from 0.02 to 6.11 mg/L, with an average of 0.46 mg/L. The concentration of ammonia nitrogen in groundwater ranges from 0.02 to 194 mg/L, with an average of 7.58 mg/L. The concentration of nitrate and nitrite in shallow water is higher than in deep water, whereas the concentration of ammonia nitrogen shows the opposite trend

3.2. Water Chemical Types

The Piper diagram of groundwater and surface water shows that the main groundwater chemical types were Ca-Mg-HCO_3, Na-Cl-SO_4, mixed Ca-Na-HCO_3 and mixed Ca-Mg-Cl, accounting for 36.49%, 27.01%, 16.11% and 14.69% of the samples, respectively (Figure 3). The chemical types of different types of groundwater are clearly distinct. Most of the clastic fissure groundwater lacks a dominant cation, with a small amount dominated by Ca^{2+}, and the anions are dominated by HCO_3^-, mainly forming the Ca-Mg-HCO_3 type, with a small amount of Na-Cl-SO_4 and mixed Ca-Mg-Cl type.

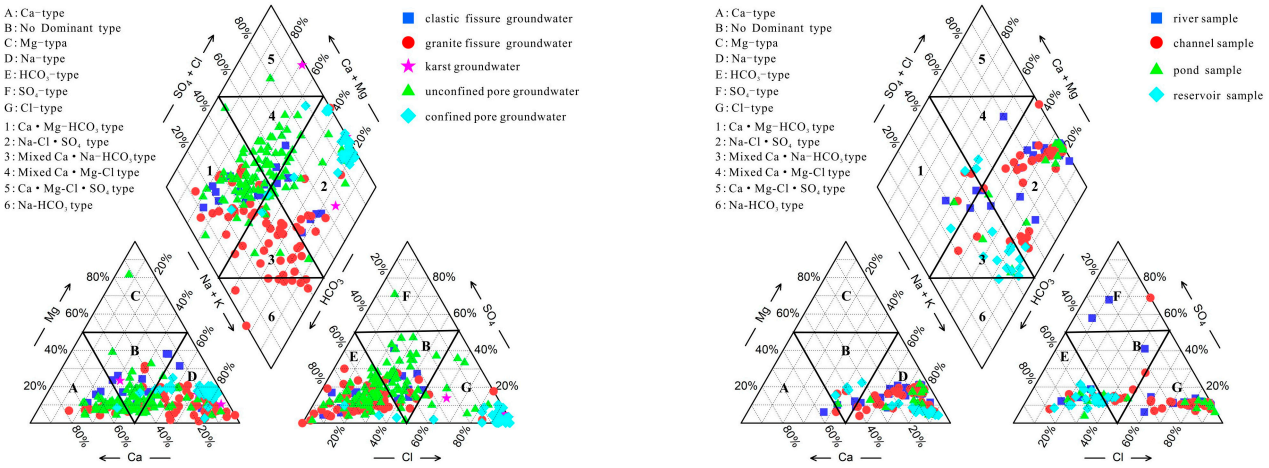

Figure 3. Piper diagram of water samples.

The chemical composition of the granite fissure groundwater is consistent with that of clastic fissure groundwater. The cations in most samples are dominated by Na^+, a small number of samples lack dominant cations or are dominated by Ca^{2+}. The anions are dominated by HCO_3^-, and the chemical type of the groundwater is predominantly the mixed Ca-Na-HCO_3 type, with a small proportion being Ca-Mg-HCO_3 type. Two out of the three karst groundwater samples are Na-Cl-SO_4 type, and the remaining one is Ca-Mg-HCO_3 type. Most of the unconfined pore groundwater samples lack dominant cations, some are dominated by Ca^{2+} or Na^+, and the anions are dominated by HCO_3^- or

lack dominant anions. The water chemical types are Ca-Mg-HCO_3 type or mixed Ca-Mg-Cl type. The cations in the confined pore groundwater samples are dominated by Na^+, a small amount lack dominant cations or are dominated by Ca^{2+}. The anions are dominated by Cl^-, and the primary water chemical type is Na-Cl-SO_4 type.

Most of the surface water samples are dominated by Na^+, and a small amount of water samples lack dominant cations. The anions in rivers, canals and pond samples are dominated by Cl^-, and the anions in reservoir samples are dominated by HCO_3^-, with a small number of water samples from canals and reservoirs lacking dominant anions. The water chemical types of surface water are predominantly Na-Cl-SO_4 type and mixed Ca-Na-HCO_3 type, accounting for 71.93% and 17.54% of the surface water samples, respectively. The water samples of reservoirs are predominantly mixed Ca-Na-HCO_3 type, accounting for 64.71% of the samples.

4. Discussion

4.1. Spatial Patterns of the Main Chemical Components

The pH of groundwater increases with the decrease in terrain elevation [27]. Most of the groundwater samples from hilly platform areas are strongly or weakly acidic, and a small number of samples are neutral (Figure 4). The main types of groundwater in these areas are clastic fissure groundwater, granite fissure groundwater and unconfined pore groundwater. Most of confined pore groundwater in the coastal plain area is neutral, and the pH values of two water samples exceed 8.0. Groundwater in this area is primarily recharged by river water that is weakly alkaline and connected to surface water and seawater. We can still find that there are some acidic samples in the plain located in the alluvial plain and the intermountain valley, which may be related to the recharge of groundwater from the hilly area. The genesis of acidic groundwater in coastal areas of Southern China is primarily related to atmospheric precipitation, the vadose zone aquifer medium, water–rock interaction, river influence and tidal action [27–29].

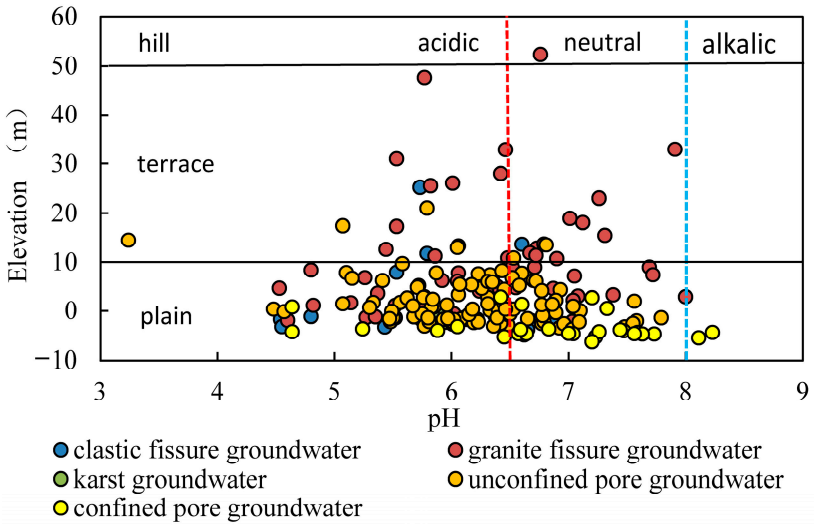

Figure 4. Relationship between acidic groundwater and landform.

The major cations and anions in different groundwater aquifers are shown in Figure 5. The spatial patterns of main anions and cations in groundwater are closely related to landform and aquifer type. The main chemical components of confine pore groundwater and karst groundwater in coastal plain areas are significantly higher than those in hilly platform areas, which may be due to the direct or indirect lateral recharge of seawater in these two aquifers. The distribution of nitrate and ammonia nitrogen in groundwater is also related to topography. The nitrate concentration in granite fissure groundwater, clastic fissure groundwater and unconfined pore groundwater distributed in the hilly platform area with higher terrain is higher, while the ammonia nitrogen content in confined pore groundwater

and karst groundwater in the coastal plain with lower terrain is higher. Studies have shown that inorganic nitrogen pollution in groundwater is primarily caused by chemical fertilizer, cultivation, urban domestic sewage and industrial activities, in addition to geological background factors [30,31]. The mineralization of organic matter, denitrification, anaerobic ammonium oxidation and dissimilatory nitrate reduction in different redox environments also affect the distribution of nitrate and ammonia nitrogen [32].

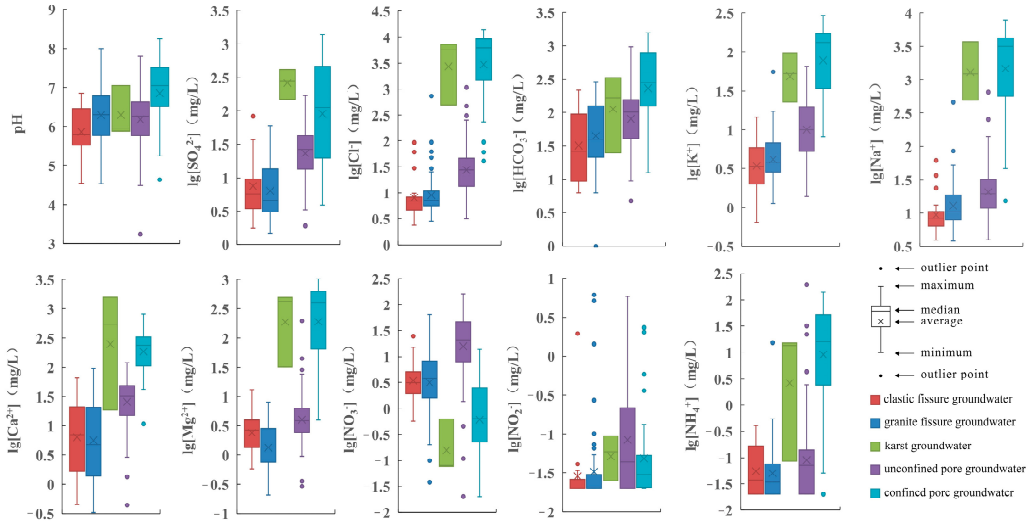

Figure 5. Box diagram of main chemical composition of groundwater.

4.2. Mechanism and Influencing Factors of Groundwater Hydrochemical Formation

The soluble ions in groundwater are mainly derived from atmospheric precipitation, lateral recharge of surface water, weathering and hydrolysis of minerals in sediments and soils [33,34], and human activities [35,36]. The chemical composition results from a long-term process of water–rock interaction between groundwater and aquifer medium, recording information about groundwater recharge, migration and circulation [37]. The main control mechanisms and influencing factors of groundwater chemical characteristics can be understood by ion ratios.

4.2.1. Rock Weathering

Gibbs identified three major mechanisms that control of world waters: atmospheric precipitation, rock dominance, and the evaporation–crystallization process, based on analytical chemical data from numerous water samples [38]. The major cations that characterize the end members of the world's waters are Ca for freshwater bodies and Na for high-saline water bodies, and the presence of chloride and bicarbonate in the world's waters is similar to the major cations. The chemical compositions of low-salinity waters are controlled by the amount of dissolved salts furnished by precipitation. The precipitation control zone is one end member of this series. The opposite end member of this series is comprised of waters having the rocks and soils of their basins as their dominant source of dissolved salts. The Na-rich, high-salinity, end-member components are the various seawaters of the earth whose compositions cluster near the Na-rich axis. Therefore, the relationship between the equivalent concentration ratios of $Na^+/(Na^+ + Ca^{2+})$ and $Cl^-/(Cl^- + HCO_3^-)$ is used to determine the origin mechanism of natural water bodies, which is controlled by rainfall dilution, evaporation concentration or rock weathering. Figure 6 shows that most of the equivalent concentration ratios of $Na^+/(Na^+ + Ca^{2+})$ and $Cl^-/(Cl^- + HCO_3^-)$ are mainly concentrated in the less than 0.5 area and are close to rock weathering zones. The ratios for confined pore groundwater, karst groundwater and most surface water are mainly concentrated in the greater than 0.5 area and near the evaporation and seawater influence area, which further indicates that the groundwater in Zhuhai City is primarily controlled

by rock weathering, and the confined pore groundwater and karst groundwater are more affected by evaporation. The confined pore groundwater, characterized by slow runoff, is influenced by a certain degree of evaporation, and it is distributed in the plain areas such as Doumen, Jinwan and Baijiao. According to the geological background conditions of the study area, the confined pore groundwater and karst groundwater are recharged by seawater that has undergone intense evaporation. Therefore, these samples appear in the top right corner of Figure 6. The surface water in Zhuhai, excluding the reservoir water, is recharged by seawater, which relates to the chemical composition of seawater. The reservoir water is primarily recharged by the surface and underground runoff from the surrounding mountains, thus falling within the rock weathering area, and its chemical composition is influenced by the lithology of the surrounding mountains.

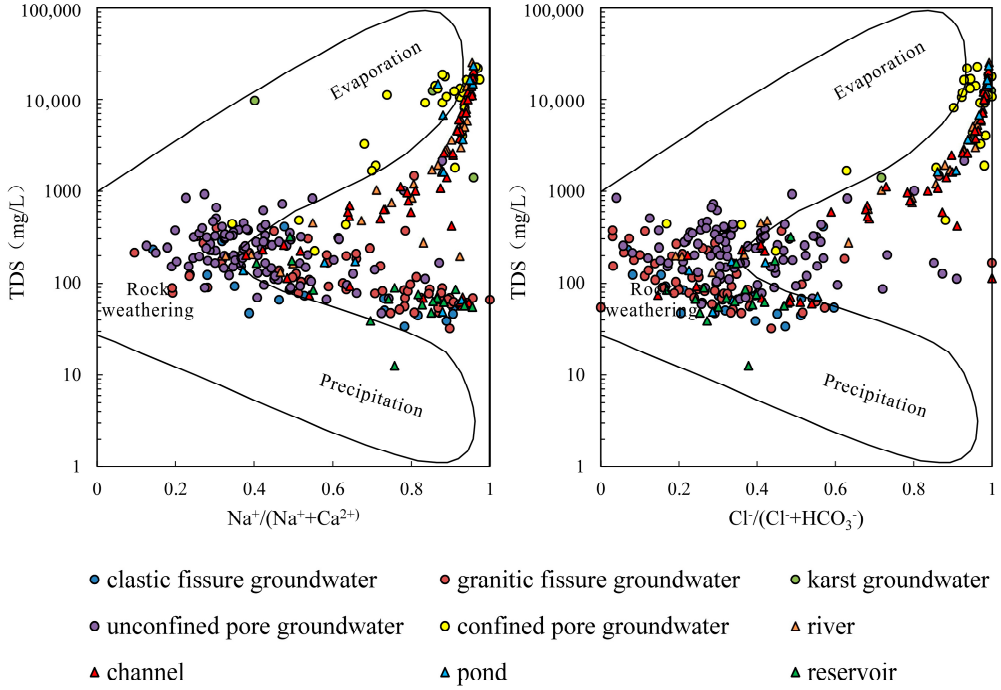

Figure 6. Gibbs diagram of water samples.

4.2.2. Ion Ratios

The equivalent concentration ratio between Na^+ and Cl^- is a hydrogeological parameter that characterizes the abundance of Na^+ [39]. Liu et al. found that the equivalent concentration ratio in natural seawater and atmospheric precipitation is approximately 0.86 [40]. The equivalent concentration ratio between Na^+ and Cl^- of the samples in the study area is showed in Figure 7. It can be seen that the equivalent concentration ratio of surface water (excluding reservoirs), confined pore groundwater and karst groundwater is mainly near the 0.86 line, indicating that the primary source of these samples is atmospheric precipitation. The ratio of samples with low Cl^- concentration is more variable, and the range of variation gradually decreases and approaches 0.86 as the Cl^- concentration increases. This further indicates that marine atmospheric precipitation or seawater is the main source of surface water, confined pore groundwater and karst groundwater. However, the Na^+ concentration in clastic fissure groundwater, granite fissure groundwater and unconfined pore groundwater is higher than that in atmospheric precipitation and seawater sources, indicating that silicate dissolution or cation exchange occurs in these three aquifers.

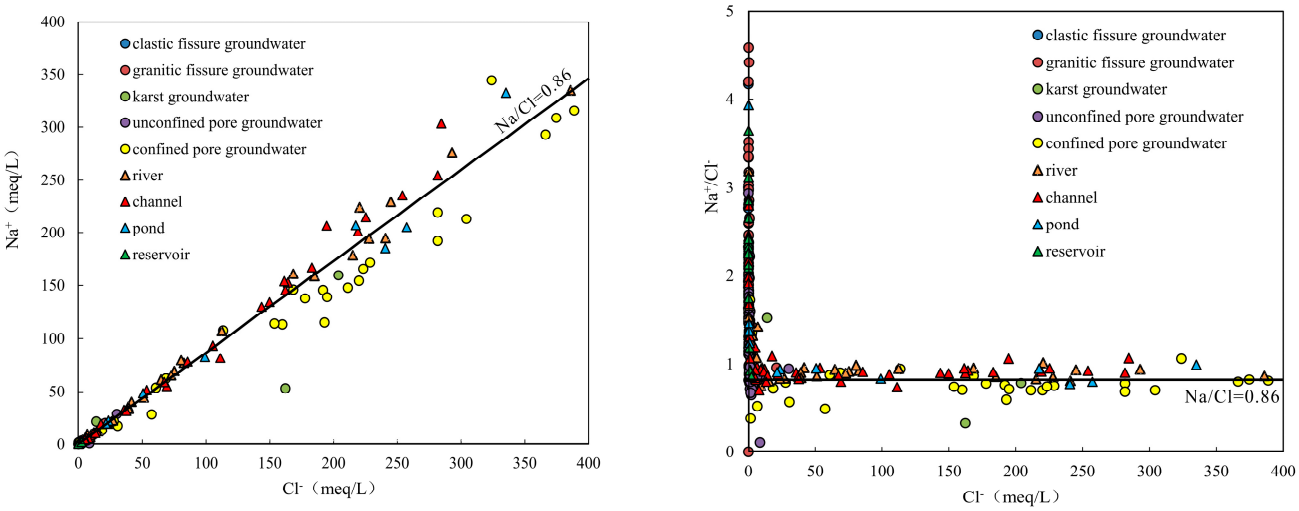

Figure 7. Relationship between Na^+ and Cl^- of water samples.

The equivalent concentration ratios of Mg^{2+}/Na^+, Ca^{2+}/Na^+ and HCO_3^-/Na^+ produced by the weathering of carbonate, silicate and evaporite minerals are significantly different, and are often used for ion genesis analysis [41]. Wu et al. and Gaillardet et al. studied the Ca^{2+}/Na^+ and Mg^{2+}/Na^+ ratios of silicate, carbonate and evaporite minerals [13,42]. The results show that the Ca^{2+}/Na^+ and Mg^{2+}/Na^+ ratios produced by silicate mineral weathering are 0.35 ± 0.15 and 0.24 ± 0.12, respectively; those produced by carbonate mineral weathering are 50 ± 20 and 20 ± 8, respectively; and those produced by evaporite mineral weathering are 0.17 ± 0.09 and 0.02 ± 0.01, respectively. The Figure 8 shows that most of the groundwater samples are located near the weathering and dissolution of silicate minerals, indicating that the weathering and hydrolysis of silicate minerals play a major role in controlling the chemical characteristics of groundwater in the study area. The confined pore groundwater, karst groundwater and most surface water samples are located at the end of the dissolution of evaporite salt rock minerals, indicating evaporation and concentration. In addition, unconfined pore groundwater and some granite fissure groundwater samples are located at the end of carbonate mineral dissolution, indicating that dissolution of carbonate minerals occurs in these samples with low Na^+ concentration.

The ratio of the equivalent concentration of $(Ca^{2+} + Mg^{2+})$ and $(HCO_3^- + SO_4^{2-})$ is an important parameter commonly used to study mineral dissolution in groundwater [10]. When the ratio of the equivalent concentration is close to 1, it indicates that Ca^{2+} and Mg^{2+} mainly originate from the dissolution of carbonate and sulfate minerals. If the ratio is greater than 1, it indicates that dissolution of carbonate and sulfate minerals is accompanied by the dissolution of silicate. If the ratio is less than 1, it indicates that the process of mineral weathering and dissolution is accompanied by ion exchange absorption [14]. The plots showing the relationships between $(Ca^{2+} + Mg^{2+})$ and $(HCO_3^- + SO_4^{2-})$ of samples demonstrate that unconfined pore groundwater, clastic fissure groundwater and granite fissure groundwater with low Ca^{2+} and Mg^{2+} concentration (<10 meq/L) mainly fall near the 1:1 line, indicating that the Ca^{2+} and Mg^{2+} in these groundwaters primarily originate from the dissolution of carbonate or sulphate (Figure 9). The confined pore groundwater and surface water samples with high Ca^{2+} and Mg^{2+} concentration (>30 meq/L) mainly fall near the 2:1 line, indicating that Ca^{2+} and Mg^{2+} in groundwater are primarily derived from the dissolution of silicate or the cation exchange of Na^+ replacing Ca^{2+} and Mg^{2+}.

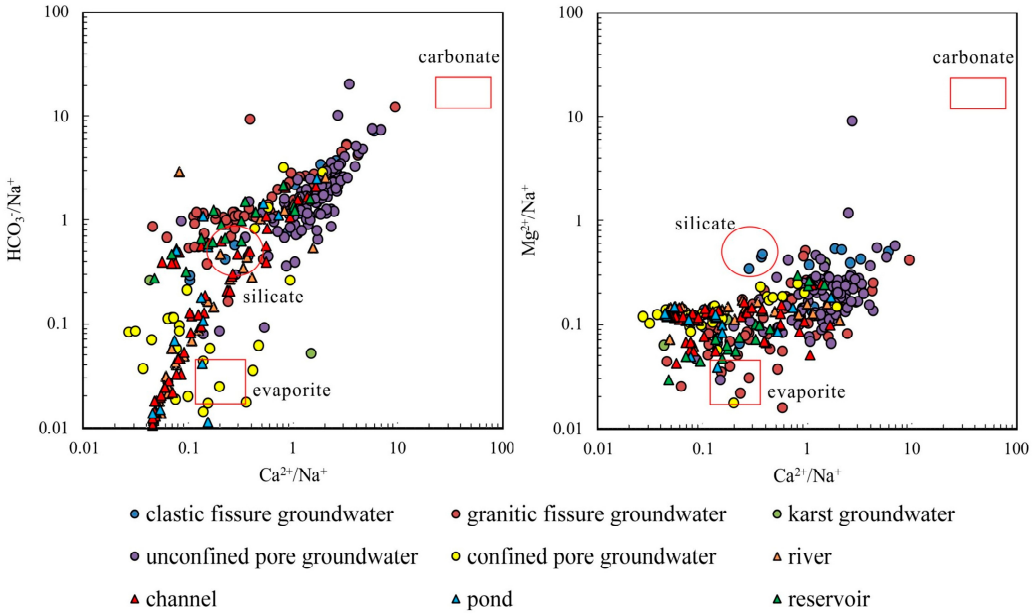

Figure 8. Relationship between HCO_3^-/Na^+, Mg^{2+}/Na^+ and Ca^{2+}/Na^+ of water samples.

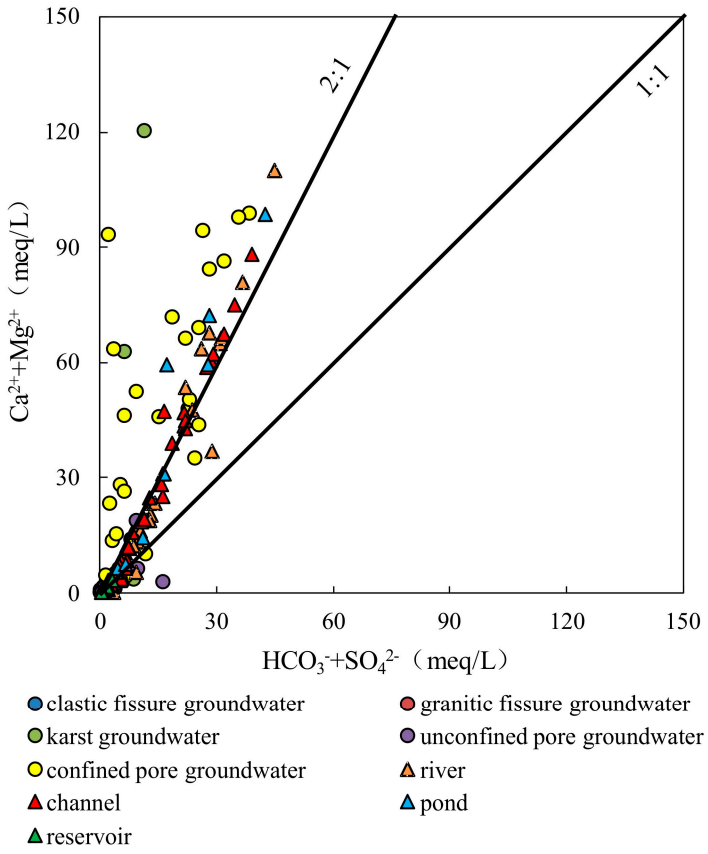

Figure 9. Relationships between $(Ca^{2+} + Mg^{2+})$ and $(HCO_3^- + SO_4^{2-})$ of water samples.

4.2.3. Cation Exchange

Cation exchange in groundwater can be verified by the correlation between the equivalent concentrations of $(Na^+ - Cl^-)$ and $(Ca^{2+} + Mg^{2+}) - (HCO_3^- + SO_4^{2-})$ [43,44]. A strong negative correlation indicates significant cation exchange in groundwater. The confined pore groundwater, karst groundwater and some surface waters fall along the 1:1 line in Figure 10, indicating that cation exchange occurs in these water bodies. In addition,

the $(Ca^{2+} + Mg^{2+}) - (HCO_3^- + SO_4^{2-})$ values for unconfined pore groundwater and clastic fissure groundwater are close to 0, which further indicates that the Ca^{2+} and Mg^{2+} in these two types of groundwaters are primarily originated from the dissolution of carbonate or sulfate minerals.

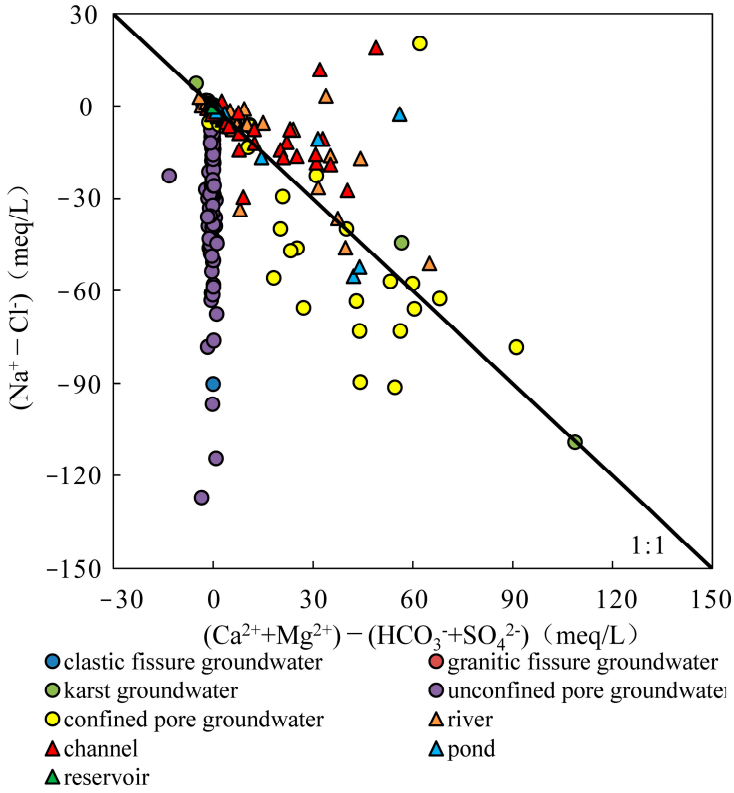

Figure 10. Relationships between $(Na^+ - Cl^-)$ and $(Ca^{2+} + Mg^{2+}) - (HCO_3^- + SO_4^{2-})$ of water samples.

Two basic exchange indexes, the chlor-alkali indices CAI 1 and CAI 2, were used to determine the replacement relationship between groundwater and cations in an aquifer medium during the cation exchange reaction [45]. Positive values of both indexes indicate that reverse ion exchange occurs, where Na^+ and K^+ in groundwater replace Ca^{2+} and Mg^{2+} in an aquifer medium. Negative values of both indexes indicate that a positive ion exchange occurs, where Ca^{2+} and Mg^{2+} in groundwater replace Na^+ and K^+ in the aquifer medium [24].

$$\text{CAI 1} = [c(Cl^-) - c(Na^+ + K^+)]/c(Cl^-) \quad (1)$$

$$\text{CAI 2} = [c(Cl^-) - c(Na^+ + K^+)]/[2c(SO_4^{2-}) + c(HCO_3^-) + c(NO_3^-)] \quad (2)$$

Figure 11 shows that the chlor-alkali indices of confined pore groundwater, karst groundwater, river, canal, lake and reservoir water in the study area are primarily positive, indicating reverse cation exchange. The replacement of Ca^{2+} and Mg^{2+} in the aquifer medium by Na^+ and K^+ in the groundwater explains why the equivalent concentration of Na^+ in these samples are less than that of Cl^-, and the content of Ca^{2+} and Mg^{2+} is excessive, exceeding the dissolution line of silicate minerals. The chlor-alkali indices of unconfined pore groundwater, clastic fissure groundwater and granite fissure groundwater are mostly negative, indicating that Ca^{2+} and Mg^{2+} in the groundwater displace Na^+ and K^+ in the aquifer medium. Consequently, there is an excess of Na^+ in these groundwaters, and a certain amount of Na^+ can be produced through the dissolution of silicate.

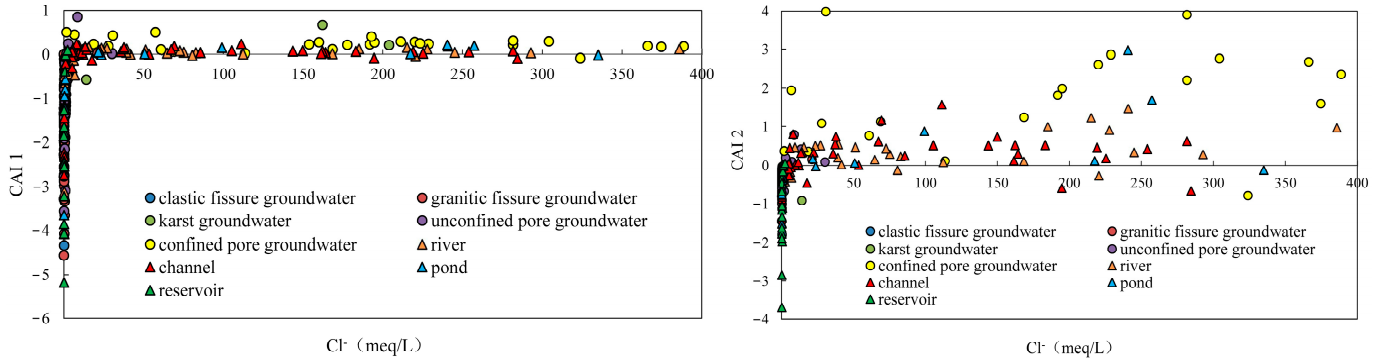

Figure 11. Chlor-alkali index of water samples.

4.2.4. Impact of Human Activities

Nitrate has become one of the primary pollutants in groundwater environments globally, originating predominantly from industrial and agricultural activities, as well as domestic sewage [46,47]. The molar concentration ratios of SO_4^{2-}/Na^+, Cl^-/Na^+ and NO_3^-/Na^+ can be used to identify the effects of agricultural or industrial activities on nitrate in groundwater [40]. In general, high-intensity human activities lead to the increased Cl^-, NO_3^- and SO_4^{2-} concentrations in groundwater, resulting in high Cl^-/Na^+ and NO_3^-/Na^+ molar ratios. Figure 12a shows the Cl^-/Na^+ and NO_3^-/Na^+ molar ratios. Most of the clastic fissure groundwater, granite fissure groundwater, unconfined pore groundwater, pond and reservoir samples are located near the upper right corner of line y = x, suggesting that most of the nitrate in these samples originates from agricultural activities in hills, such as forestry and orchards. The samples of confined pore water, rivers and ponds are primarily distributed near the evaporite and domestic sewage zones, indicating a domestic sewage source and the influence of evaporation. Figure 12b indicates that a small number of samples were mildly affected by industrial activities.

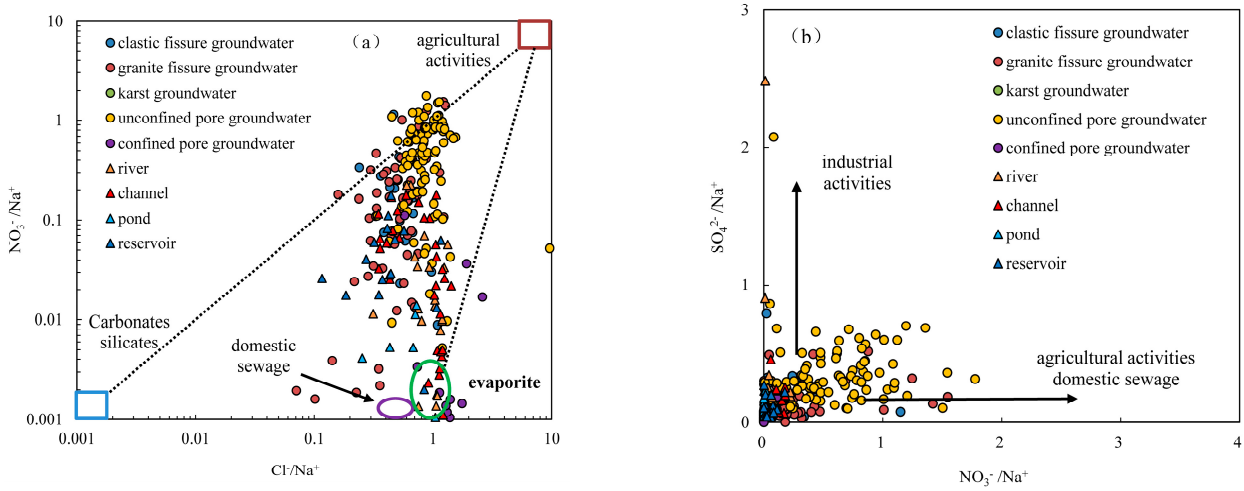

Figure 12. Relationship between NO_3^-/Na^+, Cl^-/Na^+ and SO_4^{2-}/Na^+ of groundwater. (**a**) NO_3^-/Na^+ and Cl^-/Na^+; (**b**) Cl^-/Na^+ and SO_4^{2-}/Na^+.

The halides Br^- and I^- are considered conservative anions due to their minimal interactions with the surrounding substrate during groundwater migration. Bromide may concentrate in brines due to evaporation and clay-membrane effects, which I^- tends to concentrate in marine vegetation and can also be concentrated in some brines [48]. Statistical analysis of the Br^- and I^-/Na^+ ratios in samples can help identify the source of nitrate [49]. Figure 13 illustrates that most of the clastic fissure groundwater, granite fissure groundwater, unconfined pore groundwater and reservoir samples fall within the atmospheric precipitation and soil water zone, characterized by high-concentration I^- and relatively

low Br^- concentration. This further indicates that the nitrate in the samples from hilly terraces and intermountain valleys primarily originates from atmospheric precipitation and agricultural activities, with a minor influence from domestic sewage. The confined pore groundwater, river, channel and pond samples are clearly distinct from other samples, falling within the sewage and feces contamination zones. This indicates that the nitrate in these samples primarily originates from domestic sewage and aquaculture wastewater, in conjunction with the specific land use types.

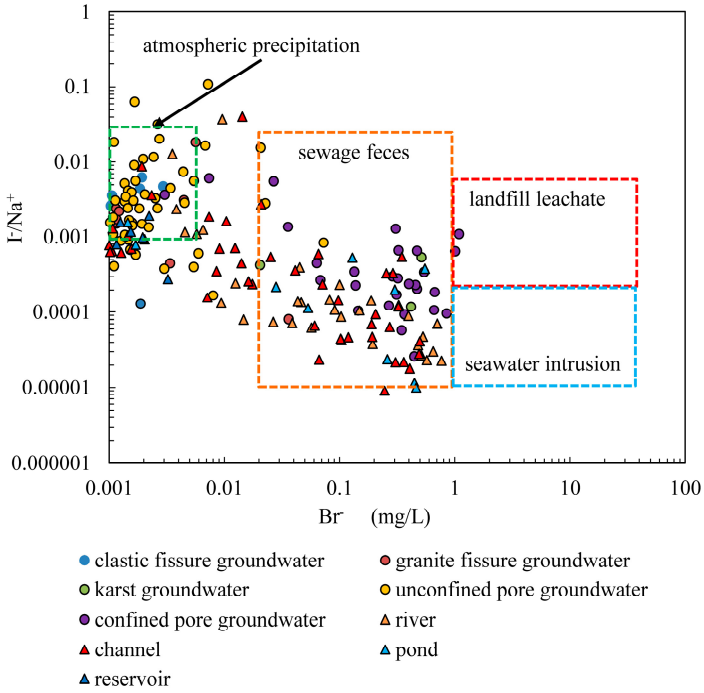

Figure 13. Relationship between I^-/Na^+ and Br^- of groundwater.

5. Conclusions

Freshwater sources in coastal areas worldwide are increasingly vulnerable due to rising sea levels and extensive abstraction for domestic, agricultural and industrial uses. Accordingly, we assessed the water system in Zhuhai city, Southern China. The chemical characteristics of the water samples and the impact of hydrogeochemical processes on mineral dissolution, evaporation and concentration, and cation exchange were evaluated using analytical and statistical methods. Our key findings are summarized as follows:

(1) The pH of groundwater in the study area ranges from 3.24 to 8.23, with most of the groundwater being slightly acidic. The pH of surface water ranges from 5.35 to 9.86, with most of it being weakly alkaline. The acidity in the groundwater is linked to acidic atmospheric precipitation, an acidic unsaturated zone, the oxidation of sulphide minerals and tidal action.

(2) The cations in groundwater are dominated by Na^+ and Ca^{2+}, with mean concentrations of 457.7 mg/L and 67.93 mg/L, respectively. The anions are dominated by Cl^- and HCO_3^-, with mean concentrations of 909.9 mg/L and 154.84 mg/L, respectively. The groundwater chemical types are predominantly mixed, followed by Ca-Mg-HCO_3 type. Surface water samples are predominantly of the Na-Cl-SO_4 type.

(3) The spatial patterns of major anions and cations in groundwater are closely related to landform and aquifer type. The main chemical components of confine pore groundwater and karst groundwater in coastal plain areas are significantly higher compared to those in hilly plateau areas.

(4) The samples from rivers, canals, lakes, ponds, confined pore groundwater and karst groundwater are strongly influenced by the dissolution of rock salts, evaporation and concentration, and reverse cation exchange. Unconfined pore groundwater,

clastic fissure groundwater, granite fissure groundwater and reservoir water are controlled by the dissolution of carbonate, sulphate and silicate, along with positive cation exchange.

(5) The nitrate concentration in groundwater ranges from 0.02 to 162 mg/L with a mean of 17.46 mg/L. Nitrate in groundwater primarily originates from atmospheric precipitation and human activities. Nitrate in clastic pore fissure groundwater, granite fissure groundwater and pore unconfined groundwater primarily originates from atmospheric precipitation, agricultural activities on slope farmland and forest land. Nitrate in pore confined groundwater and karst water primarily originates from domestic sewage and mariculture wastewater.

Overall, our findings elucidate the processes that define the hydrogeology and surface water interactions in the coastal system of Zhuhai city, which are relevant for other catchments with similar geological characteristics.

Author Contributions: Methodology, Y.L. and M.Z.; software, P.W.; validation, H.J. and X.Z.; formal analysis, J.H.; investigation, C.C. and P.W.; resources, X.Z.; data curation, Y.L.; writing—original draft preparation, J.H. and H.J.; writing—review and editing, M.Z. and P.W.; visualization, C.C.; supervision, H.J.; project administration, X.Z.; funding acquisition, X.Z. All authors have read and agreed to the published version of the manuscript.

Funding: This research was funded by urban geological survey of Zhuhai City, Zhuhai Municipal People's Government, grant number MZCD-2201-008 and monitoring and evaluation of resource and environment carrying capacity in Guangdong–Hong Kong–Macao Greater Bay Area, China Geological Survey, grant number DD20221729.

Data Availability Statement: The raw data supporting the conclusions of this article will be made available by the authors on request.

Conflicts of Interest: The authors declare no conflict of interest.

References

1. Subhankar, G.; Madan, K.J. Hydrogeochemical characterization of groundwater and critical assessment of its quality in a coastal basin. *Environ. Dev. Sustain.* **2023**. [CrossRef]
2. Adimalla, N.; Dhakate, R.; Kasarla, A.; Taloor, A.K. Appraisal of groundwater quality for drinking and irrigation purposes in central Telangana, India. *Groundw. Sustain. Dev.* **2020**, *10*, 100334. [CrossRef]
3. Salehi, S.; Chizari, M.; Sadighi, H.; Bijani, M. Assessment of agricultural groundwater users in Iran: A cultural environmental bias. *Hydrogeol. J.* **2018**, *26*, 285–295. [CrossRef]
4. Subrata, H.; Madan, K.J. Hydrogeologic and geochemical investigations in a coastal basin of West Bengal. *Arab. J. Geosci.* **2023**, *16*, 420. [CrossRef]
5. Han, D.; Kohfahl, C.; Song, X.; Xiao, G.; Yang, J. Geochemical and isotopic evidence for palaeo-seawater intrusion into the south coast aquifer of Laizhou Bay, China. *Appl. Geochem.* **2011**, *26*, 863–883. [CrossRef]
6. Angelaki, A.; Dionysidis, A.; Sihag, P.; Golia, E.E. Assessment of Contamination Management Caused by Copper and Zinc Cations Leaching and Their Impact on the Hydraulic Properties of a Sandy and a Loamy Clay Soil. *Land* **2022**, *11*, 290. [CrossRef]
7. Pavlovskiy, I.; Selle, B. Integrating hydrogeochemical, hydrogeological, and environmental tracer data to understand groundwater flow for a karstified aquifer system. *Groundwater* **2015**, *53*, 156–165. [CrossRef] [PubMed]
8. Li, P.; Tian, R.; Xue, C.; Wu, J. Progress, opportunities and key fields for groundwater quality research under the impacts of human activities in China with a special focus on western China. *Environ. Sci. Pollut. Res.* **2017**, *24*, 13224–13234. [CrossRef]
9. Tian, X.; Fei, Y.H.; Zhang, Z.J.; Li, Y.S.; Dun, Y.; Guo, C.Y. Analysis on hydrochemical characteristics of groundwater in strongly exploited area in Hutuo River Plain. *J. Groundw. Sci. Eng.* **2017**, *5*, 130–139. [CrossRef]
10. Zhang, T.; He, J.; Li, J.J.; Cao, Y.T.; Gong, L.; Liu, J.W.; Bian, C.; Cai, Y.M. Major ionic features and possible controls in the groundwater in the Hamatong River basin. *Environ. Sci.* **2018**, *39*, 4981–4990. [CrossRef]
11. Gai, J.B.; Yan, B.Z.; Fan, C.B.; Tuo, Y.P.; Ma, M.M. Hydrochemical Evolution Process and Mechanism of Groundwater in the Hutuo River Alluvial Fan, North China. *Water* **2024**, *16*, 2229. [CrossRef]
12. Jiang, W.J.; Wang, G.C.; Sheng, Y.Z.; Shi, Z.M.; Zhang, H. Isotopes in groundwater (^{2}H, ^{18}O, ^{14}C) revealed the climate and groundwater recharge in the Northern China. *Sci. Total Environ.* **2019**, *666*, 298–307. [CrossRef]
13. Wu, Y.; Luo, Z.H.; Luo, W.; Ma, T.; Wang, Y.X. Multiple isotope geochemistry and hydrochemical monitoring of karst water in a rapidly urbanized region. *J. Contam. Hydrol.* **2018**, *218*, 44–58. [CrossRef]
14. Li, X.H.; Zhang, Y.L.; Wang, R.; Li, Z.H. Hydrochemical characteristics and formation mechanism of groundwater in Hohhot basin. *South-North Water Transf. Water Sci. Technol.* **2018**, *16*, 136–145.

15. Ning, H.; Jiang, W.J.; Sheng, Y.Z.; Wang, K.L.; Chen, S.M.; Zhang, Z.; Liu, F.T. Comprehensive evaluation of nitrogen contamination in water ecosystems of the Miyun reservoir watershed, northern China: Distribution, source apportionment and risk assessment. *Environ. Geochem. Health* **2024**, *46*, 278. [CrossRef] [PubMed]
16. Jiang, W.J.; Sheng, Y.Z.; Wang, G.C.; Shi, Z.M.; Liu, F.T.; Zhang, J.; Chen, D.L. Cl, Br, B, Li, and noble gases isotopes to study the origin and evolution of deep groundwater in sedimentary basins, a review. *Environ. Chem. Lett.* **2022**, *20*, 1497–1528. [CrossRef]
17. Cheng, Y.; Wang, Y.; Zhou, Y.Z.; Gu, T. Status and sources of heavy metal/metalloid pollution in the groundwater system of Zhuhai City. *Bull. Mineral. Petrol. Geochem.* **2019**, *38*, 595–603. [CrossRef]
18. Zhao, X.F.; Chen, F.J.; Chen, J.Y.; Tang, C.Y.; Luo, Y.L.; Jia, G.D. Using nitrogen isotope to identify the sources of nitrate contamination in urban groundwater—A case study in Zhuhai City. *Hydrogeol. Eng. Geol.* **2008**, *3*, 87–92. [CrossRef]
19. Yao, P. Distribution and origin of manganese in groundwater in the eest Zhuhai coastal zone. *Groundwater* **2015**, *37*, 1–3.
20. Wang, S.; Yan, X.X.; Jie, J.; Yang, T.L.; Wu, J.Z.; Wang, H.S. Analysis on factors affecting ground settlement in plain area of Pearl River Delta. *Chin. J. Geol. Hazard Control* **2019**, *30*, 98–104. [CrossRef]
21. Xie, X.M.; Wang, S.; Li, M.; Zhou, Z.Z.; Wu, L.X. Present situation and cause analysis of land subsidence in Pearl River Delta. *West-China Explor. Eng.* **2021**, *33*, 8–10.
22. Wei, F.Y. Groundwater quality evaluation of emergency water supply in Zhuhai City. *Groundwater* **2014**, *36*, 126–128.
23. Chen, Y.M.; Gao, Z.P.; Chen, Z.L.; Li, W.; Wang, Q.; Ma, X.M.; Guo, H.M. Distribution characteristics and genesis of strontium-bearing mineral water in Tailai Basin. *Geol. China* **2019**, *46*, 1–11. [CrossRef]
24. Chen, W.; Wu, Y.; Zhang, H.X.; Liu, H.Q. Hydrochemical Characteristics and Formation Mechanism of Groundwater in the Western Region of Hepu Basin, Beihai City. *Environ. Sci.* **2024**, *45*, 194–206. [CrossRef]
25. Bello, M.; Ketchemen-Tandia, B.; Nlend, B.; Huneau, F.; Fouepe, A.; Fantong, W.Y.; Boum-Nkot, S.N.; Garel, E.; Celle-Jeanton, H. Shallow groundwater quality evolution after 20 years of exploitation in the southern Lake Chad: Hydrochemistry and stable isotopes survey in the far north of Cameroon. *Environ. Earth Sci.* **2019**, *78*, 474. [CrossRef]
26. He, J.; Xiao, P.; Xu, K.; Peng, K. Hydrogeochemical process of groundwater in western margin of Jianghan plain. *Yangtze River* **2018**, *49*, 6–10. [CrossRef]
27. He, J.; Li, Y.Y.; Zeng, M.; Wu, P.; Chen, C.; Zhao, X.W. Characteristics of Distribution and Genetic Mechanism of Acidic Groundwater in Zhuhai City. *South China Geol.* **2024**, *40*, 404–412.
28. Zhou, X.; Zhang, H.; Zhao, L.; Shen, Y.; Yan, X.; Ou, Y.C.; Huang, X.X. A preliminary analysis of the formation of the weak acidic groundwater in Beihai, Guangxi. *Acta Geol. Sin.* **2007**, *81*, 850–856.
29. Zhang, H.X.; Yu, S.W.; Zhang, Y.P.; Chen, W.; Li, Q.H.; Liu, H.Q.; Zhang, Q.Y. Spatial-temporal distribution, genesis and environmental impact of the shallow groundwater pH values in the Fangchenggang, Guangxi. *Geol. China* **2022**, *49*, 822–833. [CrossRef]
30. Naik, M.R.; Mahanty, B.; Sahoo, S.K.; Jha, V.N.; Sahoo, N.K. Assessment of groundwater geochemistry using multivariate water quality index and potential health risk in industrial belt of central Odisha, India. *Environ. Pollut.* **2022**, *303*, 119161. [CrossRef]
31. Podgorski, J.; Araya, D.; Berg, M. Geogenic manganese and iron in groundwater of Southeast Asia and Bangladesh-machine learning spatial prediction modeling and comparison with arsenic. *Sci. Total Environ.* **2022**, *833*, 155131. [CrossRef] [PubMed]
32. Gao, Z.P.; Weng, H.C.; Guo, H.M. Unraveling influences of nitrogen cycling on arsenic enrichment in groundwater from the Hetao Basin using geochemical and multi-isotopic approaches. *J. Hydrol.* **2021**, *595*, 125981. [CrossRef]
33. Yu, H.T.; Ma, T.; Deng, Y.M.; Du, Y.; Shen, S.; Lu, Z.J. Hydrochemical characteristics of shallow groundwater in eastern Jianghan Plain. *Earth Sci.* **2017**, *42*, 685–692. [CrossRef]
34. Shen, B.B.; Wu, J.L.; Jilili, A.; Saparov, A.S.; Isanova, G. Hydrochemical and Isotopic Characteristics of the Lake Balkhash Catchment, Kazakhstan. *Environ. Sci.* **2020**, *41*, 173–182. [CrossRef]
35. Xu, J.; He, J.T.; Peng, C.; Zeng, Y. Characteristics and genesis of NO_3 type water in shallow groundwater in Liujiang Basin. *Environ. Sci.* **2018**, *39*, 4142–4149. [CrossRef]
36. Zhang, Y.; Guo, C.Q.; Zhu, Y.G.; Yu, S. Chemical characteristics of groundwater and material sources analysis in Buckwheat Field, Yunnan Province. *Environ. Sci.* **2019**, *40*, 2686–2695. [CrossRef]
37. Wei, X.; Zhou, J.L.; Nai, W.H.; Zeng, Y.Y.; Bin, F. Hydrochemical characteristics and evolution of groundwater in the Kashgar delta area in Xinjiang. *Environ. Sci.* **2019**, *40*, 4042–4051. [CrossRef]
38. Gibbs, R.J. Mechanisms controlling world water chemistry. *Science* **1970**, *170*, 1088–1090. [CrossRef]
39. Su, C.T.; Yang, Y.; Nie, F.Y.; Zou, S.Z.; Zhao, G.S.; Luo, F.; Huang, Q.B.; Ba, J.J.; Li, X.P.; Liang, J.P. Hydrochemical characteristics and formation mechanism of strontium-rich groundwater in Xintian County, Hunan Province. *Geoscience* **2018**, *32*, 554–564. [CrossRef]
40. Liu, J.T.; Cai, W.T.; Cao, Y.T.; Cai, Y.M.; Bian, C.; Yong-Gao, L.; Chen, Y.M. Hydrochemical characteristics of groundwater and the origin in alluvial-proluvial fan of Qinhe River. *Environ. Sci.* **2018**, *39*, 5428–5439. [CrossRef]
41. Liu, S.T.; Zhang, D.; Li, Y.H.; Yang, J.M.; Jia, B.J. Water sources and factors controlling hydro-chemical compositions in the Yiluo River basin. *Environ. Sci.* **2020**, *41*, 1184–1196. [CrossRef]
42. Gaillardet, J.; Dupré, B.; Louvat, P.; Allègre, C.J. Global silicate weathering and CO_2 consumption rates deduced from the chemistry of large rivers. *Chem. Geol.* **1999**, *159*, 3–30. [CrossRef]
43. Lin, C.Y.; Sun, Z.X.; Gao, B.; Hua, E.X.; Zhang, H.Y.; Yang, F.; Gao, Y.; Jiang, W.B.; Jiang, X.Y. Hydrochemical characteristics and formation mechanism of groundwater in Lhasa area, China. *Earth Sci. Front.* **2021**, *28*, 49–58. [CrossRef]

44. Liu, J.; Hao, Y.; Gao, Z.; Wang, M.; Liu, M.; Wang, Z.; Wang, S. Determining the factors controlling the chemical composition of groundwater using multivariate statistics and geochemical methods in the Xiqu coal mine, North China. *Environ. Earth Sci.* **2019**, *78*, 1–11. [CrossRef]
45. Zhang, J.W.; Liang, X.; Jin, M.; Ma, T.; Deng, Y.M.; Ma, B. Identifying the groundwater flow systems in a condensed river-network interfluve between the Han River and Yangtze River (China) using hydrogeochemical indicators. *Hydrogeol. J.* **2019**, *27*, 2415–2430. [CrossRef]
46. Vaiphei, S.P.; Kurakalva, R.M. Hydrochemical characteristics and nitrate health risk assessment of groundwater through seasonal variations from an intensive agricultural region of upper Krishna River basin, Telangana, India. *Ecotoxicol. Environ. Saf.* **2021**, *213*, 112073. [CrossRef] [PubMed]
47. Liu, J.; Peng, Y.; Li, C.; Gao, Z.; Chen, S. Characterization of the hydrochemistry of water resources of the Weibei Plain, Northern China, as well as an assessment of the risk of high groundwater nitrate levels to human health. *Environ. Pollut.* **2021**, *268*, 115947. [CrossRef]
48. Panno, S.V.; Hackley, K.C.; Hwang, H.H.; Greenberg, S.E.; Krapac, I.G.; Landsberger, S.; O′Kelly, D.J. Characterization and Identification of Na-Cl Sources in Ground Water. *Groundwater* **2006**, *44*, 176–187. [CrossRef]
49. Lv, X.L.; Liu, J.T.; Han, Z.T.; Zhu, L.; Zhang, Y.X. Geochemical characteristics and driving factors of NO_3-type groundwater in the rapidly urbanizing Pearl River Delta. *Environ. Sci.* **2021**, *42*, 4761–4771. [CrossRef]

Disclaimer/Publisher's Note: The statements, opinions and data contained in all publications are solely those of the individual author(s) and contributor(s) and not of MDPI and/or the editor(s). MDPI and/or the editor(s) disclaim responsibility for any injury to people or property resulting from any ideas, methods, instructions or products referred to in the content.

water

MDPI

Article

Hydrogeochemical Characteristics and Health Risk Assessment of Groundwater in Grassland Watersheds of Cold and Arid Regions in Xilinhot, China

Yubo Xia [1,2,3], Guangfang Chen [4,*], Futian Liu [1,2,3], Jing Zhang [1,2,3] and Hang Ning [1,2,3]

[1] Tianjin Center (North China Center for Geoscience Innovation), China Geological Survey, Tianjin 300170, China; sosodragon@163.com (Y.X.); zihun@126.com (F.L.); tjcgszj@163.com (J.Z.); ninghang1123@163.com (H.N.)
[2] Tianjin Key Laboratory of Coast Geological Processes and Environmental Safety, Tianjin 300170, China
[3] Xiong'an Urban Geological Research Center, China Geological Survey, Tianjin 300170, China
[4] Inner Mongolia Ninth Geology Mineral Exploration and Development Co., Ltd., Xilinhot 026000, China
* Correspondence: guangfang0610@126.com; Tel.: +86-022-8411-2916

Abstract: Xilinhot City is a significant pastoral city in China where groundwater serves as the primary water source for the cold and arid pastoral regions. The formation and evolution of material components in groundwater, as well as groundwater quality, are directly linked to the health of pastoral residents. This study is based on the physical and chemical test results of 22 groundwater samples collected from the Xilinhot River Basin in Inner Mongolia. Various statistical analyses, including Piper and Chadha diagrams, as well as hydrogeochemical simulation methods, were employed to assess the hydrogeochemical characteristics and material composition sources of groundwater, evaluate groundwater quality and non-carcinogenic risks, and comprehensively discuss the impact of macro- and microelements on human health. The findings indicate that igneous rocks containing minerals such as potassium feldspar, plagioclase, and pyroxene contribute Na^+, Cl^-, and K^+ to the groundwater, while sedimentary rocks containing minerals like dolomite and calcite supply ions such as Ca^{2+}, Mg^{2+}, and HCO_3^-. The groundwater quality is primarily classified as Class II–V, with F^- and NO_3^- exhibiting varying hazard quotients for children and adults in the study area, though they do not pose a non-carcinogenic risk. Additionally, the enrichment of hardness, Ca^{2+}, Mg^{2+}, Na^+, SO_4^{2-}, and other indicators in localized areas exceeds the recommended values for drinking water, potentially impacting the digestive and urinary systems of the human body. There is a risk of excessive fluoride in areas where F levels exceed 1 mg/L. Furthermore, the content of beneficial micronutrients such as selenium (Se), zinc (Zn), boron (B), and germanium (Ge) is relatively low. Based on the elemental abundance characteristics and a comparative analysis of the chemical properties of groundwater across five regions of China, this comparison facilitates a discussion on the definition of healthy groundwater, particularly in relation to safe consumption in cold and arid regions. This study aims to highlight the health issues associated with drinking groundwater in the cold and arid regions of Mongolia. The findings serve as a valuable reference for efforts aimed at reducing the incidence of endemic diseases and enhancing human lifespan.

Keywords: groundwater hydrogeochemical characteristics; groundwater health risk assessment; cold and arid regions; formation and evolution of groundwater; grassland watershed

1. Introduction

The Earth system is often perceived as a unified entity [1] characterized by the similarity in the composition and prevalence of human-related elements and the typical composition and prevalence of elements within crustal rocks [2]. The relationship between the hydrosphere, which acts as a vital connector, and elements like the lithosphere and human organisms shows a stronger regression coefficient [3]. The human body takes in a

variety of chemical elements from the geological surroundings mainly through the intake of food and water. Importantly, the elements found in water are absorbed more efficiently by the human body than those sourced from food [4]. In pastoral areas where groundwater is typically the primary drinking water source, the elements contained in groundwater play a crucial role in supporting human biological functions and overall health. An inadequate or surplus intake of specific chemical elements can result in abnormal growth or health issues in humans [5]. Human activities can significantly influence hydrogeochemistry [6,7]; however, the presence and forms of elements in groundwater under natural conditions are shaped by the hydrogeological and hydrogeochemical context [8]. Therefore, examining the conditions that influence the formation and evolution of groundwater hydrochemistry can shed light on the connection between the abundant and scarcity of macro-elements and trace elements in groundwater and their impacts on human health. This analysis ultimately offers a robust geological framework for decreasing the prevalence of endemic diseases and promoting a longer human lifespan.

The inland river basins in Inner Mongolia have developed a unique water cycle system in cold and arid regions characterized by relatively closed circulation conditions, exhibiting significant regional differentiation patterns in precipitation, surface runoff, and groundwater [9]. Groundwater resources, along with their extraction outputs, are key attributes of groundwater as a resource [10], serving as strategic resources that support domestic water needs for humans and livestock [11]. When groundwater is utilized as a water source for a region, evaluating its quality becomes a crucial consideration [12]. Furthermore, the abundance or deficiency of certain elements is vital for human health [13,14]. Existing research on the genesis mechanisms of groundwater and drinking water health aimed to elucidate the chemical characteristics of groundwater [15], analyze the formation and evolution mechanisms of health-related major and trace elements [16], and explore the relationship between human health and the elemental content of groundwater in regions where it has been used as a drinking water source over extended periods. This research primarily focuses on hydrogeochemistry, examining the formation of groundwater chemical components and the migration of various chemical elements within them [17], to uncover the chemical characteristics and origins of groundwater [18]. The interactions among ions in groundwater reflect the outcomes of water–rock transformation [19], thus allowing researchers to trace its sources and infer the mechanisms of its formation and evolution through the elemental composition of groundwater [20]. The mineral saturation index in groundwater serves as a key parameter indicating the interactions between groundwater and aquifer media [21]. Various mineral saturation indices also reflect the stages and evolutionary trends of groundwater chemical formation. In the realm of investigating the relationship between heterogeneous elements in groundwater and human health, the assessment of risks associated with anthropogenic pollutants—such as inorganic contaminants like nitrates and heavy metals [22,23], as well as organic pollutants including petroleum hydrocarbons and aromatic hydrocarbons [24,25]—has consistently been a focal point of research. Additionally, the investigation of site pollution and the development of soil and water remediation methods have reached a relatively advanced stage. Studies examining native groundwater with high concentrations of arsenic, fluoride, and chromium [26–28] have emerged as critical components in understanding the interplay between groundwater quality and human health. The toxicity threshold theory for each element delineates optimal nutrition levels and their respective positive and negative impacts on human health [29,30]. Furthermore, macro-elements in groundwater are intricately linked to human health; their inherent characteristics lead to significant absorption and utilization by the human body, with their abundance or deficiency manifesting distinctly in health outcomes. Nevertheless, current research lacks sufficient examples that simultaneously analyze human health in relation to both macro-elements and trace elements in groundwater. An integrated study of these elements would enhance the relevance of hydrogeological and hydrogeochemical research, thereby providing a scientific foundation for health geology.

Groundwater serves as the primary source of drinking water, as well as for agricultural and livestock needs, in Xilinhot City and the inland river basins of Inner Mongolia. Its quality directly influences the safety and health of local residents [31]. This study aims to investigate the impact of groundwater on the health of local inhabitants and herdsmen while also reducing the adverse effects of utilizing unhealthy groundwater. By examining the geological and hydrogeological conditions of the Xilinhot area, we elucidate the distribution characteristics of key macro and micro ions present in the groundwater. A statistical analysis was conducted to explore the correlations among major ions affecting groundwater quality, alongside an assessment of groundwater quality and health risks. Furthermore, we characterized the abundance and deficiency of hydrochemical elements in the groundwater. Utilizing the theory of element poisoning thresholds, we examined the relationship between the water environment and the abundance and deficiency of macro- and microelements in relation to human health. This research proposes recommendations for ensuring safe drinking water derived from groundwater sources. By framing the health of drinking water in terms of a comparative analysis of element abundance, this study emphasizes a comprehensive and scientific approach to understanding the implications for human health across all relevant elements.

2. Materials and Methods

2.1. Study Area

The study area is located in Xilinhot, Inner Mongolia, China (Figure 1). Xilinhot City is situated in the western section of the Shengli Maodeng Basin, characterized by its surrounding low mountains, hills, and lava plateaus. The central and eastern regions of the city comprise an inclined plain that transitions into the mountains, while the central and western sections feature valley plains. The overall topography exhibits a gradient, with higher elevations in the south and east, and lower elevations in the north and west. Based on geological genesis and morphological characteristics, the monitoring area can be categorized into four genetic types and six morphological types (Figure 2): (1) The hilly region predominantly consists of light metamorphic rocks from the Lower Permian, as well as sandstone and conglomerate from the Middle and Lower Jurassic, tuff and basalt from the Upper Jurassic, and granite from the Yanshanian period. (2) The lithology of the wavy high plain is primarily composed of detrital rocks from the Tertiary and Cretaceous periods, with certain areas covered by thin layers of Quaternary strata. (3) The sloping plain in front of the mountains is characterized by Upper Pleistocene alluvial deposits and lacustrine deposits. (4) The valleys and depressions between the hills are formed from Upper Pleistocene alluvial sand and gravel, as well as fine sand mixed with gravel. (5) The river valley plain consists of Holocene alluvial deposits, Upper Pleistocene alluvial lacustrine deposits, and additional alluvial materials. (6) The volcanic-accumulation-type lava platform is formed from Quaternary Upper Pleistocene basalt.

The temperate grassland region is characterized by arid climate conditions that result in insufficient moisture, leading to sparse vegetation and limited humus. This environment is typically alkaline and strongly oxidizing. Under conditions of low rainfall intensity, significant evaporation, and minimal surface runoff, leaching processes are weak, allowing for the accumulation of various elements, with chloride (Cl), sulfate (SO_4), calcium (Ca), and sodium (Na) being particularly prevalent. Consequently, the degree of mineralization in natural water sources is generally high. Biogeochemical endemic diseases in arid grasslands are primarily associated with the enrichment of certain elements and a deficiency of humus [32].

This area is characterized by a Quaternary loose rock pore aquifer, a basalt pore fissure aquifer, and a bedrock fissure aquifer (Figure 3). The Quaternary pore groundwater aquifer serves as the primary monitoring target layer, with a lithology primarily consisting of alluvial and lacustrine fine sand. Drilling indicates that the maximum thickness of the aquifer does not exceed 100 m, and it gradually thins toward the periphery of the basin, ultimately disappearing at the basin's edge. In September 2022, the water level was

recorded at depths ranging from 0.96 to 39.74 m, with water volume varying from scarce to abundant. The next layer is the pore fissure water aquifer of Cenozoic basalt, which is primarily developed along both sides of the river valley. At their junction, this aquifer lies beneath the Quaternary loose rock pore aquifer, exhibiting a certain degree of local hydraulic connectivity. However, drilling did not reveal this aquifer, and the water level burial depth was measured at 7.1 to 51.32 m in September 2022. Groundwater flow is directed from south to north (Figure 4). Currently, no relevant studies have been conducted on the zoning of the basalt pore fissure aquifer and the bedrock fissure aquifer.

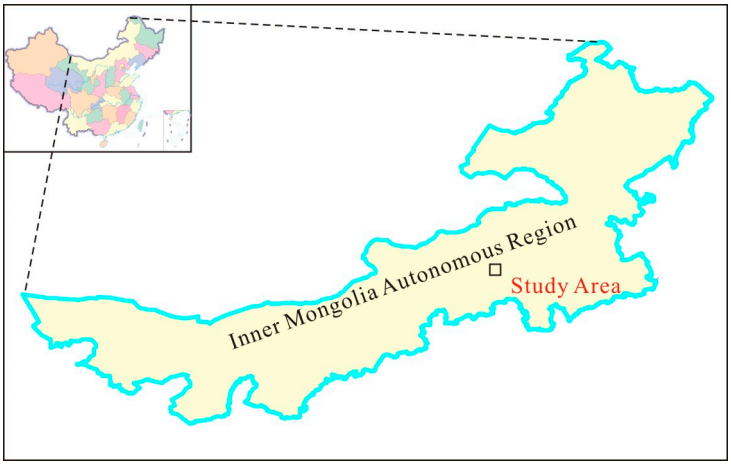

Figure 1. Location map of the study area.

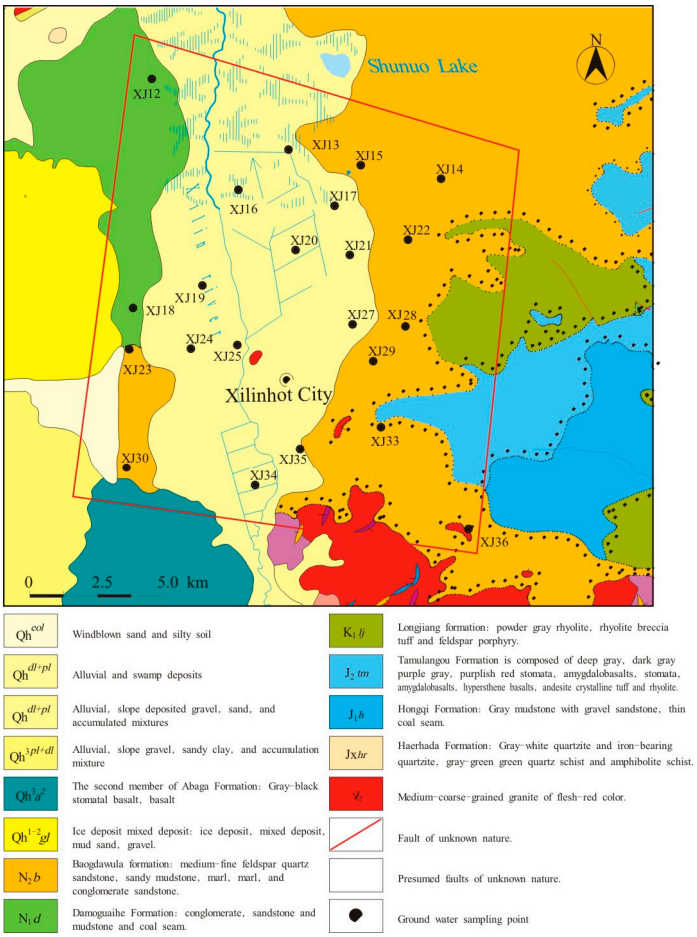

Figure 2. Geological map and sampling location map of the study area.

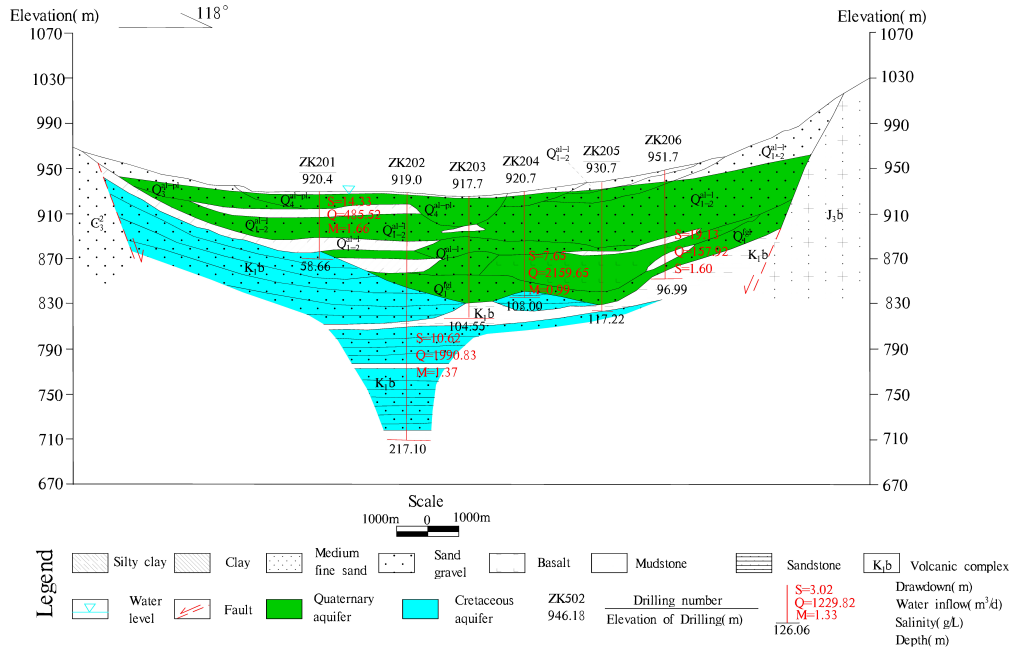

Figure 3. Typical hydrogeological profile.

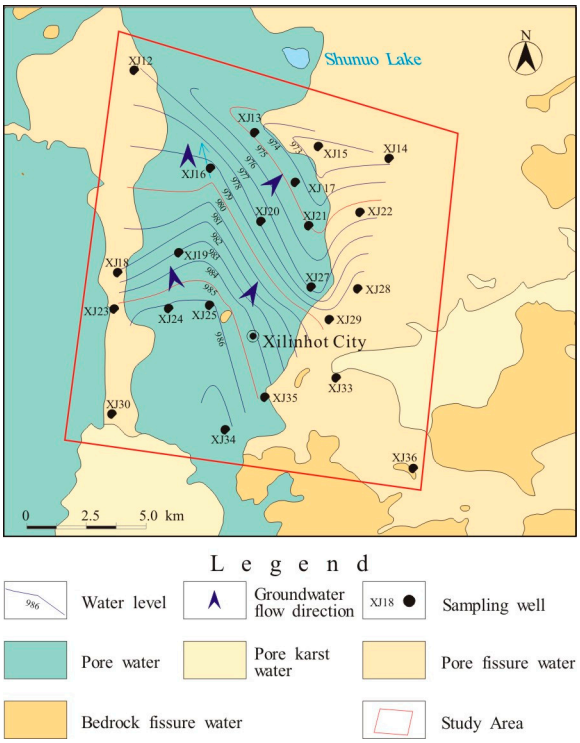

Figure 4. Hydrogeological and groundwater level map.

2.2. Experimental Methods

In 2022, chemical analysis involved the collection of water samples from 22 monitoring wells (Figure 2). The monitoring wells are all complete wells, with depths ranging from 70 to 130 m. To ensure sample quality, each well was rinsed three times with raw water prior to sampling to prevent contamination. The original sample was collected in a 2.5 L white polyethylene bucket, and an alkaline sample was transferred to a 1 L transparent polyethylene plastic bottle, to which 0.2 g of sodium hydroxide (Tianjin Zhiyuan Chemical

Reagent Co., Ltd., Tianjin, China) was added using a spoon. For each water sample, two parallel samples were taken, labeled accordingly, and stored at low temperatures.

Necessary tests were performed in line with the "Groundwater Quality Standards" GB/T 14848-2017 [33]. The laboratory evaluated the primary ions sodium (Na^+), potassium (K^+), calcium (Ca^{2+}), magnesium (Mg^{2+}), sulfate ($SO_4{}^{2-}$), bicarbonate ($HCO_3{}^-$), and chloride (Cl^-) along with nitrate ($NO_3{}^-$), nitrite ($NO_2{}^-$), phosphate ($PO_4{}^{3-}$), silica (SO_2), dissolved oxygen (DO), total dissolved solids (TDS), suspended solids, and trace elements present in the sample. Measurements were conducted within 48 h post-collection. The ICP-OES (PerkinElmer, Optima 5300 DV, MA, USA) was used to determine the concentrations of key cations (Ca^{2+}, Mg^{2+}, SiO_2), while trace element concentrations were assessed using ICP-MS (PerkinElmer, Elan DRC-e). For determining the concentration of Cl^-, the electrode method was used; flame photometry facilitated the analysis of Na^+ and K^+; and the spectrophotometric turbidity method was employed for measuring $SO_4{}^{2-}$. The detection limit for the primary cations and anions is set at 0.01 mg/L, whereas the minimum detectable level for Cl^- stands at 5.00 mg/L. TDS are derived by summing the primary ions plus SiO_2 minus half of the $HCO_3{}^-$. The calculation of total hardness (TH) is based on the levels of Ca^{2+} and Mg^{2+}.

2.3. Mineral Saturation Index

To further analyze the chemical characteristics of groundwater, it is essential to calculate the saturation index of the primary minerals present. The specific formula for this calculation is as follows [34–36]:

$$SI_i = \lg \frac{IAP}{K_i} = lg\beta_i \quad (1)$$

In the formula, SI_i represents the saturation index of the i mineral, K_i denotes the equilibrium constant for the dissolution reaction of the i mineral, and IAP refers to the ion activity product involved in mineral dissolution reactions.

2.4. Groundwater Quality Evaluation

In line with the national groundwater quality standards of China (GB/T 14848-2017) [33], the water quality within the study region is categorized into five classes (I–V) based on its status and the related health risks to humans. This classification derives from the quality requirements set for drinking water meant for domestic use, agriculture, and industrial purposes, as well as the concentration of various elements (excluding pH levels). Class I signifies excellent quality, permitting direct consumption with no need for treatment. Class II reflects good quality which is safe for consumption following minimal treatment. Class III is identified as medium quality, necessitating suitable treatment prior to consumption. Class IV is classified as poor quality, considered inappropriate for drinking yet acceptable for industrial use. Lastly, Class V is defined as very poor quality, rendering it unsuitable for any purpose unless extensive treatment is applied.

The Nemerow Composite Pollution Index (NCPI) serves as a tool for assessing overall environmental quality, formulated by combining evaluations of individual pollution indices. This index provides insights into the integrated pollution scenario by taking into account both average and peak values of various indicators, thus offering a more comprehensive and representative evaluation of groundwater quality. The assessment process is divided into two primary steps; the initial step focuses on evaluating the single factor pollution index, and the subsequent step involves the evaluation of the combined pollution index. The evaluation for each individual indicator was performed according to China's standards for groundwater quality (Classes I–V), with each category being classified based on the concentration levels of a single factor found in groundwater samples.

Composite score value F calculations were performed using the Nemerow composite index method:

$$F = \sqrt{\frac{(F_{max}^2 + F_{mean}^2)}{2}} \quad (2)$$

$$\overline{F} = \frac{1}{n}\sum_{i=1}^{n} F_i \quad (3)$$

2.5. Health Risk Assessment

Taking into account the broad and specific aspects of the study region, a health risk assessment for non-carcinogenic effects was formulated. The anticipated health risks were evaluated by employing the model suggested by the USEPA (1989) [37]. The calculation of the average daily intake for an individual contaminant is performed using Equation (4).

$$CDI = \frac{C \times IR \times ED \times EF}{AW \times AT} \quad (4)$$

where *CDI* is the chronic daily intake (mg/kg/day); *C* represents the concentration of a particular contaminant in water (mg/L). The ingestion rates (*IR*) are 2.457 L/day for adults and 0.780 L/day for children, representing the annual average daily total drinking water intake in both urban and rural areas of the Inner Mongolia Autonomous Region. The exposure duration (*ED*) is 74.44 years, based on the 2010 life expectancy for adults in the region, and 12 years for children. Given that groundwater is utilized for drinking and domestic consumption on a daily basis, the exposure frequency (*EF*) is set at 365 days per year. The average body weight (*AW*) is 66.1 kg for adults and 20.3 kg for children, reflecting the average body weight in urban and rural areas of Inner Mongolia, with the median weight of children aged 5–6 years taken into account. The average exposure duration (*AT*) is calculated as 27,171 days for adults and 4380 days for children. The data above are sourced from the Exposure Factors Handbook of the Chinese Population (adult volume) by 3045 samples and the Highlights of the Chinese Exposure Factors Handbook (children volume).

Toxic effects of a contaminant are most likely to manifest when the exposure dosage exceeds the reference dose for that specific contaminant. The safety factor (*SF*) is set at 10 [38]. The non-carcinogenic toxic effects of a contaminant are quantified using the hazard quotient (*HQ*), which is calculated according to Equation (5).

$$HQ = \frac{CDI \times SF}{RfD} \quad (5)$$

where *RfD* represents the reference dose for non-carcinogens. Ultimately, the total hazard index (*THI*) for non-carcinogens, which reflects the integrated effects of water quality evaluation results, is calculated using Equation (6).

$$THI = \sum HQ_i \quad (6)$$

According to the recommendations set forth by the USEPA [39], *THI* values should be maintained below 1. Elevated values indicate that individuals using the contaminated water may face non-carcinogenic health hazards [40].

3. Results

3.1. Hydrochemical Characteristics and Mineral Saturation Index

The pH value of groundwater in the research area ranges from 6.38 to 7.54, indicating that it is neutral water. The degree of mineralization in pore water is relatively high, while the mineralization degree of pore fissure water is comparatively low, with values ranging from 41.85 to 1980.87 mg/L (Table 1). The concentration range of HCO_3^- among anions is 196.04 to 765.8 mg/L; the concentration range of Cl^- is 33.68 to 391.72 mg/L;

the concentration range of SO_4^{2-} is 21.29 to 1206.98 mg/L; and the concentration range of NO_3^- is 1.27 to 81.97 mg/L, with some samples not detected (Table 1). The concentrations of Ca^{2+} and Mg^{2+} among cations are 26.24 to 262.4 mg/L and 11.91 to 159.19 mg/L, respectively. The concentration range of Na^+ is 44.02 to 386.26 mg/L, and the concentration range of K^+ is 2.3 to 34.25 mg/L. The saturation index of dolomite ranges from −1.17 to 1.39; the saturation index of calcite is between −0.57 and 0.68; the saturation index of gypsum is between −2.37 and −0.47; and the saturation index of rock salt ranges from −7.37 to −5.62 (Table 1).

Table 1. Descriptive statistics of physical and chemical properties of groundwater.

	Mean	Min.	Max.	SD	CV%	Sk
pH	7.25	6.38	7.54	0.27	3.72	−1.59
TDS (mg/L)	514.33	41.85	1980.87	497.02	96.63	1.57
Ca^{2+} (mg/L)	98.50	26.24	262.40	67.13	68.15	1.33
Mg^{2+} (mg/L)	58.84	11.91	159.19	38.15	64.84	1.39
Na^+ (mg/L)	154.80	44.02	386.26	95.05	61.40	0.65
K^+ (mg/L)	7.74	2.30	34.25	8.36	108.08	2.29
HCO_3^- (mg/L)	443.88	196.04	765.80	151.27	34.08	0.31
Cl^- (mg/L)	138.50	33.68	391.72	90.90	65.63	1.14
SO_4^{2-} (mg/L)	239.75	21.29	1206.98	310.18	129.38	1.97
β_d	0.19	−1.17	1.39	0.53	283.29	−0.53
β_c	0.07	−0.57	0.68	0.24	323.27	−0.34
β_g	−1.62	−2.37	−0.47	0.58	−35.52	0.74
β_h	−6.44	−7.37	−5.62	0.54	−8.43	−0.23

Descriptive statistics were calculated for nine physical and chemical parameters of groundwater samples, along with four common mineral saturation indices. The standard deviation (SD) and coefficient of variation (CV) for each groundwater parameter were calculated (Table 1). The results for the physical and chemical indicators reveal a notable degree of variability, suggesting significant changes in the hydrochemical characteristics and groundwater transport patterns within the region. The variation values for K^+ and SO_4^{2-} are the highest, followed by total dissolved solids (TDS), indicating that these ions exhibit the greatest level of activity in groundwater runoff processes, influenced by dissolution, exchange adsorption, and other mechanisms.

3.2. Sources of Substances in Groundwater

3.2.1. The Main Source of Ions

(1) The source of Na^+

The average Na^+/Cl^- millimolar equivalent ratio in groundwater is 1.83, with 91% of groundwater samples exhibiting a ratio greater than 1 (Figure 5a). This finding suggests that the dissolution of silicate minerals is the primary source of Na^+ in groundwater [41,42]. Samples with an Na^+/Cl^- ratio of less than 1 were predominantly collected from the central pore aquifer of the study area. Conversely, samples with an Na^+/Cl^- ratio exceeding 2 were primarily obtained from pore fissure aquifers, particularly in regions adjacent to the second-stage basalt and Jurassic granite of the Abaga Formation, where the ratio is notably higher and may locally exceed 3.

The basalt in the second section of the Abaga Formation is characterized by gray-black porous basalt, almond-shaped basalt, and purple-red porous basalt, primarily composed of pyroxene and plagioclase. The Middle Jurassic potassium feldspar granite rocks exhibit a flesh-red color, featuring a medium-coarse grain structure with a blocky texture. The potassium feldspar content is approximately 55%, while plagioclase accounts for about 15%, quartz for around 25%, and biotite for about 2.5%. It is theorized that plagioclase plays a pivotal role in contributing to the Na+ content. The equation representing the dissolution of plagioclase can be found in Equation (7).

$$NaCaAl_3Si_5O_{16}(\text{Plagioclase}) + 3H_2CO_3 + 5.5H_2O = Na^+ + Ca^{2+} + 3HCO_3^- + 2H_4SiO_4 + 1.5Al_2Si_2O_5(OH)_4 \quad (7)$$

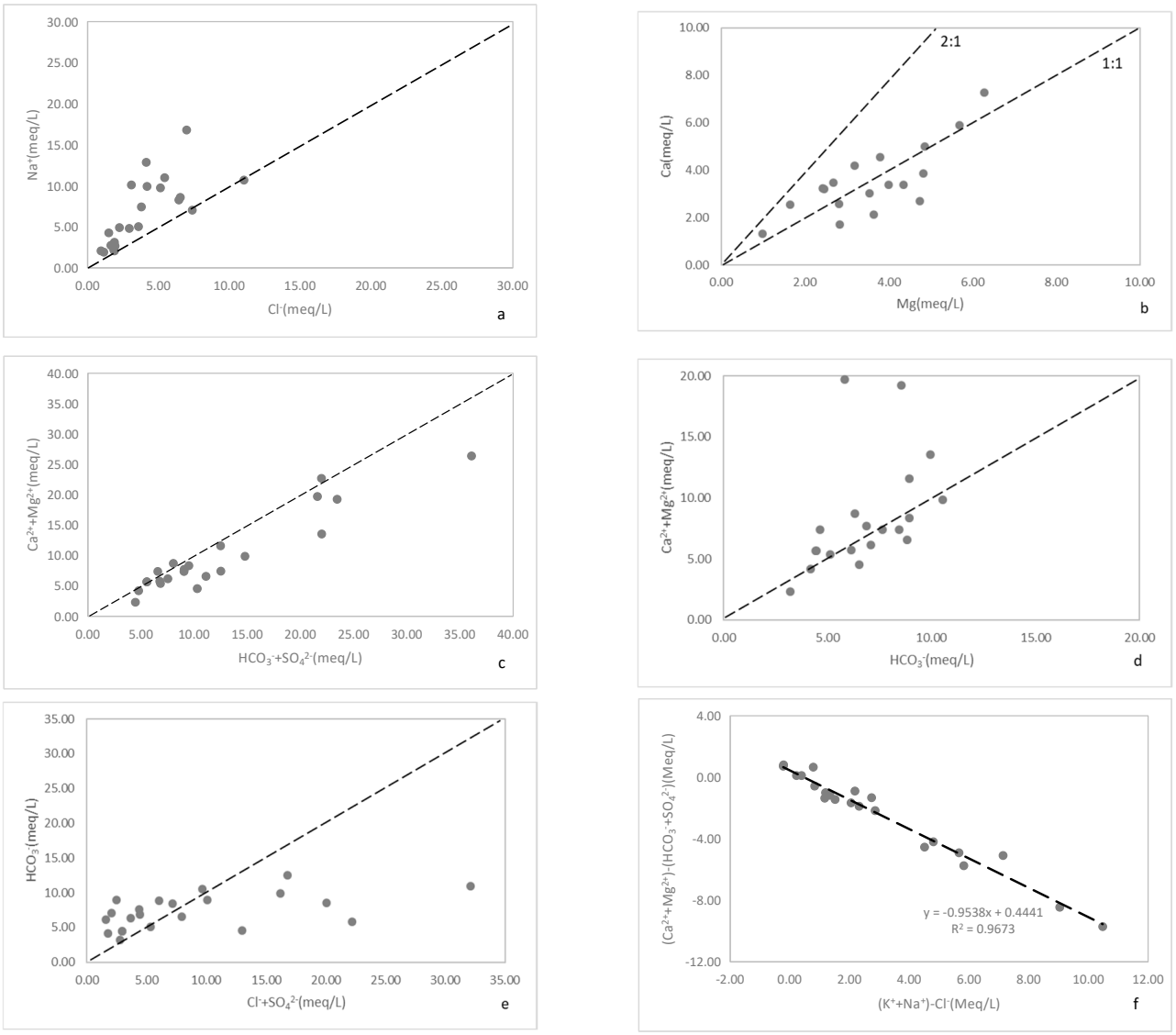

Figure 5. Correlation diagram of main ions in groundwater (mg/L). (**a**) The relationship between Na^+ and Cl^-; (**b**) The relationship between Ca^{2+} and Mg^{2+}; (**c**) The relationship between Ca^{2+} + Mg^{2+} and HCO_3^- + SO_4^{2-}; (**d**) The relationship between Ca^{2+} + Mg^{2+} and HCO_3^-; (**e**) The relationship between HCO_3^- and Cl^- + SO_4^{2-}; (**f**) The relationship between (Ca^{2+} + Mg^{2+})-(HCO_3^- + SO_4^{2-}) and (K^+ + Na^+)-Cl^-.

(2) Sources of Ca^{2+} and Mg^{2+}

The ratio of Ca^{2+}/Mg^{2+} found in groundwater varies between 0.57 and 1.56 (Figure 5b). Predominantly, samples exhibiting a ratio exceeding 1 were sourced from the pore aquifer and the northeast pore fissure aquifer, representing 59% of the overall sample size. Conversely, the regions in which the Ca^{2+}/Mg^{2+} ratio is below 1 constituted 41% of the total sample collection. The presence of Ca^{2+} and Mg^{2+} in the groundwater across the study site is mainly due to the combined dissolution of dolomite and calcite [43] (Equations (8) and (9)). Additionally, during the replenishment phase, the dissolution of pyroxene further introduces Mg^{2+} into the groundwater (Equation (10)). Around 72% of the analyzed water samples revealed a saturation index above 0 for dolomite, while approximately 68% in-

dicated a saturation index exceeding 0 for calcite, implying that the precipitation of both dolomite and calcite has occurred concurrently.

When dolomite dissolution occurs,

$$CaMg(CO_3)_2 + 2H_2O + 2CO_2 \rightarrow Ca^{2+} + Mg^{2+} + 4HCO_3^- \quad (8)$$

When calcite dissolution occurs,

$$CaCO_3 + H_2O + CO_2 \rightarrow Ca^{2+} + 2HCO_3^- \quad (9)$$

When pyroxene dissolution occurs,

$$Mg_2SiO_6(\text{pyroxene}) + 2H_2O + 4H_2CO_3 = 2Mg^{2+} + 2H_4SiO_4 + 4HCO_3^- \quad (10)$$

(3) Contribution of mineral dissolution

Figure 5c demonstrates that the curves for Ca^{2+} + Mg^{2+} and HCO_3^- + SO_4^{2-} millimolar equivalents decline and approach a 1:1 equimolar relationship. As a result, the dissolution processes of calcite, dolomite, and gypsum are the most significant, whereas the dissolution of rock salt appears in a less prominent manner. The saturation index for rock salt throughout all areas remains considerably lower than the precipitation threshold. Below the contour line, the weathering of silicate minerals takes place [44], where Ca^{2+} + Mg^{2+} does not adequately bind with all HCO_3^- + SO_4^{2-}, and the dissolved Na+ from silicates acts as an extra source of cations.

(4) Distribution relationship of anions and cations

The overall relationship between Ca^{2+} + Mg^{2+} and HCO_3^- demonstrates that the primary source of HCO_3^- is the dissolution of calcite and dolomite. Around 41% of the samples showed higher levels of Ca^{2+} + Mg^{2+} compared to HCO_3^- (Figure 5d), which implies that carbonate weathering was the dominant process, contributing Ca^{2+} and Mg^{2+} to the groundwater [45]. The surplus of Ca^{2+} + Mg^{2+} present in the groundwater samples was compensated for by SO_4^{2-} + Cl^- (Figure 5e). In contrast, nearly 59% of the samples revealed that the concentrations of Ca^{2+} + Mg^{2+} fell below that of HCO_3^-, suggesting that the excess negative charge from HCO_3^- must be neutralized by alkali metals (such as Na^+ and K^+) [46], which results in the dissolution of silicate minerals. Interestingly, the amount of HCO_3^- did not show an increase alongside the rising concentrations of SO_4^{2-} + Cl^- (Figure 5e).

(5) Ion exchange

The relationship curve between Ca^{2+} + Mg^{2+} and HCO_3^- + SO_4^{2-} in Figure 5f exhibits a slope of -0.9538. In the absence of silicate mineral weathering and/or cation exchange adsorption, all data points should cluster near the origin. The data are predominantly distributed along a straight line with a slope of -1, suggesting that Ca^{2+}, Mg^{2+}, and Na^+ are interrelated through reverse ion exchange reactions.

3.2.2. Piper Diagram

The Piper trilinear diagram (Figure 6) depicts the different processes that affect groundwater characteristics [47]. In the eastern area, the pore fissure water is primarily made up of HCO_3-Ca·Mg·Na, along with other types such as HCO_3-Ca·Na·Mg. On the other hand, the pore water is chiefly characterized by HCO_3·SO_4-Ca·Na·Mg, as well as by variations including HCO_3·Cl-Na·Ca·Mg, among others. In the western area, the pore fissure water predominantly features HCO_3·Cl·SO_4 along with sodium. This distribution highlights a distinct zoning of hydrochemical types, where anions shift from HCO_3 to HCO_3·Cl·SO_4, and cations transition from Ca·Mg·Na to Na.

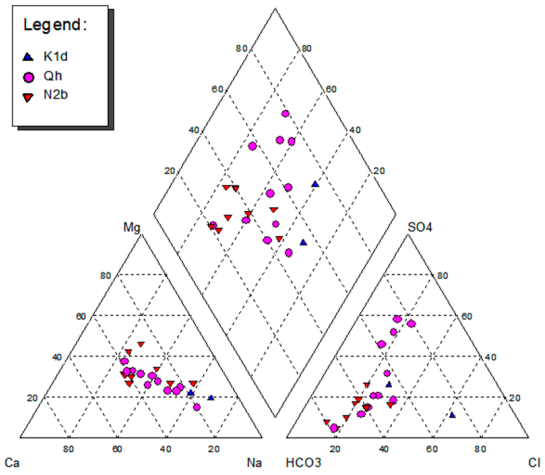

Figure 6. Piper map of Xilinhot in groundwater.

3.2.3. Chadha Diagram

The Chadha diagram [48] reveals that around 41% of groundwater is categorized as recharge water (HCO_3-Ca·Mg), while 32% is recognized as reverse ion exchange (Cl-Ca·Mg type) (Figure 7). Recharge water is mainly stored in the aquifers that contain pore fissure water, situated in the northeast and southwest areas of Xilinhot. In these locations, the saturation index of groundwater—especially for minerals like dolomite and calcite—typically falls below 0, indicating that this water remains unsaturated. On the other hand, reverse ion exchange water predominantly exists in the majority of porous aquifers, where the saturation index for dolomite and calcite frequently surpasses 0. Findings from both the Piper plot and the Chadha plot indicate that the levels of alkaline earth metals and weakly acidic anions in groundwater samples are greater than those of alkaline and strongly acidic anions, pointing to the presence of temporary hardness in the groundwater.

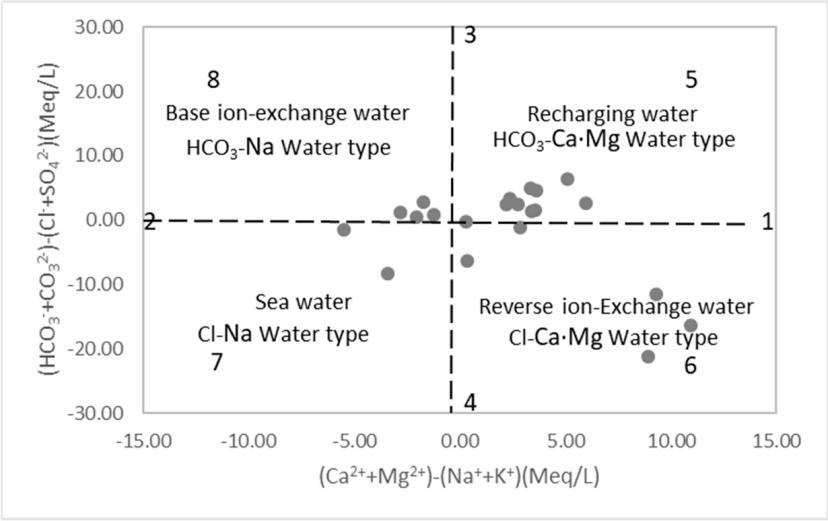

Figure 7. Chadha diagram of groundwater hydrochemical process. 1. Alkaline earth exceeds alkali metal; 2. alkali metal exceeds alkaline earth; 3. weak acidic anions exceed strong acidic anions; 4. strong acidic anions are greater than weak acidic anions; 5. recharging water (HCO_3-Ca·Mg type); 6. counter ion exchange water (Cl-Ca·Mg type); 7. seawater (Cl-Na type); 8. ion exchange water (HCO_3-Na type).

3.2.4. The Formation and Evolution Law of Groundwater

In the groundwater of the southern region's upper reaches, the predominant cation is Na^+. This ion, along with some Mg^{2+}, mainly comes from the basalt of the second

rock segment of the Abaga Formation and the Middle Jurassic potassium feldspar granite. Moreover, Ca^{2+} and the rest of the Mg^{2+} are sourced from both dolomite and calcite. The principal anion present is HCO_3^-, which originates also from carbonate minerals. In the downstream layers, particularly in porous aquifers, some degree of inverse ion exchange occurs, leading to a decrease in the relative content of Na^+. As Ca^{2+} and Mg^{2+} accumulate, certain regions may hit saturation thresholds, resulting in precipitation. Additionally, the level of SO_4^{2-} is affected by the dissolution and alteration of sulfate minerals. Although these minerals are not widely distributed, the concentration of SO_4^{2-} rises with groundwater runoff, even though the gypsum saturation index has not reached full saturation. Cl^- is liberated from specific igneous rocks after extended periods of weathering and leaching, where it remains tightly bound within the mineral crystallization lattice and engages in the cycling of elements in the surface geochemical context.

The substances found in the water can be divided into equisoluble and non-equisoluble minerals. Once these substances dissolve in water, they are influenced by the principles of mineral solubility products, the common ion effect, and the salt effect. In the upstream watershed area, characterized by volcanic rocks, Na^+ shows considerable activity, with 91% of water samples classified as containing Na^+ according to the Shukalev classification. Certain minerals made up of Ca^{2+}, Mg^{2+}, and HCO_3^- ions precipitate when their saturation values are met or exceeded in the aquifer pores, while Na^+ and K^+ persist in dissolving and accumulating, leading to a horizontal zoning characteristic of hydrochemical types.

3.2.5. Hydrogeochemical Modeling

In this research, PHREEQC (Version 2) was utilized to model the restoration of water quality and source materials. The paths being simulated are designated as XJ24 and XJ19, as depicted in Figure 3. Key minerals associated with the restoration of water quality sources encompass rock salt, gypsum, sodium feldspar, kaolinite, carbon dioxide (g), calcite, dolomite, quartz, plagioclase, potassium feldspar, and pyroxene. Silicate minerals within this list undergo enforced dissolution, while clay minerals are subjected to enforced precipitation. Regarding reverse ion exchange processes, NaX is allocated for enforced precipitation, while CaX2 and MgX2 are chosen for enforced dissolution.

The simulation outcomes reveal that the dissolution of plagioclase, potassium feldspar, and pyroxene plays a crucial role in supplying substances in the water, with plagioclase exerting the most pronounced effect, followed by minor dissolution of dolomite and calcite. Furthermore, gypsum dissolution adds to the substance sources in groundwater, leading to the precipitation of sodium-containing aluminosilicates. During the transport process, plagioclase dissolved 1092 mg, potassium feldspar dissolved 168 mg, and gypsum dissolved 818 mg, with clay minerals precipitating at 985 mg. Although this is not the only solution available, it stands out as one of the more plausible outcomes in the simulations.

3.3. The Relationship between Groundwater Components and Human Health

3.3.1. Endemic Diseases and Target Ion Screening

The Inner Mongolia Groundwater Resources Evaluation Report reveals that groundwater quality is linked primarily to endemic diseases such as fluorosis, iodine deficiency (which causes endemic goiter), and Keshan disease. This research focuses on two specific conditions: fluorosis and iodine deficiency. Reports indicate that fluorosis has been observed in every city within the league, with Xilinhot City exhibiting a dental fluorosis prevalence rate of 71.4% and a skeletal fluorosis prevalence of 0.11%. Furthermore, the recorded prevalence of iodine deficiency in Xilinhot stands at 16.88%.

3.3.2. Results of Groundwater Quality Evaluation

A thorough assessment of groundwater quality reveals that the water in this region can be mainly divided into Classes II, III, IV, and V. Within the analysis of the 22 monitoring points for water quality, one point is designated as Class II, which represents 8.7% of all monitoring locations. Moreover, there are six points identified as Class III, making up 26.1%

of the total, nine points classified as Class IV, comprising 39.1%, and six points categorized as Class V, which also accounts for 26.1% of the overall monitoring sites (Figure 8). The primary factors influencing water quality evaluation include F^-, NO_3^-, SO_4^{2-}, DO, Cl^-, Na^+, and TDS. Among these, F^- affected 23% of the samples, while both NO_3^- and SO_4^{2-} impacted 18% of the water sample evaluation results.

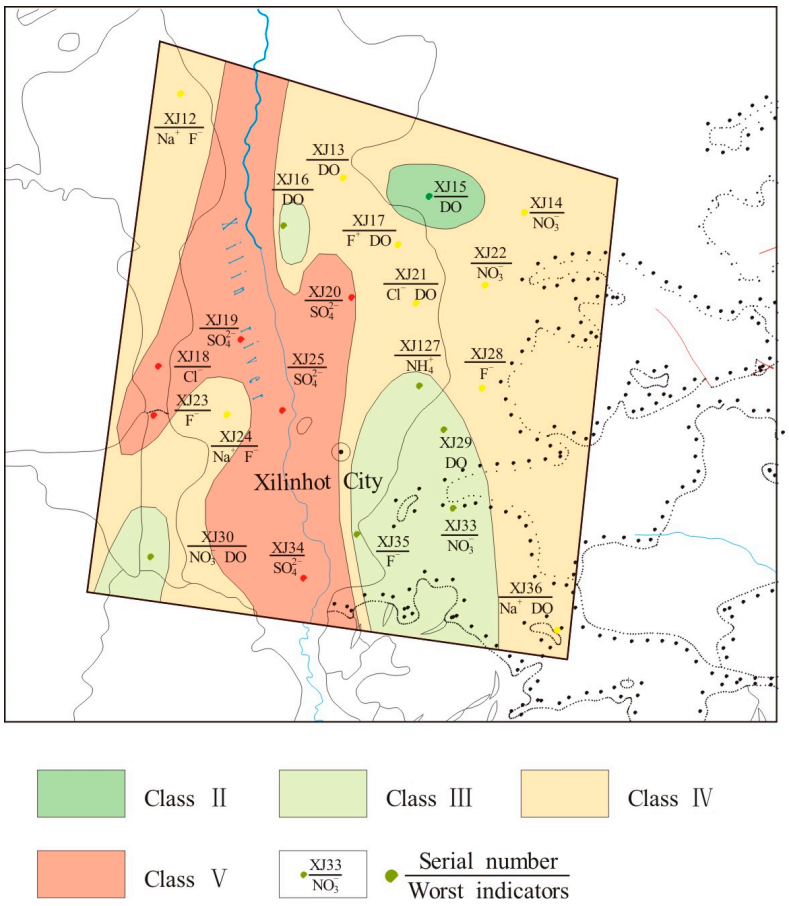

Figure 8. Groundwater quality evaluation map of Xilinhot.

3.3.3. Non-Carcinogenic Health Risks

The pollutants selected for this health risk evaluation should carefully take into account the findings from the water quality analysis and the occurrence of local diseases. Furthermore, extended exposure to these pollutants presents non-carcinogenic health hazards. Considering these elements, nitrate and fluoride have been identified as the pollutants for this assessment. These substances have the potential to expose water users in the study region to harmful health consequences [49].

The site-wise variation of the non-carcinogenic health risks posed by nitrate and fluoride for children and adults is presented in Table 2. $HQ_{Nitrate}$ varied between 0 and 0.148 (children) and 0 and 0.143 (adults). Similarly, the $HQ_{Fluoride}$ varied between 0 and 0.191 (children) and 0 and 0.185 (adults).

The findings demonstrate that F^- and NO_3^- exhibit distinct hazard quotients for children and adults within the studied region; nonetheless, neither $HQ_{Nitrate}$, $HQ_{Fluoride}$, nor THI values have led to any tangible risks. The health threats associated with nitrate and fluoride appear to be nearly equivalent for both adults and children. The hazard quotient for children is slightly higher than that for adults, likely due to their lower body weight [50].

Table 2. Results of potential health risks due to fluoride and nitrate.

	Children			Adults		
	$HQ_{nitrate}$	$HQ_{fluoride}$	THI	$HQ_{nitrate}$	$HQ_{fluoride}$	THI
XJ12	0.021	0.116	0.056	0.020	0.112	0.132
XJ13	0.003	0.061	0.022	0.003	0.059	0.062
XJ14	0.042	0.087	0.069	0.041	0.084	0.124
XJ15	0.000	0.066	0.020	0.000	0.063	0.063
XJ16	0.006	0.061	0.025	0.006	0.059	0.065
XJ17	0.084	0.105	0.116	0.081	0.102	0.183
XJ18	0.009	0.077	0.033	0.009	0.075	0.083
XJ19	0.002	0.063	0.022	0.002	0.061	0.063
XJ20	0.000	0.063	0.019	0.000	0.061	0.061
XJ21	0.000	0.068	0.021	0.000	0.066	0.066
XJ22	0.045	0.087	0.072	0.044	0.084	0.128
XJ23	0.133	0.191	0.191	0.128	0.185	0.313
XJ24	0.000	0.094	0.029	0.000	0.091	0.091
XJ25	0.004	0.050	0.019	0.004	0.048	0.052
XJ27	0.000	0.025	0.008	0.000	0.024	0.024
XJ28	0.031	0.097	0.061	0.030	0.094	0.124
XJ29	0.148	0.046	0.162	0.143	0.045	0.188
XJ30	0.027	0.094	0.056	0.026	0.091	0.117
XJ33	0.022	0.061	0.041	0.021	0.059	0.080
XJ34	0.004	0.056	0.021	0.004	0.054	0.058
XJ35	0.030	0.080	0.054	0.029	0.077	0.106
XJ36	0.135	0.046	0.149	0.131	0.045	0.176

3.3.4. Analysis of Drinking Groundwater and Human Health

(1) Comprehensive analysis of healthy geological conditions

The examination and study of groundwater, along with its influence on human health, mainly concentrate on the following points: ① The buildup of specific elements may cause considerable damage, which might arise even in natural settings. The US EPA's National Primary Drinking Water Regulations and the groundwater quality standards in China explicitly highlight the risk of such damage. ② The levels of these elements within the Earth's crust are notably high. ③ This evaluation can incorporate available data, which yields relatively clear results. ④ Furthermore, there exist advantageous elements for human health. Therefore, it is essential to further explore the elements and compounds, such as Ca, Mg, Na, K, HCO_3, CO_3, Cl, SO_4, F, I, Be, Cr, Cu, Se, Cd, Sb, Ba, Hg, and Pb, among others.

(2) Macro-elements and their compounds and human health

The influence of macro-elements and their compounds on human health is frequently neglected; nonetheless, their significance cannot be ignored.

Calcium (Ca) is plentiful in the Earth's crust, but the concentration of Ca in drinking water seldom surpasses 180 mg/L. The advised limit is 20 mg/L, and the rate of Ca exceeding this standard in groundwater is 32%. Sufficient intake of Ca is crucial for human growth, development, and the sustenance of normal metabolic functions. In contrast, elevated levels of water hardness may result in negative health consequences, such as a higher likelihood of kidney stones, gastrointestinal issues, and skin problems [51].

The amount of magnesium (Mg) found in natural water is typically low, with 27% of samples from the study area surpassing 65 mg/L. While higher Mg levels can contribute to endemic diarrhea, its presence in natural water is also advantageous for human health, and the prevalence of endemic diseases remains low.

For drinking water, the ideal sodium (Na) concentration should be less than 20 mg/L. In the study region, groundwater Na levels exceed this guideline, with the peak concentration reaching 15 times the recommended amount.

Consuming excessive sodium over extended periods can negatively impact the health of both humans and animals. Levels of potassium (K) need to be kept between 10 and

12 mg/L. In the study area, the overall K content stays within this recommended range; however, samples XJ13, XJ19, XJ25, and XJ34 surpassed this limit.

Water that contains over 1000 mg/L of bicarbonate compounds (Na, Mg) can be categorized as bicarbonate mineral water, known for enhancing gastrointestinal function and assisting in the management of hepatobiliary conditions. Moreover, bicarbonate has demonstrated a hypoglycemic effect [52]. In this study area, bicarbonate levels remained below 1000 mg/L, suggesting no harmful health consequences.

The permissible limit for Cl^- concentration in drinking water within China is set at 250 mg/L. In the examined region, groundwater typically remains within the recommended safe levels, though two locations surpass the permissible threshold of 500 mg/L. Nevertheless, this minor exceedance does not interfere with normal physiological processes in humans since significant impacts on gastric juice production and metabolic functions only occur when concentrations rise above 500 mg/L.

Sulfur (S) acts as a vital biological element, being a key part of proteins and playing an essential role in the synthesis of chondroitin sulfate, making it crucial for living organisms. The guideline for sulfate levels in drinking water is <250 mg/L. Typically, sulfate concentrations under 500 mg/L do not pose negative effects on human physiological activities. However, when sulfate is present in the form of $MgSO_4$ or Na_2SO_4, such levels can activate gastrointestinal functions and may lead to diarrhea [53]. Additionally, water with sulfate concentrations exceeding 960 mg/L is considered unsuitable for agricultural use as it hampers crop growth. In this investigation, samples XJ19 and XJ34 were above this critical limit.

The groundwater in this area shows no detectable carbonate, and, therefore, further discussion is not warranted.

(3) Micronutrients and their compounds and human health

The level of nitrate found in groundwater is closely linked to pollution, mainly arising from sources like septic tanks, agricultural fertilizers, feedlots, and wastewater from industries [54]. The impact of grazing livestock is particularly pronounced in pastoral regions. The acceptable maximum limit for nitrate in potable water is established at 10 mg/L, while the excess concentration of nitrate reaches about 18%. Nitrate concentration below 100 mg/L, or within the interval of 100 to 200 mg/L, does not represent an immediate hazard to human health. Nonetheless, when nitrate transforms into nitrite, it poses a significant health threat. It is important to note that nitrite levels in drinking water are heightened in areas impacted by Keshan disease and Kashin–Beck disease. Furthermore, regions with elevated rates of liver and esophageal cancers have also reported significantly increased nitrite concentrations in their drinking water. Crucially, no nitrite was found in the area of study.

Fluorine (F) is a crucial element required by the human body; nevertheless, both high and low levels can negatively impact health [55]. In China, the acceptable range for F concentration in water is established between 0.5 and 1.0 mg/L. Within the investigated area, F levels are categorized as moderate to high, with 45% of the samples surpassing 1.0 mg/L. Regions with increased F levels are especially vulnerable to fluorosis.

Iodine (I) concentrations varied from 0.8 mg/L to 16.4 mg/L, presenting a median of 4.34 mg/L. The hydrogeological properties of the pores and fractures in the southeastern region of Xilinhot are mainly linked to iodine deficiency in the natural setting, shaped by geomorphological factors and an unfavorable geological environment for iodine accumulation. This iodine-deficient area is located in the low mountain and hilly terrains, where rapid groundwater runoff and discharge inhibit the enhancement of iodine levels.

Compared to water quality standards, the levels of beryllium (Be), chromium (Cr), copper (Cu), selenium (Se), cadmium (Cd), antimony (Sb), barium (Ba), mercury (Hg), and lead (Pb) remain within the acceptable limits.

(4) Comprehensive

Based on the macro-elements, the geological health concerns observed in the study area include excessively high local hardness, along with increased concentrations of calcium (Ca), magnesium (Mg), and sodium (Na) ions. Moreover, the content of sulfate (SO_4) is also significantly elevated. Long-term consumption of this water may lead to health issues, such as a higher prevalence of kidney stones and gastrointestinal ailments, including endemic diarrhea. Concerning micronutrients, nearly 50% of the water samples in this region presented health hazards, which may result in conditions like fluorosis. In contrast, the levels of advantageous micronutrients, such as selenium (Se), zinc (Zn), boron (B), and germanium (Ge), were not found to be elevated.

3.3.5. A Discussion of Healthy Groundwater

Humans are organic entities that are derived from and interact with their surroundings. When comparing the concentrations of elements in the Earth's crust to those found in human blood, there is a very strong correlation in element concentrations, with exceptions for the primary components of biological protoplasm (C, H, O, N) and the key constituents of filling rocks (Si, Al) [56,57] (Figure 9). Based on the understanding of elemental abundances in humans, a deviation of certain elements from the standard abundance curve indicates potential pollution in the human body. Consequently, specific ions in groundwater might show significant deviations under natural conditions, particularly in areas where groundwater serves as the primary source of drinking water, potentially leading to endemic diseases.

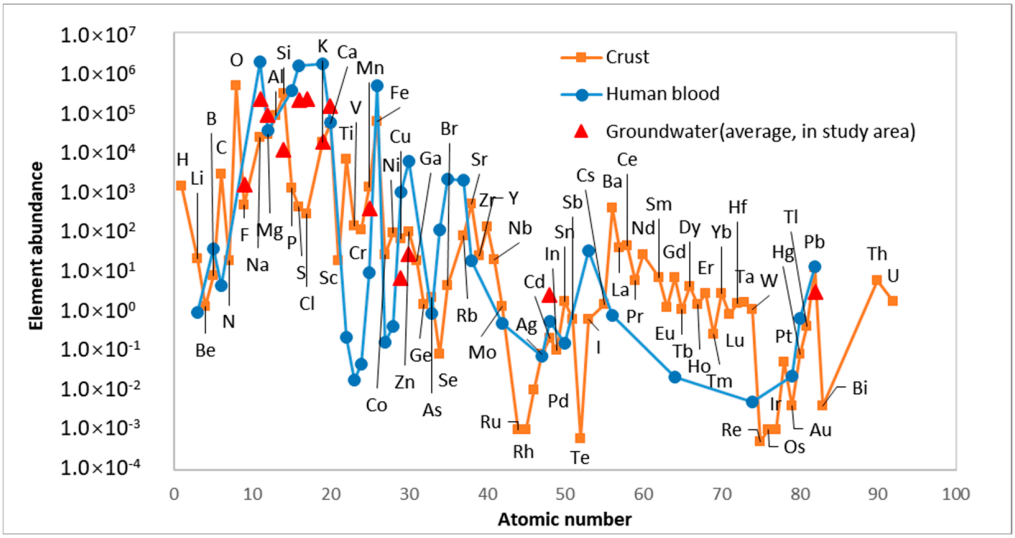

Figure 9. The abundance and atomic number variation curves of elements in the crust, human blood, and groundwater in study area.

The typical concentration of the main constituents of groundwater in the research area does not considerably differ from the typical concentrations observed in crust and human blood, indicating a stronger correlation with the average levels found in the crust. Sulfur (S) and Chlorine (Cl) show a propensity to transfer from the environment into the human system, whereas other elements maintain a state of equilibrium.

Based on the findings from the seventh national census carried out in 2020, in Xilinhot, 1.84% of the resident population is aged over 80, which is below the national average of 2.54% [58].

What defines healthy groundwater regarding its abundance? This research analyzes the ion concentrations of potable water in Jinxiang County of Jining, recognized as a region associated with longevity, and compares it with Jinan and the Guanzhong areas, emphasizing the indicators that reflect the health impacts of groundwater [59–62]. It is

noteworthy that, as of 2020, the percentage of individuals aged over 80 in Xilinhot was lower than the Jinxiang County average of 2.36% recorded in 2010, but it was slightly higher than the figures of 1.69% for Jinan and 1.07% for Guanzhong. Concerning stable elements, the study region displays a comparable scale to Jinxiang County for elements like sodium (Na), magnesium (Mg), and calcium (Ca) (Figure 10). Research findings indicate that the concentration of native heavy metal contaminants in groundwater is not significant [63,64]. Nonetheless, the levels of micronutrient elements such as manganese (Mn), copper (Cu), zinc (Zn), selenium (Se), iodine (I), and lithium (Li) were found to be lower in the study area than in Jinxiang County. The deficiencies in these micronutrients may result in insufficient intake, which can undermine the health benefits linked with these vital elements. Therefore, groundwater deemed healthy for human consumption ought to be devoid of toxic, harmful, and foul-smelling substances while maintaining a suitable equilibrium of minerals crucial for human well-being. Optimal groundwater should have a rich presence of trace elements such as calcium (Ca), magnesium (Mg), potassium (K), and sodium (Na), along with essential micronutrients like iron (Fe), silicon (Si), fluorine (F), iodine (I), selenium (Se), and lithium (Li). It is advisable to boil groundwater before consumption. Additionally, it is advisable to avoid using fluoride toothpaste in areas with elevated fluoride levels, or to implement groundwater defluoridation treatment [65,66], and nitrogen reduction treatment [67]. Instead, opt for iodized table salt and ensure adequate intake of trace elements such as zinc, iron, and selenium through various means.

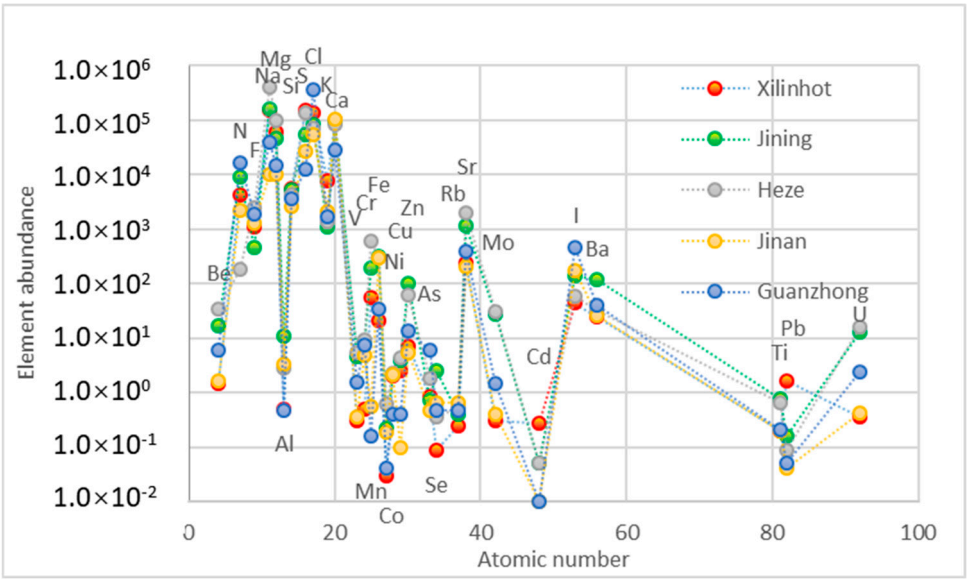

Figure 10. Comparison chart of groundwater abundance.

4. Conclusions

Based on the test results of groundwater samples collected around Xilinhot City, along with a geological overview of the area and the primary mineral components of the aquifer, the formation and evolution of groundwater were investigated. The quality of the groundwater and non-carcinogenic health risks were assessed, and the impacts of macro-elements and trace elements on human health were examined. The following conclusions were drawn:

(1) The dissolution and alteration of major minerals within the aquifer contribute to the characteristics of groundwater through various chemical reactions. Igneous rocks, which contain minerals such as potassium feldspar, plagioclase, and pyroxene, release Na^+, Cl^-, and K^+ ions into the groundwater. In contrast, sedimentary rocks that contain minerals like dolomite and calcite provide ions such as Ca^{2+}, Mg^{2+}, and HCO_3^- to the groundwater, which can accumulate and precipitate with runoff.

(2) A comprehensive assessment of groundwater quality indicates that the water in this region can be predominantly categorized into Classes II, III, IV, and V. The primary factors influencing the evaluation of water quality include fluoride (F^-), nitrate ($NO_3{}^-$), sulfate ($SO_4{}^{2-}$), dissolved oxygen (DO), chloride (Cl^-), sodium (Na^+), and total dissolved solids (TDS). Notably, fluoride affected 23% of the samples, while both nitrate and sulfate impacted 18% of the water sample evaluation results.

(3) The results of the non-carcinogenic health risk assessment indicate that F^- and ($NO_3{}^-$ exhibit distinct hazard quotients for children and adults within the studied region. However, neither $HQ_{Nitrate}$, $HQ_{Fluoride}$, nor THI values have resulted in any tangible risks. The health threats associated with nitrate and fluoride appear to be nearly equivalent for both adults and children, although the hazard quotient for children is slightly higher than that for adults.

(4) The analysis of the relationship between drinking water and human health, based on macro-elements, reveals significant geological health concerns in the study area. These concerns include excessively high local hardness, along with increased concentrations of calcium (Ca), magnesium (Mg), and sodium (Na) ions. Additionally, the content of sulfate (SO_4) is also markedly elevated. Regarding micronutrients, nearly 50% of the water samples in this region posed health hazards which could lead to conditions such as fluorosis. In contrast, the levels of beneficial micronutrients, including selenium (Se), zinc (Zn), boron (B), and germanium (Ge), were not found to be elevated.

(5) Based on the elemental abundance characteristics of the Earth's crust, human blood, and groundwater in the study area, we compared the hydrochemical characteristics of drinking groundwater in longevity areas with those in non-longevity areas. This comparison facilitated a discussion on the definition of healthy groundwater and led to recommendations for its consumption.

(6) In the next phase of our research, we will continue to collect groundwater samples to analyze both intra-annual and inter-annual variations in groundwater quality. Additionally, we will collect aquifer rock samples and analyze their mineral composition to further elucidate the processes and intensities of water–salt interactions. During the survey, we will compile statistics on the types and frequencies of endemic disease occurrences and provide detailed recommendations based on the drinking water habits observed.

Author Contributions: Conceptualization, Y.X. and F.L.; methodology, Y.X. and H.N.; investigation, Y.X., J.Z. and H.N.; data curation, G.C. writing—original draft preparation, Y.X.; writing—review and editing, F.L. and Y.X.; supervision, F.L.; project administration, G.C.; resources, Y.X., G.C., F.L., J.Z. and H.N. All authors have read and agreed to the published version of the manuscript.

Funding: This research was funded by the Department of Natural Resources, Inner Mongolia, grant number 2022-TZH08. This research was funded by the China Geological Survey, grant number DD20230431. This research was funded by The Inner Mongolia Geological Survey Institute, grant numbers NDHX[2023]NMGDXS-JC-06.

Data Availability Statement: Data is contained within the article.

Conflicts of Interest: Author Guangfang Chen was employed by the company Inner Mongolia Ninth Geology Mineral Exploration and Development Co., Ltd. The remaining authors declare that the research was conducted in the absence of any commercial or financial relationships that could be construed as a potential conflict of interest.

References

1. Wang, S.; Meng, J.; Chen, X.S.; Fan, J.F. An overview of complexity studies on Earth systems. *J. Beijing Norm. Univ. (Nat. Sci.)* **2023**, *59*, 796–805. [CrossRef]
2. Hamilton, E.I. The chemical elements and human morbidity-water, air and places—A study of natural variability. *Sci. Total Environ.* **1974**, *3*, 3–85. [CrossRef]
3. Wang, Z.M.; Liu, Y.S.; Lu, A.H.; Wang, Y. Water: The lifeblood of the Earth-human system revealed in elemental correlations. *Sci. China Earth Sci.* **2023**, *66*, 2386–2390. [CrossRef]

4. Lin, N.F. *Medical Environmental Geochemistry*; Jilin Science and Technology Press: Changchun, China, 1991; pp. 239–240.
5. Zhu, W.; Wang, C.; Wu, J.; Chen, S.; Mao, W.; Chen, Y.; Chen, M. Dietary copper intake and the prevalence of kidney stones among adult in the United States: A propensity score matching study. *Front. Public Health* **2022**, *10*, 973887. [CrossRef] [PubMed]
6. Zhang, K.; Li, Y.; Yu, Z.; Yang, T.; Xu, J.; Chao, L.; Ni, J.; Wang, L.; Gao, Y.; Hu, Y.; et al. Xin'anjiang Nested Experimental Watershed (XAJ-NEW) for Understanding Multiscale Water Cycle: Scientific Objectives and Experimental Design. *Engineering* **2022**, *18*, 207–217. [CrossRef]
7. Zhao, Y.; Zhang, M.; Liu, Z.; Ma, J.; Yang, F.; Guo, H.; Fu, Q. How Human Activities Affect Groundwater Storage. *Research* **2024**, *7*, 0369. [CrossRef]
8. Zhang, B.Y.; Zeng, F.S.; Wei, X.Z.; Khan, U.; Zou, Y.H. Three-Dimensional Hierarchical Hydrogeological Static Modeling for Groundwater Resource Assessment: A Case Study in the Eastern Henan Plain, China. *Water* **2022**, *14*, 1651. [CrossRef]
9. Chen, X.; Huang, R.C.; Huang, F.; Liu, X.F.; Zhang, Y.Y.; Zhang, R.R. A comprehensive study of the maintaining mechanisms for hydrological cycle and ecological evolution and function in the northwest inland river basins of China. *Hydrogeol. Eng. Geol.* **2022**, *49*, 12–21. [CrossRef]
10. Dang, X.Y.; Zhang, J.; Chang, L.; Gu, X.F. Hydrogeological Survey and Water Resources Security in Northwest China. *Northwest Geol.* **2022**, *55*, 81–95. [CrossRef]
11. Bodrud-Doza, M.; Didar-Ul Islam, S.M.; Rume, T.; Quraishi, S.B.; Rahman, M.S.; Bhuiyan, M.A.H. Groundwater quality and human health risk assessment for safe and sustainable water supply of Dhaka City dwellers in Bangladesh. *Groundw. Sustain. Dev.* **2020**, *10*, 100374. [CrossRef]
12. Wu, C.; Tang, K.W.; Zhang, X.H. Water Quality assessment and variation characteristics of underground drinking water sources in Hebei Province based on self-defined classification criteria. *Water Resour. Power* **2022**, *40*, 116–119+160. [CrossRef]
13. Li, Y.; Wu, P.; Zhang, B.; Huang, X.Q.; Han, Q.Q.; Li, Y.; Xu, Z.X.; Yu, K. Distribution characteristics and formation factors of high fluoride groundwater in the north of Lingwu City. *Environ. Chem.* **2020**, *39*, 2520–2528. [CrossRef]
14. Yuan, H.Q.; Li, Q.; Tao, H.F.; Aihemaiti, M.; Yang, W.X.; Su, Y.P. Groundwater arsenic enrichment factors of Kuitun River basin, Xinjiang. *Environ. Chem.* **2020**, *39*, 524–530. [CrossRef]
15. Li, Z.Y.; Cao, W.G.; Wang, Z.R.; Li, J.C.; Ren, Y. Hydrochemical Characterization and Irrigation Suitability Analysis of Shallow Groundwater in Hetao Irrigation District, Inner Mongolia. *Geoscience* **2022**, *36*, 418–426. [CrossRef]
16. Xia, Y.B.; Wang, B.; Li, H.T.; Ma, Z.; Guo, X.; Zhao, K.; Zhao, C.R.; Zhang, X.; Wang, X.X. Study on hydrochemical origins and health geology regionalization of shallow groundwater in Xiong'an New Area. *China Geol.* **2023**, 1–18. Available online: https://www.cnki.com.cn/Article/CJFDTotal-DIZI20220619002.htm (accessed on 1 August 2023).
17. Meng, R.F.; Yang, H.F.; Bai, H.; Xu, B.H. Chemical characteristics and evolutionary patterns of groundwater in the Daqing River Plain Area of Haihe Basin. *Rock Miner. Anal.* **2023**, *42*, 383–395.
18. Zhang, C.C.; Hou, X.W.; Li, X.Q.; Wang, Z.X.; Gui, C.L.; Zuo, X.F. Hydrogeochemical characteristics and evolution mechanism of karst groundwater in the catchment area of the Sangu Spring. *Hydrogeol. Eng. Geol.* **2021**, *48*, 62–71. [CrossRef]
19. Lakhvinder, K.; Madhuri, S.; Sakshi, S.; Bhavika, S.; Renu, L.; Gagandeep, S. Hydrogeochemical characterization of groundwater in alluvial plains of river Yamuna in northern India: An insight of controlling processes. *J. King Saud Univ. Sci.* **2019**, *31*, 1245–1253. [CrossRef]
20. Κατσάνου, K.; Siavalas, G.; Panagopoulos, G.; Lambrakis, N. Rare earth element patterns in a rapidly changing karst environment. *Appl. Geochem.* **2022**, *146*, 105462. [CrossRef]
21. Gayathri, J.A.; Raj, V.T.; Sreelash, K.; Maya, K.; Vandana, M.; Padmalal, D. Spatiotemporal variability in groundwater chemistry of a mountainous catchment with complex geologic and climate gradients in south west India. *Environ. Earth Sci.* **2021**, *80*, 18–28. [CrossRef]
22. Jiang, W.J.; Meng, L.S.; Liu, F.T.; Sheng, Y.Z.; Chen, S.M.; Yang, J.L.; Mao, H.R.; Zhang, J.; Zhang, Z.; Ning, H. Distribution, source investigation, and risk assessment of topsoil heavy metals in areas with intensive anthropogenic activities using the positive matrix factorization (PMF) model coupled with self-organizing map (SOM). *Environ. Geochem. Health* **2023**, *45*, 6353–6370. [CrossRef] [PubMed]
23. Ning, H.; Jiang, W.J.; Sheng, Y.Z.; Wang, K.L.; Chen, S.M.; Zhang Zhuo Liu, F.T. Comprehensive evaluation of nitrogen contamination in water ecosystems of the Miyun reservoir watershed, northern China: Distribution, source apportionment and risk assessment. *Environ. Geochem. Health* **2024**, *46*, 278. [CrossRef] [PubMed]
24. Li, X.Z. *Distribution and Health Risk Assessment of Organic Pollutants in Groundwater in the Receiving Area of the South-to-North Water Transfer Project in Mihuaishun*; China University of Geosciences: Beijing, China, 2021.
25. Zhang, Q.M.; Zhao, R.P.; Wang, X.L.; Sun, X.P. Chemical and biological remediation of soil and groundwater organic pollution. *Environ. Dev.* **2020**, *32*, 55–56. [CrossRef]
26. Zhang, Z.; Liu, F.; Jiang, W.; Chen, S.; Zhang, H.; Gao, Z.; Zhang, J.; Niu, X.; Cao, W.; Shan, Q. Quantifying the factors controlling groundwater fluoride and associated health risks in the coastal river delta, northern China. *J. Asian Earth Sci.* **2024**, *259*, 105929. [CrossRef]
27. Han, Z.H.; Ma, T.; Shen, S.; Du, Y.; Wu, X.C.; Liu, W.H. Distribution characteristics and influencing factors of poor-quality native groundwater in river percolation system in the lower reaches of the Hanjiang River. *Earth Sci. Front.* **2021**, *28*, 035–048. [CrossRef]
28. Zhang, Z.; Guo, H.; Han, S.; Gao, Z.; Niu, X. Controls of Geochemical and Hydrogeochemical Factors on Arsenic Mobility in the Hetao Basin, China. *Groundwater* **2022**, *61*, 44–55. [CrossRef]

29. Banach, A.; Kuźniar, A.; Marzec-Grządziel, A.; Wolińska, A.; Gałazką, A. Phenotype switching in metal-tolerant bacteria isolated from a hyperaccumulator plant. *Biology* **2021**, *10*, 879. [CrossRef]
30. Li, L.J.; Wang, H.J.; Ma, J.S. Pollution characteristics and health risk assessment of volatile organic compounds in groundwater in the Lower Liaohe River Plain. *Rock Miner. Anal.* **2021**, *40*, 930–943. [CrossRef]
31. Zhao, C.; Zhang, X.; Fang, X.; Zhang, N.; Xu, X.; Li, L.; Liu, Y.; Su, X.; Xia, Y. Characterization of drinking groundwater quality in rural areas of Inner Mongolia and assessment of human health risks. *Ecotoxicol. Environ. Saf.* **2022**, *234*, 113360. [CrossRef]
32. Dulamsuren, T.T.D. Effects of forest fragmentation on organic carbon pool densities in the Mongolian forest-steppe. *For. Ecol. Manag.* **2019**, *433*, 780–788. [CrossRef]
33. *GB/T 14848-2017*; Groundwater Quality Standards. Standards Press of China: Beijing, China, 2018.
34. Rajkumar, H.; Pradeep, K.N.; Gagandeep, S.; Rishi, M. Hydrogeochemical characterization, multi-exposure deterministic and probabilistic health hazard evaluation in groundwater in parts of Northern India. *Toxin Rev.* **2022**, *42*, 204–227. [CrossRef]
35. Qureshi, A.; Maurice, C.; Öhlander, B. Co-disposal of lignite fly ash and coal mine waste rock for neutralisation of AMD. *Environ. Sci. Pollut. Res. Int.* **2021**, *28*, 48728–48741. [CrossRef]
36. Choi, H.; Kim, J.; Shim, B.O.; Kim, D.H. Characterization of Aquifer Hydrochemistry from the Operation of a Shallow Geothermal System. *Water* **2020**, *12*, 1377. [CrossRef]
37. USEPA. *Risk Assessment: Guidance for Superfund Volume 1 Human Health Evaluation Manual (Part A)*; USEPA: Washington, DC, USA, 1989.
38. Sun, L.; Ma, X.; Jin, H.Y.; Fan, C.J.; Li, X.D.; Zuo, T.T.; Ma, S.C.; Wang, S.C. Geographical origin differentiation of Chinese Angelica by specific metal element fingerprinting and risk assessment. *Environ. Sci. Pollut. Res.* **2020**, *27*, 45018–45030. [CrossRef]
39. USEPA. *Risk Assessment Guidance for Superfund, Volume 1: Human Health Evaluation Manual (Part B, Development of Risk-Based Preliminary Remediation Goals)*; USEPA: Washington, DC, USA, 1991.
40. USEPA. *Human Health Evaluation Manual, Supplemental Guidance: Update of Standard Default Exposure Factors-OSWER Directive 9200.1-120*; USEPA: Washington, DC, USA, 2014.
41. Li, Y.Z.; Liu, J.T.; Gao, Z.J.; Wang, M.; Yu, L.Q. Major ion chemistry and water quality assessment of groundwater in the Shigaze urban area, Qinghai-Tibetan Plateau, China. *Water Sci. Technol. Water Supply* **2019**, *20*, 335–347. [CrossRef]
42. Sunkari, E.D.; Abu, M.; Zango, M.S.; Lomoro, W.; Alex, M. Hydrogeochemical characterization and assessment of groundwater quality in the Kwahu-Bombouaka Group of the Voltaian Supergroup, Ghana. *J. Afr. Earth Sci.* **2020**, *169*, 103899. [CrossRef]
43. Boyd, E.S.; Hamilton, T.L.; Havig, J.R.; Skidmore, M.L.; Shock, E.L. Chemolithotrophic primary production in a subglacial ecosystem. *Appl. Environ. Microbiol.* **2014**, *80*, 6146–6153. [CrossRef]
44. Suhendar, R.; Hadian, M.S.D.; Muljana, B.; Setiawan, T.; Hendarmawan, H. Geochemical Evolution and Groundwater Flow System in Batujajar Groundwater Basin Area, West Java, Indonesia. *Indones. J. Geosci.* **2020**, *7*, 87–104. [CrossRef]
45. Kuznetsova, A.; Kuznetsov, P.; Young, R.F.; Semple, K.M.; Li, C.; Foght, J.M.; Siddique, T. Microbial transformation of solid phase impacts quality of recovered water during consolidation of bioreactor-treated oil sands tailings. *J. Environ. Chem. Eng.* **2021**, *9*, 104715. [CrossRef]
46. Tiwari, A.K.; Singh, A.K. Hydrogeochemical investigation and groundwater quality assessment of Pratapgarh district, Uttar Pradesh. *J. Geol. Soc. India* **2014**, *83*, 329–343. [CrossRef]
47. Su, G.F.; Liu, G.J.; Li, Y.L.; Wang, G.Y. Analysis of groundwater ion abnormality and its cause of centralized drinking water sources in Jieshou City, China. *Front. Environ. Sci.* **2023**, *10*, 1055623. [CrossRef]
48. Hassan, A.M.; Ersoy, A.F. Hydrogeochemical and isotopic investigations on the origins of groundwater salinization in Çarşamba coastal aquifer (North Turkey). *Environ. Earth Sci.* **2022**, *81*, 128. [CrossRef]
49. Susan, A.; Katya, C.; Natasha, C.W. Chemical Contamination of Drinking Water in Resource-Constrained Settings: Global Prevalence and Piloted Mitigation Strategies. *Annu. Rev. Environ. Resour.* **2020**, *45*, 195–226. [CrossRef]
50. Zhai, Y.; Zhao, X.; Teng, Y.; Li, X.; Zhang, J.J.; Wu, J.; Zuo, R. Groundwater nitrate pollution and human health risk assessment by using HHRA model in an agricultural area, NE China. *Ecotoxicol. Environ. Saf.* **2017**, *137*, 130–142. [CrossRef] [PubMed]
51. Guo, X.D. Analysis of the Relationship between Water Hardness and Human Life and Its Determination. *Chem. Manag.* **2021**, *07*, 48–49. [CrossRef]
52. Paulson, W.D. Anion Gap-Bicarbonate Relation in Diabetic Ketoacidosis. *Am. J. Med.* **1986**, *81*, 995–1000. [CrossRef]
53. Ahmad, M.I.; Chand, S.; Rafique, H. Predicting the spatial distribution of sulfate concentration in groundwater of Jampur-Pakistan using geostatistical methods. *Desalination Water Treat.* **2016**, *57*, 28195–28204. [CrossRef]
54. Zhang, Q.Q.; Wang, H.W.; Zhai, T.L.; Hua, M.J. Characteristics and source apportionment of groundwater nitrate contamination in the Hutuo River alluvial-pluvial fan regions. *Hydrogeol. Eng. Geol.* **2017**, *44*, 110–117. [CrossRef]
55. Jagadeshan, G.; Kalpana, L.; Elango, L. Hydrogeochemistry of High Fluoride Groundwater in Hard Rock Aquifer in a Part of Dharmapuri District, Tamil Nadu, India. *Geochem. Int.* **2015**, *53*, 554–564. [CrossRef]
56. Li, T. The Earth Abundance of Chemical Elements. *Geochemistry* **1976**, *3*, 167–174.
57. Heitland, P.; Köster, H.D. Human biomonitoring of 73 elements in blood, serum, erythrocytes and urine. *J. Trace Elem. Med. Biol.* **2021**, *64*, 126706. [CrossRef] [PubMed]
58. Wang, S.; Luo, K.; Ni, R.; Yuan, T.; Xing, G. Assessment of elemental background values and their relation with lifespan indicators: A comparative study of Jining in Shandong Province and Guanzhong area in Shaanxi Province, northern China. *Sci. Total Environ.* **2017**, *595*, 315–324. [CrossRef] [PubMed]

59. Wang, Y.W.; Yu, J.Y.; Bao, M.Z.; Bai, H.M.; Hao, J.Q.; Yu, Y.Q. Investigation and Study on Chronic Diseases and Risk Factors among Residents in Xilinhot City. *Chin. J. Conval. Med.* **2014**, *23*, 360–363. [CrossRef]
60. Zheng, H.M.; Zhang, F.; Shi, Q.M.; Tong, L.; Meng, J. Analysis on the hydrochemical characteristics and genesis of shallow groundwater in coal resource-based cities: A case study of Jining urban area. *Yangtze River* **2024**, *55*, 51–56. [CrossRef]
61. Li, Y.L. Groundwater Environmental Characteristics of Beiluo River Watershed (Guanzhong Plain Section) and Its Hydrochemical Evolution Mechanism. Master's Thesis, Chang'an University, Xi'an, China, 2022. [CrossRef]
62. Jia, C.; Wang, C.; Liu, M.; Yang, X.; Liu, W. Study on hydrogeochemical characteristics of groundwater in the alluvial plain of western Jinan. *Water Resour. Hydropower Eng.* **2022**, *53*, 49–60. [CrossRef]
63. Ning, H.; Liu, F.T.; Wang, G.M.; Zhang, J.; Zhang, Z.; Chen, S.M. Evaluation of groundwater resources and analysis of related geological environment problems in Inner Mongolia Inland River Basin. *N. China Geol.* **2024**, *47*, 62–72. [CrossRef]
64. Liu, Y.; Lu, N. Hot topics and frontier evolution on soil heavy metals risk assessment in China. *N. China Geol.* **2023**, *46*, 61–69. [CrossRef]
65. Mousazadeh, M.; Alizadeh, S.M.; Frontistis, Z.; Kabdaşlı, I.; Niaragh, E.K.; Qodah, Z.A.; Naghdali, Z.; Mahmoud, A.E.D.; Sandoval, M.A.; Butler, E.; et al. Electrocoagulation as a promising defluoridation technology from water: A review of state of the art of removal mechanisms and performance trends. *Water* **2021**, *13*, 656. [CrossRef]
66. Al-Shannag, M.; Al-Qodah, Z.; Nawasreh, M.; Al-Hamamreh, Z.; Bani-Melhem, K.; Alkasrawi, M. On the performance of Ballota undulata biomass for the removal of cadmium(II) ions from water. *Desalination Water Treat.* **2017**, *67*, 223–230. [CrossRef]
67. Sheng, Y.; Baars, O.; Guo, D.; Whitham, J.; Srivastava, S.; Dong, H. Mineral-bound trace metals as cofactors for anaerobic biological nitrogen fixation. *Environ. Sci. Technol.* **2023**, *57*, 7206–7216. [CrossRef]

Disclaimer/Publisher's Note: The statements, opinions and data contained in all publications are solely those of the individual author(s) and contributor(s) and not of MDPI and/or the editor(s). MDPI and/or the editor(s) disclaim responsibility for any injury to people or property resulting from any ideas, methods, instructions or products referred to in the content.

water

MDPI

Article

Study on the Evolution Mechanism of Temporal Variability of Chloride Ions in Typical Districts of Ordos City

Letian Si [1,2], Bing Zhang [1,2,*], Ruiqing Zhou [3], Ruirui Jiang [1,2], Wanggang Dong [1,2], Rong Ma [1,2] and Sihang Liu [4]

[1] Key Laboratory of Quaternary Chronology and Hydrological Environmental Evolution, China Geological Survey, Shijiazhuang 050061, China; siletian@foxmail.com (L.S.); rayrayj@163.com (R.J.); dongwanggang61@163.com (W.D.); marong@mail.cgs.gov.cn (R.M.)
[2] The Institute of Hydrogeology and Environmental Geology, Chinese Academy of Geological Sciences, Shijiazhuang 050061, China
[3] Ordos Environmental Protection Investment Co., Ltd., Ordos 017010, China; zhouruiqing1979@163.com
[4] Hebei Provincial Prospecting Institute of Hydrogeology and Engineering Geology, Shijiazhuang 050021, China; liusihang1994@foxmail.com
* Correspondence: ihegzhang1983@163.com

Abstract: The study of the temporal evolution of chloride ions in groundwater is important for identifying whether their sources are due to anthropogenic pollution or natural factors. Groundwater in the northern part of Dalat Banner, Ordos City, has high chloride ion content and exhibits strong temporal variability. To identify the source of chloride ions and reveal their evolution mechanisms, the fast Fourier transform (FFT) was used to determine the trend and cycle of chloride ion evolution, and the groundwater dynamics field combined with multivariate statistical analysis was used to identify the source of chloride ion pollution. Calculations show that the background value of chloride ions in groundwater in the study area is 195.17 mg/L, reaching a maximum of 459 mg/L under the influence of rainfall. The fluctuation of chloride ion concentration is mainly related to the total rainfall in the study area over 165 days, and a single rainfall of more than 15 mm affects the concentration of chloride ions in groundwater. The results of this study show that the background values of chloride ions are mainly influenced by the groundwater dynamical field, and the temporal volatility is mainly influenced by atmospheric rainfall.

Keywords: source identification; groundwater environment; area under agricultural irrigation; rainfall; multivariate statistical analysis

1. Introduction

Chloride ions are naturally abundant in the environmental background and play a crucial role in the recharge and discharge dynamics of groundwater. They are also highly sensitive to external disturbances, which can lead to frequent exceedances in groundwater concentrations. Consequently, chloride ions exhibit significant spatial and temporal variability within groundwater systems. Currently, numerical simulation [1,2], isotope [3–5] tracer [6,7], multivariate statistics [8–12], and other methods are utilized both domestically and internationally for the traceability analysis of groundwater pollutants, achieving good results. Among these methods, Cl ions, as conventional ions, have been analyzed for traceability since the 1960s. Scholars commonly use hydrological modeling, water chemistry methods, isotopes, artificial sweeteners, and other methods for tracing chloride ions [13–16]. Turson–Aishan conducted a study of chloride ion concentration in the Wei-Ku region and found that the coefficient of variation of salt content in all the layers of soil in the study area exceeded 100%, with strong spatial variability [17]; Fu Tengfei carried out a study on the spatial variability of chloride ion concentration along the south coast of Laizhou Bay, and the coefficient of variation of chloride ion concentration on the spatial scale under the effect of a large amount of groundwater pumping and rainfall drenching in the rainy season was

up to 146% [18]. Liu Fei conducted a study on chloride ion concentration in Minqin Oasis and found that the coefficient of variation of chloride ion concentration was 103.83% in arable land and 102% in grassland, both of which were highly variable, depending on the land use and cropping system [19]. There are a large number of studies on the variability of Cl ions on spatial scales, but fewer studies on the mechanism of their evolution on long time series scales, especially the response mode of chloride ions to climate change, are not clearly understood.

Building on this context, we focus on the Ordos Plateau's unique meteorological and hydrological characteristics to explore the source and evolution of chloride ions. Dalat Banner, located in the northern part of Ordos City, was selected as a representative study area. Utilizing long-term groundwater monitoring wells and integrating the local hydrogeological structure and hydrodynamic field, we aim to identify the sources of chloride ions in groundwater. Additionally, we seek to determine the rainfall intensity threshold that influences chloride concentrations. This study also examines the spatial and temporal characteristics of the atmospheric precipitation and chloride distribution based on a clear understanding of the local chloride background levels. By first establishing the background levels of chloride ions in the region, we can explore the spatiotemporal evolution of the atmospheric rainfall and chloride distribution. This allows us to identify the sources of chloride ions in the regional groundwater and to determine the thresholds of rainfall intensity that impact chloride concentrations. These findings will provide essential support for the control and management of the groundwater environment in the Ordos area.

2. Materials and Methods

2.1. Study Area

The Ordos Plateau is located in the core area of the northern agricultural and pastoral intertwined belt, with strong agricultural irrigation and due to a strong evaporation effect, which leads to the rapid evaporation of irrigation water, chloride, sodium, calcium, and other ions are very easy to be enriched in the shallow soil. Meanwhile, the Ordos Plateau is rainy and hot at the same time, and rainfall is mainly concentrated between June and September [20,21], with more extreme rainfall weather, and the frequency of heavy rainfall (24 h rainfall > 50 mm) is at least one time per year in the last 40 years, and it reached 14 times in 2016 [22]. Under intense rainfall, chloride ions reenter groundwater through vertical infiltration [23,24], resulting in a strong temporal variability of chloride ions in regional groundwater.

The study area is located in the northeastern part of Dalat Banner in the northern part of Ordos, covering an area of 178 km^2. The geomorphology consists of alluvial plains with east–west distribution in the form of bands. The micro-geomorphic units mostly belong to hilly gentle slopes and river valley terraces, and the land surface is covered by wind-deposited sands forming flat sand land. The general trend of the topography is high in the west and low in the east, with a gentle transition and a steplike decrease in the north–south direction. Groundwater in the region is mainly deposited in the diving aquifer of the Upper Pleistocene to Holocene ($Q_{3–4}$), and the lithology of the aquifer is dominated by fine and powdery sand, sand and clay, locally coarse sand, gravelly sand, and gravelly sand, with a loose structure and high porosity; the thickness of the aquifer in the alluvial floodplain area varies, with the southern part of the area slightly thinned, generally between 30 and 50 m, the central and northern parts are thicker, generally between 50 and 100 m, and the northern part of the Yellow River alluvial plain is generally between 10 and 40 m. In the northern part of the Yellow River alluvial plain, the thickness of the shallow groundwater aquifer is smaller, generally between 10 and 40 m, due to the deposit of silt loam and powdery clay strips in a cascading distribution and greater thickness.

The long-term groundwater monitoring well CQ01 is located in the northeastern part of the study area, which was completed in 2017 and has a depth of 50 m. The buried depth of the groundwater table ranges from 10 to 14 m, and the buried depth of the

submersible aquifer ranges from 12 to 50 m. The well is located in the northeastern part of the study area.

2.2. Sample Collection and Measurements

2.2.1. Groundwater Sample Collection and Testing

To investigate the spatial and temporal evolution characteristics of groundwater chloride ions in the region, a total of 18 sets of groundwater chemistry samples were collected from January 2021 to November 2023 at the long-term monitoring well CQ01 at a frequency of one set every 2 months. To determine the background value of chloride ion concentration, seven sets of samples were collected in the area in May 2023 to test 39 indicators such as Cl and Na, while 23 points of groundwater level measurements were carried out in the study area to characterize the groundwater flow field in the study area.

Before the sample collection work, sampling is conducted using a low-flow submersible pump to wash the sampling point; after the pumping volume is greater than 3–5 times the volume of the well, it is regarded as the completion of the well washing and formally starts the sampling work. Sampling was carried out in polyethylene plastic bottles with a capacity of 1 L, which were moistened and washed for collection.

After completing the sampling, the samples were restored in an insulated box with built-in frozen blue ice and sent to the laboratory to test the content of each ion within 48 h. The chemical reagents for the experiments were prepared at the Institute of Hydrogeology and Environmental Geology, Chinese Academy of Geological Sciences. And the chemical reagents required for soil sample testing are also included. The main testing instruments include plasma emission spectrometer (iCAP6300, Thermo Fisher, Los Angeles, CA, USA), gas chromatography-mass spectrometry (GC-MSQP2010plus, Yidian, Shanghai, China) and atomic absorption spectrophotometer (TAS-986, Yidian, Shanghai, China).

2.2.2. Soil Sample Collection and Testing

In 2023, soil samples were collected from within the air-packed zone (0–14 m) at the long-term monitoring well CQ01 and its upstream and downstream ZK06 and ZK07, respectively, at 2 m intervals, with seven sets of soil samples collected at each point, for a cumulative total of 21 sets of soil samples.

After completing the sample collection, the chloride ion content in the soil was determined according to the industry standard "Determination of Chloride Ion Content in Soil" (NY/T1378-2007) [25].

2.2.3. Rainfall Data

In this study, daily precipitation data were obtained from the Dongsheng meteorological station (Station ID: 53543, Station Name: DONGSHENG, CH). The station is at coordinates 109.983° E, 39.833° N, at an elevation of 1461 m above sea level.

2.3. Research Methods

2.3.1. Autocorrelation Function (ACF)—Periodic Analysis

The autocorrelation function is used to characterize the degree of correlation between a set of time-series samples and itself after a certain time lag. The autocorrelation function can eliminate the random error of the data itself in the calculation. The autocorrelation function can be calculated to obtain the periodic pattern of the groundwater chloride ion concentration within the study area over time. The autocorrelation coefficient calculation formula is shown in Equation (1):

$$ACF(k) = \frac{\sum_{t=k+1}^{n} (Yt - Y^{-})(Yt - k - Y^{-})}{\sum_{t=1}^{n} (Yt - Y^{-})^{2}} \quad (1)$$

where $ACF(k)$ is the autocorrelation coefficient with lag k; Yt is the observed value of the time series; Y is the mean value of the time series; n is the length of the time series; and k is the number of lag periods.

2.3.2. Fast Fourier Transform (FFT)—Periodicity Analysis

The Fast Fourier Transform converts time-series chloride concentration test data into the frequency domain. In turn, its periodicity is analyzed in the frequency domain. The fast Fourier transform is calculated as shown in Equation (2):

$$X(k) = \sum_{n=0}^{N-1} x(n) \cdot e^{-i2\pi \frac{kn}{N}} \quad (2)$$

where $X(k)$ is the complex-valued spectral component with frequency k; $x(n)$ is the observed value of the time series; N is the length of the time series; and k is the sampling frequency.

Since the sampling frequency is one sample every two months, the period of the chloride concentration $T = 1/k \times 2$ (months).

2.3.3. Multivariate Statistical Analysis

The groundwater in the study area flows from southwest to northeast, and CQ01 is located downstream of the study area (Figure 1). During the groundwater flow, the content of chloride ions gradually increases with the groundwater flow due to water–rock interaction. On top of that, under the effect of agricultural irrigation and strong evaporation, the content of Cl ions in the air pocket is also high. Under the effect of atmospheric rainfall, the Cl ions in the air envelope enter the submerged aquifer again, and due to the fluctuation of atmospheric rainfall, the Cl ions in the groundwater in the agricultural irrigation area have a strong spatial variability on the time scale.

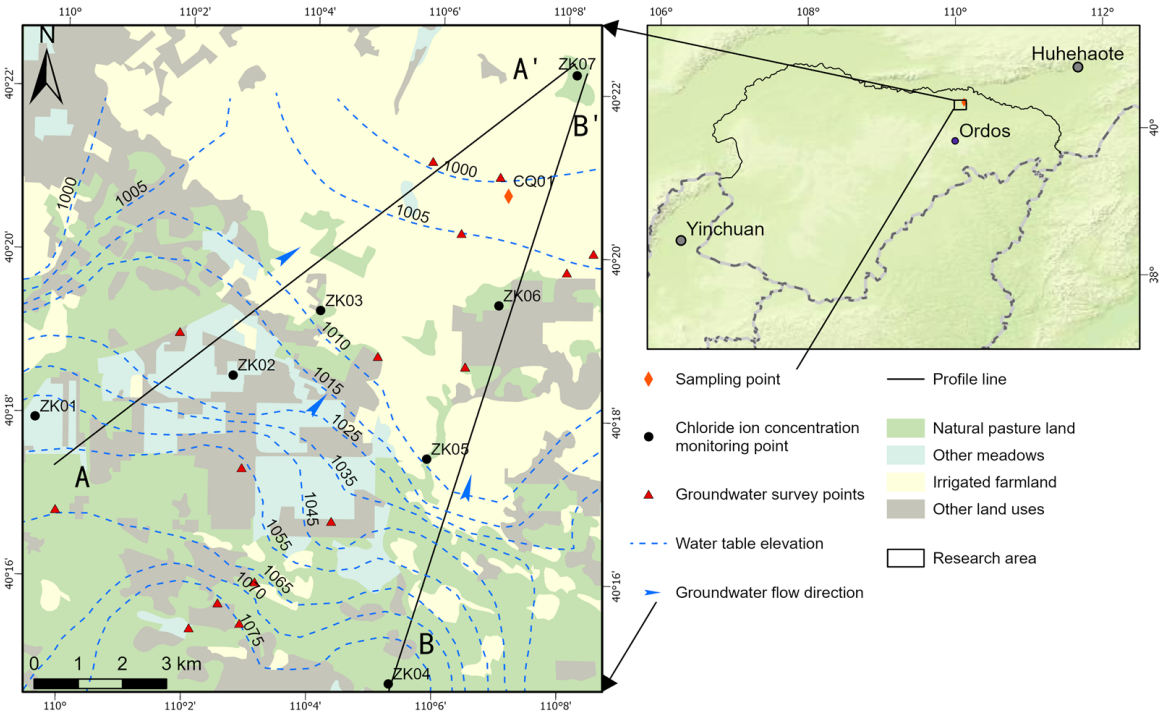

Figure 1. Location of the study area.

In the rainfall leaching of chloride ions in the air pocket, the larger the rainfall amount and the longer the time, the content of chloride ions entering the groundwater from the soil gradually increases, and with the decrease of the content of chloride ions in the soil, the

content of chloride ions entering the groundwater gradually decreases, and finally tends to be a constant amount, and its evolution of the time scale in the groundwater is close to a normal distribution.

The more fully chlorine ions are leached, the less chlorine ions are retained in the soil. Therefore, when the content of chloride ions in the soil is high, the leaching effect of rainfall on chloride ions is better. Along with the gradual increase of rainfall, the leaching effect of rainfall on chloride ions gradually decreases and finally tends to a constant amount.

In order to explore the response mode of groundwater chloride ions to atmospheric rainfall in the study area, daily rainfall data from meteorological stations in the region were collected since January 2020, and a Gaussian function was applied to fit the changes in rainfall and chloride ions concentration in the monitoring wells of CQ01; the regression Equation (3) is:

$$y = a \times \exp(-(x-b)^2/c^2) \quad (3)$$

where Chloride ion concentration is y, rainfall is x; a, b and c are constants obtained from the fitting calculation; a represents the theoretical maximum value of chloride ion concentration, i.e., the concentration of chloride ions in groundwater after all chloride ions are leached out of the soil, and b represents the amount of rainfall that achieves the maximum effect of chlorine ion leaching. When the value of x is 0, the calculated value of y is the background value of the chloride concentration in the study area when there is no interference from rainfall and other anthropogenic factors.

3. Results and Discussion

3.1. Characteristics of Rainfall and Cl Concentration Evolution with Time in the Study Area

Figure 2 illustrates the variation in chloride ion concentrations in groundwater at the sampling sites from 2021 to 2023. The average chloride ion concentrations in the monitoring wells from 2021 to 2023 were 261 mg/L, 272.83 mg/L, and 300.41 mg/L, respectively, showing an increasing trend each year. Figure 3 illustrates the variation in rainfall in the study area from 2021 to 2023. The total rainfall from 2021 to 2023 was 296.93 mm, 542.29 mm, and 425.45 mm, respectively, with the total rainfall in 2022 being higher than in 2021 and 2023.

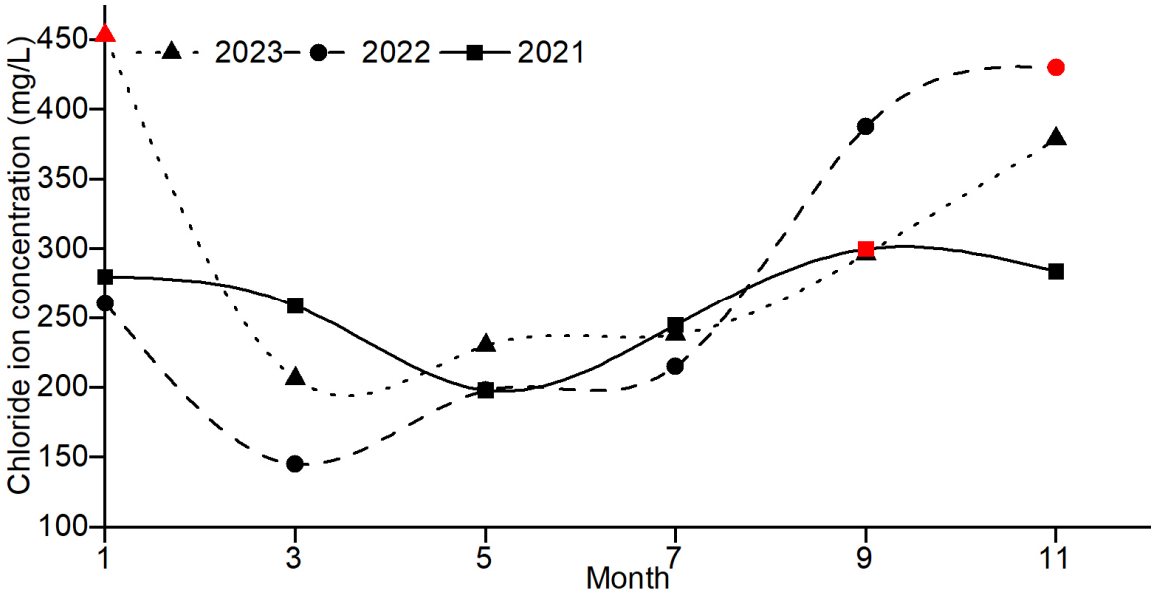

Figure 2. Changes in chloride ion concentrations by year. Note: The red symbols are the maximum chloride ion concentrations during the year.

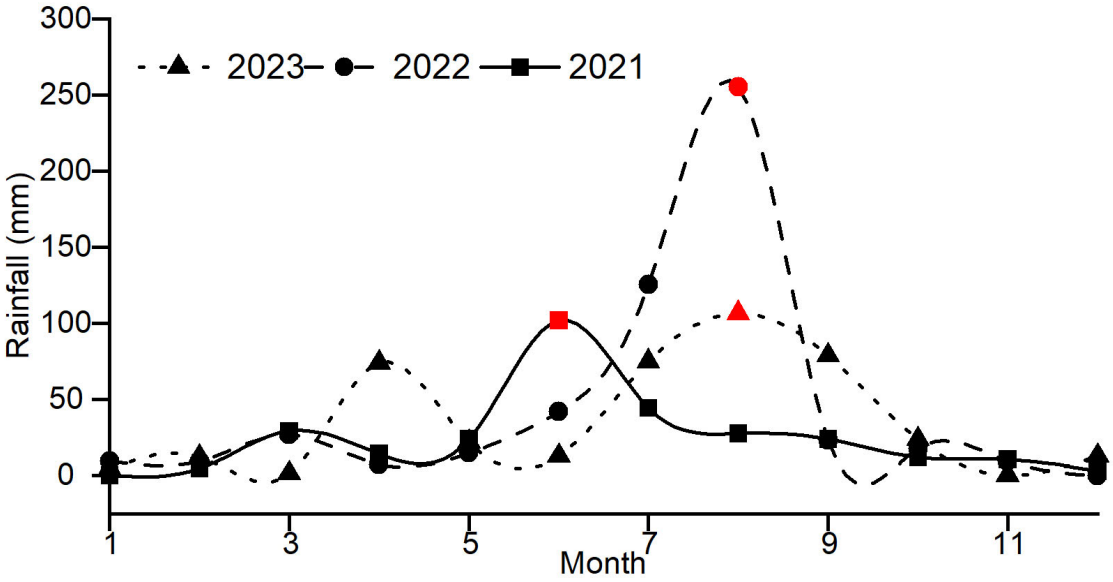

Figure 3. Monthly rainfall changes from 2021 to 2023. Note: The red symbols are the maximum rainfall during the year.

3.2. Background Values of Cl Ions in the Study Area

As shown in Figure 1, the evolution of groundwater chloride ion concentrations at the seven monitoring points along the groundwater flow path is shown in the table below:

Of the eight sampling points mentioned above, all were located within the grassy area except for CQ01, where chloride concentrations were calculated by fitting the chloride concentrations at each point of the AA′ and BB′ profiles to the distance from the first sampling point, respectively.

Table 1 shows that the Cl^- ion concentration has a significant tendency to increase with groundwater flow. At the same time, the increase of Cl^- ion concentration is smaller in the region with faster groundwater flow and larger hydraulic gradient. The increase of Cl^- ion concentration is larger in the region with a smaller hydraulic gradient and slower groundwater flow.

Table 1. Concentration of chloride ions at monitoring points.

AA′ Chloride Ion Concentration Profile				BB′ Chloride Ion Concentration Profile			
Point Serial No.	**Distance (km)**	**Chloride (mg/L)**	**Hydraulic Gradient**	**Point Serial No.**	**Distance (km)**	**Chloride (mg/L)**	**Hydraulic Gradient**
ZK01	0	19.4	-	ZK04	0	58.3	-
ZK02	4.314	21.0	0.0063	ZK05	5.326	68.1	0.0130
ZK03	6.889	80.6	0.0050	ZK06	9.011	109.0	0.0008
CQ01	12.045	**158.78**	0.0012	CQ01	11.744	**158.95**	0.0015
ZK07	14.831	226	0.0022	ZK07	14.534	226	0.0022

Note: The chloride ion concentration of CQ01 was calculated based on the regression formula.

The scatter plot of the distance–chloride ion concentration at each sampling point was graphed according to Table 1, and a fitted line was plotted. The scatter plot of the distance–chloride ion concentration of profile AA′ is shown in Figure 4; the fitting equation of the change of chloride ion concentration with distance is $y = 0.8598x^2 + 1.5849x + 14.951$, which has a coefficient of determination $R^2 = 0.9846$, indicating a good fit. The background value of the corresponding chloride ion concentration at the long-term monitoring point is 158.78 mg/L.

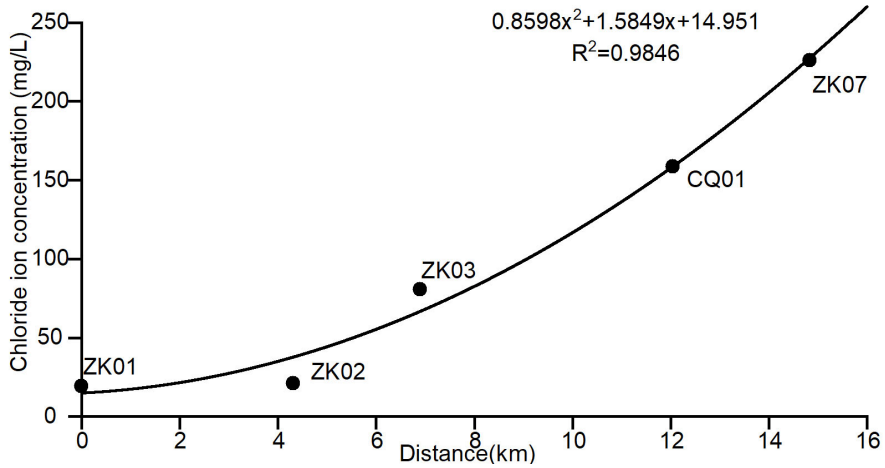

Figure 4. Scatter plot of the distance–chloride concentration for profile AA′.

The scatter plot of the distance–chloride ion concentration for profile BB′ is shown in Figure 5; the fitting equation for the variation of chloride ion concentration with distance is $y = 1.062x^2 - 3.9114x + 58.404$, which has a coefficient of determination of $R^2 = 0.998$, indicating a good fit, and the background value of the corresponding chloride ion concentration at the long-term monitoring point is 158.95 mg/L.

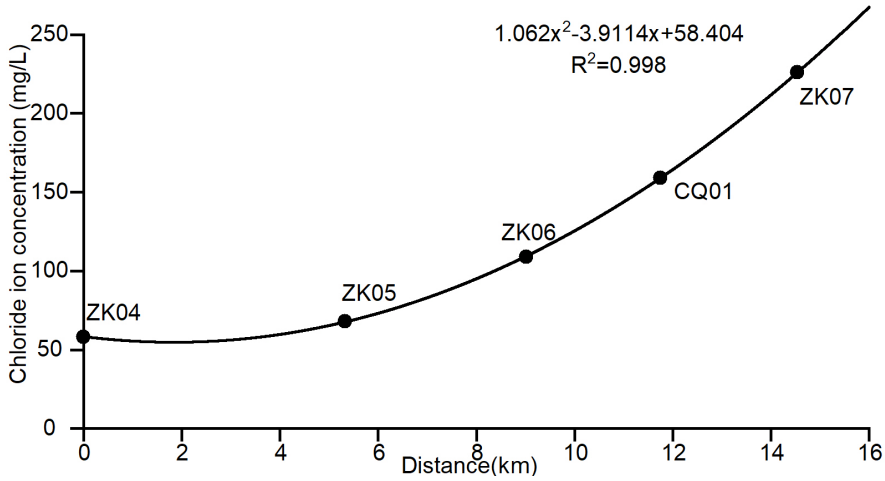

Figure 5. Scatter plot of the distance–chloride concentration profile for BB′.

Combining the distance–chloride ion concentration fitting of the monitoring points in profile AA′ and profile BB′, and taking the average value of the calculation results of the two groundwater flow directions, it can be preliminarily concluded that under the influence of water–rock interaction, the natural background value of the chloride ion concentration in groundwater of CQ01 is approximately 158.865 mg/L.

3.3. Chloride Ion Content in Soil

Using the chloride ion concentration profile, it was calculated that the chloride ion concentration at point CQ01 should be around 158.865 when it is not disturbed by human factors. However, the average values of chloride ion concentration at point CQ01 measured from 2021 to 2023 were 261 mg/L, 272.83 mg/L, and 300.41 mg/L, respectively. Therefore, there are other sources of chloride ions at CQ01.

Soil samples were taken from the sampling points CQ01, ZK06, and ZK07 to test the soluble chlorine content in the soil layers at various burial depths. The results are shown in Table 2. It can be observed that the soluble chlorine content in the soil at sampling point CQ01, which is located in an irrigated farmland area, is higher than that at ZK06 and ZK07,

which are located in a grassland area. This indicates that chloride ions in the groundwater are significantly retained in the soil due to irrigation.

Table 2. Soluble chlorine content in soil layers.

Profundity (m) Dot Mark	Soluble Chlorine (mg/kg) ZK6	CQ01	ZK7
0–2 m	131	160	86
2–4 m	57	120	120
4–6 m	91	112	111
6–8 m	120	184	85
8–10 m	104	249	88
10–12 m	83	168	68
12–14 m	62	176	54

Figure 6 shows the variation of chloride ion concentration with the depth of the vadose zone. It can be seen that the chlorine content in the soil layers of the study area is higher in the surface soil from 0 to 2 m, decreases with increasing depth, rises again at about 6 m, reaches a maximum value at about 10 m, and stabilizes at 12 m and downwards. This variation is in accordance with the conclusions reached in this study. The study area is located in an irrigated farmland area, and when groundwater is utilized for irrigation, water is lost, and salts accumulate at the surface. As a result, soluble chlorine is slightly higher in the surface soil. The process of rainfall leaching soluble chlorine to the subsurface could not leach all the chlorine ions into the subsurface. Therefore, the soluble chlorine content gradually decreases with increasing depth until it reaches a depth of 4~6 m. Along with many times of groundwater irrigation containing chloride ions and rainfall leaching without chloride ions, 71% of the chloride ions in the soil would be transported downward with the leaching solution [23], so the depth of the groundwater table at the sampling site fluctuated at about 10~14 m, and a large number of chloride ions were leached to the shallowest point of the fluctuation of the groundwater table and gradually leached into the groundwater. Therefore, the concentration of chloride ions in the soil reaches the maximum value at a depth of 8~10 m and tends to stabilize at a deeper depth.

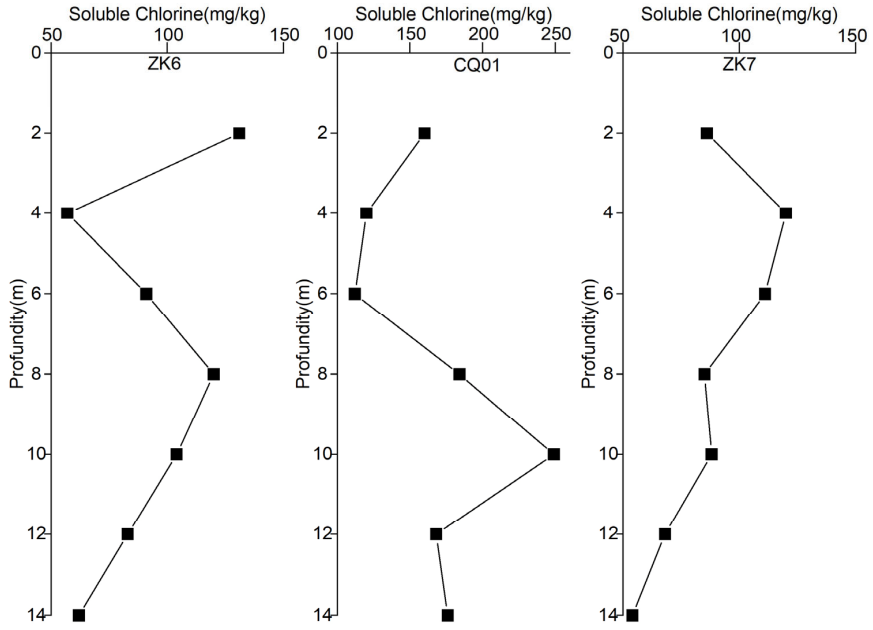

Figure 6. Distribution of soluble chlorine content by sampling point.

The difference in soluble chlorine content in the soil between the CQ01 sampling site and the ZK06 and ZK07 sampling sites indicates that irrigation has had a more pronounced effect on the chlorine ion content in the soil. Due to rainfall and other factors, this effect is applied to the groundwater so that the concentration of chloride ions in the groundwater is increased. Therefore, the correlation between groundwater chloride concentration and rainfall at CQ01 was investigated.

3.4. Analysis of the Correlation between Cl Ions and Rainfall

3.4.1. Cyclic Analysis of Chloride Ion Concentration Variations

The autocorrelation function (ACF) was used to analyze the changes in groundwater chloride ion concentration from January 2021 to November 2023, and the results of the analysis are shown in Figure 7, which shows that the autocorrelation coefficient is -0.5643 when the lag value is 3, and the autocorrelation coefficient is located outside the confidence interval; the results are significant. The results show that the concentration of chloride ions in groundwater in the study area has significant autocorrelation with a lag period of 6 months (one group of samples is collected every 2 months, the lag period is $3 \times 2 = 6$). That is to say, the concentration of groundwater chloride ions in the study area shows a regular change trend with a cycle of 6 months. This trend of changes is opposite in every two adjacent cycles.

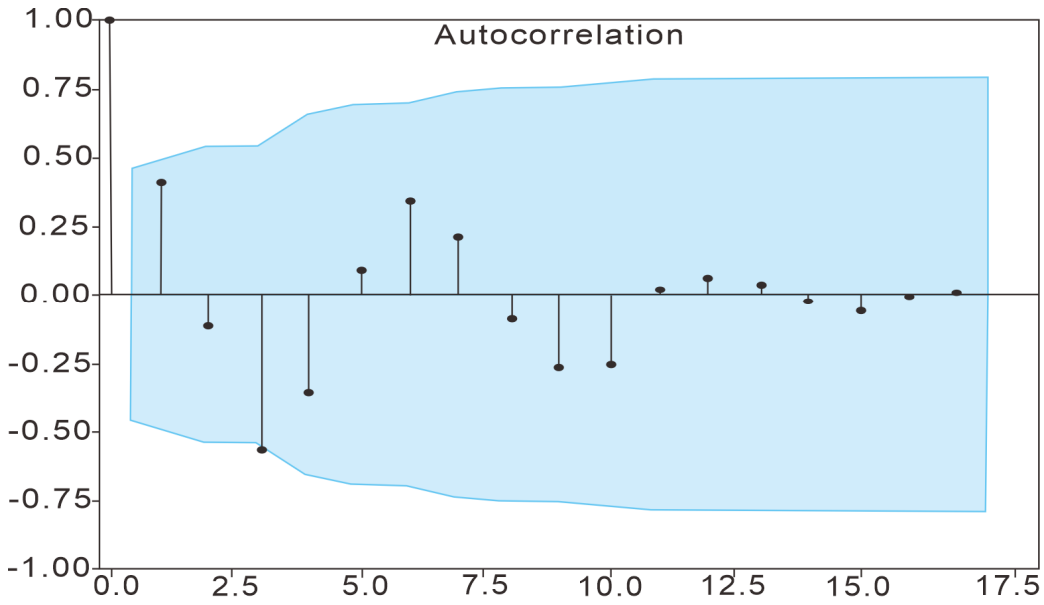

Figure 7. ACF analysis results. Note: The blue region represents the confidence interval with a confidence level of 95%.

The trend of groundwater chloride ion concentration in the study area was further analyzed using a Fast Fourier Transform (FFT); as shown in Figure 8, when the spike frequency is 0, the spike amplitude is 5000, which is much higher than the amplitude of other spike frequencies. Figure 8 shows that the baseline level (background value) accounts for the major part of the overall concentration of chloride ions in groundwater in the study area; the spike amplitude is 965.60095 when the spike frequency is 0.08333, which is the maximum value except for the spike frequency of 0. Since the sampling frequency is one sample every two months, the variation period of chloride ion concentration in the study area is $1/0.08333 \times 2 \approx 24$ months.

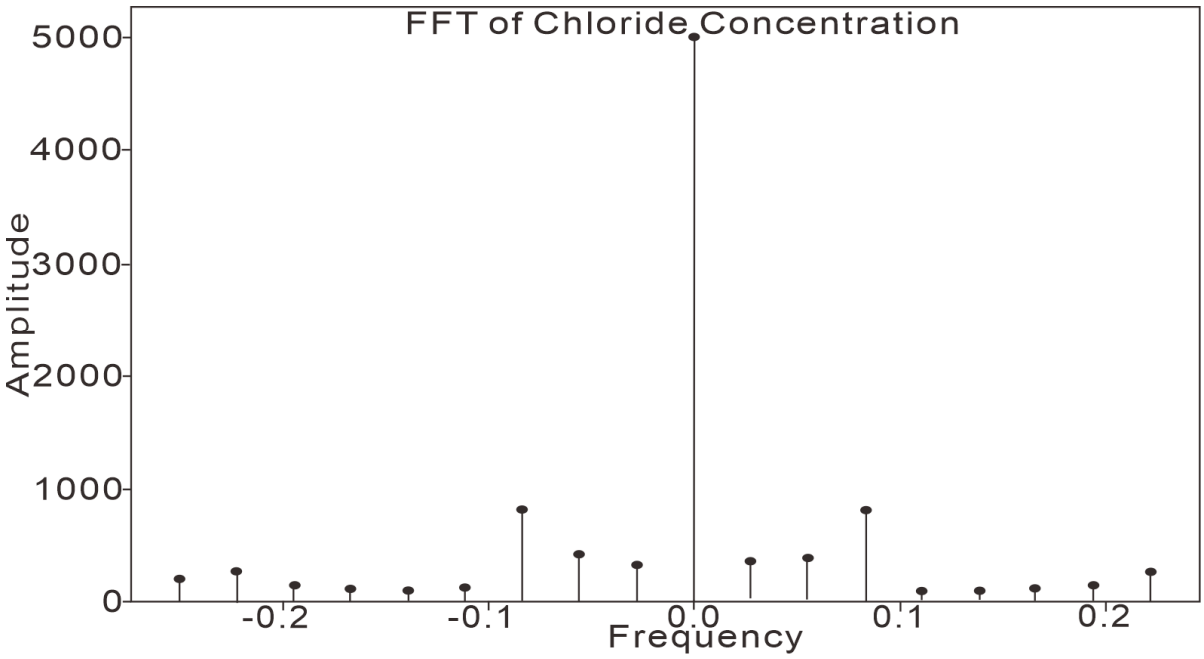

Figure 8. FFT analysis results.

As can be seen from the FFT calculations, the groundwater chloride ion concentration in the study area is mainly dominated by a baseline level that remains stable, indicating that the groundwater chloride ion concentration in the study area is mainly determined by water–rock interactions [26,27], etc., and is a characterization of the background value. The period of the changing part is 24 months, and considering the significantly larger rainfall in 2022, it is presumed that the changing part of the groundwater chloride ion concentration is mainly influenced by rainfall.

From the results of the ACF calculation, it can be seen that the trend of groundwater chloride ion concentration in the study area is opposite to that of January to June and July to December every year, and the groundwater chloride ion concentration shows a decreasing trend from January to June and an increasing trend from July to December. The rainy season in Erdos City is mainly from June to September, and after the beginning of the rainy season, the trend of groundwater chloride ion concentration changed significantly from decreasing to increasing and maintained the increasing trend after the end of the rainy season until January of the next year. The correlation between rainfall and chloride ion concentration was further analyzed.

3.4.2. Correlation Analysis between Chloride Ion Concentration and Rainfall Amount

Figure 3 shows that the rainfall is slightly higher from March to April every year. Meanwhile, from June to September, rainfall averages 71.1% of the year. Among them, 2022 was relatively rainy and had the highest rainfall for the year. This variation coincides with the variation of chloride ion concentration to some extent, and the effect of rainfall on chloride ion concentration continues for some time.

As shown in Figure 9, the trends of chloride ion concentration and rainfall over time are the same, but there is a certain lag between the chloride ion concentration and rainfall changes on the time scale, which indicates that the effect of rainfall on chloride ions is not occurring in real time, so the relationship between the chloride ion concentration and its relationship with the sum of the daily rainfall in the period prior to the time point of the test was further investigated.

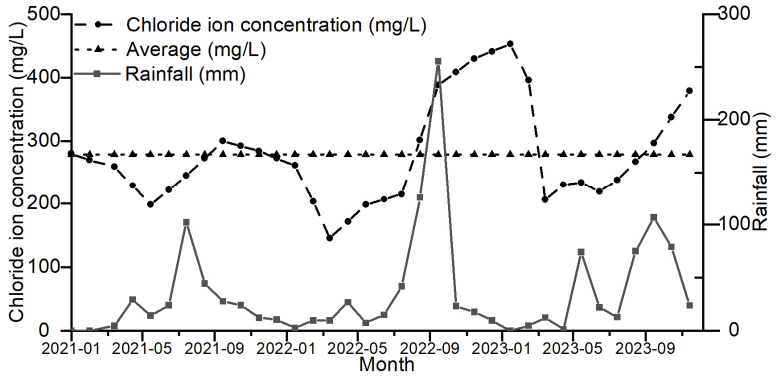

Figure 9. Temporal Trends in Chloride Ion Concentration and Rainfall.

3.4.3. Result of the Correlation Analysis

1. Rainfall period analysis

The cumulative rainfall was calculated from 10 to 200 days before the sampling date, and the trends of different rainfall periods and chloride ion concentration were observed, as shown in Figure 10, along with the increase in the cumulative time of rainfall, the trends of rainfall and chloride ion concentration were gradually the same. This indicates that rainfall over a period of time is an important factor influencing the concentration of chloride ions in the groundwater in the study area.

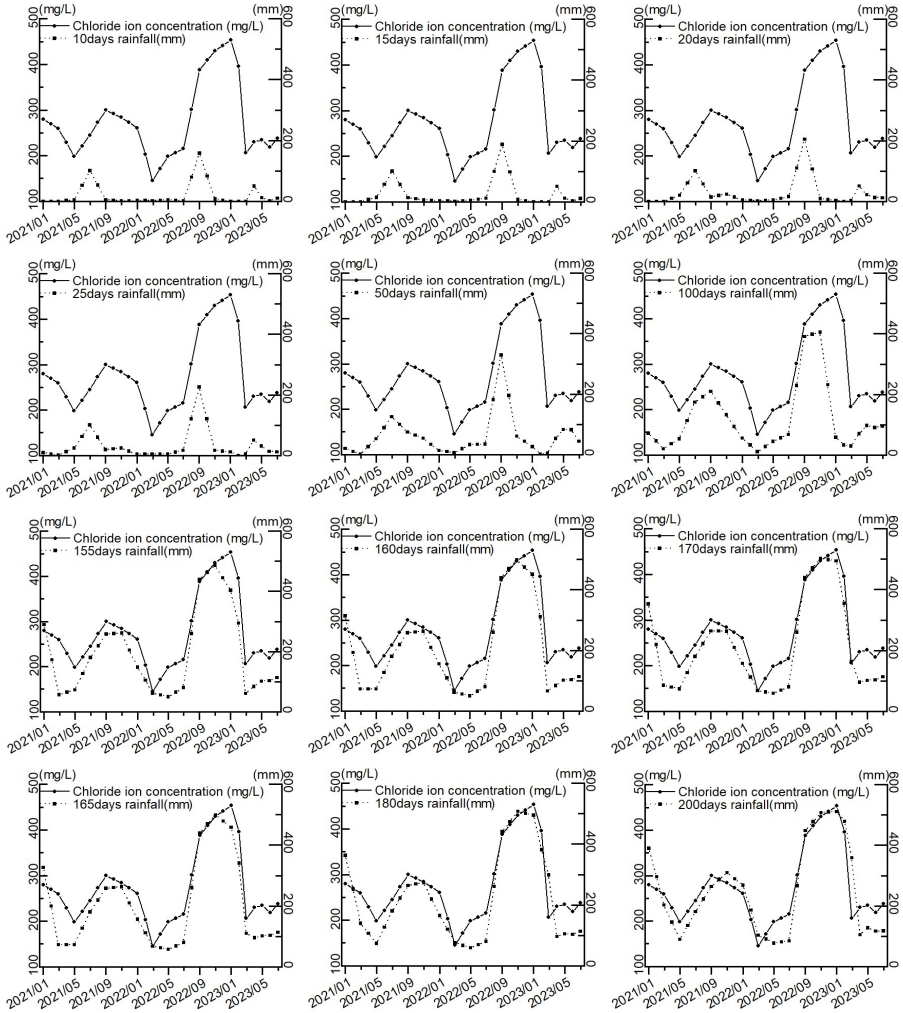

Figure 10. Trends in rainfall and chloride ion concentration at different times.

In order to find the cumulative rainfall period with the highest correlation to the chloride ion concentration, the Pearson correlation coefficient method was used to find the correlation coefficients between the cumulative rainfall and the chloride ion concentration in groundwater for the first 10, 15, 20, 25, 30, 40, 50, 60, 70, 80, 90, 100, 110, 120, 130, 140, 150, 155, 160, 165, 170, 180, 190, and 200 days, as shown in Figure 11. The correlation coefficients between the cumulative rainfall and groundwater chloride concentration for the 180, 190, and 200 days and the correlation coefficients with chloride concentration for each time are shown in Figure 11.

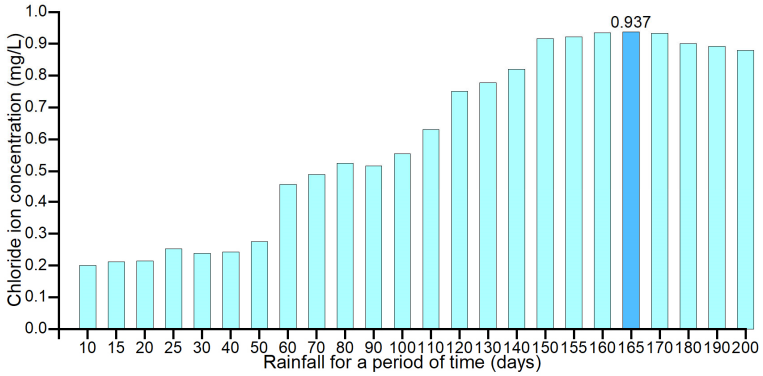

Figure 11. Histogram of the correlation coefficients for each time of rainfall statistics.

From the correlation coefficients between the rainfall and chloride ion concentration in groundwater for each period with sliding properties, it can be seen that the rainfall for 165 days in the study area is an important factor in determining the concentration of chloride ions in groundwater. It shows that the fluctuation of chloride ions in groundwater in the study area is mainly caused by rainfall leaching chloride ions from surface soil and carrying them to groundwater.

2. Analysis of the rainfall intensity

The results of this study were further analyzed by screening the number of days with single-day rainfall greater than 10 mm, 20 mm, 30 mm, 40 mm, and 50 mm within 165 days, respectively, and the number of days with single-day rainfall for each day is shown in Figure 12 and Table 3, which show that rainfall with higher intensity occurred during the 165 days prior to the collection of the samples with a higher concentration of chloride ions. At the sampling time nodes with chloride ion concentrations of 388 mg/L, 430 mg/L, 453 mg/L, and 396 mg/L, there was a single day of rainfall greater than 50 mm during the 165 days prior to sampling. This indicates a certain correlation between rainfall intensity and the concentration of chloride ions in the groundwater during the 165 days and that there is a rainfall threshold value above which rainfall on a single day will have a more obvious effect on the concentration of chloride ions in the groundwater. A single day's rainfall above this threshold has a more pronounced effect on groundwater chloride concentrations.

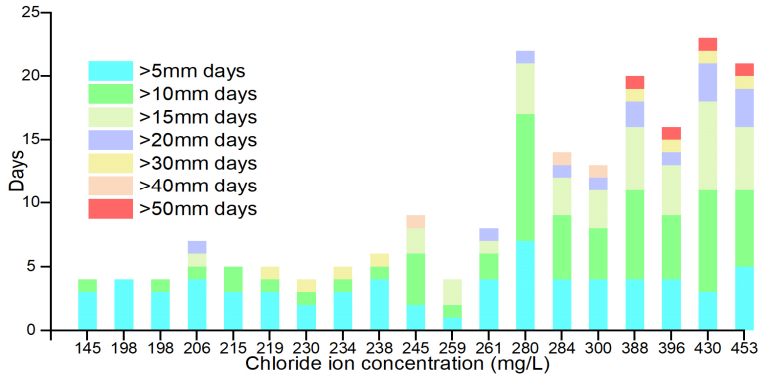

Figure 12. Histogram of the number of days of occurrence of each rainfall intensity.

Table 3. Number of days for each rainfall intensity.

Chloride Ion Concentration (mg/L)	>5 mm Days	>10 mm Days	>15 mm Days	>20 mm Days	>30 mm Days	>40 mm Days	>50 mm Days
280	22	15	5	1	0	0	0
259	4	3	2	0	0	0	0
198	4	1	0	0	0	0	0
245	9	7	3	1	1	1	0
300	13	9	5	2	1	1	0
284	14	10	5	2	1	1	0
261	8	4	2	1	0	0	0
145	4	1	0	0	0	0	0
198	4	0	0	0	0	0	0
215	5	2	0	0	0	0	0
388	20	16	9	4	2	1	1
430	23	20	12	5	2	1	1
453	21	16	10	5	2	1	1
396	16	12	7	3	2	1	1
206	7	3	2	1	0	0	0
230	4	2	1	1	1	0	0
234	5	2	1	1	1	0	0
219	5	2	1	1	1	0	0
238	6	2	1	1	1	0	0

In order to clarify the threshold value of the impact of a single rainfall on the chloride ion concentration in groundwater, the sum of rainfall intensities greater than 10 mm, 20 mm, 30 mm, 40 mm, and 50 mm in a single day within 165 days was calculated, as shown in Table 4. The trend of each rainfall intensity and chloride ion concentration is shown in Figure 4.

Table 4. Cumulative rainfall by rainfall intensity.

Chloride Ion Concentration (mg/L)	All Days Rainfall	>5 mm Rainfall	>10 mm Rainfall	>15 mm Rainfall	>20 mm Rainfall	>30 mm Rainfall	>40 mm Rainfall	>50 mm Rainfall
280	326.31	271.78	215.68	90.77	21.67	0	0	0
259	72.66	53.74	46.2	33.02	0	0	0	0
198	73.1	33.3	10.76	0	0	0	0	0
245	180.5	141.07	126.07	78.06	41.53	41.53	41.53	0
300	258.52	197.03	170.29	122.28	67.75	41.53	41.53	0
284	263.36	205.15	183.04	122.28	67.75	41.53	41.53	0
261	156.24	89.97	67.73	44.22	26.22	0	0	0
145	67.6	28.39	11.68	0	0	0	0	0
198	57.31	28.75	0	0	0	0	0	0
215	80.18	42.97	20.56	0	0	0	0	0
388	440.14	372.85	343.98	256.88	171.38	119.99	81.28	81.28
430	498.67	433.88	413.3	313.69	194.23	119.99	81.28	81.28
453	458.46	394.95	358.32	279.27	194.23	119.99	81.28	81.28
396	341.39	308.78	278.61	210.08	142.84	119.99	81.28	81.28
206	110.04	84.35	54.18	41.67	22.85	0	0	0
230	96	64.92	48.87	36.89	36.89	36.89	0	0
234	101.55	77.2	48.87	36.89	36.89	36.89	0	0
219	103	77.2	48.87	36.89	36.89	36.89	0	0
238	113.8	84.93	48.87	36.89	36.89	36.89	0	0

Figure 13 shows that with the increase in rainfall intensity threshold, the rainfall and chloride concentration curves tend to approach and then deviate from each other. Pearson's correlation coefficients between the rainfall and chloride ion concentration for each rainfall intensity were further investigated, and the correlation coefficients are shown in Figure 14 and Table 5, which show that the correlation coefficients between rainfall and chloride ion showed an increasing trend and then decreasing along with the increase of the rainfall in a single day. This indicates that when screening the single-day rainfall, the single-day rainfall that has no or very little correlation with the chloride ion concentration is first removed. The single-day rainfall with a high correlation with chloride ion concentration is removed later. Therefore, the single-day rainfall with the largest correlation coefficient with the

chloride ion concentration is the threshold of single-day rainfall that affects the chloride ion concentration, which is 15 mm. This means that a single rainfall of more than 15 mm can effectively leach chloride ions from the surface soil and carry them to the groundwater.

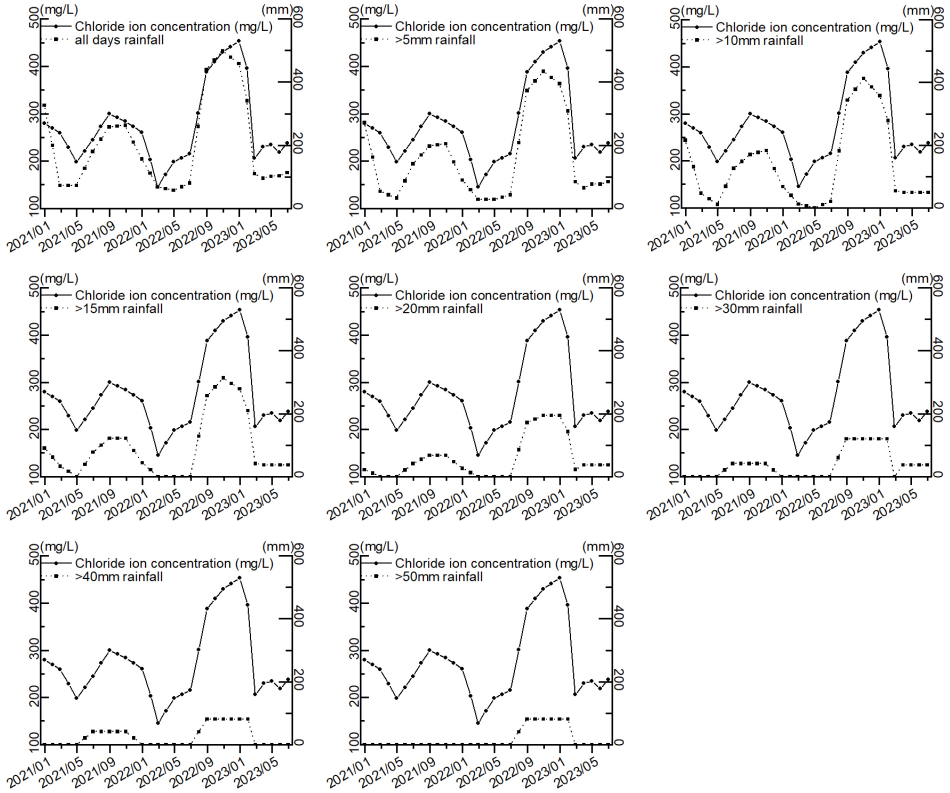

Figure 13. Trends in rainfall and chloride ion concentration at various rainfall intensities.

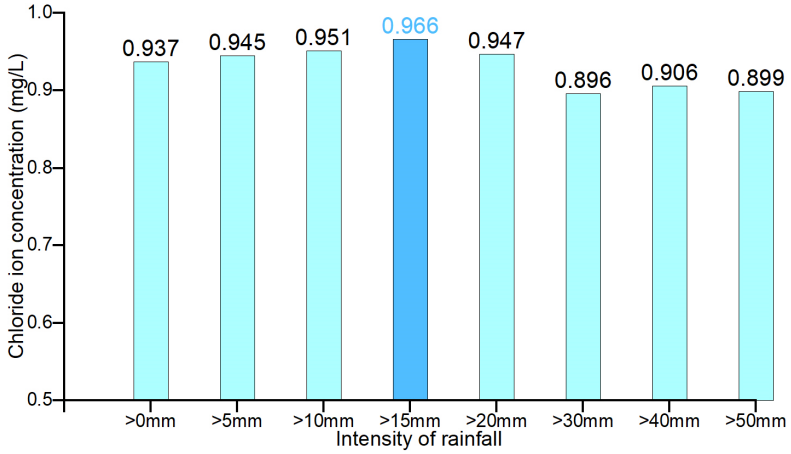

Figure 14. Correlation coefficients between rainfall and chloride concentration at various rainfall intensities.

Table 5. Correlation coefficients between rainfall intensity and chloride ion concentration for each rainfall intensity.

Rainfall Intensity	>0 mm	>5 mm	>10 mm	>15 mm	>20 mm	>30 mm	>40 mm	>50 mm
correlation coefficient	0.937 **	0.945 **	0.951 **	0.966 **	0.947 **	0.896 **	0.906 **	0.899 **
two-tailed test	0.000	0.000	0.000	0.000	0.000	0.000	0.000	0.000

Note: ** means Significant at the 0.01 level (two-tailed).

3.4.4. Result of the Regression Analysis

As shown in Figure 15, The Gaussian regression equation between groundwater chloride concentration and rainfall is $y = 459.1 \times \exp(-(x - 400.2)^2/432.7^2)$.

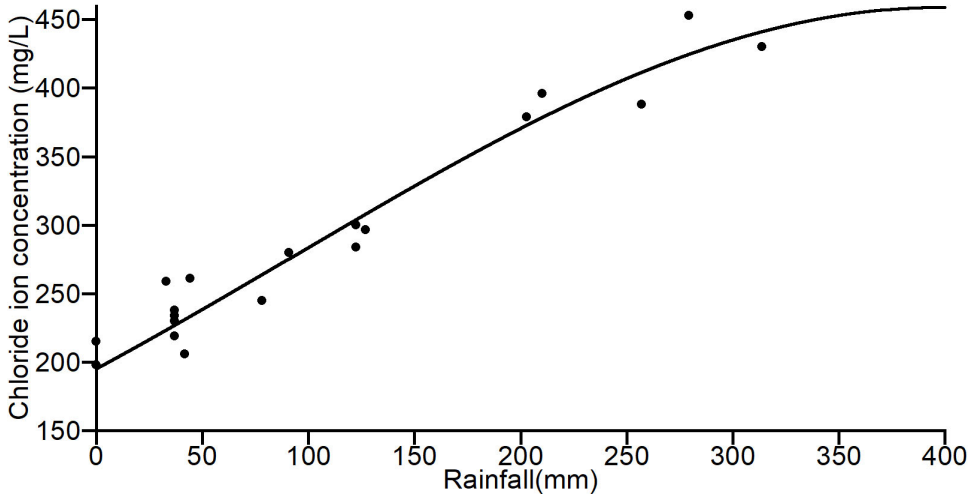

Figure 15. Chloride concentration—regression plot of single day > 15 mm rainfall in the first 165 days.

The sum of single rainfall events greater than 15 mm in the 165 days with the highest correlation with groundwater chloride concentration was used as the independent variable x, and groundwater chloride concentration was used as y.

The model efficiency coefficient of this regression equation, $R^2 = 0.936$, was a good fit, and it can be seen from the regression equation that the higher the cumulative rainfall, the less chlorine ions are leached out per unit of rainfall. It is in line with the natural law. Meanwhile, when the rainfall was 400.2 mm, the chlorine ions retained in the soil were maximally leached into the groundwater; at this time, the groundwater chloride ion concentration was 459.1 mg/L. According to the Gaussian function to find the background value of chloride ion concentration in the study area, when the rainfall (x) takes the value of 0, the background value of chloride ion in the groundwater of the monitoring wells is 195.165 mg/L, which is higher than that of the background value (158.865 mg/L) carved out according to the local profile of the concentration of chloride ions.

The effect of water–rock interaction on chloride ion concentration in the study area was calculated as 158.865 mg/L using chloride ion concentration distance, which is different from the result obtained using chloride ion concentration–rainfall in the study area (195.165 mg/L), and this difference is attributed to the fact that the sampling site of the former is a pasture land that is not affected by anthropogenic activities while the latter is located in the irrigated farmland. As shown in Figure 6 and Table 2, under the influence of perennial irrigation, the soil was endowed with more chloride ions than the pastureland. Under irrigation and rainfall, more chloride ions enter the groundwater. This leads to some elevation of the background value of groundwater chloride ion concentration.

3.5. Error Verification of the Regression Equations

To further verify the accuracy of the test results, groundwater chemistry samples were collected from the sampling sites in September 2023 and November 2023 for the determination of chloride ion concentrations.

The results of the regression equation show that in September 2023, the concentration of chloride ion at the sampling point was 296.5 mg/L, the amount of rainfall greater than 15 mm on a single day in the previous 165 days was 126.81 mm, and the concentration of chloride ion calculated according to the regression equation was 307.99 mg/L. The error between the predicted value and the measured value was 3.9%, and the two were of the same level of water quality, which are both class IV; in 2023, the concentration of chloride

ion at the sampling point was 379 mg/L in November, and the amount of rainfall greater than 15 mm on a single day in the previous 165 days was 202.95 mm. In November 2023, the chloride ion concentration at the sampling point was 379 mg/L, the rainfall amount greater than 15 mm on a single day in the previous 165 days was 202.95 mm, and the chloride ion concentration calculated according to the regression equation was 372.95 mg/L, and the error between the predicted value and the measured value was 1.6%, and the two were of the same water quality, both of which are classified as class V. The validation results showed that the Gaussian equation had a significant effect on the water quality of the sampling point. The validation results show that the Gaussian equation can accurately depict the relationship between the chloride ion concentration in the groundwater and rainfall in the study area (the sum of single-day rainfall greater than 15 mm in 165 days). For the chloride ion concentration > 380 mg/L, there were cases of rainfall higher than 50 mm in a single day in 165 days before sampling.

Sun Lei et al. found that the leaching of chloride ions from the soil reached the maximum leaching volume when the rainfall reached 440 mm [23], which is in line with the results obtained in this study (400.2 mm). Dustin W. Kincaid et al. found that contrary to the past belief that chloride ions are only stored for a short period in the soil, the soil can be a temporary reservoir of chloride ions, which can be stored in the soil over a longer time. Storage of chloride ions in a soil column 15 cm high, the leaching of chloride ions from the soil was only more effective when rainfall exceeded 150 mm and took 2 weeks, and exogenous chloride ions from the use of local snow removers in the winter still impacted the local groundwater in the summer of the following year [24], suggesting that it also took two seasons for the region to leach chloride ions into the groundwater gradually. This is consistent with the 165-day impact time obtained in this study.

The test of the regression equation and the corroboration of the results with the findings of others show that the results obtained in this study are accurate and reliable.

This paper focuses on the problem of chloride ions exceeding the standard in the typical area of Dalat Banner, Ordos City, and the main sources of chloride ions in the groundwater of the study area were determined by correlation analysis and regression analysis between the concentration of chloride ion in the groundwater of the study area and the local rainfall. The high concentration of chloride ions in groundwater in the study area is not related to human activities. This is mainly due to the high background value of chloride ion concentration caused by the geological background and the migration of chloride ions from rainfall–leaching surface soil into groundwater. Since the study area is an irrigated farmland, it is assumed that the chloride ions in the surface soil are mainly due to the loss of water due to absorption by vegetation and evaporation after pumping groundwater for irrigation and the retention of salts in the surface soil.

The study area is primarily irrigated farmland, where groundwater is extracted from aquifers and transferred to surface fields for irrigation. The region experiences high evaporation rates, which contribute to water loss and salt accumulation. This study does not consider variations in evaporation rates. However, evaporation plays a significant role in salt accumulation. This research uniquely considers the impact of rainfall when analyzing variations in chloride ion concentrations in groundwater. Yet, using only rainfall as a factor to fit chloride concentrations may not fully account for environmental changes. So, this study primarily focuses on cases where chloride concentration fluctuations are significant under stable environmental conditions over time.

4. Conclusions

Based on the measured water chemistry ion content, groundwater table burial depth, and precipitation data in the field, the background values of chloride ions in the study area were identified using FFT and multivariate statistical analyses. This study revealed the mechanisms of the cyclical changes of chloride ions and explored their contamination sources. The specific conclusions are listed below.

The chloride content in the monitoring well area is not only high but also exhibits significant temporal variability. This phenomenon can be attributed to two main reasons. First, the monitoring well is located in a groundwater discharge zone, where the interaction between groundwater and rock leads to elevated levels of chlorides as the water flows through. Consequently, the background chloride concentration in the groundwater surrounding the monitoring well is relatively high. Second, this well is situated in an irrigated agricultural area, where atmospheric precipitation causes vertical migration of chloride ions from the surface soil. Given that precipitation in Ordos City is unevenly distributed throughout the year, primarily occurring between June and September, the chloride concentration in the monitoring well also demonstrates a regular pattern of temporal and spatial variation.

The fluctuation of chloride ion concentration is primarily influenced by total precipitation over 165 days. When a single rainfall exceeds 15 mm, it effectively leaches surface soil salts from the irrigated agricultural zone into the groundwater. This leaching effect persists for 165 days following rainfall events. Rainfall in the study area mainly occurs from June to October, resulting in higher chloride ion concentrations measured from June to January and lower concentrations measured from January to June.

This temporal variability in chloride ion concentration should be taken into account by relevant authorities for improved monitoring and managing of groundwater environmental conditions in the study area.

Author Contributions: Conceptualization, L.S.; Data curation, L.S.; Formal analysis, L.S. and R.J.; Funding acquisition, B.Z., R.Z. and R.M.; Investigation, L.S. and B.Z.; Methodology, L.S.; Project administration, B.Z. and R.M.; Resources, B.Z., R.Z. and S.L.; Supervision, W.D.; Validation, R.J., W.D. and R.M.; Writing—original draft, L.S.; Writing—reviewing and editing, L.S. and R.M. All authors have read and agreed to the published version of the manuscript.

Funding: This work was funded by the "Basic Research Funds of Chinese Academy of Geological Sciences (SK202327)", "Geological Survey Projects Foundation of the Institute of Hydrogeology and Environmental Geology (DD20221773)", and "Investigation of Groundwater Environment in Ordos (Phase II) (ESZC-G-F-220140)".

Data Availability Statement: The data used to support the findings of this study are available from the corresponding author upon request.

Acknowledgments: The editor and reviewers are sincerely acknowledged for their instructive and detailed comments on the early versions of this manuscript. The authors appreciate all centers supplying open-source data sets used in the present research.

Conflicts of Interest: Ruiqing Zhou was employed by Ordos Environmental Protection Investment Co., Ltd. The remaining authors declare that the research was conducted in the absence of any commercial or financial relation-ships that could be construed as a potential conflict of interest. All authors have read and agreed to the published version of the manuscript.

References

1. Zheng, N.; Liu, J.; Xia, X.; Gu, S.; Wu, Y.; Li, X.; Jiang, S. Identification of Contaminant Source and Hydraulic Conductivity Field Based on an ILUES-SOM Surrogate Model. *Stoch. Environ. Res. Risk Assess.* **2023**, *37*, 2725–2738. [CrossRef]
2. Li, Y.; Lu, W.; Pan, Z.; Wang, Z.; Dong, G. Simultaneous Identification of Groundwater Contaminant Source and Hydraulic Parameters Based on Multilayer Perceptron and Flying Foxes' Optimization. *Environ. Sci. Pollut. Res.* **2023**, *30*, 78933–78947. [CrossRef] [PubMed]
3. Duan, L.; Wu, Y.; Fan, J.; Ye, F.; Xie, C.; Fu, X.; Sun, Y. Identification of Nitrogen Pollution Sources and Transport Transformation Processes in Groundwater of Different Landforms Using C, H, N, and O Isotope Techniques: An Example from the Lower Weihe River. *Environ. Sci. Pollut. Res.* **2023**, *30*, 29442–29457. [CrossRef] [PubMed]
4. Zhao, W.; Yang, D.; Sun, Q.; Gan, Y.; Bai, L.; Li, S.; Liu, D.; Dai, J. Combining Multi-Isotope Technology, Hydrochemical Information, and MixSIAR Model to Identify and Quantify Nitrate Sources of Groundwater and Surface Water in a Multi-Land Use Region. *Environ. Sci. Pollut. Res.* **2023**, *30*, 80070–80084. [CrossRef] [PubMed]
5. Chen, Y.; Gui, H.; Jiang, C.; Zha, J.; Zheng, L. Hydrogeochemistry and Stable Hydrogen and Oxygen Isotope Characteristics of Deep Limestone Water in the Huainan Panxie Mining Area. *Arab. J. Geosci.* **2022**, *15*, 1133. [CrossRef]

6. Irrgeher, J.; Prohaska, T. Application of Non-Traditional Stable Isotopes in Analytical Ecogeochemistry Assessed by MC ICP-MS—A Critical Review. *Anal. Bioanal. Chem.* **2015**, *408*, 369–385. [CrossRef]
7. Wang, G.; Gao, H.; Long, B.; Wu, J. Progress of Nitrate Isotope-Coupled Multi-Tracer Traceability of Groundwater Nitrate Contamination. *J. Appl. Ecol.* **2024**, *35*, 970–984.
8. Long, Z. Huangshui River Basin Water Environment Quality Comprehensive Evaluation and Typical Pollutants Traceability and Control Countermeasures Research. Ph.D. Thesis, Shandong University, Jinan, China, 2022.
9. Lin, B.; Qi, F.; An, X.; Zhao, C.; Gao, Y.; Liu, Y.; Zhong, Y.; Qiu, B.; Wang, Z.; Hu, Q.; et al. Review: The Application of Source Analysis Methods in Tracing Urban Non-Point Source Pollution: Categorization, Hotspots, and Future Prospects. *Environ. Sci. Pollut. Res.* **2024**, *31*, 23482–23504. [CrossRef]
10. Peng, L.; Jianyuan, C.; Ji, L.; Tiantian, W.; Jian, Y. Hydrogeochemical Characteristics and Solute Sources of Groundwater in the Yuhengbei Mining Area, Shaanxi Province, China. *Environ. Earth Sci.* **2022**, *81*, 516. [CrossRef]
11. Chakraborty, P.; Wood, D.A.; Singh, S.; Hazra, B. Trace Element Contamination in Soils Surrounding the Open-Cast Coal Mines of Eastern Raniganj Basin, India. *Environ. Geochem. Health* **2023**, *45*, 7275–7302. [CrossRef]
12. Han, X.; Tang, F.; Liu, A.L. Drinking Water Quality Evaluation in Supply Systems in Wuhan, China: Application of Entropy Weight Water Quality Index and Multivariate Statistical Analysis. *Environ. Sci. Pollut. Res.* **2024**, *31*, 280–292. [CrossRef] [PubMed]
13. Jean-Michel, M.; Alexandre, D. Origin of Cl− and High δ^{37}Cl Values in Radiocarbon Dated-Fracture Groundwaters at the Tournemire URL (France). *Procedia Earth Planet. Sci.* **2013**, *7*, 574–577. [CrossRef]
14. Moncada-Aguilar, A.M.; Ramírez-Hernández, J.; Quintero-Núñez, M.; Avendaño-Reyes, L. Origin of Salinity in Groundwater of Neighboring Villages of the Cerro Prieto Geothermal Field. *Water Air Soil Pollut.* **2010**, *213*, 389–400. [CrossRef]
15. Khazaei, E.; Milne-Home, W. Applicability of Geochemical Techniques and Artificial Sweeteners in Discriminating the Anthropogenic Sources of Chloride in Shallow Groundwater North of Toronto, Canada. *Environ. Monit. Assess.* **2017**, *189*, 218. [CrossRef]
16. Ma, R.; Li, L.; Zhang, B. Impact Assessment of Anthropogenic Activities on the Ecological Systems in the Xiongan New Area in the North China Plain. *Integr. Environ. Assess. Manag.* **2021**, *12*, 866–876. [CrossRef]
17. Tursun, A. Study on Spatial and Temporal Changes of Salinized Soil and Groundwater Characteristics in Wei-Ku Oasis. Ph.D. Thesis, Xinjiang University, Ürümqi, China, 2012.
18. Tengfei, F. Research Application of Spatial and Temporal Variability of Soil Salinization and Monitoring System in Typical Coastal Areas. Ph.D. Thesis, Graduate School of Chinese Academy of Sciences (Institute of Oceanography), Qingdao, China, 2015.
19. Fei, L. Soil Water-Salt Characteristics of Minqin Oasis and Its Relationship with Groundwater. Master's Thesis, Lanzhou University, Lanzhou, China, 2019.
20. Huang, G.; Sun, J.; Qi, J.; Zang, Y.; Chen, J.; Jing, J. Isotopic Composition of Ordos Groundwater in Relation to Climate Change. *J. Earth Sci.* **2007**, *06*, 550–554.
21. Xuekun, Y. Characterization of Precipitation in Ordos City in the Recent 50 Years. *Inn. Mong. Sci. Econ.* **2017**, *22*, 66–67, 81.
22. Zhang, L.; Zheng, Y.; Xu, J.; Xu, G.; Li, Y. Characteristics of Spatial and Temporal Distribution of Heavy Rainfall and Disaster Defense in Ordos City under the Background of Climate Warming. *Inn. Mong. Meteorol.* **2020**, *4*, 14–16.
23. Sun, L.; Yuan, L.; Fu, Q.; Nie, X.; Yu, H.; Tang, J.; Dong, L. Effects of Rainfall on Exogenous Cl^- Leaching Efficiency and Its Spatial Distribution in Soils with Different Textures. *J. Northeast Agric. Univ.* **2022**, *53*, 27–38.
24. Kincaid, D.W.; Findlay, S.E.G. Sources of Elevated Chloride in Local Streams: Groundwater and Soils as Potential Reservoirs. *Water Air Soil Pollut.* **2009**, *203*, 335–342. [CrossRef]
25. *NY/T 1378-2007*; Determination of Chloride Ion Content in Soil. China Standards Press: Beijing, China, 2007.
26. Jiang, W.; Sheng, Y.; Wang, G.; Shi, Z.; Liu, F.; Zhang, J.; Chen, D. Cl, Br, B, Li, and Noble Gases Isotopes to Study the Origin and Evolution of Deep Groundwater in Sedimentary Basins: A Review. *Environ. Chem. Lett.* **2022**, *20*, 1497–1528. [CrossRef]
27. Sheng, Y.; Baars, O.; Guo, D.; Whitham, J.; Srivastava, S.; Dong, H. Mineral-Bound Trace Metals as Cofactors for Anaerobic Biological Nitrogen Fixation. *Environ. Sci. Technol.* **2023**, *57*, 7206–7216. [CrossRef] [PubMed]

Disclaimer/Publisher's Note: The statements, opinions and data contained in all publications are solely those of the individual author(s) and contributor(s) and not of MDPI and/or the editor(s). MDPI and/or the editor(s) disclaim responsibility for any injury to people or property resulting from any ideas, methods, instructions or products referred to in the content.

water

MDPI

Article

Distribution and Co-Enrichment Factors of Arsenic and Fluoride in the Groundwater of the Plain Area of the Aksu River Basin, Xinjiang, PR China

Yuanyuan Ji [1,2], Yinzhu Zhou [3], Xiaoyu Zhao [1], Jinlong Zhou [1,*], Ying Sun [1] and Mi Lei [1]

[1] College of Hydraulic and Civil Engineering, Xinjiang Agricultural University, Urumqi 830052, China; xj_jiyuanyuan@163.com (Y.J.); 18135926563@163.com (X.Z.); xjsunying@xjau.edu.cn (Y.S.); leimi20203@gmail.com (M.L.)
[2] College of Agricultural Engineering, Xinjiang Agricultural Vocational and Technical University, Changji 831100, China
[3] Center for Hydrogeology and Environmental Geology, China Geological Survey, Tianjin 300309, China; zhouyinzhu@mail.cgs.gov.cn
* Correspondence: zjzhoujl@163.com

Abstract: The Aksu River Basin is located in the western region of the middle part of the southern foothills of the Tianshan Mountains and the northwestern edge of the Tarim Basin in Xinjiang, China. High-arsenic (As)/high-fluoride (F) groundwater is widely distributed in this area and is harmful to the life of local residents and to agricultural production. It is of great importance to understand the distribution and causes of As-F co-enrichment in the groundwater in this area. Based on the test results of 138 groundwater samples in the plain area of the Aksu River Basin, the hydrochemical characteristics of groundwater and the spatial distribution of As-F co-enrichment groundwater were analyzed under the following conditions: a single-structure phreatic aquifer (SSPA), a phreatic aquifer in a confined groundwater area (PACGA), a shallow confined aquifer (SCA), and a deep confined aquifer (DCA), all in a recharge area, transition area, and an evaporation area. The hydrogeochemical processes affecting the source, migration, and enrichment of As-F in the groundwater were revealed. The results showed that the chemical types of groundwater in the study area were mainly HCO_3·SO_4-Ca·Mg and SO_4·Cl-Na·Mg. Horizontally, high-As-F groundwater was mainly distributed in the transition area and evaporation area in the middle and lower reaches of the Aksu River Basin. The area is close to the edge of the desert, where the groundwater runoff is sluggish and in an alkaline-reducing groundwater environment. Vertically, high-As groundwater was mainly distributed in the PACGA at a depth of 10–20 m and in the SCA at a depth of 80–100 m. High-F groundwater was mainly concentrated in the PACGA at a depth of 10–30 m and in the SCA at a depth of 80–100 m, and As-F co-enrichment groundwater was mainly concentrated in the PACGA at a depth of 10–20 m and in the SCA at a depth of 80–100 m. The hydrochemical characteristics of the groundwater in the Aksu River Basin were closely related to geological conditions, hydrogeological conditions, and the hydrochemical environment of the groundwater. As-F co-enriched groundwater was mainly affected by the combination of a small topographic gradient, a shallow groundwater burial depth, a weak reducing alkaline groundwater environment, strong evaporation and concentration, the weathering and dissolution of evaporated salt rock, and the alternating adsorption of cations.

Keywords: the Aksu River Basin; groundwater; arsenic-fluoride co-enrichment; influencing factors

1. Introduction

The effects of drinking high-F and high-As groundwater on human health are increasingly concerning. Globally, more than 140 million people in about 70 countries are affected by arsenic pollution in groundwater, and about 200 million people in about 25 countries are suffering from fluorosis [1]. The World Health Organization (WHO) has established

allowable limits of 0.01 mg·L^{-1} for arsenic (As) [2] and 1.5 mg·L^{-1} for fluoride (F) [3] in drinking water. An appropriate amount of As has certain pharmacological effects. As, As oxides, and As-containing traditional Chinese medicine are widely used to treat leukemia and other types of cancer and have achieved remarkable results [4]. Excessive inorganic As can cause skin depigmentation or excessive deposition and palmoplantar keratosis-based systemic chronic poisoning. Severe cases can lead to skin cancer, lung cancer, and other visceral cancers [5]. A small amount of F is beneficial to the strength of bones and teeth [6], but excessive F in drinking water can cause dental fluorosis and skeletal fluorosis, which can lead to paralysis in severe cases [7]. Countries around the world that have reported co-exceeding levels of As-F in groundwater (here defined as "As-F co-enrichment") mainly include India in Asia [8–10], China [11], Argentina in the Americas [12], and Bangladesh [13]. Excessive arsenic and fluorine caused by natural environmental factors are among the main problems caused by groundwater in these areas. The research on its origin, migration, and impact on local ecology and residents' health is still in the stage of continuous exploration, and its interaction mechanism is also relatively complex. Internationally, most studies focus on either arsenic or fluoride in groundwater, and information on the simultaneous enrichment of arsenic and fluoride in groundwater is relatively limited [14].

High-As and high-F groundwater in the plain area of Xinjiang Uygur Autonomous Region (Xinjiang for short) in China is mainly distributed in the oasis belt around the Tarim Basin and the southern margin of the Junggar Basin [15,16]. There are few reports on the co-enrichment of As-F in groundwater in some areas of Xinjiang, such as the Kuitun River Basin in northern Xinjiang [17] and the oasis belt in the southern margin of the Tarim Basin in southern Xinjiang [16]. As-F co-enriched groundwater seriously affects the safety of local drinking water, threatens human health, and restricts local economic and social development.

Based on the detection data of 1412 groundwater samples in Xinjiang from 2016 to 2021, according to the Class III water standard in China's *Groundwater Quality Standard* (GB/T 14848-2017), groundwater with As at >0.01 mg·L^{-1} was defined as high-As groundwater, and groundwater with F at >1.0 mg·L^{-1} was defined as high-F groundwater. The over-standard rates of As, F, and the co-enrichment of As-F in the groundwater of three-level drainage basins in Xinjiang Plain were analyzed. It was found that the over-standard rate of groundwater As in the Aksu River Basin was as high as 26.09% (ranking second in Xinjiang, second only to the Aibi Lake Water system), the over-standard rate of groundwater F was as high as 60.87% (ranking first in Xinjiang), and the proportion of As-F co-enrichment was 18.12% (ranking first in Xinjiang). As-F and the co-enrichment of As-F in the groundwater of the Aksu River Basin were widely distributed. At present, the distribution and enrichment mechanism of As-F in the groundwater in the Kuitun River Basin and Manas River Basin in northern Xinjiang has been studied in depth, while that in southern Xinjiang has been rarely reported, especially in the Aksu River Basin. The Aksu River Basin in Xinjiang was selected as a typical study area, and a total of 138 groundwater samples were collected to clarify the occurrence and co-enrichment mechanism of arsenic and fluorine in groundwater. The obtained results can improve a comprehensive understanding of the co-enrichment mechanism of arsenic and fluorine in groundwater, and it also provides a theoretical basis for the utilization and protection of local groundwater resources.

2. Experimental Section

2.1. Study Area

2.1.1. Physical Geography

The Aksu River Basin is located in the western region of the middle part of the southern foothills of the Tianshan Mountains and the northwestern edge of the Tarim Basin in Xinjiang, China (76°29′~81°53′ E and 40°00′~42°03′ N). The total area of the Aksu River Basin is 48,806.03 km^2, including 26,900.74 km^2 in mountainous areas and 21,905.29 km^2 in the plain area. The topography of the watershed gradually decreases from north to

south and from west to east. Geomorphic zoning is more obvious. From high to low, there are middle and low mountain hills, a fore-mountain diluvial fan group, alluvial inclined plains, and alluvial plains. The basin has a temperate continental arid climate with little precipitation, strong evaporation, and a large temperature difference between day and night. The annual average precipitation in the basin is 64.2 mm; the annual average evaporation is 1890.3 mm; the annual average temperature is 9.2–11.5 °C, the annual extreme maximum temperature is 40.2 °C, the extreme minimum temperature exceeds −27.6 °C, and the annual average sunshine duration is 2850 h [18]. The administrative divisions of the basin include Aksu City, Awati County, Keping County, Wensu County, Wushi County, Xinhe County in Aksu Prefecture, Aheqi County in Kizilsu Kirgiz Autonomous Prefecture, and the 8th and 16th regiments of the First Division of Xinjiang Production and Construction Corps. The industries in the area are mainly agriculture and fruit production, mainly planting rice, wheat, cotton, and other crops, as well as fruit trees such as apples, walnuts, dates, fragrant pears, apricots, etc. The development of agriculture and forestry mainly depends on river and groundwater irrigation. The stability of natural oases mainly depends on the groundwater.

2.1.2. Hydrogeological Conditions

The vertical zonation from the mountainous area to the plain area in the Aksu River Basin is obvious. From the northernmost high mountains and extremely high mountains to the south, they gradually evolve into mid-mountains, low mountains, hills, plains, and deserts. The piedmont slope flood and gravel plain diving area is distributed along the northern mountain front. The confined water area of the river alluvial plain is distributed in the middle and lower reaches (Figure 1). As shown in the north–south hydrogeological profile of the Aksu River Basin (Figure 2), the quaternary sedimentary law gradually transitions from single gravel and pebbles in the piedmont to coarse sand, medium-coarse sand, fine sand, silty sand, and clay in the downstream area [19]. The quaternary sediments in the basin are mainly lacustrine alluvial deposits, with mainly sand and fine sand. The total thickness of the loose deposits is more than 500 m, which is interlaced with the alluvial layers dominated by clay in the northern piedmont sloping plain. The northern part is the South Tianshan fold belt, which is composed of metamorphic rocks and magmatic rocks such as biotite granite, biotite schist, and biotite quartzite. Fluoride-rich minerals such as mica, hornblende, tourmaline, apatite, fluorite, and crystal are widely distributed. These minerals, through hydrochemical processes and under alkaline conditions, provide abundant fluorine to the groundwater and become the main source of fluorine [20]. In the north of the Aksu area, there is the East Alai-Haerke manganese, iron, copper, gold, antimony, aluminum, nickel, and rare metal metallogenic belt. The arsenic element mainly exists in ores, such as antimony ore, pyrite, and pyrrhotite. Due to the change in the natural environment, arsenide precipitates or the arsenic fixed in rocks is desorbed and enters the groundwater, resulting in an increase in arsenic content in the groundwater [21].

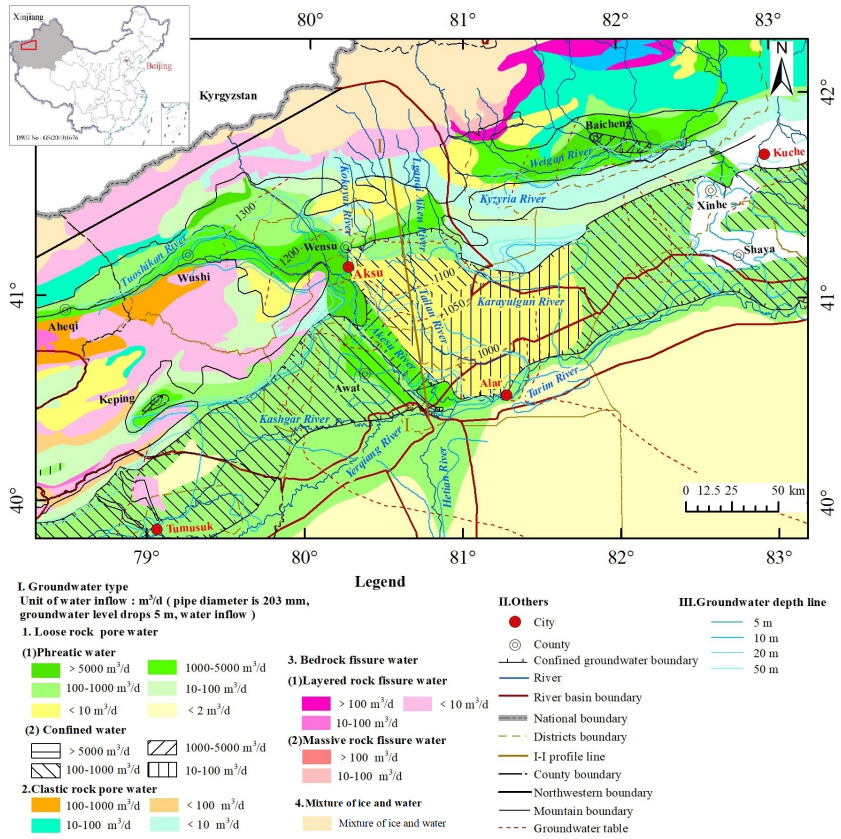

Figure 1. Hydrogeological map of the Aksu River Basin, adapted with permission from [22] (2023, China Light Industry Press Ltd., Beijing, China).

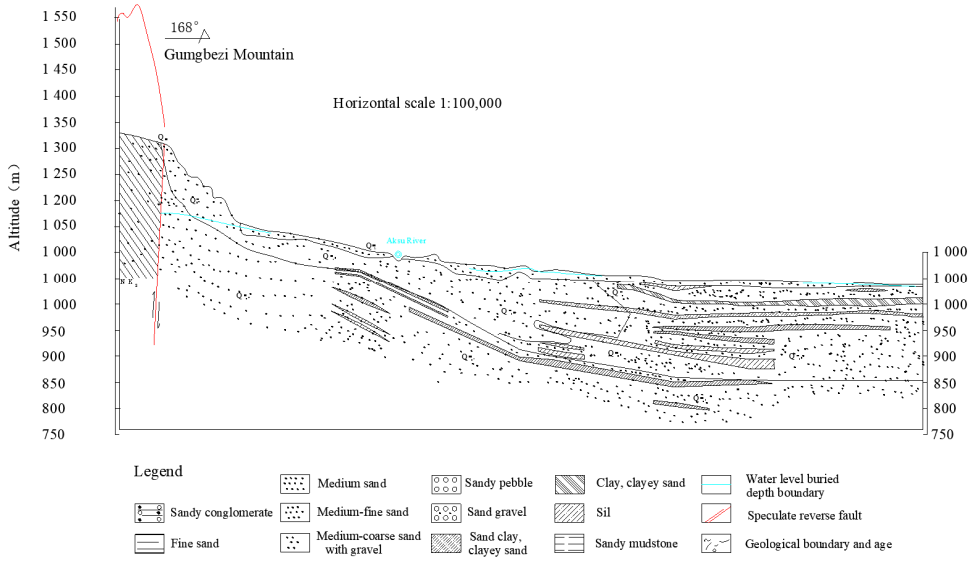

Figure 2. The north–south hydrogeological profile of the Aksu River Basin, adapted with permission from [23] (2021, China Rural Water and Hydropower).

The groundwater types in the northern and southern plains are single-structure phreatic water and multi-layer phreatic-confined water structures, respectively. The single thick phreatic aquifer in the front of Mt. Luo is mainly recharged by vertical surface water infiltration. The river network and ditches are densely distributed in the alluvial plain area of the middle and lower reaches of the river. The horizontal direction of groundwater is recharged by the lateral runoff of groundwater in the upstream aquifer, and the vertical

direction is recharged by the infiltration of river water, ditch water, reservoir water, and spring water. The direction of groundwater flow is consistent with that of the surface runoff, with both being from northwest to southeast. The groundwater discharge mode in the study area is dominated by vertical artificial mining and phreatic evaporation and transpiration [24]. There is a lateral runoff discharge of groundwater in the transition zone between the plain area and the desert area.

The depth of the groundwater sampling wells was 10–190 m. According to the isoline of the distribution of the confined water and the depth of the phreatic water in the study area (Figure 1), taking the evaporation limit depth of phreatic water as 5 m, the study area was divided into the recharge area (single-structure phreatic groundwater area), transition area (multi-layer-structure phreatic–confined groundwater aquifer distribution area with a phreatic water depth of >5 m) and the evaporation area (multi-layer-structure phreatic–confined groundwater aquifer distribution area with a phreatic water depth of $\leq$5 m).

2.2. Sample Collection and Analysis

2.2.1. Sample Collection

Based on the distribution of existing wells in the study area, a total of 138 groundwater samples, which could control the entire study area, were collected in the plain area of the Aksu River Basin in 2016 (Figure 3). According to the conditions of the aquifers, there were 56 samples from the single-structure phreatic aquifer (SSPA) (depth: 20 to 130 m), 31 samples of the phreatic aquifer in the confined groundwater area (PACGA) (depth: 10 to 30 m), 38 samples from the shallow confined aquifer (SCA) (depth: 17 to 100 m), 13 samples from the deep confined aquifer (DCA) (depth: 110 to 190 m), and 6 surface water samples were collected simultaneously. The control area of the groundwater sampling points was 21,905.29 km^2, and the density of the sampling points was 6.30 wells/103 km^2. This fully met the requirements of the groundwater quality monitoring well density of 1.0–1.6 wells/103 km^2 and the groundwater quality monitoring well density of 3.0–4.8 wells/103 km^2 in the over-exploitation area of the inland basin plain area in the *Groundwater Monitoring Specification* (SL183-2005). The groundwater and surface water samples were strictly in accordance with the *Technical Specifications for Groundwater Environmental Monitoring* (HL/T 164-2004). During field sampling, all water bottles were washed three times with the water samples and then filtered with a 0.45 μm microporous membrane to remove suspended solids. All water samples for cation analysis were acidified to pH < 2 with HNO_3 without leaving the bubble lid tight, sealed with a sealing film, labeled, stored at 4 °C, and sent for inspection.

2.2.2. Test Analysis

The groundwater and surface water samples were tested by the Mineral Water Testing Center of the Institute of Hydrogeology and Environmental Geology, Chinese Academy of Geological Sciences. The selection of testing items was based on the *Technical Specifications for Groundwater Environmental Monitoring* (HL/T 164-2004). The groundwater temperature, redox potential (Eh), pH, electrical conductivity (EC), and dissolved oxygen (DO) were measured on-site.

The laboratory test indexes included TH (total hardness), TDSs (total dissolved solids), K^+, Na^+, Ca^{2+}, Mg^{2+}, Cl^-, $SO_4{}^{2-}$, $HCO_3{}^-$, F, As, Fe, Mn, $NO_3{}^-$, $NH_4{}^+$, etc. K^+ and Na^+ were determined using flame atomic absorption spectrophotometry. Total hardness, Ca^{2+}, and Mg^{2+} were determined using EDTA titration. The 105 °C dry-weight method was used for the determination of TDS. Cl^- was determined using a silver nitrate volumetric method, $SO_4{}^{2-}$ was determined using barium sulfate turbidimetry, $HCO_3{}^-$ was determined using hydrochloric acid titration, As was determined using atomic fluorescence spectrometry (AFS-922), F was determined an using ion-selective electrode method (PHS-3D), Fe was determined using a PinAAcle-900Z single graphite furnace atomic absorption spectrophotometer, and Mn was determined using a OPTIMA8000 inductively coupled plasma emission spectrometer. The lower limit for the detection of As and Mn

was 0.001 mg·L^{-1}, the lower limit for the detection of F was 0.1 mg·L^{-1}, the lower limit for the detection of NO_3^- was 0.2 mg·L^{-1}, and the lower limit for the detection of other components was 0.01 mg·L^{-1}. The relative standard deviation (RSD) of the measured values was less than 5%.

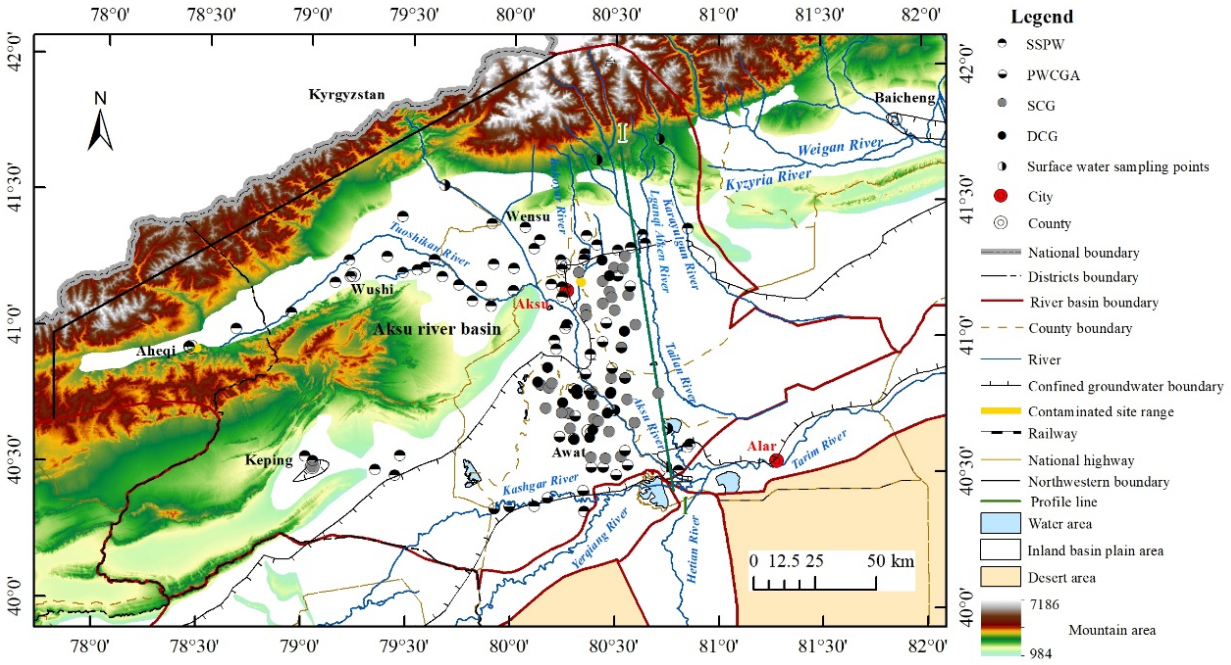

Figure 3. Distribution map of surface water and groundwater sampling points.

2.3. Data Analyses

Based on the basic theories of hydrogeology and hydrogeochemistry, the chemical characteristics, arsenic and fluorine content, and distribution of groundwater were analyzed by means of data analysis software, 3S technology, and isotope analysis. The sources of fluorine and arsenic in groundwater were identified, and the influencing factors of arsenic and fluorine co-enrichment were summarized. The typical basin of arsenic and fluorine co-enrichment was selected for in-depth study, and the reverse hydrogeochemical simulation was carried out using PHREEQC 2.12.5 software to summarize the characteristics of arsenic and fluorine co-enrichment. The distribution characteristics and occurrence environment of arsenic and fluorine co-enrichment in the study area were further analyzed, and the mechanism of arsenic and fluorine co-enrichment in groundwater was summarized. The research technology roadmap is shown in Figure 4.

The dissolution and precipitation state of minerals in groundwater was mainly determined using the saturation degree of their relative aqueous solution. Based on the calculation of the equilibrium distribution of water-soluble components, the saturation index (SI) of groundwater relative to calcite, dolomite, gypsum, and rock salt was calculated as follows (Equation (1)):

$$SI = \lg (IAP/K) \quad (1)$$

where IAP is the product of ion activity. K is the solubility product constant of minerals at a specific temperature. When SI > 0.5, it indicates mineral precipitation. When SI < −0.5, it indicates mineral dissolution. When the absolute value of SI is less than 0.5, it indicates that the mineral is in an equilibrium state.

The enrichment of As-F in groundwater is related to the alternating cation adsorption of active Ca^{2+} and Mg^{2+} with Na^+ and K^+ in the aquifers [25]. The chlor-alkali index (CAI) can reflect the cation exchange in groundwater (Equations (2) and (3)). When $CAI - 1$ and $CAI - 2$ are both positive, Na^+ and K^+ in the groundwater exchange with Ca^{2+} and Mg^{2+} in an aqueous medium. Otherwise, Ca^{2+} and Mg^{2+} in the groundwater are exchanged with

Na^+ and K^+ in aqueous media. The larger the absolute values of $CAI-1$ and $CAI-2$ are, the more intensive the cation exchange is.

$$CAI-1=\frac{Cl^- - \left(Na^+ + K^+\right)}{Cl^-} \tag{2}$$

$$CAI-2=\frac{Cl^- - \left(Na^+ + K^+\right)}{\mathrm{HCO}(_3^-)+\mathrm{SO}(_4^{2-})+\mathrm{CO}(_3^{2-})+\mathrm{NO}(_3^-)} \tag{3}$$

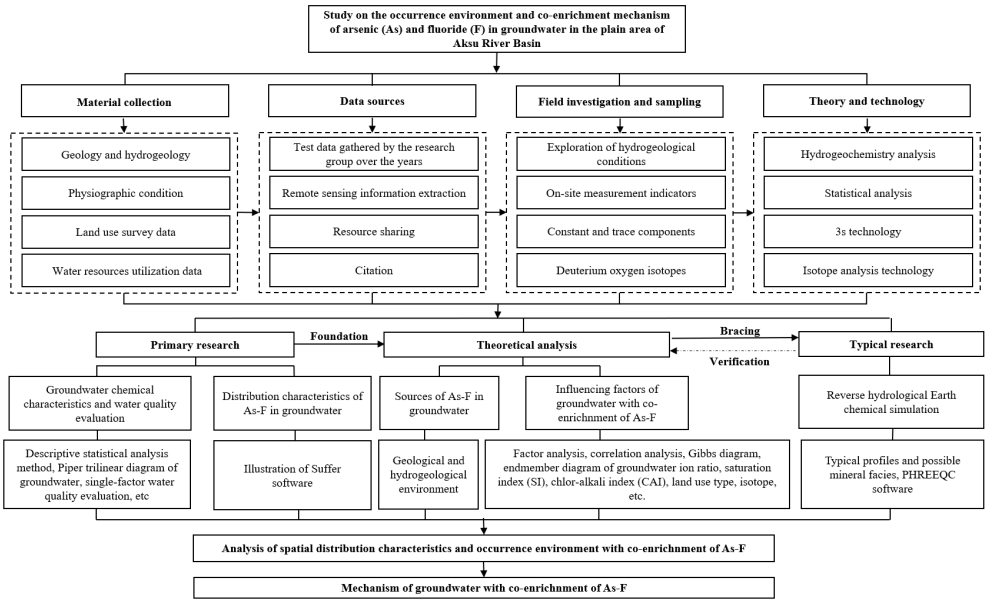

Figure 4. Research technology roadmap.

3. Results and Discussion

3.1. Groundwater Chemical Characteristics

The Piper diagram of 138 groundwater samples in the study area (Figure 5a) showed that the hydrochemical types of groundwater in the plain area of the Aksu River Basin were mainly HCO_3·SO_4-Ca·Mg and SO_4·Cl-Na·Mg types. The groundwater chemical type of the SSPA in the study area was mainly HCO_3·SO_4-Ca·Mg. The PACGA and SCA mainly contained the SO_4·Cl-Na·Mg type. The DCA mainly contained the HCO_3·SO_4·Cl-Na·Ca type. The chemical type of the groundwater in the recharge area mainly contained HCO_3·SO_4-Ca·Mg. The transition area mainly contained SO_4·Cl-Na·Mg. The evaporation area mainly contained SO_4·Cl-Na·Ca (Na·Ca·Mg).

Groundwater with As greater than 0.01 mg·L^{-1} was defined as high-As groundwater, and groundwater with F content greater than 1.0 mg·L^{-1} was defined as high-F groundwater. In the SSPA of the study area, the groundwater hydrochemical type with As-F not exceeding the standard was mainly HCO_3·SO_4-Ca·Mg, and there was no single As exceeding point. The groundwater hydrochemical type with F (single) exceeding the standard was mainly HCO_3·SO_4-Ca·Mg (Ca·Na·Mg), and the groundwater hydrochemical type with As-F co-enrichment was mainly Cl·SO_4-Na. In the PACGA, the groundwater hydrochemical type with As-F not exceeding the standard was mainly SO_4·Cl-Na·Ca (Na·Mg), and there was no As (single) exceeding the standard point. The groundwater hydrochemical type of high-F groundwater was mainly Cl·SO_4-Ca·Na·Mg, and that of high-As-F groundwater was mainly SO_4·HCO_3·Cl-Mg·Na·Ca. In the SCA, the hydrochemical type of groundwater with As-F that did not exceed the standard was mainly HCO_3·SO_4-Ca·Mg, and the hydrochemical type of groundwater with As exceeding the standard was mainly SO_4·Cl-Na·Mg. The hydrochemical type of groundwater with excessive F was mainly Cl·SO_4-Na, and the hydrochemical type of groundwater with As-F co-enrichment was mainly HCO_3·SO_4-

Ca·Na (Mg·Ca). In the DCA, the groundwater hydrochemical type of As-F not exceeding the standard was mainly HCO_3·SO_4-Na·Mg·Ca; the groundwater hydrochemical type of As exceeding the standard was mainly SO_4·Cl-Na·Mg·Ca; the groundwater hydrochemical type of F exceeding the standard was mainly HCO_3·SO_4·Cl-Mg·Na; and the groundwater hydrochemical type of As-F co-enrichment was mainly HCO_3·SO_4·Cl-Na·Ca.

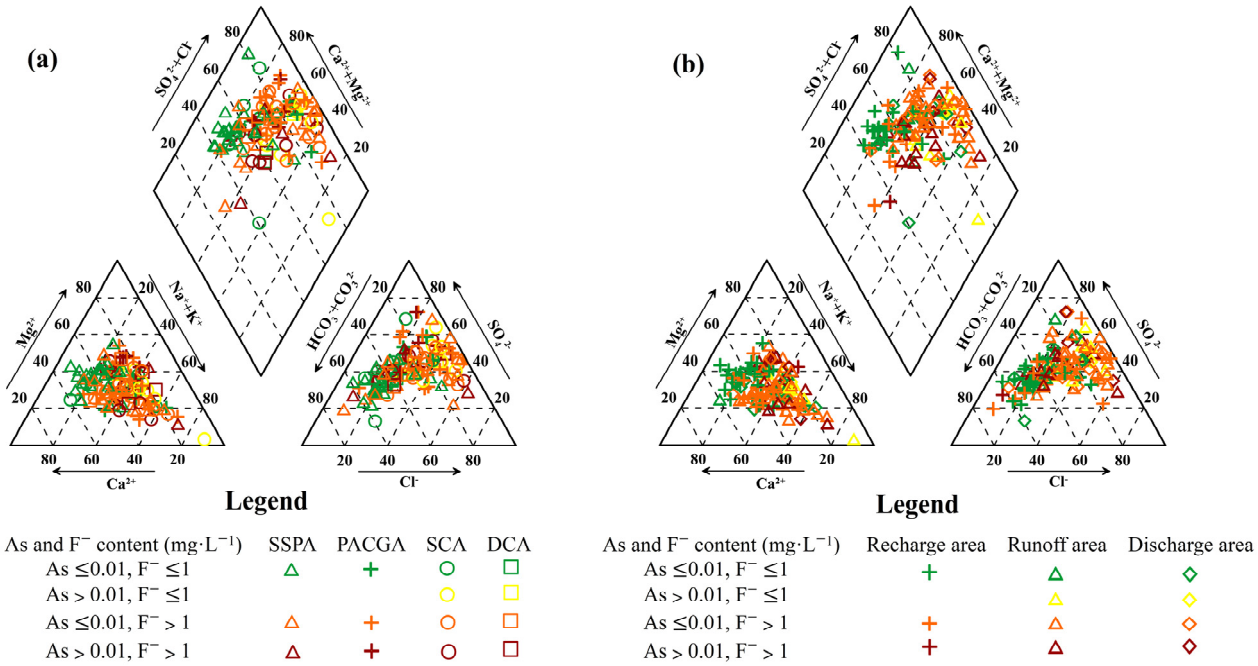

Figure 5. Piper trilinear diagram of groundwater in the study area. (**a**) Trilinear diagram of As-F content in different groundwater types. (**b**) Trilinear diagram of As-F content in groundwater based on recharge–runoff–discharge conditions.

According to the trilinear diagram of As-F content in groundwater based on recharge–runoff–discharge conditions (Figure 5b), the main chemical types of groundwater in which As-F in the recharge area did not exceed the standard were HCO_3·SO_4-Ca·Mg, with no single point exceeding the standard. The chemical type of groundwater with excessive F was mainly HCO_3·SO_4-Ca·Mg (Ca·Na·Mg), and the chemical type of groundwater with the co-enrichment of As-F was mainly HCO_3·SO_4-Na·Mg. In the transition area, the groundwater chemical type for which neither As nor F exceeded the standard was mainly SO_4·Cl-Na·Mg, the groundwater chemical type which exceeded the standard for single As was mainly SO_4·Cl-Na·Mg, and the groundwater chemical type which exceeded the standard for single F was mainly Cl·SO_4-Na. The main hydrochemical type of As-F co-enriched groundwater was HCO_3·SO_4-Na·Ca (Mg·Ca). In the evaporation area, the groundwater hydrochemical type for As-F was mainly SO_4·HCO_3-Ca·Mg; the groundwater hydrochemical type for As exceeding the single standard was mainly SO_4·Cl-Na·Mg; the groundwater hydrochemical type for F exceeding the single standard was mainly SO_4·Cl-Ca·Na; and the groundwater hydrochemical type for As-F co-enrichment was mainly SO_4·Cl-Na·Mg. The groundwater pH in the study area ranged from 6.7 to 8.6, with an average of 7.6, which was neutral–weakly alkaline (Table 1). The cations in the groundwater were mainly Na^+ (14.7 to 1577.0 mg·L^{-1}, with an average of 195.3 mg·L^{-1}). The contents of Ca^{2+} and Mg^{2+} were 9.9 to 532.4 mg·L^{-1} and 2.5 to 417.8 mg·L^{-1}, respectively, and the averages were 121.3 mg·L^{-1} and 79.2 mg·L^{-1}, respectively. The anions were mainly SO_4^{2-}, with contents of 32.0 to 2819.0 mg·L^{-1}, and the average content was 462.1 mg·L^{-1}. The contents of HCO_3^- and Cl^- were 78.9 to 573.7 mg·L^{-1} and 12.3 to 2153.0 mg·L^{-1}, respectively, and the averages were 260.0 mg·L^{-1} and 251.7 mg·L^{-1}, respectively. The Eh of groundwater ranged from −70.0 to 249.0 mV, with an average of 150.3 mV, indicating that the groundwater was in a

reduction–sub-oxidation environment. From the recharge area (average 179.1 mV) to the transition area (average 142.9 mV) and then to the evaporation area (average 115.7 mV), Eh decreased, indicating that the groundwater environment reduced. The TDSs in groundwater ranged from 192.2 to 7632.0 $mg \cdot L^{-1}$, with an increase from the recharge area (average 814.4 $mg \cdot L^{-1}$) to the transition area (average 1490.2 $mg \cdot L^{-1}$) and then to the evaporation area (average 1662.8 $mg \cdot L^{-1}$), indicating increased evaporation and excretion. In addition, the ratio of $\gamma Ca^{2+}/\gamma Cl^{-}$, which reflects the dynamic characteristics of groundwater, ranged from 0.1 to 4.0, with an average of 0.8. The $\gamma Ca^{2+}/\gamma Cl^{-}$ ratio decreased from the recharge area (average 1.2) to the transition area (average 0.6) and then to the evaporation area (average 0.8), indicating that groundwater flow conditions were deteriorating.

Table 1. Statistics of groundwater hydrochemical index content.

Distribution		Groundwater Type				Recharge–Runoff–Discharge Conditions		
		SSPW	PWCGA	SCG	DCG	Recharge Area	Transition Area	Evaporation Area
Indexes \ Samples		56	31	38	13	4	67	23
K^+	Minimum ($mg \cdot L^{-1}$)	1.3	1.5	0.9	2.4	1.3	0.9	2.1
	Maximum ($mg \cdot L^{-1}$)	28.8	55.0	28.1	22.7	17.4	45.5	55.0
	Mean ($mg \cdot L^{-1}$)	7.5	14.6	9.5	8.1	6.3	10.7	13.8
Na^+	Minimum ($mg \cdot L^{-1}$)	14.7	31.9	32.2	31.3	14.7	31.3	31.9
	Maximum ($mg \cdot L^{-1}$)	1577.0	1213.0	756.1	308.3	935.5	1577.0	838.9
	Mean ($mg \cdot L^{-1}$)	168.9	278.4	196.7	106.9	97.2	247.8	247.0
Ca^{2+}	Minimum ($mg \cdot L^{-1}$)	26.2	34.6	9.9	28.9	26.2	9.9	22.5
	Maximum ($mg \cdot L^{-1}$)	532.4	486.1	252.2	148.6	348.9	532.4	398.7
	Mean ($mg \cdot L^{-1}$)	112.0	170.9	113.6	66.1	93.3	127.2	162.8
Mg^{2+}	Minimum ($mg \cdot L^{-1}$)	10.6	8.5	2.5	11.9	10.6	2.5	13.0
	Maximum ($mg \cdot L^{-1}$)	366.6	417.8	245.7	166.4	185.7	417.8	325.7
	Mean ($mg \cdot L^{-1}$)	61.8	132	69.7	55.7	51.9	90.5	103.2
Cl^-	Minimum ($mg \cdot L^{-1}$)	12.3	28.2	26.4	42.0	12.3	29.7	26.4
	Maximum ($mg \cdot L^{-1}$)	2153.0	1681.0	989.1	384.4	1355.0	2153.0	1190.0
	Mean ($mg \cdot L^{-1}$)	220.0	353.1	252.5	143.9	129.4	318.0	313.6
SO_4^{2-}	Minimum ($mg \cdot L^{-1}$)	40.8	77.8	32.0	69.7	40.8	69.7	32.0
	Maximum ($mg \cdot L^{-1}$)	2819.0	2781.0	1272.0	617.0	1674.0	2819.0	2306.0
	Mean ($mg \cdot L^{-1}$)	367.3	768.3	424.2	250.8	251.1	544.8	661.4
HCO_3^-	Minimum ($mg \cdot L^{-1}$)	78.9	88.0	84.6	94.1	100.2	78.9	100.0
	Maximum ($mg \cdot L^{-1}$)	564.6	562.3	524.0	573.7	564.6	573.7	573.7
	Mean ($mg \cdot L^{-1}$)	249.3	339.3	225.7	216.7	255.6	256.2	279.8
pH	Minimum	6.9	6.9	6.7	7.1	6.9	6.8	6.7
	Maximum	8.2	8.6	8.3	8.3	8.2	8.6	8.3
	Mean	7.6	7.5	7.6	7.7	7.6	7.6	7.5
TDS	Minimum ($mg \cdot L^{-1}$)	192.2	327.3	274.0	269.4	192.2	269.4	300.0
	Maximum ($mg \cdot L^{-1}$)	7632.0	6804.0	3330.0	1717.0	4614.0	7632.0	4561.0
	Mean ($mg \cdot L^{-1}$)	1114.9	1903.6	1208.5	754.7	814.4	1490.2	1662.8

Table 1. *Cont.*

Distribution		Groundwater Type				Recharge–Runoff–Discharge Conditions		
		SSPW	PWCGA	SCG	DCG	Recharge Area	Transition Area	Evaporation Area
Indexes \ Samples		56	31	38	13	4	67	23
TH	Minimum (mg·L^{-1})	108.6	121.1	110.0	123.1	108.6	121.1	110.0
	Maximum (mg·L^{-1})	2827.0	2932.0	1481.0	1057.0	1636.0	2932.0	2334.0
	Mean (mg·L^{-1})	539.1	1005.3	557.1	394.7	452.6	676.3	896.6
As	Minimum (mg·L^{-1})	<0.001	<0.001	<0.001	<0.001	<0.001	<0.001	<0.001
	Maximum (mg·L^{-1})	0.060	0.038	0.099	0.023	0.050	0.094	0.099
	Mean (mg·L^{-1})	0.005	0.008	0.019	0.009	0.002	0.015	0.011
F	Minimum (mg·L^{-1})	<0.1	0.4	0.3	0.5	<0.1	0.3	0.4
	Maximum (mg·L^{-1})	2.8	4.8	4.9	3.7	2.3	4.9	2.8
	Mean (mg·L^{-1})	1.1	2.0	1.8	1.5	0.9	2.1	1.2
Fe	Minimum (mg·L^{-1})	<0.01	<0.01	<0.01	<0.01	<0.01	<0.01	<0.01
	Maximum (mg·L^{-1})	5.7	5.7	28.9	0.2	5.7	28.9	5.7
	Mean (mg·L^{-1})	0.5	1.2	1.1	0.0	0.6	1.0	1.0
Mn	Minimum (mg·L^{-1})	<0.001	0.043	<0.001	<0.001	<0.001	<0.001	0.006
	Maximum (mg·L^{-1})	0.544	1.585	1.589	1.599	0.544	1.599	1.599
	Mean (mg·L^{-1})	0.049	0.466	0.255	0.286	0.043	0.288	0.401
EC	Minimum (mg·L^{-1})	328.0	575.0	575.0	458.0	328.0	458.0	724.0
	Maximum (mg·L^{-1})	10,320.0	9130.0	4400.0	23,300.0	6660.0	10,320.0	23,300.0
	Mean (mg·L^{-1})	1993.7	3036.8	1864.5	3441.3	1463.3	2353.8	3770.3
Eh	Minimum (mg·L^{-1})	−49.0	−70.0	−53.0	121.0	−49.0	−70.0	−51.0
	Maximum (mg·L^{-1})	249.0	245.0	244.0	240.0	249.0	244.0	245.0
	Mean (mg·L^{-1})	174.2	104.4	139.6	176.7	179.1	142.9	115.7
DO	Minimum (mg·L^{-1})	1.3	0.8	0.8	1.7	1.6	0.8	0.9
	Maximum (mg·L^{-1})	9.1	3.9	4.7	4.5	9.1	4.7	4.8
	Mean (mg·L^{-1})	4.8	2.3	2.9	3.3	5.2	2.9	2.6

Note: pH is dimensionless.

According to the *Groundwater Quality Standard* (GB/T 14848-2017) for Class III water (suitable for centralized drinking water sources and industrial and agricultural water), it can be concluded that the overall water quality in the study area was poor. Class IV and V water accounted for 86.96% of the total number of samples. The main over-standard components included TH (the point over-standard rate was 57.97%), SO_4^{2-} (the point over-standard rate was 55.07%), TDSs (the point over-standard rate was 45.65%), and Mn (the point over-standard rate was 39.13%).

3.2. Distribution of Groundwater with Co-Enrichment of As-F

3.2.1. Horizontal Distribution Characteristics

The content of As in the groundwater in the study area varied from <0.001 to 0.099 mg·L^{-1}, with an average of 0.010 mg·L^{-1}. The content of F in the groundwater varied from <0.1 to 4.9 mg·L^{-1}, with an average of 1.5 mg·L^{-1}. The pH of the groundwater ranged from 7.3 to 8.3, with an average of 7.7, which was neutral to weakly alkaline. The Eh of the

groundwater ranged from −70.0 to 244.0 mV, with an average of 82.9 mV, which is a reducing–oxidizing environment. No As-F was detected in the six surface water samples.

The co-enrichment distribution of As-F content in the groundwater in the study area is shown in figure (Figure 6). The groundwater flow conditions in the groundwater recharge area near the northern mountainous area and the piedmont alluvial plain were better, the evaporation and excretion were relatively small, and the distribution area of As-F co-enrichment was less. The distribution area of As-F co-enriched groundwater in the study area reached 799.17 km^2, accounting for 3.65% of the plain area (21,905.29 km^2). The area of As exceeding the standard was 185.82 km^2, and the area of F exceeding the standard was 3001.79 km^2. As-F co-enrichment areas in the study area were mainly distributed in Awati County, meaning the middle and lower reaches of the Aksu River Basin, which is close to the edge of the desert, with slow groundwater runoff and a strong alkaline and reductive groundwater environment. A fine-grained lithology, gentle terrain, shallow groundwater burial conditions, a slightly alkaline groundwater environment, and mineral dissolution mediated by organic matter under microbial degradation were the main reasons for the co-enrichment of arsenic and fluorine.

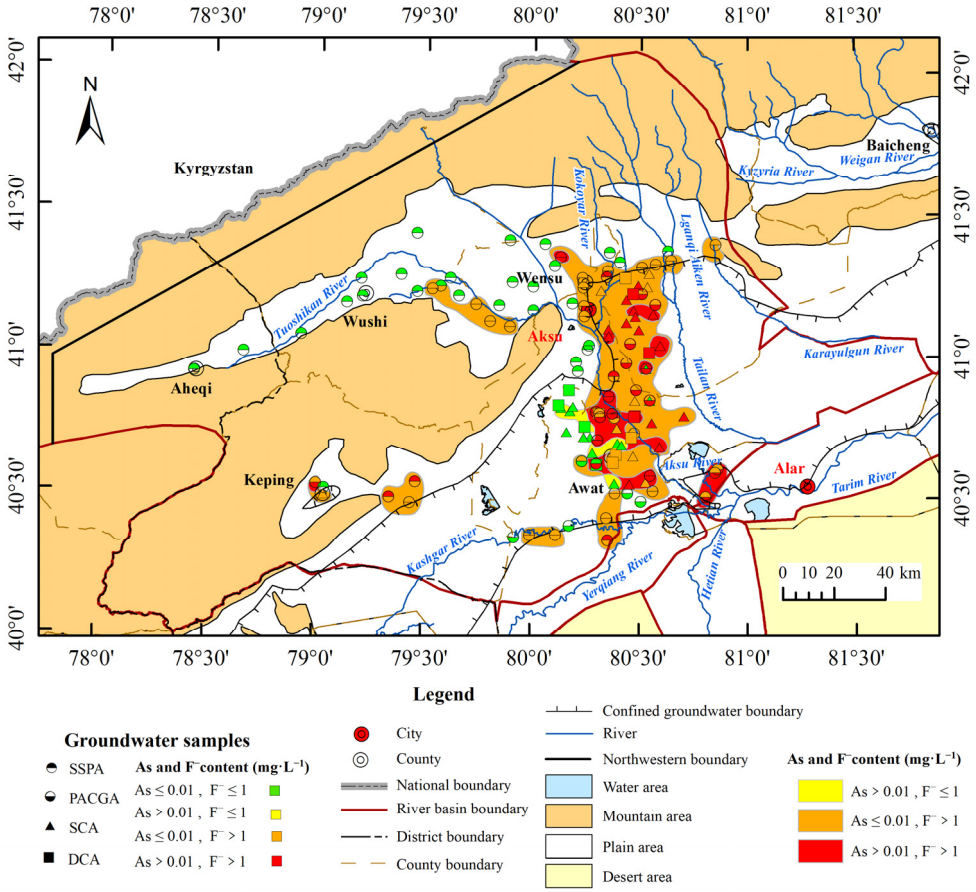

Figure 6. Distribution of groundwater with the co-enrichment of As-F.

3.2.2. Vertical Distribution

The over-standard rate of As in the groundwater in the study area was 26.09%; in more detail, the SSPA, PACGA, SCA, and DCA were 8.93% (5 samples), 25.81% (8 samples), 44.74% (17 samples), and 46.15% (6 samples), respectively. The vertical distribution of As in the groundwater system in the study area is shown in Figure 7a. It can be seen that high-As groundwater was mainly distributed in the PACGA at 10–20 m (depth) and in the SCA at 80–100 m (depth).

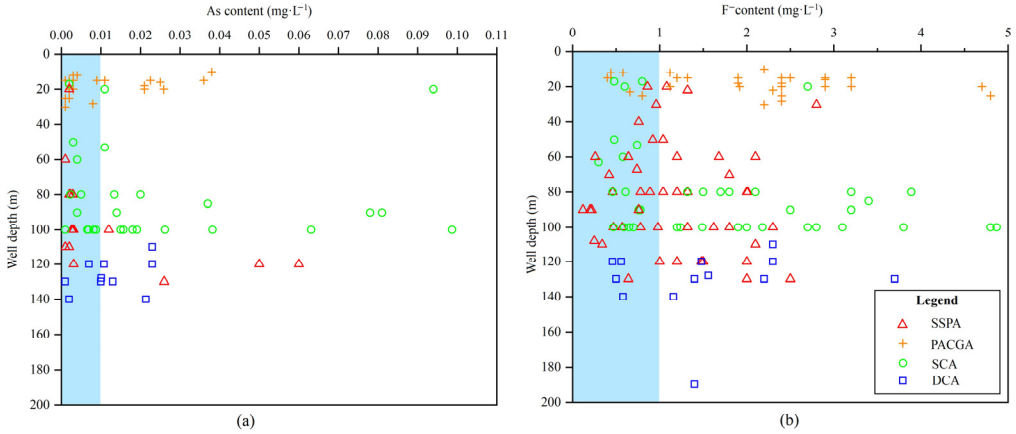

Figure 7. Relationship between groundwater As (**a**) and F (**b**) content and well depth.

The over-standard rate of F in the groundwater in the study area was 60.87%. More specifically, the over-standard rate of F in the SSPA, PACGA, SCA and DCA were 48.21% (27 samples), 80.65% (25 samples), 60.53% (23 samples), and 69.23% (9 samples). The vertical distribution of F in the groundwater system in the study area is shown in Figure 7b. It can be seen that high-F groundwater was mainly distributed in the PACGA at 10–30 m (depth) and in the SCA at 80–100 m (depth).

4. Genetic Analysis of Groundwater with the Co-Enrichment of As-F

4.1. Geological Conditions

Natural sources of As are mostly derived from gold, copper, lead, and other As-bearing minerals in the form of sulfides [26,27]. As-bearing minerals in rocks are the primary source of groundwater As, and the secondary enrichment of As in organisms and ferromanganese nodules is the secondary source of groundwater As. In nature, F is mostly present in F-containing minerals (such as fluorite, with the main component CaF_2). F released from parent rock weathering is the primary source of groundwater F, and F released from the leaching and desorption of soil and sedimentary rocks is the secondary source. The Aksu area is an important energy and mineral resource enrichment area in Xinjiang. The reserves and resources ranked first in Xinjiang are bauxite, fluorite, medical stone, etc. There are also widely distributed and large reserves of metal ores (including iron, copper, manganese, lead, zinc, gold, nickel, magnesium, etc.), coal, rock salt, fireclay, clay, quartz sand, basalt, granite, marble, phlogopite, and other minerals. Its associated indicator elements include As, Sb, Ag, and Hg [21].

In the Aksu River Basin, high-As groundwater was mainly distributed in the quaternary alluvial plain of the middle and lower reaches of the Aksu River; high-F groundwater was mainly distributed in the quaternary alluvial plain of the middle and lower reaches of the Aksu River, the diluvial plain of the Aksu River, and the Telan River; and a small amount of groundwater was distributed in the alluvial lacustrine plain of the lower reaches of the Kashgar River (Figure 8). As-F co-enriched groundwater was mainly distributed in the quaternary alluvial plain in the middle and lower reaches of the Aksu River and the flood plain in the interfluvial block of the Aksu River and Telan River. According to the geological conditions, the groundwater in the Aksu River Basin was identified as the primary high-As and high-F groundwater.

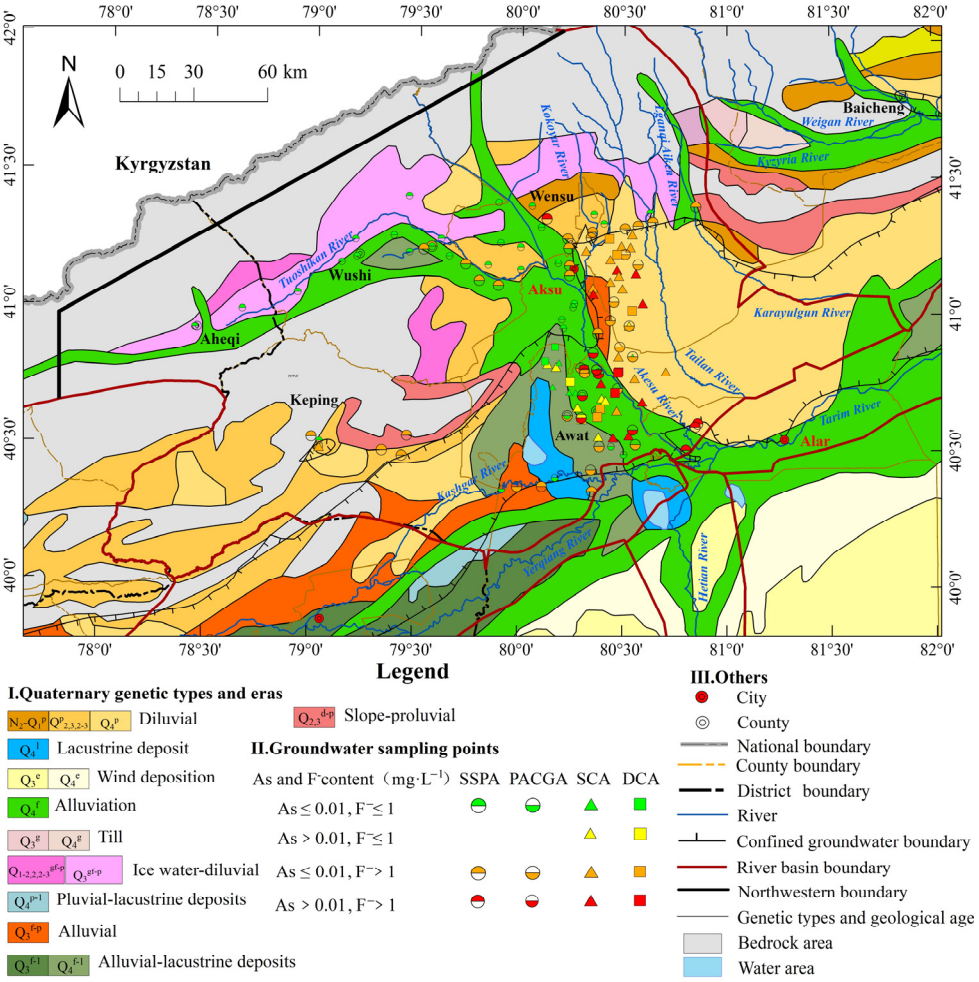

Figure 8. Quaternary geology and groundwater As-F content. Note: the quaternary genesis and geological age code are explained in Table S1.

4.2. Hydrogeological Effects

The Aksu River Basin is connected by a series of alluvial fans from north to south formed by a dozen rivers of different sizes. The upper part of the alluvial fans is a gravel belt composed of gravel with relatively single lithology, which is a good water-bearing medium. When it moves south to a fine soil plain, the medium is fine sand, silty sand, and clay soil, and the water-bearing medium presents strong heterogeneity. The transition area is the phreatic water overflow area. The sediments of the Tarim River alluvial plain in the southern part of the study area were mainly from the southern slope of the Tianshan Mountains. The water-bearing medium was mainly composed of powder, fine sand, and a thin layer of sub-clay and sub-sand, which was distributed in a strip from west to east. The thin sub-clay and sub-sandy layers were regional aquifuges [28]. The recharge area received the recharge of atmospheric precipitation and mountain bedrock fissure water. There were As-F-bearing minerals in the leaching aqueous medium. As-F in the groundwater migrated with groundwater flow to the transition area (with low topography and a low flow rate) and continuously flowed southeastward to the evaporation area. In the evaporation area, the sediment particles were fine, the runoff was blocked, and the groundwater was discharged through evaporation, resulting in the slow migration of groundwater As-F and the formation of the As-F co-enrichment in the groundwater.

4.3. Hydrochemical Environment of Groundwater Occurrence

4.3.1. Analysis of Groundwater Chemical Index Factors

Data processing software (SPSS 19.0) was used to conduct factor analysis on 18 groundwater indexes of the SSPA, PACGA, SCA, and DCA in the study area (Table 2). The KMO (Kaiser–Meyer–Olkin measure of sampling adequacy) test value of the SSPA was 0.574, and the Bartlett spherical test difference significance test value was 0.000 (<0.05 indicated a significant difference), indicating that the data could be used for factor analysis. The rotation factor load value of each index was obtained by calculating the component matrix using the maximum fifth power value method. The contribution rates of the main factors (F1, F2 and F3) were 40.52%, 13.90%, and 12.71%, respectively, and the cumulative contribution rate of the three main factors was 67.14%.

Table 2. Rotation factor load matrix of groundwater hydrochemical index.

Indexes	SSPA Factor Load			SCA Factor Load		
	F_1	F_2	F_3	F_1	F_2	F_3
K^+	**0.836**	0.294	−0.173	**0.637**	0.460	−0.518
Na^+	**0.970**	−0.074	0.136	**0.914**	−0.074	−0.285
Ca^{2+}	**0.958**	0.047	−0.049	**0.734**	0.334	−0.181
Mg^{2+}	**0.915**	0.297	−0.023	**0.862**	0.281	0.112
Cl^-	**0.965**	−0.115	0.114	**0.914**	−0.069	−0.304
$SO_4{}^{2-}$	**0.983**	0.012	0.036	**0.952**	0.031	0.035
$HCO_3{}^-$	−0.083	**0.882**	−0.190	0.157	**0.891**	−0.294
$NO_3{}^-$	0.058	0.065	−0.229	0.320	0.156	**−0.846**
$NO_2{}^-$	0.017	0.015	**0.949**	0.476	**−0.515**	0.320
Fe	0.127	**0.729**	0.338	−0.041	0.025	0.004
Mn	0.091	**0.733**	0.468	**0.599**	0.237	0.464
As	−0.007	0.147	**0.956**	−0.189	0.174	−0.025
F	**0.536**	0.281	0.265	0.318	**0.736**	0.245
TDS	**0.986**	−0.006	0.061	**0.972**	0.089	−0.175
TH	**0.959**	0.102	−0.101	**0.768**	0.457	−0.099
pH	0.072	0.116	−0.131	−0.388	−0.129	**0.850**
Eh	0.060	−0.202	−0.024	0.175	0.246	**0.528**
H_2SiO_3	0.424	**0.648**	0.050	0.154	**0.912**	0.104
Contribution rate %	40.524	13.904	12.708	36.532	17.190	14.575
Cumulative contribution rate %	40.524	54.428	67.136	36.532	53.722	68.297

The KMO test value of the SCA was 0.513, and the Bartlett spherical test difference significance test value was 0.000 (<0.05 indicated a significant difference), indicating that the data can be used for factor analysis. The rotation factor load value of each index was obtained by using the maximum seventh power value method to calculate the component matrix. The contribution rates of the main factors (F1, F2 and F3) were 36.532%, 17.190%, and 14.575%, respectively, and the cumulative contribution rate of the three main factors was 68.297%. The KMO test value of the PACGA was 0.344, and the KMO test value of the DCA was less than 0.300, both of which were less than 0.500, indicating that the control factors of the groundwater chemical process in this area were relatively complex and it was not suitable for factor analysis. Therefore, the rotation factor load matrix analysis was only carried out for the SSPA and SCA.

The results of the rotation factor load matrix showed that K^+, Na^+, Ca^{2+}, Mg^{2+}, Cl^-, $SO_4{}^{2-}$, F, TDSs, and TH have higher positive loads of F1 in the SSPA. The SSPA was mostly distributed in the groundwater recharge area near the mountain area, which had good groundwater flow conditions and relatively small evaporation and discharge. Na^+ was mainly derived from the weathering and dissolution of rock salt and sodium-containing minerals in sedimentary rocks. Ca^{2+} and Mg^{2+} were mainly derived from the weathering and dissolution of carbonate sediments and minerals containing calcium and magnesium.

Cl^- was mainly derived from the dissolution of rock salt and other chlorides in sedimentary rocks, and SO_4^{2-} was mainly derived from the dissolution of sedimentary rocks containing gypsum or other sulfate. F was mainly derived from the dissolution of F-containing minerals (such as fluorite). In summary, F1 was defined as the leaching factor of the groundwater. The indexes with higher factor loading in F2 were HCO_3, Fe, Mn, and H_2SiO_3. The Fe and Mn in the groundwater came mainly from the same source with similar migration and enrichment processes. The dissolution of As-Fe in the sediments was associated. As was adsorbed on the surface of Fe and Mn oxides. The bicarbonate solution can effectively extract As adsorbed on the surface of iron hydroxide, indicating that the bicarbonate solution can activate As in sediments, thereby replacing As on the surface of sediments and minerals and releasing it into the groundwater [29,30]. Therefore, F2 represented the adsorption release factor. The indexes with higher factor loading in F3 were NO_2^- and As. Due to the lack of human activities in the piedmont area and the deep groundwater, nitrite could be converted into ammonia nitrogen under an anaerobic environment. Ammonia nitrogen indicated a reduction environment. Therefore, F3 was a reductive environmental factor.

The indexes with the highest factor loading in the SCA for F1 were K^+, Na^+, Ca^{2+}, Mg^{2+}, Cl^-, SO_4^{2-}, Mn, TDSs, and TH. Rock leaching and intense evaporation–concentration had a great influence on the chemical composition of the water. The region is arid with little rain, a high groundwater table, strong evaporation, and slow groundwater flow, resulting in more intensive water–rock interaction. The ion concentration of each component was high, and the anions were mainly Cl^- and SO_4^{2-}. Therefore, this factor was considered a salinization factor. The indexes with higher factor loading in F2 were HCO_3^-, NO_2^-, F and H_2SiO_3. Inorganic/organic carbon sources played an important role in the formation of high-As groundwater. Dissolved carbonates can affect the adsorption of trace metals by competing for mineral surface sites, forming carbonate complexes to enhance or inhibit adsorption, and then forming precipitates. The activation of adsorbent As under the action of dissolved carbonate was considered to be one of the main reasons for the high-As in the groundwater [31]. The microbial degradation of organic matter had a significant promotion effect on the enrichment of As. The increased availability of carbon sources of micro-organisms promoted the metabolism of heterotrophic micro-organisms and consumed oxygen, and this finally formed a reducing environment conducive to the enrichment of groundwater As [32]. Therefore, F2 can be defined as a carbon-influencing factor. The indicators of high factor load in F3 were NO_3^-, pH, and Eh. Therefore, F3 was an alkaline-reducing environmental factor.

There were some limitations and uncertainties in terms of the statistical methods used in the assessment processes. The main limitation is that the factor analysis only considered the characteristics of the obtained data and ignored the hydrogeological characteristics of the study area (e.g., the potential variability in aquifers) to some extent because it was based on the principle of mathematical statistics. Despite these uncertainties, factor analysis has been widely used to determine the formation mechanisms of water chemistry [33]. Moreover, the results obtained from the factor analysis were similar to the interpretation based on the hydrogeological conditions and hydrochemical index.

4.3.2. Relationship Between As-F Content in Groundwater and Other Water Chemical Indexes

Groundwater with high As content generally has a high-HCO_3^- content (Figure 9a). Since HCO_3^- can compete with As for adsorption sites on the surface of iron and manganese oxides, this results in the desorption of As in groundwater. A high content of HCO_3^- can also replace the F adsorbed on the surface of soil colloids [34]. The HCO_3^- content in the groundwater in the study area was up to 573.7 $mg \cdot L^{-1}$. The high HCO_3^- content may result from intensive evaporation–concentration and organic degradation [35]. The concentration of As-F in groundwater increased with the increase in HCO_3^- content.

Therefore, the high content of HCO_3^- was one of the factors affecting the co-enrichment of As-F in the groundwater.

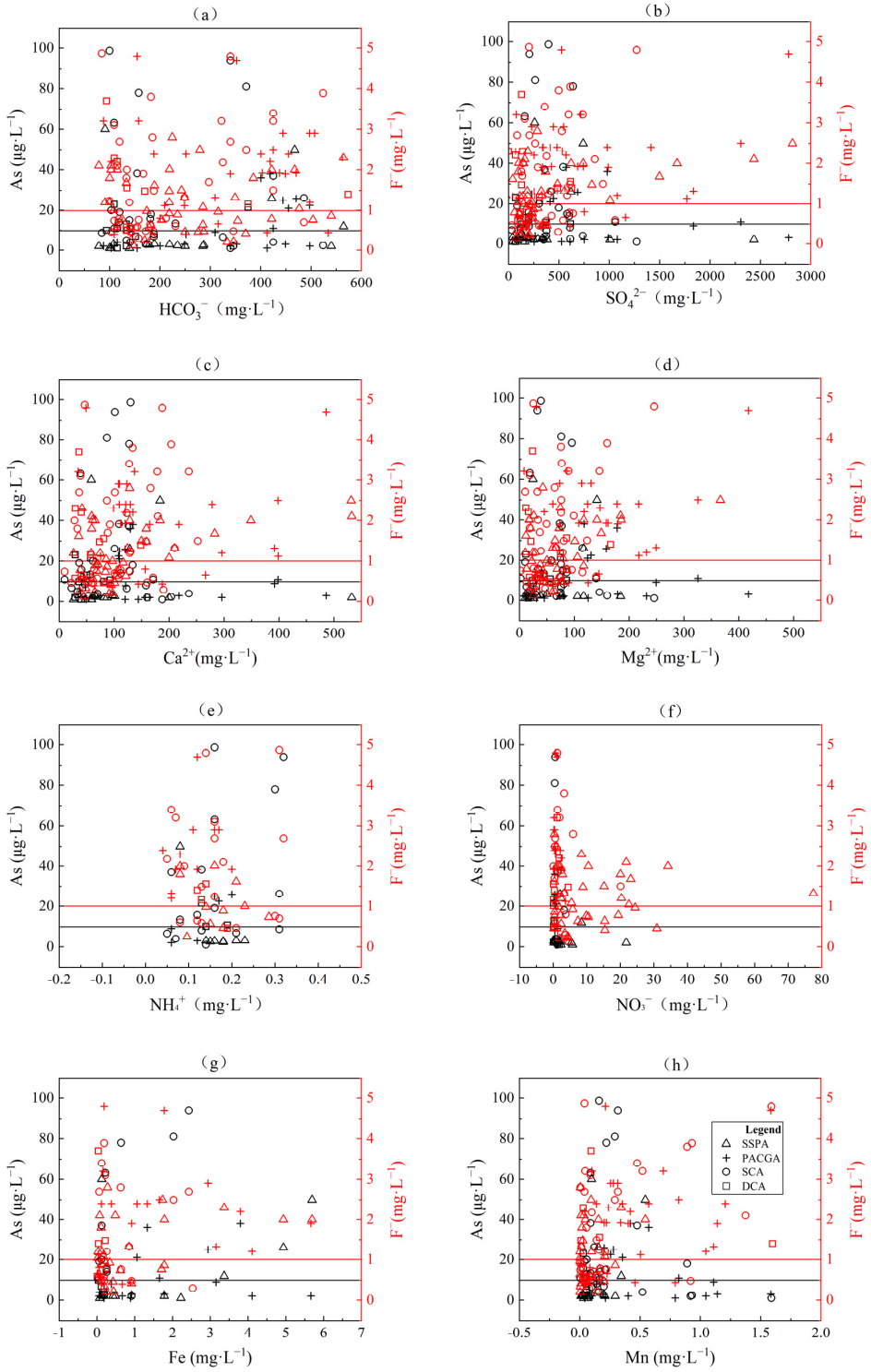

Figure 9. Relationship between As-F content and other hydrochemical indexes in the groundwater. (**a**) Relationship between As-F content and HCO^- in the groundwater; (**b**) Relationship between As-F content and SO_4^{2-} in the groundwater; (**c**) Relationship between As-F content and Ca^{2+} in the groundwater; (**d**) Relationship between As-F content and Mg^{2+} in the groundwater; (**e**) Relationship between As-F content and NH_4^+ in the groundwater; (**f**) Relationship between As-F content and NO_3^- in the groundwater; (**g**) Relationship between As-F content and Fe in the groundwater; (**h**) Relationship between As-F content and Mn in the groundwater.

The SO_4^{2-} content in the high-As groundwater was generally low (Figure 9b), indicating a strong reducing environment. As a whole, the F content in the groundwater decreased with increasing Ca^{2+} and Mg^{2+} contents (Figure 9c,d). The dissolution equilibrium of CaF_2 was an important factor controlling the concentration of F in the groundwater. The low concentration of Ca^{2+} and Mg^{2+} was conducive to F enrichment. When the mass concentration of Ca^{2+} and Mg^{2+} increased beyond the saturation of CaF_2 and MgF_2, F precipitation with Ca^{2+} and Mg^{2+} resulted in a decrease in F ion content in the water [36]. High-As groundwater was generally low in NO_3^- and high in NH_4^+ (Figure 9e,f), indicating a strong reducing environment, and NO_3^- in the groundwater could be reduced to NH_4^+, NO_2^- or N_2 [37]. The chemical properties of Fe and Mn are similar. Studies show that iron and manganese oxides and hydroxides can be reduced to highly soluble Fe^{2+} and Mn^{2+} under a reducing environment so that adsorbed As on the mineral surface can be desorbed and released into groundwater [38]. The As content of the groundwater tended to increase with the increase in Fe and Mn concentrations (Figure 9g,h), indicating that the enrichment of groundwater As was related to the reductive dissolution of iron and manganese oxides [39,40].

4.3.3. Oxidation–Reduction Environment

The groundwater in the study area was under a reducing and sub-oxidizing environment, which played an important role in the migration and enrichment of As; this can be seen from the relationship between groundwater Eh and As-F in the Aksu River Basin (Figure 10a). The Eh of As-F co-enrichment ranged from −70.0 to 244.0 mV, with an average of 82.9 mV, which was much smaller than that of the As-F (single) exceeding the standard (average of 162.4 mV) and the non-exceeding standard (142.4 mV) of groundwater. In the oxidizing environment, the As compounds in the groundwater were adsorbed by colloids or iron–manganese oxides or hydroxides. However, in the reducing environment, when the redox potential reached a certain level, the colloid which became unstable or the iron (manganese) oxide or hydroxide with strong adsorption capacity for As was reduced. More active low-valent iron (manganese) ions with great solubility were generated, and the As adsorbed on their surfaces was also released into the groundwater. In such groundwater, high As was often associated with high iron, high manganese, low dissolved oxygen, and low SO_4^{2-} [41]. Therefore, the content of As and SO_4^{2-} in groundwater with high As was generally negatively correlated. This relationship suggested that As migrated under intense reducing conditions, in parallel with the reduction of SO_4^{2-} [42]. In addition, the oxidation of As-containing minerals such as pyrite can also lead to the release of As in an oxidizing environment [43,44].

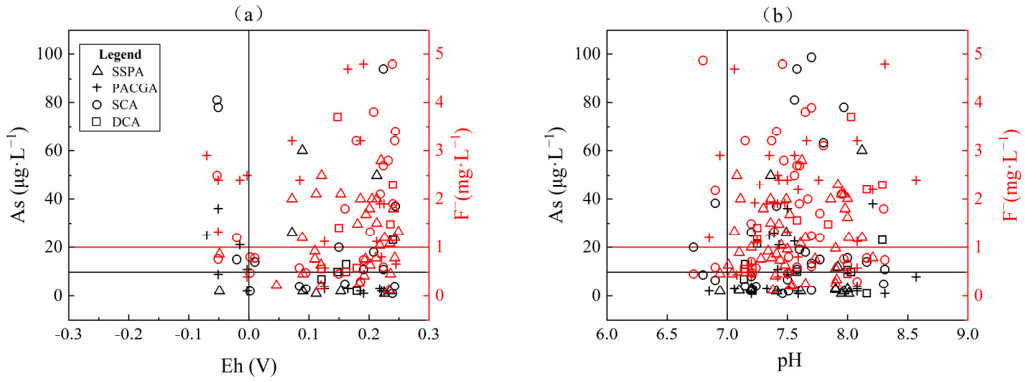

Figure 10. Relationship between As-F content and Eh (**a**) and pH (**b**) in groundwater. (**a**) Relationship between As-F content and Eh in the groundwater; (**b**) Relationship between As-F content and pH in the groundwater.

4.3.4. pH Value

The pH value of high-As-F groundwater (Figure 10b) ranged from 7.3 to 8.3 (with an average of 7.7), which was higher than that of low-As-F groundwater (average of 7.5) or groundwater with a single index (As or F) exceeding the standard (average of 7.5). The neutral–weakly alkaline environment was favorable for the co-enrichment of As-F in groundwater. As mainly occurred in the form of arsenate and arsenite in groundwater with a pH of 7–9. With the increase in pH value, colloids and clay minerals loaded more negative charge, which inhibited As adsorption and facilitated As desorption due to high groundwater pH leading to As enrichment in the groundwater. This was the same as the results of previous studies that found that groundwater with high As was generally weakly alkaline [45]. The pH value of groundwater had a decisive effect on the occurrence state of F in the water. In neutral–alkaline groundwater (pH of 7–9), there were more than 10 forms of F, such as F^-, $BF(OH)_3$, HF_{aq}, CaF^+, AlF^{2+}, MgF^+, $AlF_3{}^0$, and $AlF_4{}^-$. Alkaline and semi-alkaline water reduced the activity of Ca^{2+} in the water, thus weakening the effect of F aggregation in the water, which was conducive to the enrichment of F in the groundwater [46].

5. Formation Mechanism and Function of Groundwater Water Chemistry

5.1. Analysis of Water Chemical Formation Mechanism

A Gibbs diagram was often used to analyze the formation mechanism of the groundwater hydrochemical characteristics. When $\gamma Na^+/\gamma(Na^+ + Ca^{2+})$ or $\gamma Cl^-/\gamma(Cl^- + HCO_3{}^-)$ was greater than 0.5 and the TDSs were low, it indicated that atmospheric precipitation was the main factor affecting the chemical composition of the groundwater. When $\gamma Na^+/\gamma(Na^+ + Ca^{2+})$ or $\gamma Cl^-/\gamma(Cl^- + HCO_3{}^-)$ was less than 0.5 and TDSs were medium, it indicated that rock weathering was the main factor affecting the chemical composition of the groundwater. When $\gamma Na^+/\gamma(Na^+ + Ca^{2+})$ or $\gamma Cl^-/\gamma(Cl^- + HCO_3{}^-)$ was greater than 0.5, and the TDSs were high, it indicated that evaporation and concentration were the main factors affecting the chemical composition of the groundwater [47,48]. Intensive evaporation and concentration processes facilitate the formation of an alkaline environment and reduction conditions. Under weakly alkaline and alkaline conditions, the pH of the groundwater was usually higher than the boundary point of the surface charge properties (pHZ) of most rocks, minerals, and sediments. When pH > pHZ, the surface charge was negatively charged. The arsenic in the groundwater was usually found in the form of complex oxygen anions. The electrostatic repulsion generated caused the desorption of arsenic, resulting in an increase in arsenic content in the groundwater. In neutral and slightly alkaline aquifers, the decrease in the activity of calcium ions inhibited the formation of CaF_2 and was conducive to the enrichment of fluoride ions in the groundwater [49].

The TDSs of the groundwater generally ranged from 200 to 900 $mg \cdot L^{-1}$, indicating that the value was medium to large. The Gibbs diagram (Figure 11) showed that $\gamma Na^+/\gamma(Na^+ + Ca^{2+})$ and $(\gamma Cl^-/\gamma Cl^- + HCO_3{}^-)$ in the SSPA were mostly less than 0.5, indicating that rock weathering was the main influencing factor. $\gamma Na^+/\gamma(Na^+ + Ca^{2+})$ was more than 0.5 and $\gamma Cl^-/\gamma(Cl^- + HCO_3{}^-)$ was less than 0.5 in the PACGA, showing that the main influencing factors were evaporation and concentration and rock weathering. $\gamma Na^+/\gamma(Na^+ + Ca^{2+})$ and $\gamma Cl^-/\gamma(Cl^- + HCO_3{}^-)$ were mostly less than 0.5 in the SCA, indicating that rock weathering was the main influencing factor. $\gamma Na^+/\gamma(Na^+ + Ca^{2+})$ and $\gamma Cl^-/\gamma(Cl^- + HCO_3{}^-)$ were mostly less than 0.5 in the DCA, which indicated that rock weathering was the main influencing factor. In the heavy mineral composition of the quaternary sediments in this river basin, fluorine-containing minerals such as hornblende and mica were dominant, accounting for 45% of the total heavy minerals [20]. In the northern mountainous area, there are medium-sized arsenic mines and large iron mines [50]. The dissolution of these minerals simultaneously increased the concentrations of As and F in the groundwater.

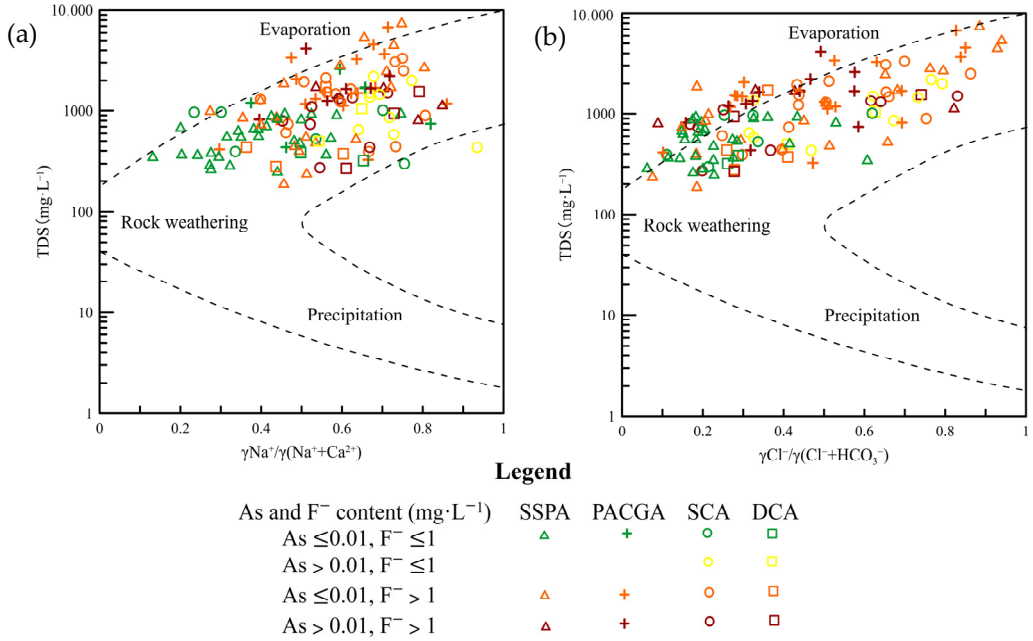

Figure 11. Relationship between TDSs and $\gamma Na^+/\gamma(Na^+ + Ca^{2+})$ (**a**) and $\gamma Cl^-/\gamma(Cl^- + HCO_3^-)$ (**b**).

The ratio of $\gamma Na^+/\gamma(Na^+ + Ca^{2+})$ and $\gamma Cl^-/\gamma(Cl^- + HCO_3^-)$ in As-F co-enriched groundwater was mostly greater than 0.5 and less than 0.5, respectively, indicating that evaporation and rock weathering were the main influencing factors; that in the high-As or -F groundwater was greater than 0.5, indicating that evaporation and concentration were the main influencing factors [51].

5.2. Identification of Rock Weathering Sources

Rock weathering sources with groundwater chemical characteristics were further determined by the ratio end element graph method of $\gamma Ca^{2+}/\gamma Na^+$ and $\gamma HCO_3^-/\gamma Na^+$ [52,53].

In Figure 12, it can be seen that the groundwater is mainly distributed near the silicate rock, in which the points of As-F co-enrichment and high-As or -F groundwater were mostly distributed near the silicate rock, while low-As-F groundwater is mostly distributed between the silicate rock and carbonate rock. Therefore, it can be concluded that the enrichment of As-F was mainly affected by the weathering and dissolution of silicate rock. This is consistent with the result of the factor analysis in that the enrichment of arsenic and fluorine ions the in groundwater was affected by the weathering and dissolution of evaporite and silicate minerals.

5.3. Leaching Effect

According to the SI of each mineral phase in the groundwater (Figure 13), it can be seen that calcite and dolomite were mainly at saturation or in an equilibrium state in each aquifer. Gypsum and rock salt were mainly dissolved in each aquifer, and the average absolute value of the saturation index of gypsum and rock salt was the smallest in high-F groundwater. The average absolute value of the saturation index of gypsum and rock salt in the As-F co-enriched aquifer was slightly higher. The average absolute value of the saturation index of gypsum and rock salt was the highest in the aquifer where As-F was not exceeded. The results show that gypsum and rock salt in high-As-F groundwater were in a solubility equilibrium state. This is consistent with the fact that SO_4·Cl-Na·Mg (Na·Ca·Mg) was the main chemical type of the groundwater with As-F co-enrichment or high-As (or -F) groundwater.

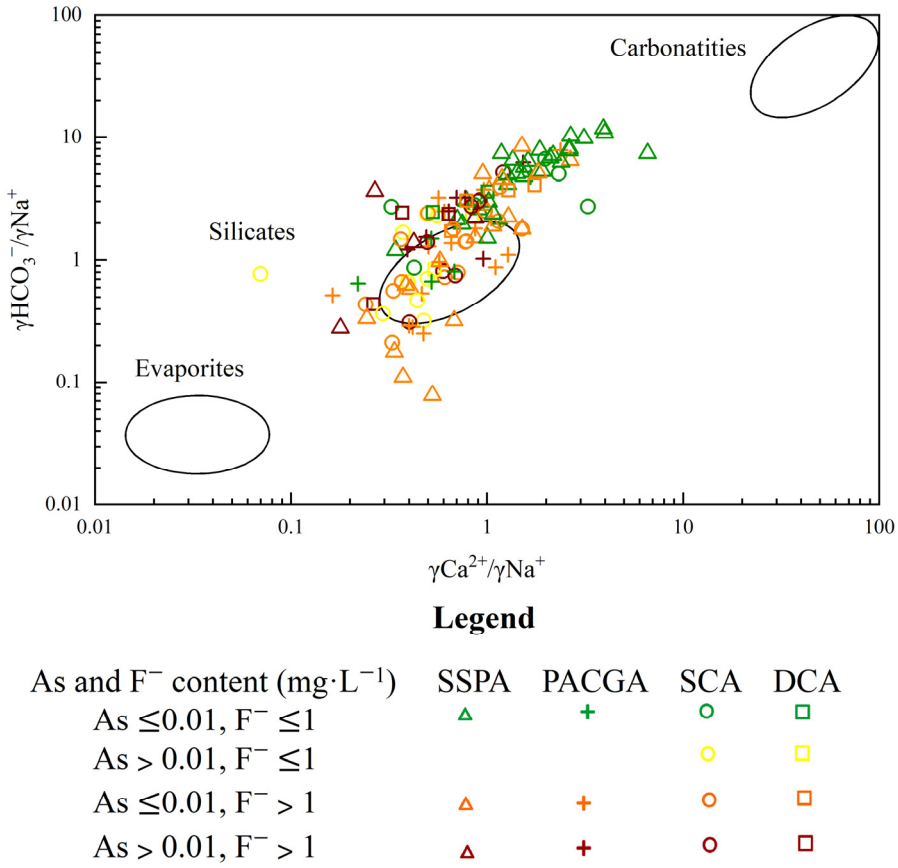

Figure 12. Endmember diagram of groundwater ion ratio.

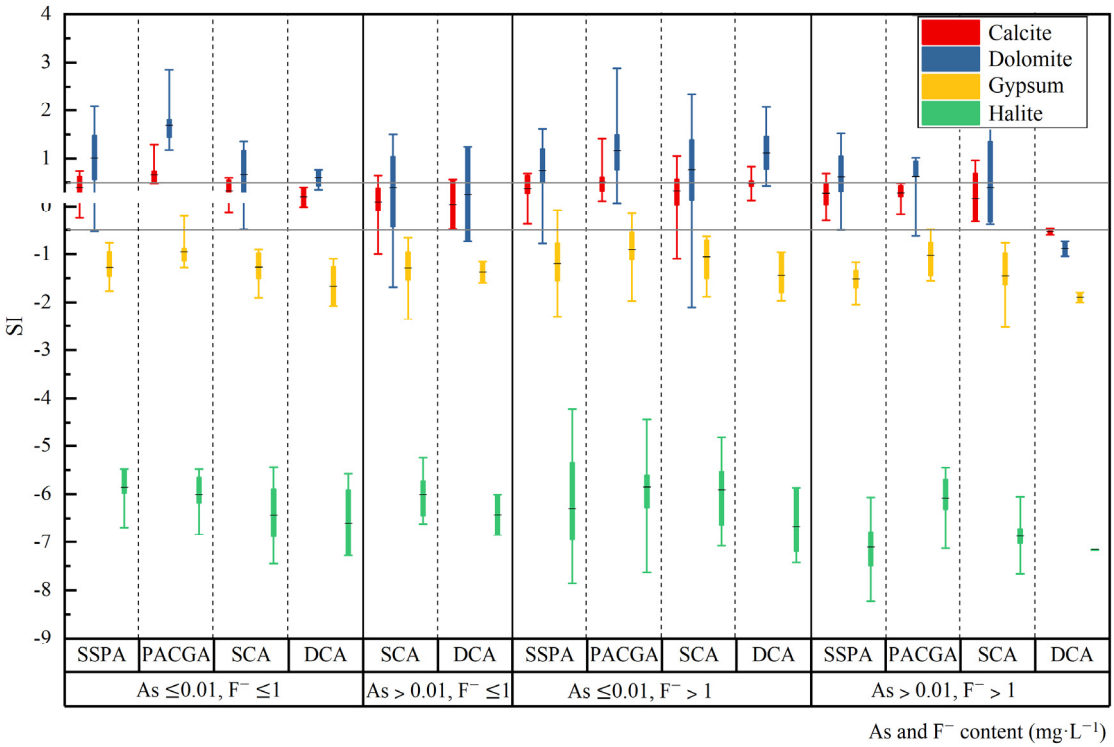

Figure 13. Mineral saturation index in the groundwater.

5.4. Cation Alternating Adsorption

According to the distribution of groundwater CAI-1 and CAI-2 (Figure 14), it can be seen that the groundwater CAI-1 and CAI-2 were mostly positive, indicating the ion exchange of groundwater Na^+ and K^+ with Ca^{2+} and Mg^{2+} in the aqueous medium. The CAI of the groundwater with As-F co-enrichment in the phreatic aquifers (including SSPA and PACGA) was mostly positive, while the groundwater CAI in the confined aquifers (including SCA and DCA) was mostly negative. Therefore, cation alternating adsorption was one of the important reasons affecting the As-F co-enrichment of the groundwater.

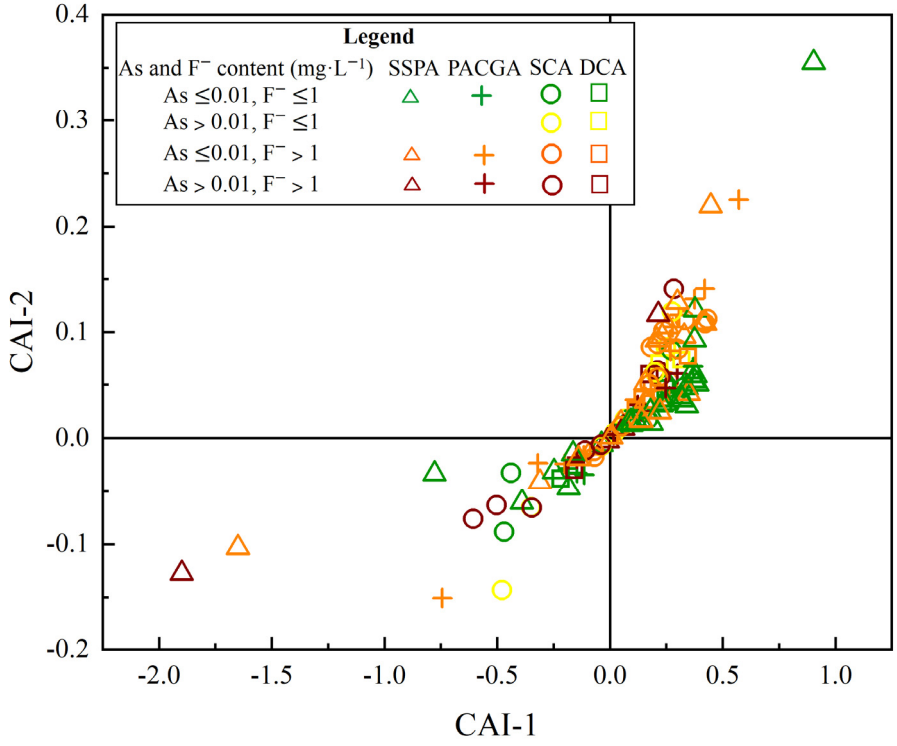

Figure 14. Distribution of groundwater CAI-1 and CAI-2.

6. Conclusions

In the plain area of the Aksu River Basin in Xinjiang, the groundwater As content ranged from <0.001 to 0.099 mg·L^{-1}, with an average of 0.010 mg·L^{-1}. High-As groundwater accounted for 26.09% of the total samples. The groundwater F content ranged from <0.1 to 4.9 mg·L^{-1} with an average of 1.5 mg·L^{-1}. High-F groundwater accounted for 60.87% of the total samples. The As-F co-enriched samples accounted for 18.12% of the total samples.

The main hydrochemical types of the groundwater were HCO_3·SO_4-Ca·Mg and SO_4·Cl-Na·Mg. The groundwater hydrochemistry types of As-F co-enrichment in SSPA, PACGA, SCA, and DCA were Cl·SO_4-Na, SO_4·HCO_3·Cl-Mg·Na·Ca, HCO_3·SO_4-Ca·Na (Mg·Ca), and HCO_3·SO_4·Cl-Na·Ca, respectively. The groundwater chemical types of As-F co-enrichment in the recharge area, transition area, and evaporation area were mainly HCO_3·SO_4-Na·Mg, HCO_3·SO_4-Na·Ca (Mg·Ca), and SO_4·Cl-Na·Mg, respectively.

Groundwater with As-F co-enrichment was mainly distributed in the transition and evaporation areas of the middle and lower reaches of the Aksu River Basin. The area is close to the edge of the desert, where the groundwater runoff is slow and the groundwater is under a reducing-alkaline environment. Vertically, high-As groundwater was concentratedly distributed in the PACGA at a depth of 10–20 m and in the SCA at depth of 80–100 m; high-F groundwater was concentratedly distributed in the PACGA at a depth of 10–30 m and in the SCA at a depth of 80–100 m.

As-F co-enriched groundwater was affected by intensive evaporation–concentration and silicate rock weathering. Gypsum and rock salt in the groundwater showed a generally

balanced dissolution state, and Na^+ and K^+ were exchanged with Ca^{2+} and Mg^{2+} in an aqueous medium.

The hydrochemical characteristics of the groundwater in the Aksu River Basin were closely related to the geological conditions, hydrogeological conditions, and hydrochemical environment of the groundwater. As-F co-enriched groundwater was mainly affected by a small topographic gradient, shallow groundwater depth, a weak reducing–alkaline groundwater environment, strong evaporation and concentration, weathering and dissolution of evaporated salt rock, and alternating adsorption of cations.

The innovation of this study is mainly reflected in the following two aspects. In terms of mechanism research, the mechanism of arsenic and fluorine co-enrichment, as well as the migration and transformation of groundwater in typical watersheds in arid inland areas, was clarified. We conclude that the formation of arsenic and fluorine co-enriched groundwater in the study area was mainly related to the dissolution of fluorite, realgar, and orpiment. In terms of research methods, based on field investigation, comprehensive isotope techniques, as well as hydrogeochemical modeling, were used to study the migration and transformation rules of arsenic and fluorine in groundwater; the contribution of key migration and transformation pathways to arsenic and fluorine in groundwater was quantitatively analyzed, which provides a reference case for the study of the arsenic and fluorine co-enrichment mechanism in groundwater in similar areas.

Supplementary Materials: The following supporting information can be downloaded at: https://www.mdpi.com/article/10.3390/w16223201/s1, Table S1: The Quaternary genesis and geological age code.

Author Contributions: Software, Y.S.; Resources, X.Z.; Data curation, M.L.; Writing—original draft, Y.J. and Y.Z.; Writing—review & editing, J.Z. All authors have read and agreed to the published version of the manuscript.

Funding: This research work was financially supported by the National Natural Science Foundation of China (No. 42067035 and 42007161).

Data Availability Statement: No new data were created or analyzed in this study.

Conflicts of Interest: The authors declare no conflict of interest.

References

1. Kumar, M.; Goswami, R.; Patel, A.K.; Srivastava, M.; Das, N. Scenario, perspectives and mechanism of arsenic and fluoride co-occurrence in the groundwater: A review. *Chemosphere* **2020**, *249*, 126126. [CrossRef] [PubMed]
2. World Health Organization. *Guidelines for Drinking Water Quality*; WHO: Geneva, Switzerland, 1993. Available online: https://www.who.int/teams/global-tuberculosis-programme/tb-reports/ (accessed on 20 August 2024).
3. Graham, N. Guidelines for drinking-water quality, 2nd edition, addendum to volume 1-recommendations, World Health Organisation, Geneva, 1998, 36 pages. *Urban Water* **1999**, *1*, 183. [CrossRef]
4. Zhang, Y.; Wu, X.X.; Zhang, H.Y.; Du, Z.M. Anti-leukemia effect and toxicity of arsenic trioxide: A review. *Chin. J. Pharmacol. Toxicol.* **2017**, *31*, 675–681. [CrossRef]
5. Jomova, K.; Jenisova, Z.; Feszterova, M.; Baros, S.; Liska, J.; Hudecova, D.; Rhodes, C.J.; Valko, M. Arsenic: Toxicity, oxidative stress and human disease. *J. Appl. Toxicol.* **2011**, *31*, 95–107. [CrossRef]
6. Rao, N.S. High-fluoride groundwater. *Environ. Monit. Assess.* **2011**, *176*, 637–645. [CrossRef] [PubMed]
7. Everett, E.T. Fluoride's effects on the formation of teeth and bones, and the influence of genetics. *J. Dent. Res.* **2011**, *90*, 552–560. [CrossRef]
8. Das, N.; Deka, J.P.; Shim, J.; Patel, A.K.; Kumar, A.; Sarma, K.P.; Kumar, M. Effect of river proximity on the arsenic and fluoride distribution in the aquifers of the Brahmaputra Floodplains, Assam, Northeast India. *Groundw. Sustain. Dev.* **2016**, *2–3*, 130–142. [CrossRef]
9. Das, N.; Sarma, K.P.; Patel, A.K.; Deka, J.P.; Das, A.; Kumar, A.; Shea, P.J.; Kumar, M. Seasonal disparity in the co-occurrence of arsenic and fluoride in the aquifers of the Brahmaputra Flood Plains, Northeast India. *Environ. Earth Sci.* **2017**, *76*, 183. [CrossRef]
10. Patel, A.K.; Das, N.; Goswami, R.; Kumar, M. Arsenic mobility and potential co-leaching of fluoride from the sediments of three tributaries of the Upper Brahmaputra Floodplain, Lakhimpur, Assam, India. *J. Geochem. Explor.* **2019**, *203*, 45–58. [CrossRef]
11. Guo, H.M.; Zhang, Y.; Xing, L.N.; Jia, Y.F. Spatial variation in arsenic and fluoride concentrations of shallow groundwater from the town of Shahai in the Hetao Basin, Inner Mongolia. *Appl. Geochem.* **2012**, *27*, 2187–2196. [CrossRef]

12. Alarcón-Herrera, M.T.; Bundschuh, J.; Nath, B.; Nicolli, H.B.; Gutierrez, M.; Reyes-Gomez, V.M.; Nuñez, D.; Martín-Dominguez, I.R.; Sracek, O. Co-occurrence of arsenic and fluoride in groundwater of semi-arid regions in Latin America: Genesis, mobility and remediation. *J. Hazard. Mater.* **2013**, *262*, 960–969. [CrossRef] [PubMed]
13. Anawar, H.M.; Akai, J.; Mihaljevič, M.; Sikder, A.M.; Ahmed, G.; Tareq, S.M.; Rahman, M.M. Arsenic contamination in groundwater of Bangladesh: Perspectives on geochemical, microbial and anthropogenic issues. *Water* **2011**, *3*, 1050–1076. [CrossRef]
14. Wang, Y.X.; Li, J.X.; Ma, T.; Xie, X.J.; Deng, Y.M.; Gan, Y.Q. Genesis of geogenic contaminated groundwater: As, F and I. *Crit. Rev. Environ. Sci. Technol.* **2020**, *51*, 2895–2933. [CrossRef]
15. Luan, F.J.; Zhou, J.L.; Zeng, Y.Y.; Gao, Y.X.; Liu, J.T. Distribution characteristics and enrichment factors of fluorine in groundwater in typical areas of Southern Xinjiang. *Environ. Chem.* **2016**, *35*, 1203–1211. [CrossRef]
16. Fan, W.; Zhou, J.L.; Zhou, Y.Z.; Zeng, Y.Y.; Chen, Y.F.; Chudaev, O.; Kharaka, Y.; Harmon, R.; Millot, R.; Shouakar-Stash, O. Factors influencing the distribution of arsenic, fluorine and iodine in shallow groundwater in the oasis zone in the southern margin of the Tarim Basin in Xinjiang, P.R. China. *E3S Web Conf.* **2019**, *98*, 09006. [CrossRef]
17. Zhou, Y.Z.; Zeng, Y.Y.; Zhou, J.L.; Guo, H.M.; Li, Q.; Jia, R.L.; Chen, Y.F.; Zhao, J.T. Distribution of groundwater arsenic in Xinjiang, P.R. China. *Appl. Geochem.* **2016**, *77*, 116–125. [CrossRef]
18. Wang, L. Study on the Law of Water and Salt Migration and Dynamic Regulation of Diving Level in the Vadose Zone in the Salinized Area of the Aksu River Basin. Master's Thesis, Xinjiang University, Urumchi, China, 2020.
19. Tang, L.J.; Qiu, H.J.; Yun, L.; Yang, Y.; Huang, T.Z.; Wang, P.H.; Xie, D.Q.; Li, M.; Jiang, H.S. Analysis of basin mountain coupling and transition of the Northern Tarim Basin Southern Tianshan Orogenic Belt. *Earth Sci. Front.* **2012**, *19*, 195–204.
20. Fu, W. The distribution of fluoride in the natural environment of the Aksu River Basin and a chemical analysis of the water in Endemic Fluorosis Regions. *J. Appl. Sci.* **2002**, *20*, 197–201.
21. Wang, Y.F.; Li, W.L. Metallogenic geological features and ore controlling factors in Akesu area. *Min. Resour.* **2018**, *11*, 102+104. [CrossRef]
22. Zhou, J.L.; Sun, Y.; Zeng, Y.Y.; Zhou, Y.Z.; Fan, W.; Zhao, J.T.; Li, L.; Ji, Y.Y. *Study on Groundwater Water Quality in the Oasis Area of Tarim Basin*; China Light Industry Press: Beijin, China, 2023.
23. Wang, Y.N.; Li, S.; Yu, B. Spatial variability analysis of permeability coefficient in Aksu River Basin. *China Rural Water Hydropower.* **2021**, *1*, 64–70+75. [CrossRef]
24. Chen, J.S.; Zhou, J.L.; Zeng, Y.Y.; Zhang, J. Spatial distribution and enrichment factors of high-arsenic groundwater in the plain area of Aksu Prefecture, Xinjiang. *Environ. Chem.* **2021**, *40*, 254–262. [CrossRef]
25. Rashid, A.; Guan, D.X.; Farooqi, A.; Khan, S.; Zahir, S.; Jehan, S.; Khattak, S.A.; Khan, M.S.; Khan, R. Fluoride prevalence in groundwater around a fluorite mining area in the flood plain of the River Swat, Pakistan. *Sci. Total Environ.* **2018**, *635*, 203–215. [CrossRef] [PubMed]
26. Wang, Y.X.; Shvartsev, S.L.; Su, C.L. Genesis of arsenic/fluoride-enriched soda water: A case study at Datong, northern China. *Appl. Geochem.* **2009**, *24*, 641–649. [CrossRef]
27. Jin, H.Z. Mineral resources distribution and the current exploration situation in Akesu area, Xinjiang. *Min. Explor.* **2017**, *8*, 325–330. [CrossRef]
28. Ye, H.C.; Chen, G.X. Groundwater resources and its rational development and utilization in Aksu area. *J. Tarim Univ. Agr. Reclam.* **2000**, *3*, 64–67.
29. Nickson, R.T.; McArthur, J.M.; Ravenscroft, P.; Burgess, W.G.; Ahmed, K.M. Mechanism of arsenic release to groundwater, Bangladesh and West Bengal. *Appl. Geochem.* **2000**, *15*, 403–413. [CrossRef]
30. Anawar, H.M.; Akai, J.; Sakugawa, H. Mobilization of arsenic from subsurface sediments by effect of bicarbonate ions in groundwater. *Chemosphere* **2004**, *54*, 753–762. [CrossRef] [PubMed]
31. Garcia, S.A.; Moyano, A.; Mayorga, P. High arsenic contents in groundwater of central Spain. *Environ. Geol.* **2005**, *47*, 847–854. [CrossRef]
32. Zheng, Y.; Stute, M.; Van Geen, A.; Gavrieli, I.; Dhar, R.; Simpson, H.J.; Schlosser, P.; Ahmed, K.M. Redox control of arsenic mobilization in bangladesh groundwater. *Appl. Geochem.* **2004**, *19*, 201–214. [CrossRef]
33. Qin, B.; Li, J.X. Hydrochemistry and occurrence of high fluoride groundwater in Datong Basin. *Geol. Sci. Technol. Inform.* **2009**, *31*, 3106.
34. Anawar, H.M.; Akai, J.; Komaki, K.; Terao, H.; Yoshioka, T.; Ishizuka, T.; Safiullah, S.; Kato, K. Geochemical occurrence of arsenic in groundwater of Bangladesh: Sources and mobilization processes. *J. Geochem. Explor.* **2003**, *77*, 109–131. [CrossRef]
35. Hasan, A.M.; Ahmed, M.K.; Sracek, O.; Bhattacharya, P.; Brömssen, M.V.; Broms, S.; Fogelström, J.; Mazumder, L.M.; Jacks, G. Arsenic in Shallow groundwater of Bangladesh: Investigations from three different physiographic settings. *Hydrogeol. J.* **2007**, *15*, 1507–1522. [CrossRef]
36. Gutiérrez, M.; Alarcón-Herrera, M.T.; Gaytán-Alarcón, A.P. Arsenic and fluorine in groundwater in northern Mexico: Spatial distribution and enrichment factors. *Environ. Monit. Assess.* **2023**, *195*, 212. [CrossRef] [PubMed]
37. Thornton, S.F.; Quigley, S.; Spence, M.J.; Banwart, A.S.; Bottrell, S.; Lerner, N.D. Processes controlling the distribution and natural attenuation of dissolved phenolic compounds in a deep sandstone aquifer. *J. Contam. Hydrol.* **2001**, *53*, 233–267. [CrossRef]
38. Guo, H.M.; Zhang, B.; Li, Y.; Berner, Z.; Tang, X.H.; Norra, S.; Stüben, D. Hydrogeological and biogeochemical constrains of as mobilization in shallow aquifers from the Hetao basin, Inner Mongolia. *Environ. Poll.* **2011**, *159*, 876–883. [CrossRef] [PubMed]

39. Han, S.B.; Zhang, F.C.; Zhang, H.; An, Y.H.; Wang, Y.S.; Wu, X.; Wang, C. Spatial and temporal patterns of groundwater arsenic in shallow and deep groundwater of Yinchuan Plain, China. *J. Geochem. Explor.* **2013**, *135*, 71–78. [CrossRef]
40. Xie, X.J.; Ellis, A.; Wang, Y.X.; Xie, Z.M.; Duan, M.Y.; Su, C.L. Geochemistry of redox-sensitive elements and sulfur isotopes in the high arsenic groundwater system of Datong Basin, China. *Sci. Total Environ.* **2009**, *407*, 3823–3835. [CrossRef]
41. Fakhreddine, S.; Prommer, H.; Scanlon, B.R.; Ying, S.C.; Nicot, J.P. Mobilization of arsenic and other naturally occurring contaminants during managed aquifer recharge: A critical review. *Environ. Sci. Technol.* **2021**, *55*, 2208–2223. [CrossRef]
42. Smedley, P.L.; Kinniburgh, D.G. A review of the source, behaviour and distribution of arsenic in natural waters. *Appl. Geochem.* **2002**, *17*, 517–568. [CrossRef]
43. Guo, H.M.; Zhou, Y.Z.; Jia, Y.F.; Tang, X.H.; Li, X.F.; Shen, M.M.; Lu, H.; Han, S.B.; Wei, C.; Norra, S.; et al. Sulfur cycling-related biogeochemical processes of arsenic mobilization in the western Hetao Basin, China: Evidence from multiple isotope approaches. *Environ. Sci. Technol.* **2016**, *50*, 12650–12659. [CrossRef]
44. Mukherjee, A.; Coomar, P.; Sarkar, S.; Johannesson, K.H.; Fryar, A.E.; Schreiber, M.E.; Schreiber, M.E.; Ahmed, K.M.; Alam, M.A.; Bhattacharya, P.; et al. Arsenic and other geogenic contaminants in global groundwater. *Nat. Rev. Earth Environ.* **2024**, *5*, 312–328. [CrossRef]
45. Park, J.M.; Lee, J.S.; Lee, J.U.; Chon, H.T.; Jung, M.C. Microbial effects on geochemical behavior of arsenic in as-contaminated sediments. *J. Geochem. Explor.* **2006**, *88*, 134–138. [CrossRef]
46. Li, Q.; Jia, R.L.; Zhou, J.L.; Yang, G.Y. Preliminary analysis of high-fluoride groundwater in Aksu Prefecture, Xinjiang, China. *Adv. Mater. Res.* **2012**, *610–613*, 1041–1046. [CrossRef]
47. Gibbs, R.J. Mechanisms controlling world water chemistry. *Science* **1970**, *170*, 1088–1090. [CrossRef]
48. Elaid, M.; Hind, M.; Abdelmadiid, B.; Mohamed, M. Contribution of hydrogeochemical and isotopic tools to the management of Upper and Middle Cheliff Aquifers. *J. Earth Sci.* **2020**, *31*, 993–1006. [CrossRef]
49. Sun, Y.; Zhou, J.L.; Yang, F.Y.; Ji, Y.Y.; Zeng, Y.Y. Distribution and co-enrichment genesis of arsenic, fluorine and iodine in groundwater of the oasis belt in the southern margin of Tarim Basin. *Earth Sci. Front.* **2022**, *29*, 99–114. [CrossRef]
50. Wang, J.N.; Zhao, Y.M.; Liu, G.H. Distribution characteristics and metallogenic types of arsenic mines in Xinjiang. *Xinjiang Nonferrous Met.* **2017**, *40*, 63–64+67. [CrossRef]
51. Zhang, Y.; Yu, Q.; Shi, C.; Li, P.; Niu, H. Environmental isotopes and Cl/Br ratios evidences for delineating arsenic mobilization in aquifer system of the Jianghan plain, central China. *J. Earth Sci.* **2023**, *34*, 571–579. [CrossRef]
52. Gaillardet, J.; Dupré, B.; Louvat, P.; Allègre, C.J. Global silicate weathering and CO_2 consumption rates deduced from the chemistry of large rivers. *Chem. Geol.* **1999**, *159*, 3–30. [CrossRef]
53. Qian, C.; Wu, X.; Mu, W.P.; Fu, R.Z.; Zhu, G.; Wang, Z.R.; Wang, D.D. Hydrogeochemical characterization and suitability assessment of groundwater in an agro-pastoral area, Ordos Basin, NW China. *Environ. Earth Sci.* **2016**, *75*, 1356. [CrossRef]

Disclaimer/Publisher's Note: The statements, opinions and data contained in all publications are solely those of the individual author(s) and contributor(s) and not of MDPI and/or the editor(s). MDPI and/or the editor(s) disclaim responsibility for any injury to people or property resulting from any ideas, methods, instructions or products referred to in the content.

water

MDPI

Article

Accumulation, Source Apportionment, and Ecological-Health Risks Assessment of Topsoil Heavy Metals in Agricultural and Pastoral Areas in the Eastern Qaidam Basin, China

Mingxia Zhu [1], Zhen Yao [1,*], Xianhong Xu [2], Youning Wei [3], Xufa Yan [4] and Ming Xiao [5]

[1] Fifth Institute of Geological and Exploration of Qinghai Province, Xining 810000, China
[2] State Key Laboratory of Plateau Ecology and Agriculture, Qinghai University, Xining 810016, China
[3] Qinghai Geological Survey, Xining 810000, China
[4] Department of Agriculture and Rural Affairs of Qinghai Province, Xining 810000, China
[5] Academy of Agriculture and Forestry, Qinghai University, Xining 810016, China
* Correspondence: qhyaozhen@163.com

Abstract: The contamination of heavy metals (HMs) in the topsoil of agricultural and pastoral areas threatens the yield and quality of agriculture and animal husbandry and also endangers regional ecological security and human health. This study analyzed the HMs (Cd, Pb, As, Cu, Zn, Hg, and Mn) in areas with intensive agricultural and pastoral activities to identify their accumulation, source apportionment, and ecological-health risks using geochemical methods coupled with positive matrix factorization (PMF). It was uncovered that the concentrations of HMs presented varying scales of enrichment and contamination levels in the topsoil. However, except for only one sample, the residual HMs concentrations fell within the associated risk screening values (the RSVs). The combined assessment of geo-accumulation index (I_{geo}) and enrichment factor (EF) pointed that Hg and Cd were the primary contaminants. The PMF identified four sources of HMs including natural geogenic, industry mining, composite (caused by multi-anthropogenic activities), and agricultural sources accounting for 33.7%, 41.0%, 7.7%, and 17.6% of contribution rates, respectively. The potential ecological risk was largely attributed to the accumulation of Hg, followed by Cd. The non-carcinogenic risk for both groups fell beneath the acceptable risk threshold, and the prospective carcinogenic health threats posed by Cd, As, and Pb for different groups should not be ignored, particularly concerning children. It is of great significance to control the HMs pollution and restore soil cleanliness in the study area.

Keywords: accumulation characteristic; source apportionment; ecological-health risks; agricultural and pastoral areas; eastern Qaidam Basin

1. Introduction

As an extremely important material for human survival and development, soil serves as a pivotal link between the atmosphere, hydrosphere, biosphere, and constitutes the bedrock for each of earth's ecosystems [1]. However, in tandem with industrial and agricultural advancements, coupled with the swift urban sprawl, HMs contamination in soil has escalated drastically, reaching alarming proportions [2–4]. Additionally, HMs, owing to their high toxicity, mobility, persistence, and non-degradability, are one of the key factors influencing ecological quality. Even some HMs required by the human body, if overexposed, will cause great harm to the ecosystem and the human body [5,6]. In this context, soil quality determines the ecological environment, human health, food security, and sustainable development of agriculture and attracts more and more attention in many part of the world [7–9].

In general, HMs accumulated in the soil are derived from both geogenic and anthropogenic sources [5,10]. Geological background conditions such as bedrock and parent material are the natural sources [11–13], while human activities such as mining and smelting,

industrial manufacturing, agricultural cultivation, urban traffic, etc., are important reasons for causing or aggravating HMs accumulation, especially in the topsoil [14–16]. Once introduced into the environmental media, the HMs undergo complex physico-chemical and biological processes that determine their behavior and fates [17,18]. Importantly, understanding the distributions and source apportionment of HMs is the basis of topsoil contamination prevention and control and is also an important mean of ecological environmental safety protection [19,20].

Recently, the positive matrix factorization (PMF) model has been frequently adopted for identifying and conducting quantitative evaluations of contaminant sources of receptors, such as atmosphere, dust fall, water body, and sediment [5,21], especially in the field of topsoil HMs [19,22,23]. In addition, geochemical methods including geo-accumulation index (I_{geo}) or enrichment factor (EF) and potential ecological-health risks assessment have been widely used in topsoil HMs contamination and ecological risk assessment [24–26].

Notably, as an ecological transition zone connecting agricultural and grassland area, the special environment of agricultural and pastoral areas makes the land use type change frequently. It has typical environmental sensitivity and vulnerability and integrates the unique economic form of the common development of agriculture and animal husbandry [14,27,28]. However, with the rapid development of agriculture and animal husbandry economy, large numbers of HMs enter and change the soil function, leading to the decline of soil environmental quality [1,4,14]. This will affect the yield and quality of agriculture and animal husbandry and also endanger regional ecological security and human health.

In this study, Cd, Pb, As, Cu, Zn, Hg, Mn, Al, and Fe in topsoil samples were analyzed to illustrate the accumulation characteristics of HMs in areas characterized by intensive agricultural and pastoral activities. Combining with PMF and Pearson correlation analysis, the source apportionment was investigated. The potential ecological-health risks caused by HMs were evaluated. It is of great significance to prevent and control the contamination of HMs while maintaining ecological environment safety and safeguarding human health in areas undergoing intensive agricultural and pastoral activities.

2. Study Area

The research area is situated in the southeast of Qaidam Basin, Qinghai Province, Northwest China (Figure 1), where agricultural and pastoral activities are predominant. The southern portion is part of the East Kunlun mountain system, which is the southern edge of the Qaidam Basin. The peak elevation is above 4500 m, and the highest peak is 5447 m. The bare bedrock or surface layer is covered with thin layers of aeolian salt-bearing soil layers, presenting a natural desert landscape. Additionally, the soil types in the study area are diverse, and the parent material of soil formation is relatively complex, mainly including meadow saline soil, semi-fixed aeolian sand soil, salinized brown calcium soil, irrigated salinized brown calcium soil, and salinized clay. In the southern mountainous region, the weathering products of granite and diorite rocks predominantly constitute the soil parent material. With the decrease in altitude, the parent material gradually changes to flood alluvial, lake sediment, ice water sediment, and residual slope sediment. In the transition area of mountainous area and basin, the soil parent material becomes complex, mainly dominated by alluvial, diluvium, and loess-like material. A number of agricultural–pastoral areas and towns have been formed in this area, spanning more than 200 km^2, which are distributed on the river alluvial plain. Additionally, the area is rich in plentiful ores of various metals such as gold, iron, lead, zinc, and copper ore resources, together with manganese, molybdenum, graphite, fluorite, and rare earth mineral resources.

According to the results of remote sensing interpretation in the study area (Figure 1), the land use types mainly include farm and wood–grass lands, urban–rural zones, water area, barren landscapes, etc. Among them, natural grassland is the largest utilization type, and the distribution characteristics of farmland determines that agriculture is mainly oasis. The old oasis agriculture is generally distributed along rivers or lakes in arid desert

areas, as well as in groundwater-exposed locations in foothills and alluvial fans. With the development of social productive forces and the improvement of water conservancy conditions, the newly reclaimed agricultural areas are mainly opened up in arid and desert areas where the resources of suitable agricultural land are abundant, and the conditions of development and utilization are superior.

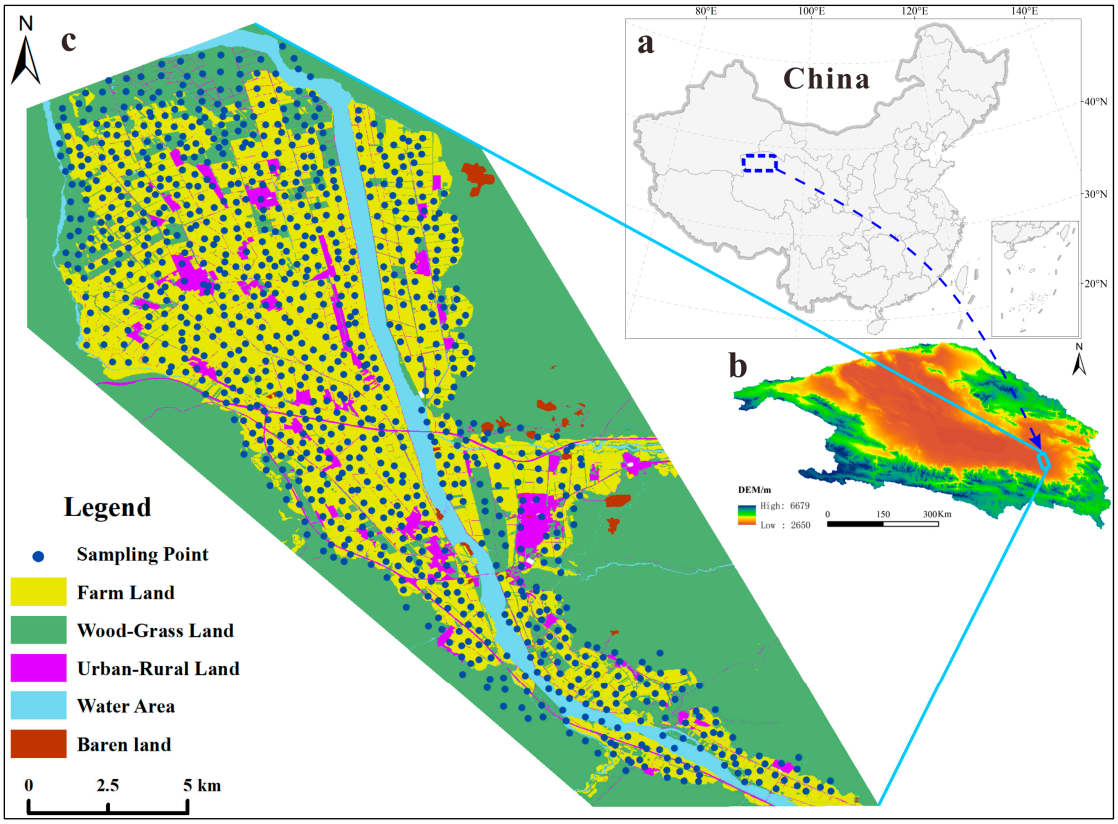

Figure 1. Land use types and sampling location of HMs in the study area: (**a**,**b**) the Qaidam Basin; (**c**) the study area.

3. Materials and Methods

3.1. Soil Sampling and Analyses

The topsoil samples were collected employing a strip-grid methodology, and the representative sample at each site was a homogenized mix of five randomly chosen subsamples. In the study area, 1013 samples (from 0 to 20 cm) were systematically gathered via soil drill, including grassplot, irrigable, nature reserve, forest–grass and residential land. And GPS was used to record the coordinates of sampling points. The sampling process avoided obvious contamination sources such as dump, mine slag, cesspit, fertilizer stacking, etc. Prior to sampling, larger stones, grass roots, and other impurities were removed, and each soil sample had an original weight of at least 1 kg. All the collected samples were kept in polythene bags, numbered, and preserved. The collected soil samples underwent an air-drying process at ambient conditions before being passed through a 2.0 mm nylon sieve to remove larger components such as macroscopic organic matter, decomposed plant residue, and miscellaneous debris. The samples were put into polyethene plastic sacks to avoid contamination, numbered, marked separately, and then sent to the laboratory for analyses.

The soil samples were subjected to digestion using a concentrated acid mixture (HNO_3-HF-$HClO_4$) in sterile dry Teflon crucibles [19,23,26]. The concentrations of Cu, Pb, Zn, Mn, Al, and Fe were measured via X-ray fluorescence spectrometry (XRF), while Hg and As were measured using atomic fluorescence spectrophotometer (AFS, HGF-V9, Beijing,

China). Additionally, the Cd concentrations were quantified using inductively coupled plasma mass spectrometry (ICP-MS, Thermo X series II, Thermo Fisher Scientific, Vacaville, CA, USA), whereas the soil pH was determined through the glass electrode technique after extraction with non-carbon dioxide distilled water. Quality assurance and control measures included the incorporation of both random replicate samples and certified reference materials (CRMs), specifically a national standard soil sample (GBW 07449). The proportion in restoration percentage for all analyzed elements ranged from 90% to 105%, with the RSD (relative standard deviation) of duplicate samples totaling to less than 5%. The method detection limits were 0.8, 2, 2, 0.02, 0.2, 0.0005, 5, 0.05, and 0.05 mg/kg for Cu, Pb, Zn, Cd, As, Hg, Mn, Al, and Fe, respectively.

3.2. Evaluation Method of Pollution Levels

Geochemical assessments, encompassing metrics like the geo-accumulation index (I_{geo}) and the enrichment factor (EF), are instrumental in evaluating contamination levels and pinpointing anthropogenic influences [24–26].

3.2.1. Geo-Accumulation Index (I_{geo})

The I_{geo} is calculated by the following expression:

$$I_{geo} = \log_2 [C_i/(K \cdot B_i)] \quad (1)$$

In this context, C_i corresponds to the detected concentration of the elements, while B_i stands for their background values (mg/kg). Meanwhile, K denotes a fixed coefficient introduced to accommodate variations in background levels, generally 1.5 [29,30]. The grading standards of I_{geo} are shown in Table S1.

3.2.2. Enrichment Factor (EF)

EF is employed to determine the enrichment degree of HMs in soil:

$$EF = \frac{(C_i/C_{ref})_{sample}}{(C_i/C_{ref})_{background}} \quad (2)$$

where C_i and C_{ref} represent the concentration of element i and the reference element for normalization, respectively (mg/kg). In general, the most common normalizing element are Al, Fe, Mn, Ti, etc. [31,32]. In this research, Al was chosen as the reference element due to its significantly higher abundance and greater stability within the Earth's crust, along with its minimal influence from anthropogenic sources. The classification criteria for EF are also presented in Table S1.

3.3. Positive Matrix Factorization Model (PMF)

In this study, the PMF model, endorsed by the United States Environmental Protection Agency (US EPA), was applied for quantitatively elucidating contamination sources using receptor-based data. Additionally, an integrated approach involving both Pearson correlation analysis and PMF model was utilized to effectively allocate the sources of HMs in topsoil. Through successive decompositions of the primary matrix X, the PMF algorithm optimizes matrices G and F, leading to the minimization of the target function Q [5,23] as follows:

$$X_{ij} = \sum_{k=1}^{p} G_{ik}F_{kj} + E_{ij} \quad (3)$$

$$Q = \sum_{i=1}^{n}\sum_{j=1}^{m}\left(\frac{X_{ij} - \sum_{k=1}^{p} G_{ik}F_{kj}}{U_{ij}}\right)^2 \quad (4)$$

In this formulation, X_{ij} signifies the content of HMs (expressed in mg/kg), whereas G_{ik} illustrates the extent of contribution from the kth source to the ith specimen. F_{kj} represents the proportion of the jth HM originating from various factors. E_{ij} designates the

residual component. Here, *n* indicates the variety of metallic elements; m identifies the individual samples, and U_{ij} represents the uncertainty associated with HMs, calculated using the method detection limit (MDL) pertinent to each species, combined with the metal concentration and error fraction.

$$\text{If c} \leq \text{MDL, } U_{ij} = \frac{5}{6}\text{MDL, else, } U_{ij} = \sqrt{(\text{Error fraction} \times \text{C})^2 + (0.5 \times \text{MDL})^2} \quad (5)$$

Here, error fraction and C represent the percentage of measurement uncertainty and the element content, respectively.

3.4. Potential Ecological-Health Risks

3.4.1. Potential Ecological Risks Assessment

The potential ecological risk index (RI), initially proposed by Hakanson (1980) [33], was formulated to evaluate the potential consequences of contaminations based on both the toxicity of heavy metals and the environmental system's sensitivity [2,23]. Its calculation is shown in the following formula:

$$RI = \sum_{i=1}^{n} E_r^i = \sum_{i=1}^{n} T_r^i \times \left(C_D^i / C_R^i\right) \quad (6)$$

where E_r^i is the potential risk index of target element i; C_D^i and C_R^i are the measured concentration and the background value of HMs, respectively (mg/kg). $T_r{}^i$ refers to the toxic response coefficient of target element, with the relevant values as follows: Zn = Mn = 1, Cu = Pb = 5, As = 10, Cd = 30, and Hg = 40 [34,35]. The classifying standards of E_R^i and RI are shown in Table S2.

3.4.2. Human Health Risks Assessment (HRA)

The HRA model proposed by the US EPA [36] was utilized to systematically estimate the potential health hazards posed by hazardous substances to the human.

This investigation synthesized multiple evaluation indexes, incorporating insights from the International Agency for Research on Cancer (IARC) and the World Health Organization (WHO) on the detrimental impacts of various noxious compounds on human health. Consequently, the model encompassed evaluations of carcinogenic threats attributable to Cd, As, and Pb in addition to non-carcinogenic risk attributable to Cd, Pb, As, Cu, Zn, Hg, and Mn.

Exposure levels incurred through oral intake, dermal absorption, and inhalation can be determined using the subsequent formulas:

$$ADI_{int\text{-}i} = C_i \times \frac{IngR \times EF \times ED}{BW \times AT} \times CF \quad (7)$$

$$ADI_{dermal\text{-}i} = C_i \times \frac{SA \times AF \times ABS \times EF \times ED}{BW \times AT} \times CF \quad (8)$$

$$ADI_{inh\text{-}i} = C_i \times \frac{InhR \times EF \times ED}{PEF \times BW \times AT} \quad (9)$$

where ADI_{ing}, ADI_{dermal}, and ADI_{inh} represent the average daily intake from soil ingestion, dermal, and inhalation absorption, respectively (mg/kg·day), The values for the above parameters are listed in Table S3.

(1) Non-carcinogenic risk assessment

The target hazard quotient (HQ) and hazard index (HI) of HMs were calculated using the following equation:

$$HI = \sum HQ_i = \sum \frac{ADI_i}{RfD_i} \quad (10)$$

Here, RfD_i denotes the reference toxicity threshold dose of target element i [mg/(kg·day)]. The calculated HQ and HI values lower than 1 suggest neglectable non-carcinogen risk, while the values higher than 1 indicate high non-carcinogen risks [37–39].

(2) Carcinogenic risk assessment

The CR value represents carcinogenic risk from a single element, and the TCR value indicates combined carcinogenic health risk, both of which were calculated as follows:

$$CR = ADI \times SF \quad (11)$$

$$TCR = \sum CR_i = \sum ADI_i \times SF_i \quad (12)$$

where SF is the cancer slope factor, and the values are shown in Table S4. The calculated TCR value lower than 10^{-6} represents acceptable cancer risk, while the TCR value higher than 10^{-4} represents unacceptable cancer risk level [40,41].

4. Results and Discussion

4.1. Description Statistics of HMs

Statistical summaries for the HMs content, including minimum, maximum, and mean values, and upper (Q1, 25%), median, and lower quartiles (Q3, 75%), are presented in Table 1 and Figure 2. Additionally, the geochemical background values (GBVs) of soil in the study area and the soil environmental quality: risk control standard for soil contamination of agricultural land issued by the Ministry of Ecology and Environment of China (RSVs, GB 15618-2018 [42]) were employed to contrastively analyze the content characteristics of HMs in the study area. Table 1 illustrates the pH levels observed in the samples that spanned between 7.89 and 9.25, with a mean value of 8.53, reflecting the mildly alkaline characteristics of topsoil. Hence, the risk control threshold of agricultural land soil with pH > 7.5 can be determined (RSVs in Table 1).

Table 1. Statistical summary of HMs concentrations in soil samples in the study area (mg/kg).

Element	Cu	Pb	Zn	Cd	As	Hg	Mn	Al	Fe	pH
Min	9.80	14.70	30.90	0.059	4.59	0.002	348.50	4.89	1.60	7.89
Mean	21.32	20.96	61.75	0.145	10.96	0.020	556.61	5.68	2.82	8.53
Max	36.50	43.00	132.30	1.129	21.67	1.386	795.20	7.97	4.56	9.25
Q_1 (25%)	19.10	19.30	55.10	0.120	9.86	0.013	522.40	5.46	2.64	8.37
Median	21.70	20.80	62.00	0.143	11.08	0.017	564.90	5.67	2.89	8.51
Q_3 (75%)	23.70	22.10	68.70	0.164	12.25	0.021	602.30	5.84	3.06	8.66
SD [a]	3.99	2.84	12.58	0.050	2.06	0.045	69.99	0.37	0.41	0.24
CV (%) [b]	0.19	0.14	0.20	0.341	0.19	2.240	0.13	0.07	0.14	0.03
BV [c]	21.70	20.80	62.00	0.143	11.10	0.017	565.00	5.66	2.79	8.51
RSV [d]	100.00	170.00	300.00	0.60	20.00	1.00	-	-	-	-

Notes: Q_1 and Q_3 correspond to the upper (25%) and lower (75%) quartiles, respectively. [a] standard deviation. [b] coefficient of variation. [c] background values [43]. [d] soil environmental quality: risk control standard for soil contamination of agricultural land (GB 15618-2018) [42].

The CV values of HMs were relatively small, except for Hg with 2.24%, indicating that the dispersion of HMs across different areas was generally uniform, pointing to convoluted sources. The average HMs concentrations (mg/kg) were 21.32 (Cu), 20.96 (Pb), 61.75 (Zn), 0.14 (Cd), 10.96 (As), 0.02 (Hg), 556.61 (Mn), 5.56 (Al), and 2.82 (Fe), respectively. The concentrations (mean) of Cu, Zn, As, Mn, and Fe were slightly below or close to the BVs, while the means of the remaining metals including Pb, Cd, Hg, and Al were slightly higher than the BVs. Additionally, apart from the outlier concentrations of Cd, As, and Hg from only one sample, the HMs contents in the other samples remained beneath their respective risk screening thresholds (the RSVs).

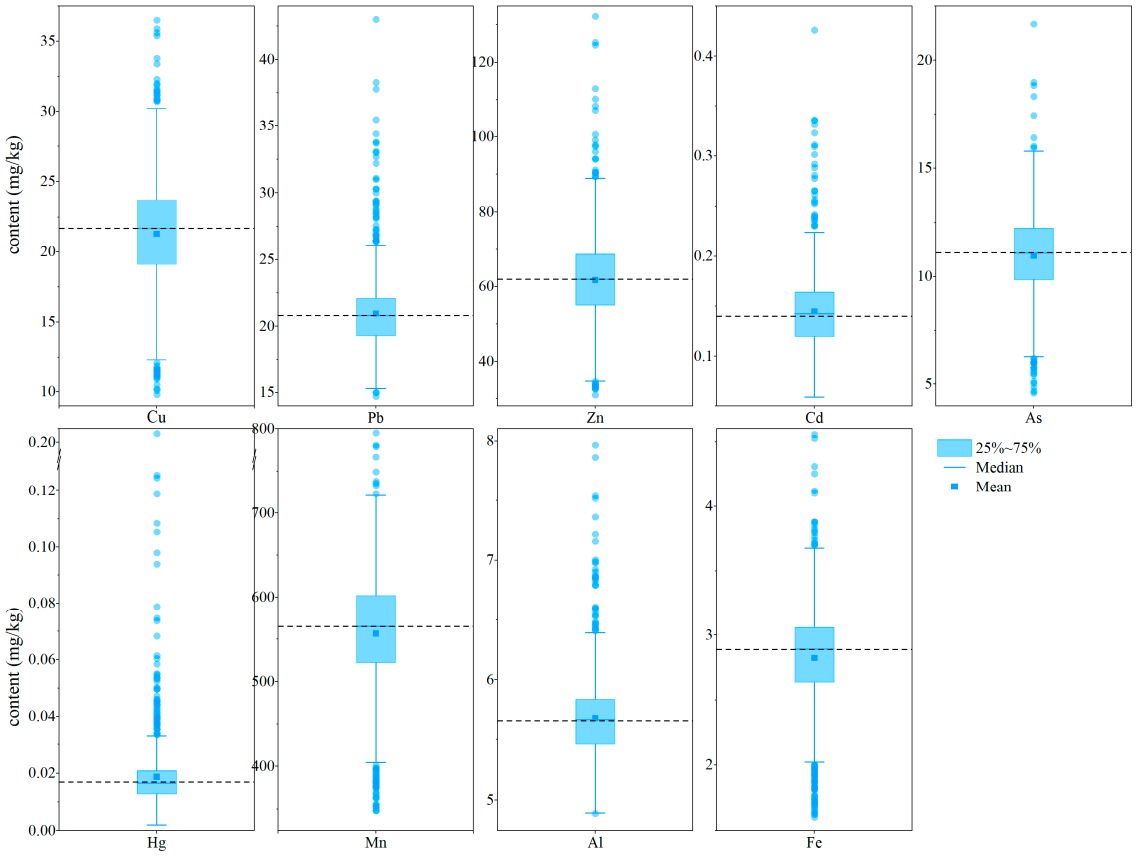

Figure 2. The concentration box diagrams of HMs in topsoil. The dashed lines represent the background values (BVs) of HMs in the study area.

However, according to the quartile (from upper to lower quartile), the contents of each HMs in many topsoil samples were still greater than the BVs (Figure 2). Specifically, in contrast to Pb and Mn, the concentrations of Cd, Cu, As, Zn, and Hg in the majority of samples exceeded the BVs. The exceeding rates of these HMs were higher than 50%, accounting for 50.64% (Cu), 50.05% (Zn), 50.15% (Cd), 50.94% (As), and 50.74% (Hg), respectively. It indicated that the HMs in the topsoil exhibited signs of contamination or enrichment, implying potential ecological hazards and health risks in the study area. Thus, in order to effectively control the harm, identifying the enrichment characteristics, quantifying the source apportionment, and calculating potential eco-health risks of these HMs in topsoil are essential [23,44].

4.2. Contamination Assessment of HMs

The contamination extent of topsoil HMs was calculated using geochemical indicators I_{geo} (Figure 3) and EF (Figure 4) to identify the impact of anthropogenic activities in the study area.

Figure 3 illustrates, except for Hg, the other HMs, ranging from the uncontaminated level ($I_{geo} \leq 0$) to the moderately contaminated level ($0 < I_{geo} \leq 1$) according to the classification of I_{geo} (Table S1). While the I_{geo} values of Hg in some samples were at the level of moderately contaminated or higher, the average I_{geo} values of HMs were less than 0, with Cu (−0.64), Pb (−0.59), Zn (−0.62), Cd (−0.61), As (−0.63), Hg (−0.64), and Mn (−0.62). Overall, the I_{geo} values of different HMs in the topsoil samples indicated a relatively low pollution extent. However, the proportion of all samples with I_{geo} above 0 decreased in the order of 12.54% (Hg) > 3.36% (Cd) > 1.38% (Zn) > 1.09% (Cd) > 0.59% (Cu) > 0.49% (As), which also represents the contamination extent of topsoil HMs.

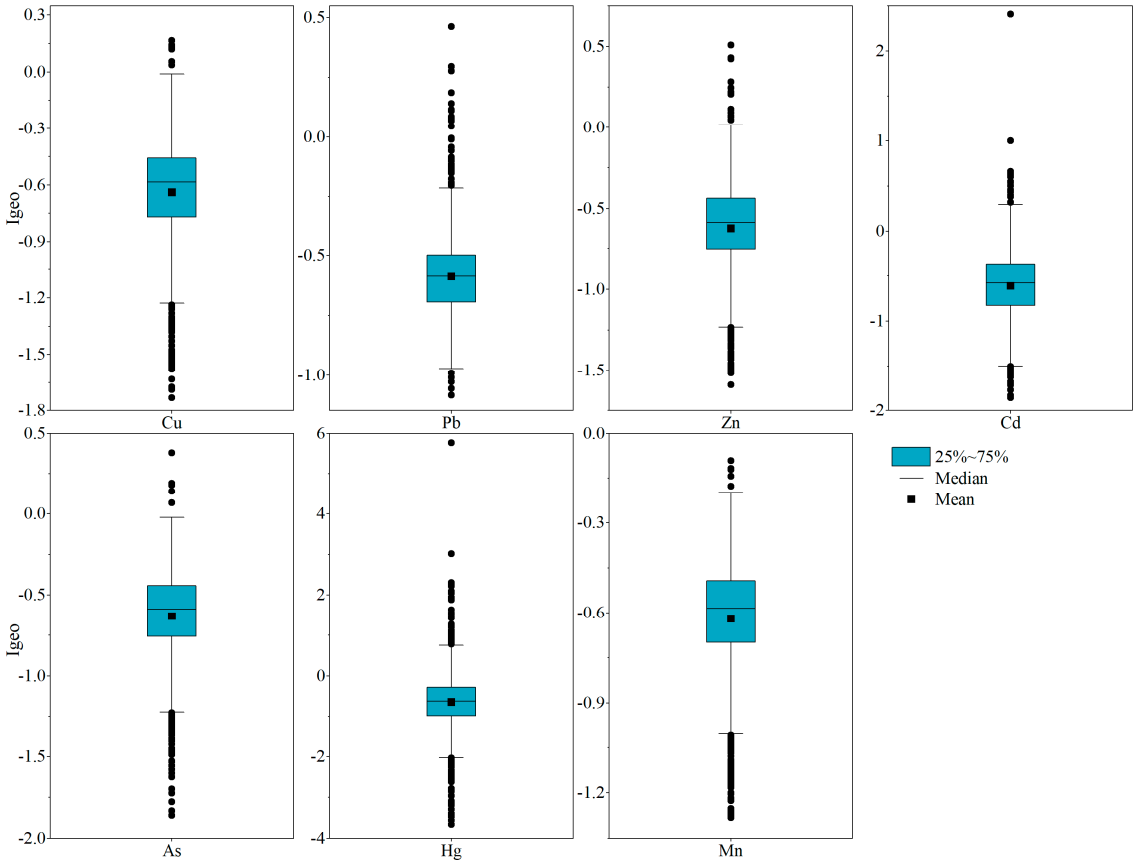

Figure 3. I_{geo} box diagrams of HMs in the study area.

Notably, regarding the contamination of samples with Hg, 10.37%, 1.48%, 0.49%, and 0.2% were uncontaminated to moderately contaminated, moderately contaminated, moderately to heavily contaminated, and heavily contaminated, respectively. Simultaneously, in the case of Cd, the proportion of samples classified as uncontaminated to moderately contaminated and moderately were 3.26% and 0.1%, respectively. While the samples were mostly unaffected by the other HM elements, the outcomes also indicate that Hg and Cd exhibited pollute levels with varying degrees and were the predominant contaminants in the topsoil samples, suggesting that these HMs have been affected by anthropogenic sources [23,45].

Based on the EF classification in Table S1, the computations disclosed that every EF value for As, Cu, and Mn in the topsoil samples pointed to the minimal enrichment level, and only one Pb and Zn showed moderate enrichment level (Figure 4). Notably, the enrichment of Hg in samples that reached moderate or above levels accounted for 89.55%, including moderate level (76.12%), significant level (11.94%), and extremely high level (1.49%), respectively. Meanwhile, the ratio of samples categorized as moderate and significant enrichment caused by Cd were 14.93% and 1.49%, respectively (Figure 4). Similar to the I_{geo}, Hg was considered to be the most enriched with EF value indicating that Hg in most topsoil samples were at a serious contamination level, followed by Cd. Relatively, the other types of HMs in samples were primarily situated at or below the level of minimal enrichment. To summarize, combining with the results of I_{geo}, this implied that the impact of anthropogenic activities on the accumulation of Hg and Cd in the topsoil should not be ignored.

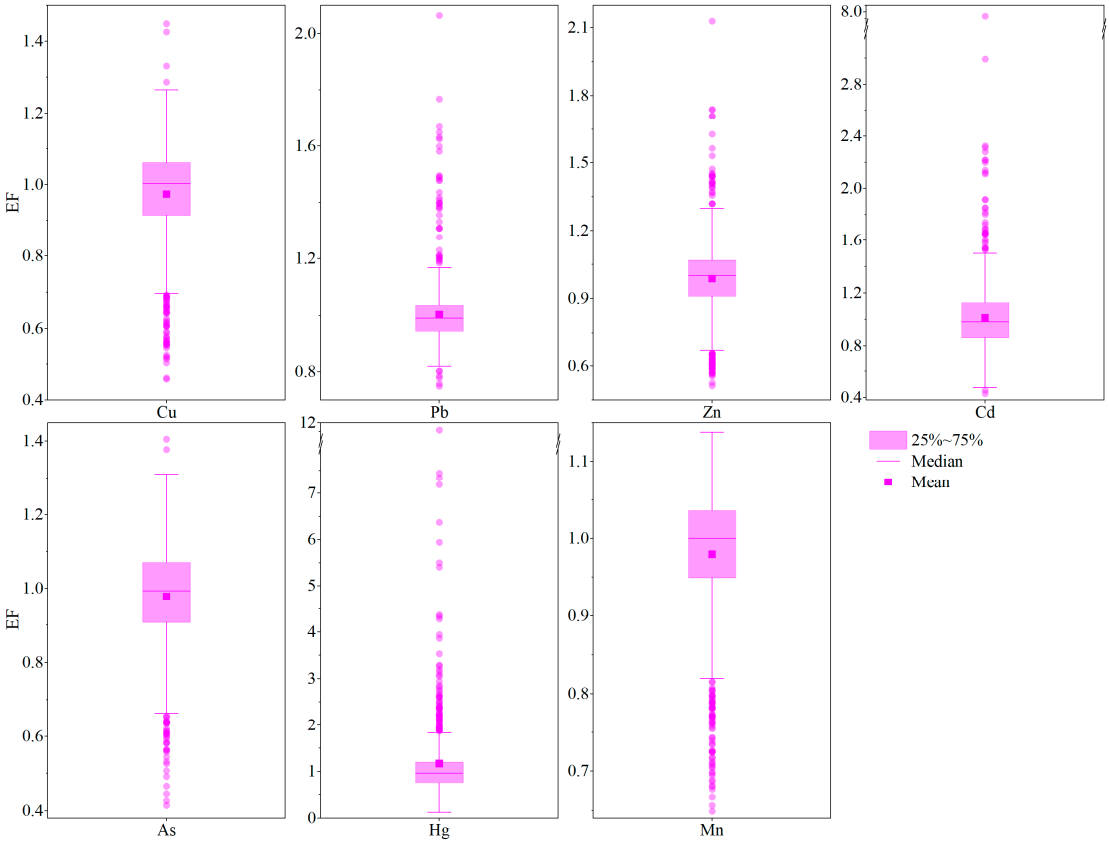

Figure 4. EF box diagrams of HMs in the study area.

4.3. Source Identification of HMs

Subsequent to executing iterative calculations in the PMF model, an integrated approach involving both Pearson correlation analysis and PMF model was utilized to effectively allocate the sources of HMs in topsoil (Figure 5). According to the Pearson correlation analysis, strong correlations ($R^2 > 0.6$) were observed in the pairwise comparisons of HMs in topsoil (Figure 5c), revealing a potential common source [5,23,46]. Upon assessing their robustness along with the lowest Q values, four factors were derived, accounting for 33.7%, 41.0%, 7.7%, and 17.6% of the contribution, respectively (Figure 5a). All elements were categorized as 'strong' due to their high signal-to-noise ratios (S/N). The scaled residuals, falling neatly within the interval of −3 to 3, effectively revealed the influences exerted by each factor. Additionally, the coefficients of determination (R^2) between the observed and predicted concentrations in PMF model were all greater than 0.75, which means that the model was appropriate, and the results were reliable [21,26].

Factor 1, responsible for 24.9% of the total contribution (Figure 5a), was chiefly dominated by Al (33.73%) and Pb (32.19%) (Figure 5b). The remaining HMs contributed less than 25% with an order of Mn (19.55%) > Cd (17.52%) > Fe (15.95%) > Zn (13.06%) > Cu (9.48%) > As (9.37%) > Hg (8.11%). In general, the primary determinants shaping the concentration and dispersion of Al and Mn in soils are attributed to the Earth's crustal materials and pedogenesis. In the metallogenic belt of the study area, some elements such as Mo, Rn, Sr, Al, Na, K, etc. are characterized by high content availability. A considerable number of Al concentration in the samples slightly exceeded the background level (Figure 2), indicating potential additional sources for the observed Al, beyond just parent materials and soil-forming processes. Pb functions as a critical signal for automotive emissions [47–49]; the metallogenic geological background, particularly linked to non-ferrous minerals such as lead–zinc ore, offers a plausible source for Pb, Zn, and Cu in topsoil [5,50,51]. Meanwhile, combining with the above I_{geo}, the EF values of Pb (Figures 3 and 4), the source of Pb could be recognized as natural background influenced by anthropogenic inputs (mainly traffic

activity). Consequently, Factor 1 might potentially represent the natural geogenic sources, but only a handful of topsoil samples exhibited signs of anthropogenic impacts.

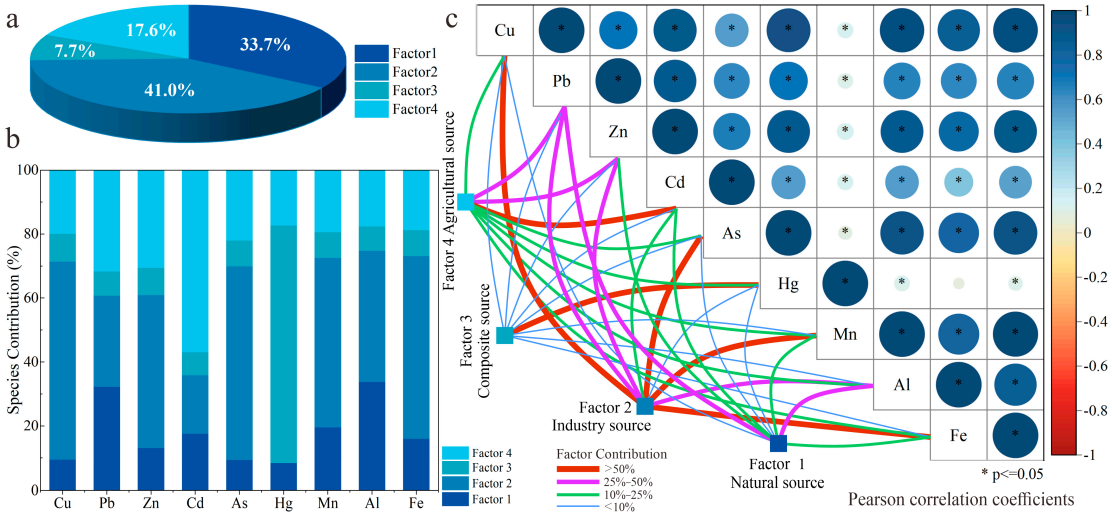

Figure 5. Source apportionment of HMs in the study area. (**a**) The contribution percentage of four factors. (**b**) Factor profiles of HMs according to the PMF result. (**c**) Determine the interrelationships among HMs by integrating correlation analysis alongside the outcomes of PMF. The degree of correlation between HMs was visualized using a color gradient in their pairwise comparisons. The extent of contribution from each factor identified in PMF was associated specifically with each HM.

Factor 2, the biggest contribution that accounted for 41.0% of the total variance, was mainly characterized by Cu (61.83%), As (60.51%), Fe (57.16%), and Mn (52.98%), followed by Zn (47.81%), Al (40.98%), and Pb (28.52%). Relevant studies have established that the emission of metals such as Cu, As, Fe, Mn, Zn, and Pb is associated with intense human activities [11,40,45,52–54], and rock weathering [55,56] could be released through atmospheric deposition. Serving as a principal indicator for automotive emissions, Pb particles originating from vehicle exhaust contribute to soil pollution via the accumulation of dust [47,48,57]. Moreover, for Cu and Zn, predominantly employed in the production of automotive components and traffic signage, their minuscule particles could also be released from tires and braking systems into the topsoil via atmospheric deposition. Additionally, As, Al, and Mn exhibit extensive presence in the Earth's crustal materials and play crucial roles in pedogenesis [52,54,58,59]. Although the I_{geo} and EF values were not too high, the concentrations of these elements in many samples (even more than 50%) exceeded the background values of the study area. Thus, it was reasonable to assign this factor to industry sources, especially mining operations due to the long mining history within the study area.

Factor 3, accounting for 7.7% source, was the strongest and mainly characterized by Hg (55.73%, Figure 5b), while all contribution rate of other HMs was below 10%. According to the concentration, I_{geo} and EF values, it revealed Hg to be the predominant contaminant from anthropogenic activities in the topsoil samples. Previous research has reported that the origins of Hg in topsoil were diversified, but mainly anthropogenic through atmospheric deposition and airborne dust adsorption. Notable Hg sources include coal combustion, the extraction and refining of gold and mercury [2,45], contaminants from copper ore smelting [60,61], emissions from fossil fuel burning [54,62,63], mercury pesticide, or sludge fertilizer [23,64]. However, it can be seen that no significant correlation was found between Hg and other HMs at the level of 0.05 (Figure 5c), indicating that the Hg and other HMSs did not exist from the same or similar source. Consequently, it can be deduced that Factor 3 likely represents a conglomerate of sources driven by multiple human activities.

Factor 4, contributing 17.6% to the overall composition, showed a substantial link to Cd (57.03%) and exhibited moderate correlations with Pb (31.72%) and Zn (30.57%).

Combined with the results of I_{geo} and EF, the influence of Cd contaminant may not to be ignored. In particular, as an element in phosphate rocks, Cd mainly exists in phosphate fertilizer [65–67], generally regarded as the hallmark of agricultural practice [24,68,69]. Additionally, studies have indicated that Zn is nearly ubiquitous across a range of agricultural inputs, encompassing fertilizers, pesticides, fungicides, and manures [45,70,71]. It indicated that agricultural activities were the main sources of Cd and Zn in topsoil [25,72,73]. Notably, according to the land use types, the proportion of farmland is very high, meaning high intensity of agricultural activities in the study area (Figure 1). Meanwhile, the contents of Cd and Zn showed significant correlation (Figure 5c). Hence, Factor 4 could be attributed to agricultural sources.

In summary, the sources of HMs in topsoil in the study area were diversified. In order to ensure the functional sustainability of the land in the study area, it is urgent to implement some management strategies and governance techniques. The results show that the strict control of anthropogenic emissions including rational use of mercury pesticide or sludge fertilizer and fossil fuels, control of mining activities, and soil remediation such as soil washing, phytoremediation, biochar, in situ chemical oxidation technique, etc., [74–79] are of great significance to curb HMs pollution and restore soil cleanliness in the study area.

4.4. Potential Ecological Risks Assessment

The results pertaining to the prospective ecological risk evaluation for topsoil in agricultural and pastoral areas are illustrated in Figure 6. The average Er values of HMs decreased in the order of Hg (47.23) > Cd (31.07) > As (9.87) > Pb (5.04) > Zn (4.98) > Cu (4.91) > Mn (0.99). With the exception of Hg and Cd (Figure 6a), the Er indices for all other metals fell below the threshold for low-risk classification (Table S2), signifying an absence of ecological hazard in the topsoil. Significantly greater ecological hazards were linked to Hg and Cd, with approximately 47.48% of Hg and 9.87% of Cd in samples corresponding to the moderate risk level or higher (Figure 6b). Notably, Hg posed moderate and considerable risk in 41.46% and 4.74% of the sampled sites, respectively. And the Er value of eleven and two samples was at high and extreme risk, respectively.

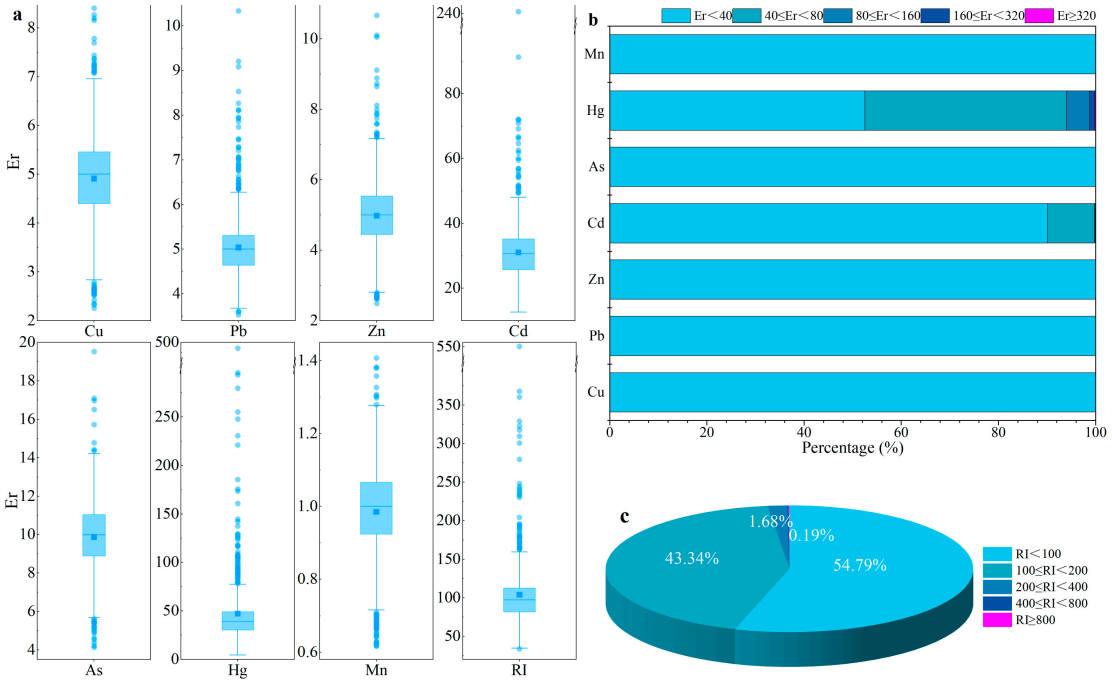

Figure 6. Statistical examination of Er and RI pertaining to different HMs in topsoil samples. (**a**) Er box diagrams of HMs in the study area; (**b**) the cumulative percentage of Er classification level of different heavy metals; (**c**) the proportion of RI classification level caused by all HMs.

Regarding the total ecological risks, 54.79%, 43.34%, and 1.68% corresponded to slight, moderate, strong, and high risk based on the RI categorization (Figure 6c, Table S2), respectively. Importantly, the calculated RI value of two sample showed quite strong and extremely strong risk levels. In general, the ecological toxicity of HMs is different, and it can lead to higher potential ecological risk due to high enrichment. However, it is crucial to note that even at relatively low levels of contamination, the high toxicity inherent in HMs has the capacity to instigate significant ecological risks [23,26,29]. Overall, the RI values revealed greater potential ecological risk in the study area, and Hg was identified as the primary contributing element, followed by Cd, which should be given more attention.

4.5. Probabilistic Health Risks Assessment

The potential carcinogenic and non-carcinogenic risk of hazardous substances to children and adult through different pathways was evaluated, and the findings are presented in Figures 7 and 8. The maximum HI caused by the HMs to both children and adults showed an acceptable risk level (<1), suggesting all topsoil samples posed negligible non-carcinogenic health risks. It is noteworthy that despite both groups presenting non-carcinogenic risks beneath the acceptable threshold, the HI values observed in children surpassed those found in adults. As such, the non-carcinogenic risk for children should also not be ignored.

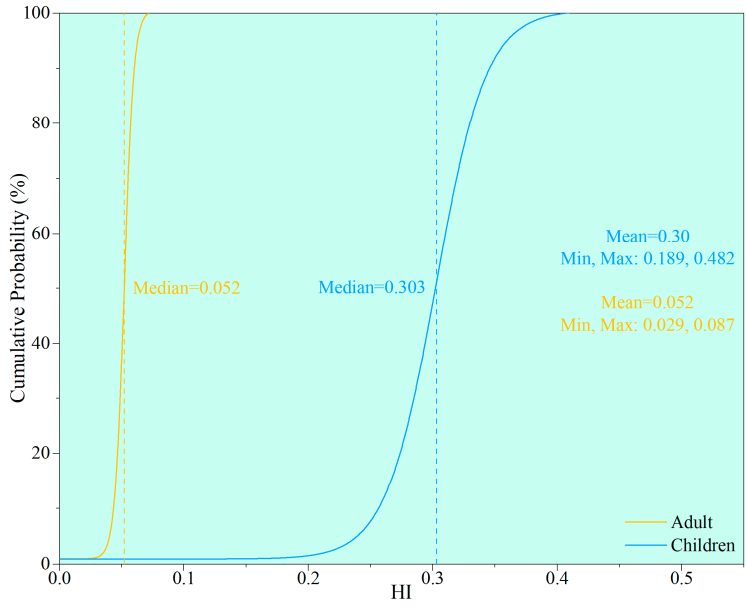

Figure 7. Cumulative probability of non-carcinogenic HI of all HMs.

Overall, the CR posed to children or adults due to Cd, As, and Pb in topsoil remained under the unacceptable level (10^{-4}) with the order of As > Cd > Pd for both groups (Figure 8). Furthermore, the CR (As), with all values higher than 10^{-6} signified the most substantial potential for carcinogenic health hazards. Simultaneously, the risk level induced by Cd ranked as the second most significant, whereas that of Pb stood as the least concerning (< 10^{-6} in all samples). It revealed that As was the main potential carcinogenic element and posed a carcinogenic risk in the topsoil.

Despite the fact that the TCR level presented to children or adults attributable to Cd, As, and Pb was both below the unacceptable level (10^{-4}), the potential carcinogenic hazards were also at high levels with varying degrees (CR > 10^{-6}) (Figure 8d). According to the results of I_{geo} and EF, the contamination and enrichment degree of Cd, As, and Pb were the relatively low among most samples (Figures 3 and 4), but these HMs still represent heightened cancerous threats to both children and adults, owing to their cancer-inducing toxicity. Notably, the overall TCR level posed by Cr, As, and Cd was considerably

more pronounced for children than for adults in the study area, indicating a heightened susceptibility in children. Thus, compared with non-carcinogenic health risks, the potential carcinogenic health risks for different groups should not be ignored, especially for children.

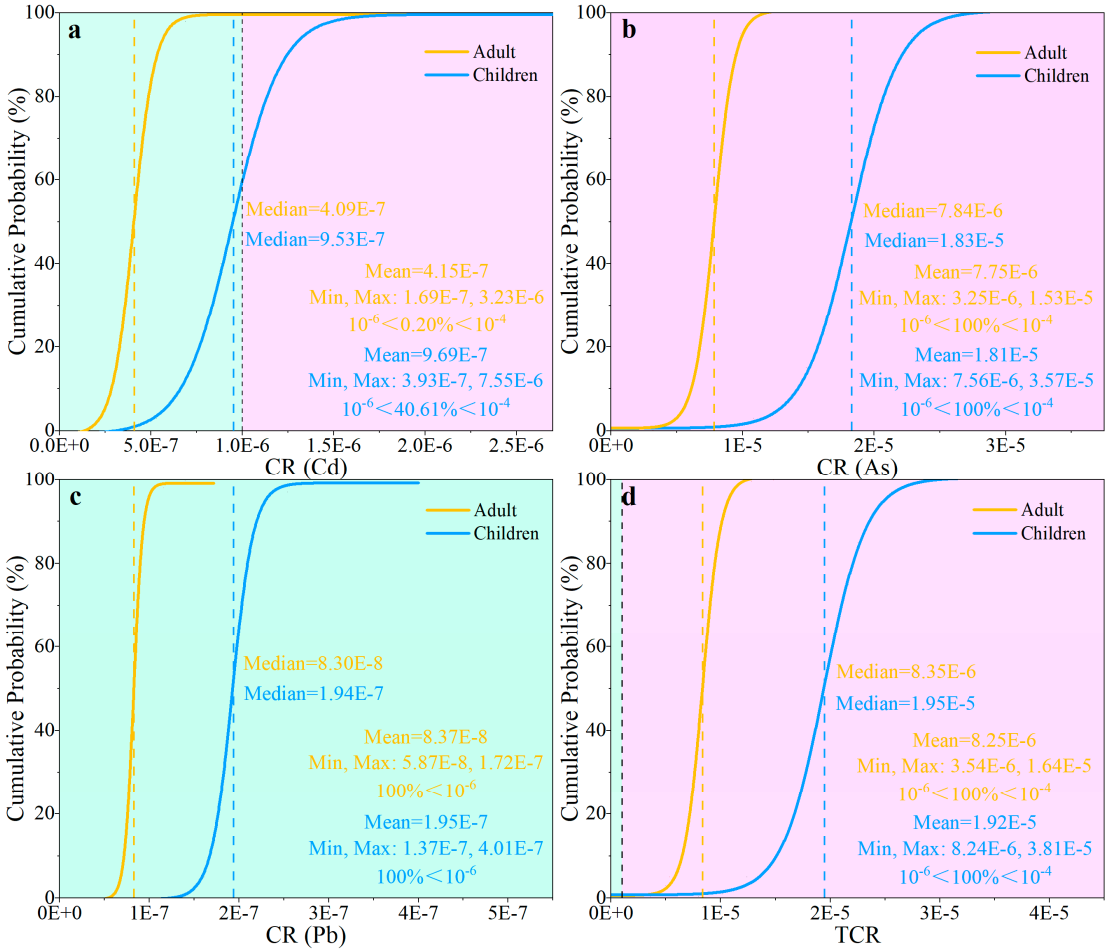

Figure 8. Box diagram of carcinogenic risk values of HMs (**a**–**d**).

5. Conclusions

This study focused on analyzing primary HMs (Cd, Pb, As, Cu, Zn, Hg, Mn, Al, and Fe) to explore the accumulation, source apportionment, and hazards associated with topsoil HMs in typical intensive agricultural and pastoral areas in the eastern Qaidam Basin, China. On the whole, the contents (mean) of the examined HMs in the topsoil displayed variability, showing different levels of contamination and enrichment. The results further pointed out that Hg and Cd, primarily affected by anthropogenic activities, exhibited accumulations at various levels and served as the leading pollutants. However, the concentrations of HMs fell within the respective risk screening values (RSVs), implying that the potential hazards for agricultural land use could be considered negligible. An integrative analysis, merging the strengths of the PMF model alongside Pearson correlation analysis, significantly enhanced the precision of source determination and successfully quantified the extent of contribution from distinct HMs contamination sources. Natural geogenic, industry mining, composite, and agricultural sources emerged as critical determinants, influencing the accumulation of HMs in the topsoil, whereas mining operations contributed the most significant portion owing to a protracted history of extraction. In summary, the RI values indicated a higher ecological threat, with Hg being distinguished as the main contributor, followed by Cd. Significantly, the non-carcinogenic risk for both groups fell beneath the acceptable risk threshold, and the prospective carcinogenic health threats posed by Cd, As, and Pb for different groups should not be ignored, particularly concerning children.

Supplementary Materials: The following supporting information can be downloaded at the following website: https://www.mdpi.com/article/10.3390/w16243719/s1, Text S1: The assessment criteria for E_R^i and RI; Table S1: The corresponding relationship between contamination level and value for geo-accumulation index (I_{geo}) and enrichment factor (EF); Table S2: Criteria of classification levels for E_r^i (a) and RI (b); Table S3: Parameters of health risk assessment model; Table S4: Reference values of SF and RfD for health risk assessment model. References [80–106] are citied in the Supplementary Materials.

Author Contributions: Conceptualization, M.Z. and Z.Y.; methodology, Z.Y. and X.X.; software, M.Z. and X.X.; validation, X.X., Y.W. and X.Y.; formal analysis, X.Y.; investigation, M.Z., X.X., Y.W. and X.Y.; resources, Y.W. and X.Y.; data curation, X.X. and M.X.; writing—original draft preparation, M.Z.; writing—review and editing, Z.Y.; All authors have read and agreed to the published version of the manuscript.

Funding: This research received no external funding.

Data Availability Statement: The original contributions presented in the study are included in the article, further inquiries can be directed to the corresponding author.

Conflicts of Interest: The authors declare no conflicts of interest.

References

1. Lehmann, J.; Bossio, D.A.; Kögel-Knabner, I.; Rillig, M.C. The concept and future prospects of soil health. *Nat. Rev. Earth Environ.* **2020**, *1*, 544–553. [CrossRef] [PubMed]
2. Árvay, J.; Demková, L.; Hauptvogl, M.; Michalko, M.; Bajčan, D.; Stanovič, R.; Tomáš, J.; Hrstková, M.; Trebichalský, P. Assessment of environmental and health risks in former polymetallic ore mining and smelting area, Slovakia: Spatial distribution and accumulation of mercury in four different ecosystems. *Ecotoxicol Environ. Saf.* **2017**, *144*, 236–244. [CrossRef] [PubMed]
3. Sheng, Y.; Jiang, W.; Zhang, M. Mobilization, Speciation, and Transformation of Organic and Inorganic Contaminants in Soil-Groundwater Ecosystems. *Appl. Sci.* **2023**, *13*, 11454. [CrossRef]
4. Wang, Z.; Xiao, J.; Wang, L.; Liang, T.; Guo, Q.; Guan, Y.; Rinklebe, J. Elucidating the differentiation of soil heavy metals under different land uses with geographically weighted regression and self-organizing map. *Environ. Pollut.* **2020**, *260*, 114065. [CrossRef]
5. Jiang, W.J.; Meng, L.S.; Liu, F.T.; Sheng, Y.Z.; Chen, S.M.; Yang, J.L.; Mao, H.R.; Zhang, J.; Zhang, Z.; Ning, H. Distribution, source investigation, and risk assessment of topsoil heavy metals in areas with intensive anthropogenic activities using the positive matrix factorization (PMF) model coupled with self-organizing map (SOM). *Envion. Geochem. Hlth.* **2023**, *45*, 6353–6370. [CrossRef]
6. Huang, Y.; Deng, M.H.; Wu, S.F.; Japenga, J.; Li, T.Q.; Yang, X.E.; He, Z.L. A modified receptor model for source apportionment of heavy metal pollution in soil. *J. Hazard. Mater.* **2018**, *354*, 161–169. [CrossRef]
7. Pavlović, P.; Mitrović, M.; Đorđević, D. Assessment of the contamination of riparian soil and vegetation by trace metals-A Danube River case study. *Sci. Total Envion.* **2016**, *540*, 396–409. [CrossRef]
8. Zhang, Y.X.; Wu, Y.; Song, B. Spatial distribution and main controlling factor of cadmium accumulation in agricultural soils in Guizhou, China. *J. Hazard. Mater.* **2022**, *424*, 127308. [CrossRef]
9. Chai, L.; Wang, Y.H.; Wang, X.; Ma, L.; Cheng, Z.; Su, L.M. Pollution characteristics, spatial distributions, and source apportionment of heavy metals in cultivated soil in Lanzhou, China. *Ecol. Indic.* **2021**, *125*, 107507. [CrossRef]
10. Kebonye, N.M.; Eze, P.N.; John, K.; Gholizadeh, A.; Dajčl, J.; Drábek, O.; Němeček, K.; Borůvka, L. Self-organizing map artificial neural networks and sequential Gaussian simulation technique for mapping potentially toxic element hotspots in polluted mining soils. *J. Geochem. Explor.* **2021**, *222*, 106680. [CrossRef]
11. Chen, T.; Chang, Q.R.; Liu, J.; Clevers, J.G.P.W.; Kooistra, L. Identification of soil heavy metal sources and improvement in spatial mapping based on soil spectral information: A case study in northwest China. *Sci. Total Environ.* **2016**, *565*, 155–164. [CrossRef] [PubMed]
12. Zhou, X.; Sheng, Y.; Zheng, Y.; Jiang, M.; Wang, M.; Zhu, Z.; Li, G.; Baars, O.; Dong, H. Bioavailability of molybdenite to support nitrogen fixation on early Earth by an anoxygenic phototroph. *Earth Planet. Sci. Lett.* **2024**, *647*, 119056. [CrossRef]
13. Sheng, Y.; Dong, H.; Coffin, E.; Myrold, D.; Kleber, M. The important role of enzyme adsorbing capacity of soil minerals in regulating β-glucosidase activity. *Geophys. Res. Lett.* **2022**, *49*, e2021GL097556. [CrossRef]
14. Liu, H.; Zhang, Y.; Yang, J. Quantitative source apportionment, risk assessment and distribution of heavy metals in agricultural soils from southern Shandong Peninsula of China. *Sci. Total Environ.* **2021**, *767*, 144879. [CrossRef]
15. Yang, J.Z.; Sun, Y.L.; Wang, Z.L. Heavy metal pollution in agricultural soils of a typical volcanic area: Risk assessment and source appointment. *Chemosphere* **2022**, *304*, 135340. [CrossRef]
16. Han, Q.; Liu, Y.; Feng, X.X. Pollution effect assessment of industrial activities on potentially toxic metal distribution in windowsill dust and surface soil in central China. *Sci. Total Environ.* **2021**, *759*, 144023. [CrossRef]
17. Sheng, Y.Z.; Kaley, B.; Bibby, K.; Grettenberger, C.; Macalady, J.L.; Wang, G.C.; Burgos, W.D. Bioreactors for low-pH iron (II) oxidation remove considerable amounts of total iron. *RSC Adv.* **2017**, *7*, 35962–35972. [CrossRef]

18. Zhang, B.; Liu, J.; Sheng, Y.; Shi, J.; Dong, H. Disentangling microbial syntrophic mechanisms for hexavalent chromium reduction in autotrophic biosystems. *Environ. Sci. Technol.* **2021**, *55*, 6340–6351. [CrossRef]
19. Liang, J.; Feng, C.T.; Zeng, G.M.; Gao, X.; Zhong, M.Z.; Li, X.D.; Li, X.; He, X.Y.; Fang, Y.L. Spatial distribution and source identification of heavy metals in surface soils in a typical coal mine city, Lianyuan, China. *Environ. Pollut.* **2017**, *225*, 681–690. [CrossRef]
20. Hu, W.Y.; Wang, H.F.; Dong, L.R.; Huang, B.; Borggaard, O.K.; Bruun, H.H.; He, Y.; Holm, P.E. Source identification of heavy metals in peri-urban agricultural soils of southeast China: An integrated approach. *Environ. Pollut.* **2018**, *237*, 650–661. [CrossRef]
21. Salim, I.; Sajjad, R.U.; Paule-Mercado, M.C.; Memon, S.A.; Lee, B.Y.; Sukhbaatar, C.; Lee, C.H. Comparison of two receptor models PCA-MLR and PMF for source identification and apportionment of pollution carried by runoff from catchment and sub-watershed areas with mixed land cover in South Korea. *Sci. Total Environ.* **2019**, *663*, 764–775. [CrossRef] [PubMed]
22. Fei, X.; Lou, Z.; Xiao, R. Contamination assessment and source apportionment of heavy metals in agricultural soil through the synthesis of PMF and GeogDetector models. *Sci. Total Environ.* **2020**, *747*, 141293. [CrossRef] [PubMed]
23. Huang, J.L.; Wu, Y.Y.; Sun, J.X.; Li, X.; Geng, X.L.; Zhao, M.L.; Sun, T.; Fan, Z.Q. Health risk assessment of heavy metal(loid)s in park soils of the largest megacity in China by using Monte Carlo simulation coupled with Positive matrix factorization model. *J. Hazard. Mater.* **2021**, *415*, 125629. [CrossRef] [PubMed]
24. Baltas, H.; Sirin, M.; Gökbayrak, E.; Ozcelik, A.E. A case study on pollution and a human health risk assessment of heavy metals in agricultural soils around Sinop province, Turkey. *Chemosphere* **2020**, *241*, 125015. [CrossRef]
25. Chen, H.Y.; Teng, Y.G.; Lu, S.J.; Wang, Y.Y.; Wang, J.S. Contamination features and health risk of soil heavy metals in China. *Sci. Total Environ.* **2015**, *512–513*, 143–153. [CrossRef]
26. Li, J.; Wang, G.C.; Liu, F.; Cui, L.F.; Jiao, Y.J. Supplementary material source apportionment and ecological-health risks assessment of heavy metals in topsoils near a factory, central China. *Expo Health* **2021**, *13*, 79–92. [CrossRef]
27. Shi, Z.Y.; Pu, W.P.; Dong, J.H. Spatiotemporal Changes of Land Use and Its Impact on Ecosystem Service Value in the Agro-pastoral Ecotone of Northern China. *Environ. Sci.* **2024**, 1–19. (In Chinese) [CrossRef]
28. Wang, W.Q.; Liu, X.; Liu, C.H. Impacts of grazing pressure on ecosystem health in the agro-pastoral intertwined areas of northern China. *Acta Ecol. Sin.* **2024**, *44*, 6288–6300.
29. Chen, R.; Chen, H.; Song, L.; Yao, Z.; Meng, F.; Teng, Y. Characterization and source apportionment of heavy metals in the sediments of Lake Tai (China) and its surrounding soils. *Sci. Total Environ.* **2019**, *694*, 445–486. [CrossRef]
30. Long, Z.J.; Zhu, H.; Bing, H.J.; Tian, X.; Wang, Z.G.; Wang, X.F.; Wu, Y.H. Contamination, sources and health risk of heavy metals in soil and dust from different functional areas in an industrial city of Panzhihua City, Southwest China. *J. Hazard. Mater.* **2021**, *420*, 126638. [CrossRef]
31. Wu, S.; Xia, X.H.; Lin, C.Y.; Chen, X.; Zhou, C.H. Levels of arsenic and heavy metals in the rural soils of Beijing and their changes over the last two decades (1985-2008). *J. Hazard. Mater.* **2010**, *179*, 860–867. [CrossRef] [PubMed]
32. Cheng, Z.; Chen, L.J.; Li, H.H.; Lin, J.B.; Yang, Z.B.; Yang, Y.X.; Xu, X.X.; Xian, J.R.; Shao, J.R.; Zhu, X.M. Characteristics and health risk assessment of heavy metals exposure via household dust from the urban area in Chengdu, China. *Sci. Total Environ.* **2018**, *619–620*, 621–629. [CrossRef] [PubMed]
33. Hakanson, L. An ecological risk index for aquatic pollution control. A sedimentological approach. *Water Res.* **1980**, *14*, 975–1001. [CrossRef]
34. Ahmad, W.; Alharthy, R.D.; Zubair, M.; Ahmed, M.; Hameed, A.; Rafique, S. Toxic and heavy metals contamination assessment in soil and water to evaluate human health risk. *Sci. Rep.* **2021**, *11*, 17006. [CrossRef]
35. Islam, M.S.; Ahmed, M.K.; Raknuzzaman, M.; Habibullah Al- Mamun, M.; Islam, M.K. Heavy metal pollution in surface water and sediment: A preliminary assessment of an urban river in a developing country. *Ecol. Indic.* **2015**, *48*, 282–291. [CrossRef]
36. USEPA. *Exposure Factors Handbook*, Final ed.; U.S. Environment Protection Agency: Washington, DC, USA, 2011.
37. Ning, H.; Jiang, W.J.; Sheng, Y.Z.; Wang, K.L.; Chen, S.M.; Zhang, Z.; Liu, F.T. Comprehensive evaluation of nitrogen contamination in water ecosystems of the Miyun reservoir watershed, northern China: Distribution, source apportionment and risk assessment. *Environ. Geochem. Health* **2024**, *46*, 278. [CrossRef]
38. Gu, Y.G.; Lin, Q.; Gao, Y.P. Metals in exposed-lawn soils from 18 urban parks and its human health implications in southern China's largest city, Guangzhou. *J. Clean. Prod.* **2017**, *163*, 164–171. [CrossRef]
39. Zhang, R.; Chen, T.; Zhang, Y.; Hou, Y.; Chang, Q. Health risk assessment of heavy metals in agricultural soils and identification of main influencing factors in a typical industrial park in northwest China. *Chemosphere* **2020**, *252*, 126591. [CrossRef]
40. Cai, L.M.; Wang, Q.S.; Wen, H.H.; Luo, J.; Wang, S. Heavy metals in agricultural soils from a typical township in Guangdong Province, China: Occurrences and spatial distribution. *Ecotoxicol. Environ. Saf.* **2019**, *168*, 184–191. [CrossRef]
41. Cui, X.T.; Wang, X.Q.; Liu, B. The characteristics of heavy metal pollution in surface dust in Tangshan, a heavily industrialized city in North China, and an assessment of associated health risks. *J. Geochem. Explor.* **2020**, *210*, 106432. [CrossRef]
42. CMEE—Ministry of Ecology and Environment of, P.R. *Soil Environmental Quality Risk Control Standard for Soil Contamination of Agricultural Land (GB15618-2018)*; China Environmental Science Press: Beijing, China, 2018; pp. 1–7. (In Chinese)
43. CNEMC—China National Environmental Monitoring Centre. *Background Values of Soil Elements in China*; China Environmental Science Press: Beijing, China, 1990; pp. 1–500. (In Chinese)

44. Jin, Y.L.; O'Connor, D.; Ok, Y.S.; Tsang, D.C.W.; Liu, A.; Hou, D.Y. Assessment of sources of heavy metals in soil and dust at children's playgrounds in Beijing using GIS and multivariate statistical analysis. *Environ. Int.* **2019**, *124*, 320–328. [CrossRef] [PubMed]
45. Marrugo-Negrete, J.; Pinedo-Hernandez, J.; Díez, S. Assessment of heavy metal pollution, spatial distribution and origin in agricultural soils along the Sinú River Basin, Colombia. *Environ. Res.* **2017**, *154*, 380–388. [CrossRef] [PubMed]
46. Cheng, W.; Lei, S.; Bian, Z.; Zhao, Y.; Li, Y.; Gan, Y. Geographic distribution of heavy metals and identification of their sources in soils near large, open-pit coal mines using Positive Matrix Factorization. *J. Hazard. Mater.* **2020**, *387*, 121666. [CrossRef] [PubMed]
47. Duzgoren-Aydin, N.S.; Li, X.D.; Wong, S.C. Lead contamination and isotope signatures in the urban environment. *Environ. Int.* **2004**, *30*, 209–217. [CrossRef]
48. Kadi, M.W. Soil pollution hazardous to environment, a case study on the chemical composition and correlation to automobile traffic of the roadside soil of Jeddah city, Saudi Arabia. *J. Hazard. Mater.* **2009**, *168*, 1280–1283. [CrossRef]
49. Peng, T.; O'Connor, D.; Zhao, B.; Jin, Y.; Zhang, Y.; Tian, L.; Zheng, N.; Li, X.; Hou, D. Spatial distribution of lead contamination in soil and equipment dust at children's playgrounds in beijing, china. *Environ. Pollut.* **2018**, *245*, 363–370. [CrossRef]
50. Liu, J.; Wang, J.; Chen, Y.H.; Lippold, H.; Xiao, T.F.; Li, H.S.; Shen, C.C.; Xie, L.H.; Xie, X.F.; Yang, H.L. Geochemical transfer and preliminary health risk assessment of thallium in a riverine system in the Pearl River Basin, South China. *J. Geochem. Explor.* **2017**, *176*, 64–75. [CrossRef]
51. Cao, J.; Ren, S.; Wang, C.; She, J.; Jiang, Y.; Liu, Y.; Zhou, Y.; Wang, L.; Wang, J.; Wang, Y.; et al. Cadmium and lead distribution in pyrite ores: Environmental concerns over geochemically mobile fractions. *Elem. Sci. Anth.* **2021**, *9*, 00093. [CrossRef]
52. Wang, S.; Cai, L.M.; Wen, H.H.; Luo, J.; Wang, Q.S.; Liu, X. Spatial distribution and source apportionment of heavy metals in soil from a typical county-level city of Guangdong Province, China. *Sci. Total Environ.* **2019**, *655*, 92–101. [CrossRef]
53. Ma, W.; Tai, L.; Qiao, Z.; Zhong, L.; Wang, Z.; Fu, K.; Chen, G. Contamination source apportionment and health risk assessment of heavy metals in soil around municipal solid waste incinerator: A case study in north china. *Sci. Total Environ.* **2018**, *631–632*, 348–357. [CrossRef]
54. Liu, L.L.; Liu, Q.Y.; Ma, J.; Wu, H.W.; Qu, Y.J.; Gong, Y.W.; Yang, S.H.; An, Y.F.; Zhou, Y.Z. Heavy metal(loid)s in the topsoil of urban parks in Beijing, China, concentrations, potential sources, and risk assessment. *Environ. Pollut.* **2020**, *260*, 114083. [CrossRef] [PubMed]
55. Sheng, Y.; Dong, H.; Kukkadapu, R.K.; Ni, S.; Zeng, Q.; Hu, J.; Coffin, E.; Zhao, S.; Sommer, A.J.; McCarrick, R.M.; et al. Lignin-enhanced reduction of structural Fe (III) in nontronite: Dual roles of lignin as electron shuttle and donor. *Geochim. Cosmochim. Acta* **2021**, *307*, 1–21. [CrossRef]
56. Sheng, Y.; Baars, O.; Guo, D.; Whitham, J.; Srivastava, S.; Dong, H. Mineral-bound trace metals as cofactors for anaerobic biological nitrogen fixation. *Environ. Sci. Technol.* **2023**, *57*, 7206–7216. [CrossRef] [PubMed]
57. Zhao, L.; Xu, Y.F.; Hou, H.; Shangguan, Y.X.; Li, F.S. Source identification and health risk assessment of metals in urban soils around the Tanggu chemical industrial district, Tianjin, China. *Sci. Total Environ.* **2014**, *468–469*, 654–662. [CrossRef] [PubMed]
58. Rodriguez, J.A.; Nanos, N.; Grau, J.M.; Gil, L.; Lopez-Arias, M. Multiscale analysis of heavy metal contents in Spanish agricultural topsoils. *Chemosphere* **2008**, *70*, 1085–1096. [CrossRef]
59. Šajn, R.; Halamić, J.; Peh, Z.; Galović, L.; Alijagić, J. Assessment of the natural and anthropogenic sources of chemical elements in alluvial soils from the Drava River using multivariate statistical methods. *J. Geochem. Explor.* **2011**, *110*, 278–289. [CrossRef]
60. Tomiyasu, T.; Kodamatani, H.; Imura, R.; Matsuyama, A.; Miyamoto, J.; Akagi, H.; Kocman, D.; Kotnik, J.ž.; Fajon, V.; Horvat, M. The dynamics of mercury near Idrija mercury mine, Slovenia, horizontal and vertical distributions of total, methyl, and ethyl mercury concentrations in soils. *Chemosphere* **2017**, *184*, 244–252. [CrossRef]
61. Xiao, R.; Wang, S.; Li, R.; Wang, J.J.; Zhang, Z. Soil heavy metal contamination and health risks associated with artisanal gold mining in Tongguan, Shaanxi, China. *Ecotoxicol. Environ. Saf.* **2017**, *141*, 17–24. [CrossRef]
62. Jiang, G.B.; Shi, J.B.; Feng, X.B. Mercury pollution in China. *Environ. Sci. Technol.* **2006**, *40*, 3672–3678. [CrossRef]
63. Pacyna, E.G.; Pacyna, J.M.; Sundseth, K.; Munthe, J.; Kindbom, K.; Wilson, S.; Steenhuisen, F.; Maxson, P. Global emission of mercury to the atmosphere from anthropogenic sources in 2005 and projections to 2020. *Atmos. Environ.* **2010**, *44*, 2487–2499. [CrossRef]
64. Dong, H.; Lin, Z.; Wan, X. Risk assessment for the mercury polluted site near a pesticide plant in Changsha, Hunan, China. *Chemosphere* **2017**, *169*, 333–341. [CrossRef] [PubMed]
65. Luo, W.; Wang, T.; Lu, Y.; Giesy, J.P.; Shi, Y.; Zheng, Y. Landscape ecology of the Guanting Reservoir, Beijing, China: Multivariate and geostatistical analyses of metals in soils. *Environ. Pollut.* **2007**, *146*, 567–576. [CrossRef] [PubMed]
66. Nan, Z.R.; Li, J.J.; Zhang, J.M.; Cheng, G.D. Cadmium and zinc interactions and their transfer in soil crop system under actual field conditions. *Sci. Total Environ.* **2002**, *285*, 187–195. [CrossRef] [PubMed]
67. Nicholson, F.A.; Smith, S.R.; Alloway, B.J.; Carlton-Smith, C.; Chambers, B.J. An inventory of heavy metals inputs to agricultural soils in England and Wales. *Sci. Total Environ.* **2003**, *311*, 205–219. [CrossRef] [PubMed]
68. Abollino, O.; Aceto, M.; Malandrino, M.; Mentasti, E.; Sarzanini, C.; Petrella, F. Heavy metals in agricultural soils from Piedmont, Italy: Distribution, speciation and chemometric data treatment. *Chemosphere* **2002**, *49*, 545–557. [CrossRef]
69. Sun, C.Y.; Liu, J.S.; Wang, Y.; Sun, L.Q.; Yu, H.W. Multivariate and geostatistical analyses of the spatial distribution and sources of heavy metals in agricultural soil in Dehui, Northeast China. *Chemosphere* **2013**, *92*, 517–523. [CrossRef]

70. Mcbride, M.B.; Spiers, G. Trace element content of selected fertilizers and dairy manures as determined by ICP-MS. *Commun. Soil Sci. Plant Anal.* **2001**, *32*, 139–156. [CrossRef]
71. Li, J.T.; Qiu, J.W.; Wang, X.W.; Zhong, Y.; Lan, C.Y.; Shu, W.S. Cadmium contamination in orchard soils and fruit trees and its potential health risk in Guangzhou, China. *Environ. Pollut.* **2006**, *143*, 159–165. [CrossRef]
72. Nogueirol, R.C.; Alleoni, L.R.F.; Nachtigall, G.R.; de Melo, G.W. Sequential extraction and availability of copper in Cu fungicide-amended vineyard soils from Southern Brazil. *J. Hazard. Mater.* **2010**, *181*, 931–937. [CrossRef]
73. Lu, A.X.; Wang, J.H.; Qin, X.Y.; Wang, K.Y.; Han, P.; Zhang, S.Z. Multivariate and geostatistical analyses of the spatial distribution and origin of heavy metals in the agricultural soils in Shunyi, Beijing, China. *Sci. Total Environ.* **2012**, *425*, 66–74. [CrossRef]
74. Liu, Z.C.; Chen, B.N.; Wang, L.A.; Urbanovich, O.; Nagorskaya, L.; Li, X.; Tang, L. A review on phytoremediation of mercury contaminated soils. *J. Hazard. Mater.* **2020**, *400*, 123138. [CrossRef] [PubMed]
75. Chen, Y.L.; Yang, W.T.; Zou, Y.Z.; Wu, Y.H.; Mao, W.J.; Zhang, J.; Zia-ur-Rehman, M.; Wang, B.; Wu, P. Quantification of the effect of biochar application on heavy metals in paddy systems: Impact, mechanisms and future prospects. *Sci. Total Environ.* **2024**, *912*, 168874. [CrossRef] [PubMed]
76. Sizmur, T.; Fresno, T.; Akgül, G.; Frost, H.; Moreno-Jiménez, E. Biochar modification to enhance sorption of inorganics from water. *Bioresour. Technol.* **2017**, *246*, 34–47. [CrossRef] [PubMed]
77. Yang, J.P.; Zhao, Y.C.; Ma, S.M.; Zhu, B.B.; Zhang, J.Y.; Zheng, C.G. Mercury Removal by Magnetic Biochar Derived from Simultaneous Activation and Magnetization of Sawdust. *Environ. Sci. Technol.* **2016**, *50*, 12040–12047. [CrossRef]
78. Guo, W.P.; Yao, X.; Chen, Z.; Liu, T.; Wang, W.; Zhang, S.J.; Xian, J.Q.; Wang, Y.H. Recent advance on application of biochar in remediation of heavy metal contaminated soil: Emphasis on reaction factor, immobilization mechanism and functional modification. *J. Environ. Manag.* **2024**, *371*, 123212. [CrossRef]
79. Song, P.P.; Xu, D.; Yue, J.Y.; Ma, Y.C.; Dong, S.J.; Feng, J. Recent advances in soil remediation technology for heavy metal contaminated sites: A critical review. *Sci. Total Environ.* **2022**, *838*, 156417. [CrossRef]
80. Astel, A.; Tsakovski, S.; Barbieri, P.; Simeonov, V. Comparison of self-organizing maps classification approach with cluster and principal components analysis for large environmental data sets. *Water Res.* **2007**, *41*, 4566–4578. [CrossRef]
81. Bian, B.; Lin, C.; Wu, H.S. Contamination and risk assessment of metals in road-deposited sediments in a medium-sized city of China. Ecotoxicol. *Environ. Saf.* **2015**, *112*, 87–95. [CrossRef]
82. Céréghino, R.; Park, Y.S. Review of the Self-Organizing Map (SOM) approach in water resources: Commentary. *Environ. Model. Softw.* **2009**, *24*, 945–947. [CrossRef]
83. Chen, Y.; Jiang, X.; Wang, Y.; Zhuang, D. Spatial characteristics of heavy metal pollution and the potential ecological risk of a typical mining area: A case study in China. *Process. Saf. Environ. Prot.* **2018**, *113*, 204–219. [CrossRef]
84. Clark, S.; Sisson, S.A.; Sharma, A. Tools for enhancing the application of selforganizing maps in water resources research and engineering. *Adv. Water Resour.* **2020**, *143*, 103676. [CrossRef]
85. CMEP; Ministry of Environmental Protection of P.R. China. *Technical Guidance for Risk Assessment of Contaminated Sites, (HJ 25.3-2014)*; China Environmental Science Press: Beijing, China, 2014. (In Chinese)
86. Fernández, J.; Carballeira, A. Evaluation of contamination, by different elements, in terrestrial mosses. *Arch. Environ. Contam. Toxicol.* **2001**, *40*, 461–468. [PubMed]
87. Ferreira-Baptista, L.; Miguel, E. Geochemistry and risk assessment of street dust in Luanda, Angola: A tropical urban environment. *Atmos. Environ.* **2005**, *38*, 4501–4512. [CrossRef]
88. Huang, Y.; Wang, L.Y.; Wang, W.J.; Li, T.Q.; He, Z.L.; Yang, X. Current status of agricultural soil pollution by heavy metals in China: A meta-analysis. *Sci. Total Environ.* **2019**, *651*, 3034–3042. [CrossRef]
89. Jiang, H.H.; Cai, L.M.; Wen, H.H.; Hu, G.C.; Chen, L.G.; Luo, J. An integrated approach to quantifying ecological and human health risks from different sources of soil heavy metals. *Sci. Total Environ.* **2020**, *701*, 134466. [CrossRef]
90. Kusin, F.M.; Azani, N.N.M.; Hasan, S.N.M.S.; Sulong, N.A. Distribution of heavy metals and metalloid in surface sediments of heavily-mined area for bauxite ore in Pengerang, Malaysia and associated risk assessment. *Catena* **2018**, *165*, 454–464. [CrossRef]
91. Li, Z.Y.; Ma, Z.W.; Kuijp, T.J.; Yuan, Z.W.; Huang, L. A review of soil heavy metal pollution from mines in China: Pollution and health risk assessment. *Sci. Total Environ.* **2014**, *468-469*, 843–853. [CrossRef]
92. Lu, X.; Wu, X.; Wang, Y.; Chen, H.; Gao, P.; Fu, Y. Risk assessment of toxic metals in street dust from a medium–sized industrial city of China. *Ecotoxicol. Environ. Saf.* **2014**, *106*, 154–163. [CrossRef]
93. Ma, J.; Wang, X.; Hou, Q.; Duan, J. Pollution and potential ecological risk of heavy metals in surface dust on urban kindergartens. *Geogr. Res.* **2011**, *30*, 486–495.
94. Mao, H.R.; Wang, G.C.; Rao, Z.; Liao, F.; Shi, Z.M.; Huang, X.J.; Chen, X.L.; Yang, Y. Deciphering spatial pattern of groundwater chemistry and nitrogen pollution in Poyang Lake Basin (eastern China) using self-organizing map and multivariate statistics. *J. Clean. Prod.* **2021**, *329*, 129697. [CrossRef]
95. Singh, U.K.; Ramanathan ALSubramanian, V. Groundwater chemistry and human health risk assessment in the mining region of East Singhbhum, Jharkhand, India. *Chemosphere* **2018**, *204*, 501–513. [CrossRef] [PubMed]
96. Tong, S.M.; Li, H.R.; Tudi, M.; Yuan, X.; Yang, L.S. Comparison of characteristics, water quality and health risk assessment of trace elements in surface water and groundwater in China. *Ecotox. Environ. Safe.* **2021**, *219*, 112283. [CrossRef] [PubMed]
97. USEPA. *Supplemental Guidance for Developing Soil Screening Levels for Superfund Sites*; U.S. Environmental Protection Agency, Office of Emergency and Remedial Response: Washington, DC, USA, 2002.

98. USEPA. Region IX, Regional Screening Levels (Formerly PRGs). San Francisco, CA 94105. 2013. Available online: http://www.epa.gov/region9/superfund/prg/ (accessed on 23 November 2014).
99. USEPA. U.S. Environmental Protection Agency, Integrated Risk Information System. 2014. Available online: http://www.epa.gov/iris/ (accessed on 23 November 2014).
100. Vesanto, J.; Alhoniemi, E. Clustering of the self-organizing map. *IEEE Trans. Neural Netw.* **2000**, *11*, 586–600. [CrossRef] [PubMed]
101. Wang, Z.Y.; Meng, B.; Zhang, W.; Bai, J.H.; Ma, Y.X.; Liu, M.D. Multi-Target Risk Assessment of Potentially Toxic Elements in Farmland Soil Based on the Environment-Ecological-Health Effect. *Int. J. Environ. Res. Public Health* **2018**, *15*, 1101. [CrossRef]
102. Wang, S.Y.; Wang, L.Q.; Huan, Y.Z.; Wang, R.; Liang, T. Concentrations, spatial distribution, sources and environmental health risks of potentially toxic elements in urban road dust across China. *Sci. Total Environ.* **2022**, *805*, 150266. [CrossRef]
103. Wu, H.; Yang, F.; Li, H.; Li, Q.; Zhang, F.; Ba, Y.; Cui, L.; Sun, L.; Lv, T.; Wang, N. Heavy metal pollution and health risk assessment of agricultural soil near a smelter in an industrial city in China. *Int. J. Environ. Health Res.* **2019**, *30*, 174–186. [CrossRef]
104. Xiao, J.; Wang, L.; Deng, L.; Jin, Z. Characteristics, sources, water quality and health risk assessment of trace elements in river water and well water in the Chinese Loess Plateau. *Sci. Total Environ.* **2019**, *650 Pt 2*, 2004–2012. [CrossRef]
105. Xie, X.F.; Liu, Y.X.; Qiu, H.; Yang, X.S. Quantifying ecological and human health risks of heavy metals from different sources in farmland soils within a typical mining and smelting industrial area. *Environ. Geochem. Health* **2020**, *45*, 5669–5683. [CrossRef]
106. Zuo, L.; Lu, X.W.; Fan, P.; Wang, L.Q.; Yu, B.; Lei, K.; Yang, Y.F.; Chen, Y.R. Concentrations, sources and ecological–health risks of potentially toxic elements in finer road dust from a megacity in north China. *J. Clean. Product.* **2022**, *358*, 132036. [CrossRef]

Disclaimer/Publisher's Note: The statements, opinions and data contained in all publications are solely those of the individual author(s) and contributor(s) and not of MDPI and/or the editor(s). MDPI and/or the editor(s) disclaim responsibility for any injury to people or property resulting from any ideas, methods, instructions or products referred to in the content.

water

MDPI

Article

Status, Sources, and Risks of Heavy Metals in Surface Sediments of Baiyangdian Lake and Inflow Rivers, North China

Hongwei Liu [1,2,3,4], Yaonan Bai [1,3,4], Yihang Gao [1,3,4,*], Bo Han [1,3,4], Jinjie Miao [1,3,4], Yanchao Shi [5,*] and Fengtian Yang [6]

[1] Tianjin Center, China Geological Survey (North China Center for Geoscience Innovation of China Geological Survey), No. 4 Dazhigu 8th Road, Tianjin 300170, China; liuhenry022@163.com (H.L.); byaonan@mail.cgs.gov.cn (Y.B.); hanbo1984@126.com (B.H.); tjmiaojj@163.com (J.M.)
[2] Chinese Academy of Geological Sciences, No. 26 Baiwanzhuang Street, Beijing 100037, China
[3] Xiong'an Urban Geological Research Center, China Geological Survey, No. 4 Dazhigu 8th Road, Tianjin 300170, China
[4] Tianjin Key Laboratory of Coast Geological Processes and Environmental Safety, No. 4 Dazhigu 8th Road, Tianjin 300170, China
[5] Hebei Geo-Environment Monitoring, Shijiazhuang 050021, China
[6] Key Laboratory of Groundwater Resources and Environment, Ministry of Education, Jilin University, Changchun 130021, China; yangfengtian@jlu.edu.cn
* Correspondence: gaoyihang1988@163.com (Y.G.); shiyanchao521@126.com (Y.S.)

Abstract: Baiyangdian Lake, recognized as the largest freshwater body in northern China, plays a vital role in maintaining the regional eco-environment. Prior studies have pointed out the contamination of sediments with heavy metals, raising concerns about eco-environmental challenges. Therefore, it is imperative to evaluate the current pollution levels and ecological threats related to heavy metals found in the sediments of Baiyangdian Lake as well as in its inflow rivers. In May 2022, surface sediments with a depth of less than 20 cm were analyzed for Cu, Zn, Pb, Cr, Ni, As, Cd, and Hg to determine the pollution status, identify sources of pollution, and evaluate potential ecological risks. A range of evaluation methods used by predecessors such as geo-accumulation index (I_{geo}), enrichment factor (*EF*), ecological risk index (*RI*), sediment quality guidelines (*SQGs*), positive matrix factorization (*PMF*), absolute principal component score-multiple linear regression model (*APCS-MLR*), chemical mass balance (*CMB*), and *UNMIX* model were analyzed. After comparison, multi-methods including the geo-accumulation index (*Igeo*), absolute principal component score-multiple linear regression model (*APCS-MLR*), ecological risk index (*RI*), and sediment quality guidelines (*SQGs*) were utilized this time, leading to a better result. Findings reveal that pollution levels are generally low or non-existent, with only 1.64% of sampling sites showing close to moderate pollution levels for Cu, Pb, and Zn, and 4.92% and 1.64% of sites exhibiting close to moderate and moderate pollution levels for Cd, respectively. The main contributors to heavy metal presence are pinpointed as industrial wastewater discharge, particularly Cu, Zn, Pb, Cd, and Hg. The ecological risks are also relatively low, with 4.92%, 1.64%, and 1.64% of sampling sites demonstrating close to moderate, moderate, and strong risks in the inflow rivers, respectively. Additionally, only one site shows moderate potential biological toxicity, while the rest display non-toxicity. These findings will update our cognition and offer a scientific basis for pollution treatment and ecosystem enhancement for government management.

Keywords: heavy metals; pollution sources; potential risks; multi-methods (*RI*) (*APCS-MLR*) (I_{geo}) (*SQGs*); surface sediments; Baiyangdian Lake

1. Introduction

Pollution from heavy metals has become a significant worldwide concern [1–6], with rivers, lakes, and oceans serving as primary repositories for these contaminants [7–9]. The heavy metals are discharged into water bodies through anthropogenic activities such as industrial, agricultural, and daily life practices [10–12], as well as natural processes like

rock weathering [13–15]. Upon entering the water, heavy metals settle in sediments at the bottom [13,16], where they can persist for extended periods [17]. When disturbed, these contaminated sediments can act as secondary sources of pollution [9], negatively impacting water quality and ecological health. The long residual and chronic toxic nature of heavy metals in sediments will lead to environmental deterioration, the degradation of water quality [3,18,19], and pose a threat to human health and aquatic life by entering into the food chain and causing various diseases, including genetic mutations [20–24]. Assessing the pollution and identifying the driving factors of heavy metals in sediments can provide worthy insights for contamination mitigation and ecosystem enhancement [10,25]. As a result, the pollution of heavy metals in sediments has garnered global attention and has become a hotspot of academic research [26–28].

To date, pollution and ecological risk evaluation for heavy metals have primarily relied on methods such as geo-accumulation index (*Igeo*) [29,30], enrichment factor (*EF*) [31,32], ecological risk index (*RI*) [33,34], sediment quality guidelines (*SQGs*) [35,36], pollution index (*RI*) [37], and pollution load index (*PLI*) [37]. The comprehensive use of multiple methods is a clear trend in this field [38–40]. It is important to note that obtaining an objective background or reference value is crucial in determining the validity of evaluation results. Additionally, the quantitative identification of contaminant sources often involves receptor models [41] like positive matrix factorization (*PMF*) [42,43], absolute principal component score–multiple linear regression model (*APCS-MLR*) [44–46], chemical mass balance (*CMB*) [47,48], and *UNMIX* model [49,50]. Each of these models has its own strengths and weaknesses [51,52], and sometimes different models may yield similar results, such as *APCS-MLR* and *PMF* [53,54]. Recent studies suggest that *APCS-MLR* generally outperforms other common models [51].

In China, over the past few decades, heavy metal pollution has occurred in the sediments of some rivers and lakes due to human activities such as industrial production. In the past ten years, China has attached great importance to the protection of the ecological environment and the treatment of pollution and has adopted many remediation measures, which have improved the quality of surface water and sediment environment. Turning to Baiyangdian Lake and its inflow rivers, focusing on heavy metals, many scholars have conducted studies on the pollution status and ecological risks in surface sediments. Although previous research reveals that heavy metals such as As, Cd, Cr, Co, Cu, Fe, Pb, Hg, Mn, Ni, and Zn et al., when their concentration reaches a certain value, may have a negative impact on lakes and rivers [37], published papers have been concluded that heavy metals have presented eco-environmental challenges in both past and recent years in the surface sediments mainly due to Cu, Zn, Pb, Cr, Ni, As, Cd, and Hg in the study area [9,55,56]. Previous research indicates that heavy metals may derive from various sources including industrial wastewater discharge, agricultural and domestic sewage discharge, and rock weathering deposition [2,57,58]. Specifically, Cd, As, Hg, Pb, and Zn are closely linked to wastewater discharge from refining and electroplating activities [59,60], and, to a certain extent, domestic sewage discharge [61]. The As element is also influenced by rock weathering deposition [37], as well as agricultural and domestic sewage discharge [62]. Cu, Zn, and Cd are additionally sourced from rock weathering deposition [19], automobile exhaust emissions, and tire wear sediment [59,60], while Hg is also impacted by atmospheric deposition [63]. Moreover, Cr and Ni are notably also influenced by rocks weathering deposition [59,60,63]. From the perspective of the source location for heavy metals, the concentrations of Zn, Hg, Cu, Cd, Ni, and Cr are affected by external input from rivers [37], with Cu, Cd, and Zn showing significant changes due to this input [30]. Pb and Cr are also influenced by human activities [30,37], while As is significantly impacted by local human activities [30]. The sources and relationships among these heavy metals are complex, making traditional quantitative research methods like correlation analysis and hierarchical clustering less applicable. The above findings provide a solid foundation for current research efforts.

However, previous studies have primarily been concerned with the pollution of the surface sediments in Baiyangdian Lake, with limited attention given to pollution in the

inflow rivers that recharge the lake. Only a few rivers, such as Fuhe, Tanghe, Xiaoyihe, and Zhulonghe, have been studied [37,57,58,61]. Additionally, previous research did not quantitatively identify the contribution of diverse pollution sources, such as industry and rock weathering, to heavy metals pollution in the surface sediments of Baiyangdian Lake and its inflow rivers. Building upon these gaps, this study aims to: (1) identify the current pollution status of heavy metals in surface sediments of Baiyangdian Lake and all its inflow rivers using the *Igeo* index; (2) determine pollution sources and respective contribution rates through the *APCS-MLR* model; and (3) recognize potential ecological risks and biological toxicity applying the *RI* and *SQGs*.

2. Study Area

Baiyangdian Lake, acknowledged as the largest freshwater body in Northern China [64], is situated in the central region of Hebei Province, with central coordinates around (116°00′ E, 38°52′ E) (Figure 1). It has the characteristics of a monsoon, continental, and semi-arid climate; 80% of precipitation in the year is concentrated from July to September, and the average water surface evaporation is 925 mm. The typical annual temperature fluctuates between 7.3 °C and 12.7 °C, with an average annual precipitation of approximately 563.9 mm [17]. Baiyangdian Lake is crucial for preserving the eco-environment of the surrounding area [8], with several inflow rivers including Fuhe, Nanpuhe, Pinghe, Baigouyinhe, Tanghe, Xiaoyihe, Zhulonghe, Renwenganqu, and Zhaowangxinqu within its watershed (Figure 1). Under natural conditions, the rivers of Fuhe, Baigouyinhe, and Xiaoyihe input water into the lake all year round, and other rivers run into the lake in wet seasons. In recent years, the annual ecological water replenishment through the rivers into Baiyangdian Lake is more than 4.0×10^8 m^3, and the water level of the lake is maintained at 6.5~7.4 m. The mean water storage capacity of Baiyangdian Lake reaches about 13.2×10^8 m^3, with a total area of 366 km^2. The surface ground around Baiyangdian Lake and its inflow rivers primarily consist of Quaternary alluvial, diluvial, and lacustrine deposits [65], while silt, sandy mud, and muddy sand are prevalent in the shallow sediments of the lake and its inflow rivers. Human activities during a historical period have led to heavy metals pollution in this region, deteriorating the water and sediment quality of Baiyangdian Lake [17,62]. The main sources of pollution include domestic waste, agricultural chemicals from residents, and industrial pollutants from both local and upstream areas carried by the inflowing rivers [66–68].

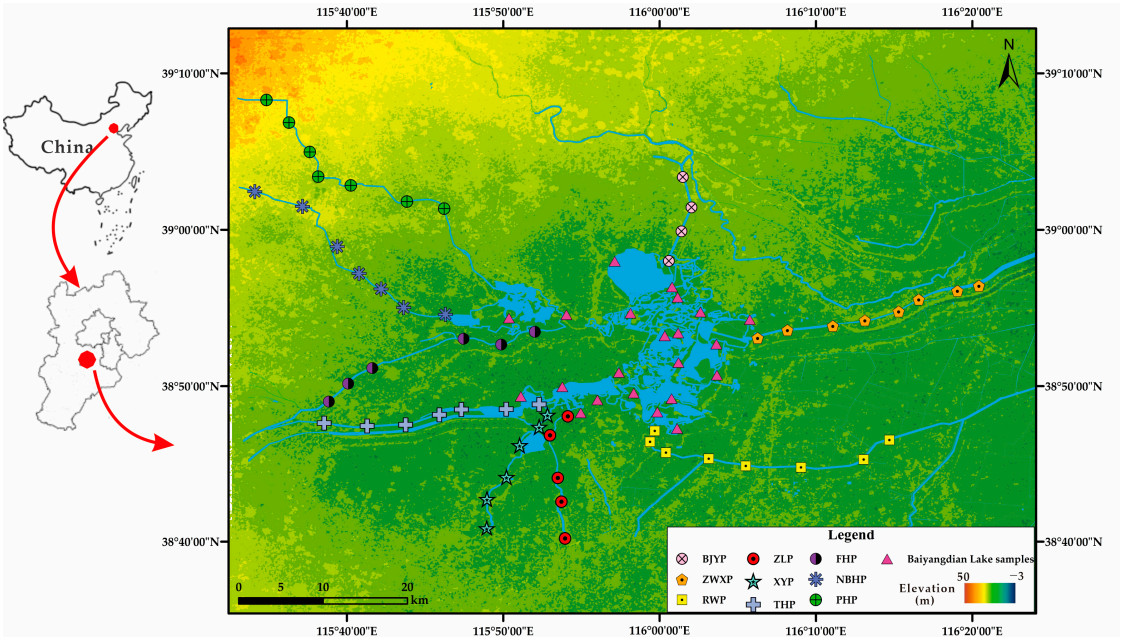

Figure 1. Location of sampling sites and study area.

3. Materials and Methods

3.1. Sampling and Analysis

In May 2022, 83 surface sediment samples were gathered from depths from 0 to 20 cm in the study area using a plastic columnar sampler. These samples were obtained from 61 sites across 9 rivers, namely, Fuhe (FHP), Nanpuhe (NBHP), Pinghe (PHP), Baigouyinhe (BJYP), Tanghe (THP), Xiaoyihe (XYP), Zhulonghe (ZLP), Renwenganqu (RWP), and Zhaowangxinqu (ZWXP), as well as 22 sites within Baiyangdian Lake (BYD) (Figure 1). Upon collection, the samples were meticulously labeled, numbered, refrigerated at 4 °C, and then transferred to a laboratory for heavy metal concentration measuring, including Cu, Zn, Pb, Cr, Cd, As, Ni, and Hg. Subsequently, the samples underwent natural drying at 20 °C until reaching a consistent weight. Following the manual removal of plant roots, shellfish residues, and gravel, the samples were crushed and sifted through a mesh made of nylon fiber filaments with a pore diameter of 2 mm to produce sediment powder, which was then stored in clean and dry glass bottles for further analysis.

After that, the powder samples were firstly dissolved in a mixture of HNO_3, HF, and $HClO_4$ inside a clean and dry Teflon crucible, and then a mixture of HCl and HNO_3 was introduced into the crucible for digestion, followed by evaporation under ventilated conditions. Subsequently, a certain amount of HNO_3 was added to the residue, which was then dissolved under heat. After cooling, the samples were transferred to a flask, diluted with ultrapure water, and prepared for testing using various instruments. The concentrations of Zn and Cr were measured using inductively coupled plasma atomic emission spectrometry (ICP-AES, iCAP6300, USA), whereas As and Hg concentrations were determined with an atomic fluorescence spectrophotometer (AFS-230, China). Cu, Pb, Cd, and Ni concentrations were analyzed using inductively coupled plasma mass spectrometry (ICP-MS, Thermo X-II, USA). To guarantee the reliability and accuracy of the test results, national standard materials [5], repeated samples, and blank samples were included in the analysis.

3.2. Pollution Levels of Heavy Metals

After obtaining the precise concentration data of heavy metals by integrated use of these automatic instruments mentioned in the last paragraph, the geo-accumulation index (I_{geo}) is utilized to estimate the pollution levels of heavy metals, which takes into account the effects of natural geological processes and human activities on heavy metals [5,13]. By comparing the concentration of heavy metals found in stream sediments to local background values, this index is expressed as [13,69]:

$$I_{geo} = log_2(C_i/1.5B_i) \quad (1)$$

where C_i is the measured concentration of heavy metal i (mg/kg), and B_i represents the local background value of heavy metal i (mg/kg) (Table 1). The pollution levels are classified as practically no pollution ($Igeo \leq 0$), light pollution ($0 < Igeo \leq 1$), close to moderate pollution ($1 < Igeo \leq 2$), moderate pollution ($2 < Igeo \leq 3$), close to strong pollution ($3 < Igeo \leq 4$), strong pollution ($4 < Igeo \leq 5$), and extreme pollution ($Igeo > 5$) [27,70].

Table 1. The background values of heavy metals for surface sediments in the study area.

Item	Cu	Zn	Pb	Cr	Cd	As	Ni	Hg
Background value/(mg·kg^{-1})	22.6	78.4	26	68.3	0.097	13.6	30.8	36
Data sources	[71]	[9,17]	[71]	[9,17]	[9,17,71]	[9,17]	[9]	[72]

3.3. Pollution Sources of Heavy Metals

The recognition of pollution sources of heavy metals can be achieved through *APCS-MLR* [73,74]. Initially, a concept of dimensionality reduction is applied to condense multiple indicators into a few comprehensive ones. Principal component analysis (*PCA*) serves to

investigate the connections among various indicators and to derive a condensed set of representative indicators that encapsulate critical information [21,75]. Subsequently, the rotation indicator load matrix and eigenvalues are obtained through varimax rotation based on *PCA* results, leading to the calculation of the absolute principal component score (*APCS*). Finally, by integrating *APCS* with multiple linear regression (*MLR*), the mean contribution rate (F_j) of each pollution source to every indicator can be determined [76–78].

The *MLR* is expressed as [73,74]:

$$C_j = b_{j0} + \sum_{p=1}^{m}(b_{pj}APCS_p) \quad (2)$$

where C_j denotes the measured concentration of heavy metal j (mg/kg), b_{j0} stands for the multiple regression constant term of heavy metal j, and b_{pj} is the regression coefficient of heavy metal j to pollution source p. m represents the number of pollution sources, $APCS_p$ stands for the absolute principal component factor score, and $b_{pj}APCS_p$ indicates the contribution of pollution source p to C_j.

The F_j is expressed as [76–78]:

$$F_j = (\mid b_{pj}\left(APCS_{\,p}\right)_{mean} \mid)/(\mid b_{j0} \mid + \sum_{p=1}^{m} \mid b_{pj}APCS_p \mid) \quad (3)$$

3.4. Potential Ecological Risks of Heavy Metals Pollution

The potential ecological risks associated with heavy metal pollution can be assessed according to the comprehensive ecological risk index (*RI*) and the sediment quality guidelines (*SQGs*), respectively.

3.4.1. Comprehensive Ecological Risk Index (RI)

The potential ecological risks can be evaluated using *RI* by integrating the concentrations of heavy metals, alongside their ecological, environmental, and toxicological impacts, in accordance with sedimentology principles. The equations are expressed as [71,79]:

$$E_i = T_i(C_i/B_i) \quad (4)$$

$$RI = \sum_{i=1}^{n} E_i \quad (5)$$

where C_i represents the measured concentration of heavy metal i (mg/kg), and B_i stands for the local background value of heavy metal i (mg/kg) (Table 1). T_i represents the toxicity parameter of heavy metal i, and the values are 30 (Cd), 5 (Cu, Pb, Ni), 2 (Cr), 1 (Zn), 10 (As), and 40 (Hg), respectively [59]. E_i denotes the ecological risk index to heavy metal i, n means the number of heavy metal species. The classification of *RI* is displayed in Table 2 [9].

Table 2. Grading criteria to pollution levels of heavy metals according to the ecological risk index.

Ecological Risk Index to Single Heavy Metal	Comprehensive Ecological Risk Index to Multiple Heavy Metals	Risk Levels
$E_i < 40$	$RI < 150$	light
$40 \leq E_i < 80$	$150 \leq RI < 300$	close to moderate
$80 \leq E_i < 160$	$300 \leq RI < 600$	moderate
$160 \leq E_i < 320$	$RI \geq 600$	strong
$E_i \geq 320$	-	extreme

3.4.2. Sediment Quality Guidelines (SQGs)

The potential biological toxicity of heavy metals to benthic organisms or overlying aquatic organisms can be estimated by the sediment quality guidelines (*SQGs*). The equations are expressed as [17,80]:

$$TUs_i = C_i/PEC_i \quad (6)$$

$$\sum TUs = \sum_{i=1}^{n} C_i / PEC_i \quad (7)$$

$$I_{SQGs} = (\sum TUs)/n \quad (8)$$

where C_i is the measured concentration of heavy metal i (mg/kg), PEC_i stands for the probable effect concentration of heavy metal i (mg/kg) (Table 3), and n means the number of heavy metal species. TUs_i denotes the toxicity unit of heavy metal i, and I_{SQGs} is the sediment quality guidelines index.

When $\Sigma TUs < 4$, heavy metals in sediments can be deemed as non-toxic; when $\Sigma TUs \geq 6$, it can be classified as having acute toxicity; and when $4 \leq \Sigma TUs < 6$, it can be categorized as having moderate toxicity [81–83]. Moreover, if the C_i is below the threshold effect concentration (*TEC*) (mg/kg) (Table 3), the toxic effect rarely occurs; if the C_i exceeds the *PEC* (mg/kg), the toxic effect will occur frequently; and if the C_i is within the range of *TEC* and *PEC*, the toxic effect will occasionally occur [84–86]. The classification of I_{SQGs} is displayed in Table 4 [16,87,88].

Table 3. Threshold criteria to *TEC* and *PEC*.

	Cu	Zn	Pb	Cr	Cd	As	Ni	Hg
$TEC/(mg{\cdot}kg^{-1})$	31.6	121	35.8	43.4	0.99	9.79	22.7	0.18
$PEC/(mg{\cdot}kg^{-1})$	149	459	128	111	4.98	33	48.6	1.06
Data sources	[9,84,89]	[84,89]	[84,89]	[9,84,89]	[9,84,89]	[9,84,89]	[9,84,89]	[84,89]

Table 4. Grading criteria to potential biological toxicity of heavy metals according to I_{SQGs}.

Item	$I_{SQGs} \leq 0.1$	$0.1 < I_{SQGs} \leq 1$	$1 < I_{SQGs} \leq 5$	$I_{SQGs} > 5$
Probability of biological toxicity (PBT)	PBT < 14%	15% < PBT ≤ 29%	33% < PBT ≤ 58%	75% < PBT ≤ 81%
Risk levels	no	low	moderate	high

4. Results and Discussion

4.1. Pollution Levels of Heavy Metals

With the exception of Hg in inflow rivers and As and Hg in Baiyangdian Lake, the concentration of other heavy metals in certain sites, both in the surface sediments of inflow rivers and Baiyangdian Lake, was found to be higher than their background values based on statistical data analysis. Among the 61 sites in inflow rivers, the concentrations of Cu, Zn, Pb, Cr, Cd, As, and Ni were larger than their background values in 45, 32, 22, 33, 41, 51, and 5 sites, respectively, accounting for 73.77%, 52.46%, 36.07%, 54.10%, 67.21%, 83.61%, and 8.20% of the sites. In Baiyangdian Lake, out of the 22 sites, the concentrations of Cu, Pb, Zn, Cr, Ni, and Cd exceeded their background values in 16, 3, 8, 7, 11, and 17 sites, representing proportions of 72.73%, 13.64%, 36.36%, 31.82%, 50.00%, and 77.27%, respectively. Furthermore, the mean and median values of heavy metal concentrations in inflow rivers are almost all larger than those in Baiyangdian Lake, indicating a higher overall pollution level of heavy metals in the upstream region of the watershed (Table 5). Additionally, the variation coefficient of heavy metal concentrations in inflow rivers was also larger than that in Baiyangdian Lake, with a relatively large variation coefficient among different heavy metals, suggesting significant differences in pollution levels among various heavy metals in inflow rivers (Table 5). This phenomenon might be attributed to two primary factors: (1) the relatively large interval distance between sampling sites, and (2) the distinct locations of different sampling sites, which were significantly influenced by human activities and various pollution sources. This underscored the importance of identifying the sources of pollution.

Table 5. Concentration statistics of heavy metals at sampling sites.

Item	Cu	Zn	Pb	Cr	Cd	As	Ni	Hg
Max/(mg·kg^{-1})	81.200	372.000	123.000	92.600	2.250	28.700	54.200	0.200
Mean/(mg·kg^{-1})	27.746	82.849	30.269	69.931	0.207	9.544	33.669	0.042
Min/(mg·kg^{-1})	15.200	41.900	14.900	46.100	0.038	2.080	20.600	0.010
Standard deviation	9.796	38.495	14.308	9.855	0.294	4.073	6.226	0.034
Variation coefficient	35.305%	46.464%	47.270%	14.092%	141.765%	42.673%	18.493%	81.556%
Upper quartile (75%)	30.500	88.900	34.900	76.050	0.200	11.250	37.000	0.041
Median	26.000	72.700	26.900	70.300	0.150	8.880	33.600	0.029
Lower quartile (25%)	21.750	64.500	21.600	63.550	0.110	7.235	29.050	0.024
Max/(mg·kg^{-1})	33.100	91.300	30.500	75.300	0.220	13.500	40.700	0.074
Mean/(mg·kg^{-1})	25.159	72.918	22.768	62.927	0.136	8.191	31.800	0.035
Min/(mg·kg^{-1})	18.100	50.400	15.300	48.800	0.056	4.800	24.300	0.015
Standard deviation	3.887	12.457	3.755	8.474	0.051	1.778	4.767	0.015
Variation coefficient	15.450%	17.083%	16.493%	13.467%	37.623%	21.706%	14.990%	44.508%
Upper quartile (75%)	27.800	86.750	25.025	72.800	0.178	8.925	36.675	0.045
Median	24.100	72.900	23.150	62.250	0.130	8.255	30.750	0.030
Lower quartile (25%)	22.450	64.100	20.250	55.425	0.096	7.242	28.100	0.025

The I_{geo} values calculated for both the surface sediment of the inflow rivers and Baiyangdian Lake suggest that the levels of heavy metal pollution were relatively low (Figure 2). Among the 63 sites in inflow rivers, negative values for Cr and Hg displayed no pollution from these heavy metals. However, Cu, Zn, Pb, Cd, As, and Ni were found in 8, 5, 9, 27, 1, and 1 sites, respectively, with proportions of 13.11%, 8.20%, 14.75%, 44.26%, 1.64%, and 1.64%, showing light pollution. Cu, Pb, Zn, and Cd were present in one, one, one, and three sites, respectively, with proportions of 1.64%, 1.64%, 1.64%, and 4.92%, indicating close to moderate pollution levels. Additionally, Cd was found in one site, accounting for 1.64%, showing moderate pollution. In Baiyangdian Lake, out of the 22 sites, Cu, Zn, Pb, Cr, As, Ni, and Hg were at no pollution level, while Cd was present in eight sites, representing 36.36% of places displaying light pollution. Furthermore, the median values of I_{geo} for Cu were −0.413 (no pollution), 0.204 (light pollution), and 1.260 (close to moderate pollution). For Pb, the median values of I_{geo} were −0.700 (no pollution), 0.219 (light pollution), and 1.496 (close to moderate pollution). The median values of I_{geo} for Zn were −0.716 (no pollution), 0.188 (light pollution), and 1.408 (close to moderate pollution). The median value of I_{geo} for Cr was −0.600 (no pollution). For Ni, the median values of I_{geo} were −0.013 (no pollution) and 0.230 (light pollution). The median values of I_{geo} for Cd were −0.404 (no pollution), 0.307 (light pollution), 1.918 (close to moderate pollution), and 2.563 (moderate pollution). The median values of I_{geo} for As were −1.271 (no pollution) and 0.492 (light pollution). Lastly, the median value of I_{geo} for Hg was −10.814 (no pollution). These values were crucial for enhancing our understanding of the average pollution levels associated with various heavy metals.

4.2. Pollution Sources of Heavy Metals

Principal component analysis (*PCA*) was performed on the surface sediments of inflow rivers and Baiyangdian Lake, revealing that the sum of the first three principal component eigenvalues for the eight heavy metals was 6.817 and 6.921, respectively (Figure 3). These values accounted for 84.214% and 86.517% of the total information, respectively. The main load heavy metals (Tables 6 and 7) of the principal component PC01 for the inflow rivers were Cu, Zn, Pb, Cr, Cd, As, Ni, and Hg; the principal component PC02 consisted of Cr, Cd, and Ni, and the principal component PC03 included As and Hg. On the other hand, for Baiyangdian Lake, the principal component PC01 encompassed Cu, Zn, Pb, Cr, Cd, and Ni. PC02 included As, and PC03 was comprised of As and Hg.

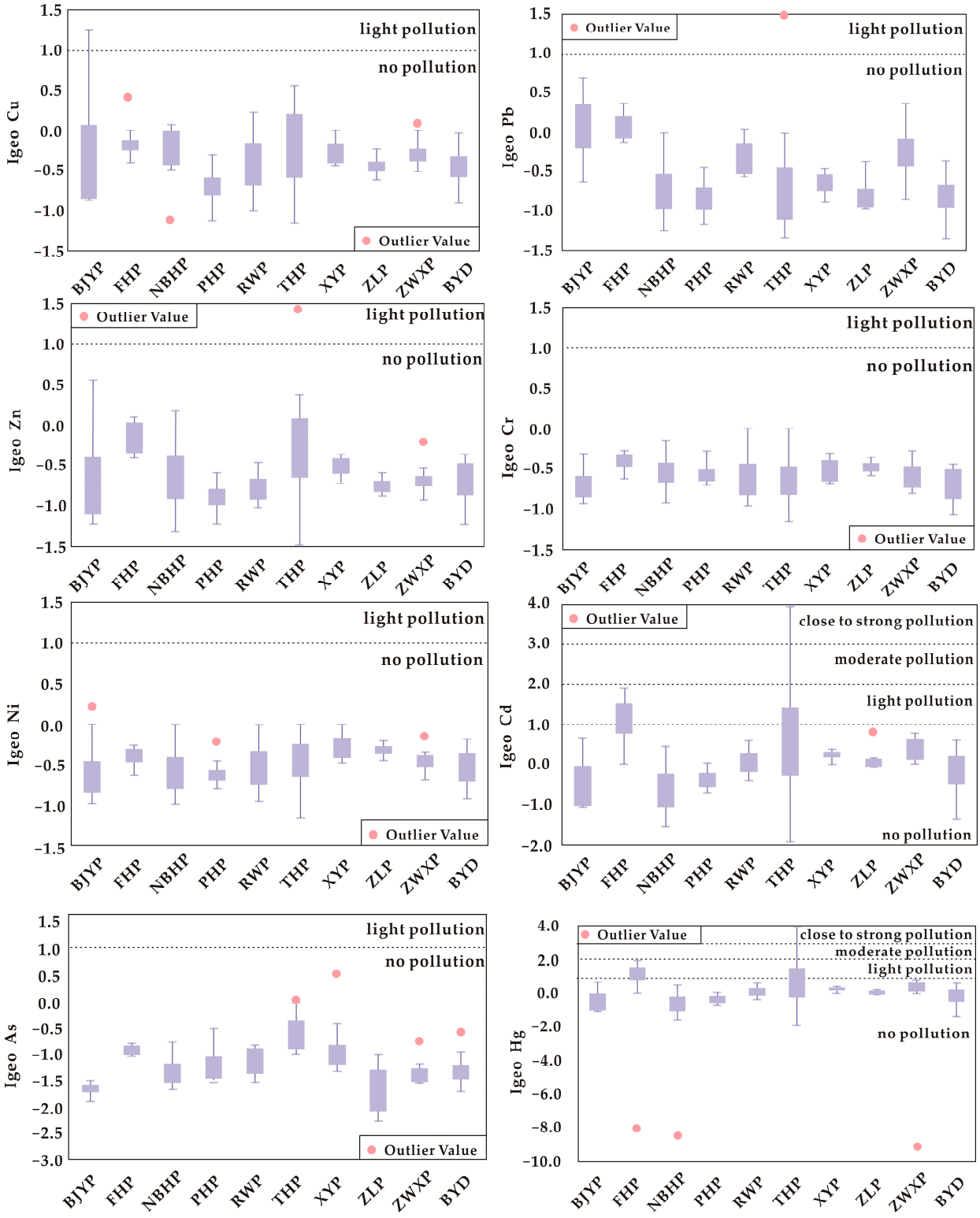

Figure 2. The *Igeo* values and pollution levels of heavy metals at sampling sites.

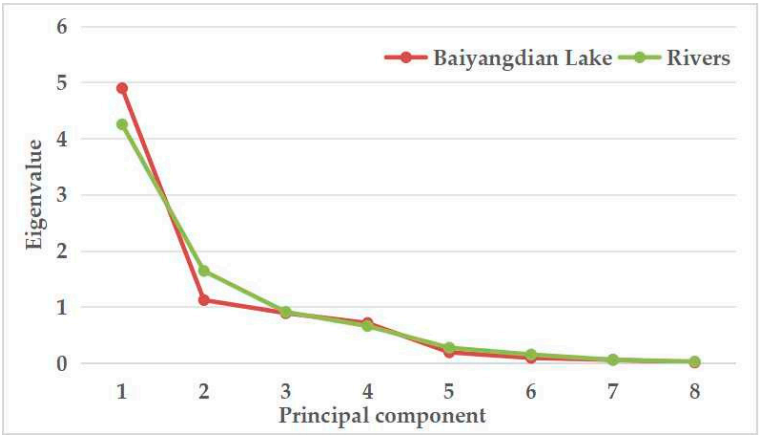

Figure 3. Gravel figure of principal component analysis of heavy metals at sampling sites.

Table 6. PCA of heavy metals in surface sediment of inflow rivers.

Heavy Metal	Load Coefficient of *PCA*		
	PC01	PC02	PC03
Cu	0.828	0.311	0.182
Zn	0.92	−0.322	−0.01
Pb	0.817	−0.303	0.184
Cr	0.615	0.695	−0.002
Cd	0.738	−0.583	−0.219
As	0.62	−0.12	−0.626
Ni	0.683	0.689	−0.113
Hg	0.533	−0.204	0.628

Table 7. PCA of heavy metals in surface sediment of Baiyangdian Lake.

Heavy Metal	Load Coefficient of *PCA*		
	PC01	PC02	PC03
Cu	0.965	−0.083	−0.079
Zn	0.941	0.181	−0.047
Pb	0.787	0.476	−0.183
Cr	0.842	−0.383	−0.314
Cd	0.707	0.439	0.086
As	0.472	−0.522	0.587
Ni	0.889	−0.398	−0.129
Hg	0.493	0.299	0.62

Based on the *APCS-MLR* model, multiple linear regression equations were developed, and the constant terms and coefficients were presented in Tables 8 and 9. The fitting coefficient of determination (R^2) for the measured concentration of heavy metals and the model-calculated concentration mostly ranges from 0.693 to 0.984, indicating a strong level of agreement. This suggests that the model is dependable and appropriate for analyzing the sources of heavy metal pollution. The calculations reveal that (1) in the surface sediments of inflow rivers, heavy metals Cu, Zn, Pb, As, Cd, and Hg are predominantly attributed to industrial wastewater discharge, with mean contribution rates of 78.07%, 64.45%, 62.12%, 57.28%, 53.66%, and 57.27%, respectively. However, the primary source of Cr remains unidentified (Table 10); (2) in the surface sediments of Baiyangdian Lake, heavy metals Cu, Zn, Pb, Cd, Ni, and Hg are primarily linked to industrial wastewater discharge, with mean contribution rates of 62.13%, 63.87%, 46.39%, 86.19%, 53.18%, and 68.12%, respectively. Nevertheless, the major contributor of Cr and As are yet to be determined (Table 11); (3) in contrast, the contribution of agricultural and domestic sewage discharge to heavy metals

in the surface sediments of both inflow river and Baiyangdian Lake is relatively minimal (Tables 10 and 11).

Table 8. Regression constant terms and coefficients based on the *APCS-MLR* model in surface sediments of inflow rivers.

Heavy Metal	Constant Term	*APCS*01 Coefficient	*APCS*02 Coefficient	*APCS*03 Coefficient	R^2
Cu	−8.439	5.799	\	−3.032	0.848
Zn	−8.118	27.557	−18.352	6.767	0.932
Pb	1.780	10.416	−8.126	−2.076	0.843
Cr	27.851	2.156	6.314	−1.425	0.868
Cd	−0.095	0.177	−0.177	0.116	0.829
As	0.962	0.983	0.436	3.835	0.986
Ni	5.567	1.611	3.973	−0.704	0.954
Hg	0.003	0.018	−0.017	−0.008	0.473

Table 9. Regression constant terms and coefficients based on the *APCS-MLR* model in surface sediments of Baiyangdian Lake.

Heavy Metal	Constant Term	*APCS*01 Coefficient	*APCS*02 Coefficient	*APCS*03 Coefficient	R^2
Cu	9.315	1.693	\	\	0.930
Zn	24.835	5.297	2.121	\	0.919
Pb	11.746	1.335	1.686	−0.725	0.880
Cr	31.810	3.224	−3.060	−2.814	0.955
Cd	−0.002	0.016	0.021	\	0.693
As	3.579	0.379	−0.874	1.104	0.839
Ni	12.927	1.914	−1.788	−0.653	0.965
Hg	0.001	0.003	0.004	0.010	0.717

Table 10. Mean contribution rate of pollution sources to heavy metals in surface sediment of inflow rivers.

Pollution Sources	Cu	Zn	Pb	Cr	Cd	As	Ni	Hg
Industrial wastewater discharge	78.07%	64.45%	62.12%	19.00%	53.66%	57.28%	29.62%	57.27%
Rocks weathering deposition	\	31.16%	35.14%	39.99%	38.87%	18.58%	52.49%	39.18%
Agricultural and domestic sewage discharge	3.06%	1.22%	0.96%	1.00%	2.68%	14.78%	1.02%	1.96%
Unknown source	18.87%	3.17%	1.77%	40.02%	4.80%	9.36%	16.87%	1.59%

Table 11. Mean contribution rate of pollution sources to heavy metals in surface sediment of Baiyangdian Lake.

Pollution Sources	Cu	Zn	Pb	Cr	Cd	As	Ni	Hg
Industrial wastewater discharge	62.13%	63.87%	46.39%	44.12%	86.19%	39.35%	53.18%	68.12%
Rocks weathering deposition	\	2.93%	6.54%	4.71%	12.59%	10.00%	5.59%	10.26%
Agricultural and domestic sewage discharge	\	\	2.26%	3.43%	\	9.94%	1.63%	19.07%
Unknown source	37.87%	33.21%	44.81%	47.74%	1.21%	40.71%	39.59%	2.55%

4.3. Potential Ecological Risks of Heavy Metals Pollution

4.3.1. Potential Ecological Risks of Heavy Metals Pollution Based on RI

The potential ecological risks linked to heavy metals in both the surface sediments of inflow rivers and Baiyangdian Lake are relatively low, with the exception of Cd, based on the calculated E_i (Figure 4). Among the 61 sites in inflow rivers, the ecological risk index was below 40 for Cu, Zn, Pb, Cr, As, Ni, and Hg, indicating a light level of potential ecological risk posed by these heavy metals. However, Cd showed levels ranging from close to moderate to extreme in 34, 3, 2, and 1 sites, respectively, accounting for 55.74%, 4.92%, 3.28%, and 1.64% of the total sites. In Baiyangdian Lake, only Cd in 13 sites (59.09%) exhibited a close to moderate level of risk, while the other heavy metals remained at a light level. The comprehensive ecological risk in most sites in both the surface sediment of inflow rivers and Baiyangdian Lake was also relatively low, as determined by the calculated *RI* (Figure 4). Out of the 61 sites in inflow rivers, the levels of risk were categorized as light, close to moderate, moderate, and strong in 56, 3, 1, and 1 sites, respectively, representing proportions of 91.80%, 4.92%, 1.64%, and 1.64%. On the other hand, all 22 sites in Baiyangdian Lake were classified as having a light level of risk.

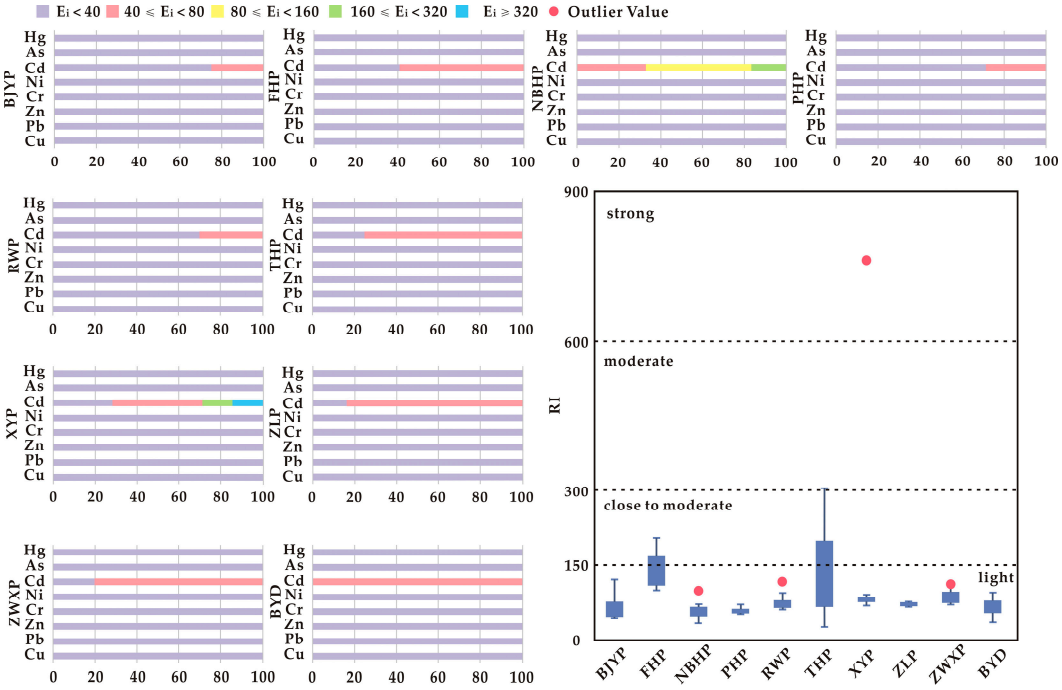

Figure 4. Statistical figure of E_i and *RI* for heavy metals at sampling sites.

4.3.2. Potential Ecological Risks of Heavy Metals Pollution Based on SQGs

The potential biological toxicity of heavy metals to benthic organisms or overlying aquatic organisms in both the surface sediment of inflow rivers and Baiyangdian Lake was found to be at a low-risk level based on the calculated I_{SQGs}. The values exhibited all less than 1 but more than 0.1 (Figure 5). Additionally, the probability of biological toxicity (*PBT*) ranged between 15% and 29% (Table 4). When looking at the calculated ΣTUs, 1 out of the 61 sites in inflow rivers indicated moderate toxicity, while the rest were considered non-toxic (Figure 6). In Baiyangdian Lake, all 22 sites were identified as non-toxic (Figure 6).

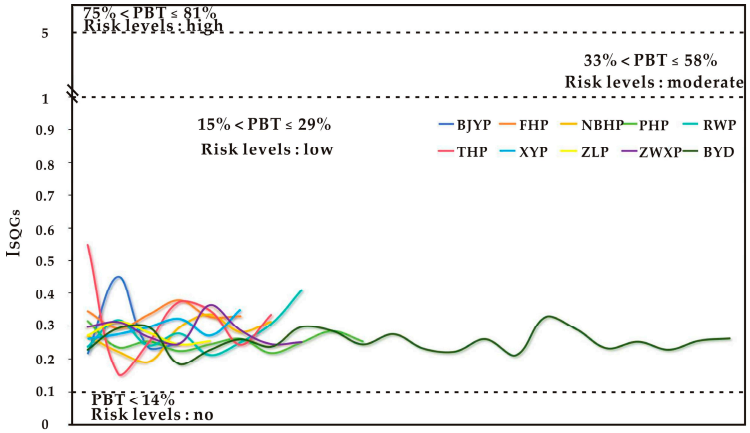

Figure 5. Statistical figure of I_{SQGs} for heavy metals at sampling sites.

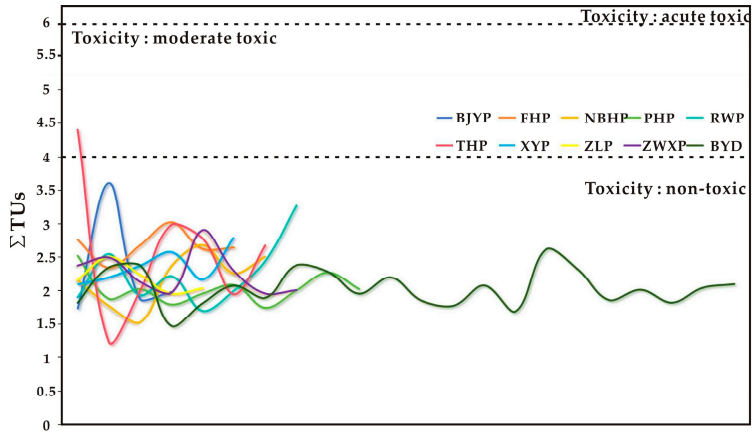

Figure 6. Statistical figure of Σ*TUs* for heavy metals at sampling sites.

According to the values of C_i, *TEC*, and *PEC*, there were evident variations in the frequency of toxic effects among different heavy metals. Among the 61 sites in inflow rivers, Ni was found to frequently cause toxic effects in one site, while Cu, Zn, Pb, Cr, Cd, As, Ni, and Hg were associated with occasional toxic effects in 11, 14, 6, 61, 59, 1, 25, and 1 sites, respectively, with proportions of 18.03%, 22.95%, 9.84%, 100.00%, 96.72%, 1.64%, 40.98%, and 1.64%. Additionally, other sites exhibited rare occurrences of toxic effects from these heavy metals (Figure 7). In the case of the 22 sites in Baiyangdian Lake, Cu, Cr, Ni, and As were found to occasionally cause toxic effects in 2, 22, 22, and 2 sites, respectively, with proportions of 9.09%, 100.00%, 100.00%, and 9.09%, while other sites experienced rare toxic effects from these heavy metals (Figure 7).

4.4. Comparison of the Results with Published Study

Several published studies have reported the average concentration of different heavy metals in the sediments of Baiyangdian Lake at different times (Table 12). Nonetheless, owing to differences in the number and distribution of sampling sites, as well as sampling depth, accurately identifying changes in the average concentration of heavy metals is challenging. Subjectively, there appears to be a decreasing trend in the average concentration of heavy metals, aligning with the findings of Wei's study [17]. This trend could be attributed to eco-environmental management and restoration efforts [9,90]. Comparing the results to previous studies since 2019, it is more consistent that the pollution levels of heavy metals are generally at a lower degree. However, some sites still exhibit relatively higher pollution levels for Cd [9,55], highlighting the need for attention from the ecological environment management department.

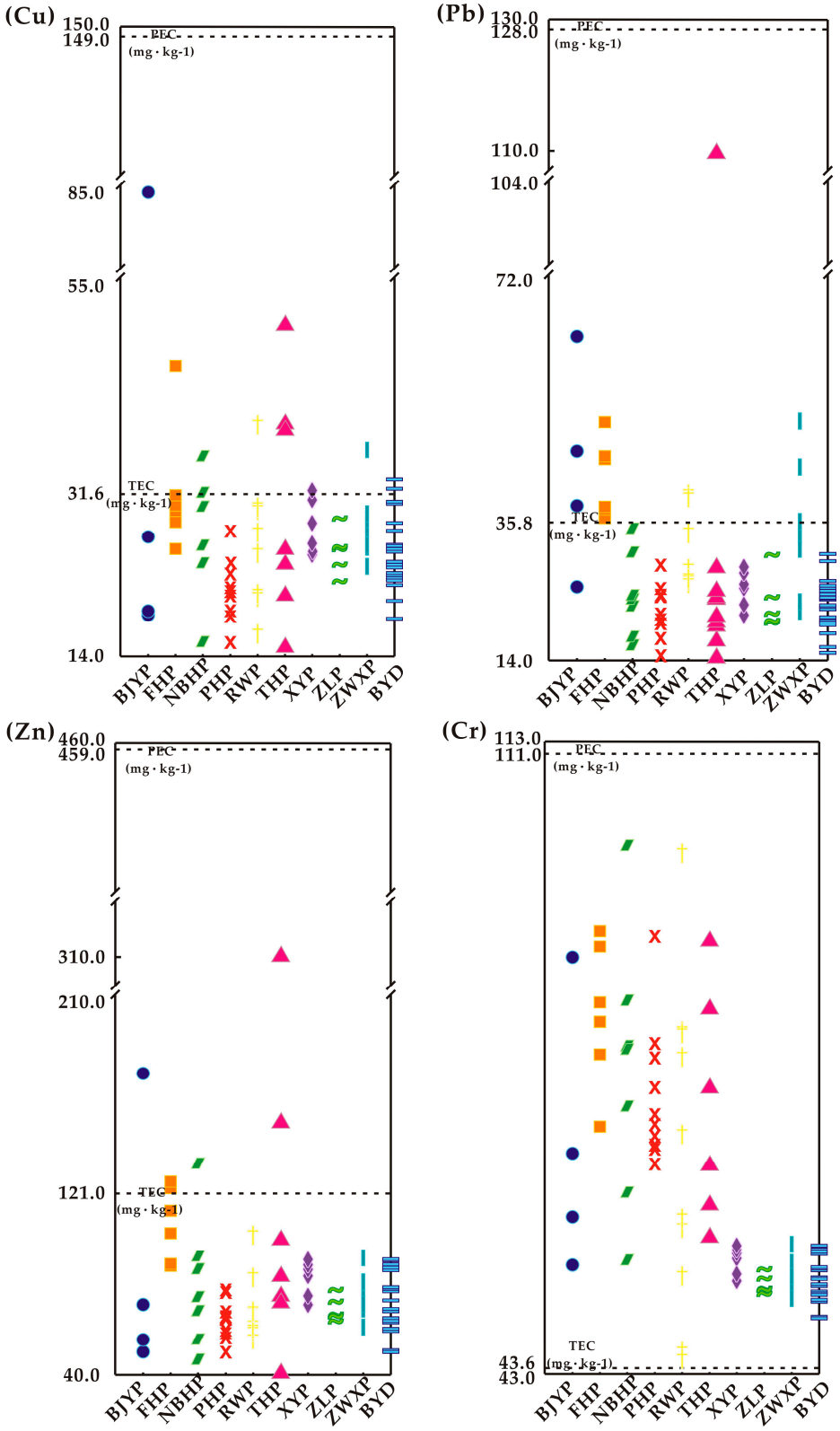

Figure 7. *Cont.*

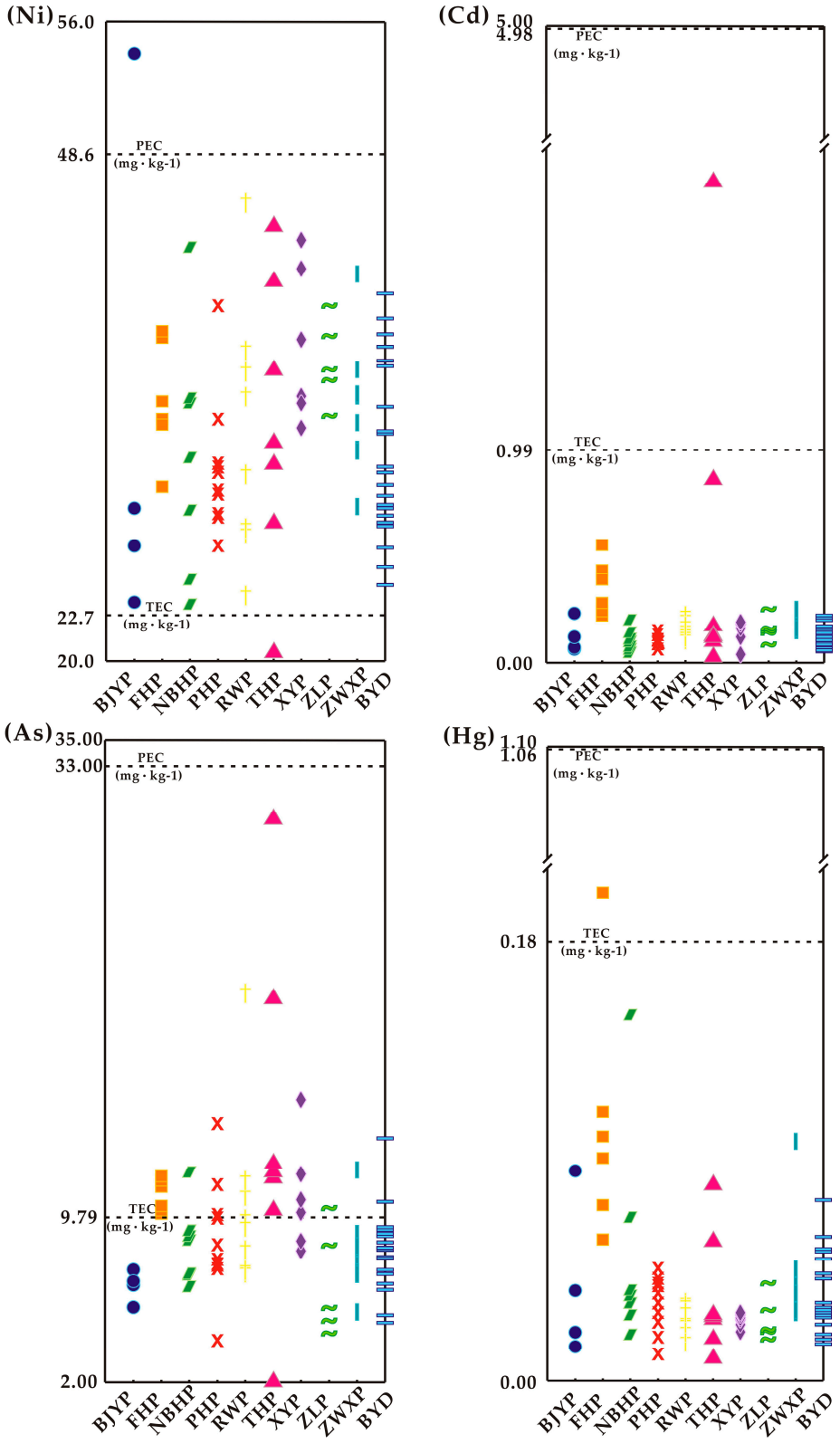

Figure 7. Statistical figure of the frequency of toxic effects for heavy metals Cu, Pb, Zn, Cr, Ni, Cd, As, and Hg based on C_i, *TEC*, and *PEC* at sampling sites.

Table 12. Comparison of the average concentration of heavy metals in the sediments of Baiyangdian Lake ($mg \cdot kg^{-1}$).

Sampling Time	Cu	Zn	Pb	Cr	Cd	As	Ni	Hg	Data Sources
2022	25.159	72.918	22.768	62.927	0.136	8.191	31.800	0.035	Present study
2020	31.02	93.06	39.8	82.56	0.32	18.96	\	\	[17]
2019–2020	37.43	102.43	27.78	75.46	0.33	9.91	37.22	0.054	[55]
2019	32.33	84.24	19.17	56.37	0.35	9.53	30.18	\	[9]
2019	28.79	56.77	19.01	59.68	0.25	\	28.85	\	[91]
2016	32.27	137.84	66.96	54.52	1.22	\	27.58	\	[92]
2010	28.19	150.88	33.50	41.34	0.80	32.08	35.04	\	[56]

5. Conclusions

(1) Pollution levels of heavy metals exhibited relatively low in both the surface sediments of inflow rivers and Baiyangdian Lake. However, it is important to note that Cu, Zn, Pb, and Cd, with proportions of 1.64%, 1.64%, 1.64%, and 4.92%, respectively, indicated close to moderate pollution levels. Specifically, Cd, with a proportion of 1.64%, displayed moderate pollution at sampling sites of inflow rivers. Compared with previous studies, it is evident that heavy metal pollution levels were generally low, but Cd showed relatively higher pollution degrees at some sites.

(2) Heavy metals found in the surface sediments of inflow rivers and Baiyangdian Lake originated from various sources such as industrial wastewater discharge, rock weathering deposition, and agricultural and domestic sewage discharge during the historical period. In the case of inflow rivers, industrial wastewater discharge was identified as the primary source of Cu, Zn, Pb, As, Cd, and Hg, contributing mean rates of 78.07%, 64.45%, 62.12%, 57.28%, 53.66%, and 57.27%, respectively. Rock weathering deposition was determined to be the main source of Ni, with a mean contribution rate of 52.49%. However, the main contributor to Cr, accounting for 40.02%, was not definitively identified, while rock weathering deposition contributed 39.99%. As for heavy metals in Baiyangdian Lake, industrial wastewater discharge was the primary source of Cu, Zn, Pb, Cd, Ni, and Hg, with mean contribution rates of 62.13%, 46.39%, 63.87%, 53.18%, 86.19%, and 68.12%, respectively. The main sources of Cr (47.74%) and As (40.71%) were not clearly identified, although industrial wastewater discharge contributed 44.12% and 39.35%, respectively. Additionally, heavy metals from the water recharging of the nine inflow rivers and local industrial activities, particularly for Cr, Ni, Cd, and Hg, also contributed to the heavy metals content in Baiyangdian Lake.

(3) The comprehensive ecological risk indicated relatively low in most sites, both in the surface sediment of inflow rivers and Baiyangdian Lake. However, it is important to highlight that a small proportion of sampling sites (4.92%, 1.64%, and 1.64%) showed varying degrees of risk in inflow rivers, ranging from close to moderate to strong. The potential biological toxicity of heavy metals to benthic organisms or overlying aquatic organisms at all sites in inflow rivers and Baiyangdian Lake was also low, with a probability of biological toxicity (*PBT*) between 15% and 29%. Only one site was identified as having moderate toxicity, while the rest were considered non-toxic. Furthermore, variations were observed in the occurrence frequency of toxic effects among different heavy metals. Specifically, Ni was found to frequently cause toxic effects in one site, whereas other heavy metals caused toxic effects rarely or occasionally.

(4) This study offered a comprehensive understanding of the heavy metal pollution status, sources, and potential ecological risks associated with various heavy metals in the surface sediments of Baiyangdian Lake and its inflow rivers. The research findings provided a crucial basis for government departments to formulate effective ecological restoration measures. Notably, for certain inflow rivers, there had been

limited research or reporting on sediment heavy metal pollution, and this study contributed valuable new insights. Although the overall pollution level of surface sediments was low and had demonstrated a decreasing trend over recent years, it was important to highlight that some areas still exhibited Cd pollution at relatively higher concentrations. Nevertheless, due to financial constraints, the sample quantity and depth in this study were limited. Future researchers should enhance sample density to improve the accuracy of the findings.

Author Contributions: Conceptualization, H.L.; methodology, H.L.; software, Y.G.; validation, H.L., Y.S., and F.Y.; formal analysis, H.L.; investigation, H.L., Y.B., B.H., and J.M.; resources, H.L.; data curation, H.L. and B.H.; writing—original draft preparation, H.L.; writing—review and editing, Y.G.; visualization, Y.G.; supervision, Y.B., B.H. and J.M.; project administration, H.L.; funding acquisition, H.L. All authors have read and agreed to the published version of the manuscript.

Funding: This research was funded by the China Geological Survey, grant numbers DD20221727 and DD20243452.

Data Availability Statement: The data presented in this study are available on request from the corresponding author.

Conflicts of Interest: The authors declare no conflicts of interest.

References

1. Palansooriya, K.N.; Li, J.; Dissanayake, P.D.; Suvarna, M.; Li, L.Y.; Yuan, X.Z.; Sarkar, B.; Tsang, D.C.W.; Rinklebe, J.; Wang, X.N.; et al. Prediction of soil heavy metal immobilization by biochar using machine learning. *Environ. Sci. Technol.* **2022**, *56*, 4187–4198. [CrossRef] [PubMed]
2. Wang, Y.; Yang, Y.; Li, Q.; Zhang, Y.; Chen, X. Early warning of heavy metal pollution after tailing pond failure accident. *J. Earth Sci.* **2022**, *33*, 1047–1055. [CrossRef]
3. Zaynab, M.; Al-Yahyai, R.; Ameen, A.; Sharif, Y.; Ali, L.; Fatinma, M.; Khan, K.; Li, S.F. Health and environmental effects of heavy metal. *J. King Saud Univ. Sci.* **2022**, *34*, 101653. [CrossRef]
4. Zhang, Q.; Wang, C. Natural and human factors affect the distribution of soil heavy metal pollution: A review. *Water Air Soil Pollut.* **2020**, *231*, 1–13. [CrossRef]
5. Jiang, W.J.; Meng, L.S.; Liu, F.T.; Sheng, Y.Z.; Chen, S.M.; Yang, J.L.; Mao, H.R.; Zhang, J.; Zhang, Z.; Ning, H. Distribution, source investigation, and risk assessment of topsoil heavy metals in areas with intensive anthropogenic activities using the positive matrix factorization (PMF) model coupled with self-organizing map (SOM). *Environ. Geochem. Health* **2023**, *45*, 6353–6370. [CrossRef]
6. Gulan, L.; Stajic, J.M.; Zeremski, T.; Durlević, U.; Valjarević, A. Radionuclides and metals in the parks of the city of Belgrade, Serbia: Spatial distribution and health risk assessment. *Forests* **2022**, *13*, 1648. [CrossRef]
7. An, Y.; Zhou, S.; Sun, C.L.; Wang, S.Y.; Zhang, X.; Lv, J.Q. Heavy metal pollution of sediments in northern Jiaozou Bay and influence of DOM on their environmental behavior. *Earth Sci.* **2024**, *48*, 2901–2913. [CrossRef]
8. Yao, X.; Wang, Z.; Liu, W.; Zhang, Y.; Wang, T.H.; Li, Y.L. Pollution in river tributaries restricts the water quality of ecological water replenishment in the Baiyangdian watershed, China. *Environ. Sci. Pollut. Res.* **2023**, *30*, 51556–51570. [CrossRef]
9. Zerizghi, T.; Yang, Y.F.; Wang, W.J.; Zhou, Y.; Zhang, J.; Yi, Y.J. Ecological risk assessment of heavy metal concentrations in sediment and fish of a shallow lake: A case study of Baiyangdian Lake, North China. *Environ. Monit. Assess.* **2020**, *192*, 154. [CrossRef]
10. Mitra, S.; Chakraborty, A.J.; Tareq, A.M.; Emran, T.B.; Nainu, F.; Khusro, A.; Idris, A.M.; Khandaker, M.U.; Osman, H.; Alhumaydhi, F.A.; et al. Impact of heavy metals on the environment and human health: Novel therapeutic insights to counter the toxicity. *J. King Saud Univ. Sci.* **2022**, *34*, 101865. [CrossRef]
11. Hou, D.; O'Connor, D.; Igalavithana, A.D.; Alessi, D.S.; Luo, J.; Tsang, D.C.W.; Sparks, D.L.; Yamauchi, Y.; Rinklebe, J.; Ok, Y.S. Metal contamination and bioremediation of agricultural soils for food safety and sustainability. *Nat. Rev. Earth Environ.* **2020**, *1*, 366–381. [CrossRef]
12. Paul, D. Research on heavy metal pollution of river Ganga: A review. *Ann. Agrar. Sci.* **2017**, *15*, 278–286. [CrossRef]
13. Hou, W.L.; Wang, Q.X.; Xiang, Z.Z.; Jia, N.; Hu, J.W.; Wu, Z.H.; Dong, W.L. Comprehensive assessment of occurrence, temporal-spatial variations, and ecological risks of heavy metals in Jiaozhou Bay, China: A comprehensive study. *Mar. Pollut. Bull.* **2024**, *198*, 115883. [CrossRef] [PubMed]
14. Abd, E.M.K.; Elkaliny, N.E.; Elyazied, M.M.; Azab, S.H.; Elkhalifa, S.A.; Elmasry, S.; Mouhamed, M.S.; Shalamesh, E.M.; Alhorieny, N.A.; Elaty, A.E.A.; et al. Toxicity of heavy metals and recent advances in their removal: A review. *Toxics* **2023**, *11*, 580. [CrossRef]
15. Sheng, Y.Z.; Baars, O.; Guo, D.Y.; Whitham, J.; Srivastava, S.; Dong, H. Mineral-bound trace metals as cofactors for anaerobic biological nitrogen fixation. *Environ. Sci. Technol.* **2023**, *57*, 7206–7216. [CrossRef]

16. Feng, H.; Jiang, H.; Gao, W.; Weinstein, M.P.; Zhang, Q.; Zhang, W.; Yu, L.; Yuan, D.; Tao, J. Metal contamination in sediments of the western Bohai Bay and adjacent estuaries, China. *J. Environ. Manag.* **2011**, *92*, 1185–1197. [CrossRef]
17. Wei, H.; Wang, J.Z.; Zhu, S.J.; Yu, K.N.; Cai, K.; Li, X.; Song, Z.F. Ecological assessment and source identification based on chemical forms and content of heavy metals in the sediment of Baiyangdian Lake. *Front. Earth Sci.* **2022**, 1–15. [CrossRef]
18. Dhaliwal, S.S.; Singh, J.; Taneja, P.K.; Mandal, A. Remediation techniques for removal of heavy metals from the soil contaminated through different sources: A review. *Environ. Sci. Pollut. Res.* **2020**, *27*, 1319–1333. [CrossRef]
19. Valdés, J.; Guiñez, M.; Castillo, A.; Vega, S.E. Cu, Pb, and Zn content in sediments and benthic organisms from San Jorge Bay (northern Chile): Accumulation and biotransference in subtidal coastal systems. *Cienc. Mar.* **2014**, *40*, 45–58. [CrossRef]
20. Mao, K.Z.; Li, H.M.; Ming, Q.; Liu, H.; Zhao, H.; Lu, B.S.; Hao, W.J. Health risk assessment in the groundwater of a certain mine in Hunan. *North China Geol.* **2023**, *46*, 57–66. [CrossRef]
21. Mishra, S.P.; Sarkar, U.; Taraphder, S.; Swain, D.; Saikhom, R.; Panda, S.; Laishram, M. Multivariate statistical data analysis-principal component analysis (PCA). *Int. J. Livest. Res.* **2017**, *7*, 60–78. [CrossRef]
22. Albarano, L.; Lofrano, G.; Costantini, M.; Zupo, V.; Carraturo, F.; Guida, M.; Libralato, G. Comparison of in situ sediment remediation amendments: Risk perspectives from species sensitivity distribution. *Environ. Pollut.* **2021**, *272*, 115995. [CrossRef] [PubMed]
23. Palansooriya, K.N.; Shaheen, S.M.; Chen, S.S.; Tsang, D.C.W.; Hashimoto, Y.; Hou, D.; Bolan, N.S.; Rinklebe, J.; Ok, Y.S. Soil amendments for immobilization of potentially toxic elements in contaminated soils: A critical review. *Environ. Int.* **2020**, *134*, 105046. [CrossRef] [PubMed]
24. Singh, U.K.; Kumar, B. Pathways of heavy metals contamination and associated human health risk in Ajay River basin, India. *Chemosphere* **2017**, *174*, 183–199. [CrossRef]
25. Zhang, W.; Liu, M.; Li, C. Soil heavy metal contamination assessment in the Hun-Taizi River watershed, China. *Sci. Rep.* **2020**, *10*, 8730. [CrossRef]
26. Liu, Y.; Lu, N. Hot topics and frontier evolution on soil heavy metals risk assessment in China. *North China Geol.* **2023**, *46*, 61–69. [CrossRef]
27. Xu, Y.; Shi, H.; Fei, Y.; Wang, C.; Mo, L.; Shu, M. Identification of soil heavy metal sources in a large-scale area affected by industry. *Sustainability* **2021**, *13*, 511. [CrossRef]
28. Hu, B.; Wang, J.Y.; Jin, B.; Li, Y.; Zhou, S. Assessment of the potential health risks of heavy metals in soils in a coastal industrial region of the Yangtze river delta. *Environ. Sci. Pollut. R.* **2017**, *24*, 19816–19826. [CrossRef]
29. Soodmand, A.; Ebrahimi, S.; Kiani, F. Monitoring and assessment of contamination and ecological risk of heavy metals in Hezarpich surface soils. *Int. J. Environ. Sci. Technol.* **2024**, 1–14. [CrossRef]
30. Wardani, N.K.; Prartono, T.; Sulistiono, S. Sediments quality based on Geo-Accumulation Index in heavy metals (Pb, Cu, and Cd) of Cengkok coastal waters, Banten Bay. *J. Pendidik. IPA Indones.* **2020**, *9*, 574–582. [CrossRef]
31. Lao, X.; Tam, N.F.Y.; He, H.; Su, X.T.; Zhong, M.L.; Wu, Q.H.; Liu, Y.H.; Huang, X.X.; Wei, L.Z.; Liu, Y.; et al. Distribution Characteristics and Assessment of Heavy Metal Pollution in Sediments of Fengyuan River, Guangdong. *Environ. Forensics* **2024**, 1–13. [CrossRef]
32. Jaskuła, J.; Sojka, M. Assessment of spatial distribution of sediment contamination with heavy metals in the two biggest rivers in Poland. *Catena* **2022**, *211*, 105959. [CrossRef]
33. Han, X.; Wu, H.; Li, Q.; Cai, W.R.; Hu, S.Y. Assessment of heavy metal accumulation and potential risks in surface sediment of estuary area: A case study of Dagu river. *Mar. Environ. Res.* **2024**, *196*, 106416. [CrossRef] [PubMed]
34. Khalili, R.; Zali, A.; Motaghi, H. Evaluating the heavy metals in the water and sediments of Haraz River, using pollution load index (PLI) and geo accumulation index (Igeo). *Iran. J. Soil Water Res.* **2021**, *52*, 933–942. [CrossRef]
35. Lasheen, E.L.S.R.; Mansour, A.M.; Mohamed, A.W.; Osman, M.R.; Khaleal, F.M.; Tahoon, M.A.; Alarifi, N.; Jordan, G.; Abdelaal, A. Assessing the Heavy Metals in Surface Sediments of Wadi El-Gemal Island, Red Sea, Egypt: Pollution Levels, Sources, and Associated Risks. *Water Air Soil Pollut.* **2024**, *235*, 461. [CrossRef]
36. Zhang, Y.; Li, H.; Yin, J.; Zhu, L.Y. Risk assessment for sediment associated heavy metals using sediment quality guidelines modified by sediment properties. *Environ. Pollut.* **2021**, *275*, 115844. [CrossRef]
37. Wołowiec, M.; Komorowska-Kaufman, M.; Pruss, A.; Rzepa, G.; Bajda, T. Removal of heavy metals and metalloids from water using drinking water treatment residuals as adsorbents: A review. *Minerals* **2019**, *9*, 487. [CrossRef]
38. Zaakour, F.; Kholaiq, M.; Khouchlaa, A.; Ikram, E.M.; Abdelmejid, R.; Najib, S. Assessment of heavy metal contamination using pollution index, geo-accumulation index, and potential ecological risk index in agricultural soil—A case study in the coastal area of Doukkala (Morocco). *Ecol. Eng. Environ. Technol.* **2023**, *24*, 38–44. [CrossRef]
39. Hadif, W.M.; Abd Rahim, S.; Sahid, I.; Rahman, A.; Ibrahim, I. Assessment of Heavy Metal Pollution Using the Geo-accumulation Index (I-Geo), Pollution Load Index (PLI) and Potential Ecological Risk Index (RI) in Paddy Field Soils Adjacent to Ultrabasic Soils. *Univ. Thi-Qar J. Agric. Res.* **2020**, *9*, 85–97. [CrossRef]
40. Xu, Y.F.; Wu, Y.; Han, J.; Li, P.P. The current status of heavy metal in lake sediments from China: Pollution and ecological risk assessment. *Ecol. Evol.* **2017**, *7*, 5454–5466. [CrossRef]
41. Zhao, Y.J.; Deng, Q.Y.; Lin, Q.; Zeng, C.Y.; Zhong, C. Cadmium source identification in soils and high-risk regions predicted by geographical detector method. *Environ. Pollut* **2020**, *263*, 114338. [CrossRef] [PubMed]

42. Jin, Z.; Zhang, L.; Lv, J.; Sun, X.F. The application of geostatistical analysis and receptor model for the spatial distribution and sources of potentially toxic elements in soils. *Environ. Geochem. Health* **2021**, *43*, 407–421. [CrossRef] [PubMed]
43. Zhang, J.; Li, R.F.; Zhang, X.Y.; Bai, Y.; Cao, P.; Hua, P. Vehicular contribution of PAHs in size dependent road dust: A source apportionment by PCA-MLR, PMF, and Unmix receptor models. *Sci. Total Environ.* **2019**, *649*, 1314–1322. [CrossRef]
44. Peng, Y.; Yu, G.I. Assessment of heavy metal pollution on agricultural land in Chengdu city under different anthropogenic pressures based on APCS-MLR modelling. *Ecol. Indic.* **2024**, *165*, 112183. [CrossRef]
45. Shi, H.; Zeng, M.; Peng, H.; Huang, C.S.; Sun, H.M.; Hou, Q.Q.; Pi, P.C. Health risk assessment of heavy metals in groundwater of Hainan island using the Monte Carlo simulation coupled with the APCS/MLR model. *Int. J. Environ. Res. Public Health* **2022**, *19*, 7827. [CrossRef] [PubMed]
46. Zhang, M.; Wang, X.; Liu, C.; Lu, J.Y.; Qin, Y.H.; Mo, Y.K.; Xiao, P.J.; Liu, Y. Quantitative source identification and apportionment of heavy metals under two different land use types: Comparison of two receptor models APCS-MLR and PMF. *Environ. Sci. Pollut. Res.* **2020**, *27*, 42996–43010. [CrossRef]
47. Hsieh, P.Y.; Ho, C.C.; Wang, G.S.; Hsu, Y.C.; Wang, D.W.; Shang, Y.M.; Wu, C.F. Use of an Effective Variance Chemical Mass Balance Model for Source Apportionment of Metal Elements in a Polluted River. *Environ. Process.* **2022**, *9*, 51. [CrossRef]
48. Zhang, F.G.; Wang, C.W.; Cheng, X.M.; Ma, H.H.; He, L. Ecological Assessment, Spatial Analysis, and Potential Sources of Heavy Metals (HMs) in Soils with High Background Values in the Lead-Zinc Mine, Hezhang County, Southwestern China. *Water* **2022**, *14*, 783. [CrossRef]
49. Wu, J.; Fang, F.; Ma, K.; Li, Y.S.; Ge, L.; Chen, H.; Zhou, H. Spatial Distribution and Source Analysis of Soil Heavy Metals in Lujiang County Based on Unmix Model. *J. Ecol. Rural Environ.* **2022**, *38*, 1204–1210. [CrossRef]
50. Li, Y.; Kuang, H.; Hu, C.; Ge, G. Source apportionment of heavy metal pollution in agricultural soils around the Poyang Lake region using UNMIX model. *Sustainability* **2021**, *13*, 5272. [CrossRef]
51. Gong, C.; Xia, X.; Lan, M.; Shi, Y.C.; Lu, H.C.; Wang, S.X.; Chen, Y. Source identification and driving factor apportionment for soil potentially toxic elements via combining APCS-MLR, UNMIX, PMF and GDM. *Sci. Rep.* **2024**, *14*, 10918. [CrossRef] [PubMed]
52. Wei, R.; Meng, Z.; Zerizghi, T.; Luo, J.; Guo, Q.J. A comprehensive method of source apportionment and ecological risk assessment of soil heavy metals: A case study in Qingyuan city, China. *Sci. Total Environ.* **2023**, *882*, 163555. [CrossRef] [PubMed]
53. Chen, H.Y.; Teng, Y.G.; Chen, R.H.; Li, J.; Wang, J.S. Contamination characteristics and source apportionment of trace metals in soils around Miyun Reservoir. *Environ. Sci. Pollut. Res.* **2016**, *23*, 15331–15342. [CrossRef]
54. Zhang, Y.; Guo, C.; Xu, J.; Tian, Y.Z.; Shi, G.L.; Feng, Y.C. Potential source contributions and risk assessment of PAHs in sediments from Taihu Lake, China: Comparison of three receptor models. *Water Res.* **2012**, *46*, 3065–3073. [CrossRef]
55. Yin, D.C.; Qi, X.F.; Wang, Y.S.; Xu, R.Z.; An, Y.H.; Wang, X.Q.; Geng, H.J. Geochemical characteristics and ecological risk assessment of heavy metals in surface sediments of Baiyangdian Lake, Xiong'an New Area. *Geol. China* **2022**, *49*, 979–992.
56. Zhao, Y.; Dong, L.M.; Zhang, Y.P.; Zhang, M.L.; Sun, X.T. Speciation distribution and pollution assessment of heavy metals in sediment of Baiyangdian Lake. In Proceedings of the Agricultural Environment and Ecological security—The 5th National Symposium on Agricultural Environment Science, Nanjing, China, 19–22 April 2013; pp. 537–545.
57. Wang, J.Z.; Liu, Z.; Wei, H.; Wu, Y.H.; Zhan, S.E.; Zhu, C.; Zhang, Y.M. Spatial characteristics, risk assessment, and source analysis of elements in surface sediments from the Baiyangdian Lake. *Environ. Sci.* **2020**, *41*, 224–231. [CrossRef]
58. Zhang, H.; Liu, M.Z.; Liao, P.P.; Zhou, X.S.; Guo, L.F.; Gao, J.Q. Analysis of spatial characteristics and source of main pollutants in Baiyangidan before and after flood season. *J. Water Resour. Water Eng.* **2016**, *27*, 28–31.
59. Zhang, Q.; Zhao, Y.X.; Yang, Y.; Guo, W.C.; Yue, Y.P.; Xu, J. The ecological risk assessment of heavy metals in the sediments of Fu River Baiyangdian Lake system. *Acta Sci. Circumstantiae* **2024**, *44*, 167–176. [CrossRef]
60. Zhang, S.R.; Wang, C.Y.; Liu, J.H.; Xing, Y.; Liu, Q.X.; Yang, J.Q.; He, F.Q. Assessments of heavy metal pollution in soils of the southwestern Xiong'an District and its ecological risk. *Earth Sci. Front.* **2021**, *28*, 238–249. [CrossRef]
61. Wang, J.; Wei, H.; Liang, Z.; Zhan, S.E.; Jia, H.J.; Guo, S.; Ge, P.X. Contamination, risk and quantitative identification of nutrients and potentially toxic elements in the surface sediments of Baiyangdian Lake, North China. *Ecotoxicology* **2022**, *31*, 289–298. [CrossRef]
62. Gao, H.; Bai, J.; Xiao, R.; Liu, P.P.; Jiang, W.; Wang, J.J. Levels, sources and risk assessment of trace elements in wetland soils of a typical shallow freshwater lake, China. *Stoch. Environ. Res. Risk Assess.* **2012**, *27*, 275–284. [CrossRef]
63. Han, S.B.; Yuan, L.; Zhang, Q.X.; Zheng, Y.; Li, F.C. Heavy metal content and risk assessment of sediments and soil in the Juma river basin. *Environ. Sci.* **2024**, *45*, 2962–2970. [CrossRef]
64. Zeng, Y.; Zhao, Y.; Qi, Z. Evaluating the ecological state of Chinese Lake Baiyangdian (BYD) based on ecological network analysis. *Ecol. Indic.* **2021**, *127*, 107788. [CrossRef]
65. Wang, X.C.; Zhi, Q.Q.; Zhang, J.; Yang, Y.; Wu, J.J.; Wang, J.H.; Liu, D.M.; Deng, X.H. Application of Transient Electromagnetic Method in Investigation of Underground Water in Xiong'an New Area. *Earth Sci.* **2023**, *48*, 4243–4255.
66. Liu, X.S.; Wang, Y.S.; Wang, X.Q.; Yin, D.C. Distribution characteristics and source of the main environmental elements in the surface soil of lake Baiyangdian wetlands. *J. Lake Sci.* **2022**, *34*, 496–505. [CrossRef]
67. Ji, Z.; Zhang, H.; Zhang, Y.; Chen, T.; Long, Z.W.; Li, M.; Pei, Y.S. Distribution, ecological risk and source identification of heavy metals in sediments from the Baiyangdian Lake, Northern China. *Chemosphere* **2019**, *237*, 124425. [CrossRef] [PubMed]
68. Chen, C.Y.; Pickhardt, P.C.; Xu, M.Q.; Folt, C.L. Mercury and arsenic bioaccumulation and eutrophication in Baiyangdian Lake, China. *Water Air Soil Pollut.* **2008**, *190*, 115–127. [CrossRef]

69. Arisekar, U.; Shakila, R.J.; Shalini, R.; Jeyasekaran, G.; Keerthana, M.; Arumugam, N.; Almansour, A.I.; Perumal, K. Distribution and ecological risk assessment of heavy metals using geochemical normalization factors in the aquatic sediments. *Chemosphere* **2022**, *294*, 133708. [CrossRef] [PubMed]
70. Chen, T.B.; Zheng, Y.M.; Lei, M.; Huang, Z.C.; Wu, H.T.; Chen, H.; Fan, K.K.; Yu, K.; Wu, X.; Tian, Q.Z. Assessment of heavy metal pollution in surface soils of urban parks in Beijing, China. *Chemosphere* **2005**, *60*, 542–551. [CrossRef]
71. Zhang, C.; Zhang, Y.; Shan, B. Heavy metal distribution, fractionation, and biotoxicity in sediments around villages in Baiyangdian Lake in North China. *Environ. Monit. Assess.* **2023**, *195*, 86. [CrossRef]
72. Sun, L.; Dong, Y.; Feng, W.; Zhang, Z.C.; Guo, X.B.; Li, H.T. Geochemical characteristics of soil elements and its driving mechanisms in the Xiong'an New Area, China. *Geogr. Res.* **2022**, *41*, 1715–1730.
73. Wu, J.; Margenot, A.J.; Wei, X.; Fan, M.M.; Zhang, H.; James, L.B.; Wu, P.B.; Chen, F.R.; Gao, C. Source apportionment of soil heavy metals in fluvial islands, Anhui section of the lower Yangtze River: Comparison of APCS–MLR and PMF. *J. Soils Sediments* **2020**, *20*, 3380–3393. [CrossRef]
74. Jin, G.; Fang, W.; Shafi, M.; Wu, D.T.; Li, Y.Q.; Zhong, B.; Ma, J.W.; Liu, D. Source apportionment of heavy metals in farmland soil with application of APCS-MLR model: A pilot study for restoration of farmland in Shaoxing City Zhejiang, China. *Ecotoxicol. Environ. Saf.* **2019**, *184*, 109495. [CrossRef]
75. Duan, W.; He, B.; Nover, D.; Yang, G.S.; Chen, W.; Meng, H.F.; Zou, S.; Liu, C.M. Water quality assessment and pollution source identifica tion of the eastern Poyang Lake basin using multivariate statistical methods. *Sustainability* **2016**, *8*, 133. [CrossRef]
76. Mu, D.; Wu, J.; Li, X.; Xu, F.; Yang, Y.Q. Identification of the spatiotemporal variability and pollution sources for potential pollutants of the Malian River water in northwest China using the PCA-APCS-MLR receptor model. *Expo. Health* **2024**, *16*, 41–56. [CrossRef]
77. Li, W.; Wu, J.; Zhou, C.; Abel, N. Groundwater pollution source identification and apportionment using PMF and PCA-APCS-MLR receptor models in Tongchuan City, China. *Arch. Environ. Contam. Toxicol.* **2021**, *81*, 397–413. [CrossRef]
78. Zhang, H.; Cheng, S.; Li, H.; Fu, K.; Xu, Y. Groundwater pollution source identification and apportionment using PMF and PCA -APCA-MLR receptor models in a typical mixed land-use area in Southwestern China. *Sci. Total Environ.* **2020**, *741*, 140383. [CrossRef]
79. Hakanson, L. An ecological risk index for aquatic pollution control. A sedimentological approach. *Water Res.* **1980**, *14*, 975–1001. [CrossRef]
80. Caeiro, S.; Costa, M.H.; Ramos, T.B.; Fernandes, F.; Sileira, N.; Coimbra, A.; Medeiros, G.; Painho, M. Assessing heavy metal contamination in Sado Estuary sediment: An index analysis approach. *Ecol. Indic.* **2005**, *5*, 151–169. [CrossRef]
81. Chen, X.X.; Zhang, M.; Li, B.; Wen, P.Z.; Ding, P.; Yao, L.A.; Ma, Q.L.; Li, T.Z.; Cai, D.; Hu, G.C. Risk assessment and source analysis of heavy metal pollution in surface sediments from major river systems in Maoming city, Guangdong province. *Environ. Sci.* **2023**, *44*, 1397–1406. [CrossRef]
82. Chai, M.W.; Li, R.L.; Ding, H.; Zan, Q.J. Occurrence and contamination of heavy metals in urban mangroves: A case study in Shenzhen, China. *Chemosphere* **2019**, *219*, 165–173. [CrossRef] [PubMed]
83. Pedersen, F.; Bjørnestad, E.; Andersen, H.V.; Jesper, K.; Christian, P. Characterization of sediments from Copenhagen Harbour by use of biotests. *Water Sci. Technol.* **1998**, *37*, 233–240. [CrossRef]
84. Bai, G.Y.; Zhao, K.L.; Liu, E.F.; Zhang, E.L. Accumulation characteristics and risk assessment of heavy metals in sediments of Fuxian Lake. *China Environ. Sci.* **2023**, *43*, 3625–3633. [CrossRef]
85. Apitz, S.E.; Barbanti, A.; Bernstein, A.G.; Martina, B.; Eugeia, D.; Laura, M. The assessment of sediment screening risk in Venice Lagoon and other coastal areas using international sediment quality guidelines. *J. Soil. Sediment* **2007**, *7*, 326–341. [CrossRef]
86. Lacey, E.M.; King, J.W.; Quinn, J.G.; Mecray, E.L.; Appleby, P.G.; Hunt, A.S. Sediment quality in Burlington harbor, lake champlain, U.S.A. *Water Air Soil Pollut.* **2001**, *126*, 97–120. [CrossRef]
87. Huang, C.S.; Zhang, Q.; Tang, F.K.; Zhang, L.J.; Yu, Y.J.; Zhou, K.X.; Hu, G.C. Profiles of heavy metals pollution and potential influence to aquatic environment of Doushui reservoir from Jiangxi province. *Environ. Chem.* **2022**, *41*, 2919–2930.
88. Bian, B.; Zhou, Y.; Zhang, Q. Pluution characteristics and risk assessment of heavy metals from river network sediment in western area of Taihu Lake. *Environ. Sci.* **2017**, *38*, 1442–1450. [CrossRef]
89. MacDonald, D.D.; Ingersoll, C.G.; Berger, T.A. Development and evaluation of consensus-based sediment quality guidelines for freshwater ecosystems. *Arch. Environ. Contam. Toxicol.* **2000**, *39*, 20–31. [CrossRef]
90. Chen, P.; Fu, C.G.; Ji, X.G.; Kang, G.Q. Research on the optimization and implementation effect of Baiyangdian water quality improvement plan. *J. Water Ecol.* **2022**, *43*, 48–55.
91. Xiang, Y.X.; Wang, X.; Shan, B.Q.; Zhao, Y.; Tang, W.Z.; Shu, L.M.; Jiang, S.X.; Cao, Y. Spatial distribution, fractionation and ecological risk of heavy metals in surface sediments from Baiyangdian Lake. *Acta Sci. Circumstantiae* **2020**, *40*, 2237–2246. [CrossRef]
92. Zhang, C.; Shan, B.; Zhao, Y.; Song, Z.X.; Tang, W.Z. Spatial distribution, fractionation, toxicity and risk assessment of surface sediments from the Baiyangdian Lake in northern China. *Ecol. Indic.* **2018**, *90*, 633–642. [CrossRef]

Disclaimer/Publisher's Note: The statements, opinions and data contained in all publications are solely those of the individual author(s) and contributor(s) and not of MDPI and/or the editor(s). MDPI and/or the editor(s) disclaim responsibility for any injury to people or property resulting from any ideas, methods, instructions or products referred to in the content.

water

MDPI

Article

Spatial Distribution, Leaching Characteristics, and Ecological and Health Risk Assessment of Potential Toxic Elements in a Typical Open-Pit Iron Mine Along the Yangzi River

Yifan Zeng, Zuxin Xu * and Bin Dong *

State Key Laboratory of Pollution Control and Resource Reuse, College of Environmental Science and Engineering, Tongji University, Shanghai 200092, China; zengyifan93@outlook.com
* Correspondence: zuxinxu111@126.com (Z.X.); dongbin@tongji.edu.cn (B.D.)

Abstract: Potential toxic elements (PTEs) pollution in the soil of abandoned open-pit mines can lead to great ecological risk to the areas around the mining districts. This study selected a typical abandoned open-pit iron mine along the Yangzi River in southeast China to investigate the spatial distribution, leaching characteristics, and ecological and health risk of the soil PTEs (As, Pb, Cd, Ni, Cr, Cu, and Zn). Leaching tests and sequential extraction were applied to study the migration of PTEs under the condition of rainfall. Different risk assessment methods were used to analyze the pollution and ecological risk of PTEs. The contents of As and Cu exceeded the background value of the Chinese soil guideline, with average contents of 50.71 ± 1.59 and 197.47 ± 16.09, respectively. The leaching test and sequential extraction indicated that sites 8 and 9 posed the greatest risk of PTE migration. According to the map of the Nemerow integrated pollution index (*NIPI*), the pollution level of the middle bare area of the study area was the highest, and Cu possessed the highest pollution index (*PI*) of 3.92. The average geo-accumulation index (I_{geo}) of As and Cu was between 1 and 2, reaching the pollution level of moderately contaminated. The average potential ecological risk coefficient (E_i) of As was the highest, and the contributions of As, Cu, and Cd to the potential ecological risk of the whole study area were 46.7%, 29.7%, and 14.3%, respectively. The range of the hazard index (*HI*) and the range of the As carcinogenic risk (CR_{As}) of all the sampling sites for children were 1.30–3.94 and 2.19×10^{-4}–7.20×10^{-4}, and As accounted for more than 85% of the total noncarcinogenic risk, indicating that the comprehensive pollution of PTEs in the study area posed great carcinogenic and noncarcinogenic risks to children. This study can be a proper reference for the subsequent recovery methods and environmental management of the whole mining area.

Keywords: open-pit iron mine; potential toxic elements pollution; leaching potential; pollution risk assessment

1. Introduction

During the process of exploitation and abandonment of metal mines, large amounts of potential toxic elements (PTEs) will enter and accumulate in the soil around the mines [1–3], and the mobile part of PTEs can migrate with rainwater, leading to environmental risk to the nearby rivers and lakes [2,4]. Moreover, PTEs will accumulate through the food chain and cause great risk to humans and ecosystems [5]. With the fast development of mining in China in the past few decades, the PTE pollution of soil caused by abandoned bare mines is getting more and more serious [6] Taking the banks of the Yangtze River as an example, according to the remote sensing data in 2019 from the Chinese Ministry of Natural Resources, the area of abandoned bare mines within 10 km along the river mainstream and primary tributaries is 17,431.82 hectares, and under rough estimation, the amount of PTEs (Cd, Zn, Pb, Cr, Cd, As, and Hg) discharged into the environment could reach 5300 tons, which will cause great damage to the soil and water [7,8].

Among different kinds of metal mines, sulfur-bearing metal mines cause extreme pollution because of acid mine drainage (AMD) [9–11]. The pyrite mine is a typical sulfur-bearing mine, which continuously generates Fe^{2+}, $SO_4{}^{2-}$, and H^+ with the existence of oxygen, water (especially rainfall), and sulfur-oxidizing bacteria, then forming the acid mine drainage [12,13]. PTEs are inclined to leach from the soil and migrate to further regions under the washing of AMD [14]. The combination of low pH and high concentrations of PTEs can pose severe toxicological effects on edaphic and aquatic systems [15]. Previous studies have shown that AMD could bring massive PTEs to nearby regions, and the acid-soluble fraction of PTEs is easy to leach from the soil affected by AMD [16,17].

Assessing the extent of PTE pollution and the potential environmental risk of open-pit mines can offer a guideline for the subsequent pollution remediation and environmental management of mining areas [18]. Spatial distribution analysis of PTEs is conducive to seeking the seriously polluted areas and the priority control PTEs. In mine pollution studies, the leaching tests of PTEs are often ignored [19]. Also, there are few methods to assess the leaching risk based on a leaching test [20]. However, the leaching tests can offer valuable reference on the migration risk of PTEs [21]. It is reported that acid rainfall can greatly increase the average annual leach of PTEs (Zn, Cu, Pb, and Cd, etc.) from mine soils [22,23], and the leaching behavior and mechanism varied with elements and pH conditions [24]. Therefore, before the remediation of abandoned bare mines, it is necessary to analyze the distribution, mobility, and ecological risk of PTEs.

In view of that, a typical and abandoned bare pyrite mine along the Yangzi River was chosen for assessment. Before the application of remediation methods, this study investigated and assessed the PTE pollution for the first time, and the objectives of this study are to (1) quantify the contents and fractionation of PTEs: arsenic(As), lead(Pb), cadmium(Cd), nickel(Ni), chromium(Cr), copper(Cu), and zinc(Zn); (2) investigate the spatial distributions of PTEs in the study area; (3) investigate the leaching characteristics of PTEs; (4) assess the pollution level, ecological risk, and human health risk of PTEs.

2. Materials and Methods

2.1. Study Area

The city of Maanshan (longitude 31°24′~32°02′ N, latitude 117°53′~118°52′ E) is located 10 km east of Anhui province, and the Yangtze River runs across the city. Maanshan is famous for its iron mines, and the city is one of the seven biggest iron mine producing regions [25]. As time goes by, many bare iron mines are left without being restored, and the Xiaonanshan pyrite mine is a typical bare mine that has not been remediated. The Xiaonanshan pyrite mine (longitude 31°40′12″ N, latitude 118°36′51″ E) is located 10 km east of Maanshan city (Figure 1). The mining history of the Xiaonanshan mine can be traced back to 1916, and the mine is abandoned now, leaving bare regions and a water pit to be restored. It can be seen from the satellite map that nearly half of the mountain soil was bare, and the middle part of the bare area is red because of the iron mine corrosion. Moreover, there are ponds, farmlands, and villages on the north side of the iron mine.

2.2. Sampling and Analysis

To better investigate the distributions of PTE pollution in the bare area, 10 sampling sites were chosen according to the terrain of the mountain, and the sample locations were evenly spread at a distance of 150–200 m. Moreover, two sampling sites at the Northwest foot of the mountain were chosen to investigate the migration of PTEs (Figure 1). The sampling sites were located via a GPS app on a mobile phone. To make the samples more representative, 5 topsoil samples (a total of 60 samples) within 5 m from each site were collected according to the 5-point sampling method in July 2023 [26]. A stainless-steel shovel was used to collect all soil samples at a depth of 0–20 cm. All the samples were sealed in plastic bags for later analyses.

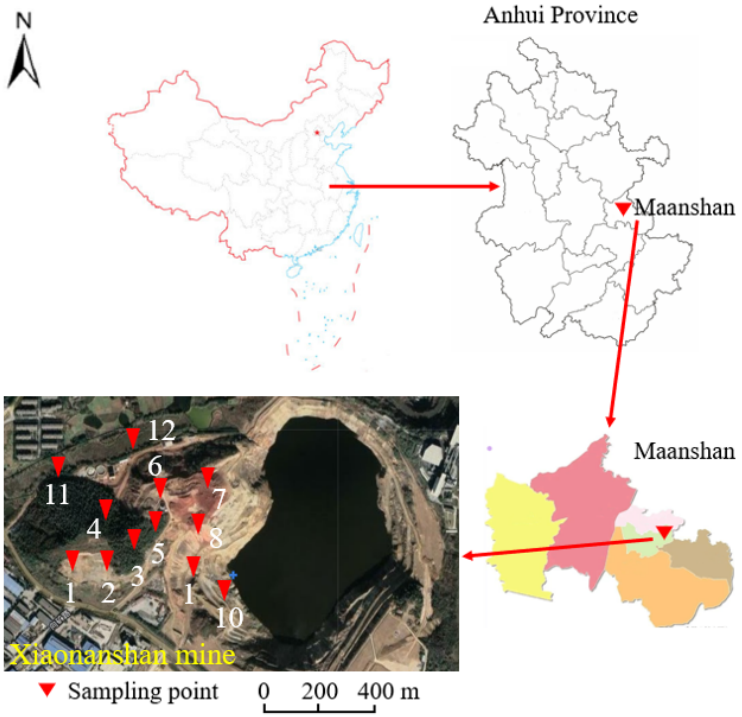

Figure 1. Location of the study area and sampling locations.

The soil samples were air-dried and passed through a 2 mm Nylon sieve. The pH values of the soil samples were determined at a 1:5 mass ratio using a Leici PHS-3F digital ion meter [27]. To measure the concentration of As, Pb, Cd, Ni, Cr, Cu, and Zn in the soil samples, 1.0 g of soil sample was digested with a mixture of acids (9 mL of HNO_3 + 3 mL of HCl + 5 mL of HF). After digestion, the PTEs' concentration was measured with an inductively coupled plasma spectrometer (ICP-OES, Agilent 720ES) [28]. The detection limits of As, Pb, Cd, Ni, Cr, Cu, and Zn are 1 μg/L, 0.8 μg/L, 0.05 μg/L, 0.3 μg/L, 0.15 μg/L, 0.3 μg/L, and 0.2 μg/L, respectively. During the testing process of PTE concentration, various quality assurance and quality control (QA/QC) steps were conducted to make the results accurate and reliable, including instrument calibration, blank analysis, replicate analysis, and a quality control sample set, etc. The relative standard deviation (RSD) was less than 5%, and the recovery rate of the standard sample was between 92% to 110% in this study.

To determine the PTEs' fractionation in the soil samples, the BCR sequential extraction procedure was applied. The details of this method are available elsewhere, and the detailed procedure is summarized in Table 1 [29,30].

Table 1. Modified BCR three-step sequential extraction procedure.

Extraction Steps	Reagent/Concentration/pH	Soil Phase
1	0.5 g sample + 20 mL of 0.11 M Acetic acid CH_3COOH, pH 2.85	Exchangeable; water and acid-soluble
2	20 mL 0.5 M NH_2OH-HCl, pH 1.5	Reducible
3	5 mL H_2O_2 (30% *w*/*v*) + 20 mL 1 M CH_3COONH_4, pH 2	Oxidizable
4	4 mL aqua regia (HCl:HNO_3, 3:1)	Residual

2.3. Leaching Test

2.3.1. Leaching Potential Test

To determine the leaching potential of PTEs in the soil samples, a modified toxicity characteristic leaching procedure (TCLP) test was conducted, according to the Chinese

standard (GB 5085.3-2007) [31]. In brief, 4.0 g of a soil sample was added to 50 mL sulphuric acid solution (pH = 3), and the mixture was agitated on a shaker at 120 rpm for 2, 4, 8, and 24 h at 50 °C. Then, the mixture was centrifuged, and the supernatant was filtered with a 0.45 µm membrane filter. The PTEs' concentration in the supernatant were measured via ICP-OES in an Agilent 720ES spectrometer.

2.3.2. Dynamic Leaching Test

The dynamic leaching test of PTEs from two typical sites was investigated in two down-flow columns (Figure 2), according to Method 1314 of the USEPA [32]. The inner diameter and height of the column are 8 and 15 cm. A 1000 g air-dried soil sample (maximum particle size is 3 mm) was filled into the column. To prevent potential migration of the particles out of the column, both ends of the columns were filled with washed fine-grained quartz sand and filter papers before being sealed. The filling materials in both columns were saturated with rainwater for 24 h before the test. According to Chinese Standard Weather Data, the flow rate for columns was 0.69 mL/min to simulate the local annual precipitation, and the process was conducted for 12 h every day, leaving the other 12 h to collect the leachate. Every day after 12 h of leaching, 20 mL of leachate samples were taken for measurement of PTE contents via ICP-OES. The dynamic leaching test was conducted for 7 days.

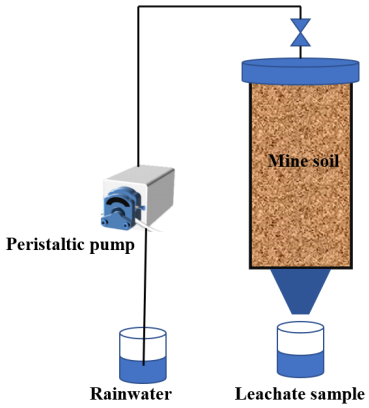

Figure 2. Schematic illustration of the dynamic column experiment.

2.4. Contamination Assessment

2.4.1. Nemerow Integrated Pollution Index

The Nemerow integrated pollution index (*NIPI*) was applied to assess the pollution level of PTEs in the soil [33,34], and the calculation formula is as follows:

$$P_i = \frac{C_i}{C_0} \tag{1}$$

$$NIPI = \sqrt{\frac{P_{ave}^2 + P_{max}^2}{2}} \tag{2}$$

where C_i is the content of heavy metal i in soil, C_0 is the background value of soil heavy metal i, P_i is the single pollution index of soil heavy metal i, P_{ave} is the average index of single pollution of heavy metal i, P_{max} is the maximum *PI* of each heavy metal, and *NIPI* refers to the comprehensive index of each heavy metal. The *NIPI* values can be divided as safe ($NIPI \leq 0.7$), precaution ($0.7 < NIPI \leq 1.0$), slight pollution ($1.0 < NIPI \leq 2.0$), moderate pollution ($2.0 < NIPI \leq 3.0$), and heavy pollution ($NIPI > 3$).

2.4.2. Geo-Accumulation Index

As one of the evaluation methods widely used for soil PTEs, the geo-accumulation index (I_{geo}) method was used to analyze and evaluate the PTE pollution of the Xiaonanshan pyrite mine [35,36]. The calculation formula is as follows:

$$I_{geo} = \log_2\left[\frac{C_i}{(K \times C_0)}\right] \quad (3)$$

where C_i is the content of heavy metal i in the soil (mg kg^{-1}), C_0 is the background value of soil heavy metal i (mg kg^{-1}), and K is a coefficient taken to consider the variation of the background value caused by the difference of rocks in different places (this study, K = 1.5). The I_{geo} value can be classified into seven grades, which represent different contaminated levels (Table S1).

2.4.3. Potential Ecological Risk Assessment

The Hakanson potential ecological risk index method was used to evaluate the potential ecological risk of PTEs in the samples [37]. The calculation formula is as follows:

$$E_r^i = T_r^i \times PI \quad (4)$$

$$RI = \sum_{i=1}^{n} E_r^i \quad (5)$$

where PI refers to the single pollution factors of each heavy metal, ${E_r}^i$ refers to the potential ecological risk factors of each heavy metal, ${T_r}^i$ refers to the toxic response factors of each heavy metal (the toxic response factors of As, Pb, Cd, Ni, Cr, Cu, and Zn are 10, 30, 5, 5, 2, 5, and 1), and RI is the potential ecological risk index. The ${E_r}^i$ and RI values can be classified into five grades, which are shown in Table S2.

2.5. Health Risk Assessment

Besides the soil environment, PTEs also threaten human health [38]. Half of the Xiaonanshan pyrite mine is totally bare, causing large amounts of polluted dust to be brought to nearby places. Considering the nearest village is within 350 m of the pyrite mine, the adults and children are likely to be affected by the PTEs through all three routes. In order to evaluate the risk extent of human health led by PTEs, the health risk assessment model from the USEPA was applied in this study [39]. Considering the differences in vulnerability of different age groups, residents are divided into children and adults [38,40]. The calculation formula is as follows:

$$ADI_{ing} = \frac{C_i \times IngR \times EF \times ED \times CF}{BW \times AT} \quad (6)$$

$$ADI_{inh} = \frac{C_i \times InhR \times EF \times ED}{PEF \times BW \times AT} \quad (7)$$

$$ADI_{der} = \frac{C_i \times CF \times EF \times ED \times AF \times SA \times ABS}{BW \times AT} \quad (8)$$

where ADI_{ing}, ADI_{inh}, and ADI_{dern} are the average daily dose of metals by ingestion, respiration, and dermal absorption, respectively (mg kg^{-1} d^{-1}); C_i refers to the content of heavy metal i in the soil (mg kg^{-1}), $IngR$ refers to the ingestion soil rate (mg d^{-1}), $InhR$ refers to the inhalation rate of soil (m^3 d^{-1}), EF refers to the exposure frequency (d a^{-1}), ED refers to the exposure duration (a), CF refers to the conversion factor (mg kg^{-1}), BW refers to the body weight (kg), AT refers to the average time (days), PEF refers to the particle emission index (m^3 kg^{-1}), SA refers to the exposed skin surface (cm^2), AF refers to the adhered skin index (mg cm^{-2} d), and ABS refers to the dermal adsorption index. Values of the above parameters are shown in Table S3.

The noncarcinogenic and carcinogenic health risks of soil PTEs are calculated with the following formula:

$$HQ_i = \sum \frac{ADI_{ij}}{RfD_{ij}} \quad (9)$$

$$HI = \sum HQ_i \quad (10)$$

where HQ_i refers to the hazard quotient of each heavy metal on the noncarcinogenic risk, ADI_{ij} refers to the average daily intake through of the jth exposure route of each heavy metal (mg kg^{-1} d^{-1}), RfD_{ij} refers to the reference amount of the average daily intake of the jth exposure route of each heavy metal (mg kg^{-1} d^{-1}), and HI refers to the hazard factor. When HQ_i or $HI < 1$, the noncarcinogenic risk is low; when HQ_i or $HI \geq 1$, the noncarcinogenic risk is evident.

$$CR_i = ADI_{ij} \times SF_{ij} \quad (11)$$

$$TCR = \sum CR_i \quad (12)$$

where CR_i refers to the carcinogenic risk of each heavy metal, SF_{ij} refers to the carcinogenic slope factor of the jth exposure route of each heavy metal (mg kg^{-1} d^{-1}), and TCR refers to the total carcinogenic risk. When $1.00 \times 10^{-6} \leq CR_i$ (or TCR) $< 1.00 \times 10^{-4}$, the carcinogenic risk is low; when CR_i (or TCR) $\geq 1.00 \times 10^{-4}$, the cancer risk is evident. In this study, the carcinogenic risk of As was calculated. The toxicity index reference values of PTEs are presented in Table S4.

3. Results and Discussion

3.1. Contents and Fractionation of PTEs in Mine Soils

The average PTEs contents of As, Pb, Cd, Ni, Cr, Cu, and Zn in the study area were 50.71 ± 1.59, 0.13 ± 0.01, 29.30 ± 0.75, 14.51 ± 0.44, 36.30 ± 1.06, 197.47 ± 16.09, and 74.40 ± 2.63 mg/kg, respectively (Table 2). The average concentration of each metal at different sites is shown in Table S5. The average value of As and Cu exceeded the background value of Maanshan soil and the value of Chinese soil guideline (pH ≤ 5.5). The coefficient of variation (CV) showed the average degree of variation of each sampling site in the study area. The CV value of Cu is 97.79%, while the other six PTEs showed slight spatial changes with CV values ranging from 30.82 to 48.49%. The high CV value of Cu indicated that the concentration of Cu in the soil fluctuated greatly, leading to strong spatial changes. Considering that copper ore is often associated with iron ore, the spatial change for Cu was possibly due to the original distribution of copper ore [41]. The content Kurtosis values of each PTE is less than 3, indicating that the contents' distribution is a flatter-than-normal distribution [42]. The content skewness values of As, Pb, Cr, Cu, and Zn are more than 0, indicating the contents of the mentioned metals present an evident right deviation from the normal distribution, while the contents of Cd and Ni present a small deviation. The average value of the soil pH is 4.23 ± 0.06, which may contribute to the process of acid leaching [43].

Table 2. Summary statistics of PTEs' concentrations (mg kg^{-1}) and pH in the soils around the iron mine.

	As	Cd	Pb	Ni	Cr	Cu	Zn	pH
Min	29.94	0.03	14.85	4.73	19.72	23.31	38.74	2.97
Mean ± SE [a]	50.71 ± 1.59	0.13 ± 0.01	29.30 ± 0.75	14.51 ± 0.44	36.30 ± 1.06	197.47 ± 16.09	74.40 ± 2.63	4.23 ± 0.06
Max	98.32	0.21	49.28	23.15	65.52	621.81	155.46	5.66
SD [b]	19.14	0.06	9.03	5.28	12.73	193.09	31.57	0.81
CV [c] (%)	37.74	48.49	30.82	36.40	35.06	97.79	42.44	19.23
Kurtosis	1.62	−1.59	0.51	−0.44	0.68	1.10	2.58	−0.88
Skewness	1.32	−0.06	0.78	−0.22	1.01	1.50	1.56	0.14
Background [d]	10.55	0.26	24.43	38.90	86.40	32.37	84.73	-
Chinese soil guideline (pH ≤ 5.5) [e]	40	0.3	70	60	150	50	200	-

Notes: [a] Standard error; [b] Standard deviation; [c] Coefficient of variation; [d] Soil background values for soils in Maanshan; [e] Soil environment quality risk control standard for soil contamination of agricultural land.

3.2. Spatial Distribution of PTEs

The spatial distribution of As, Cd, Pb, Ni, Cr, Cu, and Zn concentrations and pH values in the study area are presented in Figure 3. According to the maps, the distribution trends of Cu and Zn were similar. The areas with higher concentrations of Cu and Zn were

confined to sites 8 and 9, and site 10 presented the highest concentration, indicating the possible migration of Cu from sites 8 and 9 to site 10. The distribution trends of As, Pb, Ni, and Cr are different from Cu, Cd, and Zn. The maximum concentration of As, Pb, Ni, and Cr came from the bare area (middle and southwest part) of the mine, where human activities like transportation were frequent, indicating the contaminants may be released from human activities [44]. The highest concentration of Cd came from sites 6, 8, and 9, and the Cd concentration of site 10 was less than the above sites, indicating that the migration speed of Cd was slower than Cu. The lowest pH values came from the bare area of the north and south part, and the pH value of sites 8 and 9 was higher, which was probably caused by the wash of large amounts of rainwater [45].

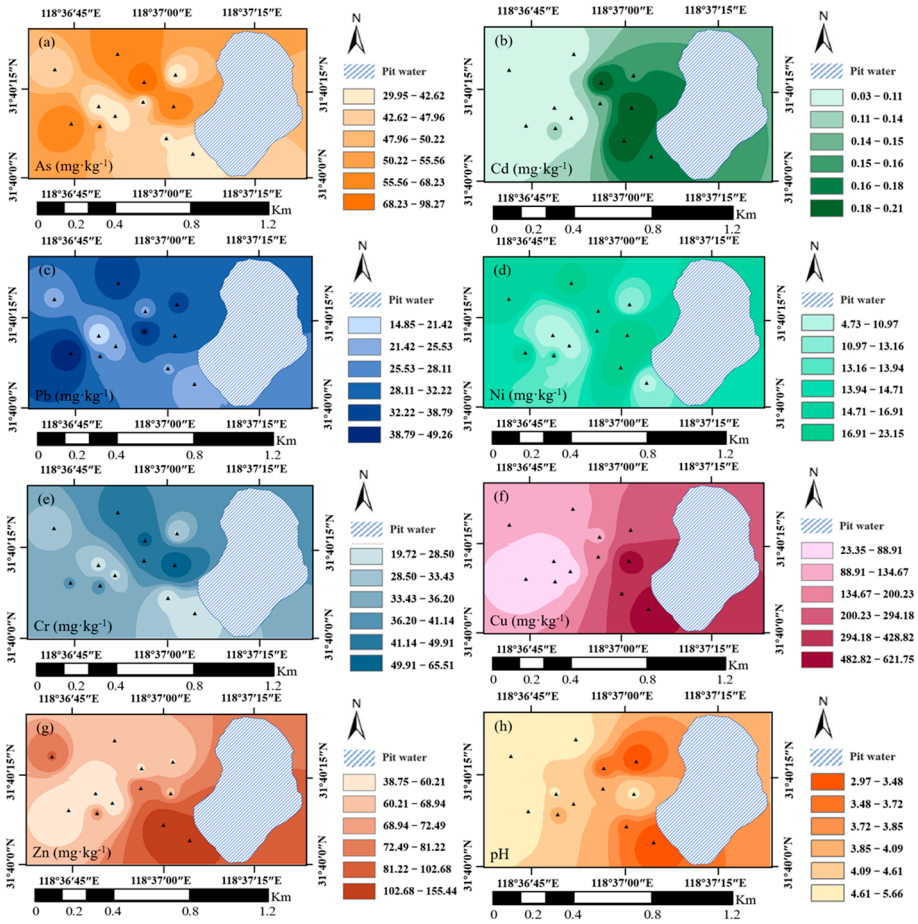

Figure 3. Maps of As (**a**), Cd (**b**), Pb (**c**), Ni (**d**), Cr (**e**), Cu (**f**), and Zn (**g**) concentrations and pH value (**h**) in the study area.

3.3. Sequential Extraction

The mobility and availability decrease in the order of acid-soluble fraction > reducible fraction > oxidizable fraction [46]. The PTE fractionations of Pb, Ni, Cd, As, Cr, Zn, and Cu in the soil samples are shown in Figure 4, and the results are described in terms of the percentage distribution. Acid-soluble fraction PTEs are mobile and bioavailable, leading environmental threats to nearby soil and water. Therefore, the percentage of acid-soluble fraction indicates the migration risk of PTEs. According to Figure 4, the largest percentage of all the PTEs (except for sample 8 from Cu fractionation) is the residual fraction. The acid-soluble and reducible fraction of Pb are less than 1%, and several samples possess a certain percentage of reducible Pb. For As and Cr, the fractionation difference among different samples is small. The acid-soluble fractions of Cr samples are less than 1%, and for As they are between 2 and 7%. For Ni, Cd, Zn, and Cu, there are obvious differences between samples 8, 9, and other samples. The acid-soluble fractions of sample 8 and 9 of

Ni, Cd, Zn, and Cu are 15.8% and 23.6%, 13.9% and 27.5%, 17.6% and 16.2%, and 56.0% and 6.7%, indicating great migration risk of PTEs. Considering the great proportion of the acid-soluble fraction of Cu in sample 8 (56.0%), site 8 might possess a higher amount of copper ore than other sites, and site 8 was the primary Cu pollution source of the study area. Moreover, the soil at site 8 was more porous than other sites, which accelerated the corrosion of copper ore. Though the contents of Cd, Ni, and Zn in soil are not high, given the large area of the mine, the leaching amount of acid-soluble PTEs could accumulate and cause damage to the environment [47]. It can be seen from Figure 1 that there are ponds and farmlands on the north side of the bare mine, which are only several hundred meters away from the mountain. PTE ions would transport with rainfall to the nearby ponds and farmlands. With the progress of agricultural activities, PTEs might accumulate through the food chain and threaten human health [48].

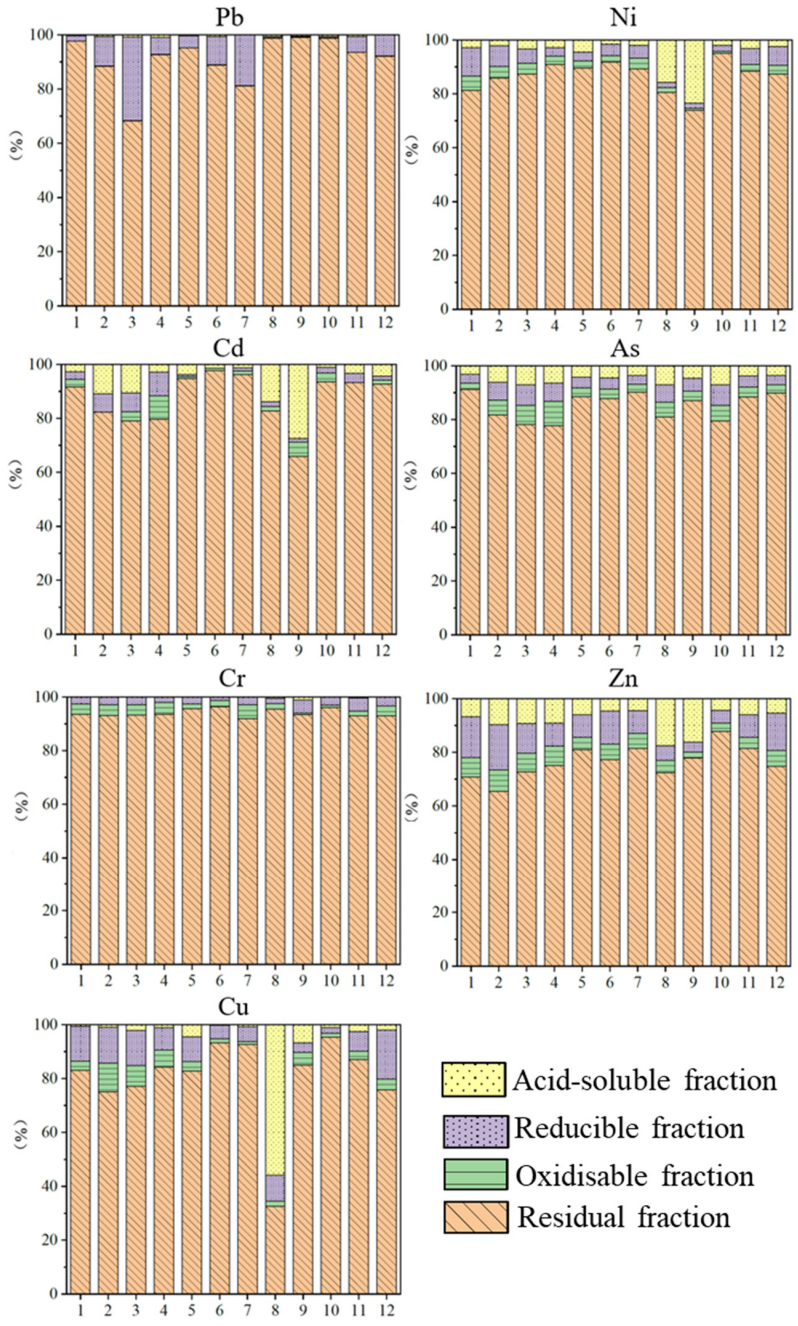

Figure 4. BCR extractable fractionations (%) of PTEs in soil samples of the study area.

3.4. Leaching Potential and Dynamic Leaching Tests

3.4.1. Leaching Potential of PTEs

Figure S1 presents the PTEs' leaching amount to the unit mass of the soil samples (mg/kg) in batch leaching tests. The test was designed to simulate severe leaching conditions to determine the largest leaching potential of different PTEs. According to Figure 5, the PTE leaching amount of soil sample 8 (brown) and 9 (deep green) were much higher than other samples, which was in accordance with the sequential extraction results that the percentage of acid-soluble fractions of PTEs of sample 8 and 9 are higher than other samples. The leaching amounts of Cd, Cr, Cu, and Pb from sample 8 were 0.07, 0.33, 172.8, and 0.54 mg/kg, and the leaching amounts of Ni, Zn, and As from sample 9 were 3.13, 19.28, and 0.082 mg/kg, which were the maximum leaching amount of all the samples. Meanwhile, based on the trend of curves in Figure S1, the leaching amount reached the maximum at 4 h, and the leaching amount began to decrease after 4 h, which was probably caused by the readsorption of heavy metal ions by soil samples [49,50]. Therefore, the leaching amount at 4 h can represent the highest PTE leaching potential of the soil samples.

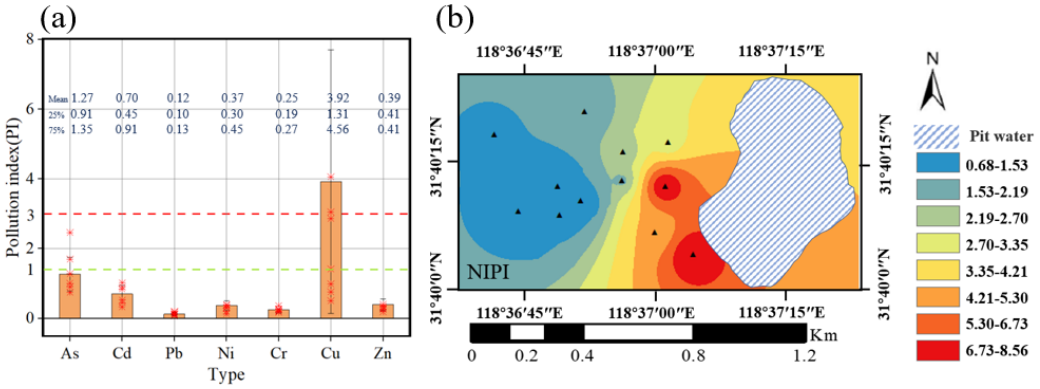

Figure 5. *PI* values (**a**) and map of *NIPI* values (**b**) of PTEs in the study area.

3.4.2. Dynamic Leaching of PTEs

According to the results of the leaching potential test, soil samples 8 and 9 were selected to conduct the dynamic leaching test because of their high leaching potential. Figure S2 presents the leaching contents of PTEs from soil sample 8 (a) and soil sample 9 (b). The amounts of Cd, Cr, Cu, Ni, Pb, Zn, and As released from soil samples 8 and 9 on the first day were the highest, which were 2.70×10^{-2}, 6.40×10^{-2}, 2.67×10^{1}, 1.19×10^{0}, 3.33×10^{-1}, 1.08×10^{1}, and 6.00×10^{-4} mg/g for soil sample 8 and 1.77×10^{-2}, 3.40×10^{-2}, 3.12×10^{0}, 2.13×10^{0}, 2.80×10^{-1}, 2.71×10^{1}, and 1.20×10^{-2} mg/g, respectively. The contents of PTEs released from the two samples decreased with time, and the leaching amounts of Cd, Cr, Cu, and Zn on the second day were less than 50% of the amounts on the first day, while the decreasing ranges of Pb and Ni were small.

The ratios of the PTE contents released on the first day/the total PTE contents released for 7 days and the total PTE contents released for 7 days/the highest leaching potential were calculated, and the results are shown in Figure S3. The ratios calculated from sample 8 and 9 are nearly the same. Based on the yellow bars, the ratios of contents released on the first day/the total PTEs contents released for 7 days of Cd, Cr, Cu, and Zn were more than 40%, and the highest ratio was 58.60% for Zn of sample 9, indicating that Cd, Cr, Cu, and Zn showed higher leaching efficiency than other PTEs on the first day. Based on the green bars, the ratios of the total PTE contents released for 7 days/the highest leaching potential of Ni, Pb, and Zn were more than 90%, and the highest ratio was 98.06% for Ni of sample 9, indicating that Ni, Pb, and Zn were more inclined to migrate with rainwater than other PTEs. The average difference among the ratios of the total PTE contents released for 7 days/the highest leaching potential between samples 8 and 9 was 4.13%, indicating that the highest leaching potential determined via the leaching potential test was an effective reference for mine soil leaching pollution assessment.

Notably, results of the leaching potential test and dynamic leaching test indicated that samples 8 and 9 possessed the highest leaching amount of PTEs. As the proportions of the acid-soluble fraction of Cu and Cd in samples 8 and 9 were much higher than other samples, the results of the leaching experiment were in accordance with the results of sequential extraction. Moreover, Cd, Cu, Zn, and Cr presented higher leaching efficiency. The wash of rainfall brought a large amount of PTEs to sites 8 and 9 [22], and a part of the PTEs settled in the two sites in an acid-soluble fraction which would leach out with the subsequent rainfall. Therefore, sites 8 and 9 became the confluence and origin of PTEs. Urgent actions should be taken to prevent the migration of PTEs in sites 8 and 9, and Cd, Cu, Zn, and Cr are the primary targets.

3.5. Contamination Assessment of PTEs

3.5.1. Pollution Index of PTEs

Figure 5 presents the *PI* and *NIPI* values of PTE pollution in the study area. The average *PI* values of As, Cd, Pb, Ni, Cr, and Zn were less than 1, indicating that the six PTEs are in the safe class and pose little threat to the nearby environment. The average *PI* value of Cu was more than 3, and the pollution of Cu was serious and posed a great threat to the quality and safety of the soil. From the map of *NIPI* values, the *NIPI* values increased from the west part of the mine to the east, and the *NIPI* value of sampling site 10 was the highest. From the middle part to the east of the mine, the *NIPI* values were more than 3, indicating that the pollution level was severe. The sites with green plants (the western part of the mine) were still clean with an *NIPI* value of less than 1.5, and the level of the middle part of the mine was between slight and moderate pollution. As the mine terrain was high in the west and low in the east, most rainfall flowed by sites 8 and 9 to the mine pit, making it difficult for the PTEs to migrate toward the west. Therefore, mountain terrain could be an important factor that influences the risk distribution [51,52].

3.5.2. Geo-Accumulation Index of PTEs

Figure 6 presents the I_{geo} values of PTEs in the study area. According to the results, the average I_{geo} values of Cd, Pb, Ni, Cr, and Zn were below 0, indicating that the overall pollution level of these PTEs was practically uncontaminated. The average I_{geo} values of As and Cu were between 1 and 2, reaching the pollution level of moderately contaminated, and certain sites showed higher environmental risk of $2 < I_{geo} < 4$, reaching the pollution level of moderately to heavily contaminated and heavily contaminated. As I_{geo} is calculated to assess the PTEs' accumulation degree in soil, the accumulation level of As and Cu in the study area is high.

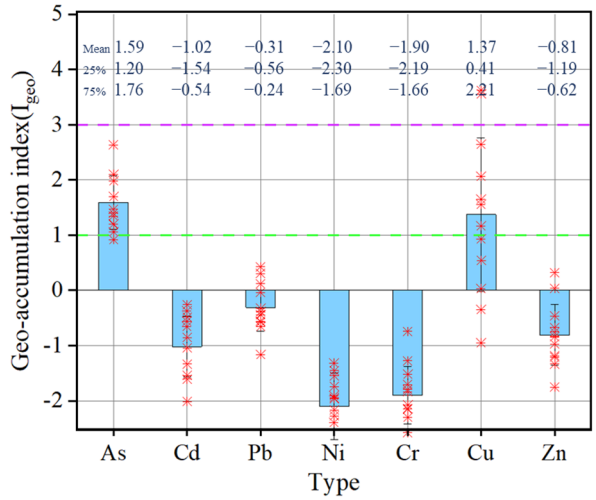

Figure 6. I_{geo} values of PTEs in the study area.

3.5.3. Potential Ecological Risk Index of PTEs

Figure 7 presents the E_i values(a) and the map of *PERI* values of PTEs in the study area. According to the E_i values, the average E_i value of As was the highest, reaching the level of intermediate pollution, and other PTEs' pollution was at the level of slight pollution. The E_i values of an As sample and two Cu samples were more than 80, reaching the level of strong pollution, which indicated that the pollution level of the study area was uneven. From the map of *PERI* values, the highest *PERI* value was at sampling site 8, reaching the level of intermediate pollution. Pollution of the bare part in the middle of the mine was more serious than that of surrounding areas, leading to a great threat to the nearby plants and soils if no appropriate remediation method was applied in time. According to Figure 8, the contributions of As, Cu, and Cd to the *PERI* value of the whole study area were 46.7%, 29.7%, and 14.3%, respectively, which accounted for a 90% pollution risk for the study area. Therefore, most of the remediation attention should be paid to the three kinds of PTEs in the future.

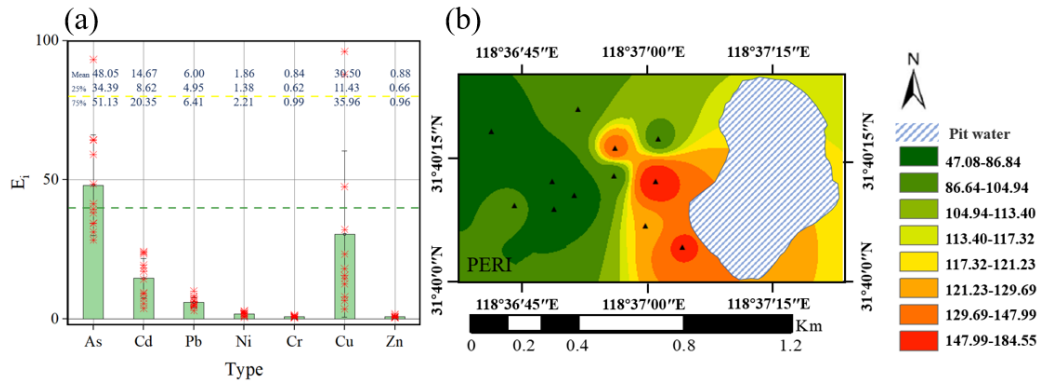

Figure 7. E_i values (**a**) and map of *PERI* values (**b**) of PTEs in the study area.

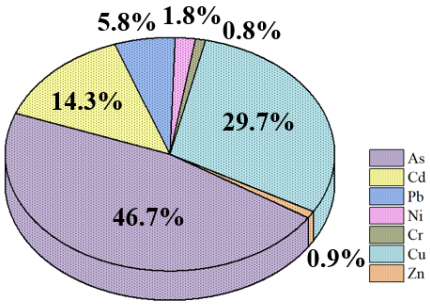

Figure 8. Contributions of PTEs to *PERI* value of the whole study area.

3.6. Health Risk Assessment of PTEs

Table 3 presents the noncarcinogenic and carcinogenic risks (As) to adults and children. Because of the low contents of Cd, Ni, and Cr, this study only calculated the carcinogenic risks of As. The range of *HI* of all the sampling sites for adults and children were 0.16–0.50 and 1.30–3.94, and the range of CR_{As} of all the sampling sites for adults and children were 2.76×10^{-5}–9.06×10^{-5} and 2.19×10^{-4}–7.20×10^{-4}, respectively. All the *HI* and CR_{As} values were less than the risk value, indicating that the comprehensive pollution of PTEs in the study area had no carcinogenic and noncarcinogenic risk to adults. As for children, all the *HI* and CR_{As} values were more than the risk value, which posed great carcinogenic and noncarcinogenic risks to children. As content of sampling site 6 and Cu content of sampling site 8 were the highest of all the sampling sites; the *HI* and CR_{As} values of the two sampling sites were higher than other sites, indicating great health risk in the bare areas. Figure 9 presents the Contributions of PTEs to *HI* values of the whole study area. The percentages of different PTEs' contributions to HI_{adults} and $HI_{children}$ were almost the

same, with As accounting for more than 85% of the total noncarcinogenic risk. The results revealed that As was the main PTE in this mine that would pose potential risk on children's health.

Table 3. Noncarcinogenic and carcinogenic risks posed to adults and children.

Sampling Sites	Adults		Children	
	Noncarcinogenic Risks (*HI*)	Carcinogenic Risks of As (*CR*)	Noncarcinogenic Risks (*HI*)	Carcinogenic Risks of As (*CR*)
1	0.35	6.26×10^{-5}	2.80	4.97×10^{-4}
2	0.27	4.72×10^{-5}	2.12	3.74×10^{-4}
3	0.16	2.76×10^{-5}	1.30	2.19×10^{-4}
4	0.19	3.34×10^{-5}	1.49	2.65×10^{-4}
5	0.23	3.71×10^{-5}	1.82	2.94×10^{-4}
6	0.50	9.06×10^{-5}	3.94	7.20×10^{-4}
7	0.20	3.35×10^{-5}	1.62	2.66×10^{-4}
8	0.38	6.25×10^{-5}	3.04	4.96×10^{-4}
9	0.23	3.84×10^{-5}	1.79	3.05×10^{-4}
10	0.19	3.04×10^{-5}	1.54	2.41×10^{-4}
11	0.23	4.03×10^{-5}	1.84	3.20×10^{-4}
12	0.33	5.74×10^{-5}	2.62	4.56×10^{-4}
Average	0.27	4.68×10^{-5}	2.16	3.71×10^{-4}

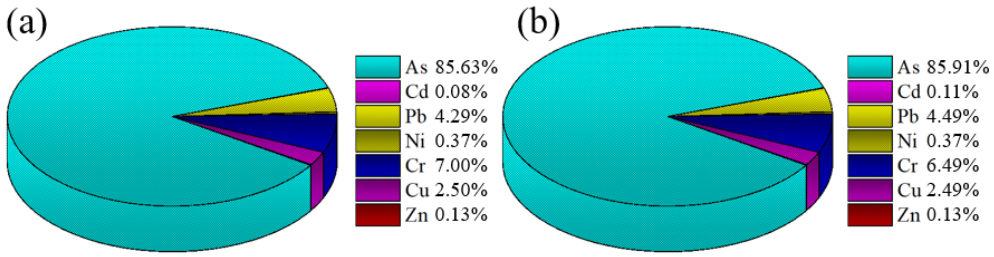

Figure 9. Contributions of PTEs to HI_{adults} (**a**) and $HI_{children}$ (**b**) values of the whole study area.

3.7. Limitations and Perspectives

This paper presented an in-depth study of PTEs' pollution assessment for the Xiaonanshan pyrite mine, but there are some limitations worth discussing. Firstly, this study only analyzed the contents of PTEs in summer, while the content variations during a long period have not been studied. Secondly, the PTEs' distributions and variations in the nearby ponds and farmlands are vacant, which are also important to the environmental risk assessment. Thirdly, we have not raised new or modified evaluation methods to properly assess the migration risk of PTEs in soils after rainfall. Therefore, in future studies, the perspectives should include the following: (1) study the variations in PTEs (contents and fractions) in the soils with time; (2) expand the study area to the nearby ponds and farmlands; (3) study the influence of rainfall on the transport of PTEs ions to nearby areas; (4) create new assessment methods to better evaluate the potential ecological risk of PTEs.

4. Conclusions

In this study, the spatial distribution, leaching potential, and ecological and health risk assessment of PTEs in soils around the Xiaonanshan pyrite mine in Maanshan were investigated for the first time. The average concentrations of As and Cu were 50.71 ± 1.59 and 197.47 ± 16.09, which were 4.8 and 6.1 times the background value of Maanshan soil. The results of sequential extraction indicated that the acid-soluble fraction of the PTEs in sites 8 and 9 was much higher than that in other areas, which posed great risk of PTEs leaching. In addition, the leaching test proved that the leaching amount of PTEs on sites 8 and 9 was much higher than that of other areas. The highest leaching potential was an

effective reference in assessing the leaching risk of PTEs. According to the results of the PTE contamination assessment, site 10 showed the highest *NIPI* value with the risk level of severe pollution, and the pollution of Cu is the most serious. The I_{geo} values indicated that the accumulation level of As and Cu in the study area is high. According to the results of *PERI*, pollution at site 8 was the worst, reaching the level of intermediate pollution, and As, Cu, and Cd accounted for 90% of the ecological risk for the study area. The health risk assessment results presented that noncarcinogenic and carcinogenic risks were likely to occur in children, and As accounted for more than 85% of the total noncarcinogenic risk.

According to this study, soil remediation methods are urgently needed to restore the soil of abandoned bare mines along the Yangzi River. More attention should be paid to the areas where PTEs are easier to leach out from the soil. PTE fixation technologies should be developed and applied to impede the migration of PTEs. Local residents, especially children, should avoid activities near the iron mine.

Supplementary Materials: The following supporting information can be downloaded at: https://www.mdpi.com/article/10.3390/w16213017/s1, Figure S1: PTEs contents in the leachate of the soil samples; Figure S2: Leaching contents of PTEs from soil sample 8(a) and soil sample 9(b); Figure S3: The ratios of the PTEs contents released on the first day/the total PTEs contents released for 7 days (yellow bar) and the total PTEs contents released for 7 days/the highest leaching potential(green bar); Table S1: Seven grades comprising the geo-accumulation index; Table S2: Five grades comprising the $E_r{}^i$ and *RI* valu; Table S3: Values of relevant parameters.

Author Contributions: Z.X. contributed to the study conception and design. Sample collection and data analysis were performed by Y.Z. The first draft of the manuscript was written by Y.Z., and the draft was reviewed and revised by Z.X. and B.D. All authors have read and agreed to the published version of the manuscript.

Funding: This research was supported by the National Key Research and Development Program of China 2021YFC3200700.

Institutional Review Board Statement: The authors declare that this manuscript has not been published previously.

Informed Consent Statement: All authors voluntarily participated in this research study.

Data Availability Statement: The raw data supporting the conclusions of this article will be made available by the authors on request.

Conflicts of Interest: The authors declare no conflicts of interest.

References

1. Davila, R.B.; Fontes MP, F.; Pacheco, A.A.; da Silva Ferreira, M. Heavy metals in iron ore tailings and flood plain soils affected by the Samarcodam collapse in Brazil. *Sci. Total Environ.* **2020**, *709*, 11. [CrossRef] [PubMed]
2. Qiao, P.; Wang, S.; Li, J.; Zhao, Q.; Wei, Y.; Lei, M.; Yang, J.; Zhang, Z. Process, influencing factors, and simulation of the lateral transport of heavy metals in surface runoff in a mining area driven by rainfall: A review. *Sci. Total Environ.* **2023**, *857*, 159119. [CrossRef]
3. Qin, H.; Takeichi, Y.; Nitani, H.; Terada, Y.; Takahashi, Y. Tellurium Distribution and Speciation in Contaminated Soils from Abandoned Mine Tailings: Comparison with Selenium. *Environ. Sci. Technol.* **2017**, *51*, 6027–6035. [CrossRef]
4. Kefeni, K.K.; Msagati, T.A.M.; Mamba, B.B. Acid mine drainage: Prevention, treatment options, and resource recovery: A review. *J. Clean. Prod.* **2017**, *151*, 475–493.
5. Du, B.; Zhou, J.; Lu, B.; Zhang, C.; Li, D.; Zhou, J.; Jiao, S.; Zhao, K.; Zhang, H. Environmental and human health risks from cadmium exposure near an active lead-zinc mine and a copper smelter, China. *Sci. Total Environ.* **2020**, *720*, 137585. [CrossRef] [PubMed]
6. Zhao, F.; Ma, Y.; Zhu, Y.-G.; Tang, Z.; McGrath, S.P. Soil Contamination in China: Current Status and Mitigation Strategies. *Environ. Sci. Technol.* **2015**, *49*, 750–759. [PubMed]
7. Yu, J.; Liu, X.; Yang, B.; Li, X.; Wang, P.; Yuan, B.; Wang, M.; Liang, T.; Shi, P.; Li, R.; et al. Major influencing factors identification and probabilistic health risk assessment of soil potentially toxic elements pollution in coal and metal mines across China: A systematic review. *Ecotoxicol. Environ. Saf.* **2024**, *274*, 116231.
8. Jiang, Y.; Guo, Q.; Deng, Y. Research progress in the distribution of heavy metals in sediments and soils in the Yangtze River Basin. *Chin. J. Ecol.* **2022**, *41*, 804–812.

9. Rodríguez-Sierra, C.J.; Adelman, D.; Vojta, Š.; Mansilla-Rivera, I.; Lohmann, R. Passive Sampling of Persistent Organic Pollutants in Four Coastal Aquatic Systems of Puerto Rico: A Pilot Study. *Bull. Environ. Contam. Toxicol.* **2019**, *103*, 770–775. [CrossRef]
10. Alegbe, M.J.; Ayanda, O.; Ndungu, P.; Nechaev, A.; Fatoba, O.; Petrik, L. Physicochemical characteristics of acid mine drainage, simultaneous remediation and use as feedstock for value added products. *J. Environ. Chem. Eng.* **2019**, *7*, 103097. [CrossRef]
11. Luo, Y.; Zheng, Z.; Wu, P.; Wu, Y. Effect of different direct revegetation strategies on the mobility of heavy metals in artificial zinc smelting waste slag: Implications for phytoremediation. *Chemosphere* **2022**, *286*, 131678. [PubMed]
12. Mohan, D.; Chander, S. Removal and recovery of metal ions from acid mine drainage using lignite—A low cost sorbent. *J. Hazard. Mater.* **2006**, *137*, 1545–1553. [CrossRef] [PubMed]
13. Tu, Z.H.; Wu, Q.; He, H.; Zhou, S.; Liu, J.; He, H.; Liu, C.; Dang, Z.; Reinfelder, J.R. Reduction of acid mine drainage by passivation of pyrite surfaces: A review. *Sci. Total Environ.* **2022**, *832*, 155116. [CrossRef]
14. Tabelin, C.B.; Uyama, A.; Tomiyama, S.; Villacorte-Tabelin, M.; Phengsaart, T.; Silwamba, M.; Jeon, S.; Park, I.; Arima, T.; Igarashi, T. Geochemical audit of a historical tailings storage facility in Japan: Acid mine drainage formation, zinc migration and mitigation strategies. *J. Hazard. Mater.* **2022**, *438*, 129453.
15. He, M.; Wang, Z.; Tang, H. Spatial and temporal patterns of acidity and heavy metals in predicting the potential for ecological impact on the Le An river polluted by acid mine drainage. *Sci. Total Environ.* **1997**, *206*, 67–77. [CrossRef] [PubMed]
16. Akcil, A.; Koldas, S. Acid Mine Drainage (AMD): Causes, treatment and case studies. *J. Clean. Prod.* **2006**, *14*, 1139–1145. [CrossRef]
17. Skousen, J.G.; Ziemkiewicz, P.F.; McDonald, L.M. Acid mine drainage formation, control and treatment: Approaches and strategies. *Extr. Ind. Soc.* **2019**, *6*, 241–249. [CrossRef]
18. Chen, R.; Han, L.; Liu, Z.; Zhao, Y.; Li, R.; Xia, L.; Fan, Y. Assessment of Soil-Heavy Metal Pollution and the Health Risks in a Mining Area from Southern Shaanxi Province, China. *Toxics* **2022**, *10*, 385. [CrossRef]
19. Lim, M.; Han, G.-C.; Ahn, J.-W.; You, K.-S.; Kim, H.-S. Leachability of Arsenic and Heavy Metals from Mine Tailings of Abandoned Metal Mines. *Int. J. Environ. Res. Public Health* **2009**, *6*, 2865–2879. [CrossRef]
20. Nguyen, X.P.; Islam, M.N.; Jo, Y.-T.; Park, J.-H. Variation of Cu and Zn Fractionation and Mobility in Mine Tailing Soil Due to Experimental Leaching. *Soil Sediment Contam. Int. J.* **2017**, *26*, 210–219. [CrossRef]
21. Zha, F.; Zhu, F.; Xu, L.; Kang, B.; Yang, C.; Zhang, W.; Zhang, J.; Liu, Z. Laboratory study of strength, leaching, and electrical resistivity characteristics of heavy-metal contaminated soil. *Environ. Earth Sci.* **2021**, *80*, 184. [CrossRef]
22. Wang, F.; Li, W.; Wang, H.; Hu, Y.; Cheng, H. The leaching behavior of heavy metal from contaminated mining soil: The effect of rainfall conditions and the impact on surrounding agricultural lands. *Sci. Total Environ.* **2024**, *914*, 169877. [CrossRef] [PubMed]
23. Tian, S.; Liu, Z.; Mao, Q.; Ye, H.; Tian, C.; Zhu, Y.; Zhang, L. Leaching characteristics and environmental impact of heavy metals in tailings under rainfall conditions: A case study of an ion-adsorption rare earth mining area. *Ecotoxicol. Environ. Saf.* **2024**, *281*, 116642. [CrossRef] [PubMed]
24. Li, W.; Deng, Y.; Wang, H.; Hu, Y.; Cheng, H. Potential risk, leaching behavior and mechanism of heavy metals from mine tailings under acid rain. *Chemosphere* **2024**, *350*, 140995. [CrossRef] [PubMed]
25. Xu, S.; Wang, W. The significance of different scale copper geochemical anomalies and large ore deposit prediction in the middle-lower Yangtze River. *Earth Sci. Front.* **2012**, *19*, 84–92.
26. Yang, H.; Wang, F.; Yu, J.; Huang, K.; Zhang, H.; Fu, Z. An improved weighted index for the assessment of heavy metal pollution in soils in Zhejiang, China. *Environ. Res.* **2021**, *192*, 110246. [CrossRef]
27. Liu, B.; Xu, M.; Wang, J.; Wang, Z.; Zhao, L. Ecological risk assessment and heavy metal contamination in the surface sediments of Haizhou Bay, China. *Mar. Pollut. Bull.* **2021**, *163*, 111954. [CrossRef]
28. Ouyang, X.; Wang, Z.; Liu, X. Distribution patterns, risk assessment and potential sources of heavy metals in sediment in the Qiongzhou Strait, China. *Mar. Pollut. Bull.* **2024**, *203*, 116481. [CrossRef] [PubMed]
29. Ure, A.M.; Quevauviller, P.; Griepink, B. Speciation of heavy metals in soils and sediments an account of the improvement and harmonization of extraction techniques undertaken under the auspices of the bcr of the commission of the european communities. *Int. J. Environ. Anal. Chem.* **1993**, *51*, 135–151. [CrossRef]
30. Guillén, M.T.; Delgado, J.; Albanese, S.; Nieto, J.M.; Lima, A.; De Vivo, B. Heavy metals fractionation and multivariate statistical techniques to evaluate the environmental risk in soils of Huelva Township (SW Iberian Peninsula). *J. Geochem. Explor.* **2012**, *119–120*, 32–43. [CrossRef]
31. Huang, M.; Feng, H.; Shen, D.; Li, N.; Chen, Y.; Shentu, J. Leaching Behavior of Heavy Metals from Cement Pastes Using a Modified Toxicity Characteristic Leaching Procedure (TCLP). *Bull. Environ. Contam. Toxicol.* **2016**, *96*, 354–360. [CrossRef] [PubMed]
32. USEPA. *Liquid-Solid Partitioning as a Function of Liquid-solid Ratio for Constituents in Solid Materials Using an Up-Flow Percolation Column Procedure*; USEPA: Washington, DC, USA, 2013.
33. Jamali, M.K.; Kazi, T.G.; Arain, M.B.; Afridi, H.I.; Jalbani, N.; Memon, A.R.; Shah, A. Heavy metals from soil and domestic sewage sludge and their transfer to Sorghum plants. *Environ. Chem. Lett.* **2007**, *5*, 209–218. [CrossRef]
34. Yi, Y.; Yang, Z.; Zhang, S. Ecological risk assessment of heavy metals in sediment and human health risk assessment of heavy metals in fishes in the middle and lower reaches of the Yangtze River basin. *Environ. Pollut.* **2011**, *159*, 2575–2585. [CrossRef]
35. Muller, G. Index of Geoaccumulation in Sediments of the Rhine River. *GeoJournal* **1969**, *2*, 109–118.

36. Loska, K.; Wiechuła, D.; Korus, I. Metal contamination of farming soils affected by industry. *Environ. Int.* **2004**, *30*, 159–165. [CrossRef]
37. Hakanson, L. An ecological risk index for aquatic pollution control.a sedimentological approach. *Water Res.* **1980**, *14*, 975–1001. [CrossRef]
38. Xiao, X.; Zhang, J.; Wang, H.; Han, X.; Ma, J.; Ma, Y.; Luan, H. Distribution and health risk assessment of potentially toxic elements in soils around coal industrial areas: A global meta-analysis. *Sci. Total Environ.* **2020**, *713*, 135292.
39. USEPA. *Exposure Factors Handbook (Final Report)*; US Environmental Protection Agency: Washington, DC, USA, 2011.
40. Kumar, V.; Parihar, R.D.; Sharma, A.; Bakshi, P.; Sidhu, G.P.S.; Bali, A.S.; Karaouzas, I.; Bhardwaj, R.; Thukral, A.K.; Gyasi-Agyei, Y.; et al. Global evaluation of heavy metal content in surface water bodies: A meta-analysis using heavy metal pollution indices and multivariate statistical analyses. *Chemosphere* **2019**, *236*, 124364. [PubMed]
41. Heydartaemeh, M.; Karamoozian, M.; Potgieter, H. Application of Nano High-Entropy Alloys to Reduce Energy Consumption and Wear of Copper Oxide and High-Grade Iron Ores in Heavy Mining Industries—A Case Study. *Minerals* **2019**, *10*, 16. [CrossRef]
42. Liu, S.; Hou, S.; He, K.; Yang, W. L-Kurtosis and its application for fault detection of rolling element bearings. *Measurement* **2018**, *116*, 523–532. [CrossRef]
43. Zhang, S.Q.; Zhang, X.; Guo, Z.; Ren, D.; Zhang, X.; Wang, S. Study on the remediation of heavy metal contaminated soils by citric acid and polyepoxysuccinic acid complex leaching. *Environ. Technol.* **2024**, *45*, 705–715. [CrossRef] [PubMed]
44. Faisal, M.; Wu, Z.; Wang, H.; Hussain, Z.; Azam, M.I.; Muzammil, M. Assessment and source apportionment of water-soluble heavy metals in road dust of Zhengzhou, China. *Environ. Sci. Pollut. Res.* **2022**, *29*, 68857–68869. [CrossRef]
45. Montoya-Mayor, R.; Fernández-Espinosa, A.; Seijo-Delgado, I.; Ternero-Rodríguez, M. Determination of soluble ultra-trace metals and metalloids in rainwater and atmospheric deposition fluxes: A 2-year survey and assessment. *Chemosphere* **2013**, *92*, 882–891. [CrossRef] [PubMed]
46. Zimmerman, A.J.; DWeindorf, C.; Cifuentes, A. Heavy Metal and Trace Metal Analysis in Soil by Sequential Extraction: A Review of Procedures. *Int. J. Anal. Chem.* **2010**, *2010*, 387803. [CrossRef] [PubMed]
47. Xu, J.C.; Wang, S.; Yao, T.; She, X.; Gan, Z. Vertical Distributions and Bioavailabilities of Heavy Metals in Soil in An-Tea Plantations in Qimen County, China. *Processes* **2022**, *10*, 664. [CrossRef]
48. Qing, X.; Yutong, Z.; Shenggao, L. Assessment of heavy metal pollution and human health risk in urban soils of steel industrial city (Anshan), Liaoning, Northeast China. *Ecotoxicol. Environ. Saf.* **2015**, *120*, 377–385. [CrossRef]
49. Gómez-Ariza, J.L.; Giráldez, I.; Sánchez-Rodas, D.; Morales, E. Metal readsorption and redistribution during the analytical fractionation of trace elements in oxic estuarine sediments. *Anal. Chim. Acta* **1999**, *399*, 295–307. [CrossRef]
50. Davranche, M.; Bollinger, J. Heavy Metals Desorption from Synthesized and Natural Iron and Manganese Oxyhydroxides: Effect of Reductive Conditions. *J. Colloid Interface Sci.* **2000**, *227*, 531–539. [CrossRef]
51. Meng, Q.P.; Zhang, J.; Zhang, Z.; Wu, T. Influence of ore deposits on river sediment compositions in Dan River drainage, China. *J. Geochem. Explor.* **2015**, *159*, 8–19. [CrossRef]
52. Ding, Q.; Cheng, G.; Wang, Y.; Zhuang, D. Effects of natural factors on the spatial distribution of heavy metals in soils surrounding mining regions. *Sci. Total Environ.* **2017**, *578*, 577–585. [CrossRef]

Disclaimer/Publisher's Note: The statements, opinions and data contained in all publications are solely those of the individual author(s) and contributor(s) and not of MDPI and/or the editor(s). MDPI and/or the editor(s) disclaim responsibility for any injury to people or property resulting from any ideas, methods, instructions or products referred to in the content.

water

MDPI

Article

Changing Soil Water Content: Main Trigger of the Multi-Phase Mobilization and Transformation of Petroleum Pollution Components—Insights from the Batch Experiments

Mingxing Yang [1], Bing Wang [2,*], Yubo Xia [3], Yan Qiu [1], Chunling Li [1] and Zhendong Cao [4]

[1] School of Resource and Environment Engineering, Guizhou Institute of Technology, Guiyang 550003, China; yangmingxing@git.edu.cn (M.Y.); qiuyan@git.edu.cn (Y.Q.); lichunling@git.edu.cn (C.L.)
[2] Tianjin Geothermal Exploration and Development Design Institute, Tianjin 300250, China
[3] Tianjin Center (North China Center for Geoscience Innovation), China Geological Survey, Tianjin 300170, China; sosodragon@163.com
[4] No.111 Gecological Party, Guizhou Bureau of Geology and Mineral Exploration & Development, Guiyang 550081, China; caozd16@mails.jlu.edu.cn
* Correspondence: wangbingdry@126.com

Abstract: Soil moisture content continuously alters the types and forms of petroleum organic pollutants in the soil through processes such as dissolution, convection, and dilution, forming complex migration and transformation in a water–air–soil–NAPL system. Field investigations and traditional indoor simulation experiments have difficulty in terms of accurately diagnosing the state of different petroleum pollutants due to the influence of environmental factors and the difficulty of controlling single factors. Batch experiments were conducted to simulate the mobilization and differentiation processes of petroleum pollutants under the influence of soil water content. The results show that (1) the residual content of components is the lowest in coarse sand and the highest in clay, which is mainly affected by soil particles; meanwhile, the residual saturation value of octanoic acid is the largest, and that of toluene is the smallest, as determined in terms of their viscosity and volatility. (2) The infiltration processes of the components are affected by their properties and medium characteristics. Due to its small particle size and strong adsorption, clay has the highest residual saturation of petroleum pollutants (28.8%). This can even be more than twice that of coarse sand (13.3%). For different components, the residual saturations of octanoic acid and toluene are the highest and lowest, respectively (taking fine sand as an example: 25.3% and 13.2%), with a relatively large difference, as determined in terms of viscosity and solubility. (3) As the free phase can migrate freely, it is transformed most rapidly in the pores. The changes in the dissolved phase of each component are relatively small and tend to be gentle. The changes in the residual phase are mainly affected by volatility, viscosity, soil particles, and pore and cosmid content; the degree of change is ordered as follows: toluene > cyclohexane > hexadecane > octanoic acid.

Keywords: petroleum contamination; soil water content; NAPL multi-phase; residual saturation; batch experiments

1. Introduction

In oil spilling, extraction, refining, and transportation, the leakage of underground storage tanks and the rupture of oil pipelines will inevitably cause soil and groundwater contamination, posing serious environmental threats [1–4]. Petroleum organic components have become an important pollutant in groundwater systems, and various oil pollution incidents and their impacts on soil and groundwater have been reported worldwide [5–8]. Due to the carcinogenic and teratogenic nature of petroleum pollutants, they pose significant threats to human health and ecology [9–11]. Petroleum is a complex mixture composed of a variety of organic substances with very low solubility, usually existing in soil and

groundwater aquifers in the form of non-aqueous-phase liquids (NAPLs) [12,13]. When petroleum pollutants are discharged to the surface through various channels, they will continue to penetrate into the vadose zone and aquifers. The vadose zone is a key area where the atmosphere, surface water, and groundwater are connected and exchange water. It forms a complex system where rock and soil particles, water, and air coexist, which has the ability to absorb, retain, and transmit water, resulting in a changeable environment with complex hydrogeochemistry. More specifically, petroleum organic pollutants continuously migrate downward in the subsurface environment, undergoing various phase transitions such as volatilization, adsorption, degradation, and dissolution, forming a complex system with multiple phases and components [14–16]. Upon infiltration into the subsurface environment, organic pollutants in the NAPL phase migrate downward, with some being retained in soil pores through adsorption or capillary action—referred to as the residual phase [17–19]—while others continue to migrate in a fluid form under the influence of gravity—referred to as the free phase [20–22]. Additionally, NAPLs can also enter the air and water through volatilization and dissolution processes, forming gas and liquid phases (i.e., dissolved phase). Qi et al. showed that benzene was likely residual at the water–NAPL interface in fine-to-medium sand aquifers [23]. Mohamed et al. concluded that long-term mass removal for a glop of NAPL located close to an air channel was dependent on the aqueous diffusion of the dissolved phase towards the air–water interface, which, in turn, increases with the increase in the mean particle size of the contaminated soil [24]. Petri et al. conducted an experiment to show that the morphology of vadose-zone NAPL strongly controls mass transfer, with occluded NAPL sources emitting considerably lower mass flux than exposed NAPL sources [25]. In reality, influenced by the properties of the subsurface medium, biochemical conditions, and environmental factors, continuous transformations occur throughout the NAPL phase, gas phase, and liquid phase, as depicted in Figure 1 [26]. During the movement of groundwater, hydrodynamic dispersion and convection will cause free NAPLs to continue to migrate and, at the same time, cause NAPLs to continue to dissolve into groundwater, eventually forming a soluble plume hydrocarbon zone [27]. Podgorski et al. found that the upward flow of groundwater forms a dissolved pollution plume, and with the movement of groundwater and microorganisms, the pollutant components will shift low-molecular-weight (MW) aliphatic, reduced compounds to high-MW unsaturated (alicyclic/aromatic), which are high-oxygen compounds that are consistent with carboxyl-rich alicyclic molecules [28]. When there is a saturated lens of free NAPLs in a body of groundwater, it will rise or fall with the same trend as the phreatic surface of the groundwater, and some free NAPLs will migrate downward into the saturated zone, leading to contamination of the soil and groundwater [29].

During these processes, changes in water content caused by fluctuations in groundwater levels control the redistribution processes that affect petroleum components [30–32]. First of all, oil is a mixed liquid substance with high viscosity and low solubility. Although it is affected by gravity after leakage, its contact with soil particles generates a strong viscous force, thus blocking downward penetration [33–35]. Fluctuations in groundwater levels caused by rainfall can cause water to mix with components and change their viscosity. Therefore, changes in soil moisture content caused by rainfall leaching or large-scale intermittent irrigation are the main forces that cause pollutants to enter the underground environment, directly affecting the mobilization process of pollutants [36–38]. Moreover, due to the spatial differences in soil mediums in the vadose zone, different pore sizes, soil compositions, and initial water contents will lead to differences in the rate, content, and transformation of pollutants during mobilization and will ultimately affect their distribution and complicate the mobilization of pollutant components [39–41].

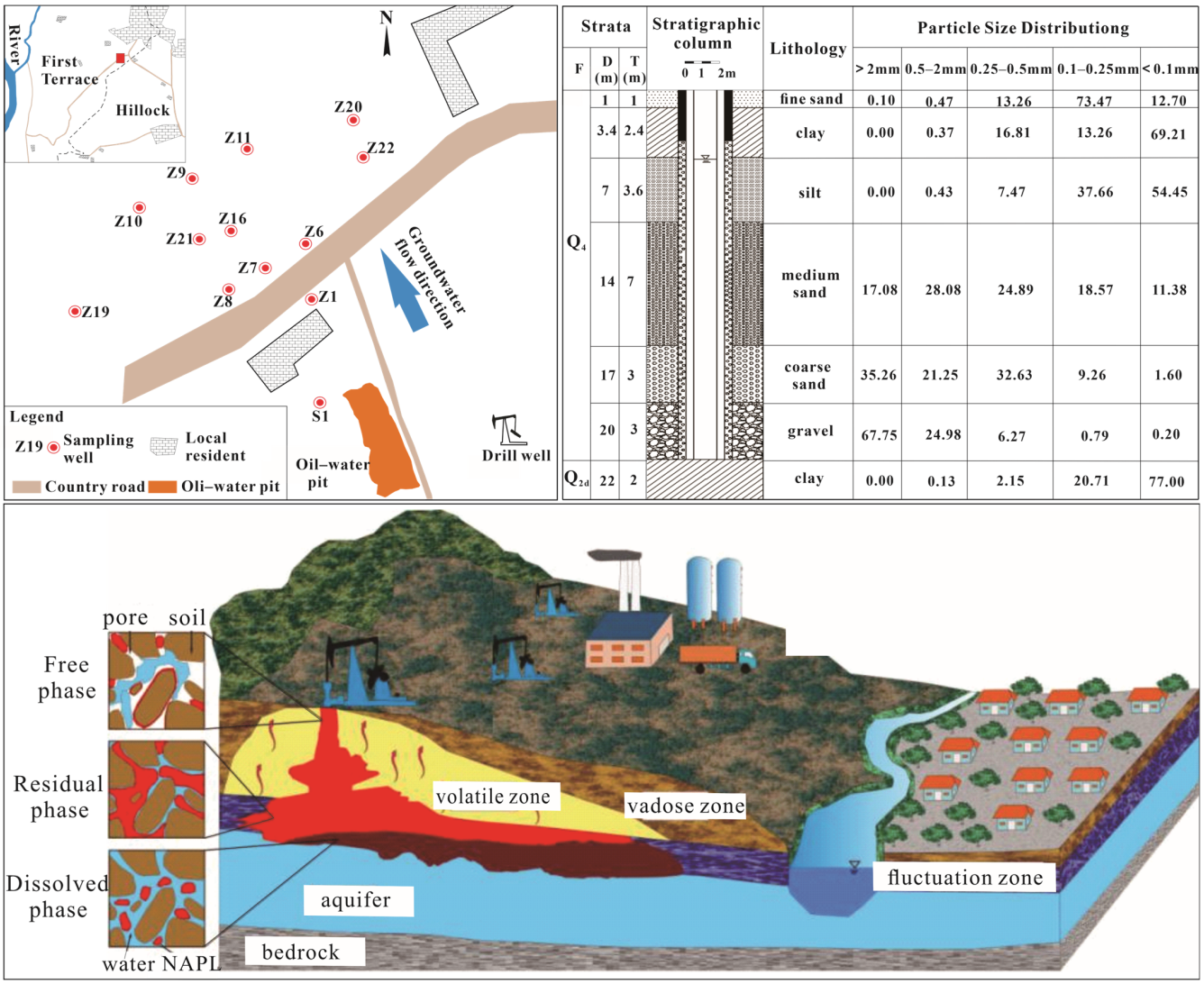

Figure 1. Conceptual model of the transportation of NAPL pollutants in the groundwater and soil system based on the contaminated site and stratigraphic column [26].

In summary, the changing patterns of NAPL substances in relation to fluctuations in groundwater levels determine the content and type of pollutants entering the groundwater [42–44]. This is also a key component of a final pollution risk assessment and the formulation of corresponding remediation plans. For example, An et al. showed that sandy soil contaminated with a higher petroleum concentration showed markedly higher potential risk than sandy loam in relation to frequently fluctuating groundwater levels [40]. The importance of groundwater resources, the hazards posed by oil pollutants, the complexity of changes in organic components, physical–chemical–biological reaction systems, and the mutual transformation systems between substances during water level fluctuation processes that affect pollution components are important prerequisites for remediating groundwater oil pollution reasonably, efficiently, and economically. For example, Teramoto et al. showed that mass transfer is governed by both LNAPL saturation and seasonal water table fluctuations within the LNAPL smear zone [45]. Zhao et al. pointed out that the capillary fringe boundary (the interface between an aquifer and an unsaturated water zone), due to its constantly changing moisture content, is a major zone involved in the transport and transformation of contaminants [46]. Sakr et al. emphasized that before selecting PRB technology to remediate BTEX contamination, it is important to determine the migration trend of the groundwater contaminants at the site [47]. However, existing

studies still lack details on the mobilization differences between different types and phases of petroleum pollutants due to the impacts of changing soil water content. Traditional research methods are based on actual field measurements or indoor simulation experiments, which can simulate and reflect real pollution in an environment. However, field conditions are very complex and the mobilization and transformation processes between different components are difficult to analyze individually due to their different characteristics; therefore, it is especially difficult to accurately study and evaluate the influence of a single factor [48–50]. Batch experiments are a commonly used experimental method when conducting small-scale experimental studies. They usually involve processing multiple samples or test conditions simultaneously in a relatively short period of time in order to obtain more data and compare the obtained results. Batch experiments can better control experimental conditions, reduce interference factors, and provide important information about reaction kinetics, material transformation processes, biological activities, and so on; therefore, they are widely used in fields such as chemistry, biology, and environmental sciences [51–53].

Based on a detailed investigation (pollution sources, pollutant types, pollutant migration, soil media, groundwater level fluctuations, and moisture content variation characteristics) of a site in northeast China that has experienced long-term pollution due to petroleum leakage, and combined with the need to address the bottleneck arising from the unclear role of soil moisture content on the complex migration and transformation system of petroleum organic pollutants and analyze the challenges that face field investigations and traditional indoor simulation experiments (such as numerous environmental influencing factors and difficulty in controlling single factors), this study innovatively employed batch experiments to simulate the mobilization and differentiation processes of multi-phase pollutants in an underground environment under the influence of these factors. The main aims of this study are as follows: (1) to determine the influencing mechanisms of different soil water contents on the mobilization and differentiation of pollution components; (2) to obtain the residual saturation of different pollution components in different soil media and discuss the change processes; and (3) to elucidate the relationship between the changes in the saturation of water, oil, and gas in soil pores. This study provides a theoretical basis for the design of reasonable and efficient restoration plans; therefore, it has very important practical significance and scientific value.

2. Materials and Methods

2.1. Experimental Pollutants and Media

This study was carried out based on an actual site investigation of a petroleum-contaminated area in an oil field in northeast China. An oily water pit located at a higher elevation was identified as a significant source of contamination at the site under investigation. Site assessments revealed that the shallow aquifer consisted of fine-to-coarse sands/gravels with a thickness of 15–20 m, overlaying Pleistocene silty clay acting as an aquitard in the area. The groundwater level was observed to be 2.0–4.0 m below the ground surface, with fluctuations of up to 0.5 m annually. The flow direction of the groundwater was predominantly from southeast to northwest. The spillage of various petroleum hydrocarbons (PHCs) from this pit resulted in severe pollution of both soil and groundwater (Figure 1). In order to better simulate the actual pollution situation, soil samples from different depths of the oil field pollution site were collected for this experiment. More specifically, in order to obtain uncontaminated original soils corresponding to the stratigraphic column at the site, we collected soil from a natural profile adjacent to the site layer by layer and then sieved and processed these soils in the laboratory to obtain clay and fine, medium, and coarse sand from the respective layers for the batch experiment. When investigating the contaminated groundwater and soil sites in the oil field, it was found that the lithology of the vadose zone was mainly composed of coarse, medium, and fine sand and clay. Therefore, these soils were used as the experimental media; their particle size distribution and main properties are shown in Figure 2 and Table 1. The petroleum

components in the groundwater at the site mainly included alkanes, cycloalkanes, aromatic hydrocarbons, and some non-hydrocarbon substances. Based on the differences in their functional groups, hexadecane, cyclohexane, toluene, and octanoic acid were utilized as representatives. Their properties are shown in Figure 3 and Table 2 [54].

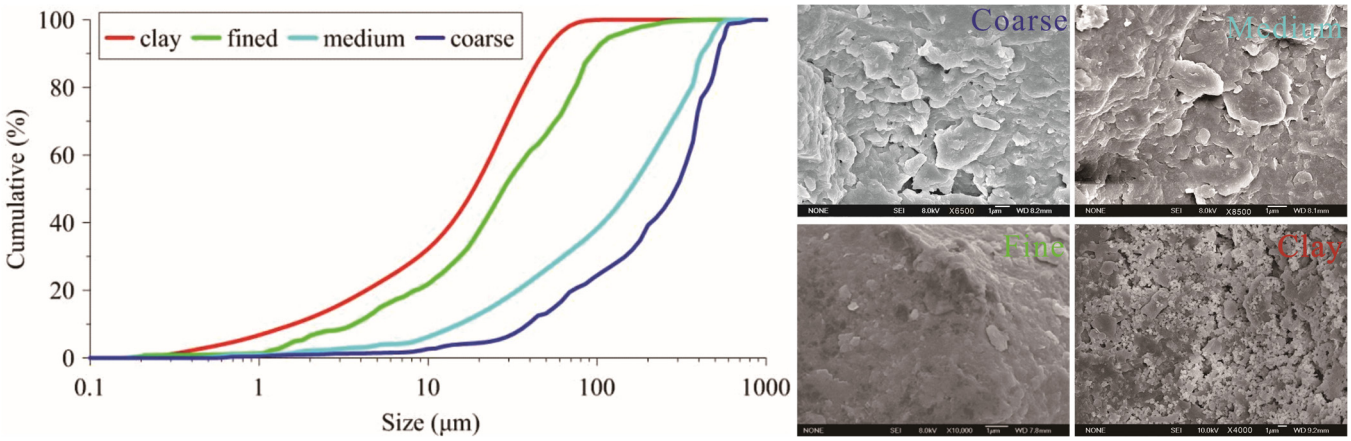

Figure 2. Grain size distribution and SEM (scanning electron microscope) images of the experimental soil media [26].

Table 1. Characteristics of the soil media at the actual oil-contaminated site.

Media Type	Coarse Sand	Medium Sand	Fine Sand	Clay
Packing density (g/cm^3)	1.83	1.72	1.63	1.52
Porosity (%)	30.9	35.2	38.6	42.7
Specific surface area (m^2/kg)	58.8	126.4	231.8	449.6
Organic matter content (%)	1.5	2.2	3.6	3.8
Mean diameter (μm)	653.55	281.21	129.32	45.53

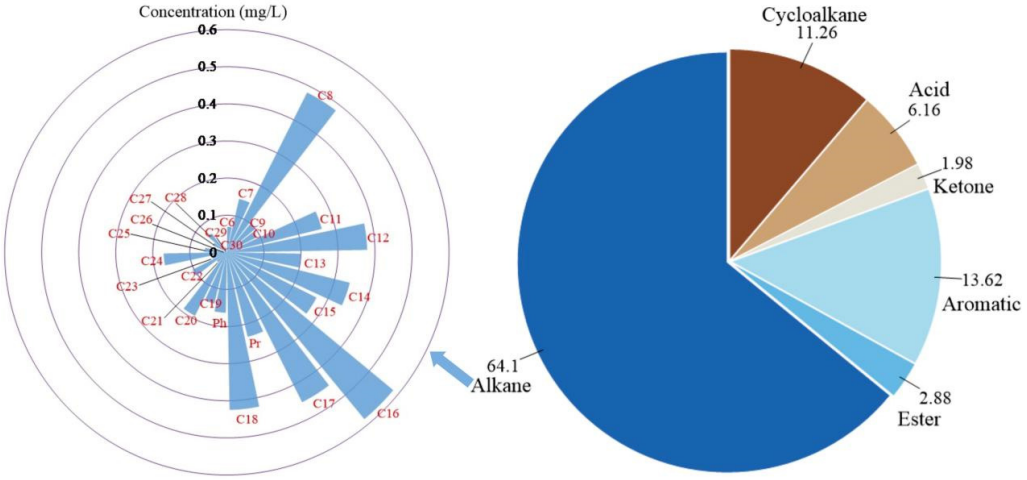

Figure 3. Types of organic matter and average n-alkane concentration in groundwater at the actual oil-contaminated site.

Table 2. Properties of the petroleum compounds at the actual oil-contaminated site.

	MW (g/mol)	FG	A (cm^{-1})	S (mg/L)	ρ (g/cm^3)	BP (°C)	η (mPa·s)	H (cm^3/cm^3)	log K_{ow}	K_{oc} (cm^3/g)	Dair (cm^2/s)	Dwater (cm^2/s)
Hexadecane	226.4	-(CH_2)n-	2960	26	0.773	287	3.34	1.6×10^2	8.24	8.47×10^6	0.037	4.2×10^{-6}
Cyclohexane	84.2		1450	55	0.779	80.7	0.98	7.8×10^0	3.44	9.63×10^2	0.084	9.1×10^{-6}
Toluene	92.1		748	515	0.866	110.6	0.59	2.7×10^{-1}	2.69	2.34×10^2	0.087	8.6×10^{-6}
Octanoic acid	144.2	-COOH	1244	680	0.911	239.7	5.83	5.0×10^2	3.05	1.10×10^4	0.023	3.6×10^{-6}

MW = molar mass; S = solubility; ρ = density; BP = vapor pressure; η = viscosity; H = Henry's constant; K_{ow} = partition coefficient of n-octanoic alcohol; K_{oc} = partition coefficient of organic carbon; Dair = dispersion coefficient in gas; Dwater = dispersion coefficient in water; FG = characteristic functional group; A = absorption wave number.

2.2. Experimental Devices and Processes

2.2.1. Experimental Aims

Two batch experiments were designed to simulate the multi-phase flow of different petroleum organic pollutants in soil and groundwater under the influence of different soil water content factors, as well as the mobilization and mutual transformation processes between different phases. Batch experiment 1 (i.e., the experiment on changes in mobilization morphological characteristics of pollution components) was conducted to obtain the residual saturation of different pollution components in different soil media in order to explore the change processes of pollution components under different water content conditions and to study the relationship between the saturation changes of water, oil, and gas in soil pores. Batch experiment 2 (i.e., the experiment on the influence of different water contents on changes in pollution components) was conducted based on batch experiment 1 (using the same experimental device, experimental materials, and pollution components), observing the changes in moisture content, the diffusion pattern of the tracer dyeing area, and the change process of gas phase saturation with the aim of exploring the changing mobilization characteristics of different components under different water contents and studying the influencing mechanisms of water content on the morphological changes of three NAPL phases. The batch experiments emphasized the highly consistent initial conditions, but differences in pollutant distribution, soil filling, and moisture content control may lead to variations in terms of the experimental conditions, ultimately affecting the precision of the experiments. To address this, the experiments were conducted in small batches, and the total number of batch experiments was divided into several sessions. With a smaller experiment volume, there is relatively sufficient operation time, which can help avoid many errors that may occur during batch experiments.

2.2.2. Experimental Devices and Steps

Batch experiment 1: A diagram of the experimental device is shown in Figure 4. The specific steps used are as follows: (1) First, fill the soil medium. A glass tube with an inner diameter of 4 cm and a length of 12 cm was filled with soil medium in order to simulate the soil conditions in the vadose zone. The upper and lower ports of the experimental device were blocked with rubber plugs and wrapped with gauze to prevent the loss of soil medium particles. The soil was filled layer by layer and tamped down continuously to ensure uniform filling. In addition, before filling the soil, we calculated the total weight of soil required based on the soil density measured in the field and the dimensions of the experimental setup. Then, we filled each layer uniformly according to the corresponding filling height per volume, ensuring that the filling density matched that of natural soil. (2) Water was injected into the tube from the bottom to the top, which was stopped when a stable liquid level appeared on the upper surface of the soil. The volume of water entering was measured to calculate the porosity of the soil. In this process, a TRIME PICO-32 (Germany IMKO; this instrument was linked to the computer via a probe. It automatically

reads soil moisture content; it has a data monitoring frequency of 2 min) meter was used to measure the water content of the soil. (3) After achieving water saturation, a syringe was used to continuously inject the petroleum component, dyed with Sudan IV (mass ratio 1:10,000), into the upper port of the tube. (4) In order to allow the components to fill the entire soil layer to achieve saturation, drainage was performed from the lower port after water saturation. Therefore, when the water in the soil pores was drained, the components also seeped downward into the pores. (5) When the entire soil column was filled with red-stained contaminating components, it was considered that the NAPL in the pores had reached saturation (refer to Stafford's method) [55]. (6) Then, water was injected from the lower port of the soil column, the upper port was opened, and the NAPL filled with pores was discharged from the upper port; here, the remaining NAPL that was not discharged formed a residual phase. (7) In terms of water injection and the discharge of NAPL, when the measured moisture content value had almost no change, a balance between the phases was reached. At this time, the components in the soil formed a residual phase and were difficult to discharge. During the experiment, the moisture content instrument continuously sampled the tube to measure the moisture content, and the discharged liquid was collected. Then, GC-MS, infrared spectrophotometer, and liquid viscometer instruments were utilized to measure the type and content of organic matter, functional group composition, and viscosity of the discharged liquid, respectively.

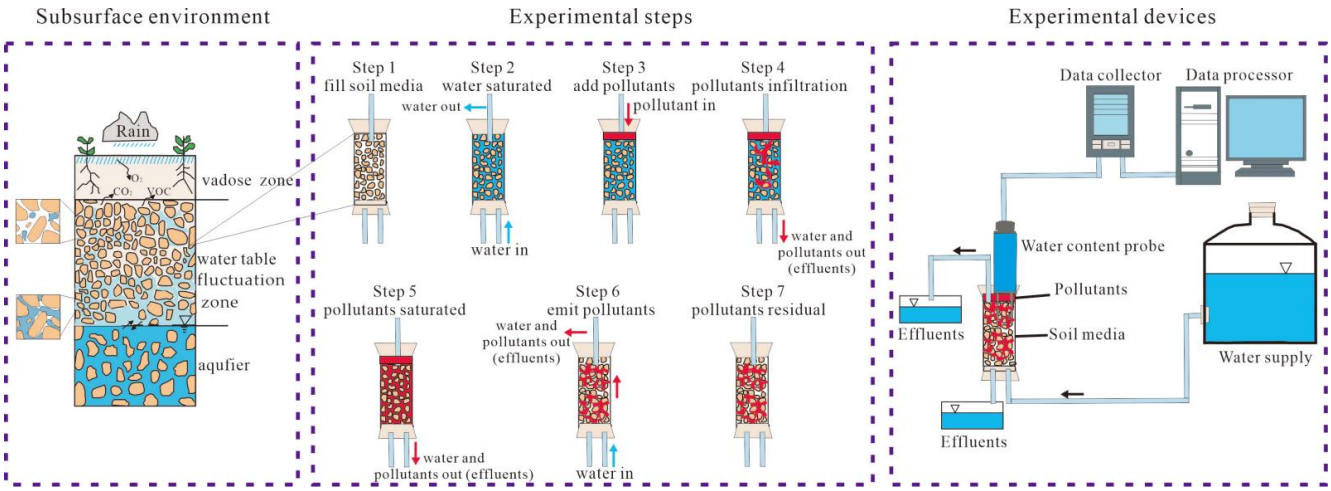

Figure 4. Residual phase saturation experimental device (batch experiment 1).

Batch experiment 2: The change processes of different petroleum pollution components in soil and groundwater can be summarized into the gas phase formed via volatilization, the dissolved and free phases of the liquid phase, and the residual phase confined to soil pores and adsorbed by soil particles. These three types coexist in soil pores, transforming and influencing each other. When the soil moisture content changes, the mobilization patterns of the components of NAPL pollution will also change accordingly. The multiphase mobilization process was also studied based on $S_i = V_i/V_{pore} = \theta_i/n$ (where i indexes water, NAPL, and air) and $S_{water} + S_{NAPL} + S_{air} = 1$. $S_{water} = \theta_{water}/n$, $S_{air} = S_{air\text{-}initial}(P_{measured}/P_{initial})$, $S_{air\text{-}initial}$ and $P_{initial}$ are the gas saturation and pressure at the initial moment, respectively; $P_{measured}$ is the gas pressure measured during the experiment. The saturation relationship at the initial moment is $S_{air\text{-}initial} = 1 - S_{water\text{-}initial}$. According to the pore properties of different media, four moisture content conditions of 25%, 20%, 10%, and 5% were set for comparison when different soil moisture contents were simulated in the experiment. During the soil media filling process, the specific steps involved (1) evenly mixing a certain weight of soil and water, according to the required moisture content ratio, and (2) then adding it layer by layer while continuously tamping it to ensure the uniformity of filling (Figure 5). (3) After filling, a syringe was used to inject 15 mL of the petroleum component (with Sudan IV) into the upper port of the glass tube. (4) The dyed

contamination components located on the surface began to slowly penetrate the soil pores due to gravity. However, due to the different moisture contents in the soil and different properties of the medium, there were obvious differences in the infiltration process. In order to reflect these differences, the soil moisture content and gas pressure were monitored in real time during the infiltration process, and the corresponding saturation was calculated to explore the change patterns of the three phases. (5) When the measured soil moisture content reached equilibrium, it was considered that the mutual transformation between the three phases reached equilibrium, and the experiment was stopped. (6) In addition, in order to obtain the change pattern relating to the concentration of the components in the three phases, a parallel experiment method was used; that is, four sets of experiments were set up under the same conditions. When the mobilization reached a certain time, the samples were taken out and the component concentrations were measured. The time series for hexadecane and octanoic acid were 0.5, 1.5, 2.5, and 3.5 h, while the time series for toluene and cyclohexane were 0.5, 1, 1.5, and 2 h.

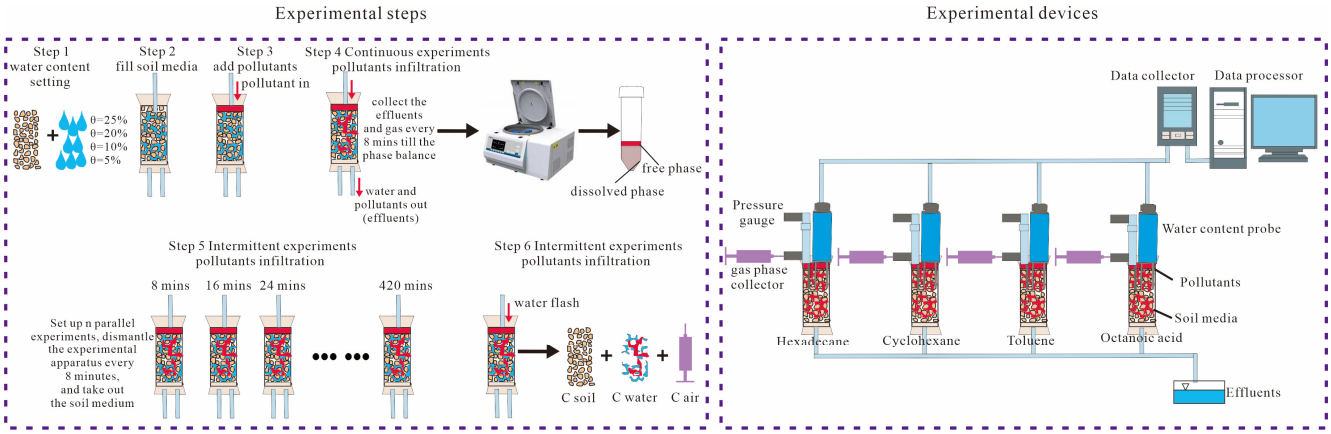

Figure 5. Diagram of the experimental design and device for the assessment of the effects of different moisture contents on component mobilization.

2.3. Sample Analysis

In the experiment, GC-MS (Agilent, 6890N-5975, Santa Clara, CA, USA) was used to qualitatively and quantitatively test the organic components, including petroleum organic components in water and soil. Organic components in the water were sampled and dichloromethane was added for liquid–liquid extraction. After extracting the organic components from the water sample, a sampling rotary evaporator was used for a concentration of 1 mL, and the resulting sample was then subjected to GC-MS for measurement. The organic components in the soil were measured using a Soxhlet drawer instrument. After the separation treatment, a rotary evaporation instrument was also used for a concentration of 1 mL, followed by measurement with GC-MS. The specific GC-MS measurement process and conditions are as follows: During the test process, the gas sample was collected using a 15 mL Agilent vial. The injection needle was inserted to take 10 μL for measurement. The GC-MS test conditions were as follows: (1) Concerning the chromatographic conditions, a capillary chromatography column (30 m × 0.25 mm × 0.25 μm) was used, and the gas chromatography inlet temperature was 250 °C; split injection was performed with a split ratio of 10:1; high-purity helium was used as the carrier gas with a purity of 99.999% in a constant-flow mode with a column flow of 10 mL/min. Regarding the programmed temperature rise, the initial column oven temperature was 35 °C, which was maintained for 3 min and then increased in 10 °C/min increments to 150 °C and held for 2 min before finally being increased to 200 °C at 20 °C/min and held for 2 min. (2) The conditions used for mass spectrometry are as follows: An electron multiplier voltage of 2108 eV was used with a GC-MS interface temperature of 250 °C and an ion source temperature of 230 °C in a quadrupole configuration. The rod temperature was 150 °C and the electron energy was

70 eV. The full scan mass range was 50–400 m/z. (3) Purge and trap: The OI4560 instrument was used (HP), and the purge time of the purge and trap concentrator was 11 min, the temperature was 34 °C, the desorption time was 2 min, the desorption temperature was 180 °C, the baking time was 10 min, and the baking temperature was 200 °C. The purge gas was high-purity nitrogen with a purity of 99.999% at a purge flow of 40 mL/min, with Tenax used as the adsorbent. The quantitative method used for this measurement adopted the internal standard method; that is, a solution of known concentration was prepared in advance and, after being subjected to GC-MS, a standard curve of concentration and peak area was developed. Then, the peak area of the test sample was compared with the standard curve for quantification. The functional group characteristics of the organic components in the soil and water were measured using a Shimadzu Fourier transform infrared spectrophotometer (Shimadzu, IRPrestige-21, Tokyo, Japan); the specific steps were to take a 5 mL liquid sample for measurement. The soil sample was extracted using the Soxhlet extraction method, using methylene chloride to extract the organic components from the soil for measurement. The moisture content in the soil was measured in real time using a moisture content meter (IMKO, TRIME-PICO32, Ettlingen, Germany). At the same time, a laser particle size distribution analyzer (Better, BT-9300H, Dandong, China), a viscometer (Brookfield, DV-I, Middleboro, MA, USA), and a specific surface meter (Builder, SSA-4000, Beijing, China) were used to measure the size of the soil particles, clay content, liquid viscosity, and specific surface area of the soil. The experimental materials used in this experiment included hexadecane, cyclohexane, toluene, octanoic acid, methylene chloride, carbon tetrachloride (all chromatographically pure), and Sudan IV stain.

2.4. Saturation of Multi-Phase Pollutants

The transport and transformation of pollutants in the underground environment can be attributed to the interactions resulting from different substances in the soil pore space. Underground soil pores contain three types of substances—water, organic pollutants (NAPLs), and air—which together fill the entire pore space. According to the ratio of the soil pore space they occupy to the entire soil pore volume, their saturation in the underground environment can be described; that is, when the soil pores are filled with two or more immiscible fluids (liquid or gas), the saturation Si of a certain phase fluid (i) at a certain point is defined as the characteristic unit around that point in terms of the ratio of the volume of fluid (V_i) occupied by the volume of soil pores (V_{pores}). In particular, $S_i = V_i/V_{pores} = \theta_i/n$, where i indicates water, NAPL, and air (where the sum of the three is 1; that is, $S_{water} + S_{NAPL} + S_{air} = 1$); θ_i represents the moisture content; and n represents the porosity. Therefore, to calculate the residual phase saturation of NAPLs, it is necessary to obtain the saturation of water and air. Based on this principle, the soil column was first completely filled with NAPL to form residual saturation, after which water was injected to discharge the free NAPL while ensuring that the entire pore only contained water and NAPL; that is, there was no gas in the pore ($S_{air} = 0$). Then, $S_{NAPL} = 1 - S_{water}$, and $S_{water} = \theta_{water}/n$ (where θ_{water} represents the moisture content). After measuring the moisture content with a moisture content meter, the residual saturation of the component in the soil medium can be calculated. In addition, during the experiment, the interconversion mechanism between the three phases was also studied based on the relationship between moisture content and changes in component concentration.

3. Results and Discussions

3.1. Analysis of Mobilization Morphology Characteristics of Pollution Components

3.1.1. Component Mobilization Morphology Formation Process

The mobilization of pollution components requires power and space. Water is the main carrier of pollution components. Its content in the pores seriously affects the mobilization and fate of components; meanwhile, the interaction between the viscosity of components and soil particles is another major factor. In the experiments, a soil moisture content meter was used to monitor the change processes relating to the moisture content in the soil column

in real time for 2 min each time, and the concentration, viscosity, and functional groups of the liquid during the discharge of NAPL were analyzed. The results are shown in Figure 6.

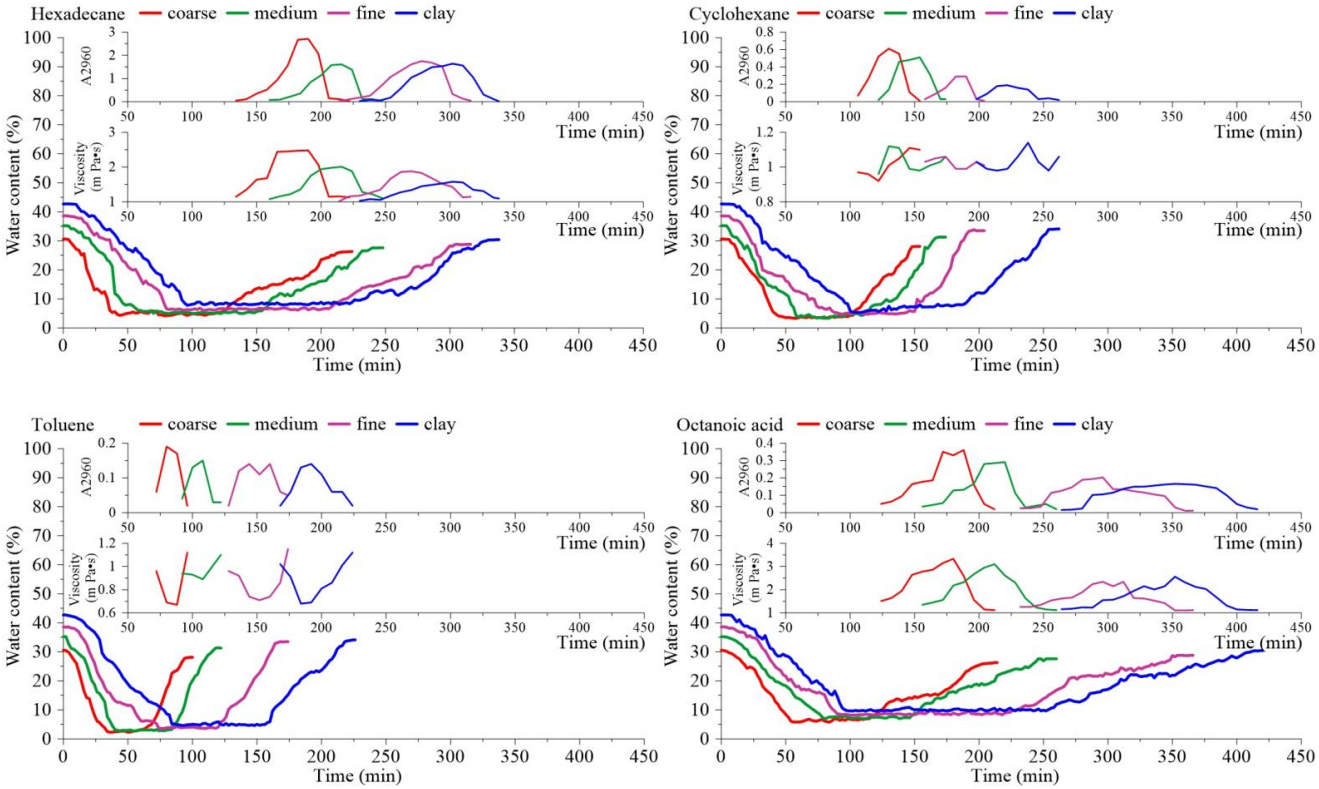

Figure 6. Moisture content and physical and chemical parameters of the outflow liquid when discharging NAPL.

As can be seen in Figure 6, the moisture content mainly presented three stages—decreasing, balancing, and increasing—which correspond to the infiltration, saturation, and discharge of NAPL in the soil, respectively, indicating that changes in moisture content are closely related to component concentrations and soil properties, and there are differences between different components and different media. First, this is due to the large differences in pore size, soil particle size, and adsorption performance in different media. The particle size of coarse sand is larger, with an average particle size (d50) of 653.55 μm. During the drainage stage, the time for the moisture content to reach equilibrium is the shortest (average 173 min), while, in clay (d50 is 45.53 μm), the time was the longest (average 312 min)—about 1.8 times that of coarse sand. In the NAPL saturation stage, due to the different clay particles contained in the medium, the adsorption capacity for components also differed. The clay content in coarse sand was only 1.01%, and the components moved faster in it; thus, it took the shortest time to fill the entire soil column. Meanwhile, when the clay content was 11.82%, it had the strongest ability to block the components. In addition, the differences between components are also obvious. The viscosity of hexadecane is relatively high (3.34 mPa·s), but its solubility is extremely low, and it is difficult to volatilize. Therefore, water is mainly displaced slowly during the mobilization process, and it takes a long time for the moisture content to reach equilibrium—about 338 min. The change process relating to moisture content for octanoic acid (viscosity 5.83 mPa·s) is similar to that of hexadecane, and the time required to reach equilibrium is 420 min. The viscosity of naphthenic hydrocarbon is 0.98 mPa·s, which is close to that of water. Therefore, it was less hindered during the infiltration process, and the time to reach final equilibrium was faster—about 262 min. Relatively speaking, toluene has the lowest viscosity, the strongest volatility, and the highest solubility; therefore, it mainly tends towards the water and gas phases and its residence time in the soil was the

shortest—about 226 min. The moisture content in the soil after finally reaching equilibrium can be calculated as S residual = (n − θw)/n (where S residual represents the soil residual saturation, n represents soil porosity, and θw represents the final soil column moisture content). The residual phase saturation values of each component in different media are provided in Table 3.

Table 3. Residual phase saturation values (%) of different components in different media.

Residual Saturation (%)	Hexadecane	Cyclohexane	Toluene	Octanoic Acid
Coarse sand	13.3	10.6	8.2	14.2
Medium sand	16.2	15.2	11.1	21.8
Fine sand	21.6	18.8	13.2	25.3
Clay	28.1	24.2	20.1	28.8

It can be seen in Table 3 that the residual phase of the components was the lowest in coarse sand and the highest in clay, which is mainly related to soil particles, porosity, clay content, and other factors; meanwhile, the residual saturation value of octanoic acid was the largest and that of toluene was the smallest, as determined in terms of viscosity and solubility.

3.1.2. Hysteresis Effect Analysis

When the NAPL in the soil column became residually saturated, water was injected from the bottom to the top to discharge the NAPL, and the viscosity and infrared functional group absorbance values of the discharged liquid were measured at the same time. The results indicate that the change in moisture content is caused by the mutual displacement between water and NAPL. However, this displacement did not occur instantaneously. Instead, the obviously dyed NAPL flowed out after water was injected for a period of time. This phenomenon is called the material hysteresis effect of inter-transportation. Observing the material properties revealed that the main cause of hysteresis was the difference in viscosity between the components. Taking the mobilization of hexadecane in coarse sand as an example, in the initial stage, the change in the moisture content was low, with a rate of about 0.09%/min (increasing from 9.5% to 12.2% in 30 min), but the viscosity changed drastically during this time—increasing from 1.15 mPa·s to 2.44 mPa·s in 30 min. This result demonstrates that the water in the outflow liquid decreased while NAPL increased. The water mixed with NAPL, thus changing the viscosity of the components. The rate in the middle section increased to 0.26%/min (from 12.7% to 25.8% in 50 min), but the viscosity remained at a stable level with little change, showing that the oil–water mixture tended to become stable at this time, and NAPL entered the water from the residual phase and floated on the surface of the water. When NAPL was discharged in large quantities in the later period, the outflowing liquid was mainly water, with its viscosity tending towards 1 mPa·s. In addition, the infrared absorption wavelengths of different components corresponding to the characteristic functional groups showed a trend of first increasing and then decreasing, further indicating that water displaced the residual NAPL trapped in the pores and then carried it out of the soil column.

3.2. Mobilization Characteristics of Each Component

In the experiment, a digital camera was used to record the mobilization of the dyeing components, and image processing software was used to extract the RGB values in the picture, allowing for a comparison of the dyed area (Figure 7) in order to clarify the change rules relating to the pollution halo. Figure 7 shows that the processes relating to oil components infiltrating from surface leakage through the vadose zone into groundwater can be summarized into three stages: (1) Free-phase infiltration—a large amount of pollutants leak due to gravity and dispersion. As a result, components migrate to the lower layers and continuously fill the pores. At the same time, free components continue to come into contact with water and soil and begin to displace water in the pores, causing the

moisture content to change greatly (Figure 6). (2) The formation of residual phases—during the mobilization of a large number of free components, as soil particles contain a large number of clay particles that can adsorb components, the components are retained on the surfaces of these clay particles. In addition, there are dead-end pores in the pores and, when components enter these, they are difficult to discharge. This part of the component is not easily soluble in water, has difficulty moving freely, and will exist in the soil pores for a long time. (3) A continuous but slow dissolution process—due to constant contact with water, the component is continuously dissolved in the water. As shown in the figure, it can be seen that the red color in the middle area gradually fades; however, as the solubility is low and it is in a flowing phase, this change occurs relatively slowly.

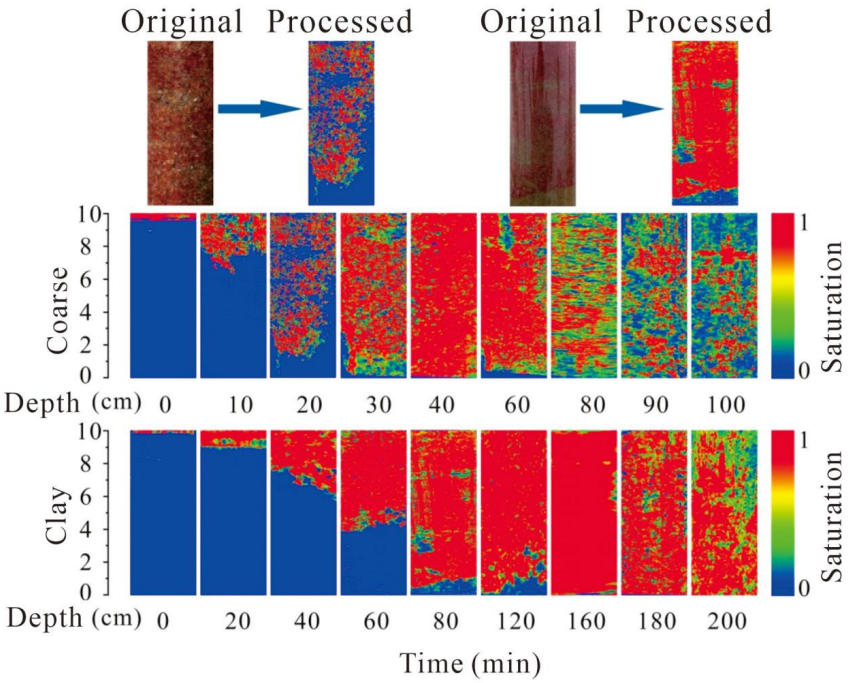

Figure 7. Changes in toluene pollution areas in different media.

There were obvious differences in the infiltration processes relating to organic components in different media. When NAPL was injected in the case of coarse sand, it was found that NAPL quickly penetrated into the soil; however, its red color did not appear as a whole but, instead, as sparse red spots. This is because the coarse sand particles are large and the pores formed are wide. When NAPL migrates, it first enters along the large pores and then spreads to the entire soil column. The most obvious is toluene, which had the fastest diffusion rate and filled the entire soil column within 30 min (Figure 7). This is mainly because toluene has strong volatility and its viscosity is much lower than that of the other components, so its transportation occurs faster. This infiltration method can be summarized as a convective influx, which quickly spreads along the large pores; however, the process differs in clay. When NAPL is injected into the clay, it remains on the surface for a long time, resulting in fewer red contaminated areas in the soil. After about 30 min, the overall penetration of the red area was only 1.0 cm. This indicates that the penetration of NAPL into clay is very slow and difficult to detect. Therefore, the mobilization characteristics of this NAPL in low-permeability media can be summarized as slow infiltration as a whole and gradual dispersion among soil particle sizes. NAPL enters the pores and displaces water. At the same time, it continuously interacts with water and soil, causing the three forms to continuously transform into each other.

3.3. Different Transformation Processes

As petroleum components mainly exist in three forms when migrating in pores, in order to grasp the component concentration distribution, the content and type of the three forms must first be clarified. During the experiment, the discharged liquid was continuously collected, taking a sample every 8 min, which was put into a 10 mL centrifuge tube and centrifuged for 3 min at 10,000 rpm in a Sigma3-18K high-speed centrifuge. As the density of the component is less than that of water, free components will remain in the upper layer in an undissolved free phase; meanwhile, the stained component in the lower layer will be in a dissolved phase. GC-MS scanning analysis was performed on the two forms of samples, where the liquid in the lower layer was the dissolved phase concentration, and the upper layer was the free phase concentration. The components in the soil are in a residual phase. The relationships between the three-phase concentration changes with time are shown in Figure 8.

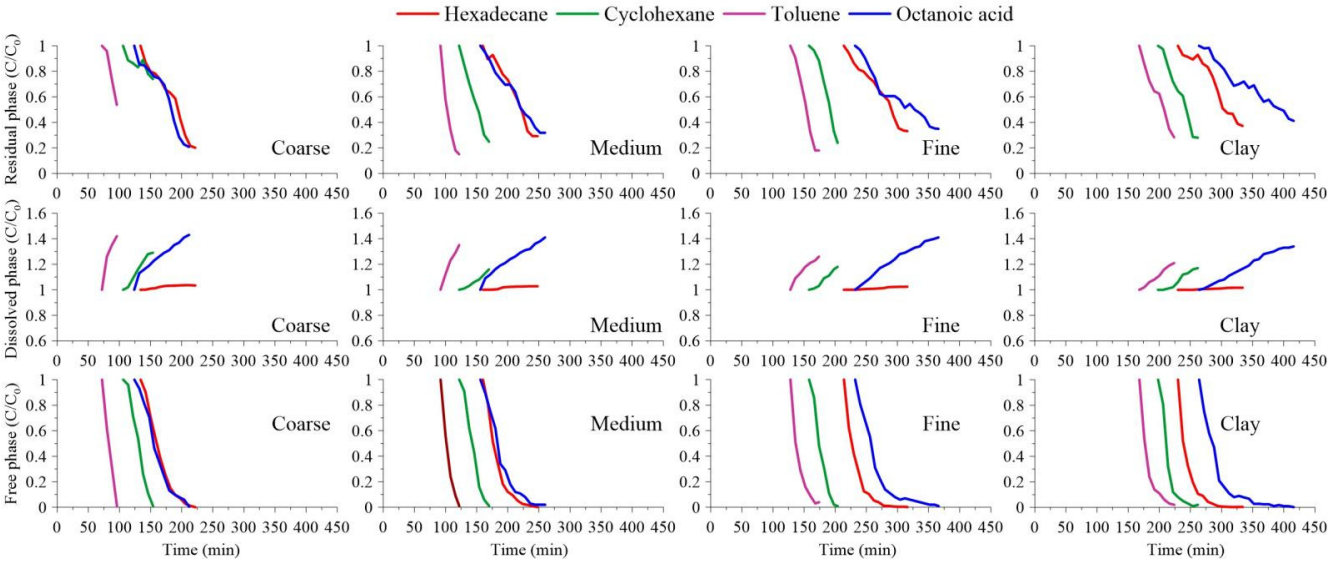

Figure 8. Changes in the concentrations of the three pollutant species over time.

It can be seen in Figure 8 that the largest change among the three phases was presented by the free phase, and the free phases of the four components in different media almost all showed a rapidly decreasing trend. This is mainly due to the fact that during the water injection and NAPL drainage process, the freely moving components in the soil column are continuously washed out; however, with time, the content of the free phase decreases, and the discharged concentration also decreases. The concentration comparison of the dissolved phase curve tends to be flat, the change amplitude is relatively small, and the dissolved phase of hexadecane presents almost no change. This is mainly determined by the solubility of the components; the changes in the residual phase mainly reflect the differences between the components. Among them, the change in the residual phase of toluene was the largest. This is because toluene is highly volatile and has a relatively low viscosity. In the soil column, internal mobilization is less hindered; thus, most of it is expelled and the residual phase changes greatly. The residual phases of the other three components also decreased with time but were significantly slower than toluene.

3.4. Effect of Soil Moisture Content on the Mobilization and Distribution of Pollution Components

3.4.1. Mobilization Characteristic Analysis

During the experiment, a high-definition digital camera was used to record the mobilization process of the dyed pollutants, and image processing software was used to analyze the changes in the red area in the images, allowing for comparison and determination of the

mobilization rules relating to the pollutant components. The obtained results are provided in Figure 9.

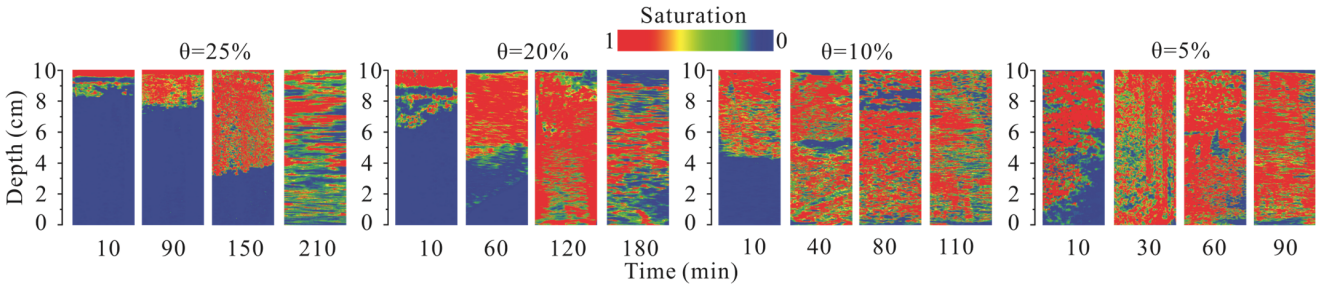

Figure 9. Change map of hexadecane pollution area in medium sand column under different soil water content conditions.

As can be seen in Figure 9, the differences in mobilization under different moisture contents are relatively obvious, which is consistent with the previous mechanism analysis. After entering the soil, the pollutant components continue to displace water and are gradually distributed to different locations. Therefore, the moisture content in the soil controls the mobilization of pollutant components. As the pollutant components are all substances with densities lower than that of water, with a high water content, the NAPLs mainly tend to float in the water, making penetration difficult. From the figure, the change observed when the moisture content is 25% illustrates this mechanism well. The red contaminated area was mainly concentrated on the surface of the soil for a long time (about 1.5 h), then began to slowly expand under the action of gravity, penetrating deep into the soil. Even at about 150 min, the entire soil column was not completely filled. On the contrary, the red area in the low-moisture-content experiment almost filled the soil column within 10 min.

In addition, when the contaminated components fill the soil column, the red-stained area will decline to varying degrees. The decline that occurs with a low moisture content is less obvious, while the decline observed with a high moisture content is more obvious. This is due to the fact that when the moisture content is low, the mixing of the two after injection of NAPLs is poor and, so, the ability of NAPL to flow with water is weak, resulting in a large amount of residue in the soil. Meanwhile, when NAPL is in an environment with a high moisture content, it is constantly mixed with water and migrates to the lower layer, eventually causing a large amount of NAPL in the soil column to be discharged, while the remaining part is relatively small.

Therefore, pollution components in underground environments tend to be stored in areas that have a low moisture content. This also explains why the pollution concentration in the water-saturated zone of actual contaminated sites is often smaller, while the vadose zone is where the main pollution components accumulate. Therefore, in actual remediation processes, more emphasis should be placed on considering the contaminated components in the soil.

3.4.2. Differences in Component Mobilization under Different Moisture Content Conditions

When components of pollutants migrate into an underground environment, they are mainly affected by environmental media, such as soil, moisture, and gases. Therefore, the properties of the environmental medium determine the mobilization process and final fate of the components. As the most active medium, water plays a key role in the interactions between substances. Therefore, the relationship between the saturation of different forms with time was measured and calculated in the experiment, and the results are shown in Figure 10.

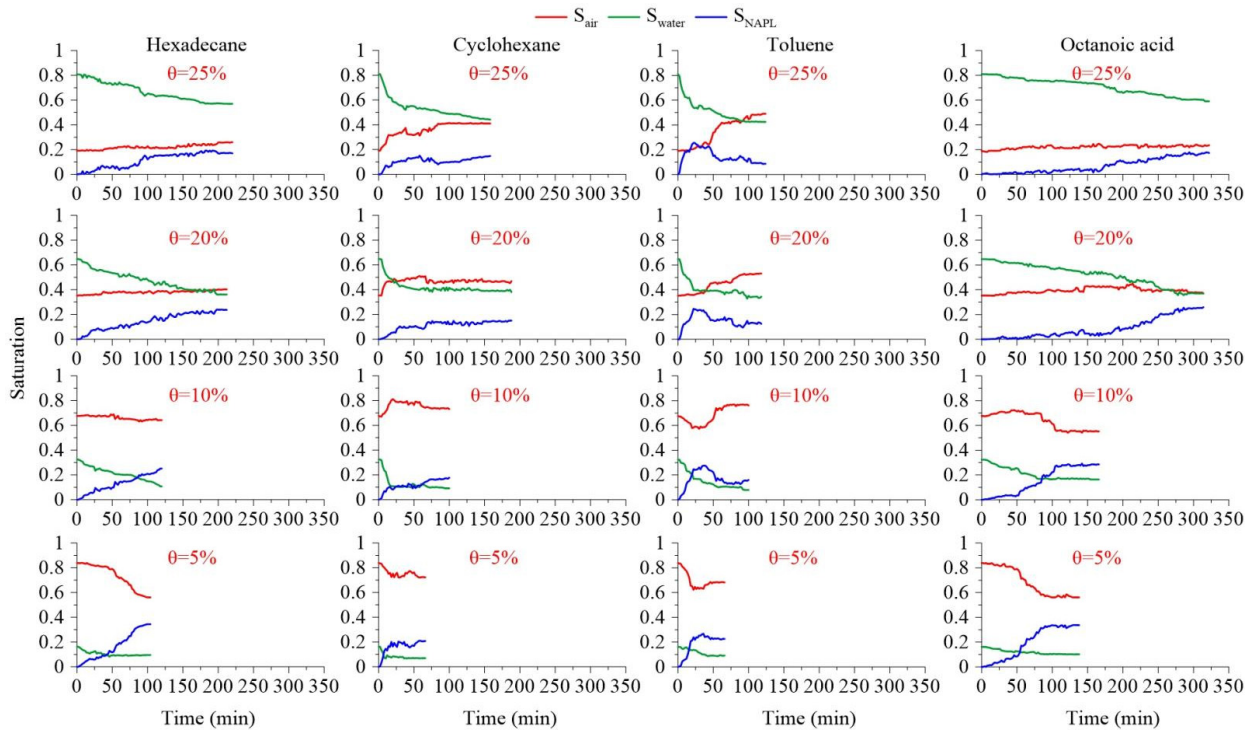

Figure 10. Change in saturation of three phases (air, water, and NAPL) in coarse sand under different soil water content conditions.

Figure 10 demonstrates that when components migrate into soil media with different moisture contents, there are large differences in the mutual changes between water, NAPL, and air. When the soil medium and components change, there are also varying degrees of differences. The specific discussion can be divided into the following:

(1) Effect of soil medium: When the moisture content is very small, the components entering the pores will change the saturation of gas and water, mainly manifesting as a decrease in the gas saturation of the pores. This is mainly due to the low moisture content, the large remaining pore space in the soil, and the small infiltration resistance of the components, which can discharge gas, thus resulting in a phenomenon of reduced gas saturation. However, there are large differences between different media. In coarse sand, the mobilization of components, water, and gas is relatively smooth and changes rapidly. In clay, due to the small pore space and strong adsorption capacity, the components can only seep underground slowly.

During this process, NAPL gradually accumulates on the surface layer and, when it reaches a certain amount, begins to accelerate downward. If NAPL is highly volatile, the remaining components will gradually decrease and turn into gas. For example, toluene has a special three-phase change curve, in which the gas first decreases, then increases, and then maintains equilibrium. This is because the gas is first discharged during early infiltration and displaces water, allowing toluene to penetrate downward into the pores. As toluene continues to accumulate in the pores, significant volatilization begins to occur, forming gas-phase toluene in the pores, leading to increased gas saturation in the pores. At the same time, the residual saturation first increases and then decreases. This is also caused by the fact that the toluene that enters first remains in the pores and then volatilizes. When the water content is very high, as the components are less dense than water, they will float on the water surface at the beginning and cannot penetrate quickly. At this time, the water and components are continuously mixed and enter the soil pores under the influence of gravity. However, as the components are not easily soluble in water, and it is difficult to drain water in a short period of time, the pore space can only be obtained by exhausting gas, reducing the gas saturation. When a large number of components enter, an equilibrium

phase is gradually reached. Likewise, the rate of change is faster in coarse sand and lower in clay. Therefore, the influence of the medium is mainly reflected in the following: NAPL displacement is smoother in coarse-grained soil but more difficult in fine-grained soil; that is, low permeability makes it difficult for NAPL to penetrate the soil layer. Furthermore, when the soil is filled with water, NAPL mainly floats on the surface layer.

(2) Component type: Another factor that affects component mobilization is the physical and chemical properties of the component. The biggest difference between petroleum pollution components and other pollutants is that they have lower water solubility and stronger volatility. Therefore, clarifying the mobilization differences between different components is also a prerequisite for studying and analyzing pollutant distributions. Taking toluene as an example, when it migrates into soil with a moisture content of 25% due to its low viscosity (0.59 mPa·s), the adsorption capacity of the soil is weak, and it migrates quickly. It continuously displaces water, causing the moisture content to decrease at the fastest rate; when toluene migrates into soil with a low moisture content due to its strong volatility, it will gradually volatilize after entering the soil pores, resulting in the evaporation of the components that have remained in the pores, forming gases that escape from the soil. Therefore, the amount of residual toluene in the soil decreased in the later period. Both hexadecane and octanoic acid have high viscosity and can only displace water slowly, slowly increasing NAPL and gas saturation in the pores.

3.4.3. Phase Transformation Analysis

During the experiment, parallel batch experiments were conducted to assess the processes relating to concentration change in soil over time. The gas sample was collected from the gas sampler at the upper port of the soil column, with a sampling volume of 5 mL. After reaching the specified time, as there was still free NAPL in the soil migrating in the pores, part of the NAPL entered the pores at this time, and a residual phase was formed. In order to distinguish between the two, referring to Rhee's method [56], water with five times the pore volume was injected into the soil column from the top to the bottom, and the NAPL that was still in the free phase was washed out and designated as the water phase until the flushed liquid was no longer red. Meanwhile, the NAPL that was difficult to wash out remained in the soil. The data relating to the three phases were compared, and the effects of moisture content on the mutual transformation between component forms were further determined. The experimental results are shown in Figure 11.

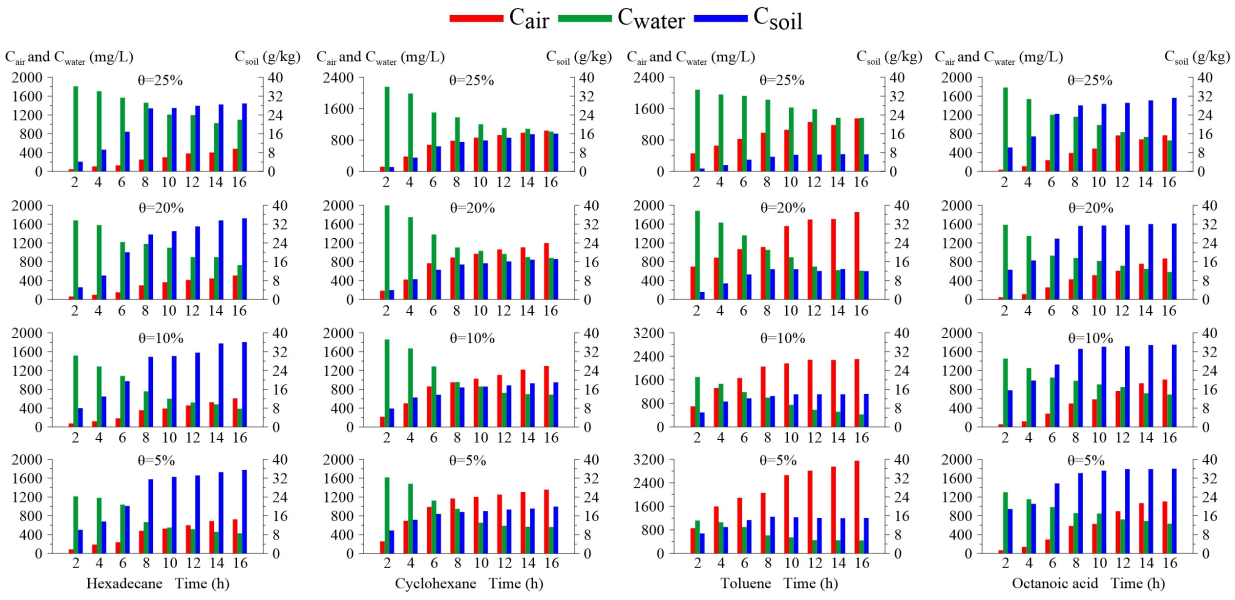

Figure 11. Concentration change in water–soil–gas three-phase components in coarse sand.

As can be seen in Figure 11, only toluene had a higher concentration in the gas samples obtained (with an average value of 1597.3 mg/L), which gradually increased with time; furthermore, volatilization at a low moisture content was stronger than at a high moisture content. This is mainly because, when the moisture content is high, the pore space is smaller, the volatilization is lower, and the components are mainly miscible with water; meanwhile, when the moisture content in the soil is low, the components tend to enter the soil pores, where the large pore space results in greater volatilization. However, after entering the soil pores, the volatilized toluene cannot escape from the soil column immediately. Instead, it is still imprisoned in the soil pores, causing the gas phase concentration in the pores to increase. The concentrations of hexadecane, cyclohexane, and octanoic acid were maintained at very low levels, with average values of 334.4, 868.3, and 502.6 mg/L, respectively. Similarly, hexadecane and octanoic acid remained in the soil in the highest amounts due to their strong viscosity, while toluene and cyclohexane left fewer residues. As the water solubility of petroleum components is low, their dissolved concentration in water is very low, and they are mainly free in water.

4. Conclusions

According to the results of the batch experiments, the existence and mobilization of petroleum components in the water–soil–NAPL–gas complex system were determined to possess the following main characteristics: (1) The residual content of components is the lowest in coarse sand and the highest in clay, which is mainly affected by the soil particles; meanwhile, the residual saturation value of octanoic acid is the largest, and that of toluene is the smallest, as determined by their viscosity and volatility. (2) The infiltration processes of the components are affected by their properties and medium characteristics. Due to its small particle size and strong adsorption, clay has the highest residual saturation of petroleum pollutants (28.8%). This can even be more than twice that of coarse sand (13.3%). For different components, the residual saturations of octanoic acid and toluene are the highest and lowest, respectively (taking fine sand as an example: 25.3% and 13.2%), with a relatively large difference, as determined in terms of viscosity and solubility. (3) As the free phase can migrate freely, it is transformed most rapidly in the pores. The changes in the dissolved phase of each component are relatively small and tend to be gentle. The changes in the residual phase are mainly affected by volatility, viscosity, soil particles, and pore and cosmid content, and the degree of change is ordered as follows: toluene > cyclohexane > hexadecane > octanoic acid. According to Sun et al., the total saturation of benzene decreased from 71.9% to 10.1% under a controlled system as the soil moisture content increased from 6.4% to 25.4% [57]. Similarly, we observed that the volatilization of toluene decreased from 68.2% to 49.0% as the water saturation increased from 5% to 25% (Figure 10). The results obtained from the two analyses are similar, with the difference relating to the petroleum components (benzene and toluene). Considering a residual concentration of approximately 7700 mg/kg for diesel and sandy soil proposed by Brost and De Vaull, the final residual concentrations of toluene in our experiment were as follows: 5.471, 10.407, 12.244625, and 13.74625 mg/kg when the soil water contents were 25%, 20%, 10%, and 5%, respectively, and with an average value of 10,467.2 mg/kg [58]. Therefore, whether using residual saturation or the residual concentration values, our experiments are comparable.

In summary, the influence of the medium is mainly reflected in the following: NAPL displacement is smoother in coarse-grained soil and more difficult in fine-grained soil; that is, low permeability makes it difficult for NAPL to penetrate the soil layer. When the soil is filled with water, NAPL mainly floats on the surface layer. Volatilization at a low moisture content is stronger than that at a high moisture content; this is mainly because, when the moisture content is higher, the pore space is smaller, volatilization is lower, and the components are mainly miscible with water. Meanwhile, when the moisture content in the soil is low, volatilization is stronger, the components tend to enter the soil pores, and the soil pore space is large and, therefore, facilitates volatilization. However, after entering the soil pores, the volatilized toluene cannot escape from the soil column immediately. Instead,

it is still imprisoned in the soil pores, increasing the gas phase concentration in the pores. The concentrations of hexadecane, cyclohexane, and octanoic acid were maintained at very low levels, with average values of 334.4, 868.3, and 502.6 mg/L, respectively. Similarly, hexadecane and octanoic acid remained in the soil in the highest amounts due to their strong viscosity, while toluene and cyclohexane left fewer residues. Due to the low water solubility of petroleum components, their dissolved concentrations in water are very low, and they are mainly free in water.

This experiment systematically studied the saturation and transformation processes relating to NAPL (non-aqueous phase liquid) petroleum pollutants in water–air–soil–NAPL systems. However, there are still some challenges and development trends that need to be addressed. Firstly, the conditions at actual contaminated field sites are extremely complex, making it difficult to accurately predict and control the migration and transformation characteristics of different types of pollutants. This necessitates research and development of effective and accurate monitoring and diagnostic technologies. Additionally, there should be continuous development and improvement of integrated remediation technologies based on actual pollution surveys, as well as the establishment of corresponding technology suitability evaluation systems to provide scientific support for selecting efficient and cost-effective remediation schemes.

Author Contributions: Conceptualization, M.Y.; methodology, M.Y. and B.W.; software, Y.Q. and C.L.; validation, M.Y. and B.W.; formal analysis, M.Y. and Z.C.; investigation, M.Y. and Y.X.; resources, M.Y. and Y.Q.; data curation, M.Y. and Y.X.; writing—original draft preparation, M.Y. and B.W.; writing—review and editing, M.Y. and C.L.; visualization, B.W. and Z.C.; supervision, M.Y. and B.W.; project administration, M.Y. and Y.X.; funding acquisition, B.W. All authors have read and agreed to the published version of the manuscript.

Funding: This research was sponsored by the Guizhou Provincial Basic Research Program (Natural Science) (QKHJC-ZK(2022)-General 186); the National Natural Science Foundation of China (grant Nos. 41602275, 41977298); the High-Level Talent Introduction Program for The Guizhou Institute of Technology (2023GCC085); the Guizhou Provincial Key Technology R&D Program (QKHZC(2023)-General 143); the Provincial Higher Education Teaching Content and Curriculum System Reform Project of Guizhou Province (2023223); the Education and Teaching Reform Research Project of Guizhou Institute of Technology (XJJG-2022-22533); the Open Fund from the Key Lab of Eco-restoration of Regional Contaminated Environment (Shenyang University); the Ministry of Education (KF-22-02); and the Provincial Key Disciplines of Guizhou Province-Geological Resources and Geological Engineering (ZDXK (2018)001).

Data Availability Statement: The original contributions presented in this study are included in the article; further inquiries can be directed to the corresponding author.

Conflicts of Interest: The authors declare no conflicts of interest.

References

1. Zhang, H.; Han, X.; Wang, G.; Mao, H.; Chen, X.; Zhou, L.; Huang, D.; Zhang, F.; Yan, X. Spatial distribution and driving factors of groundwater chemistry and pollution in an oil production region in the Northwest China. *Sci. Total Environ.* **2023**, *875*, 162635. [CrossRef] [PubMed]
2. Sattar, S.; Hussain, R.; Shah, S.M.; Bibi, S.; Ahmad, S.R.; Shahzad, A.; Zamir, A.; Rauf, Z.; Noshad, A.; Ahmad, L. Composition, impacts, and removal of liquid petroleum waste through bioremediation as an alternative clean-up technology: A review. *Heliyon* **2022**, *8*, e11101. [CrossRef] [PubMed]
3. Guo, Y.; Wen, Z.; Cheng, Z.; Jakada, H. Contamination and natural attenuation characteristics of petroleum hydrocarbons in a fractured karst aquifer, North China. *Environ. Sci. Pollut. R.* **2020**, *27*, 22780–22794. [CrossRef] [PubMed]
4. Mukhopadhyay, A.; Quinn, M.; Al-Haddad, A.; Al-Khalid, A.; Al-Qallaf, H.; Rashed, T.; Bhandary, H.; Al-Salman, B.; Bushehri, A.; Boota, A. Pollution of fresh groundwater from damaged oil wells, North Kuwait. *Environ. Earth Sci.* **2017**, *76*, 145. [CrossRef]
5. Ukhurebor, K.E.; Athar, H.; Adetunji, C.O.; Aigbe, U.O.; Onyancha, R.B.; Abifarin, O. Environmental implications of petroleum spillages in the Niger Delta region of Nigeria: A review. *J. Environ. Manag.* **2021**, *293*, 112872. [CrossRef] [PubMed]
6. Cagle, G.A.; Chen, H.; Fleeger, J.W.; Deis, D.R.; Lin, Q.; Hou, A. Spatial heterogeneity and oil pollution structured the soil microbial community in salt marshes in Barataria Bay, Louisiana, USA, eight years after the Deepwater Horizon oil spill. *Ecol. Indic.* **2024**, *160*, 111884. [CrossRef]

7. Al-Mebayedh, H.; Niu, A.; Lin, C. Strategies for cost-effective remediation of widespread oil-contaminated soils in Kuwait, an environmental legacy of the first Gulf War. *J. Environ. Manag.* **2023**, *344*, 118601. [CrossRef] [PubMed]
8. Yuan, L.; Wu, Y.; Fan, Q.; Li, P.; Liang, J.; Wang, Z.; Li, R.; Shi, L. Spatial distribution, composition, and source analysis of petroleum pollutants in soil from the Changqing Oilfield, Northwest China. *Mar. Pollut. Bull.* **2022**, *185*, 114338. [CrossRef] [PubMed]
9. Kuppusamy, S.; Maddela, N.R.; Megharaj, M.; Venkateswarlu, K. An overview of total petroleum hydrocarbons. In *Total Petroleum Hydrocarbons*; Springer: Berlin/Heidelberg, Germany, 2020; pp. 1–27.
10. Varjani, S.; Gnansounou, E.; Pandey, A. Comprehensive review on toxicity of persistent organic pollutants from petroleum refinery waste and their degradation by microorganisms. *Chemosphere* **2017**, *188*, 280–291. [CrossRef]
11. Xu, C.; Qaria, M.A.; Xu, Q.; Zhu, D. The role of microorganisms in petroleum degradation: Current development and prospects. *Sci. Total Environ.* **2023**, *865*, 161112.
12. Sheng, Y.; Zhang, X.; Zhai, X.; Zhang, F.; Li, G.; Zhang, D. A mobile, modular and rapidly-acting treatment system for optimizing and improving the removal of non-aqueous phase liquids (NAPLs) in groundwater. *J. Hazard Mater.* **2018**, *360*, 639–650. [CrossRef] [PubMed]
13. De Simone, G.; Lai, C.; Pompilj, F.; Galli, G.; Tuccimei, P. Laboratory simulation of recent NAPL spills to investigate radon partition among NAPL vapours and soil air. *Appl. Radiat. Isot.* **2017**, *120*, 106–110. [CrossRef] [PubMed]
14. Ossai, I.C.; Ahmed, A.; Hassan, A.; Hamid, F.S. Remediation of soil and water contaminated with petroleum hydrocarbon: A review. *Environ. Technol. Innov.* **2020**, *17*, 100526. [CrossRef]
15. Zargar, M.; Sarrafzadeh, M.H.; Taheri, B.; Keshavarz, A. Assessment of In Situ Bioremediation of Oil Contaminated Soil and Groundwater in a Petroleum Refinery: A Laboratory Soil Column Study. *Petrol. Sci. Technol.* **2014**, *32*, 1553–1561. [CrossRef]
16. Liu, J.; Wei, K.; Xu, S.; Cui, J.; Ma, J.; Xiao, X.; Xi, B.; He, X. Surfactant-enhanced remediation of oil-contaminated soil and groundwater: A review. *Sci. Total Environ.* **2021**, *756*, 144142. [CrossRef] [PubMed]
17. Wang, Z.; Yang, P.; Guo, H.; Wang, Y. Enhanced mass transfer of residual NAPL by convection in stagnant zone. *J. Hydrol.* **2023**, *625*, 130050. [CrossRef]
18. Ramezanzadeh, M.; Aminnaji, M.; Rezanezhad, F.; Ghazanfari, M.H.; Babaei, M. Dissolution and remobilization of NAPL in surfactant-enhanced aquifer remediation from microscopic scale simulations. *Chemosphere* **2022**, *289*, 133177. [CrossRef]
19. Mobile, M.A.; Widdowson, M.A.; Stewart, L.; Nyman, J.; Deeb, R.A.; Kavanaugh, M.C.; Mercer, J.W.; Gallagher, D.L. In-situ determination of field-scale NAPL mass transfer coefficients: Performance, simulation and analysis. *J. Contam. Hydrol.* **2016**, *187*, 31–46. [CrossRef] [PubMed]
20. Sakhaei, Z.; Daryaee, R.; Moosavi, A.A.; Carrasco-Marin, F.; Betancur, S.; Bailón-García, E.; Pérez-Cadenas, A.F.; Riazi, M. Chemical-assisted biological methods for in situ remediation of petroleum hydrocarbon-contaminated soils. In *Biotechnology of Emerging Microbes*; Sarma, H., Joshi, S.J., Eds.; Academic Press: Cambridge, MA, USA, 2024; pp. 217–261.
21. Guan, J.; Huang, J.; Sun, Y.; Li, C.; Wan, Y.; Guo, W.; Kang, R.; Pang, H.; Shi, Q.; McHugh, T.J. Understanding petroleum vapor fate and transport through high resolution analysis of two distinct vapor plumes. *Sci. Total Environ.* **2024**, *912*, 169464. [CrossRef]
22. Fatehbasharzad, P.; Aliasghari, S.; Tabrizi, I.S.; Khan, J.A.; Boczkaj, G. Microbial fuel cell applications for removal of petroleum hydrocarbon pollutants: A review. *Water Resour. Ind.* **2022**, *28*, 100178. [CrossRef]
23. Qi, S.; Luo, J.; O'Connor, D.; Wang, Y. A numerical model to optimize LNAPL remediation by multi-phase extraction. *Sci. Total Environ.* **2020**, *718*, 137309. [CrossRef]
24. Mohamed, A.; El-Menshawy, N.; Saif, A.M. Remediation of saturated soil contaminated with petroleum products using air sparging with thermal enhancement. *J. Environ. Manag.* **2007**, *83*, 339–350. [CrossRef] [PubMed]
25. Petri, B.G.; Fučík, R.; Illangasekare, T.H.; Smits, K.M.; Christ, J.A.; Sakaki, T.; Sauck, C. Effect of NAPL source morphology on mass transfer in the vadose zone. *Groundwater* **2014**, *53*, 685–698. [CrossRef] [PubMed]
26. Cao, Z.; Yang, M.; Tan, T.; Song, X. Vertical transportation diversity of petroleum pollutants under groundwater fluctuations and the instructions for remediation strategy. *Sustainability* **2023**, *15*, 6514. [CrossRef]
27. Sookhak, L.K.; Rayner, J.L.; Davis, G.B. Towards optimizing LNAPL remediation. *Water Resour. Res.* **2019**, *55*, 923–936. [CrossRef]
28. Podgorski, D.C.; Zito, P.; Kellerman, A.M.; Bekins, B.A.; Cozzarelli, I.M.; Smith, D.F.; Cao, X.; Schmidt-Rohr, K.; Wagner, S.; Stubbins, A. Hydrocarbons to carboxyl-rich alicyclic molecules: A continuum model to describe biodegradation of petroleum-derived dissolved organic matter in contaminated groundwater plumes. *J. Hazard Mater.* **2021**, *402*, 123998. [CrossRef]
29. Ciampi, P.; Esposito, C.; Cassiani, G.; Deidda, G.P.; Rizzetto, P.; Papini, M.P. A field-scale remediation of residual light non-aqueous phase liquid (LNAPL): Chemical enhancers for pump and treat. *Environ. Sci. Pollut. R.* **2021**, *28*, 35286–35296. [CrossRef]
30. Wei, K.; Ma, J.; Xi, B.; Yu, M.; Cui, J.; Chen, B.; Li, Y.; Gu, Q.; He, X. Recent progress on in-situ chemical oxidation for the remediation of petroleum contaminated soil and groundwater. *J. Hazard Mater.* **2022**, *432*, 128738. [CrossRef] [PubMed]
31. Kechavarzi, C.; Soga, K.; Illangasekare, T.H. Two-dimensional laboratory simulation of LNAPL infiltration and redistribution in the vadose zone. *J. Contam. Hydrol.* **2005**, *76*, 211–233. [CrossRef]
32. He, Z.; Liang, F.; Meng, J.; Li, N. Effects of groundwater fluctuation on migration characteristics and representative elementary volume of entrapped LNAPL. *J. Hydrol.* **2022**, *610*, 127833. [CrossRef]
33. Onaa, C.; Emmanuel Olaobaju, A.; Amro, M. Experimental and numerical assessment of Light Non-Aqueous Phase Liquid (LNAPL) subsurface migration behavior in the vicinity of groundwater table. *Environ. Technol. Innov.* **2021**, *23*, 101573. [CrossRef]

34. Karthick, A.; Roy, B.; Chattopadhyay, P. A review on the application of chemical surfactant and surfactant foam for remediation of petroleum oil contaminated soil. *J. Environ. Manag.* **2019**, *243*, 187–205. [CrossRef] [PubMed]
35. Ding, F.; Gao, M. Pore wettability for enhanced oil recovery, contaminant adsorption and oil/water separation: A review. *Adv. Colloid. Interfac.* **2021**, *289*, 102377. [CrossRef]
36. Chen, T.; Zhang, Y.; Fu, B.; Huang, W. An evaluation model for in-situ bioremediation technology of petroleum hydrocarbon contaminated soil. *Environ. Pollut.* **2024**, *344*, 123299. [CrossRef] [PubMed]
37. Qing, L.; Tan, X.; Almatrafi, E.; Yang, Y.; Wang, W.; Luo, H.; Qin, F.; Zhou, C.; Zeng, G.; Zhang, C. Effects of biochar-based materials on the bioavailability of soil organic pollutants and their biological impacts. *Sci. Total Environ.* **2022**, *826*, 153956.
38. Haruna, A.; Tanimu, G.; Ibrahim, I.; Garba, Z.N.; Yahaya, S.M.; Musa, S.G.; Merican, Z.M.A. Mitigating oil and gas pollutants for a sustainable environment—Critical review and prospects. *J. Clean. Prod.* **2023**, *416*, 137863. [CrossRef]
39. Jiang, W.; Meng, L.; Liu, F.; Sheng, Y.; Chen, S.; Yang, J.; Mao, H.; Zhang, J.; Zhang, Z.; Ning, H. Distribution, source investigation, and risk assessment of topsoil heavy metals in areas with intensive anthropogenic activities using the positive matrix factorization (PMF) model coupled with self-organizing map (SOM). *Environ. Geochem. Hlth.* **2023**, *45*, 6353–6370. [CrossRef] [PubMed]
40. An, S.; Woo, H.; Kim, S.; Yun, S.; Chung, J.; Lee, S. Complex behavior of petroleum hydrocarbons in vadose zone: A holistic analysis using unsaturated soil columns. *Chemosphere* **2023**, *326*, 138417. [CrossRef]
41. Han, K.; Zuo, R.; Cao, X.; Xu, D.; Zhao, X.; Shi, J.; Xue, Z.; Xu, Y.; Wu, Z.; Wang, J. Spatial distribution characteristics and degradation mechanism of microorganisms in n-hexadecane contaminated vadose zone. *Sci. Total Environ.* **2024**, *924*, 171462. [CrossRef]
42. Shi, J.; Yang, Y.; Lu, H.; Xi, B.; Li, J.; Xiao, C.; Wang, Y.; Tang, J. Effect of water-level fluctuation on the removal of benzene from soil by SVE. *Chemosphere* **2021**, *274*, 129796. [CrossRef]
43. Cavelan, A.; Faure, P.; Lorgeoux, C.; Colombano, S.; Deparis, J.; Davarzani, H.; Enjelvin, N.; Oltéan, C.; Tinet, A.J.; Domptail, F. An experimental multi-method approach to better characterize the LNAPL fate in soil under fluctuating groundwater levels. *J. Contam. Hydrol.* **2024**, *262*, 104319. [CrossRef] [PubMed]
44. Koohbor, B.; Colombano, S.; Harrouet, T.; Deparis, J.; Lion, F.; Davarzani, H.; Ataie-Ashtiani, B. The effects of water table fluctuation on LNAPL deposit in highly permeable porous media: A coupled numerical and experimental study. *J. Contam. Hydrol.* **2023**, *256*, 104183. [CrossRef]
45. Teramoto, E.H.; Chang, H.K. Field data and numerical simulation of btex concentration trends under water table fluctuations: Example of a jet fuel-contaminated site in Brazil. *J. Contam. Hydrol.* **2017**, *198*, 37–47. [CrossRef] [PubMed]
46. Zhao, S.; Wang, J.; Feng, S.; Xiao, Z.; Chen, C. Effects of ecohydrological interfaces on migrations and transformations of pollutants: A critical review. *Sci. Total Environ.* **2022**, *804*, 150140. [CrossRef]
47. Sakr, M.; El Agamawi, H.; Klammler, H.; Mohamed, M.M. A review on the use of permeable reactive barriers as an effective technique for groundwater remediation. *Groundw. Sust. Dev.* **2023**, *21*, 100914. [CrossRef]
48. Gatsios, E.; García-Rincón, J.; Rayner, J.C.W.; McLaughlan, R.; Davis, G.B. LNAPL transmissivity as a remediation metric in complex sites under water table fluctuations. *J. Environ. Manag.* **2018**, *215*, 40–48. [CrossRef] [PubMed]
49. Mineo, S. Groundwater and soil contamination by LNAPL: State of the art and future challenges. *Sci. Total Environ.* **2023**, *874*, 162394. [CrossRef] [PubMed]
50. Javanbakht, G.; Arshadi, M.; Qin, T.; Goual, L. Micro-scale displacement of NAPL by surfactant and microemulsion in heterogeneous porous media. *Adv. Water Resour.* **2017**, *105*, 173–187. [CrossRef]
51. Yang, Z.; Verpoort, F.; Dong, C.; Chen, C.; Chen, S.; Kao, C. Remediation of petroleum-hydrocarbon contaminated groundwater using optimized in situ chemical oxidation system: Batch and column studies. *Process Saf. Environ.* **2020**, *138*, 18–26. [CrossRef]
52. Sun, Y.; Gu, Y.; Zha, Q. A novel surface imprinted resin for the selective removal of metal-complexed dyes from aqueous solution in batch experiments: ACB GGN as a representative contaminant. *Chemosphere* **2021**, *280*, 130611. [CrossRef]
53. Negarestani, M.; Reisi, S.; Sohrabi, M.; Shayesteh, H.; Farimaniraad, H.; Mollahosseini, A.; Hosseinzadeh, M.; Tavassoli, S. In-situ growth of Al/Ni layered double hydroxide onto polyaniline-wrapped sisal fibers for highly efficient removal of pharmaceutical Ketoprofen and Ibuprofen contaminants: Batch and fixed-bed column studies. *J. Water Process Eng.* **2024**, *57*, 104657. [CrossRef]
54. Xia, Y.; Wang, B.; Yang, Y.; Du, X.; Yang, M. Quantitative assessment of organic mass fluxes and natural attenuation processes in a petroleum-contaminated subsurface environment. *Appl. Sci.* **2023**, *13*, 12782. [CrossRef]
55. Stafford, B.P.; Cápiro, N.L.; Alvarez, P.J.J.; Rixey, W.G. Pore Water Characteristics following a release of neat ethanol onto pre-existing NAPL. *Ground Water Monit. R.* **2009**, *29*, 93–104. [CrossRef]
56. Rhee, S.; Lee, S.; Park, J. Effect of soil organic carbon on the quantification of jet-fuels in soil using partitioning tracer method. *J. Hazard Mater.* **2010**, *184*, 49–57. [CrossRef] [PubMed]
57. Sun, Y.; Yue, G.; Ma, J. Transport and natural attenuation of benzene vapor from a point source in the vadose zone. *Chemosphere* **2023**, *323*, 138222. [CrossRef]
58. Brost, E.J.; DeVaull, G.E. Non-aqueous phase liquid (NAPL) mobility limits in soil. *API Soil Groundw. Res. Bull.* **2000**, *9*, 1–9.

Disclaimer/Publisher's Note: The statements, opinions and data contained in all publications are solely those of the individual author(s) and contributor(s) and not of MDPI and/or the editor(s). MDPI and/or the editor(s) disclaim responsibility for any injury to people or property resulting from any ideas, methods, instructions or products referred to in the content.

water

MDPI

Article

Mechanisms of Non-Aqueous Phase Liquid Retention in Low-Permeability Aquifer Lenses: Effects on Contaminant Remediation

Weichao Sun [1,2,3], Shuaiwei Wang [3], Jianzhou Yu [4], Huimin Lin [5] and Lin Sun [3,*]

[1] Institute of Hydrogeology and Environmental Geology, Chinese Academy of Geological Sciences, Shijiazhuang 050061, China; 17730568088@163.com
[2] School of Chinese Academy of Geological Sciences, China University of Geosciences (Beijing), Beijing 100086, China
[3] Key Laboratory of Groundwater Remediation of Hebei Province & China Geological Survey, Zhengding 050083, China; tarin_w@163.com
[4] The Fourth Hydrogeological Engineering Geological Brigade of Hebei Bureau of Geological and Mineral Resources Exploration, Cangzhou 061000, China; swsdyjz@163.com
[5] Hebei Provincial Hydrological and Engineering Geological Survey Institute (Hebei Provincial Remote Sensing Center), Shijiazhuang 050000, China; 18810886141@163.com
* Correspondence: sunlin@mail.cgs.gov.cn

Abstract: The residual non-aqueous phase liquid (NAPL) within low-permeability lenses of aquifers is a major contributor to "tailing", a phenomenon that complicates the remediation of NAPL-contaminated sites. A fundamental challenge in addressing this issue is the lack of understanding of the primary controlling factors and underlying effects of NAPL residuals in these aquifer lenses. This study aims to identify the key factors and mechanisms affecting NAPL residuals in low-permeability lenses through a series of experimental approaches. These include soil column simulation experiments on NAPL residuals in various low-permeability lenses, adsorption experiments on aquifer and lens particles, pore mercury intrusion testing, and particle size distribution analysis. The experiments provided valuable data on residual NAPL saturation S_R, particle adsorption capacity, particle size, gradation, and pore size and distribution in different lenses. Using a mass conservation approach, the particle adsorption contributed less than 0.5% to the total NAPL residuals, while retention accounted for more than 99.5%, highlighting that retention is the dominant mechanism governing NAPL persistence in these lenses. The mechanism underlying this result was further clarified through an analysis of particle size characteristics. Correlation analysis was conducted to examine the relationships between residual NAPL and macropore porosity (n_{max}, diameter > 60 μm), mesopore porosity (n_{mid}, diameter = 30~60 μm), and small pore porosity (n_{min}, diameter < 30 μm). The results demonstrated that mesopores exhibited the strongest correlation with NAPL retention, due to their pronounced capillary action and sufficient storage capacity for NAPL.

Keywords: aquifer; low-permeability lens; NAPL residuals; particle adsorption; retention; pore diameter

1. Introduction

In recent years, the increased utilization of organic chemical products has led to a significant influx of organic compounds into the subsurface environment during processes such as refining, storage, transportation, and usage [1–4]. Among these compounds,

petroleum and petroleum-based chemical pollutants frequently manifest in water as non-aqueous phase liquid (NAPL) [5–7]. NAPL can be classified into two categories according to their density. One category is Light Non-Aqueous Phase Liquids (LNAPLs) with a density less than that of water. Common LNAPLs include diesel, benzene, xylene, etc. The other category is Dense Non-Aqueous Phase Liquids (DNAPLs) with a density greater than that of water. Common DNAPLs include tetrachloroethylene, chlorinated organic solvents, etc. NAPL pollutants are characterized by their high toxicity, chemical stability, and resistance to degradation [8–10], which contributes to their prolonged persistence in subsurface soil and water environments, thereby posing significant threats to both ecological and human health. During the remediation of NAPL-contaminated sites, it has been observed that the "tailing" phenomenon, resulting from residual NAPL in low-permeability lenses (a low-permeability lens refers to a geological body whose permeability is poorer than that of the surrounding aquifer media and whose volume is much smaller than that of the aquifer) of aquifers (Figure 1), is a primary factor contributing to the failure of pollution treatment efforts [11–14]. Therefore, it is imperative to identify the key controlling factors and mechanisms that affect the presence of residual NAPL in low-permeability lenses of aquifers to enhance the effectiveness of NAPL pollution remediation strategies.

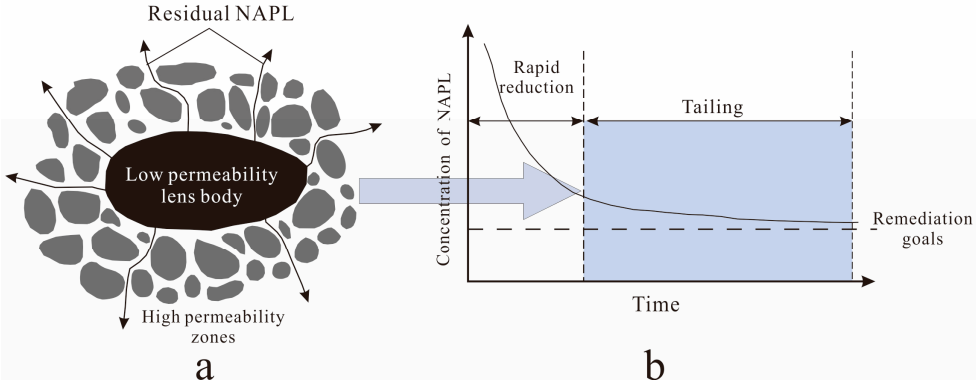

Figure 1. Residual NAPL in low-permeability lens body (**a**) leads to "tailing" (**b**).

To investigate the effect of aquifer lenses on NAPL residuals, researchers both domestically and internationally have undertaken a series of studies. The findings suggest that NAPL residuals in aquifers are primarily composed of pore retention and particle adsorption [15–17]. The particle size of the lens plays a significant role in affecting NAPL residuals: in fine-grained media, coarser lenses facilitate NAPL migration, thereby reducing residuals; conversely, in coarse-grained media, finer lenses impede migration, resulting in increased NAPL residuals [18–20]. Additionally, alterations in the pore structure of the lenses also affect NAPL residuals. Smaller pores elevate the critical displacement pressure, hindering water flow from overcoming capillary forces to penetrate low-permeability regions. In these zones, residual NAPL aggregates form NAPL-contaminated areas, consequently increasing NAPL residuals [21–26].

In summary, NAPL residuals in aquifers are affected by particle adsorption and pore retention mechanisms. Variations in NAPL residuals are associated with the grain size and pore characteristics of aquifer lenses. However, the extent to which NAPL residuals are sensitive to particle adsorption and pore retention, as well as the underlying mechanisms driving these effects, remain inadequately understood. To investigate this issue, this study designed soil column simulation experiments that varied permeability coefficient ratios K_{mn}, which represent the ratio of the permeability coefficient of the aquifer medium to the lens. By modifying the permeability of the lenses, this study simulated aquifers containing different lens types to examine the variations in NAPL residuals under diverse lens

conditions. Additionally, particle adsorption experiments were conducted to quantify the maximum adsorption capacity of the lenses for NAPL. Utilizing the law of mass conservation, this study calculated the sensitivity ranking of NAPL residuals in relation to particle adsorption and pore retention, thereby identifying the primary factors that control NAPL behavior in aquifer lenses. Furthermore, particle size distribution experiments and mercury intrusion tests were performed to ascertain the grain size and pore characteristics of both aquifers and lenses. By integrating the influence rankings of particle adsorption and retention on residual NAPL, correlation analysis was employed to elucidate the mechanisms that affect NAPL residuals in aquifer lenses.

2. Materials and Methods

To achieve the objectives of this study, a series of experiments were designed, including soil column simulation experiments, particle adsorption experiments, mercury intrusion porosimetry, and particle size analysis. Furthermore, a standard curve for NAPL concentration was established based on experimental measurements. The materials and methods employed in each experiment are detailed below.

2.1. Soil Column Simulation Experiment

2.1.1. Experimental Materials

No. 0 diesel is a non-toxic and easily accessible LNAPL. Its properties, such as density, viscosity, solubility, etc., are similar to those of common NAPL pollutants like xylene, crude oil, and aviation kerosene. So, in this experiment, non-toxic and available No. 0 diesel was utilized as a substitute for NAPL pollutants. The properties of the diesel are summarized in Table 1. To prevent microbial degradation from affecting the experimental results [27], white quartz sand with low clay content was selected to simulate the aquifer medium. This sand was procured from Henan Minghai Environmental Technology Co., Ltd. (Zhengzhou City, Henan Province, China) and underwent sterilization at high temperatures (105) prior to its application. The physical properties of the quartz sand are outlined in Table 2.

Table 1. Physicochemical properties of diesel used in NAPL experiments.

Viscosity (mPa·s)	Surface Tension (mN·m)	Liquefied Density ρ_o (g/mL)	Boiling Point (°C)	Octane Number
287	2.68	0.83	180–360	40–55

Table 2. Physical and permeability characteristics of quartz sand used in NAPL simulations.

Medium ID	Particle Size D (mm)	Bulk Density ρ (g/cm^3)	Permeability Coefficient K (m/d)	Permeability Coefficient Ratio K_{mn}	Porosity n (%)
No. 1 quartz sand (simulating aquifer)	0.25–4.00	1.53	137.84	1	42.85
No. 2 quartz sand (simulating low-permeability lens body)	0.09–1.75	1.61	30.04	5	41.07
No. 3 quartz sand (simulating low-permeability lens body)	0.063–1.00	1.69	12.45	11	40.67
No. 4 quartz sand (simulating low-permeability lens body)	0.063–0.75	1.69	5.93	23	40.61
No. 5 quartz sand (simulating low-permeability lens body)	0.053–0.425	1.73	2.78	50	40.59

The experimental setup included a HACH DR3900 spectrophotometer, an emulsifier, a HACH DRB200 digester, 500 mL beakers, pipettes, and HACH reagent tubes.

2.1.2. Experimental Apparatus and Design

In this study, soil column simulation experiments were employed to investigate the variations in NAPL residuals under varying conditions by modifying the permeability, size, and hydraulic gradient of the lens. The soil column was constructed from polymethyl methacrylate (PMMA), measuring 95 cm in height and 7 cm in diameter, with a maximum filling height of 75 cm. A sampling port and a downstream head measurement device were installed at the base of the column, while an inlet connected to a constant-head water supply was positioned 10 cm from the top (Figure 2a). The lens was designed with a diameter of φ = 3.5 cm and a height of h = 20 cm, taking into account the dimensions of the soil column, the flow characteristics of liquids within the column, and the effect of the lens on NAPL residuals. Based on the permeability coefficients of the media in Table 2, five levels of K_{mn} were established at 1, 5, 11, 23, and 50. Previous research indicates that the hydraulic gradient of groundwater in plain areas typically ranges from 1‰ to 12‰ [28,29]. For the permeability coefficients of the media utilized in this experiment, the flow velocity was set at 0.14 cm/min to facilitate monitoring; the filled soil column is shown in Figure 2b. A comprehensive overview of the experimental design is summarized in Table 3.

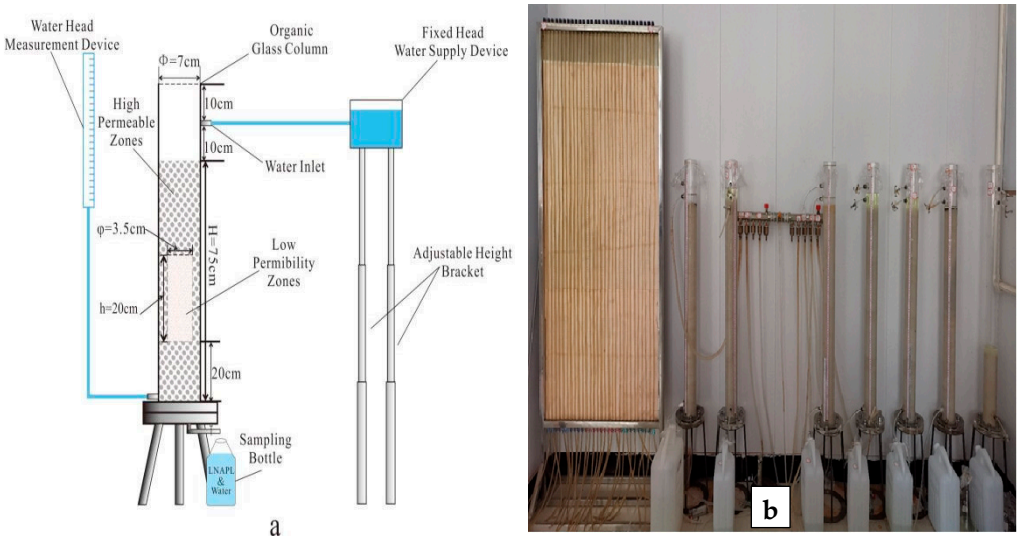

Figure 2. Schematic diagram of filling soil column (**a**) and photos of completed filling (**b**).

Table 3. Experimental design for soil column simulations of NAPL residuals.

Experiment ID	Aquifer Particle Size (mm)	Lens Particle Size (mm)	Permeability Coefficient Ratio K_{mn}	Lens Size Φ/φ × h (cm × cm)	Lens Volume V_t/ (cm^3)	Groundwater Flow Velocity V (cm/min)	Aquifer Mass m_w (g)	Lens Mass m_t (g)
1	0.25–4.00	0.25–4.00	1	3.5 × 20	192.325	0.14	4119.61	294.26
2	0.25–4.00	0.09–1.75	5	3.5 × 20	192.325	0.14	4056.32	309.64
3	0.25–4.00	0.063–1.00	11	3.5 × 20	192.325	0.14	4018.11	325.04
4	0.25–4.00	0.063–0.75	23	3.5 × 20	192.325	0.14	4216.24	324.29
5	0.25–4.00	0.053–0.425	50	3.5 × 20	192.325	0.14	4055.37	332.70

Following the completion of the packing process, NAPL was introduced from the top of the column with the assistance of a glass rod to facilitate the flow. Liquid samples were collected from the sampling port located at the bottom of the column, and the injection of NAPL was halted once the collected liquid was entirely composed of NAPL. At this

juncture, the total volume of NAPL injected into the plexiglass column (V_0) was recorded. Subsequently, the constant head water supply apparatus was activated, and the experiment commenced in accordance with the design in Table 3. Samples were taken from the sampling port at the base of the soil column, and the volume of the effluent was documented. The concentration of NAPL in the effluent was measured at various time intervals (NAPL concentration determination method in Section 2.5) until a steady concentration was achieved, at which point the experiment was complete. The total volume of NAPL discharged (V_c) was calculated utilizing the mass conservation principle. Residual NAPL saturation (Sr) in each soil column was determined using Equation (1) [30–32].

$$Sr = \frac{V_0 - V_c}{V} \times 100\% \quad (1)$$

where V represents the total pore volume, V_0 represents the total volume of NAPL injected into the plexiglass column, and V_c represents the volume of NAPL discharged.

2.2. Adsorption Experiment

2.2.1. Experimental Equipment and Materials for Adsorption Experiments

The materials and equipment utilized in the adsorption experiment comprised a THZ-82 constant temperature water bath oscillator (Figure 3), 250 mL stoppered Erlenmeyer flasks, quartz sand (Table 2), a HACH DR3900 spectrophotometer, and an FA2004N electronic balance.

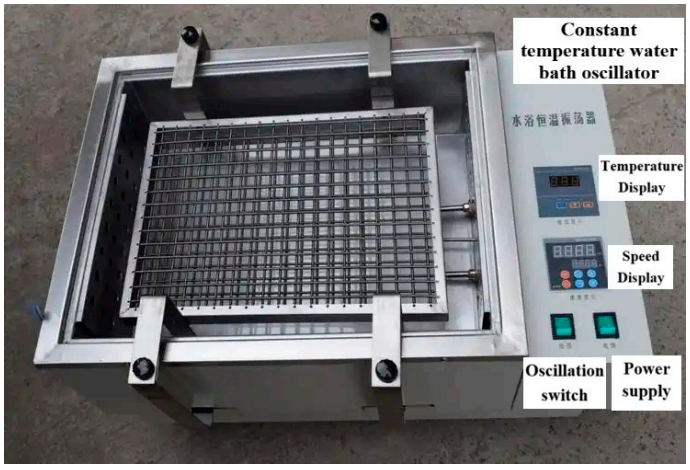

Figure 3. Image of THZ-82 thermostatic oscillator used in adsorption experiments.

2.2.2. Experimental Design for Adsorption Experiments

1. Adsorption Equilibrium Time

In the work of Xia et al. [33], the adsorption kinetics experiments revealed that NAPL is adsorbed by fine micro-sized sand aggregates in less than 24 h. To ensure the accuracy of the data obtained, the adsorption time between quartz sand and NAPL solution in this study was established at intervals of 1 h, 3 h, 6 h, 9 h, 12 h, 24 h, and 48 h. A total of 150 mL of NAPL solution was measured using a graduated cylinder and subsequently added to seven stoppered Erlenmeyer flasks, labeled 1 through 7. The thermostatic water bath oscillator was set to the desired temperature and oscillation frequency, with a preheating period of 20 min following stabilization of the water temperature at 20 °C, after which the flasks were placed into the oscillator. Subsequently, 3 g of quartz sand was introduced into each flask, and the water bath oscillator was activated. One flask was removed from the oscillator at each of the specified time intervals: 1 h, 3 h, 6 h, 9 h, 12 h, 24 h, and 48 h. For the determination of NAPL concentration (NAPL concentration determination

method in Section 2.5), 2 mL of the middle-layer solution was extracted from each flask. A curve depicting the relationship between NAPL concentration (C) and time (t) was plotted. The experiment was concluded when the slope of the curve stabilized, indicating that the medium had reached adsorption equilibrium.

2. Theoretical Maximum Adsorption Capacity

A series of NAPL solutions with varying concentration gradients, including the maximum NAPL concentration observed at the conclusion of the soil column experiment, was prepared. For each concentration, 150 mL of NAPL solution was transferred into a 250 mL stoppered Erlenmeyer flask. The temperature and oscillation frequency of the thermostatic water bath oscillator were adjusted, and once the water temperature stabilized at 20 °C, the flasks were placed into the oscillator for a preheating period of 20 min. Subsequently, 3 g of quartz sand was added to each flask, and the oscillator was activated. Oscillation was ceased once the adsorption equilibrium time was attained. A 2 mL sample from the middle layer of each solution was extracted, and NAPL concentration was determined (NAPL concentration determination method in Section 2.5). The adsorption capacity of each medium was calculated using the mass conservation method, and an isothermal adsorption curve was plotted and fitted. Utilizing the packing mass of the lens in Table 3 and NAPL concentration at the conclusion of the soil column experiment, the maximum adsorption capacity of each lens for NAPL was calculated.

2.3. Mercury Intrusion Porosimetry

2.3.1. Experimental Equipment and Materials for Mercury Intrusion Experiment

The mercury intrusion porosimetry test was conducted at Qinghai University, and experiment was MicroActive Autopore V 9620 mercury intrusion porosimeter, produced by Micromeritics, Norcross, GA, USA (Figure 4). The principal materials employed in the experiment comprised quartz sand, with its specifications and physical properties in Table 2, as well as an FA2004N electronic balance.

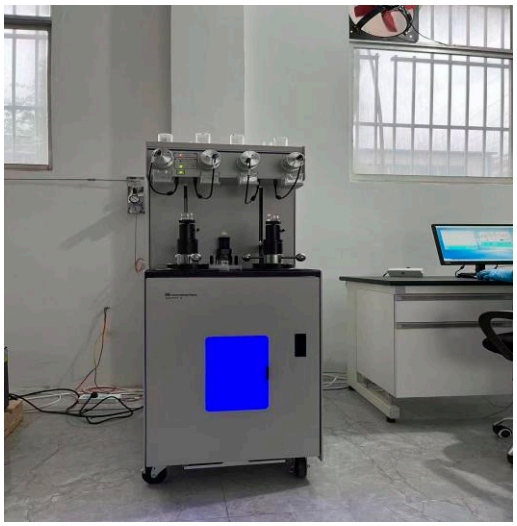

Figure 4. Image of mercury intrusion porosimeter for pore structure analysis.

2.3.2. Experimental Design for Mercury Intrusion Porosimetry

According to the principles of mercury intrusion porosimetry [34,35], the testing process begins with mercury entering larger pores at a specified pressure. The porosimeter measures these larger pores. As the pressure is incrementally increased, mercury progressively penetrates smaller pores, thereby facilitating the determination of pore size and the characteristics of pore volume distribution within the sample.

To measure the pore size distribution of each lens, a predetermined amount of quartz sand was accurately weighed and subsequently placed into 5 cc sample tubes. Mercury intrusion experiments were performed to ascertain the pore size distribution of each sample.

2.4. Particle Size Analysis

2.4.1. Experimental Apparatus and Materials for Particle Size Analysis

The primary apparatus utilized for particle size analysis comprised sieves with varying mesh sizes and a Mastersizer 3000 laser particle size analyzer (The Mastersizer 3000 laser particle size analyzer is produced by Malvern Instruments Limited in Malvern, UK). The principal materials employed in this analysis included quartz sand, with the specifications and physical properties in Table 2, as well as an FA2004N electronic balance.

2.4.2. Particle Size Analysis Design

The analysis boundaries were established utilizing both the sieving method and the laser particle size analyzer, tailored to the characteristics of the media under investigation. For the aquifer media, specifically Quartz Sand 1, which exhibits relatively large particle sizes, the sieving method was employed. A sample weighing 50 g of Quartz Sand 1 was accurately measured using a balance and subsequently placed in a series of sieves arranged in descending order of mesh size, from top to bottom. The sieves were subjected to horizontal shaking to facilitate the measurement of the mass of quartz sand retained on each sieve. A particle size distribution curve was generated based on the mass percentage of quartz sand corresponding to various particle sizes, thereby yielding the results of the particle size analysis. In contrast, for Quartz Sands 2, 3, 4, and 5, the particle size distribution was determined through the use of a laser particle size analyzer. The percentage of particles within each size range was quantified, and cumulative particle size curves were constructed to derive the particle size analysis results.

2.5. NAPL Concentration Determination

The liquid collected in the sampling bottles from the soil column simulation experiment comprised a mixture of NAPL and water. To accurately quantify NAPL concentration in the effluent, a standard curve correlating NAPL concentration with chemical oxygen demand (COD_{Cr}) was developed by preparing standard solutions [36]. Subsequently, NAPL concentration in the effluent was determined using this standard curve.

2.5.1. Experimental Apparatus and Materials for NAPL Concentration Determination

HACH DR3900 spectrophotometer(The HACH DR3900 spectrophotometer is produced by Hash Corporation in Loveland, CO, USA), an emulsifier, HACH DRB200 digester, 500 mL beakers, pipettes, and HACH reagent tubes.

2.5.2. Establishment of Standard Curve

The procedure for establishing the standard curve was conducted as follows: Eight NAPL–water mixed solutions were prepared, exhibiting concentration gradients of 20 mg/L, 50 mg/L, 100 mg/L, 200 mg/L, 400 mg/L, 600 mg/L, 800 mg/L, and 1200 mg/L, with each solution having a volume of 500 mL in separate beakers. The emulsifier speed was set to 5000 r/min, and each solution was emulsified from low to high concentration for a duration of 3 min. Following the emulsification process, 2 mL of each sample was extracted using a pipette and transferred into HACH COD_{Cr} tubes containing potassium dichromate as the indicator. The samples were then digested at a temperature of 150 °C for 2 h utilizing a HACH DRB200 digester. After digestion, the tubes were allowed to cool to room temperature, and the COD_{Cr} values of the samples were measured using a spectrophotometer.

A standard curve correlating the concentration of NAPL with COD_{Cr} was established using the aforementioned procedure (Figure 5). The fitted equation is expressed as C_{sj} = 0.9754 C_{cs} + 33.555, where C_{sj} represents NAPL concentration in the prepared solution and C_{cs} represents NAPL concentration as determined by the spectrophotometer. The correlation coefficient (R^2) was 0.987, indicating a strong degree of correlation and thereby validating the feasibility of utilizing COD_{Cr} measurements to quantify diesel concentration. All experiments conducted for the determination of NAPL concentration in this study adhered to this method for NAPL quantification.

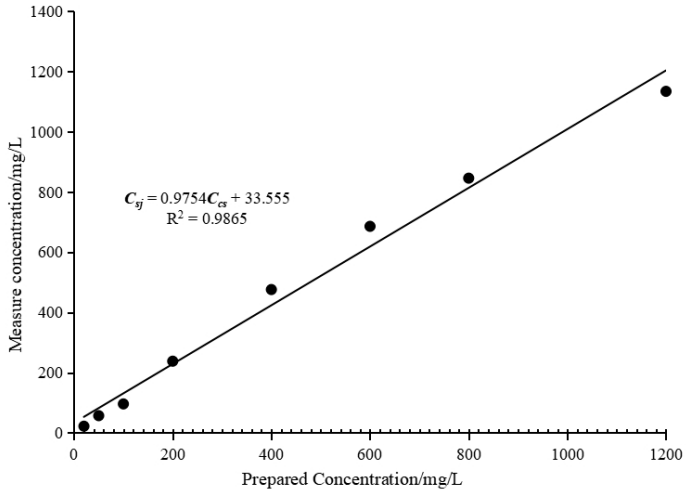

Figure 5. NAPL relationship between NAPL concentration and CODCr for quantification.

3. Results

3.1. Soil Column Experiment Results

3.1.1. Experimental Results of Soil Columns with Different K_{mn}

Following the conclusion of the soil column simulation experiments, the residual saturation of NAPL in each experimental group Sr, the residual saturation of NAPL in the lens S_R, and the concentration of NAPL in the solution of each experimental group C_D are summarized in Table 4.

Table 4. Results of soil column simulation experiments for NAPL residuals.

Experiment No.	Permeability Coefficient Ratio K_{mn}	Residual NAPL Saturation S_r (%)	Residual NAPL Saturation in Lens S_R (%)	NAPL Concentration in Effluent C_D (mg/L)
1	1	8.54	8.54	17.9
2	5	8.71	11.19	22.3
3	11	9.09	17.20	27.2
4	23	9.93	30.46	29.7
5	50	10.22	35.05	34.2

3.1.2. Relationship Between Overall Sr and K_{mn}

Low-permeability lenses significantly affect the overall Sr of NAPL within the medium. The data obtained from the soil column simulation experiments (Table 4) illustrate the relationship between Sr and K_{mn} (Figure 6).

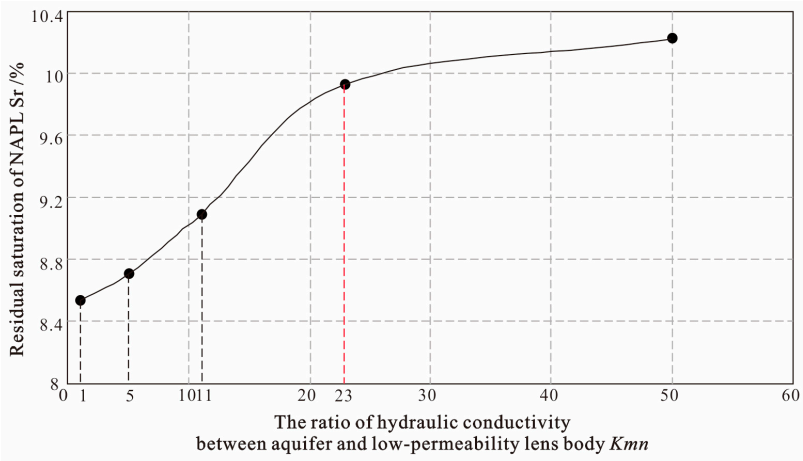

Figure 6. Relationship curve between NAPL residual saturation (Sr) and permeability coefficient gradient (K_{mn}).

As shown in Figure 6, Sr tends to increase with an increase in K_{mn}. However, when K_{mn} surpasses 23, the slope of the curve exhibits a reduction in steepness. For $K_{mn} < 23$, variations in K_{mn} exert a more significant impact on Sr compared to the range where K_{mn} is between 23 and 50.

According to existing studies, NAPL residuals in aquifers characterized by lenses predominantly arise from adsorption and entrapment processes. To investigate the sensitivity of NAPL residuals to particle adsorption and pore entrapment within low-permeability lenses, a series of particle adsorption experiments were conducted on both the aquifer and the lenses. The results of these experiments are detailed in Section 3.2.

3.2. Adsorption Experiment Results

3.2.1. Adsorption Equilibrium Time

Utilizing five types of quartz sand (1, 2, 3, 4, and 5) as adsorbents, an NAPL solution with a concentration of 35.2 mg/L was formulated, informed by the results from the soil column experiment (Table 4). An adsorption kinetics experiment was subsequently performed, and analysis of the adsorption kinetics curve (Figure 7) revealed that the time required to reach adsorption equilibrium was 24 h.

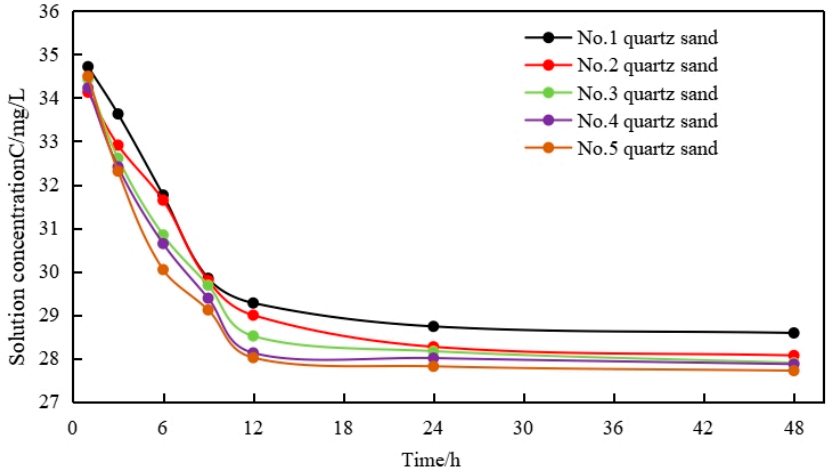

Figure 7. Adsorption kinetics curves of different quartz sands.

3.2.2. Maximum Adsorption Capacity

Isothermal adsorption experiments were conducted over a duration of 24 h, utilizing varying concentrations of NAPL solutions. Figure 8 illustrates the isothermal adsorption

curves corresponding to each individual medium. To ascertain the theoretical maximum adsorption capacity of each medium, a Langmuir-type equation was employed, which delineates the relationship between the theoretical maximum adsorption capacity of the particle surface (y, μg/g) and the equilibrium solute concentration (C_P, mg/L) in the solution. All experimental data were analyzed using the Langmuir adsorption model, and the isothermal adsorption equilibrium equations for the two different media are presented in Table 5. The NAPL concentration in the solution, as recorded upon the completion of the soil column experiment C_D (Table 4), represents the equilibrium concentration. The y of the quartz sand particle surfaces was determined by substituting the corresponding C_D into the adsorption equilibrium equation.

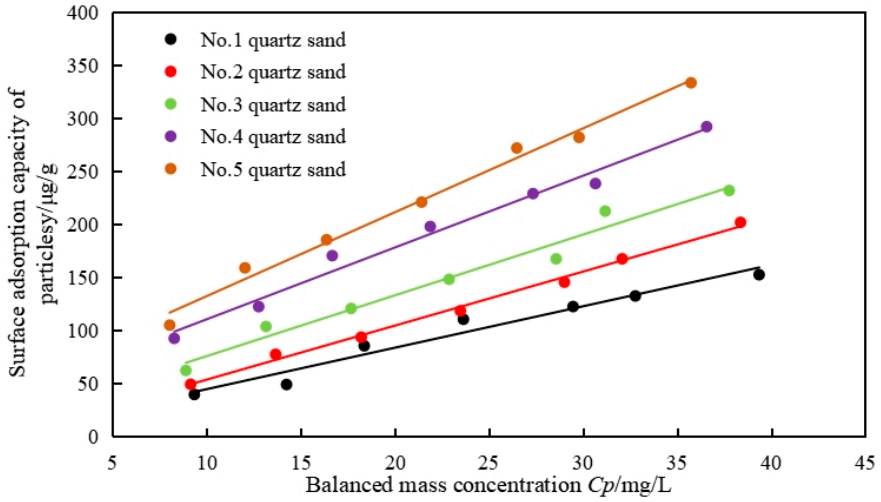

Figure 8. Isothermal adsorption curves of various quartz sands.

Table 5. Adsorption isotherm equations for quartz sands of varying particle sizes.

Medium	Langmuir	Correlation Coefficient (R^2)	Equilibrium Concentration C_D (mg/L)	Theoretical Maximum Adsorption Capacity y (μg/g)
No. 1 quartz sand	$y = 3.906 \times C_P + 5.5742$	0.9893	17.9	75.297
No. 2 quartz sand	$y = 5.093 \times C_P + 2.6649$	0.9826	22.3	107.228
No. 3 quartz sand	$y = 5.729 \times C_P + 18.499$	0.9717	27.2	156.936
No. 4 quartz sand	$y = 6.766 \times C_P + 42.869$	0.995	29.7	208.288
No. 5 quartz sand	$y = 7.907 \times C_P + 53.288$	0.9604	34.2	297.091

Based on the theoretical maximum adsorption capacity y in Table 5, in conjunction with m_t (Table 3) and ρ_o (Table 1), the maximum adsorption capacity in the lens body Sc can be determined as follows:

$$S_c = \frac{y \times m_t}{10^6 \times \rho_0} \quad (2)$$

Based on S_R in Table 4, the porosity n in Table 2, and the lens body volume V_t, the residual amount of NAPL in the lens body S_t can be determined. The equation for this calculation is given as follows:

$$S_t = S_R \times n \times V_t \quad (3)$$

The proportion of the adsorption quantity in relation to the residual amount of NAPL within the lens body is $\frac{Sc}{St} \times 100\%$, and the percentage of the retention amount in relation to the residual amount of NAPL within the lens body is $100\% - \frac{Sc}{St} \times 100\%$. The results of the aforementioned calculations are outlined in Table 6.

Table 6. Summary of NAPL residual quantities, adsorption, and retention in low-permeability lenses.

Experiment Number	NAPL Residual Amount in Lens Body S_t (mL)	Maximum Adsorption Amount of NAPL in Lens Body S_c (mL)	Percentage of Adsorption Amount in NAPL Residual Volume (%)	Percentage of Retention Amount in NAPL Residual Volume (%)
1	7.038	0.027	0.38	99.62
2	8.841	0.040	0.45	99.55
3	13.456	0.061	0.45	99.55
4	23.793	0.082	0.34	99.66
5	27.361	0.119	0.43	99.57

As shown in Table 6, the maximum adsorption capacity of NAPL by low-permeability lens body particles constitutes only 0.45% of the total residual volume of NAPL, whereas the retention capacity accounts for over 99.5% of the total NAPL residual volume. Therefore, retention emerges as the primary factor affecting NAPL residuals within the low-permeability lens body of the aquifer. The adsorption of NAPL by particles is affected by both particle size and specific surface area. To further investigate the relationship between particle size and NAPL adsorption, particle size distribution tests were conducted.

3.3. Particle Size Distribution Results

Figure 9 depicts the cumulative particle size distribution curves for each type of quartz sand, as derived from the results of the particle size distribution experiment. Table 7 summarizes the average particle diameter, uniformity coefficient Cu, and curvature coefficient ***Cs*** for each type of quartz sand, as determined from the cumulative distribution curve.

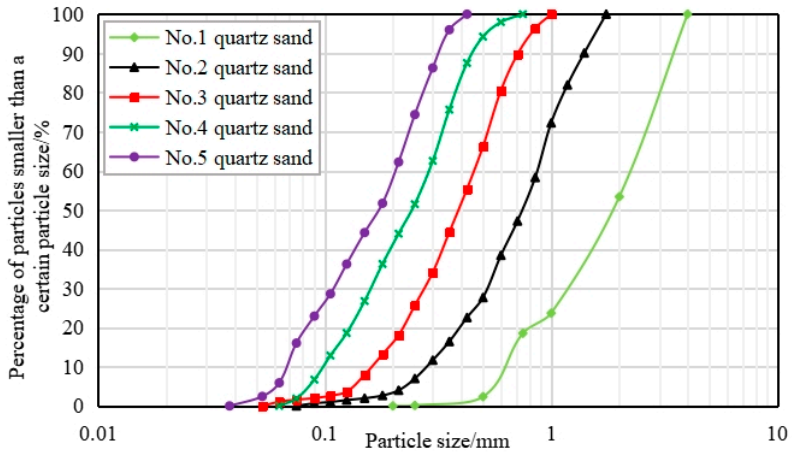

Figure 9. Cumulative curve of particle distribution.

Table 7. Particle size and distribution metrics for quartz sand types.

Medium No.	Average Particle Diameter D_{50} (mm)	Uniformity Coefficient C_u	Curvature Coefficient C_s
No. 1 quartz sand	1.80	3.77	1.03
No. 2 quartz sand	0.75	3.15	1.14
No. 3 quartz sand	0.39	2.94	1.04
No. 4 quartz sand	0.24	3.13	1.11
No. 5 quartz sand	0.18	3.01	1.03

The average particle size is a physical parameter that characterizes the overall dimensions of particles within a given medium. C_u and C_s serve as indicators of the distribution of various particle sizes. A C_u value of less than 5 signifies a relatively uniform distribution of particles, while a C_s value between 1 and 3 suggests that there are no missing

particle sizes within the specified range. As shown in Table 8, the particle sizes of different quartz sands in the lenses exhibit variability. However, the values of C_u and C_s remain notably similar.

Table 8. Proportions of pore categories in quartz sand samples.

Medium No.	The Proportion of Macropores n_{max} (%)	The Proportion of Mesopores n_{mid} (%)	The Proportion of Small Pores n_{min} (%)
No. 1 quartz sand	91.83	5.35	2.82
No. 2 quartz sand	86.12	10.64	3.24
No. 3 quartz sand	69.29	25.25	5.46
No. 4 quartz sand	36.04	56.11	7.85
No. 5 quartz sand	9.98	63.1	26.92

The difference between low-permeability lenses and aquifer media is primarily attributed to the permeability coefficient. The pore characteristics serve as a direct factor affecting the disparity in permeability, which in turn affects the retention of residual NAPL. To investigate the mechanisms underlying residual NAPL retention in lenses, mercury intrusion experiments were performed, and the results are presented in Section 3.4.

3.4. Mercury Intrusion Experiment Results

3.4.1. Pore Distribution of Each Low-Permeability Lens Body

The cumulative pore size distribution curves are presented in Figure 10, where the horizontal axis represents the pore diameter and the vertical axis denotes the volume fraction of pores with diameters smaller than a specified value. An analysis of these curves reveals that the pores in quartz sands 1, 2, 3, 4, and 5 are predominantly concentrated within the diameter range of 20 μm to 300 μm. Notably, quartz sand 1 exhibits the highest curve among all the samples, indicating that it possesses the largest pore sizes across the various diameter ranges when compared to the other groups of quartz sands.

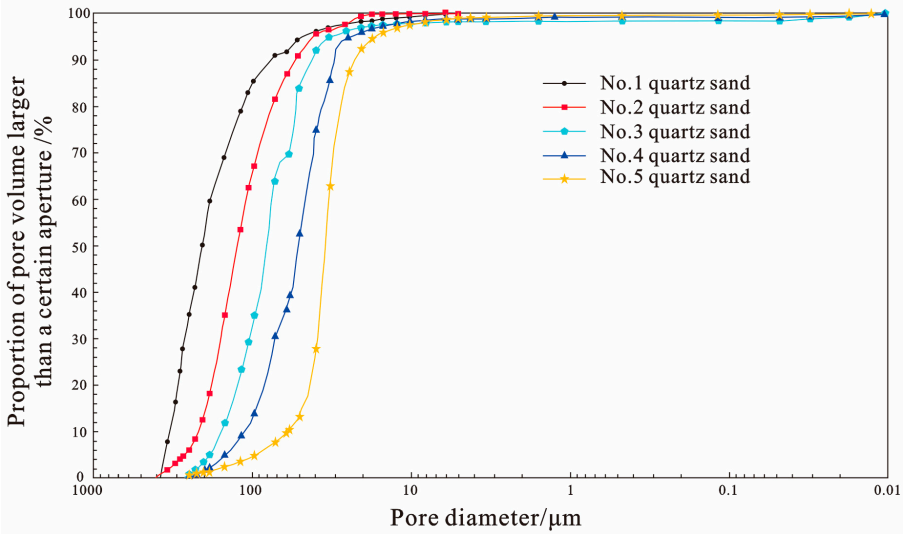

Figure 10. Cumulative curve of pore diameter distribution.

Huang et al. [37] suggested that pores with diameters ranging from 0 μm to 30 μm are classified as storage pores, which encompass bound water pores. Pores with diameters between 30 and 100 μm are identified as capillary pores, whereas pores exceeding 100 μm exhibit minimal capillary force and are categorized as gravity water pores. Thomasson [38] revealed that when pore diameters surpass 60 μm, the capillary forces diminish, resulting in these pores showing characteristics typical of gravity water

pores. Consequently, pores are categorized into three classifications based on their diameters: macropores (diameter > 60 μm), mesopores (diameter = 30~60 μm), and small pores (diameter < 30 μm). The proportions of the pore volume of each type are outlined in Table 8.

3.4.2. Experimental Results

To elucidate the mechanism by which a low-permeability lens affects residual NAPL, a correlation analysis was conducted between the porosity of the aforementioned pore types and S_R of both the aquifer and the lens body (Figure 11).

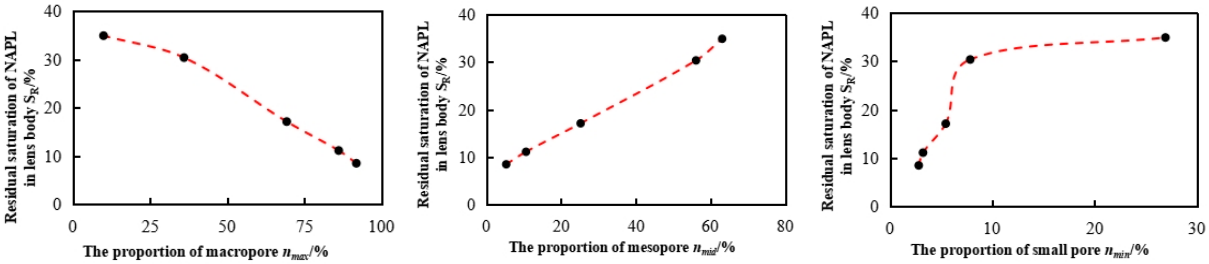

(**a**) (**b**) (**c**)

Figure 11. The variation curve of residual saturation SR of lens body with the proportion of various pore volumes. NOTE: (**a**) is the variation curve of S_R with macropore porosity, (**b**) is the variation curve of S_R with mesopore porosity, and (**c**) is the variation curve of S_R with small pore porosity.

As shown in Figure 11, the S_R of the aquifer and lens body exhibits a negative correlation with the proportion of macropore volume (n_{max}). Specifically, when the volume fraction of macropores surpasses 36.04%, the slope of the curve increases, resulting in an accelerated rate of change in S_R (Figure 11a). Conversely, S_R shows a positive correlation with the proportion of mesopore volume (n_{mid}), exhibiting an approximately linear increase (Figure 11b). Additionally, S_R is positively correlated with the small pore volume (n_{min}). Notably, when nmin is below 7.85%, the slope of the curve also increases, which contributes to a heightened rate of change in S_R (Figure 11c).

4. Discussion

4.1. Effects of Particle Adsorption on NAPL

Based on y in Table 6 and the average particle diameter (D_{50}) in Table 7, a curve illustrating the relationship between theoretical maximum adsorption capacity and particle size was generated (Figure 12). The data indicate that the adsorption capacity diminishes as particle size increases, conforming to a power-law function. The ability of quartz sand to adsorb NAPL in solution can be attributed to the similarity in the double electric layer structure present on the surfaces of both quartz sand and NAPL particles. Upon contact, a common counter-ion layer is established. Given the substantial disparity in particle size and mass between the two, the attractive force of the common counter-ion layer is adequate to facilitate the adherence of dissolved NAPL to the surfaces of quartz sand particles, thereby forming a relatively stable structure [39–41]. Therefore, water flow alone is insufficient to completely separate these entities, enabling quartz sand particles to effectively adsorb dissolved NAPL.

The observed decrease in adsorption capacity, which follows a power-law function as particle size increases, can be attributed to the relationship between the adsorption of soluble NAPL by quartz sand and the specific surface area of the particles. Specifically, a larger specific surface area correlates with a greater quantity of NAPL that can be adsorbed. The specific surface area increases exponentially as particle size decreases [42–44]. Therefore,

smaller particles exhibit higher adsorption capacities, and y can be represented in the form of a power-law function.

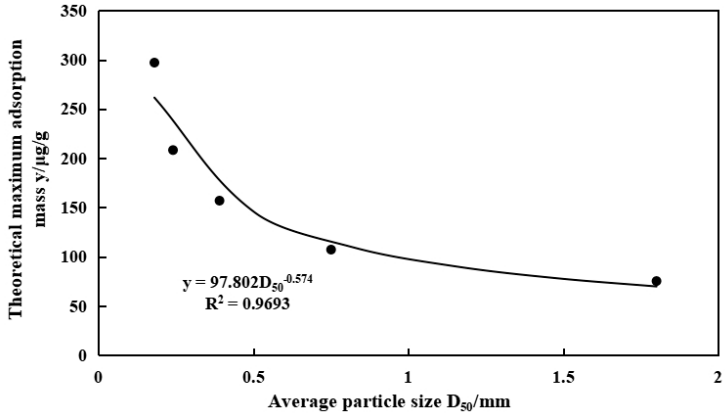

Figure 12. The variation law of adsorption capacity with particle size.

This study elucidates that the adsorption capacity of quartz sand particles for NAPL is relatively limited for the following reasons: 1. The water solubility of NAPL is exceedingly low, with concentrations typically in ppm range. As a result, the maximum adsorption of NAPL onto quartz sand particles is constrained. 2. This study utilized high-purity quartz sand, primarily composed of silicon dioxide, which possesses a crystalline structure and a smooth surface with few active adsorption sites. Its ability to adsorb NAPL is relatively low. Therefore, the retention of low-permeability lens bodies is the most important cause of residual NAPL.

4.2. Effects of Pore Characteristics on NAPL Retention

To elucidate the relationship between various types of porosity and the residuals of NAPL, as well as to investigate the effects underlying the variations in *Sr* across different pore size ranges, an analysis of the forces acting on residual NAPL droplets within the pores was performed (Figure 13).

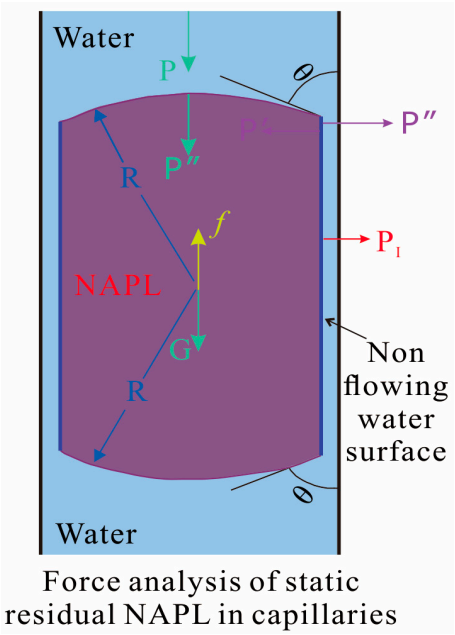

Figure 13. Force analysis of static residual NAPLs in capillaries.

As shown in Figure 13, the pores function as capillary tubes with a uniform diameter, while the residual NAPL is represented as a stationary spherical droplet. This droplet is subjected to several forces: the water flow pressure (p), its own gravitational force (G), buoyancy (f), the spherical capillary force exerted on the pore wall (P″), and the cylindrical capillary force acting at the center of the pore (P′). The resultant force (P_I), which is directed towards the pore wall, is the vector sum of P″ and P′. The calculations for P″, P′, and P_I are derived based on the Laplace equation [45], where P″ and P′ can be obtained as follows:

$$P'' = \frac{2\sigma cos\theta}{r} \tag{4}$$

$$P' = \frac{\sigma}{r} \tag{5}$$

Therefore, P_I can be determined as follows:

$$P_I = \frac{2\sigma}{r}(cos\theta - 0.5) \tag{6}$$

The function of P_I is to enhance the adhesion of an NAPL droplet to the pore wall. For the droplet to migrate, the additional frictional resistance along the pore wall induced by P_I must be surmounted. Given that the residual NAPL exists as a spherical droplet, θ remains constant, while the magnitude of P_I is contingent upon the pore radius (r). An increase in pore radius results in a reduction in resistance to NAPL migration, thereby decreasing Sr. Conversely, a decrease in pore radius leads to an increase in resistance to NAPL migration, resulting in a higher Sr.

Huang [37] and Thomasson [38] suggested that when the pore diameter exceeds 60 μm, the capillary forces within the pores become weak. In such instances, the driving force for the migration of NAPL surpasses the capillary force, resulting in reduced resistance to NAPL migration and a decreased likelihood of NAPL retention. Therefore, Sr demonstrates a negative correlation with n_{max}; specifically, as n_{max} increases, Sr decreases (Figure 11a). Conversely, when the pore diameter ranges from 30 μm to 60 μm, the pores exhibit enhanced capillary action. In this scenario, the capillary force exceeds the driving force for NAPL migration, thereby increasing resistance to NAPL movement and enhancing the probability of NAPL residuals. Therefore, Sr is positively correlated with n_{mid}. As nmid increases, Sr also increases (Figure 11b). In cases where the pore diameter is less than 30 μm, the pores exhibit very strong capillary forces and may contain certain extremely small capillary pores. In these situations, discontinuous NAPL droplets that enter these pores can become encapsulated by water and retained within the pores [46]. However, the storage capacity for residual NAPL within these pores is limited, which consequently restricts the amount of NAPL that can be retained. Although there is a positive correlation between Sr and n_{min}, this correlation diminishes when the porosity exceeds 7.8%, as the increase in Sr slows down (Figure 11c). Therefore, while small pores do contribute to NAPL residuals, their effect on Sr is less pronounced than mesopores.

4.3. Effects of K_{mn} *on* Sr

To examine the effect of K_{mn} on Sr, K_{mn} was designated as the independent variable. The proportions of various pore types in Table 8 were utilized as dependent variables. The resulting correlation variation curves are illustrated in Figure 14.

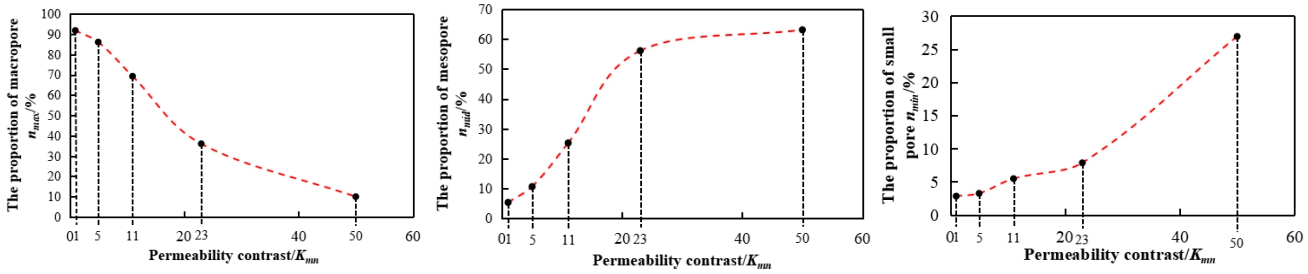

Figure 14. Correlation curve between the proportions of various pore volumes and the permeability contrast K_{mn}. NOTE: (**a**) is the variation curve of n_{max} with K_{mn}, (**b**) is the variation curve of n_{mid} with K_{mn}, and (**c**) is the variation curve of n_{min} with K_{mn}.

As shown in Figure 14, an increase in K_{mn} is associated with a decrease in n_{max}. Specifically, when K_{mn} is less than 23, the rate of change in the curve is relatively pronounced, suggesting that for K_{mn} values below 23, n_{max} diminishes rapidly as K_{mn} increases. In the range of K_{mn} between 23 and 50, the rate of decrease in n_{max} diminishes with further increases in K_{mn} (Figure 14a). Conversely, n_{mid} shows an increasing trend with rising K_{mn}. For K_{mn} values below 23, the rate of change is significant, indicating that n_{mid} increases rapidly as K_{mn} rises. However, within the interval of K_{mn} from 23 to 50, the rate of increase in n_{mid} begins to slow (Figure 14b). Similarly, n_{min} also increases with an increase in K_{mn}. Notably, when K_{mn} is less than 23, the rate of change is relatively modest, indicating that n_{min} increases gradually as K_{mn} rises. In contrast, for K_{mn} values within the range of 23 to 50, the increase in n_{min} accelerates (Figure 14c).

The integration of the experimental results in Section 3.1 with the effect of NAPL residuals discussed in Section 4.2 allows for the conclusion that the inflection point observed at K_{mn} = 23 in Sr versus K_{mn} curve (Figure 6) is attributable to specific changes in pore volume distribution. When K_{mn} is less than 23, there is a rapid decrease in n_{max} (diameter > 60 μm), accompanied by a rapid increase in n_{mid} (diameter = 30~60 μm), while n_{min} (diameter < 30 μm) increases at a slower rate. This dynamic results in a significant increase in the space available for NAPL residuals. Conversely, within the range of $K_{mn} \in (23, 50)$, the rate of increase in Sr diminishes primarily due to a slower increase in n_{mid}, contrasted with a rapid increase in n_{min}. This shift leads to a more gradual increase in the space available for NAPL residuals.

5. Conclusions and Outlook

5.1. Conclusions

1. Experimental Results from Soil Columns with Different K_{mn}: Sr generally increases with K_{mn}, as demonstrated by the experimental results. However, when K_{mn} exceeds 23, an inflection point is observed. Specifically, for K_{mn} less than 23, Sr increases rapidly with increasing K_{mn}. In the range $K_{mn} \in (23, 50)$, the increase in Sr slows down. This phenomenon can be attributed to the following: when $K_{mn} < 23$, n_{max} (diameter > 60 μm) decreases sharply, n_{mid} (diameter = 30~60 μm) increases significantly, and n_{min} (diameter < 30 μm) increases gradually. This leads to an enhanced availability of space for NAPL residuals. However, when $K_{mn} \in (23, 50)$, the rate of increase in Sr slows down primarily because n_{mid} increases at a reduced rate, while n_{min} increases rapidly, limiting the available space for NAPL residuals.
2. Contribution of Particle Adsorption and Retention to NAPL Residuals: The maximum contribution of NAPL adsorption by particles in low-permeability lenses to the total NAPL residual is only 0.45%, while retention accounts for over 99.5% of the total

NAPL residual. This indicates that the primary factor affecting NAPL residuals in low-permeability lenses is retention. This result is explained by the fact that although both quartz sand and NAPL particles exhibit similar double-layer structures on their surfaces, enabling the formation of a common ion layer upon contact, the attraction between these particles is sufficient to cause NAPL to adhere to the surface of quartz sand particles. This interaction forms a stable structure that facilitates NAPL adsorption. However, due to the extremely low solubility of NAPL in water, and because the quartz sand used in this study is of high purity with a highly crystalline structure and few active adsorption sites, its capacity for NAPL adsorption is limited. Therefore, retention is the dominant factor controlling NAPL residuals in low-permeability lenses.

3. Effect of Pore Size Distribution on NAPL Residuals: The primary reason for the formation of NAPL residuals in low-permeability lenses is the differential distribution of pore sizes, specifically n_{max} (diameter > 60 μm), n_{mid} (diameter = 30~60 μm), and n_{min} (diameter < 30 μm). In macropores, the resistance to NAPL migration is minimal, meaning that the larger n_{max}, the lower Sr. In contrast, mesopores exhibit the strongest capillary action, which hinders NAPL migration, thereby facilitating the formation of NAPL residuals. Therefore, a larger n_{mid} results in a higher Sr. Small pores, which contain bound water, exhibit strong capillary action but are limited in their ability to store NAPL due to the small volume of space available for liquid flow. Consequently, while small pores contribute to NAPL residuals, their effect on NAPL saturation is less significant than mesopores.

5.2. Outlook

This study takes diesel as an example to investigate the primary controlling factors of NAPL residuals in low-permeability lenses of aquifers and examines the effects underlying their persistence. However, diesel is an LNAPL, and its properties differ significantly from those of DNAPLs. Therefore, the conclusions of this study are applicable to LNAPL pollutants with properties similar to diesel, such as aviation kerosene and xylene. In addition, high-purity quartz sand was used for the low-permeability lenses in this study. But, in actual subsurface lenses, there are often a large number of clay minerals, which can increase the influence of adsorption on NAPL residues. Whether the conclusions of this study are applicable when clay minerals are present in low-permeability lenses remains unknown.

Consequently, in the next step, we will use trichloroethylene (TCE) as a representative of DNAPLs to continue the research on NAPL residues in low-permeability lenses of aquifers [47]. Different proportions of clay minerals will be added to the low-permeability lenses to explore whether DNAPL residues in low-permeability lenses of aquifers conform to this conclusion, and whether the presence of clay minerals in low-permeability lenses will change the NAPL residue mechanism. This will further reveal the influencing mechanism of NAPL residues in low-permeability lenses of aquifers.

Author Contributions: Conceptualization, W.S., L.S. and S.W.; methodology, W.S. and S.W.; software, W.S., J.Y. and H.L.; validation, W.S. and S.W.; formal analysis, W.S. and H.L.; investigation, S.W., L.S. and J.Y.; resources, W.S., L.S. and S.W.; data curation, W.S. and J.Y.; writing—original draft preparation, W.S.; writing—review and editing, W.S. and L.S.; project administration, J.Y. and H.L.; funding acquisition, W.S. and L.S. All authors have read and agreed to the published version of the manuscript.

Funding: This research was supported by the National Natural Science Foundation of China (No. 42007171), the S&T Program of Hebei, (grant number 242S4201Z, 22377602D) and Basal Research Found of IHEG (CAGS:sk202319).

Data Availability Statement: The original contributions presented in this study are included in this article; further inquiries can be directed to the corresponding author.

Acknowledgments: The authors are thankful for the support from the laboratory of Qinghai University in terms of experiments.

Conflicts of Interest: The authors declare no conflicts of interest.

References

1. Qiu, J. China faces up to groundwater crisis. *Nature* **2010**, *466*, 308. [CrossRef] [PubMed]
2. Sheng, Y.; Tian, X.; Wang, G.; Hao, C.; Liu, F. Bacterial Diversity and Biogeochemical Processes of Oil-Contaminated Groundwater, Baoding, North China. *Geomicrobiol. J.* **2016**, *33*, 537–551. [CrossRef]
3. Fei, G.; Feng, L.; Wang, H. Numerical modelling of the dynamic process of oil displacement by water in sandstone reservoirs with random pore structures. *J. Groundw. Sci. Eng.* **2021**, *9*, 233–244.
4. Li, S.; Liu, F.; Li, W.; Li, C.; Huang, F.; Jin, S.; Liu, J.; Yang, L.; Piao, H.; Zhang, Y.; et al. Prioritization of organic contaminants in China's groundwater based on national-scale monitoring data and their persistence, bioaccumulation, and toxicity. *Sci. Total Environ.* **2024**, *929*, 172656. [PubMed]
5. Zhang, M.; Guo, C.; Shi, C.; Ning, Z.; Chen, Z. A quantitative redox zonation model for developing natural attenuation-based remediation strategy in hydrocarbon-contaminated aquifers. *J. Clean. Prod.* **2021**, *290*, 125743. [CrossRef]
6. Ye, W.; Jin, Q.; Huang, Y.; Tang, Y. Progress in Experimental Research on Groundwater Pollution. *J. Hydraul. Eng.* **2005**, *36*, 251–255.
7. Monteiro, L.; Traunspurger, W.; Roeleveld, K.; Lynen, F.; Moens, T. Direct toxicity of the water-soluble fractions of a crude and a diesel-motor oil on the survival of free-living nematodes. *Ecol. Indic.* **2018**, *93*, 13–23.
8. Sheng, Y.; Liu, Y.; Yang, J.; Dong, H.; Liu, B.; Zhang, H.; Li, A.; Wei, Y.; Li, G.; Zhang, D. History of petroleum disturbance triggering the depth-resolved assembly process of microbial communities in the vadose zone. *J. Hazard. Mater.* **2021**, *402*, 124060. [CrossRef]
9. Zheng, F.; Gao, Y.; Shi, X.; Wu, J. Influence of groundwater flow velocity and geological heterogeneity on DNAPL migration in saturated porous media. *J. Hydraul. Eng.* **2015**, *46*, 925–933.
10. Shi, Y. Fate and Transport of Typical Organic Pollutants in Saturated Porous Media. Ph.D. Thesis, Nanjing University, Nanjing, China, 2019.
11. Chrysikopoulos, C.V.; Lee, K.Y. Contaminant transport resulting from multicomponent nonaqueous phase liquid pool dissolution in three-dimensional subsurface formations. *J. Contam. Hydrol.* **1998**, *31*, 1–21. [CrossRef]
12. Pan, Y.; Yang, J.; Jia, Y.; Xu, Z. Experimental study on non-aqueous phase liquid multiphase flow characteristics and controlling factors in heterogeneous porous media. *Environ. Earth Sci.* **2016**, *75*, 1–13. [CrossRef]
13. Song, Y.; Hou, D.; Zhao, Y.; Zhu, J.; Zhang, Q.; Qin, C.; Wang, W. Remediation strategies for contanminated groundwater at chemical industrial sites in the Bejing-Tianjin-Hebei region. *Res. Environ. Sci.* **2020**, *33*, 1345–1356.
14. Mateas, D.J.; Tick, G.R.; Carroll, K.C. In situ stabilization of NAPL contaminant source-zones as a remediation technique to reduce mass discharge and flux to groundwater. *J. Contam. Hydrol.* **2017**, *204*, 40–56. [CrossRef] [PubMed]
15. Zhang, X. Identification of the Dominated Soil Structure Factors for Diesel Migration and Residual Under Leaking Condition. Master's Thesis, Chinese Research Academy of Environmental Sciences, Beijing, China, 2015.
16. Shu, S.; Liang, H.; Yuan, Y. Numerical analysis of transportation and distribution of light non-aqueous phase liquids in partially saturated heterogeneous soils. *J. Hydraul. Eng.* **2002**, *11*, 31–37.
17. Cheng, Z.; Wu, J.; Xu, H.; Wang, J.; Gao, Y.; Li, J.; Dong, S. Investigation of the migration characteristic of DNAPL in aquifer with lenses and under the action of surfactant. *China Environ. Sci.* **2014**, *34*, 2888–2896.
18. Wang, L. Experimental Study on Multiphase Flow in Soil Contaminated with Light Non-Aqueous Phase Liquid (LNAPL). Master's Thesis, Chang'an University, Xi'an, China, 2009.
19. Panter, S.E. The Hidden Potential of Mass-based Treatment: A Method for Preventing Rebound. *Remediat. J.* **2015**, *25*, 99–109. [CrossRef]
20. Tao, J.; Shi, X.; Kang, X.; Xu, H.; Wu, J. Numerical analyses of factors affecting the LNAPL source-zone architecture. *Hydrogeol. Eng. Geol.* **2018**, *45*, 132–140.
21. Kueper, B.H.; Abbott, W.; Farquhar, G. Experimental observations of multiphase flow in heterogeneous porous media. *J. Contam. Hydrol.* **1989**, *5*, 83–95. [CrossRef]
22. Liu, H.; Zhou, Q.; Xu, S. Anexperimental investigationof LNAPL migration and redistribution in unsaturated heterogeneous porous media. *Hydrogeol. Eng. Geol.* **2006**, *33*, 52–57.
23. Zhang, Y.; Zhu, S.; Xiao, R.; Wang, J.; Li, F. Vertical transport of polycyclic aromatic hydrocarbons in different particle-size fractions of sandy soils. *Environ. Geol.* **2008**, *53*, 1165–1172. [CrossRef]

24. Shi, X.; Wu, J.; Liu, D.; Jiang, S.; Sun, Y.; Xu, H. Numerical simulation of transportation of dense non-aqueous phase liquids in the subsurface environment. *J. Nanjing Univ.* **2011**, *47*, 299–307.
25. Al-Raoush, R.I. Experimental investigation of the influence of grain geometry on residual NAPL using synchrotron microtomography. *J. Contam. Hydrol.* **2014**, *159*, 1–10. [CrossRef] [PubMed]
26. Zhang, J.; Liu, Z.; Liu, S.; Wei, Q.; Wang, Y.; Lu, L. *Study on Influence of Geological Heterogeneity on Migration of LNAPL in Contaminated Site Through Numerical Analysis*; Springer: Singapore, 2019; pp. 834–841.
27. Chen, X.; Sheng, Y.; Wang, G.; Guo, L.; Zhang, H.; Zhang, F.; Yang, T.; Huang, D.; Han, X.; Zhou, L. Microbial compositional and functional traits of BTEX and salinity co-contaminated shallow groundwater by produced water. *Water Res.* **2022**, *215*, 118277. [CrossRef] [PubMed]
28. Liu, C.; Zhang, F.; Zhang, Y.; Song, S.; Zhang, S.; Ye, H.; Hou, H.; Yang, L.; Zhang, M. Experimental and numerical study of pollution process in an aquifer in relation to a garbage dump field. *Environ. Geol.* **2005**, *48*, 1107–1115.
29. Ning, Z.; Sheng, Y.; Gan, S.; Guo, C.; Wang, S.; Cai, P.; Zhang, M. Metagenomic and Isotopic Insights into Carbon Fixation by Autotrophic Microorganisms in a Petroleum Hydrocarbon Impacted Red Clay Aquifer. *Environ. Pollut.* **2024**, *361*, 124824. [CrossRef]
30. Heidari, P.; Li, L. Solute transport in low-heterogeneity sandboxes: The role of correlation length and permeability variance. *Water Resour. Res.* **2015**, *50*, 8240–8264. [CrossRef]
31. Mackay, D.M.; Cherry, J.A. Groundwater contamination: Pump-and-treat remediation. *Environ. Sci. Technol.* **1989**, *23*, 630–636. [CrossRef]
32. Hunt, J.R.; Sitar, N.; Udell, K.S. Nonaqueous phase liquid transport and cleanup: 1. Analysis of mechanisms. *Water Resour. Res.* **1988**, *24*, 1247–1258. [CrossRef]
33. Xia, Y.; Wang, B.; Qu, Z.; Zhao, Y. Research on the natural attenuation of diesel in aeration zone. *Environ. Eng.* **2024**, *32*, 1085–1089.
34. Li, Y.; Zhang, Y.; Zhang, L.; Hou, J. Characterization on pore structure of tectonic coals based on the method of mercury intrusion, carbon dioxide adsorption and nitrogen adsorption. *J. China Coal Soc.* **2019**, *44*, 1188–1196.
35. Zhang, X.; Kong, L.; Guo, A.; Tuo, Y. Experiment study of pore distribution of strong structural clay under different consolidation pressures. *Rock Soil Mech.* **2014**, *35*, 2794–2800.
36. Sun, L.; Wang, S.-W.; Guo, C.-J.; Shi, C.; Su, W.-C. Using pore-solid fractal dimension to estimate residual LNAPLs saturation in sandy aquifers: A column experiment. *J. Groundw. Sci. Eng.* **2022**, *10*, 87–98.
37. Huang, C.; Xu, J. *Soil Science*; China Agricultural Press: Beijing, China, 2010.
38. Thomasson, A.J. Towards an Objective Classification of Soil Structure. *Eur. J. Soil Sci.* **1978**, *29*, 38–46. [CrossRef]
39. Qian, N.; Wang, Z. *Mechanics of Sediment Transport*; Science Press: Beijing, China, 1986; pp. 28–32.
40. Becher, P. *Emulsions: Theory and Practice*; Reinhold Publishing Corp: New York, NY, USA, 1965.
41. Zhao, G. *Physical Chemistry of Surfactants*; Peking University Press: Beijing, China, 1991; pp. 65–127.
42. Xiao, Y.; Lu, Q.; Cheng, H.; Zhu, X.; Tang, H. Surface properties of sediments and its effect on phosphorus adsorption. *J. Sediment Res.* **2011**, *6*, 64–68.
43. Xiao, Y.; Han, K.; Cheng, H.; Li, Q. Surface Properties of Sediments in the Waterway of Poyang Lake to YangtzeRiver and the Nanjing Reach of Yangtze River. *South-North Water Transf. Water Sci. Technol.* **2014**, *12*, 47–50.
44. Wu, J.; Zheng, X.; Li, L.; Sun, J. Adsorption of Aqueous Oil on Sands and Its Studies of Effective Factors. *Environ. Sci.* **2006**, *27*, 2019–2023.
45. Fetter, C.W.; Boving, T.; Kreamer, D. *Contaminant Hydrogeology*, 2nd ed.; Zhou, N.; Huang, Y., Translators; Higher Education Press: Beijing, China, 2011.
46. Wang, X.; Wang, X.; Li, T.H.Y.; Hou, L. The mechanism of NAPL layer formation in a microfluidic device with dual-permeability: Experiments and numerical simulation. In *IOP Conference Series: Earth and Environmental Science*; IOP Publishing: Bristol, UK, 2021; Volume 675, p. 012175.
47. Chrysikopoulos, C.V.; Harmon, T.C.; Lee, K.Y. Dissolution of a well-defined trichloroethylene pool in saturated porous media: Experimental design and aquifer characterization. *Water Resour. Res.* **2000**, *36*, 1687–1696. [CrossRef]

Disclaimer/Publisher's Note: The statements, opinions and data contained in all publications are solely those of the individual author(s) and contributor(s) and not of MDPI and/or the editor(s). MDPI and/or the editor(s) disclaim responsibility for any injury to people or property resulting from any ideas, methods, instructions or products referred to in the content.

water

MDPI

Article

Field Demonstration of In Situ Slow-Release Oxygen Chemicals Coupled with Microbial Agents for Injection to Remediate BTEX Contamination

Shuai Yang, Shucai Zhang *, Shici Ma, Sheng Zhao and Zhengwei Liu

State Key Laboratory of Chemical Safety, SINOPEC Research Institute of Safety Engineering Co., Ltd., Qingdao 266000, China; yangshu.qday@sinopec.com (S.Y.); masc.qday@sinopec.com (S.M.); zhaos.qday@sinopec.com (S.Z.); liuzw.qday@sinopec.com (Z.L.)

* Correspondence: zhangsc.qday@sinopec.com

Abstract: The global concern for risk control of organic contaminated sites is becoming more and more prominent. Traditional ex situ remediation techniques are costly and damage the site, seriously destroying the soil structure and ecological functions. Therefore, in situ means of combining material injection and microbial remediation have become a potential pathway for the green, economical, and efficient remediation of contaminated sites. In this work, a 200 m^2 test block was selected for the coupled injection of slow-release oxygen materials and microbial agents, and long-term monitoring of groundwater was carried out. The results showed that the slow-release materials could release oxygen for a period of 90 days, which provided an oxidizing environment for microorganisms to rapidly degrade BTEX. For the pre-adapted indigenous degradation bacterial agent test group, the degradation degree of BTEX was up to 98% after 40 days of injection. The results of the application on the field scale proved the feasibility of reinforcing biostimulation for remediation of underground organic contamination through the coupled injection of slow-release oxygen materials and microbial agents. The results provided theoretical and technical support for the in situ remediation of petroleum hydrocarbon-contaminated sites.

Keywords: slow-release oxygen materials; indigenous degrading bacteria; coupled injection; BTEX contamination; aquifer remediation

1. Introduction

BTEX (benzene, toluene, ethylbenzene, and xylene) is a common raw and auxiliary material in the process of petroleum extraction and refining. The structure of the benzene ring means that it can exist stably in the environment, and it is carcinogenic, teratogenic, mutagenic, and highly biotoxic [1]. It causes ecological damage to the ecological environment when it enters into the ground due to accidents, leakage, and other reasons during the production process [2,3]. For a long time, as a difficult point in the treatment of petroleum hydrocarbon pollutants, it has received great attention [4–7]. BTEX contamination remediation commonly uses technologies including gas-phase extraction, enhanced desorption, and chemical oxidation. However, the above remediation technologies have different degrees of technical limitations, such as high safety risks, large treatment costs, and secondary pollution [8]. Microbial degradation technology has received widespread attention because of its advantages of high economic efficiency, simple operation, greenness, and absence of secondary pollution [5,9,10].

There are many microorganisms that can degrade BTEX in nature. Up to now, hundreds of microorganisms that can degrade BTEX have been found around the world, with most of them distributed in ecosystems contaminated by BTEX, and microbial degradation is an effective way to remove BTEX pollutants [11]. Most of the research has focused on

the basic principle, the method of biodegradation, and the growth conditions of the BTEX-degrading bacterial group [12,13]. The degradation pathway and microbial community structure have also received significant attention [14,15]. A variety of microorganisms (e.g., *Pseudomonas* spp., *Pseudomonas syringae*, *Erythrobacter* spp., *Sphingomonas* spp., and *Streptomyces* spp.) can degrade BTEX aerobically, with oxygen as the electron acceptor, and anaerobically under anoxic conditions, with NO_3^-, Fe^{3+}, or SO_4^{2-} as the electron acceptor [16–19]. Wu et al. showed that the microbial community could be remodeled by changing the electron acceptor and the microbial function to improve the degradation of BTEX [10]. Currently, studies on the addition of electron acceptors to enhance the degradation of BTEX are mostly at the stage of indoor experiments or small-scale trials [12,20]. Yang Chufang collected groundwater from a real contaminated site and utilized indoor batch experiments to improve the degradation of BTEX by providing sufficient DO (dissolved oxygen) and obtained suitable parameters for microbial remediation of the contaminated site [21]. Ali et al. added vegetable oils to the contaminated soil and used indoor simulation experiments to conclude that microbial function was significantly enhanced, and therefore vegetable oils can be used as biostimulants to enhance the remediation of BTEX-contaminated soils [22]. Groundwater and soil contamination is a multiscale process and the development of efficient remediation technologies requires research across multiple spatial and temporal scales [23]. Microscale experiments under well-controlled and reproducible setups provide fundamental insights into the mechanisms and optimal conditions of biodegradation [24]. However, the transition from the laboratory to the pilot scale and, ultimately, to the field scale remains challenging as greater uncertainties exist under real-world conditions [25]. The paper by Ellis et al. (2000) presents a landmark study on the successful demonstration of field-scale bioremediation of soil contaminated by trichloroethene (TCE) through the coupled injection of chemical and microbial agents [26]. Therefore, field demonstrations are of far-reaching significance to verify whether the available means of enhanced biostimulation can work for contamination degradation in a real site [27].

BTEX-degrading bacteria can rapidly degrade BTEX under aerobic conditions [28]. The main limitation of in situ microbial remediation technology that failed to be engineered for application and promotion is as follows: the environmental oxygen content of the aquifer location is low [17,29]. After the injection of aerobic bacteria, it cannot be adapted to the micro-oxygenated environment for the bio-utilization of BTEX. It is more likely to die due to the lack of oxygen and the existence of competing flora under the ground, which makes it difficult for the degradation effects to meet expectations [30]. The underground matrix is anisotropic and the pollution is non-homogeneous, which limits microbial activity [31]. It is necessary to define the status of the pollution and utilize the equipment to inject the bacterial agent into the underground pollution-enriched area precisely to make the bacteria play a role [32,33]. Through long-term research and practice, it has been proven that microbial degradation technology has achieved remarkable results in the treatment of petroleum hydrocarbon pollution. In this study, the feasibility and efficiency of microbial degradation technology were further improved by screening and optimizing efficient degradation strains and fine-tuning environmental conditions. This provides strong support for the application of microbial degradation technology to the remediation of actual contaminated sites. Therefore, it is important to further investigate the coupled injection of degrading bacteria and other materials to produce a lasting degradation effect and the precise injection of bacteria and materials to validate the feasibility of in situ enhanced biostimulation for the remediation of BTEX contamination at petrochemical sites. We screened and cultivated highly efficient BTEX indigenous degrading bacterial strains suitable for low-temperature environments based on the contaminated sites, and prepared green and low-cost slow-release oxygen agents to ensure suitable environments for microbial degradation. The degradation effects of contamination under different coupling conditions through indoor batch experiments and sand-box experiments determined the key conditions of the agents and the ratio of the agents, laying the groundwork for the on-site application of the present

project. The main objectives of this work are investigating the spatial and temporal injection conditions of materials/bacteria at the site scale by monitoring the groundwater quality during the injection process and evaluating the pollution degradation effects of commercial and pre-adapted bacterial agents at the site scale by determining the concentration of pollutants in the monitoring wells after injection and remediation. In summary, this study shows remarkable novelty in the microbial degradation of petroleum pollutants (especially BTEX) in groundwater. By exploring the optimization strategy and application conditions of microbial degradation technology, a new idea and method are provided for the ecological restoration of groundwater pollution.

2. Experimental Methodology

2.1. Experimental Materials

The slow-release oxygen material is pre-adapted and based on the reaction between $Ca(OH)_2$ (calcium hydroxide, Sigma-Aldrich, St. Louis, MO, USA, 450146) and hydrogen peroxide (Sigma-Aldrich, HX0636). The purity of the micron-sized material is more than 70% and the oxygen release period is 90–220 days. The slow-release oxygen material was used to provide a suitable aerobic environment for the microbial degradation of pollutants.

Indigenous degrading bacteria were screened from contaminated areas at the test site. The acclimation factor gradient method was used to screen BTEX-degrading bacteria. A mixed bacterial solution that can withstand a high concentration of BTEX and a low-temperature environment was obtained. After further domestication and purification, the highly efficient benzene-degrading strain F was obtained. It belongs to the *Bacillus* sp. F, as determined by molecular biology. The commercial benzene-degrading strain is a ring-opening bacterial agent (VlandSaide, KH, VlandSaide Co., Ltd., Qingdao, China) produced by VlandSaide Enterprises, which is a functional microorganism that can decompose all kinds of BTEX under aerobic conditions to break the benzene ring into small molecules of organic acids, thus reducing the content of BTEX.

2.2. Hydrogeologic Conditions of the Test Site

The test site is located in the Ordos Basin, in the hinterland of Mao Wusu Desert. The terrain is relatively flat and the surface is mostly covered by the wind-deposited sands. The layer is mainly composed of fine sand, the thickness of which is about 40 m. The lithology of this set of strata in the horizontal and vertical directions does not have a big difference. The groundwater table is relatively shallow, about 4.0 m, and the main source of its recharge is atmospheric precipitation and direct infiltration. The main discharge pathway is atmospheric evaporation and lateral runoff. The hydraulic gradient of groundwater is relatively small, about 0.3%, and the annual change of the water level at the site is relatively small, ranging from 0.6 to 1.0 m, as shown in Figure 1. The permeability coefficient of the aquifer is 18.9 m/d according to the pumping test.

2.3. Injection Impact Radius Test

In order to detect the instantaneous influence radius of the injection process under different pressures and the range of influence of the diffusion of the injected material, two test groups were set up. One injection point was set for each test group, and monitoring wells were set up along the direction of the groundwater flow at a distance of 0.5, 1, 2, and 3 m from the injection point. The arrangements of the injection point and the monitoring point are shown in Figure 2. Two test groups were injected with 110 kg of slow-release oxygen material (configured as a suspension with water at a mass ratio of 1:3 before injection) in sequence with two different injection pressures, a high pressure of 5 MPa and a low pressure of 0.5 MPa, and stirred continuously during the process to ensure the homogeneity of the injected material. After the injection was completed, water quality monitoring was carried out in different monitoring wells at the same time, and soil cores were collected at different distances from the injection point to visually determine the instantaneous influence radius of the material in the horizontal direction under different

pressures. In order to investigate the long-term diffusion influence range of the slow-release oxygen material, long-term monitoring of DO value, redox potential value, and other parameters in each monitoring well was carried out for a period of 90 days.

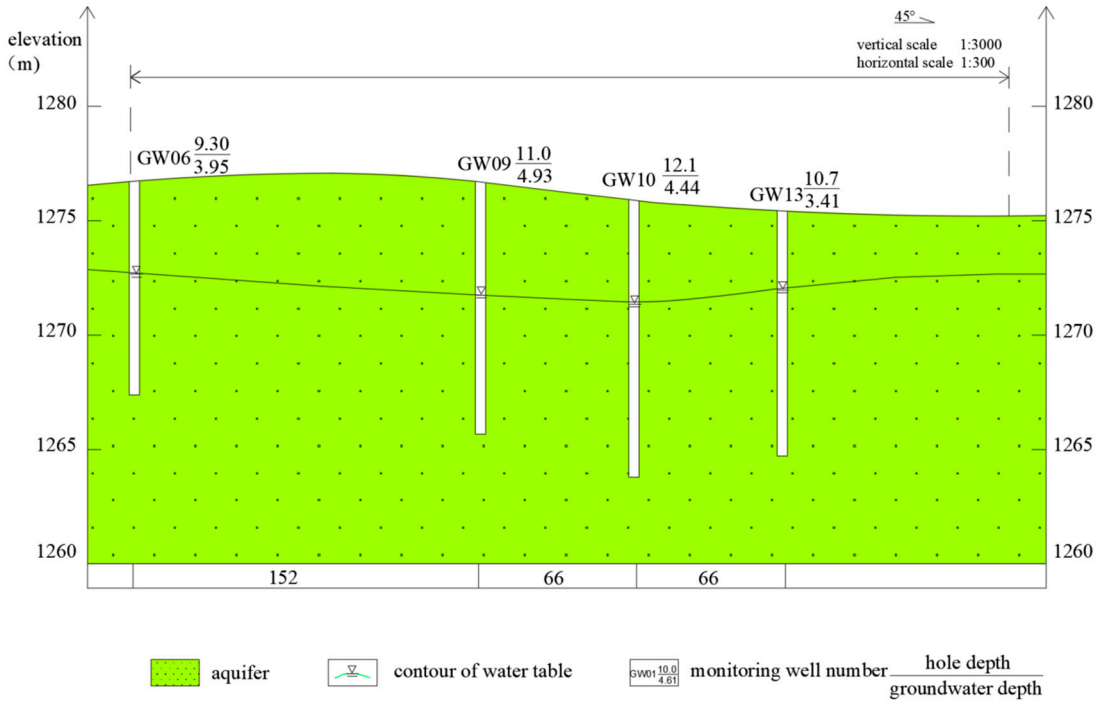

Figure 1. The hydrogeological profile of the site.

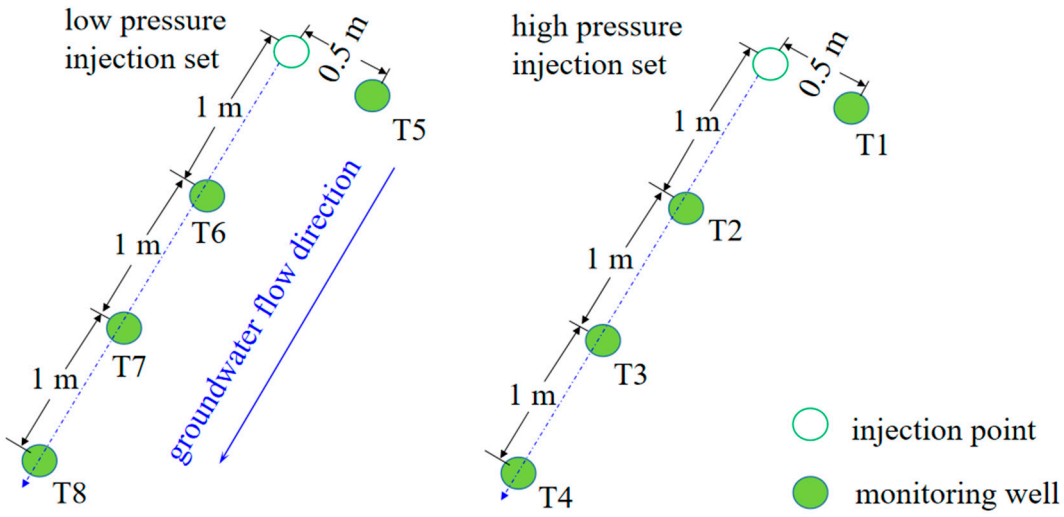

Figure 2. The spatial distributions of monitoring wells in the test of impact radius.

2.4. Monitoring Well Placement and Test Program

In the selected test site, four test groups were set up. The four experimental groups were a blank control group, slow-release oxygen material, coupled slow-release oxygen material/commercial bacteria, and coupled slow-release oxygen material/screening soil bacteria. Combined with the direction of groundwater flow in the test site, each group set up four groundwater monitoring points and one background monitoring point, as shown in Figure 3. According to the design of the test program, a total of 19 groundwater monitoring wells were constructed, and the depth of the wells was 12 m to ensure that groundwater samples could be taken from all layers.

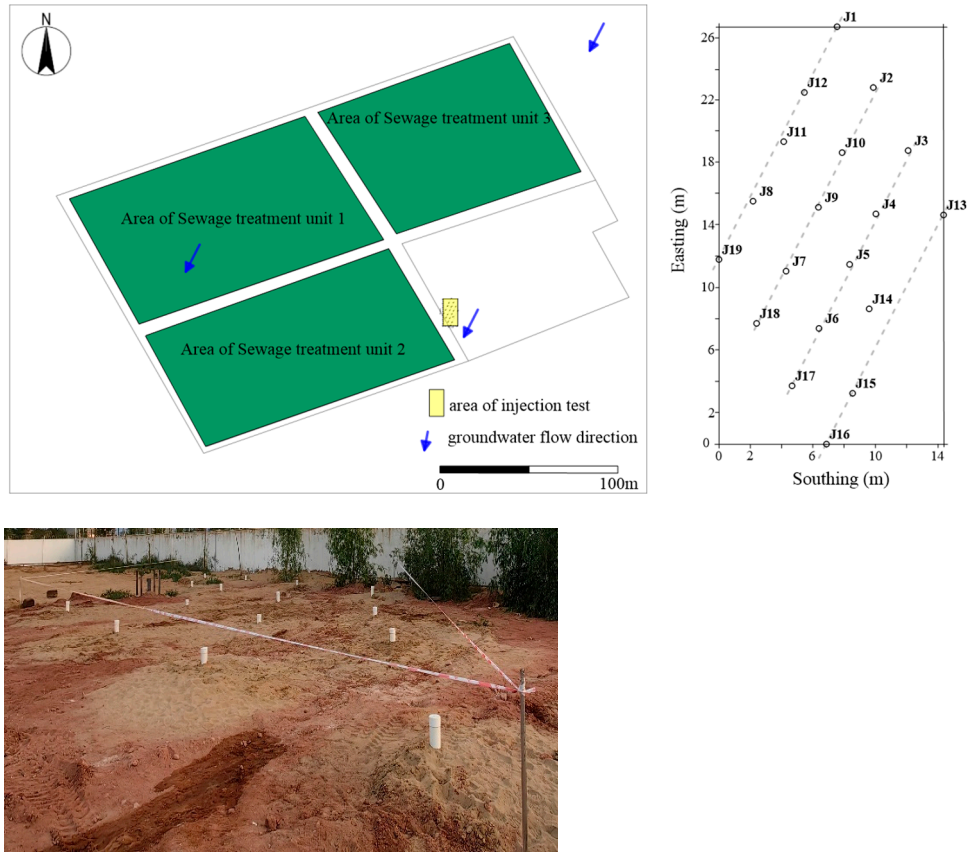

Figure 3. The spatial distributions of monitoring wells in the selected test site.

2.5. Initial Contamination Conditions at the Site

Next to the test site is the wastewater treatment plant of an enterprise, and the main pollutants in the wastewater are BTEX, halogenated hydrocarbons, petroleum hydrocarbons, etc. In the previous stage, the underground pollution of the wastewater treatment plant was detected using an MIP (membrane interface probe), and the planar distribution range of the wastewater treatment plant is shown in Figure 4. In order to explore the feasibility of coupled injection for the remediation of the BTEX contamination, the edge area of the contaminated plume was selected for this test (shown by the blue box in Figure 4). The current status of BTEX contamination in groundwater is shown in Figure 5. All samples were taken from 50 cm below the groundwater surface. BETX was detected by the purge-and-trap gas chromatography/mass spectrometry method (HJ 605-2011). The monitoring results showed that the distribution of BTEX concentration in the groundwater was basically the same between 7 days before injection and 1 day before injection, indicating that the concentration field in the test area was basically stable at this time and suggesting that the natural attenuation effect was not obvious. The concentration of BTEX was high at the location close to the contaminated plume of the plant, with the concentration reaching 3058 μg/L at the point of J11. The concentration in the blank control group, which was far away from the contaminated plume, was low. The concentration at the lowest point, J13, was 74 μg/L. In terms of composition, m/p-xylene was the main component of BTEX, accounting for about 50%, and benzene accounted for about 25%. The composition was basically the same at all points, proving that they had a consistent source of pollution. In addition, the saturation degree of BTEX in this area is relatively low, and there is no NAPL phase pooling.

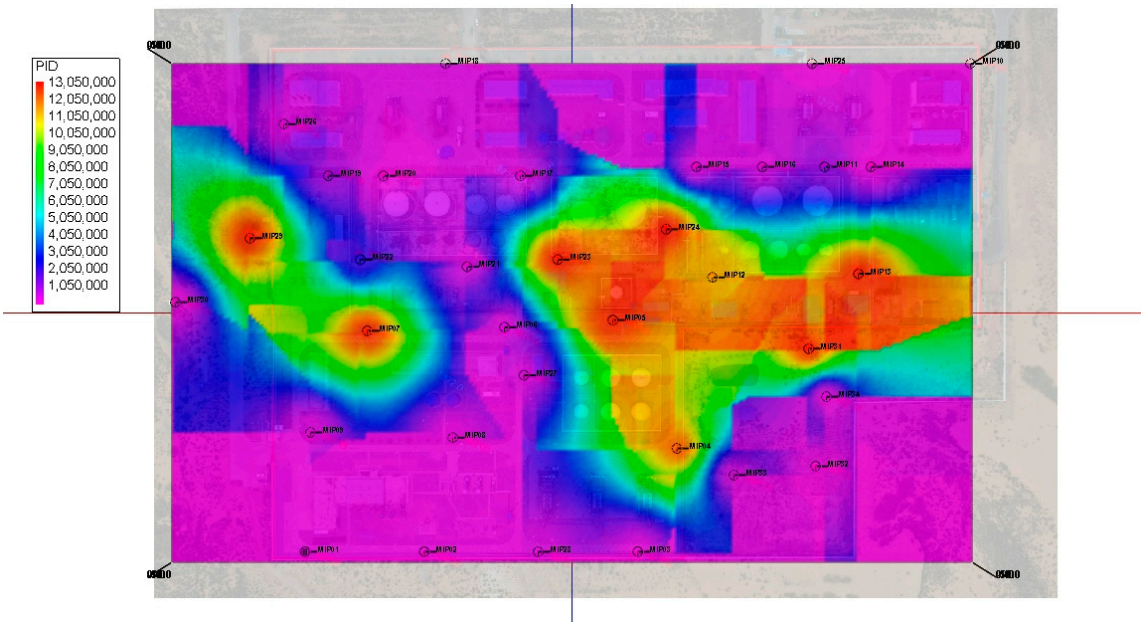

Figure 4. The spatial distributions of contamination detected using an MIP.

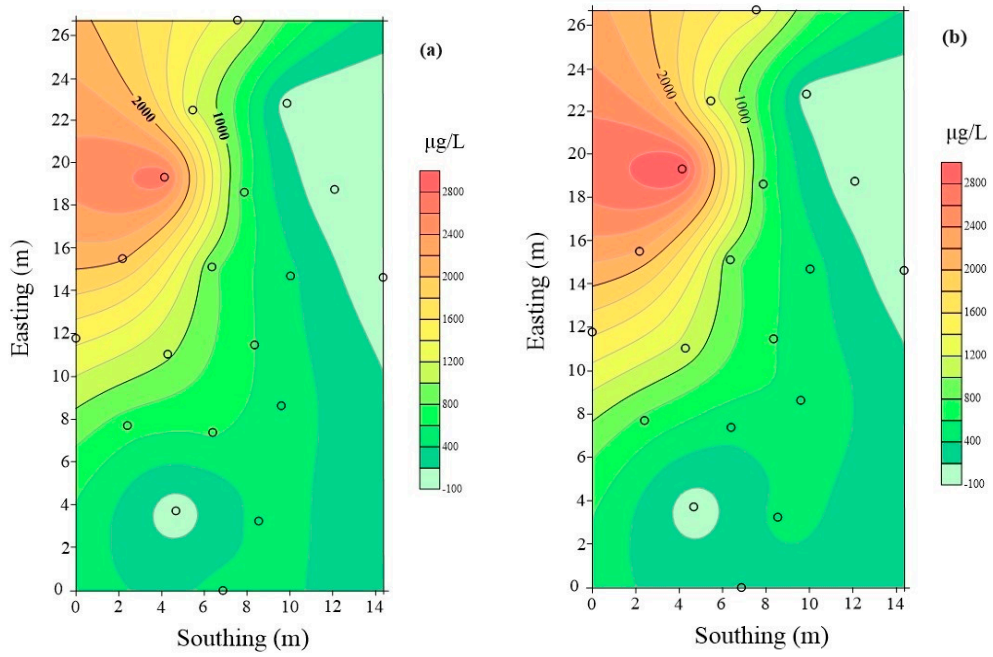

Figure 5. The total BTEX concentration (μg/L) distribution, based on groundwater samples taken prior to injection: (**a**) 7 d before injection, (**b**) 1 d before injection.

2.6. Coupling Injection Test

According to the indoor microbial remediation batch experimental data, the bacterial load Log (CFU/g) was ≥9.7. The best mass ratio of pollutant and degrading bacterial input under a low temperature (17 °C) was 1:6. Combined with the initial concentration of groundwater contamination in the field test plots and the hydrogeological conditions, it was determined that the amount of bacterial products injected into each group was 115 kg, and the bacterial products were 80 mesh powder formulations. Before injection, the bacterial product was mixed with activation matrix alginate (0.5%) and water in a ratio of 1:9 to form a suspension for activation and then injected 1 h after mixing. The oxygen demand of the bacteria was used to calculate the amount of slow-release oxygen material injected into each group of tests for 330 kg. The slow-release materials and water were

mixed in a ratio of 1:3 and configured into a suspension, with constant stirring during the injection process to ensure the homogeneity of the injected material.

Geoprobe 7822DT (Geoprobe Co., Ltd., Salina, KS, USA) was used for injection during the test, and the injection system included storage tanks, injection pumps, mixing equipment, flow meters, pressure gauges, and so on. According to the parameters determined by the injection impact radius test, a reasonable injection point and radius were set up, as shown in Figure 6. In order to ensure the degradation effect of coupled pollution, each group of microorganisms/agents was set up with three injection points, slow-release oxygen material injection points, and microorganisms, using upstream and downstream double-point injection. The upstream point for the slow-release oxygen material injection was 2.5 m downstream of the microorganism injection position. Vertical injection was performed at a depth of 7, 6, 5, 4, and 4.5 m in five layers.

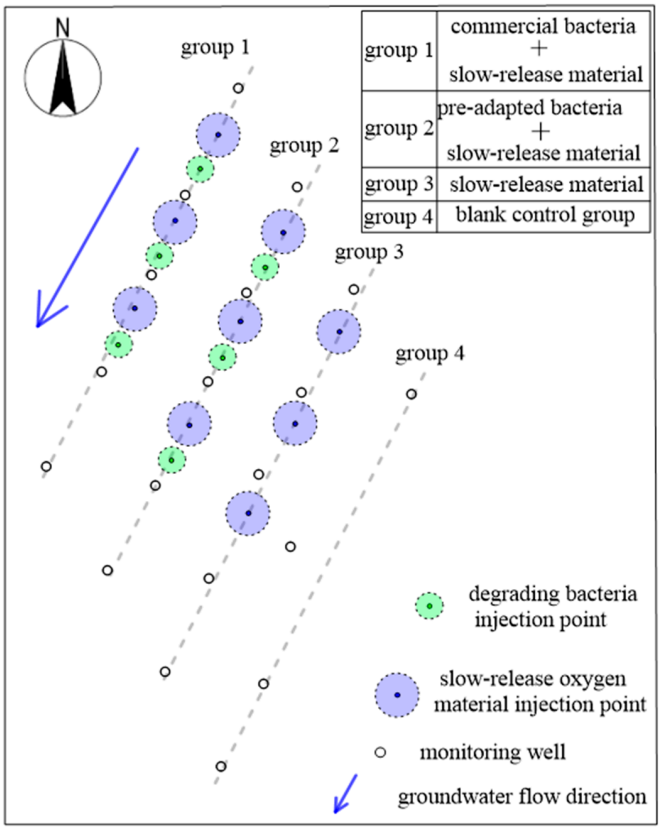

Figure 6. The spatial distributions of monitoring wells and injection points in the test.

A long-term monitoring program was designed for water quality in the groundwater monitoring wells, which were carried out on the 1st, 3rd, 5th, 10th, 20th, 40th, 60th, and 90th days after the injection. The indicators of the tests were BTEX and microbiological indicators, including the structure of microbial communities, the total number of microorganisms, the activity of lipase, dehydrogenase activity, monooxygenase activity, and so on. The degradation effect of pollutants in different test groups was compared with the groundwater samples before and after the test through the collection and analysis of the samples, so as to validate the effectiveness of the present test. The samples were sampled and detected by the Institute of Hydrogeology and Environmental Geology, Chinese Academy of Geological Sciences, as previously described [34,35].

3. Results and Discussion

3.1. Injection Instantaneous Influence Radius

Slow-release materials will lead to increases in pH and dissolved oxygen in direct contact with groundwater. Both of the phenomena were detected instantaneously in

the monitoring wells 0.5 m away from the injection point under both high-pressure and low-pressure injection modes. The dissolved oxygen concentrations of t1 and T5 were 22.5 mg/L and 14.2 mg/L, and the pH levels were 12.3 and 12.5, respectively, proving that the instantaneous influence radius of high-pressure and low-pressure injection can reach 0.5 m. The T2 wells were also found to have a rising dissolved oxygen concentration of 19.2 mg/L and a pH of 10.5, proving that the instantaneous influence radius of high-pressure injection can reach 1 m. The T6 well did not register obvious changes, proving that the instantaneous influence radius of low-pressure injection is greater than 0.5 m and less than 1 m. The soil sampling work was carried out at different distances of 0.75 m and 1.2 m from high-pressure and low-pressure injection points. The low-pressure group did not show obvious traces of material injection, while the high-pressure group showed traces of material injection at 0.75 m. Non-detection at 1.2 m determined that the instantaneous influence radius of high-pressure and low-pressure injection was 1 m and 0.5 m, respectively.

3.2. Changes in Groundwater Dissolved Oxygen Concentration after Injection of Slow-Release Oxygen Materials

The dissolved oxygen concentrations of groundwater monitoring wells in the test area were continuously monitored. Under the effect of groundwater flow, the dissolved oxygen has always been maintained at a high level, averaging around 20 mg/L, which creates an oxidizing environment suitable for the microbial aerobic degradation of BTEX in the groundwater aquifer. The influence range of the slow-release material expanded continuously with the groundwater flow. The T3 well, which is 1 m away from the T2 well, showed DO elevation 7 days after the injection. The diffusion rate of dissolved oxygen is about 0.15 m/d. The results of pH monitoring found that, except for the phenomenon of pH elevation in the monitoring wells within the transient radius of influence, the pH elevation phenomenon was not found in the downstream monitoring wells. It was presumed that the pH elevation caused by material injection was buffered by soil and did not spread downstream. The monitoring results after 90 days in wells T2, T3, T4, T5, T6, and T7 were 17.67 mg/L, 15.8 mg/L, 13.71 mg/L, 19.58 mg/L, 15.66 mg/L, and 11.71 mg/L, respectively. It shows that the slow-release oxygen material can release oxygen stably for a long period.

3.3. Characterization of Spatial and Temporal Changes in Microbial Abundance after Coupled Injection

In comparing the results of the samples with the effects of different bacterial agents, we observed significant differences, as shown in Figure 7. In the pre-adapted bacterial agent group (group 2), after the addition of *Bacillus* spp., its relative abundance climbed rapidly, not only being stable at more than 10% but also increasing to values more than 50% under certain conditions, showing strong adaptability and growth vigor. At the same time, the abundance of *Bacillus* spp. in the commercial bacterial agent group (group 1) also increased rapidly after its addition, but the average value was stable at about 10%, which indicated that the added bacterial agent could be effectively dispersed in the aquifer and survive for a long time. However, group 3 did not perform well in stimulating indigenous degrading bacteria. Despite the addition of slow-release oxygen materials, the abundance of *Bacillus* spp. in this test group always remained below 1%, indicating that the addition of slow-release oxygen materials alone could not effectively stimulate the growth of the indigenous *Bacillus* spp. In contrast, the abundance of *Bacillus* spp. in the control group also remained at a low level, which further verified that the injection of *Bacillus* spp. was significant in promoting the growth of *Bacillus* spp. Combined with the efficiency of pollutant degradation in different experimental groups, it was found that the injected *Bacillus* spp. could persistently and efficiently participate in the degradation of pollutants in the process of pollution degradation in conjunction with the slow-release material.

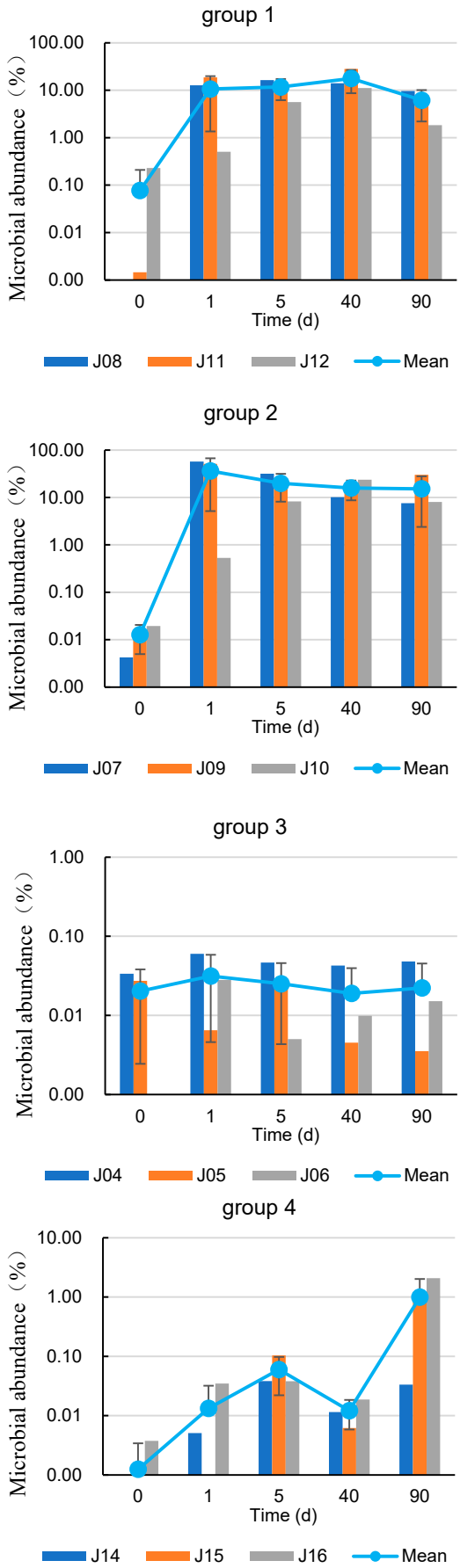

Figure 7. Abundance statistics of *Bacillus* spp. in monitoring wells.

3.4. Characterization of Spatial and Temporal Changes in Pollution after Coupled Injection

BTEX concentration in each well was examined after coupling injection, and the results are shown in Figure 8. The pollutant concentration in the test plots on the first day after injection increased slightly, and this phenomenon also appeared in other cases [36], mainly due to the pressure pulse and turbulence of the injected suspension. On the 3rd–10th days after injection, the test area's pollution plume concentration showed a significant reduction. The pollution concentration in the circled areas of J4, J9, J10, and J11 was reduced by an average of 50%. The pollution distribution was the same as before the injection, and the pollution near the plant was more serious. In the late stage of the experiment, the concentrations in the monitoring wells generally showed a large increase, and the results of pollution interpolation are shown in Figure 8. Affected by the migration of lateral pollution to the experimental area, BTEX concentration in the test area has increased. The highest increase in the concentration appeared in the blank control group of J13, which increased from 63.5 μg/L to 3180 μg/L. The average concentration in the blank control group was the lowest level in the test area before the injection, while the concentration continued to rise and became the highest concentration of BTEX in the test area. As shown in Figure 8h, the concentration of the test group closer to the pollution source was lower than that of the blank control group, which demonstrated that the injection of slow-release materials and microorganisms played a significant role in the process of pollutant degradation.

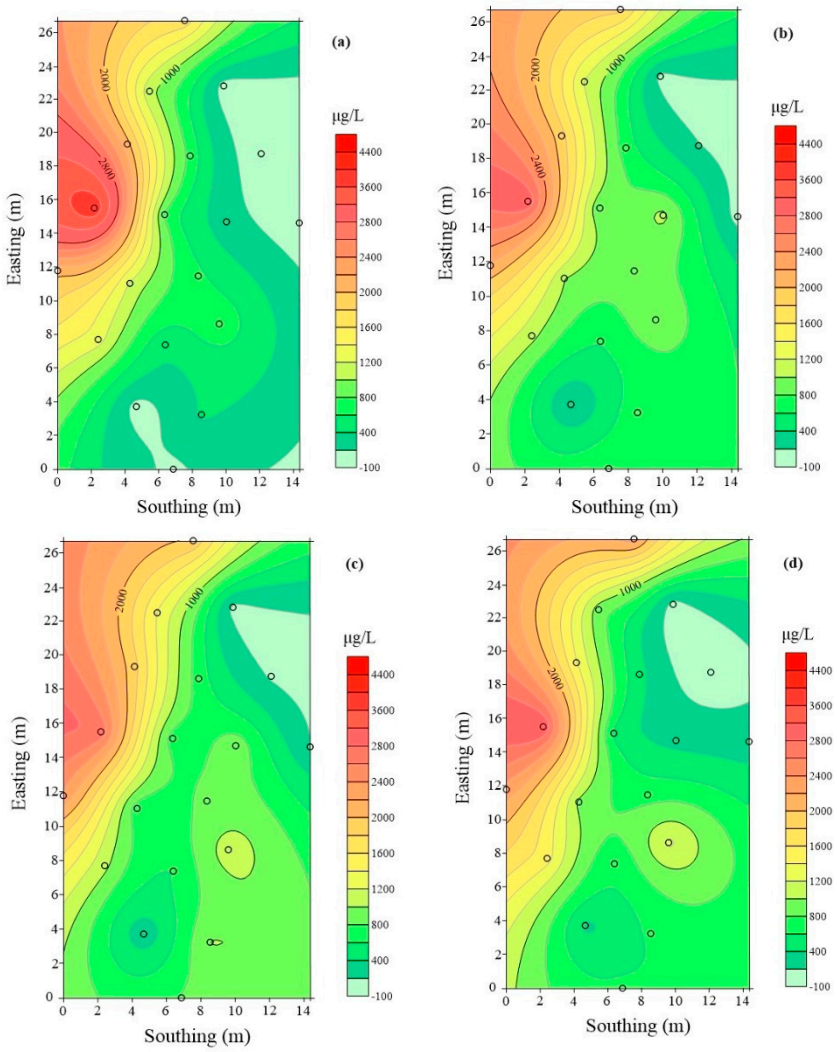

Figure 8. *Cont.*

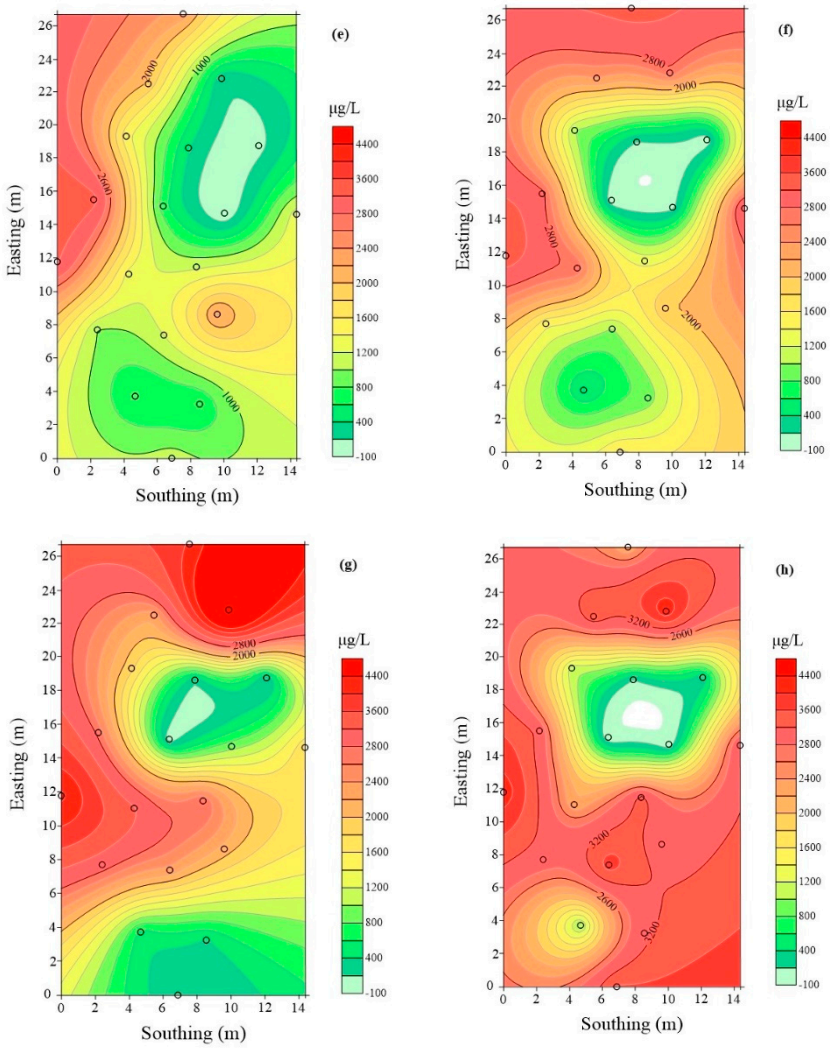

Figure 8. Total BTEX concentration (μg/L) distribution, based on groundwater samples taken after injection: (**a**) 1 d after injection, (**b**) 3 d after injection, (**c**) 5 d after injection, (**d**) 10 d after injection, (**e**) 20 d after injection, (**f**) 40 d after injection, (**g**) 60 d after injection, and (**h**) 90 d after injection.

3.5. Actual BTEX Degradation Efficiencies after Pollution Effects

In order to deduct the influence of flanking pollution, the actual degradation efficiency of BTEX was calculated using two methods: ratio analysis and computer numerical simulation. The pollutant concentration in the control groups of J14, J15, and J16 was not affected by the injection of slow-release materials and bacteria. It was affected by the spread of the flanks of the contaminated plume. Since the test area is very small compared to the whole area of the pollution plume, the test area can be approximated as homogeneous. To calculate the degradation efficiency of the injection of the slow-release materials and fungicides, the growth rate of pollutant concentrations in the control group can be used to speculate on the impact of the dispersion pollution plume at other sites.

The growth rate of BTEX concentrations in the blank control group is shown in Table 1. According to this growth rate, the theoretical pollutant concentration at other points after 90 days is calculated, as shown as Table 2. The real degradation efficiency after the injection of slow-release materials and bacterial agents can be calculated by combining the actual test concentrations. The degradation degree of BTEX in the group of slow-release materials is 9.84–99.78%, with an average value of 42.37%. The degradation efficiency of BTEX in the coupling test group of slow-release materials and pre-adapted bacterial agents ranged from 67.97% to 98.82%, with a mean value of 87.78%. The degradation efficiency of benzene in

the test group of slow-release materials coupled with commercial fungicides ranged from 58.34% to 94.02%, with an average value of 76.57%.

Table 1. Growth rate of BTEX concentration pre- and post-injection in the control group.

Well	7 d before Injection BTEX (μg/L)	90 d after Injection BTEX (μg/L)	Growth Rate (%)
J14	514.72	2876.67	458.88
J15	446.80	3098.78	593.55
J16	474.46	3642.29	667.67
Average value	478.66	3205.91	573.37

Table 2. BTEX degradation efficiencies calculated by ratio analysis.

Group	Well	7 d before Injection BTEX (μg/L)	90 d after Injection BTEX Ratio Analysis Value (μg/L)	90 d after Injection BTEX Detection Value (μg/L)	Calculated BTEX Degradation Efficiencies (%)
Group of slow-release materials	J04	445.15	2995.85	35.34	98.82
	J05	602.64	4055.77	3307.19	18.46
	J06	624.96	4205.97	3792.03	9.84
			Average value		42.37
Group of slow-release materials and pre-adapted bacterial agents	J07	1033.84	6957.75	2228.64	67.97
	J09	850.20	5721.85	12.48	99.78
	J10	690.10	4644.36	205.13	95.58
			Average value		87.78
Group of slow-release materials coupled with commercial fungicides	J08	2019.71	13,592.65	3080.80	77.33
	J11	2740.37	18,442.66	1102.06	94.02
	J12	1231.42	8287.46	3452.41	58.34
			Average value		76.57

Groundwater flow and solute transport were modeled using the GSM 10.2(groundwater modeling system) to simulate the transport of BTEX without injection of degrading bacteria and slow-release materials and test site concentrations. The actual degradation efficiency of degrading bacteria and slow-release materials was calculated according to the measured and simulated concentrations, which are shown in Table 3. Compared with the three test groups, the highest BTEX degradation efficiency occurred in the group of slow-release materials and pre-adapted fungicides, with an average degradation efficiency of 88.25%. The results were similar to those of the ratio analysis method, proving the feasibility of these two methods.

Table 3. BTEX degradation efficiencies calculated by computer numerical simulation.

Group	Well	90 d after Injection BTEX-Detection Value (μg/L)	90 d after Injection BTEX-Simulation Value (μg/L)	Calculated BTEX Degradation Efficiencies (%)
Group of slow-release materials	J04	35.34	5376.23	99.34
	J05	3307.19	5794.89	42.93
	J06	3792.03	6025.91	37.07
		Average value		59.78
Group of slow-release materials and pre-adapted bacterial agents	J07	2228.64	6849.18	67.46
	J09	12.48	8780.12	99.86
	J10	205.13	7952.25	97.42
		Average value		88.25
Group of slow-release materials coupled with commercial fungicides	J08	3080.8	8428.11	63.45
	J11	1102.06	15,936.54	93.08
	J12	3452.41	15,959.31	78.37
		Average value		78.29

In summary, the comprehensive calculation of the actual degradation efficiency at different time points in this test was carried out. The change in the BTEX degradation efficiency, calculated by numerical simulation, is shown in Figure 9. The highest degradation efficiency of 98% was reached at 40 d. Both groups in the coupled injection test group showed good pollution degradation effects, in which the indigenous bacterial agent was more effective.

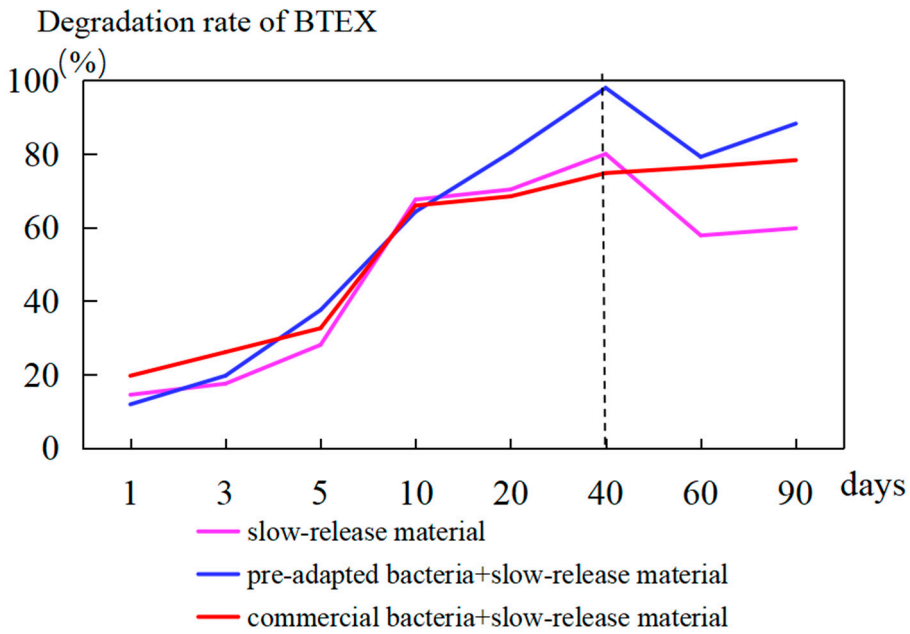

Figure 9. The actual BTEX degradation efficiencies as a function of time.

Previous studies have focused on petroleum hydrocarbon pollution in groundwater and BTEX degradation. However, they focus on different aspects, such as the degradation ability of a single strain, comparisons of different degradation techniques, and microbial community changes during degradation. This study focuses on the microbial degradation of petroleum-based pollutants, especially BTEX, in groundwater. The optimization strategy and application conditions of microbial degradation technology were studied by screening

and optimizing efficient degradation strains and fine-tuning environmental conditions. The degradation efficiency of a simple microbial injection is usually between 70% and 90%, and we further improve the degradation efficiency to more than 90% by injecting pre-adapted microbial agents under finely regulated environmental conditions. It is verified that the technology can be used in the treatment of medium- and low-concentration site pollution.

4. Conclusions

(1) Through the on-site injection test, it was verified that the radius of influence of the injection transient under the two pressures of high pressure (5 MPa) and low pressure (0.5 MPa) were 1 m and 0.5 m, respectively. The upstream and downstream dual-point coupled injection of slow-release oxygen materials and microbial agents was determined based on the results, with spacing between injection points being not less than 1.5 m.

(2) The monitoring results of dissolved oxygen concentrations after the injection of slow-release materials showed that the groundwater changed to an oxidizing environment. The dissolved oxygen content in the groundwater is continuously maintained above 15 mg/L, which ensures that microorganisms require the aerobic degradation of pollution. Elevated pH levels due to material injection are buffered by the soil medium and do not diffuse downstream.

(3) Both groups of coupled injection tests achieved positive pollutant degradation effects, in which the pre-adapted bacterial agent has a faster start rate of pollution degradation and higher pollution degradation efficiency due to the screening of local soil samples from the purification plant. The degradation effect has a long-lasting effect, reaching the highest BTEX degradation efficiency of 98% at 40 d. There were no significant changes in dissolved oxygen concentration except for redox conditions and dissolved oxygen, demonstrating that the coupled injection did not result in secondary contamination.

(4) The scope of application of this technology is areas with low- and medium-concentration pollution. When designing risk control programs for specific enterprises, it is necessary to cooperate with the use of pollution source cutting technology, and then continue to carry out in situ long-term remediation projects using the green and low-risk pollution control technology in this study. It will ensure that companies can safely and cost-effectively manage the risk of stock contamination.

Author Contributions: All authors contributed to the study conception and design. S.Y. (First Author): Conceptualization, Methodology, Investigation, Formal Analysis, Writing—Original Draft; S.Z. (Shucai Zhang) (corresponding Author): Conceptualization, Funding Acquisition, Resources, Supervision, Writing—Review & Editing; S.M.: Data Curation, Investigation; S.Z. (Sheng Zhao): Visualization, Writing—Original Draft; Z.L.: Resources, Validation. All authors have read and agreed to the published version of the manuscript.

Funding: This work was supported financially by the project of SINOPEC Science and Technology Department "Demonstration of site pollution risk control technology and equipment for typical sites of oil and gas field exploitation" (321089). Author Shuai Yang has received research support from SINOPEC.

Institutional Review Board Statement: This project has been confirmed to meet the standards of academic integrity, ensuring that the data are authentic and reliable, and the research process is transparent and open, without the need for specific ethical approval.

Data Availability Statement: The data presented in this study are available on request from the corresponding author.

Conflicts of Interest: All authors were employed by the company SINOPEC. The authors have no relevant financial or non-financial interests to disclose.

References

1. Zhao, B.; Huang, F.; Zhang, C.; Huang, G.; Xue, Q.; Liu, F. Pollution characteristics of aromatic hydrocarbons in the groundwater of China. *J. Contam. Hydrol.* **2020**, *233*, 103676. [CrossRef] [PubMed]

2. Ma, L.; Hurtado, A.; Eguilior, S.; Borrajo, J.F.L. Acute and chronic risk assessment of BTEX in the return water of hydraulic fracturing operations in Marcellus Shale. *Sci. Total Environ.* **2024**, *906*, 167638. [CrossRef] [PubMed]
3. Khaled, I.; Saidi, I.; Ferjani, H.; Ahmed, R.B.; Alrezaki, A.; Guesmi, F.; Bouzenna, H.; Harrath, A.H. BTEX induces histopathological alterations, oxidative stress response and DNA damage in the testis of the freshwater leech Erpobdella johanssoni (Johansson, 1927). *J. King Saud Univ.-Sci.* **2022**, *34*, 102196. [CrossRef]
4. Sheng, Y.; Wang, G.; Hao, C.; Xie, Q.; Zhang, Q. Microbial community structures in petroleum contaminated soils at an oil field, Hebei, China. *CLEAN–Soil Air Water* **2016**, *44*, 829–839. [CrossRef]
5. Kaur, G.; Lecka, J.; Krol, M.; Brar, S.K. Novel BTEX-degrading strains from subsurface soil: Isolation, identification and growth evaluation. *Environ. Pollut.* **2023**, *335*, 122303. [CrossRef]
6. Yu, B.; Yuan, Z.; Yu, Z.; Feng, X.-S. BTEX in the environment: An update on sources, fate, distribution, pretreatment, analysis, and removal techniques. *Chem. Eng. J.* **2022**, *435*, 134825. [CrossRef]
7. Vaezihir, A.; Bayanlou, M.B.; Ahmadnezhad, Z.; Barzegari, G. Remediation of BTEX plume in a continuous flow model using zeolite-PRB. *J. Contam. Hydrol.* **2020**, *230*, 103604. [CrossRef] [PubMed]
8. Ossai, I.C.; Ahmed, A.; Hassan, A.; Hamid, F.S. Remediation of soil and water contaminated with petroleum hydrocarbon: A review. *Environ. Technol. Innov.* **2020**, *17*, 100526. [CrossRef]
9. Huang, H.; Jiang, Y.; Zhao, J.; Li, S.; Schulz, S.; Deng, L. BTEX biodegradation is linked to bacterial community assembly patterns in contaminated groundwater ecosystem. *J. Hazard. Mater.* **2021**, *419*, 126205. [CrossRef] [PubMed]
10. Wu, Z.; Liu, G.; Ji, Y.; Li, P.; Yu, X.; Qiao, W.; Wang, B.; Shi, K.; Liu, W.; Liang, B.; et al. Electron acceptors determine the BTEX degradation capacity of anaerobic microbiota via regulating the microbial community. *Environ. Res.* **2022**, *215*, 114420. [CrossRef]
11. Hauptfeld, E.; Pelkmans, J.; Huisman, T.T.; Anocic, A.; Snoek, B.L.; von Meijenfeldt, F.A.B.; Gerritse, J.; van Leeuwen, J.; Leurink, G.; van Lit, A.; et al. A metagenomic portrait of the microbial community responsible for two decades of bioremediation of poly-contaminated groundwater. *Water Res.* **2022**, *221*, 118767. [CrossRef]
12. Dou, J.; Liu, X.; Hu, Z. Anaerobic BTEX degradation in soil bioaugmented with mixed consortia under nitrate reducing conditions. *J. Environ. Sci.* **2008**, *20*, 585–592. [CrossRef] [PubMed]
13. Huang, L.; Ye, J.; Jiang, K.; Wang, Y.; Li, Y. Oil contamination drives the transformation of soil microbial communities: Co-occurrence pattern, metabolic enzymes and culturable hydrocarbon-degrading bacteria. *Ecotoxicol. Environ. Saf.* **2021**, *225*, 112740. [CrossRef] [PubMed]
14. Sheng, Y.; Dong, H.; Kukkadapu, R.K.; Ni, S.; Zeng, Q.; Hu, J.; Coffin, E.; Zhao, S.; Sommer, A.J.; McCarrick, R.M.; et al. Lignin-enhanced reduction of structural Fe (III) in nontronite: Dual roles of lignin as electron shuttle and donor. *Geochim. Cosmochim. Acta* **2021**, *307*, 1–21. [CrossRef]
15. Lin, C.-W.; Cheng, Y.-W.; Tsai, S.-L. Multi-substrate biodegradation kinetics of MTBE and BTEX mixtures by *Pseudomonas aeruginosa*. *Process Biochem.* **2007**, *42*, 1211–1217. [CrossRef]
16. Wang, M.; Jiang, D.; Yang, L.; Wei, J.; Kong, L.; Xie, W.; Ding, D.; Fan, T.; Deng, S. Natural attenuation of BTEX and chlorobenzenes in a formerly contaminated pesticide site in China: Examining kinetics, mechanisms, and isotopes analysis. *Sci. Total Environ.* **2024**, *918*, 170506. [CrossRef] [PubMed]
17. Sheng, Y.; Tian, X.; Wang, G.; Hao, C.; Liu, F. Bacterial diversity and biogeochemical processes of oil-contaminated groundwater, Baoding, North China. *Geomicrobiol. J.* **2016**, *33*, 537–551. [CrossRef]
18. Sun, P.; Hua, Y.; Zhao, J.; Wang, C.; Tan, Q.; Shen, G. Insights into the mechanism of hydrogen peroxide activation with biochar produced from anaerobically digested residues at different pyrolysis temperatures for the degradation of BTEXS. *Sci. Total Environ.* **2021**, *788*, 147718. [CrossRef]
19. Chen, X.; Sheng, Y.; Wang, G.; Guo, L.; Zhang, H.; Zhang, F.; Yang, T.; Huang, D.; Han, X.; Zhou, L. Microbial compositional and functional traits of BTEX and salinity co-contaminated shallow groundwater by produced water. *Water Res.* **2022**, *215*, 118277. [CrossRef]
20. Tang, X.; Li, Z.; Wang, Z.; Yu, C.; Sun, H.; Wang, J.; Wang, C. Efficient remediation of PAHs contaminated site soil using the novel slow-release oxidant material. *Chem. Eng. J.* **2023**, *472*, 144713. [CrossRef]
21. Yang, C.-F.; Liu, S.-H.; Su, Y.-M.; Chen, Y.-R.; Lin, C.-W.; Lin, K.-L. Bioremediation capability evaluation of benzene and sulfolane contaminated groundwater: Determination of bioremediation parameters. *Sci. Total Environ.* **2019**, *648*, 811–818. [CrossRef] [PubMed]
22. Ali, M.; Song, X.; Wang, Q.; Zhang, Z.; Che, J.; Chen, X.; Tang, Z.; Liu, X. Mechanisms of biostimulant-enhanced biodegradation of PAHs and BTEX mixed contaminants in soil by native microbial consortium. *Environ. Pollut.* **2023**, *318*, 120831. [CrossRef] [PubMed]
23. Li, L.; Maher, K.; Navarre-Sitchler, A.; Druhan, J.; Meile, C.; Lawrence, C.; Moore, J.; Perdrial, J.; Sullivan, P.; Thompson, A.; et al. Expanding the role of reactive transport models in critical zone processes. *Earth-Sci. Rev.* **2017**, *165*, 280–301. [CrossRef]
24. Kapellos, G.E. Microbial strategies for oil biodegradation. In *Modeling of Microscale Transport in Biological Processes*; Academic Press: Cambridge, MA, USA, 2017; pp. 19–39.
25. Scammacca, O.; Sauzet, O.; Michelin, J.; Choquet, P.; Garnier, P.; Gabrielle, B.; Baveye, P.C.; Montagne, D. Effect of spatial scale of soil data on estimates of soil ecosystem services: Case study in 100 km^2 area in France. *Eur. J. Soil Sci.* **2023**, *74*, e13359. [CrossRef]
26. Ellis, D.E.; Lutz, E.J.; Odom, J.M.; Buchanan, R.J.; Bartlett, C.L.; Lee, M.D.; Harkness, M.R.; DeWeerd, K.A. Bioaugmentation for accelerated in situ anaerobic bioremediation. *Environ. Sci. Technol.* **2000**, *34*, 2254–2260. [CrossRef]

27. Mo, Y.; Dong, J.; Zhao, H. Field demonstration of in-situ microemulsion flushing for enhanced remediation of multiple chlorinated solvents contaminated aquifer. *J. Hazard. Mater.* **2024**, *463*, 132772. [CrossRef]
28. El-Naas, M.H.; Acio, J.A.; El Telib, A.E. Aerobic biodegradation of BTEX: Progresses and Prospects. *J. Environ. Chem. Eng.* **2014**, *2*, 1104–1122. [CrossRef]
29. Wang, W.; Jia, J.; Zhang, B.; Xiao, B.; Yang, H.; Zhang, S.; Gao, X.; Han, Y.; Zhang, S.; Liu, Z.; et al. A review of Sustained release materials for remediation of organically contaminated groundwater: Material preparation, applications and prospects for practical application. *J. Hazard. Mater. Adv.* **2024**, *13*, 100393. [CrossRef]
30. Nwankwegu, A.S.; Zhang, L.; Xie, D.; Onwosi, C.O.; Muhammad, W.I.; Odoh, C.K.; Sam, K.; Idenyi, J.N. Bioaugmentation as a green technology for hydrocarbon pollution remediation. Problems and prospects. *J. Environ. Manag.* **2022**, *304*, 114313. [CrossRef] [PubMed]
31. Sheng, Y.; Baars, O.; Guo, D.; Whitham, J.; Srivastava, S.; Dong, H. Mineral-bound trace metals as cofactors for anaerobic biological nitrogen fixation. *Environ. Sci. Technol.* **2023**, *57*, 7206–7216. [CrossRef] [PubMed]
32. Ning, Z.; Sheng, Y.; Guo, C.; Wang, S.; Yang, S.; Zhang, M. Incorporating the Soil Gas Gradient Method and Functional Genes to Assess the Natural Source Zone Depletion at a Petroleum-Hydrocarbon-Contaminated Site of a Purification Plant in Northwest China. *Life* **2022**, *13*, 114. [CrossRef]
33. Sheng, Y.; Liu, Y.; Yang, J.; Dong, H.; Liu, B.; Zhang, H.; Li, A.; Wei, Y.; Li, G.; Zhang, D. History of petroleum disturbance triggering the depth-resolved assembly process of microbial communities in the vadose zone. *J. Hazard. Mater.* **2021**, *402*, 124060. [CrossRef] [PubMed]
34. Ning, Z.; Sheng, Y.; Gan, S.; Guo, C.; Wang, S.; Cai, P.; Zhang, M. Metagenomic and Isotopic Insights into Carbon Fixation by Autotrophic Microorganisms in a Petroleum Hydrocarbon Impacted Red Clay Aquifer. *Environ. Pollut.* **2024**, *361*, 124824. [CrossRef]
35. Zhang, M.; Ning, Z.; Guo, C.; Shi, C.; Zhang, S.; Sheng, Y.; Chen, Z. Using Compound Specific Isotope Analysis to decipher the 1, 2, 3-trichloropropane-to-Allyl chloride transformation by groundwater microbial communities. *Environ. Pollut.* **2023**, *316*, 120577. [CrossRef] [PubMed]
36. Lhotský, O.; Kukačka, J.; Slunský, J.; Marková, K.; Němeček, J.; Knytl, V.; Cajthaml, T. The effects of hydraulic/pneumatic fracturing-enhanced remediation (FRAC-IN) at a site contaminated by chlorinated ethenes: A case study. *J. Hazard. Mater.* **2021**, *417*, 125883. [CrossRef] [PubMed]

Disclaimer/Publisher's Note: The statements, opinions and data contained in all publications are solely those of the individual author(s) and contributor(s) and not of MDPI and/or the editor(s). MDPI and/or the editor(s) disclaim responsibility for any injury to people or property resulting from any ideas, methods, instructions or products referred to in the content.

water

MDPI

Article

A Risk Assessment of the Vegetation Ecological Degradation in Hunshandake Sandy Land, China: A Case Study of Dabusennur Watershed

Peng Chen [1,2], Rong Ma [1,2,*], Letian Si [2,3], Lefan Zhao [2,4], Ruirui Jiang [2] and Wanggang Dong [2,5]

[1] Key Laboratory of Quaternary Chronology and Hydrological Environmental Evolution, China Geological Survey, Shijiazhuang 050061, China; chenpeng789@foxmail.com
[2] The Institute of Hydrogeology and Environmental Geology, Chinese Academy of Geological Sciences, Shijiazhuang 050061, China
[3] School of Urban Geology and Engineering, Hebei GEO University, Shijiazhuang 050031, China
[4] School of Earth Science and Resources, China University of Geosciences (Beijing), Beijing 100083, China
[5] Department of Geology, Northwestern University, Xi'an 710069, China
* Correspondence: marong@mail.cgs.gov.cn

Abstract: In the context of climate change, it is essential for sustainable development to assess the risks associated with climate change and human-induced vegetation degradation. The Hunshandake Sandy Land provides a variety of ecosystem services and is a substantial ecological security barrier in the Beijing–Tianjin–Hebei area of China. This study used the Normalized Difference Vegetation Index (NDVI) to analyze the spatiotemporal variation trend in vegetation in the Dabusennur Watershed using linear trend analysis and the GeoDetector model to identify the main drivers of vegetation change in the watershed. Finally, the study assessed the risk of ecological degradation in the vegetation of the watershed. The results show that the NDVI in the study area has had a fluctuating trend in the last 22 years, and the change has been small. Precipitation and groundwater depth are the key factors affecting vegetation change. The NDVI reaches its maximum value when the groundwater depth is at 2.75 m. The vegetation ecology of the basin is relatively fragile, mainly with medium risk and large risk. To cope with the ecological risk of vegetation degradation caused by climate change, appropriate water use strategies should be formulated to ensure ecological water use. The present study's outcomes provide the basis for developing ecological engineering solutions in the arid and semi-arid parts of northern China.

Keywords: vegetation; driving factors; ecological degradation; risk assessment; Hunshandake Sandy Land

1. Introduction

Ecological degradation is a significant environmental challenge [1–3] that affects both human existence and the ability of economies to grow sustainably [4,5]. China is the country where ecological degradation is occurring at one of the highest rates in the world [6–8]. Ecological degradation has attracted considerable interest from a wide range of people and has become one of the hottest areas of modern ecological research [9,10]. Vegetation is an essential part of ecosystems and plays a crucial role in global energy and material cycles [11], as well as in the management of climate change [12]. Moreover, it offers a comprehensive reflection of human activity features, water quantity, and the impacts of climate change [6,13,14]. Its coverage can potentially depict the growth status and patterns of vegetation in respective regions [15]. Investigating vegetation degradation and restoration from a time-series perspective is imperative as they represent dynamic equilibrium processes that are both regional and relative [14,16]. The extensive coverage, strong spatiotemporal continuity, and lengthy data series provided by satellite remote sensing data

enable the study of large-scale ecological changes [15,17,18]. The Normalized Difference Vegetation Index (NDVI) is a valuable metric for assessing vegetation quality, influenced by various driving factors [19,20]. Among these factors, precipitation plays a crucial role and cannot be disregarded as one of the natural forces impacting the NDVI dynamics [13]. The relationship between NDVI and temperature is intricate and closely linked to the magnitude of temperature increase [19]. Additionally, the altitude [21], groundwater depth (GD) [22,23], and soil type [24], along with other variables, exert significant influence on the NDVI. Regarding human factors, ecological restoration projects [14,25], land use and land cover (LULC) [18], and large-scale groundwater exploitation [6,26], among others, substantially contribute to the dynamics of the NDVI. The aforementioned studies have examined the relationship between ecological variables and the NDVI at various spatiotemporal scales in multiple study sites [24,27,28]. However, there is limited research on the vegetation ecological degradation risk (VEDR). Quantitatively describing the VEDR of local vegetation using the primary factors that influence NDVI distribution remains a challenging task [29–31]. Regions characterized by mountains and plateaus are particularly susceptible to climate change impacts [32]. The fragility and irreversibility of ecosystems in these regions have garnered significant attention towards understanding vegetation changes in such areas [33,34]. Hunshandake Sandy Land is located in an arid and semi-arid, ecologically sensitive area in northern China, which is a transitional zone between grassland animal husbandry and agriculture. As agricultural irrigation water occupies ecological water, ecological problems such as land desertification and lake wetland shrinkage are caused, which is one of the main reasons for the prominent dust weather in the Beijing–Tianjin–Hebei region. [14,35–37]. Therefore, we employ the Dabusennur Watershed (DW) in Hunshandake Sandy Land as our research subject. Conducting a risk assessment of ecological degradation will serve as a crucial guiding principle for future ecological protection and sustainable development within this basin, while also providing a foundation for developing ecological engineering strategies in the arid and semi-arid regions of northern China.

The objectives of the study are as follows: (1) to analyze the spatiotemporal dynamics of the NDVI in the DW from 1998 to 2019; (2) to investigate the relationships between ecological factors and their interaction with the NDVI; (3) to describe how the NDVI responds to the primary driver; and (4) to quantify and evaluate the VEDR of the DW.

2. Materials and Methods

2.1. Study Area

The DW, situated in the southwestern region of the Xilingol Grassland in Inner Mongolia, represents a typical grassland area located on the southern edge of the Hunshandake Sandy Land (Figure 1). Its geographical coordinates are 42°20–43°00′ N, 114°00′–115°20′ E, with an elevation ranging from 1077 to 1476 m; it experiences pronounced continental climate characteristics influenced by cold and high-pressure airflow originating from Mongolia. The notable climatic features include extreme coldness, aridity, strong winds, limited and concentrated precipitation patterns, an annual average temperature of ~1.9 C, annual average precipitation of ~270 mm, and annual average evaporation reaching ~210 mm. The predominant soil type is chestnut calcareous soil followed by Brown calcareous soil. The dominant land use/land cover (LULC) consists of grasslands and unused land. The primary vegetation types encompass *Caragana microphylla*, *Artemisia desertorum*, *Hedysarum laeve*, *Cleistogenes squarrosa*, *Achnatherum splendens*, and *Stipa capillata*. The unused land includes mainly saline-alkali land, marshland, and bare land.

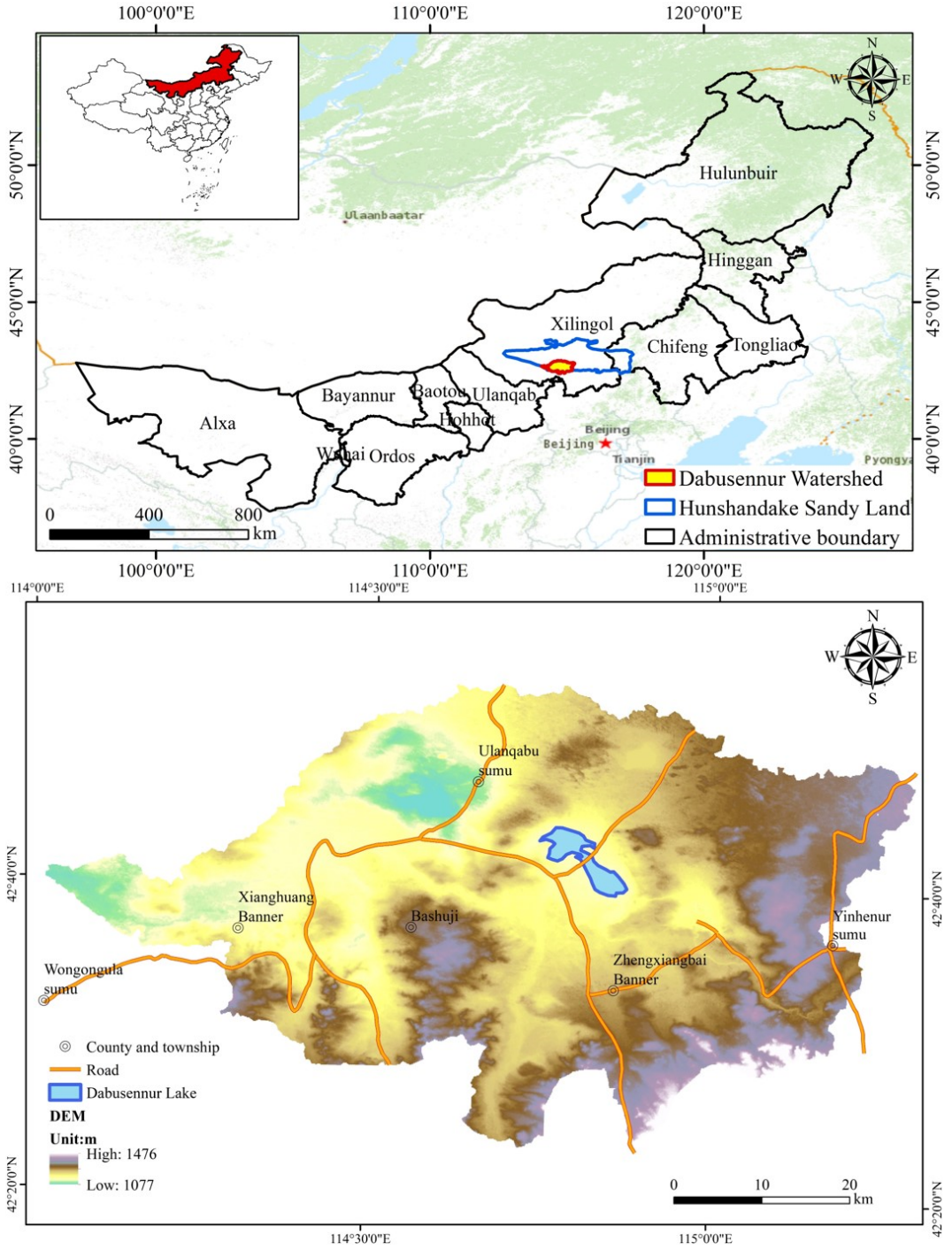

Figure 1. Location of the study area.

2.2. Data Collection

Meteorological data (precipitation and temperature) from 1998 to 2019 were obtained from the Chinese National Meteorological Information Centre (NMIC) (http://data.cma.cn, accessed on 3 August 2024). We collected the Normalized Difference Vegetation Index (NDVI) dataset for the same period from the Data Center for Resources and Environmental Sciences, Chinese Academy of Sciences (RESDC) (http://www.resdc.cn, accessed on 3 August 2024). The maximum value of NDVI in a year was selected to reduce the impact of the cloud on remote sensing data [38]. Furthermore, the land use and land cover (LULC) remote sensing monitoring data and socio-economic data were acquired from RESDC.

Meanwhile, the groundwater depth (GD) data were collected in the field. The GD was interpolated into the whole basin by ArcGIS 10.2 (https://www.esri.com, accessed on 3 August 2024) through ordinary kriging interpolation [39]. For spatial analysis and regional comparison, all data were standardized to 1000 m × 1000 m grid data. Further information regarding the data can be found in Table 1.

Table 1. Principal data sources.

Date Name	Date Type	Time	Data Source
NDVI	Raster (1000 m)	1998–2019	RESDC (http://www.resdc.cn, accessed on 3 August 2024)
Precipitation	Stations	1998–2019	NMIC (http://data.cma.cn, accessed on 3 August 2024)
Temperature	Stations	1998–2019	NMIC (http://data.cma.cn, accessed on 3 August 2024)
GD	Points (6/10 km^2)	2020	Field survey
LULC	Raster (1000 m)	2000, 2005, 2010, 2015	RESDC (http://www.resdc.cn, accessed on 3 August 2024)
Population	Raster (1000 m)	2010	RESDC (http://www.resdc.cn, accessed on 3 August 2024)
GDP	Raster (1000 m)	2010	RESDC (http://www.resdc.cn, accessed on 3 August 2024)

2.3. Research Methods

2.3.1. Workflow

Firstly, remote sensing data, field data, geographic data, and socio-economic data were fused to create a GIS spatial database of the study region. Subsequently, we examined the multi-year dynamics of the NDVI in the study region, detected the primary factors, and established a VEDR assessment model. Lastly, a quantitative evaluation, grading, and analysis of the ecological degradation risk of vegetation in the study region were executed. The workflow is depicted in Figure 2.

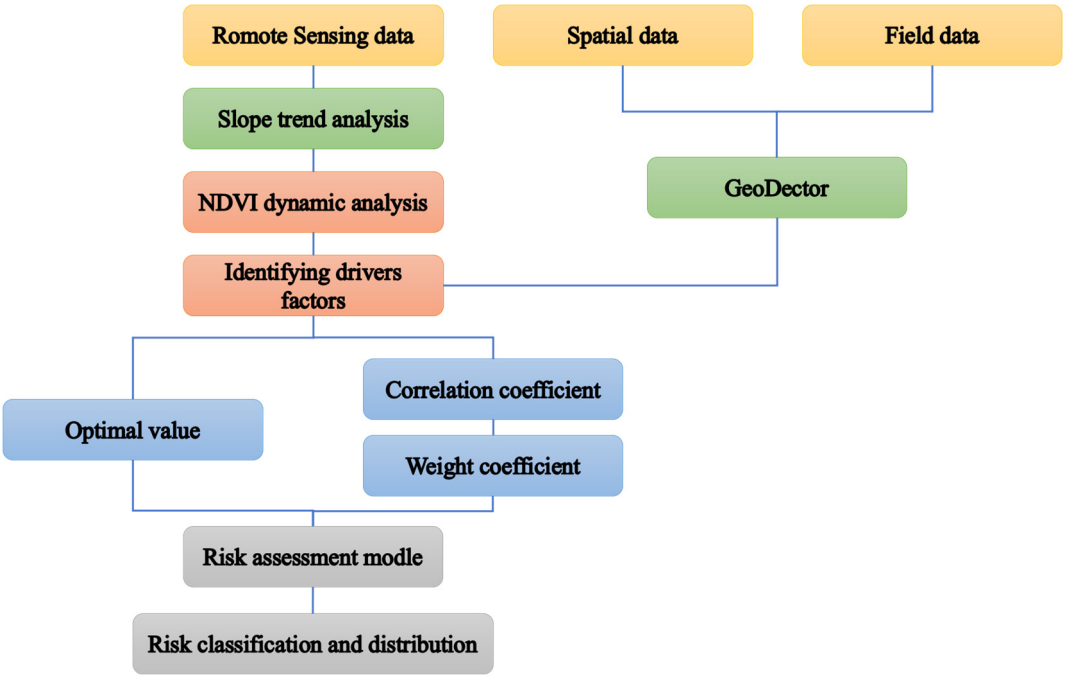

Figure 2. Workflow of study on assessment of VEDR.

2.3.2. NDVI Trend Analysis

Trend analysis involves conducting a linear regression analysis on time-dependent variables [24,40]. By applying linear trend analysis, the dynamic characteristics of vegetation can be captured through the changing trend in the NDVI for each grid. In this study, we employed a unified linear regression model to determine the vegetation change trend in DW from 1998 to 2019 and calculated the slope of the trend using the least squares method:

$$Slope = \frac{n\sum_{i=1}^{n}(i \times NDVI_i) - \sum_{i=1}^{n} \times \sum_{i=1}^{n} NDVI_i}{n\sum_{i=1}^{n} i^2 - (\sum_{i=1}^{n} i)^2} \quad (1)$$

where slope refers to the trend in vegetation change, n is the number of years studied (n = 22 in this study), i is the ordinal number of a given year, and $NDVI_i$ denotes the NDVI value for the year i; in the case of a slope >0, this indicates that the NDVI trend is increasing.

In order to better express the change trend in vegetation cover, the F-test was used to test the significance of the change trend in NDVI, and the results of the significance test reflected the reliability of the trend change [24]. The calculation formula is as follows:

$$F = U \times \frac{n-2}{Q} \quad (2)$$

$$U = \sum_{i=1}^{n}(\hat{y}_i - \overline{y})^2 \quad (3)$$

$$Q = \sum_{i=1}^{n}(y_i - \hat{y}_i)^2 \quad (4)$$

where U refers to the sum of squares of errors, Q is the regression square sum, y_i is the NDVI value for year i, $\hat{y}_i$ is the NDVI regression value for fear I, $\overline{y}$ is the average NDVI value in n year, and i is the ordinal number of a given year.

2.3.3. GeoDetector

The Geodetector method is a statistical approach that utilizes spatial statistics and spatial autocorrelation [41]. It can conduct spatial anisotropy exploration, reveal the influence and significance of each driving factor, the interaction strength between the exploration factors, and carry out risk detection and other research tasks. It consists of four components: factor detector, interaction detector, risk detector, and ecological detector, which collectively assess spatially stratified heterogeneity. In this study, we employ the factor detector and interaction detector from this model to investigate the impact of the NDVI driving factor in this region.

(1) Factor detector

The purpose of this method is to assess the spatial heterogeneity of the dependent variable Y (NDVI value) and examine the impact of independent variable X (diverse natural and socio-economic factors) on the spatial heterogeneity of Y, which is quantified by q-value. The formula for calculating it is as follows:

$$q = 1 - \frac{\sum_{h=1}^{L} N_h {\sigma_h}^2}{N\sigma^2} \quad (5)$$

where h(1,2,. . ., L) is the number of classifications of the factor; N_h and N are the numbers of units in class h and the whole area, respectively; ${\sigma_h}^2$ and σ^2 are the variance of Y for the units in class h and the whole area, respectively; the q-value represents the degree of explanatory power for each factor, with $q \in [0, 1]$, and its strength increases as the q-value approaches 1.

(2) Interaction detector

The interaction detector can be utilized to determine whether the interactions between any two influencing factors $(X_1 \cap X_2)$ are weakened, enhanced, or influenced Y independently. The types of interactive influences are determined by comparing the q-value

of the interacting factors with each of the two involved factors, as presented in Table 2. The GeoDetector utilized in this study can be further explored at http://geodetector.cn, accessed on 3 August 2024.

Table 2. Model driving force size criterion of interval and interaction.

Criterion of Interval	Interaction
$q(X_1 \cap X_2) < Min[q(X_1), q(X_2)]$	Nonlinear weakening
$Min[q(X_1), q(X_2)] < q(X_1 \cap X_2) < Max[q(X_1), q(X_2)]$	Single-factor nonlinear weakening
$q(X_1 \cap X_2) > Max[q(X_1), q(X_2)]$	Dual factor enhancement
$q(X_1 \cap X_2) = q(X_1) + q(X_2)$	Independence
$q(X_1 \cap X_2) > q(X_1) + q(X_2)$	Nonlinear enhancement

2.3.4. Risk Assessment

Defining the VEDR as the deviation of the risk factor x_{ij} from the optimal value x_{aj}, the VEDR F_i at sampling point i has the following assessment model:

$$F_i = \sum_{j=1}^{m} w_j \frac{|x_{ij} - x_{aj}|}{max|x_{ij} - x_{aj}|} \quad (6)$$

where w_j is the weight coefficient of the risk assessment factor j on evaluation objective $\sum_{j=1}^{m} w_j = 1$ and x_{ij} is the value of risk assessment factor j at sampling point i.

In this study, we employed the correlation coefficient method to ascertain the weight of each assessment factor for the VEDR. Initially, Pearson correlation coefficients were computed for the evaluated factors, and subsequently, normalization treatment was applied to derive weight coefficients for each assessed factor.

3. Results

3.1. NDVI Dynamics in the DW from 1998 to 2019

To accurately describe the DW vegetation distribution pattern, we analyzed its spatial distribution properties based on the mean value of the NDVI over these years (Figure 3). As depicted in Figure 3, clear regional differences are observed in the spatial distribution of the NDVI, with a gradual decrease from south to north. We employed an equal-spacing reclassification method to categorize the NDVI into five levels. Table 3 illustrates that most areas within the basin belong to the low-medium coverage category, accounting for approximately 74.81% of the total basin area; while low-medium and medium coverage areas together account for about 99.27% of the basin area. From the perspective of time change, the NDVI distribution pattern of DW from 1998 to 2019 has little change, showing a fluctuation type change (Figure 4). This indicates that the overall growth state of the DW vegetation is poor.

Table 3. Classification standard for vegetation coverage based on NDVI.

Level	NDVI	Area (km^2)	Percentage
Low coverage area	0–0.2	18.10	0.62%
Low-medium coverage area	0.2–0.4	2173.91	74.81%
Medium coverage area	0.4–0.6	710.89	24.46%
Medium-high coverage area	0.6–0.8	3.02	0.10%
High coverage area	0.8–1	0.00	0

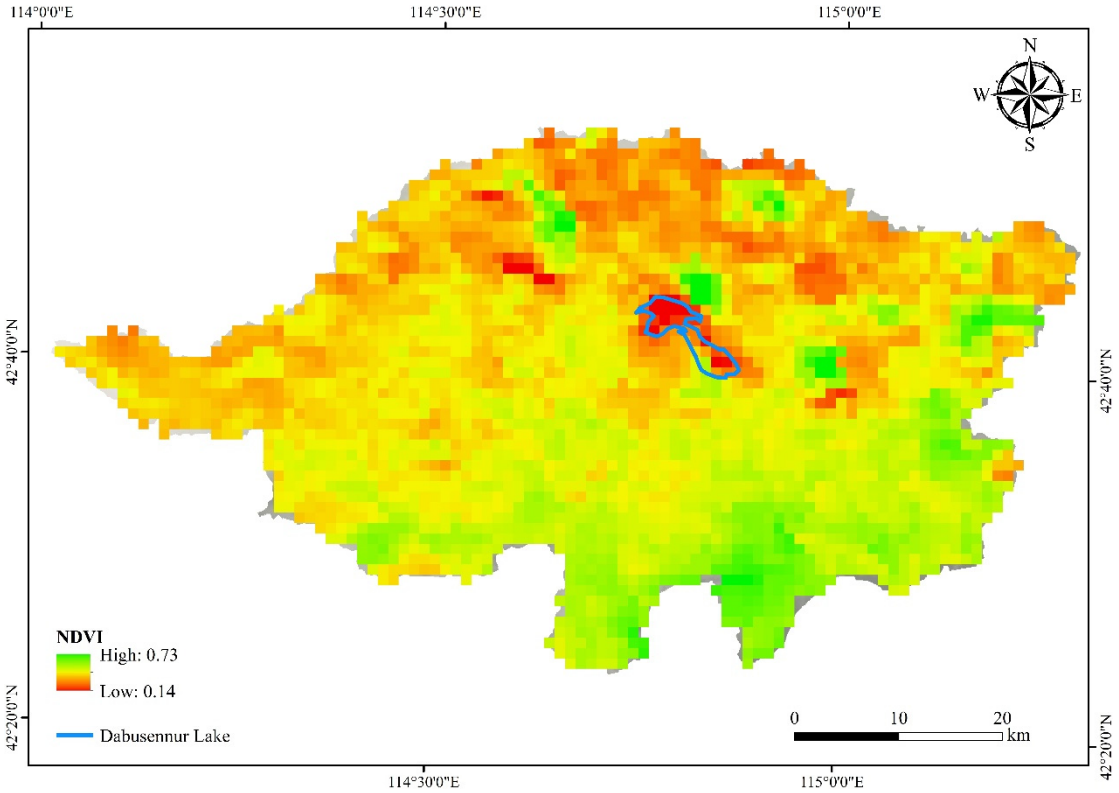

Figure 3. Spatial distribution of NDVI in DW.

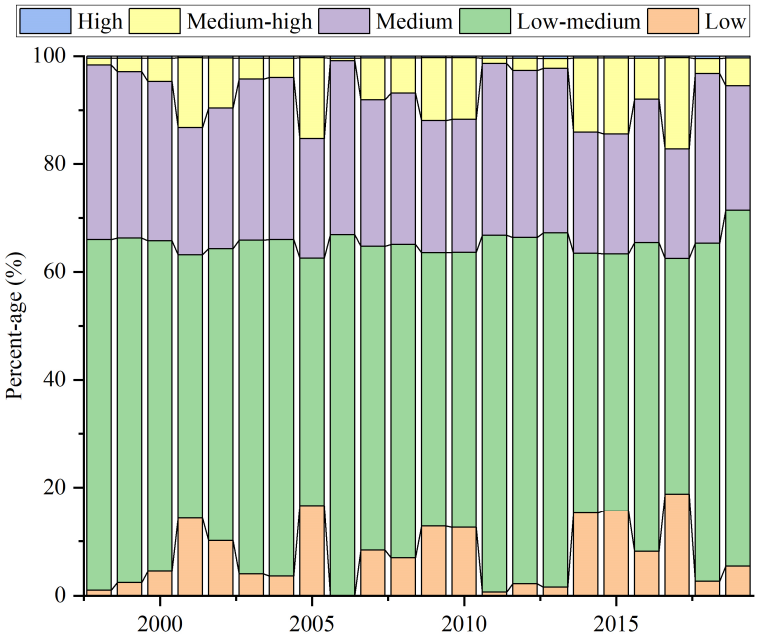

Figure 4. Percentage of different levels of NDVI in DW from 1998 to 2019.

Based on the temporal change trend in the watershed average NDVI (Figure 5), it is evident that the vegetation in the DW exhibited variation from 1998 to 2019, displaying a fluctuating pattern with a rate of change of 0.01/10 years. Notably, the mean NDVI value reached its lowest point in 2005 at 0.28 and peaked in 2018 at a maximum value of 0.47, while the multi-year average stood at 0.36.

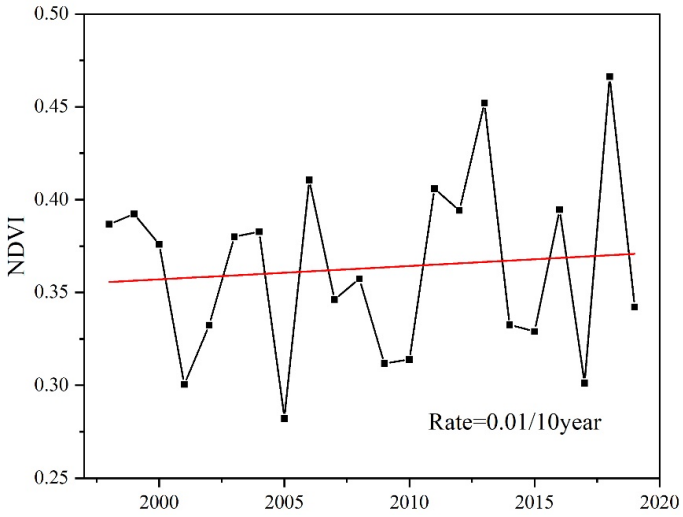

Figure 5. NDVI change trend in DW from 1998 to 2019.

The NDVI trend analysis was employed to calculate the dynamic slope of NDVI of over 22 years in DW. The spatial distribution results of NDVI variation trends in DW were obtained by conducting significance tests using the F-test (Figure 6). Based on the test results, the change trends were categorized into six levels and statistically analyzed for different change trends (Table 4).

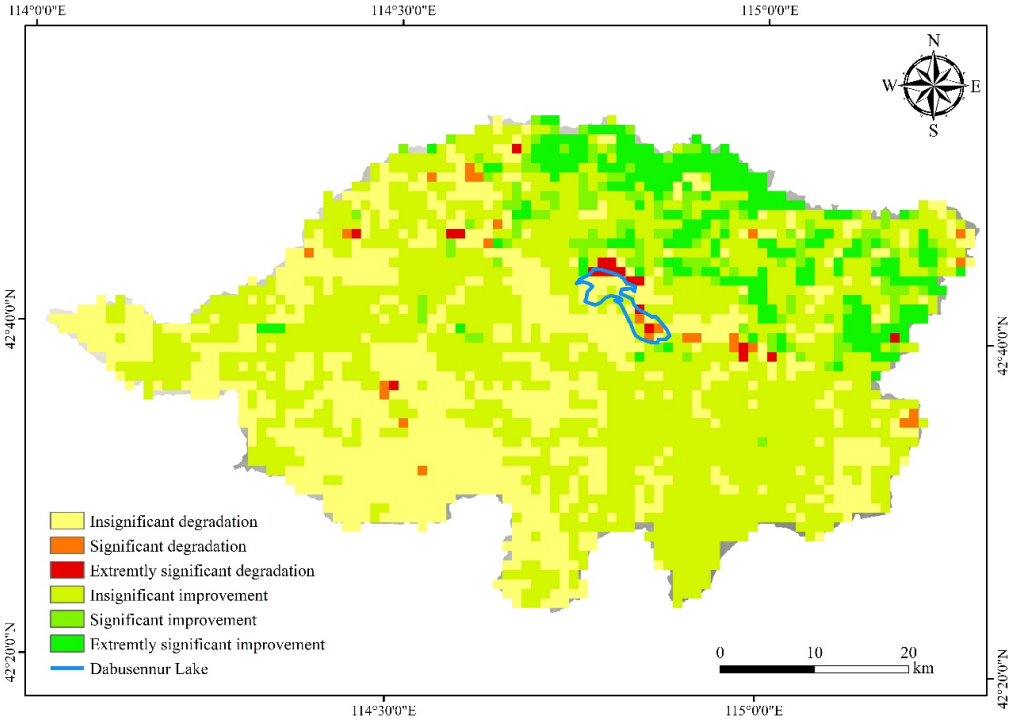

Figure 6. Slope trend analysis results in DW from 1998 to 2019.

According to Figure 4 and Table 4, approximately 36.61% of the basin exhibits a degradation trend, while around 63.69% shows an improvement trend. The majority of regions within the basin display an insignificant change trend, accounting for approximately 85.22% of the total area; notable improvements are observed in about 13.22% of the basin, primarily concentrated in its northeastern region; significant degradation is identified in approximately 1.56% scattered across the entire basin area. These findings suggest a potential association between human activities and the pronounced degradation of NDVI.

Table 4. Classification and statistical results of F-test of NDVI trend from 1998 to 2019.

Level	Change Degree	Area (km^2)	Percentage
Slope > 0, $p < 0.01$	Extremely significant improvement	241.32	8.30%
Slope > 0, $0.01 \leq p < 0.05$	Significant improvement	142.78	4.91%
Slope > 0, $p \geq 0.05$	Insignificant improvement	1457.99	50.17%
Slope < 0, $p \geq 0.05$	Insignificant degradation	1018.58	35.05%
Slope < 0, $0.01 \leq p < 0.05$	Significant degradation	26.14	0.90%
Slope < 0, $p < 0.01$	Extremely significant degradation	19.10	0.66%

3.2. Analysis of Spatial Distribution Driving Forces of NDVI in DW

To investigate the extent to which each driver factor and their interactions, as well as the combined influence of natural and human factors, affect the vegetation coverage. By analyzing the q-value of each factor, we can identify the dominant drivers influencing NDVI distribution, including precipitation, temperature, GD, LULC, population, and gross domestic product (GDP) (Figure 7).

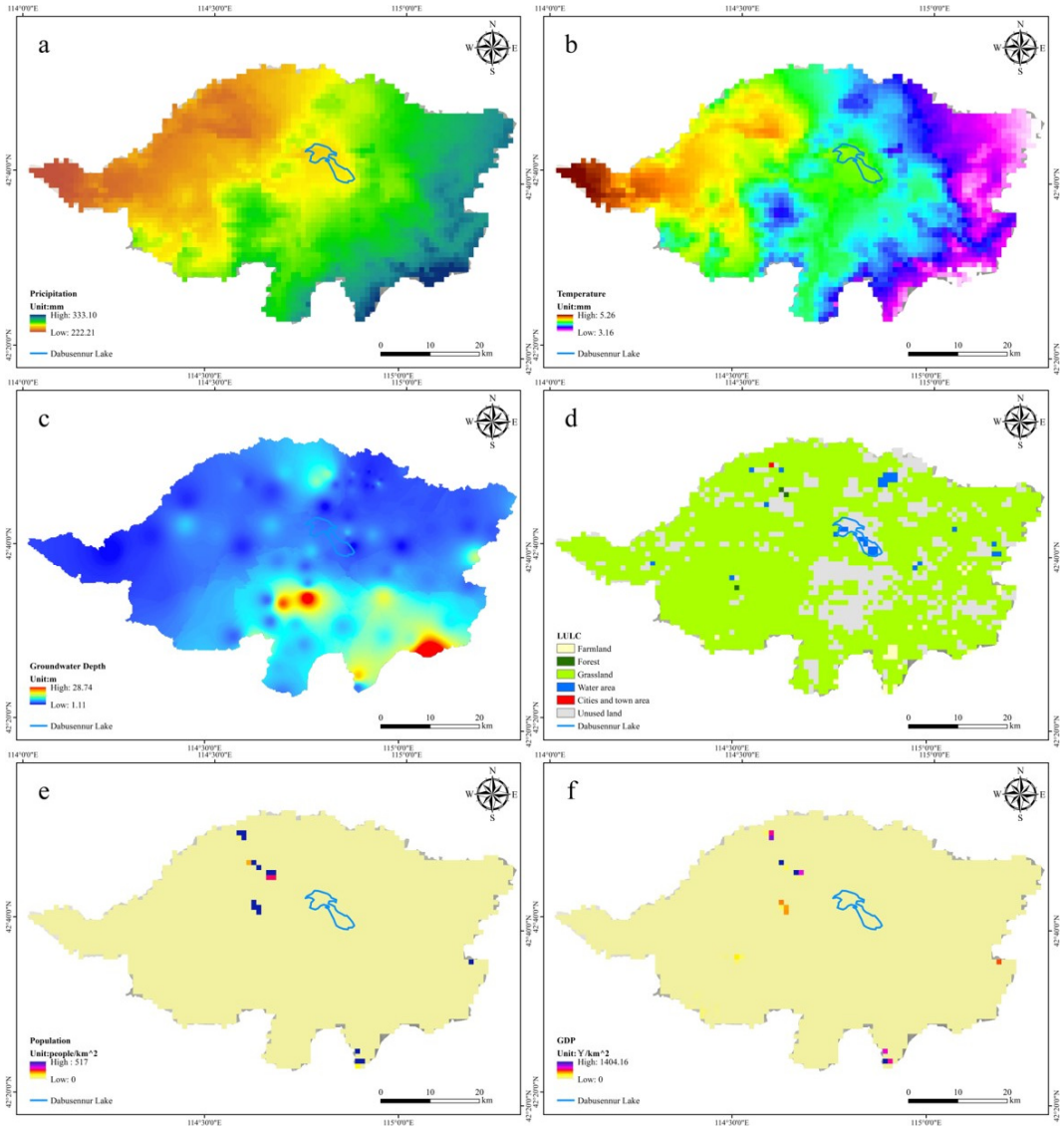

Figure 7. Spatial distribution of driving factors precipitation (**a**), temperature (**b**), GD (**c**), LULC (**d**), population (**e**), GDP (**f**), in DW.

Based on the Geodetector, the q-value of each driving factor in the area was calculated and analyzed (Table 5). The results revealed that the impact of individual driving factors on NDVI within the region can be ranked as follows: precipitation (0.231) > GD (0.200) > LULC (0.149) > temperature (0.114) > GDP (0.015) > population (0.005). The spatial heterogeneity of NDVI within the basin is the result of combined influences from natural and human factors, with the precipitation and GD exhibiting significant contribution rates, having q-value $\geq$ 0.2 and explanatory power exceeding 20%. These two factors emerge as primary influencers, while other contributing factors exhibit a relatively minor influence.

Table 5. q-value of different factors on NDVI in DW.

Precipitation	Temperature	GD	LULC	Population	GDP
0.231	0.114	0.199	0.149	0.005	0.015

The interplay between natural and human factors on the NDVI variability was investigated by employing GeoDector to analyze the interaction among different drivers and their influence on the spatial differentiation of the NDVI (Figure 8).

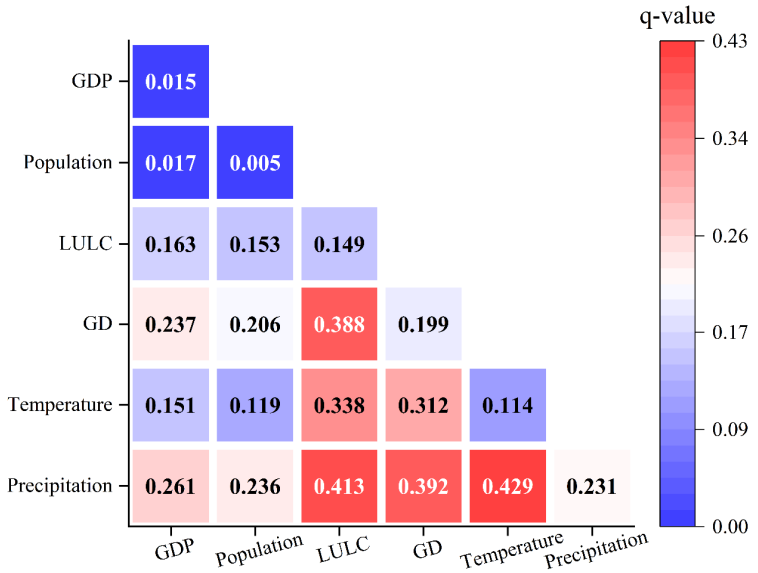

Figure 8. Interactions detected between different factors on NDVI.

The q-value obtained from the interaction of driving factors, as shown in Table 6, exhibited varying degrees of improvement. Specifically, the combined effect of the two factors was found to be stronger than that of a single factor, leading to an enhanced explanatory power for the spatial differentiation of NDVI. From a perspective on interaction types, eight out of the interaction factors demonstrated nonlinear enhancement, while seven showed double enhancement. Notably, based on these interaction results, it is evident that both annual average precipitation and GD play important roles in driving the spatial differentiation of the NDVI in the DW region. Moreover, among all interactions examined, those involving precipitation and temperature (both natural factors) were particularly significant with a large q-value (0.429), indicating their substantial influence on the NDVI values in this area. Additionally, there was also a noteworthy interaction between precipitation (representing natural factors) and LULC (representing human factors), with an interaction q-value of 0.413. This suggests that the interplay between natural factors and human factors exerts a substantial influence on the NDVI values within the region.

Table 6. Weight of VEDR factors.

Assessment Factors	Optimal Value	Correlation Coefficient	Weight Coefficient
Precipitation	333.10 mm	0.47 *	0.55
GD	2.75 m	0.38 *	0.45

Note: *, $p \leq 0.05$.

3.3. Response of NDVI to Variation of Precipitation and GD

According to Table 4, the low-medium and medium coverage areas collectively encompass 99.27% of the basin area. Consequently, we examine the response of the NDVI to variations in precipitation and groundwater in regions with medium-low coverage ($0 \leq$ NDVI < 0.4) and medium-high coverage ($0.4 \leq$ NDVI < 1), respectively. The GD was measured at intervals of 0.5 m, while precipitation was measured at intervals of 5 mm. The average value of the NDVI within each interval was utilized for analysis (Figure 9).

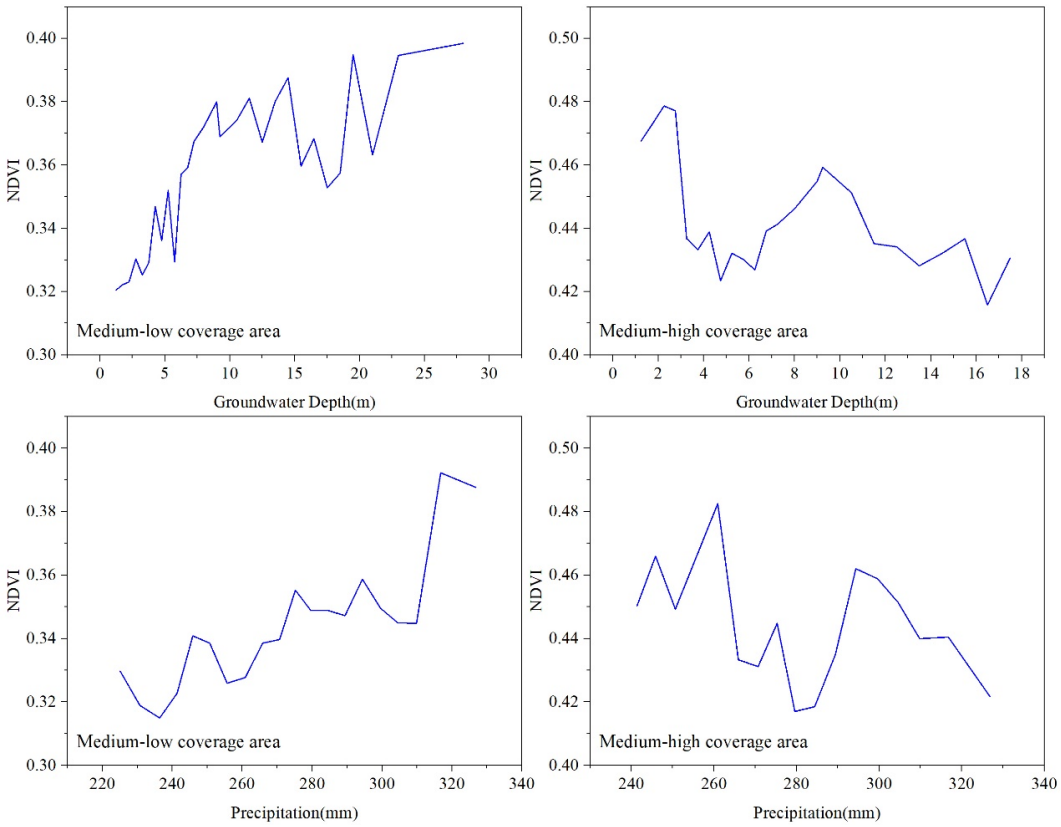

Figure 9. Response of NDVI to variations of precipitation and GD.

The NDVI in the medium-low coverage area exhibits an increase in both GD and precipitation, while the NDVI demonstrates limited dependence on GD but a strong correlation with precipitation. In this area, the vegetation primarily relies on precipitation for growth. The maximum NDVI of vegetation in the medium-high coverage area is observed at a GD of 2.75 m and a precipitation level of 260 mm, indicating that groundwater plays a crucial role in supporting vegetation growth when the GD is shallow. With increasing GD, the NDVI experiences a rapid decline under low precipitation conditions. However, as precipitation reaches 280 mm, there is another sharp rise in the NDVI, suggesting an increasing reliance on precipitation as the GD increases. In conclusion, an optimal range for achieving high NDVI values lies within the interval of 2.5–3 m for GD, and higher levels of precipitation are more favorable for promoting vegetative growth.

3.4. Risk Assessment of Vegetation Ecological Degradation

The weight coefficients of each evaluation factor are presented in Table 6. The classification criteria for the VEDR in this region were determined based on the ecological environment of the Hunshandake Sandy Land and by referencing classification methods employed in relevant studies, resulting in a four-level division, as illustrated in Table 7.

Table 7. Criteria of VEDR classification and area statistics.

Risk Level	Risk Degree	Risk Value	Area (km^2)	Percentage
4	Less risk	$R < 0.1$	0	0%
3	Medium risk	$0.1 \leq R < 0.3$	894.13	30.77%
2	Large risk	$0.3 \leq R < 0.5$	1922.99	66.17%
1	Great risk	$R \geq 0.5$	88.80	3.06%

The assessment results are presented in Table 7 and Figure 10. In the study area, the VEDR values ranged from 0.12 to 0.60, with an average value of 0.35.

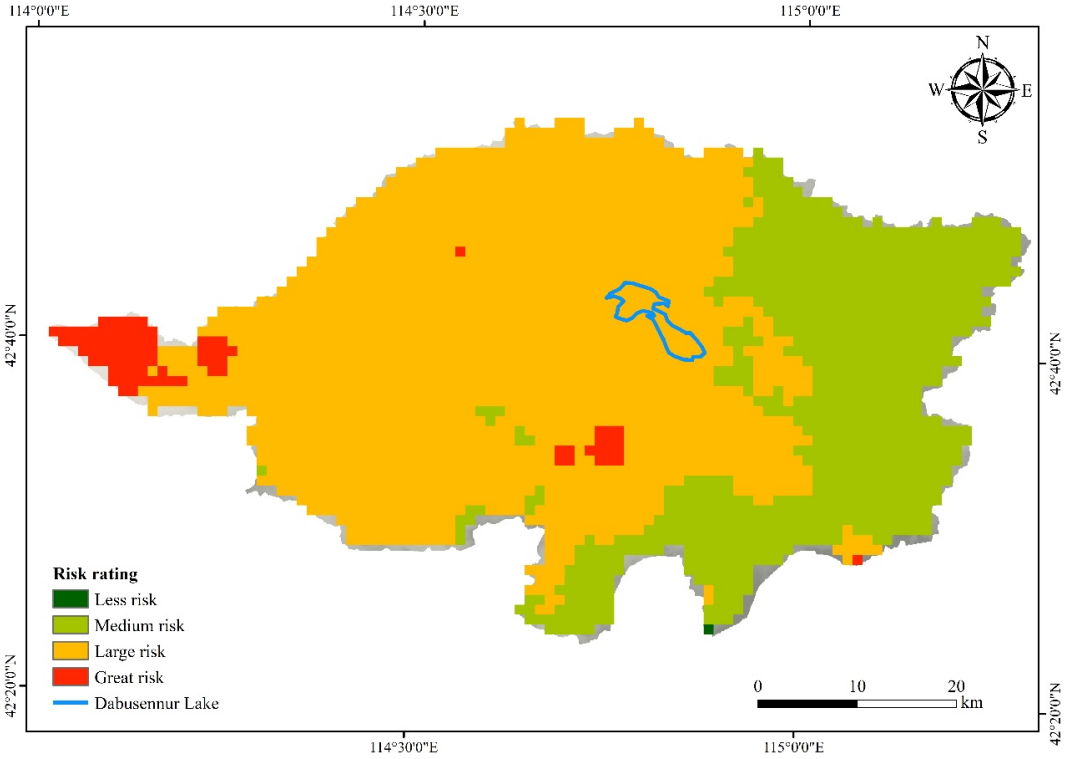

Figure 10. Spatial distribution of VEDR.

The regional VEDR levels exhibit distinct spatial variations, primarily in Level 2 (large risk), encompassing 66.17% (1922.99 km^2) of the total area, predominantly situated in the central and western regions of the basin. This region serves as a transitional zone between Level 3 (medium risk) and Level 1 (great risk), with a relatively low NDVI value, shallow GD, and insufficient precipitation. Meanwhile, Level 3 (medium risk) is predominantly situated in the eastern part of the basin, covering approximately 30.77% (894.13 km^2) of its total area, characterized by a shallow GD and sufficient precipitation. The smallest proportion belongs to Level 1 (great risk), which only accounts for a mere 3.06% (88.80 km^2), with a deep GD and insufficient precipitation. There are no Level 4 (less risk) areas in the basin. Overall, Level 2 and Level 3 dominate the basin, encompassing 96.94% of its total area. The vegetation ecology exhibits fragility and susceptibility to exceedingly arid weather conditions as well as extensive human exploitation of groundwater resources.

Additionally, the implementation of artificial rainfall or ecological water transport could be considered by local authorities to facilitate the restoration of the basin's vegetation ecology.

4. Discussion

4.1. Spatiotemporal Vegetation Changes

Previous studies have demonstrated significant improvements in vegetation conditions across different spatiotemporal scales in Inner Mongolia [18,42–44]. Our research reveals a gradual enhancement of vegetation over the past two decades, with an average increase rate of 0.01 per decade, which exhibits fluctuations potentially attributed to precipitation variations. Interestingly, our findings diverge from those reported for other high-altitude regions such as the Yunnan Plateau [24], while aligning with recent discoveries within other parts of Inner Mongolia [13,14,28]. These distinct patterns may be explained by disparities in the research scope, temporal coverage, and regional climatic characteristics.

4.2. Vegetation Dynamics in Response to Climate Change and Human Activities

In arid and semi-arid climates, where temperature and radiation are also crucial factors, precipitation plays a pivotal role in constraining plant development [45,46]. According to our research, the combined influence of temperature and precipitation significantly enhances the explanatory power of vegetation change [23,47], accounting for over 40% of the variations in vegetation dynamics. GD contributes approximately 20% of vegetation change, representing another crucial factor. The primary anthropogenic factors driving changes in the ecological environment of the watershed encompass the implementation of ecological protection and restoration, alongside agricultural practices [6,8,19,33]. In this study, LULC may account for approximately 15% of the variations in vegetation dynamics. However, when combined with precipitation, temperature, and GD, it can explain more than 30% of these changes. GD, temperature, and precipitation are representative natural variables that amplify the influence of LULC on vegetation dynamics. Moreover, our findings demonstrate a nonlinear strengthening effect of interaction variables on vegetation dynamics, rather than a simple additive relationship [24,27,28]. Recent studies have indicated that Hunshandake Sandy Land has experienced both warming trends and increased precipitation over the past 40 years [32]. Under the trend in climate change, agricultural irrigation strategies should be developed considering ecological water use to ensure the appropriate depth of groundwater.

4.3. Vegetation Ecological Threshold

Vegetation plays a crucial role in ecology, and understanding its ecological threshold is essential for comprehending the external forces driving dynamic changes and maintaining steady-state conditions. Moreover, studying this threshold provides a theoretical framework for effective resource management and ecological restoration [48–51]. To comprehend the climatic environmental thresholds of plants, numerous scholars have researched vegetation's response to climate change using pollen analysis [52,53]. In studies focused on lake wetlands in arid and semi-arid regions, the ecological threshold for vegetation is typically defined by the optimum GD required for plant development without salinization [22,54]. The investigation did not consider the production of salinization. In the DW, the optimum GD required for plant development was determined to be 2.75 m, which could be used as an ecological constraint index for groundwater extraction. These findings will contribute to forecasting future water resource utilization possibilities and serve as a fundamental basis for implementing ecological conservation strategies in the area.

4.4. The Dependence of Vegetation on Groundwater and Precipitation

The association between GD and the NDVI or vegetation coverage has been established by several researchers at the regional scale. To investigate the interaction between groundwater and ecology, GD is utilized as a classification indicator for evaluating vegeta-

tion dependency on groundwater [55–57]. The qualitative analysis in this study reveals that vegetation in regions with medium-high coverage exhibits a greater dependence on groundwater, while vegetation in areas with medium-low coverage shows a stronger dependence on precipitation. Subsequently, stable isotopes will be employed to quantitatively assess the water sources of plants and determine the extent of their dependency on both precipitation and groundwater [58,59]. The three representative plant species, *Caragana sinica*, *Artemisia desertorum* Spreng, and *Hedysarum laeve* Maxim, were selected based on the ecological characteristics of the research region. Samples of plants, soil, groundwater, and precipitation were collected for analysis, and stable isotopes ^{2}H and ^{18}O were employed to investigate the water sources utilized by these vegetation types [60–62].

5. Conclusions

The spatio-temporal evolution characteristics and main driving factors of vegetation cover in the DW, a typical watershed in the southern Hunshandake Sandy Land, were analyzed using univariable linear regression and the Geodetector method, with a primary focus on assessing the risk of vegetation ecological degradation. Precipitation and groundwater are the main factors influencing the risk of vegetation ecological degradation in the basin. The VEDR evaluation results show that the vegetation ecology of the basin is relatively fragile, mainly with medium risk and large risk. In order to cope with the potential impact of climate change on future vegetation dynamics, more reasonable water use strategies should be formulated to ensure ecological water use. A depth of 2.75 m can be used as the ecological constraint index of groundwater exploitation to reduce the interference of human activities and actively restore vegetation. The present study's outcomes provide the basis for developing ecological engineering solutions in arid and semi-arid parts of northern China.

Author Contributions: Conceptualization, P.C. and R.M.; methodology, P.C.; validation, R.M.; formal analysis, P.C.; investigation, P.C. and L.S.; resources, L.Z., R.J. and W.D.; data curation, L.Z., R.J. and W.D.; writing—original draft preparation, P.C.; writing—review and editing, R.M.; visualization, L.S.; supervision, P.C.; project administration, R.M.; funding acquisition, R.M. All authors have read and agreed to the published version of the manuscript.

Funding: This work was funded by the "Basic Research Funds of Chinese Academy of Geological Sciences (SK202327)", "Geological Survey Projects Foundation of the Institute of Hydrogeology and Environmental Geology (DD20221773)", "Investigation of Groundwater Environment in Ordos (Phase II) (ESZC-G-F-220140)", and "National Natural Science Foundation of China (4237070832; 42307555)".

Informed Consent Statement: Not applicable.

Data Availability Statement: The data used to support the findings of this study are available from the corresponding author upon request.

Acknowledgments: The editor and reviewers are sincerely acknowledged for their instructive and detailed comments on the early versions of this manuscript. The authors appreciate all centers supplying open-source datasets used in the present research.

Conflicts of Interest: The authors declare no conflicts of interest.

References

1. Das, A.; Basu, T. Assessment of Peri-Urban Wetland Ecological Degradation through Importance-Performance Analysis (IPA): A Study on Chatra Wetland, India. *Ecol. Indic.* **2020**, *114*, 106274. [CrossRef]
2. Dias, T.; Crous, C.J.; Liberati, D.; Munzi, S.; Gouveia, C.; Ulm, F.; Afonso, A.C.; Ochoa-Hueso, R.; Manrique, E.; Sheppard, L.; et al. Alleviating Nitrogen Limitation in Mediterranean Maquis Vegetation Leads to Ecological Degradation: N Enrichment Degrades Ecological Partnerships and Its Functions. *Land Degrad. Develop.* **2017**, *28*, 2482–2492. [CrossRef]
3. Park, C.Y.; Takahashi, K.; Takakura, J.; Li, F.; Fujimori, S.; Hasegawa, T.; Ito, A.; Lee, D.K. How Will Deforestation and Vegetation Degradation Affect Global Fire Activity? *Earth's Future* **2021**, *9*, e2020EF001786. [CrossRef]
4. Bernard, B.; Aron, M.; Loy, T.; Muhamud, N.W.; Benard, S. The Impact of Refugee Settlements on Land Use Changes and Vegetation Degradation in West Nile Sub-Region, Uganda. *Geocarto Int.* **2022**, *37*, 16–34. [CrossRef]

5. Luo, J.; Huai, W.; Wang, P. Contaminant Transport in a Three-Zone Wetland: Dispersion and Ecological Degradation. *J. Hydrol.* **2016**, *534*, 341–351. [CrossRef]
6. Chen, X.; Wang, F.; Jiang, L.; Huang, C.; An, P.; Pan, Z. Impact of Center Pivot Irrigation on Vegetation Dynamics in a Farming-Pastoral Ecotone of Northern China: A Case Study in Ulanqab, Inner Mongolia. *Ecol. Indic.* **2019**, *101*, 274–284. [CrossRef]
7. Li, T.; Zhang, Q.; Singh, V.P.; Zhao, J.; Song, J.; Sun, S.; Wang, G.; Shen, Z.; Wu, W. Identification of Degradation Areas of Ecological Environment and Degradation Intensity Assessment in the Yellow River Basin. *Front. Earth Sci.* **2022**, *10*, 922013. [CrossRef]
8. Zhang, Q.; Wang, G.; Yuan, R.; Singh, V.P.; Wu, W.; Wang, D. Dynamic Responses of Ecological Vulnerability to Land Cover Shifts over the Yellow River Basin, China. *Ecol. Indic.* **2022**, *144*, 109554. [CrossRef]
9. Jiang, W.; Meng, L.; Liu, F.; Sheng, Y.; Chen, S.; Yang, J.; Mao, H.; Zhang, J.; Zhang, Z.; Ning, H. Distribution, Source Investigation, and Risk Assessment of Topsoil Heavy Metals in Areas with Intensive Anthropogenic Activities Using the Positive Matrix Factorization (PMF) Model Coupled with Self-Organizing Map (SOM). *Env. Geochem. Health* **2023**, *45*, 6353–6370. [CrossRef]
10. Wang, M. Accelerating Collaborative Innovation in Hydrological, Engineering, and Environmental Fields. *J. Groundw. Sci. Eng.* **2024**, *12*, 1. [CrossRef]
11. Wang, J.; Zhang, C.; Luo, P.; Yang, H.; Luo, C. Water Yield Response to Plant Community Conversion Caused by Vegetation Degradation and Improvement in an Alpine Meadow on the Northeastern Tibetan Plateau. *Sci. Total Environ.* **2023**, *856*, 159174. [CrossRef] [PubMed]
12. Li, Y.; Xie, Z.; Qin, Y.; Zheng, Z. Estimating Relations of Vegetation, Climate Change, and Human Activity: A Case Study in the 400 Mm Annual Precipitation Fluctuation Zone, China. *Remote Sens.* **2019**, *11*, 1159. [CrossRef]
13. Gu, Y.; Pang, B.; Qiao, X.; Xu, D.; Li, W.; Yan, Y.; Dou, H.; Ao, W.; Wang, W.; Zou, C.; et al. Vegetation Dynamics in Response to Climate Change and Human Activities in the Hulun Lake Basin from 1981 to 2019. *Ecol. Indic.* **2022**, *136*, 108700. [CrossRef]
14. Yu, L.; Wu, Z.; Du, Z.; Zhang, H.; Liu, Y. Insights on the Roles of Climate and Human Activities to Vegetation Degradation and Restoration in Beijing-Tianjin Sandstorm Source Region. *Ecol. Eng.* **2021**, *159*, 106105. [CrossRef]
15. Zhumanova, M.; Mönnig, C.; Hergarten, C.; Darr, D.; Wrage-Mönnig, N. Assessment of Vegetation Degradation in Mountainous Pastures of the Western Tien-Shan, Kyrgyzstan, Using eMODIS NDVI. *Ecol. Indic.* **2018**, *95*, 527–543. [CrossRef]
16. Sun, B.; Li, Z.; Gao, W.; Zhang, Y.; Gao, Z.; Song, Z.; Qin, P.; Tian, X. Identification and Assessment of the Factors Driving Vegetation Degradation/Regeneration in Drylands Using Synthetic High Spatiotemporal Remote Sensing Data—A Case Study in Zhenglanqi, Inner Mongolia, China. *Ecol. Indic.* **2019**, *107*, 105614. [CrossRef]
17. Liu, Y.; Liu, R.; Ge, Q. Evaluating the Vegetation Destruction and Recovery of Wenchuan Earthquake Using MODIS Data. *Nat. Hazards* **2010**, *54*, 851–862. [CrossRef]
18. Yin, H.; Pflugmacher, D.; Li, A.; Li, Z.; Hostert, P. Land Use and Land Cover Change in Inner Mongolia—Understanding the Effects of China's Re-Vegetation Programs. *Remote Sens. Environ.* **2018**, *204*, 918–930. [CrossRef]
19. Liu, Q.; Wang, X.; Zhang, Y.; Zhang, H.; Li, L. Vegetation Degradation and Its Driving Factors in the Farming–Pastoral Ecotone over the Countries along Belt and Road Initiative. *Sustainability* **2019**, *11*, 1590. [CrossRef]
20. Peng, Y.; Wang, Q.; Fan, M. Identification of the Key Ecological Factors Influencing Vegetation Degradation in Semi-Arid Agro-Pastoral Ecotone Considering Spatial Scales. *Acta Oecologica* **2017**, *85*, 62–68. [CrossRef]
21. Piao, S.; Cui, M.; Chen, A.; Wang, X.; Ciais, P.; Liu, J.; Tang, Y. Altitude and Temperature Dependence of Change in the Spring Vegetation Green-up Date from 1982 to 2006 in the Qinghai-Xizang Plateau. *Agric. For. Meteorol.* **2011**, *151*, 1599–1608. [CrossRef]
22. Chen, P.; Ma, R.; Shi, J.; Si, L. Effects of Groundwater Depth and Salt Content on Vegetation in Dry Lake Basins: A Case Study of Chahan Lake, Northern China. *Geofluids* **2022**, *2022*, e7393247. [CrossRef]
23. Qin, D.; Zhao, Z.; Han, L.; Qian, Y.; Ou, L.; Wu, Z.; Wang, M. Determination of Groundwater Recharge Regime and Flowpath in the Lower Heihe River Basin in an Arid Area of Northwest China by Using Environmental Tracers: Implications for Vegetation Degradation in the Ejina Oasis. *Appl. Geochem.* **2012**, *27*, 1133–1145. [CrossRef]
24. Huo, H.; Sun, C. Spatiotemporal Variation and Influencing Factors of Vegetation Dynamics Based on Geodetector: A Case Study of the Northwestern Yunnan Plateau, China. *Ecol. Indic.* **2021**, *130*, 108005. [CrossRef]
25. Han, Y.; Ke, Y.; Zhu, L.; Feng, H.; Zhang, Q.; Sun, Z.; Zhu, L. Tracking Vegetation Degradation and Recovery in Multiple Mining Areas in Beijing, China, Based on Time-Series Landsat Imagery. *GIScience Remote Sens.* **2021**, *58*, 1477–1496. [CrossRef]
26. Jiang, W.; Wang, G.; Sheng, Y.; Shi, Z.; Zhang, H. Isotopes in Groundwater (2H, 18O, 14C) Revealed the Climate and Groundwater Recharge in the Northern China. *Sci. Total Environ.* **2019**, *666*, 298–307. [CrossRef]
27. Wang, Y.; Zhang, Z.; Chen, X. Quantifying Influences of Natural and Anthropogenic Factors on Vegetation Changes Based on Geodetector: A Case Study in the Poyang Lake Basin, China. *Remote Sens.* **2021**, *13*, 5081. [CrossRef]
28. Zhu, L.; Meng, J.; Zhu, L. Applying Geodetector to Disentangle the Contributions of Natural and Anthropogenic Factors to NDVI Variations in the Middle Reaches of the Heihe River Basin. *Ecol. Indic.* **2020**, *117*, 106545. [CrossRef]
29. Jiang, W.; Lv, J.; Wang, C.; Chen, Z.; Liu, Y. Marsh Wetland Degradation Risk Assessment and Change Analysis: A Case Study in the Zoige Plateau, China. *Ecol. Indic.* **2017**, *82*, 316–326. [CrossRef]
30. Muqi, X.; Jiang, Z.; Yuyao, H.; Yurong, G.; Shen, Z.; Yijian, T.; Chengqing, Y.; Zijian, W. The Ecological Degradation and Restoration of Baiyangdian Lake, China. *J. Freshw. Ecol.* **1998**, *13*, 433–446. [CrossRef]
31. Zhao, Q.; Guo, F.; Zhang, Y.; Ma, S.; Jia, X.; Meng, W. How Sulfate-Rich Mine Drainage Affected Aquatic Ecosystem Degradation in Northeastern China, and Potential Ecological Risk. *Sci. Total Environ.* **2017**, *609*, 1093–1102. [CrossRef] [PubMed]

32. Ma, R.; Chen, P.; Zhang, B.; Zhao, L.; Ning, K. Identification of Ecological Restoration Standard for Lakes on the Inner Mongolia Plateau, China. *Ecol. Indic.* **2024**, *162*, 111993. [CrossRef]
33. Yuan, L.; Gao, Y.; Cheng, F.; Du, J.; Hu, Z.; Yang, X.; Wang, H.; Kong, X.; Fu, Z.; Wang, W.; et al. The Influence of Oil Exploitation on the Degradation of Vegetation: A Case Study in the Yellow River Delta Nature Reserve, China. *Environ. Technol. Innov.* **2022**, *28*, 102579. [CrossRef]
34. Zhang, X.; Wang, N.; Xie, Z.; Ma, X.; Huete, A. Water Loss Due to Increasing Planted Vegetation over the Badain Jaran Desert, China. *Remote Sens.* **2018**, *10*, 134. [CrossRef]
35. Yang, X.; Scuderi, L.A.; Wang, X.; Scuderi, L.J.; Zhang, D.; Li, H.; Forman, S.; Xu, Q.; Wang, R.; Huang, W.; et al. Groundwater Sapping as the Cause of Irreversible Desertification of Hunshandake Sandy Lands, Inner Mongolia, Northern China. *Proc. Natl. Acad. Sci. USA* **2015**, *112*, 702–706. [CrossRef] [PubMed]
36. Zhang, G.; Cheng, Y.; Liu, H.; Xiao, C.; Nie, H.; Zhu, Z.; Zhao, D.; Zan, Y. Evaluation of the Groundwater Ecological Water Requirement in the Southeast Margin of Otindag Sandy Land Based on Allowable Groundwater Depth Drawdown. *Water* **2023**, *15*, 3504. [CrossRef]
37. Chu, Y.; Li-jie, W.; Yi-long, Z.; Xiu-ya, W.; Zhan-chuan, W.; Zhou, Z. Effect of Groundwater on the Ecological Water Environment of Typical Inland Lakes in the Inner Mongolian Plateau. *J. Groundw. Sci. Eng.* **2022**, *10*, 353.
38. Liang, W.; Quan, Q.; Wu, B.; Mo, S. Response of Vegetation Dynamics in the Three-North Region of China to Climate and Human Activities from 1982 to 2018. *Sustainability* **2023**, *15*, 3073. [CrossRef]
39. Li, C.; Men, B.; Yin, S. Spatiotemporal Variation of Groundwater Extraction Intensity Based on Geostatistics—Set Pair Analysis in Daxing District of Beijing, China. *Sustainability* **2022**, *14*, 4341. [CrossRef]
40. Wang, Z.; Xu, D.; Peng, D.; Zhang, Y. Quantifying the Influences of Natural and Human Factors on the Water Footprint of Afforestation in Desert Regions of Northern China. *Sci. Total Environ.* **2021**, *780*, 146577. [CrossRef]
41. Wang, J.; Li, X.; Christakos, G.; Liao, Y.; Zhang, T.; Gu, X.; Zheng, X. Geographical Detectors-Based Health Risk Assessment and Its Application in the Neural Tube Defects Study of the Heshun Region, China. *Int. J. Geogr. Inf. Sci.* **2010**, *24*, 107–127. [CrossRef]
42. Li, S.; Li, X.; Gong, J.; Dang, D.; Dou, H.; Lyu, X. Quantitative Analysis of Natural and Anthropogenic Factors Influencing Vegetation NDVI Changes in Temperate Drylands from a Spatial Stratified Heterogeneity Perspective: A Case Study of Inner Mongolia Grasslands, China. *Remote Sens.* **2022**, *14*, 3320. [CrossRef]
43. Wang, S.; Li, R.; Wu, Y.; Zhao, S. Effects of Multi-Temporal Scale Drought on Vegetation Dynamics in Inner Mongolia from 1982 to 2015, China. *Ecol. Indic.* **2022**, *136*, 108666. [CrossRef]
44. You, G.; Liu, B.; Zou, C.; Li, H.; McKenzie, S.; He, Y.; Gao, J.; Jia, X.; Altaf Arain, M.; Wang, S.; et al. Sensitivity of Vegetation Dynamics to Climate Variability in a Forest-Steppe Transition Ecozone, North-Eastern Inner Mongolia, China. *Ecol. Indic.* **2021**, *120*, 106833. [CrossRef]
45. Ebrahimi Khusfi, Z.; Khosroshahi, M.; Roustaei, F.; Mirakbari, M. Spatial and Seasonal Variations of Sand-Dust Events and Their Relation to Atmospheric Conditions and Vegetation Cover in Semi-Arid Regions of Central Iran. *Geoderma* **2020**, *365*, 114225. [CrossRef]
46. Jin, K.; Wang, F.; Zong, Q.; Qin, P.; Liu, C. Impact of Variations in Vegetation on Surface Air Temperature Change over the Chinese Loess Plateau. *Sci. Total Environ.* **2020**, *716*, 136967. [CrossRef] [PubMed]
47. Yin, L.; Zhou, Y.; Huang, J.; Wenninger, J.; Zhang, E.; Hou, G.; Dong, J. Interaction between Groundwater and Trees in an Arid Site: Potential Impacts of Climate Variation and Groundwater Abstraction on Trees. *J. Hydrol.* **2015**, *528*, 435–448. [CrossRef]
48. James-Pirri, M.-J.; Swanson, J.L.; Roman, C.T.; Ginsberg, H.S.; Heltshe, J.F. Ecological Thresholds for Salt Marsh Nekton and Vegetation Communities. In *Application of Threshold Concepts in Natural Resource Decision Making*; Guntenspergen, G.R., Ed.; Springer: New York, NY, USA, 2014; pp. 291–319. ISBN 978-1-4899-8040-3.
49. Rong, H.; Shan, D.; Guo, J.Y. Analysis Threshold Value of Ecological Water Require-Ment for Vegetation Restoration on Northern Grassland. *Appl. Mech. Mater.* **2012**, *212*, 549–553. [CrossRef]
50. Sasaki, T.; Koyama, A.; Okuro, T. Coupling Structural and Functional Thresholds for Vegetation Changes on a Mongolian Shrubland. *Ecol. Indic.* **2018**, *93*, 1264–1275. [CrossRef]
51. Zhao, M.; Wang, C.; He, Y.; He, T. Soil Characteristics and Response Thresholds of Salt Meadow on Lake Beaches of the Ordos Platform. *Front. Environ. Sci.* **2022**, *10*, 1050757. [CrossRef]
52. Tzedakis, P.C.; Frogley, M.R.; Lawson, I.T.; Preece, R.C.; Cacho, I.; de Abreu, L. Ecological Thresholds and Patterns of Millennial-Scale Climate Variability: The Response of Vegetation in Greece during the Last Glacial Period. *Geology* **2004**, *32*, 109. [CrossRef]
53. Vegas-Vilarrúbia, T.; González-Sampériz, P.; Morellón, M.; Gil-Romera, G.; Pérez-Sanz, A.; Valero-Garcés, B. Diatom and Vegetation Responses to Late Glacial and Early Holocene Climate Changes at Lake Estanya (Southern Pyrenees, NE Spain). *Palaeogeogr. Palaeoclimatol. Palaeoecol.* **2013**, *392*, 335–349. [CrossRef]
54. Qi, Z.; Xiao, C.; Wang, G.; Liang, X. Study on Ecological Threshold of Groundwater in Typical Salinization Area of Qian'an County. *Water* **2021**, *13*, 856. [CrossRef]
55. Huntington, J.; McGwire, K.; Morton, C.; Snyder, K.; Peterson, S.; Erickson, T.; Niswonger, R.; Carroll, R.; Smith, G.; Allen, R. Assessing the Role of Climate and Resource Management on Groundwater Dependent Ecosystem Changes in Arid Environments with the Landsat Archive. *Remote Sens. Environ.* **2016**, *185*, 186–197. [CrossRef]
56. Mpakairi, K.S.; Dube, T.; Dondofema, F.; Dalu, T. Spatio–Temporal Variation of Vegetation Heterogeneity in Groundwater Dependent Ecosystems within Arid Environments. *Ecol. Inform.* **2022**, *69*, 101667. [CrossRef]

57. Zhang, H.; Wang, X.-S. The Impact of Groundwater Depth on the Spatial Variance of Vegetation Index in the Ordos Plateau, China: A Semivariogram Analysis. *J. Hydrol.* **2020**, *588*, 125096. [CrossRef]
58. Sohel, M.S.I.; Grau, A.V.; McDonnell, J.J.; Herbohn, J. Tropical Forest Water Source Patterns Revealed by Stable Isotopes: A Preliminary Analysis of 46 Neighboring Species. *For. Ecol. Manag.* **2021**, *494*, 119355. [CrossRef]
59. Wang, J.; Lu, N.; Fu, B. Inter-Comparison of Stable Isotope Mixing Models for Determining Plant Water Source Partitioning. *Sci. Total Environ.* **2019**, *666*, 685–693. [CrossRef] [PubMed]
60. Allen, S.T.; Sprenger, M.; Bowen, G.J.; Brooks, J.R. Spatial and Temporal Variations in Plant Source Water: O and H Isotope Ratios from Precipitation to Xylem Water. In *Stable Isotopes in Tree Rings*; Siegwolf, R.T.W., Brooks, J.R., Roden, J., Saurer, M., Eds.; Tree Physiology; Springer International Publishing: Cham, Switzerland, 2022; Volume 8, pp. 501–535. ISBN 978-3-030-92697-7.
61. Landgraf, J.; Tetzlaff, D.; Dubbert, M.; Dubbert, D.; Smith, A.; Soulsby, C. Xylem Water in Riparian Willow Trees (Salix Alba) Reveals Shallow Sources of Root Water Uptake by in Situ Monitoring of Stable Water Isotopes. *Hydrol. Earth Syst. Sci.* **2022**, *26*, 2073–2092. [CrossRef]
62. Li, Y.; Ma, Y.; Song, X.; Wang, L.; Han, D. A δ2H Offset Correction Method for Quantifying Root Water Uptake of Riparian Trees. *J. Hydrol.* **2021**, *593*, 125811. [CrossRef]

Disclaimer/Publisher's Note: The statements, opinions and data contained in all publications are solely those of the individual author(s) and contributor(s) and not of MDPI and/or the editor(s). MDPI and/or the editor(s) disclaim responsibility for any injury to people or property resulting from any ideas, methods, instructions or products referred to in the content.

water

MDPI

Article

Spatiotemporal Dynamics and Drivers of Coastal Wetlands in Tianjin–Hebei over the Past 80 Years

Feicui Wang [1], Fu Wang [1,*], Ke Zhu [2], Peng Yang [1], Tiejun Wang [3], Yunzhuang Hu [1] and Lijuan Ye [1]

[1] Tianjin Center (North China Center of Geoscience Innovation), China Geological Survey (CGS), CGS Key Laboratory of Coast Geo-Environment and Tianjin Key Laboratory of Coast Geological Processes and Environmental Safety, Tianjin 300170, China; wfeicui0503@126.com (F.W.); dcyangpeng@163.com (P.Y.); huyunzhuang@163.com (Y.H.); didaduzhe2007@163.com (L.Y.)

[2] Tianjin Tian Ke Digital Innovation Science and Technology Co., Ltd., Tianjin 300100, China; 15620699565@163.com

[3] Institute of Surface-Earth System Science, School of Earth System Science, Tianjin University, Tianjin 300072, China; tiejun.wang@tju.edu.cn

* Correspondence: tjwangfu@163.com

Abstract: Coastal wetland ecosystems are critical due to their diverse ecological and economic benefits, yet they have been significantly affected by human activities over the past century. Understanding the spatiotemporal changes and underlying factors influencing these ecosystems is crucial for developing effective ecological protection and restoration strategies. This study examines the Tianjin–Hebei coastal wetlands using topographic maps from the 1940s and Landsat satellite imagery from 1975, 2000, and 2020, supplemented by historical literature and field surveys. The aim is to analyze the distribution and classification of coastal wetlands across various temporal intervals. The findings indicate an expansion of the Tianjin–Hebei coastal wetlands from 7301.34 km^2 in the 1940s to 8041.73 km^2 in 2020. However, natural wetlands have declined by approximately 44.36 km^2/year, while constructed wetlands have increased by around 53.61 km^2/year. The wetlands have also become increasingly fragmented, with higher numbers of patches and densities. The analysis of driving factors points to human activities—such as urban construction, cultivated land reclamation, sea aquaculture, and land reclamation—as the primary contributors to these changes. Furthermore, the study addresses the ecological and environmental issues stemming from wetland changes and proposes strategies for wetland conservation. This research aims to enhance the understanding among researchers and policymakers of the dynamics and drivers of coastal wetland changes, as well as the major challenges in their protection, and to serve as a foundation for developing evidence-based conservation and restoration strategies.

Keywords: coastal wetlands; spatiotemporal changes; human activities; Tianjin and Hebei

1. Introduction

Coastal wetlands, which are vital ecosystems closely linked to the ocean, play a crucial role in maintaining ecological integrity and enhancing economic prosperity. In China, coastal areas support 46% of the population and contribute 60% to its GDP [1]. These regions have seen a significant depletion of natural wetlands due to intensive human activities. Global studies indicate that since 1900, 64% of wetlands worldwide have been lost [2], with China experiencing a 54% reduction in wetland area since 1980 [3]. National surveys conducted between 2003 and 2013 reveal a total decrease of nearly 34,000 km^2 in China's wetlands, primarily in natural wetlands [4]. This decline has disrupted the natural processes of coastal evolution, as well as hydrological regimes, leading to soil and water quality degradation, vegetation loss, and a reduction in biodiversity and ecosystem services [5–7]. Consequently, there is an urgent need for enhanced wetland conservation efforts.

Understanding the dynamics of wetlands and the forces driving their changes is essential for developing effective conservation and restoration strategies. Previous studies have explored changes in coastal wetlands using remote sensing and field surveys [8–10]. For example, the wetlands in Louisiana are shaped by a combination of natural factors, such as hurricanes, and human activities [11]. Likewise, Mexican coastal wetlands are influenced by sea-level rise, tropical storm frequency, and changes in coastal watershed elevations [12]. In Sri Lanka, the decline of mangroves in the Puttlam Lagoon has been attributed to shrimp farming and salt industries [13]. Along China's coast, human activities since 2000 have significantly altered coastal wetlands, as evidenced by studies from the Bohai Bay area [14–17]. Despite these insights, distinguishing between natural evolution and human-induced degradation remains challenging due to extensive human modification. Therefore, long-term research is crucial to assess the impacts of natural processes versus human activities on coastal wetlands.

Although Landsat satellites have provided high-quality earth observation data with extensive spatial and temporal coverage since the 1970s, these data only reflect changes over the past 50 years. To gain a more comprehensive understanding of long-term wetland evolution, a multi-source data-integration approach is needed. For example, combining historical maps, remote sensing imagery, and extensive field surveys can address the limitations of relying on a single data source. Existing studies have used multi-temporal maps and broad field investigations to establish coastline data for mainland China since the 1940s [18]. This multi-source approach extends the temporal scale and helps to more accurately reveal the natural evolution trends of wetlands and the impacts of human activities.

This study utilizes a combination of multi-source remote sensing data, topographic maps, and field surveys to reconstruct the spatiotemporal distribution of Tianjin and Hebei coastal wetlands over the past eight decades. It investigates the factors driving changes in wetlands, assesses the influences of natural and human activities, and seeks to provide scientific insights and decision-making support for their conservation.

2. Materials and Methods

2.1. Study Area

The study area is located in the mid-latitude zone on the western coast of the Bohai Sea, characterized as a semi-closed marine environment [19]. It includes three prefecture-level cities in Tianjin and Hebei—Binhai New Area, Tangshan, and Cangzhou (115.7° E–119.6° E, 37.5° N–40.5° N)—covering approximately 39,574 km^2 (Figure 1). These cities are strategically significant and play crucial roles in the coordinated development of the Beijing–Tianjin–Hebei region.

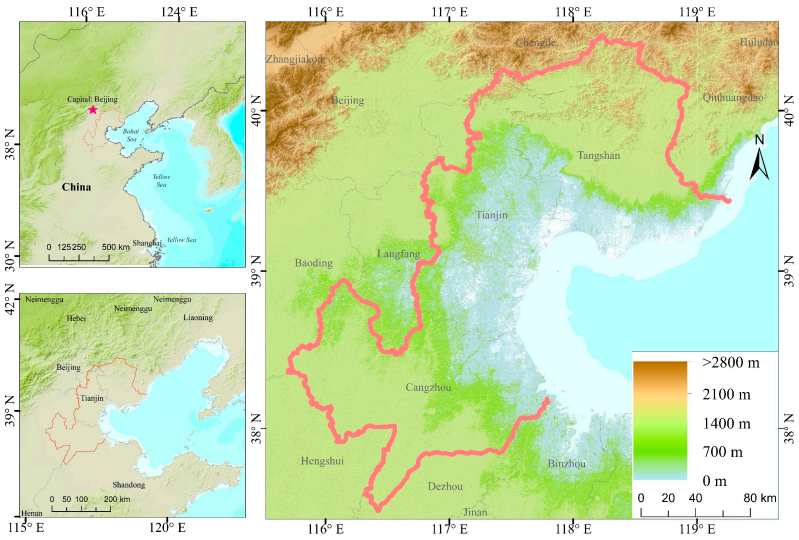

Figure 1. Location map of the study area.

The area connects with the Pacific Ocean and the Yellow Sea through straits between the Liaodong Peninsula and the Shandong Peninsula. The seabed deepens gradually from the coastline into the gulf, averaging a depth of 12.5 m (https://www.stats.gov.cn/sj/ndsj/2011/indexeh.htm (accessed on 6 June 2024)). The coastal terrain, typically below +5 m above sea level, features a west-to-east gradient, sloping gently towards the sea from north to south and west to east. Numerous rivers, including the Haihe, Duliujian, and Dagu Rivers, traverse the coastal plain and flow into the gulf. Notably, Tianjin City is undergoing long-term tectonic subsidence, estimated at approximately 1.3 to 2.0 mm per year [20]. This geological process has a significant impact on the local coastline morphology, marine environments, and ecosystems [21,22].

2.2. Data Source

This study utilizes a combination of Landsat series satellite images, topographic maps from the U.S. Army Map Service, and field survey data to comprehensively and accurately analyze the ecological and environmental changes in Bohai Bay and its surrounding areas. The remote sensing images provide long-term observational data, the topographic maps reflect historical topographic conditions, and the field surveys ensure the authenticity and reliability of the data.

2.2.1. Coastal Area Images

For this study, Landsat MSS/TM/OLI series sensor image data from 1975, 2000, and 2020 were obtained. The data underwent processing, including geometric correction, radiometric calibration, atmospheric correction, and mosaic registration. This ensured consistency in the projection of the imagery and vector data.

2.2.2. Topographic Map Data

The U.S. Army Map Service compiled a set of 1:250,000 topographic maps of China's coastal areas, primarily reflecting the coastal terrain conditions of the early 1940s (https://maps.lib.utexas.edu/maps/ams/china/ (accessed on 7 May 2024)). These maps employ the Universal Transverse Mercator (UTM) projection and adhere to rigorous cartographic standards suitable for modern mapping. This includes standardized map sheet numbering, map title, mosaic diagrams, scale, legend, textual annotations, latitude and longitude grid, kilometer grid, control points, contour lines, depth contours, elevation points, boundary lines, shorelines, schematic distribution of information sources, and accuracy specifications. Evaluated from the perspectives of cartographic standards, coverage, scale, and printing quality, this set of map data is the only available large-scale spatial data relevant to research in this area, making it of significant reference value for related studies.

2.2.3. Field Survey Data

To ensure the accuracy and reliability of data on coastal wetland changes, this study conducted field verifications at 119 points to assess the coastal wetland distribution as of 2020. During these verifications, high-precision GPS equipment was employed to calibrate geographic coordinates and compare these with remote sensing images, ensuring precise positioning. Moreover, this study incorporates previous field survey data, historical maps, literature, and images from the Google Earth platform. In-depth discussions with local residents and experts were also conducted to gain insight into the historical changes in wetlands and the impact of human activities. These field verifications confirmed that the indoor interpretations of wetland distribution aligned with the actual conditions, providing a reliable data foundation for subsequent research.

2.3. Methods

2.3.1. Definition and Classification of Coastal Wetlands

Coastal wetlands, defined as water areas not exceeding a depth of 6 m and their adjacent submerged zones, include permanent water bodies, intertidal areas, and coastal

lowlands. This definition follows the guidelines set by the Wetland classification (GB/T 24708-2009) [23]. According to the convention, wetlands are categorized into two levels: the first classifies the coastal wetland systems in Tianjin and Hebei as either natural or constructed wetlands; the second further classifies natural wetlands based on their geomorphological features and constructed wetlands based on their primary functional uses. Detailed classifications are depicted in Table 1.

Table 1. Wetland classification.

Level 1	Level 2	Interpretation Markers
Natural Wetland	River Wetland	
	Lake Wetland	
	Neritic Wetland	
	Marsh Wetland	
Constructed Wetland	Reservoir Pond Wetland	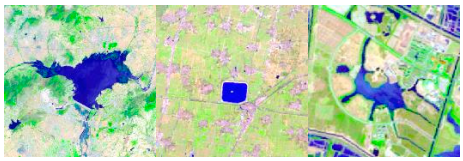
	Paddy, Mariculture, and Saltern Wetland	

Using multi-temporal Landsat remote sensing images and field survey data processed, water boundaries were extracted. Visual interpretation methods were used to derive spatial and attribute data for coastal wetlands. Additionally, topographic map data underwent spatial registration, which facilitated the reconstruction and measurement of coastal wetland areas in Tianjin and Hebei from the 1940s, thus restoring the historical distribution patterns of these wetlands.

2.3.2. Extraction Methods for Coastal Wetlands

In analyzing coastal wetlands, it is crucial to accurately differentiate between water bodies and vegetation. The Modified Normalized Difference Water Index (MNDWI) is a valuable tool for this purpose. It leverages satellite imagery bands, specifically focusing on the distinct spectral properties of water and vegetation.

Water strongly absorbs and minimally reflects in the shortwave infrared (SWIR) band, while vegetation reflects more light. This contrast is enhanced by the MNDWI, effectively highlighting water bodies and suppressing vegetation signals. This method is particularly beneficial in urban environments, where shadows from buildings might otherwise mimic water bodies in spectral data, leading to potential misclassification.

The MNDWI improves the accuracy of water extraction by enhancing contrast and reducing confusion in complex landscapes [24–26]. The formula for the MNDWI is:

$$\text{MNDWI} = (\text{GREEN} - \text{SWIR})/(\text{GREEN} + \text{SWIR}) \quad (1)$$

where "GREEN" refers to the green light band and "SWIR" refers to the shortwave infrared band.

Following the index calculation, threshold segmentation is applied to accurately delineate water boundaries. Optimal thresholds are determined through iterative adjustments and the incorporation of auxiliary data, such as higher-resolution remote sensing images and topographic information. The aim is to maximize the accuracy of water body extraction while minimizing the misclassification of other land features. After segmentation, manual visual editing refines and adjusts the water boundary, finalizing the attributes of identified water bodies based on researcher expertise.

2.3.3. Calculation Method for Wetland Dynamic Changes

The change in area for various wetland types over time is quantified using the following formula to calculate the dynamic change (K) of a single wetland type:

$$K = \frac{U_b - U_a}{U_a} \times \frac{1}{T} \times 100\% \quad (2)$$

Here, K represents the annual change in area of a specific wetland type within the study area, and U_a and U_b denote the area of the wetland type at the beginning and end of the study period T years, respectively.

2.3.4. Trajectory Analysis Method

The trajectory analysis method clarifies the temporal evolution of specific attributes within time-series data, suitable for both continuous and discontinuous phenomena. Trajectories are denoted by codes such as "111" or "AAB", each representing types of coastal wetlands across geographic grid cells at different times within the study period. This analysis effectively illustrates changes in coastal wetland types across various locations [27,28]. The formula for this is expressed as:

$$CT = 10^{n-1}P_1 + 10^{n-2}P_2 + \cdots + 10^{n-i}P_i + \cdots + P_n \quad (3)$$

Here, CT represents the change trajectory code for each grid within the study time series; n denotes the number of time nodes within the series ($n > 1$); and P_i represents the coastal wetland type data at the n-th time node.

Using raster data from 1940, 1975, 2000, and 2020, this paper conducted an analysis with ArcGIS 10.2 to examine the changes in coastal wetlands. With four time points, there are theoretically 2401 different change trajectory codes. After empirical analysis and field investigations, we excluded codes that indicated no change, were deemed unreasonable, or covered small and insignificant areas. The remaining codes were then ranked by the number of raster cells they included. It was determined that the top 20 trajectory codes, which cover 75.27% of all areas showing change, effectively represent the primary types of changes in coastal wetlands over the study period.

2.3.5. Landscape Pattern Analysis Method

To thoroughly understand the development and evolution of the coastal region around Bohai Bay, landscape ecological research methods are utilized. Key indicators, such as patch density (PD) and number of patches (NP), are analyzed using Fragstats 4.2 software to study the landscape pattern characteristics of the study area [29,30].

3. Results

3.1. Changes in Coastal Wetland Area

3.1.1. Coastal Wetland Area Changes in Total

The spatial distribution of coastal wetlands in Tianjin–Hebei has seen significant alterations from 1940 to 2020, as depicted in Figure 2 and Table 2. During this 80-year period, there were considerable shifts in wetland types and areas.

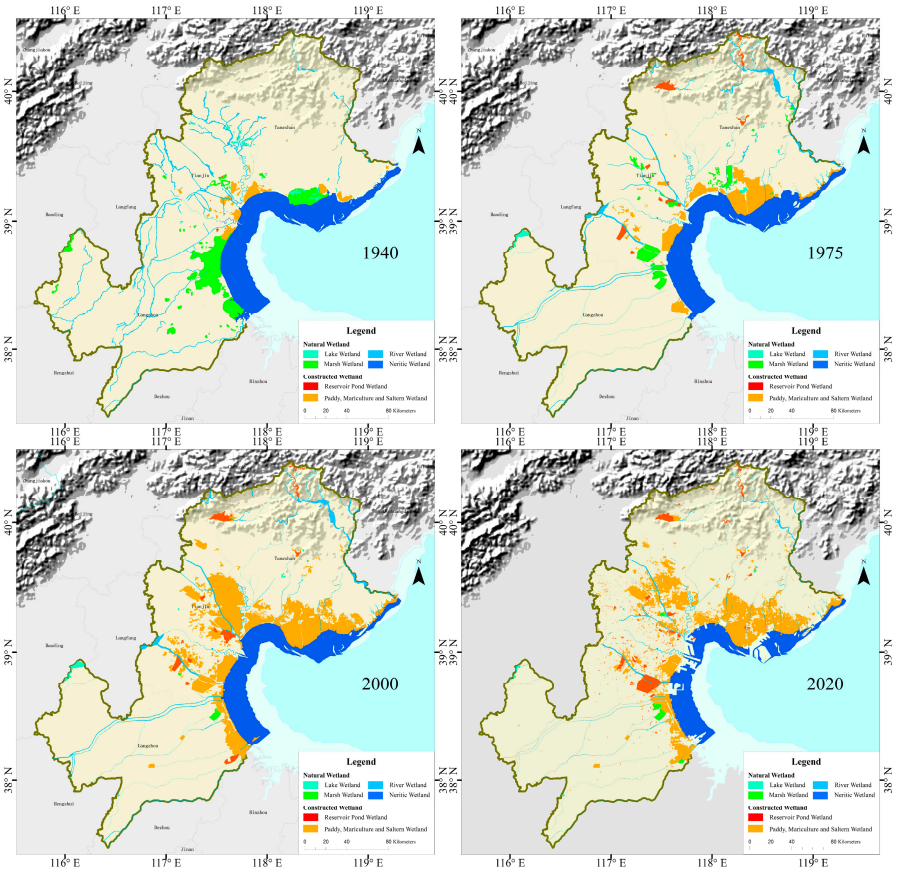

Figure 2. Distribution of wetlands in different periods.

Table 2. Area of wetland types in different periods (Unit: km^2).

Primary	Secondary	1940	1975	2000	2020
Constructed Wetland	Paddy, Mariculture, and Saltern Wetland	521.82	1655.9	4933.54	4194.18
	Reservoir Pond Wetland	14.39	269.3	371.04	631.12
Natural Wetland	River Wetland	1044.87	930.16	864.41	493.25
	Lake Wetland	132.12	103.59	69.72	33.83
	Neritic Wetland	3965.25	3506.52	3253.48	2588.52
	Marsh Wetland	1622.89	647.43	54.08	100.83
Total		7301.34	7112.9	9546.27	8041.73

(Note: High-resolution aerial image analysis and field verification were conducted to validate remote sensing interpretations of coastal wetlands in 2020. The classification accuracy achieved was 88.80%.)

Initially, in the constructed wetland categories, areas of paddy, mariculture, and saltern wetlands exhibited steady growth from 1940 to 1975, with an average annual increase of 32.40 km^2 (Table 3). This increase accelerated to 131.11 km^2 annually between 1975 and 2000. However, starting in the 21st century, this trend reversed, with the area of constructed wetlands experiencing an annual loss of 36.97 km^2 from 2000 to 2020. Conversely, the area of reservoir pond wetlands consistently expanded, increasing by 7.28 km^2 annually from 1940 to 1975, by 4.07 km^2 annually from 1975 to 2000, and by 13.00 km^2 annually since 2000, marking a nearly 44-fold increase over the entire study period.

Table 3. Wetland types' changes in different periods (Unit: km^2/a).

Primary	Secondary	1940–1975	1975–2000	2000–2020	1940–2020
Constructed Wetland	Paddy, Mariculture, and Saltern Wetland	32.40	131.11	−36.97	45.90
	Reservoir Pond Wetland	7.28	4.07	13.00	7.71
Natural Wetland	River Wetland	−3.28	−2.63	−18.56	−6.90
	Lake Wetland	−0.82	−1.35	−1.79	−1.23
	Neritic Wetland	−13.11	−10.12	−33.25	−17.21
	Marsh Wetland	−27.87	−23.73	2.34	−19.03
Total		−45.07	97.33	−75.23	9.25

Natural wetlands, on the other hand, have generally exhibited a declining trend (Figure 3). Lake wetlands steadily decreased, with an annual reduction ranging between 0.82 km^2 and 1.79 km^2. Neritic wetlands remained relatively stable from 1940 to 1975, experienced a slight annual reduction from 1975 to 2000, and then saw a sharp increase in the annual reduction to 33.25 km^2 after 2000. River wetlands displayed the most significant decrease from 2000 to 2020, with an annual reduction of 18.56 km^2. The changes in marsh wetlands were notably complex: these wetlands experienced an average annual reduction of 25.8 km^2 from 1940 to 2000, but from 2000 to 2020, they saw a slight increase, growing by 2.34 km^2 annually.

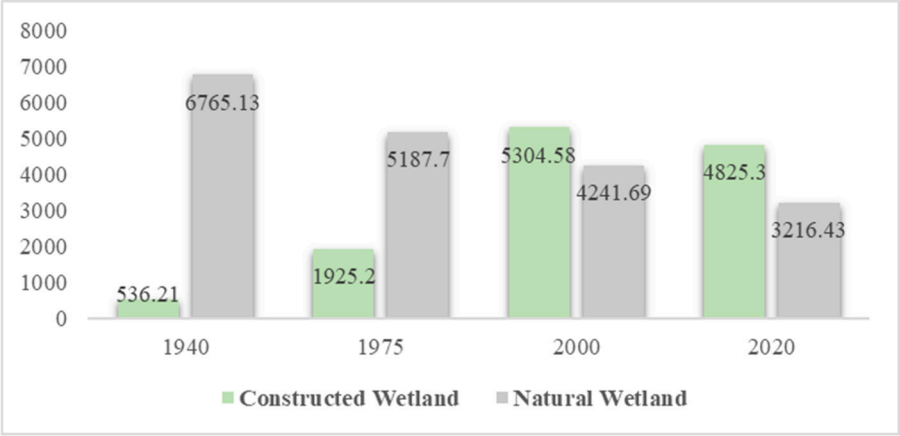

Figure 3. Nature and constructed wetland in different periods (Unit: km^2).

Overall, the area of coastal wetlands demonstrated a pattern of decrease, increase, and subsequent decrease again over the study period. Initially, there was a slight decrease from 1940 to 1975, followed by a significant increase from 1975 to 2000, reaching a historical peak of 9546.27 km^2. However, from 2000 to 2020, there was another decline, although the area remained relatively high.

3.1.2. Coastal Wetland Area Changes in Different Cities

Regional analysis reveals distinct trends in wetland area changes across Tianjin, Tangshan, and Cangzhou (Tables 4 and 5). In Tianjin, the wetland area decreased from 1940

to 1975, followed by a significant increase from 1975 to 2000. However, it exhibited a decreasing trend again from 2000 to 2020. In Tangshan, wetland areas showed relatively stable fluctuations overall but experienced a decrease from 2000 to 2020. Conversely, in Cangzhou, the wetland area decreased from 1940 to 1975, saw a slight increase from 1975 to 2000, and then decreased again from 2000 to 2020.

Table 4. Wetland changes in different regions (Unit: km^2).

	1940	1975	2000	2020
Tianjin	2890.21	2681.75	4402.61	3508.33
Constructed Wetland	420.87	797.38	2898.92	2378.43
Natural Wetland	2469.34	1884.37	1503.69	1129.9
Tangshan	2352.85	3016.18	3412.93	3048.34
Constructed Wetland	113.13	1005.02	1838.71	1922.08
Natural Wetland	2239.72	2011.16	1574.22	1126.26
Cangzhou	2058.28	1414.97	1730.73	1485.06
Constructed Wetland	2.21	122.8	566.95	524.79
Natural Wetland	2056.07	1292.17	1163.78	960.27

Table 5. Wetland dynamic changes in different regions (Unit: km^2/a).

	1940–1975	1975–2000	2000–2020	1940–2020
Tianjin	−5.96	68.83	−44.71	7.73
Constructed Wetland	10.76	84.06	−26.02	24.47
Natural Wetland	−16.71	−15.23	−18.69	−16.74
Tangshan	18.95	15.87	−18.23	8.69
Constructed Wetland	25.48	33.35	4.17	22.61
Natural Wetland	−6.53	−17.48	−22.40	−13.92
Cangzhou	−18.38	12.63	−12.28	−7.17
Constructed Wetland	3.45	17.77	−2.11	6.53
Natural Wetland	−21.83	−5.14	−10.18	−13.70

3.2. Changes in Coastal Wetland Landscape Patterns and Types

From 1940 to 2020, the fragmentation of the Tianjin–Hebei coastal wetlands has consistently increased. The fragmentation indices, NP and PD, for various wetland types over different periods are detailed in Table 6. Over the last 80 years, there have been significant changes in the NP values. Specifically, the NP value for paddy fields, mariculture zones, and saltern wetlands surged from 27 in 1940 to 559 in 2020, marking a more than 20-fold increase and highlighting severe fragmentation in these areas. River wetlands also saw increased fragmentation, with NP values rising from 40 to 307. Reservoir pond wetlands initially experienced a slight decrease, followed by stabilization, and then a significant increase to 420 from 2000 to 2020, indicating heightened fragmentation. Conversely, the NP values for lake wetlands decreased from 26 in 1940 to 14 in 2020, suggesting improved connectivity and reduced fragmentation. Coastal wetlands showed a slight overall increase in NP but remained relatively stable. However, marsh wetlands saw a marked decrease in NP, dropping from 32 in 1940 to 4 in 2020, signifying a substantial reduction in fragmentation.

The PD values highlight distinct trends across various wetland types from 1940 to 2020. The PD for paddy fields, mariculture zones, and saltern wetlands continued to increase, from 0.0037 to 0.0693, indicating a growing number of patches per unit area and further deepening the fragmentation. Reservoir pond wetlands initially remained stable and then experienced a slight increase in PD, reflecting a gradual rise in patch density. River wetlands saw an initial increase followed by a slight decrease, yet overall, the PD remained higher than in 1940, suggesting a general upward trend in patch density. Conversely, lake and marsh wetlands displayed significant decreases in PD, dropping from 0.0036 to 0.0017 and from 0.0044 to 0.0005, respectively. These reductions indicate decreased patch densities,

suggesting improved connectivity within lake and marsh wetland landscapes. Finally, neritic wetlands showed minor fluctuations but a slight overall increase in PD.

Table 6. Changes in number of landscape patches (NP) and patch density (PD) since 1940.

Primary	Secondary	1940		1975		2000		2020	
		NP	PD	NP	PD	NP	PD	NP	PD
Constructed Wetland	Paddy, Mariculture, and Saltern Wetland	27	0.0037	38	0.0053	184	0.0193	559	0.0693
	Reservoir Pond Wetland	15	0.0021	14	0.0020	16	0.0017	420	0.0521
Natural Wetland	River Wetland	40	0.0055	100	0.0141	163	0.0171	307	0.0381
	Lake Wetland	26	0.0036	8	0.0011	7	0.0007	14	0.0017
	Neritic Wetland	5	0.0007	9	0.0013	15	0.0016	8	0.0010
	Marsh Wetland	32	0.0044	32	0.0045	2	0.0002	4	0.0005

Furthermore, from 1940 to 2020, significant land-use transformations occurred in the study area, particularly in coastal wetlands (Figure 4). Key changes include the conversion of non-wetland areas into paddy, mariculture, and saltern wetlands (codes "7711" and "7771"), primarily in central eastern Tianjin and southern Tangshan. Additionally, code "3777" indicates a decline in riverine wetlands, with sections along major rivers being converted into non-wetland areas before 1975. Other codes, such as "7717", "5577", and others, represent wetlands transformed into non-wetland zones, concentrated along coastal regions where land reclamation is prevalent. Internal transformations within wetlands, such as code "6111", which denotes the conversion of marsh wetlands into paddy fields, mariculture zones, and saltern wetlands, were primarily observed in the Caofeidian region of Tangshan.

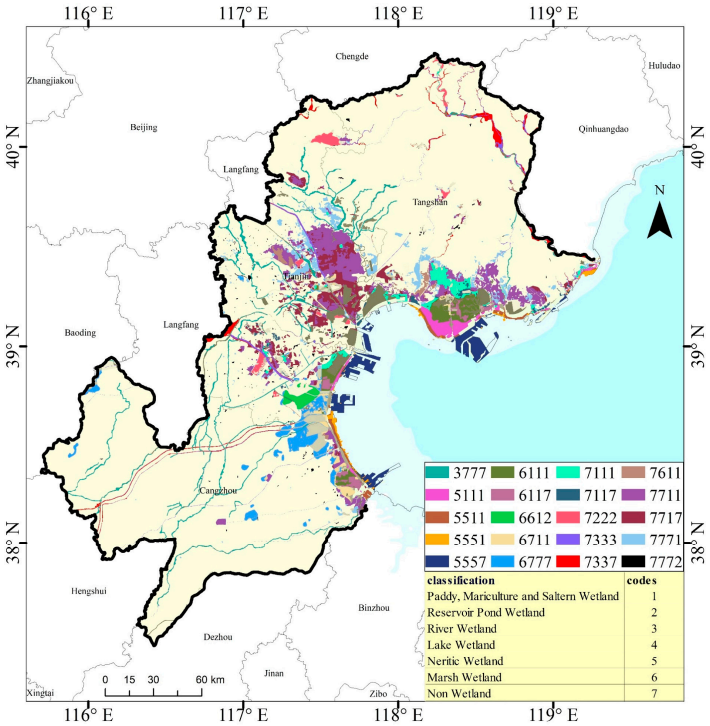

Figure 4. Spatial distribution of the main trajectory codes for wetland changes in the study area.

In summary, over the past 80 years, coastal wetlands have undergone significant changes in landscape patterns, with a notable increase in landscape fragmentation. Additionally, the primary trajectories of wetland-type changes include the conversion of wetlands into non-wetlands. These changes indicate major adjustments in landscape structure and may have profound impacts on the stability and functionality of the ecosystem.

4. Discussion

4.1. Analysis of Driving Mechanisms

Over the past 80 years, the landscape of the Tianjin–Hebei coastal wetlands has undergone substantial changes. The area of natural wetlands decreased by 3549 km^2, while constructed wetlands increased by 4289 km^2. The primary transformations included conversions from wetlands to non-wetland areas and from non-wetland areas to paddy fields, mariculture zones, and saltern wetlands. The expansion of constructed wetlands is directly linked to human activities, whereas the decline in natural wetlands can be attributed to both natural processes and human impacts.

From 1940 to 1975, constructed wetlands expanded by 1389 km^2, an increase of 259% from 1940 levels. Concurrently, natural wetlands decreased by 1577 km^2, a 23% reduction from 1940. This period saw 868 km^2 of natural wetlands converted to constructed types, with an additional 749 km^2 of non-wetland areas also being transformed. This phase was marked by rapid growth in constructed wetlands and significant declines in natural wetlands, largely driven by intensified human land-use activities.

Between 1975 and 2000, constructed wetlands further expanded by 3379 km^2, a 176% increase compared to 1975. During the same period, natural wetlands decreased by 946 km^2, an 18% decline from 1940. In this era, 752 km^2 of natural wetlands were converted into constructed wetlands, and 2766 km^2 of non-wetlands were transformed. While the expansion of constructed wetlands continued robustly, the annual loss of natural wetlands slowed. The development and utilization of non-wetland areas also played crucial roles in shaping wetland dynamics during this time.

From 2000 to 2020, constructed wetlands decreased slightly by 479 km^2, a 1% decline compared to 2000. In contrast, natural wetlands experienced a more substantial reduction of 1025 km^2, a 24% decrease from 2000. This period involved the conversion of 148 km^2 of natural wetlands into constructed wetlands, while 952 km^2 of non-wetlands were also converted. Despite the decrease in the area of constructed wetlands, the trend of natural wetland reduction persisted. The significant conversion of non-wetlands into constructed wetlands underscores the ongoing demand for coastal land for economic development.

The observed patterns of coastal wetland changes from 1940 to 1975, from 1975 to 2000, and from 2000 to 2020, reflecting the enduring and evolving impacts of human activities on these ecosystems. These changes not only mirror the evolution of economic and social needs in the coastal regions but also illuminate the varied development strategies adopted across different historical periods.

In the early years following the establishment of the People's Republic of China, constrained by a nascent economic foundation, the government prioritized the development of salt production in coastal regions to bolster national economic growth and support livelihoods [31]. This strategic emphasis led to substantial expansions in areas such as the Hangu Salt Field in Tianjin, the Nanpu Salt Field in Tangshan, and the Daqinghe Salt Field, collectively growing from 386 km^2 during the early founding period to 1452 km^2 by 2000, establishing a widespread distribution of salt pans.

During the 1980s and 1990s, as China embarked on profound economic reforms and opened its markets internationally, there was a concerted effort to develop the marine economy along the coastal regions, catalyzing the rapid growth of mariculture [32]. On the Cangzhou coast of the Tianjin–Hebei region, mariculture expanded by 50 km^2, leading to an artificial extension of the shoreline by approximately 3 km.

As the 21st century began, globalization accelerated international trade, intensifying the demand for logistical hubs such as ports [14]. This dynamic spurred extensive land

reclamation efforts in coastal zones, including Dalian Port, the Tianjin Port–Lingang Economic Zone, and Caofeidian, where reclaimed land areas exceeded 100 km^2, pushing the shoreline seaward by up to approximately 23 km.

Since 2014, recognizing the need to safeguard marine ecological resources and achieve sustainable development in the marine economy [33], the Chinese government has implemented policies to suspend the approval of new sea reclamation projects and regional plans. This regulatory shift has contributed significantly to stabilizing the coastal shoreline and enhancing environmental conservation efforts.

Upon examining the continuous evolution of human activities alongside economic and social developments in the study area, it is clear that these activities have not only spurred regional growth on a large scale but also had significant impacts on wetland ecosystems at a more localized level. This impact underscores the complex relationship between economic development and the natural environment. Despite the fact that the expansion of constructed wetlands has somewhat compensated for the reduction of natural wetlands, the concurrent expansion of reservoirs and land reclamation activities has exacerbated the pressure on wetland ecosystems.

Since 1949, China has made significant advances in reservoir construction, beginning with six large reservoirs in the early 1940s. Today, after more than 70 years, the number has soared to over 98,000 [34]. These reservoirs have played crucial roles in flood control, disaster mitigation, energy provision, and securing stable water supplies for agriculture across China [35,36]. At the same time, the development of basic water conservancy infrastructure, coupled with human activities such as agricultural irrigation, has significantly expanded the Reservoir Pond Wetlands in the study area, from 14 km^2 in 1940 to 631 km^2 by 2020.

Figure 4 shows that from 1940 to 1975, river wetlands in the study area underwent a significant narrowing of river channels. This change was driven by factors such as rapid population growth and increasing land demands, leading to extensive development along riverbanks. This development encroached upon or diverted river channels, consequently reducing their width. For example, the width of the Xuanhui River near Baoguantun Town in Nanpi County, Cangzhou City, Hebei Province, decreased from 387 m in 1940 to 68 m by 2020. Additionally, reservoir construction likely disrupted natural water flows, reducing upstream water volumes and contributing to the narrowing of downstream river channels. Furthermore, increased agricultural water usage in some areas has led to significant groundwater depletion, posing serious threats to the sustainability of wetland ecosystems [37–39], particularly evident in the extensive drying of lakes and marsh wetlands.

Concurrently, the rapid growth of port clusters has driven extensive land reclamation efforts, significantly altering wetland distributions and types. Notably, the reclamation projects at Caofeidian Port, Tianjin Port, and Dalian Port are among the largest in China, together reclaiming 310 km^2 from shallow waters to develop deep-water ports and industries such as steel, chemicals, and power [40]. During the study period, paddy, mariculture, and saltern wetlands expanded by 3672 km^2, while neritic wetlands experienced an annual loss of 1377 km^2, indicating worrying trends in both the amount of change and the reduction in area. Moreover, rising sea levels pose additional challenges, intensifying the impact on shallow sea wetlands [41–45].

Since 1940, activities such as land reclamation, water conservancy projects, agricultural development, and urbanization have profoundly and irreversibly impacted the wetland ecosystems of the Tianjin–Hebei coastal region. Initially, natural erosion processes, including shoreline degradation and widespread erosion due to rising sea levels, primarily shaped these wetlands, particularly in Northern Dashentang and Southern Xujiabao to Dakouhe areas [46,47]. However, from the 1960s onward, human activities have become the dominant forces reshaping the coastal wetland landscape, marking a significant shift. Tianjin and Hebei provinces experienced land gains of 412 km^2 and 938 km^2, respectively, between 1940 and 2014, which are primarily attributed to human activities. The areas of sea encroachment were 2 km^2 and 20 km^2, respectively, likely dominated by erosion in

the estuarine delta regions [18]. These findings underscore that although human factors are now predominant, natural factors such as extreme climate events and sea-level rise continue to subtly influence coastal wetland dynamics [48].

In conclusion, the evolution of wetlands in the Tianjin–Hebei coastal region over the past 80 years has predominantly featured a decline in natural wetlands coupled with an increase in artificial wetlands. This shift reflects a gradual transition from natural processes to human-driven forces as the primary drivers of change in these ecosystems.

4.2. Analysis of Ecological and Environmental Problems Caused by Changes in Coastal Wetlands

The changes in coastal wetland types and the degree of fragmentation will ultimately manifest in the ecological environment. Figure 5 highlights the evolving distribution of wetlands around Tianjin Port, showing a trend towards increased fragmentation as formerly contiguous wetlands have fragmented into smaller, scattered patches. With the intensification of human activities such as port construction, industrial development, agricultural expansion, and aquaculture, wetland distribution has increasingly become fragmented, and wetland types have frequently changed. This situation has significantly reduced the ecological connectivity of wetlands and undermined the overall integrity and stability of the ecosystem, with this trend becoming more pronounced [49,50].

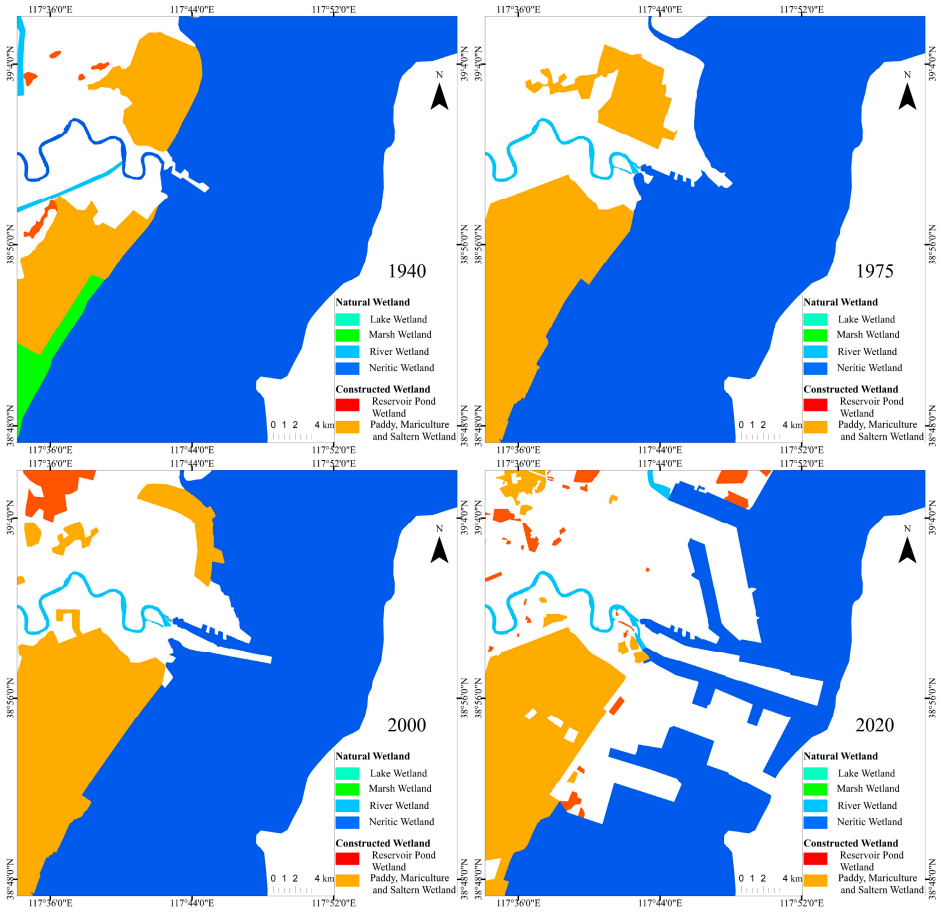

Figure 5. Illustrates the wetland distribution around Tianjin Port.

Fragmentation not only involves the physical separation and dispersion of landscapes but also profoundly disrupts the continuity and natural fluidity of ecosystems, thereby weakening interdependence and ecological cooperation. Land reclamation activities disrupt ecological connectivity, leading to the reduction or disappearance of original habitats that are crucial for various fish and bird species. Research has indicated varying impacts of coastal wetland changes on different waterbird species, particularly migratory, transient,

and endangered birds, which face heightened risks during migration, reproduction, and survival [51–53]. Furthermore, the use of fertilizers, pesticides, and pharmaceuticals in fisheries and agriculture contributes to water and environmental pollution, directly affecting waterbirds through poisoning and mortality [54]. The NP and PD values for reservoir pond wetlands also show a progressive increase, indicating worsening landscape fragmentation. Reservoir construction alters hydrological conditions, significantly affecting animal behavior, vegetation phenology, and the seasonal dynamics of the hydrological cycle [55,56]. The fragmentation of river wetlands into smaller patches, influenced by both natural and anthropogenic factors, has complex and enduring effects on biodiversity. While these impacts may not manifest immediately, extensive and rapid human-induced fragmentation can disrupt ecosystem integrity and connectivity over the long term, adversely affecting biodiversity and habitat quality [57,58].

In contrast, lake Wetlands and marsh wetlands show a slight decline in NP and PD values, likely stemming from significant reductions in their respective areas. This trend signals ongoing environmental concerns. The stability of woody plant communities may be compromised due to water source depletion, while aquatic organisms face potential population declines or even extinction risks due to habitat loss. Furthermore, unique species within marsh communities may struggle to adapt to changing environmental conditions [59]. However, this decline could also reflect conservation efforts such as the establishment of wetland reserves and ecological water replenishment initiatives, which have facilitated the expansion and connectivity of wetland patches, thereby enhancing overall wetland connectivity. Conversely, neritic wetlands exhibit relatively stable fragmentation levels, likely influenced by their inherent characteristics, geographic positioning, and environmental conditions.

The observed trend of landscape fragmentation in the Tianjin–Hebei coastal wetlands underscores the diverse adverse impacts on the ecological environment. Effective strategies must be implemented to mitigate wetland fragmentation and uphold the health and stability of these critical ecosystems.

4.3. Suggestions for Protection and Restoration

Based on a detailed analysis of changes and driving factors in coastal wetlands over the last 80 years, along with an assessment of current challenges, we propose the following recommendations:

4.3.1. Addressing the Decline in Natural Wetlands

- Government authorities should enact rigorous regulations and policies aimed at halting further development and destruction of natural wetlands. This includes stringent measures to protect existing wetlands and prevent their degradation [60].
- Focus should be on ecological restoration initiatives in heavily impacted wetland areas. Strategies may include reclaiming aquaculture zones for wetland purposes, restoring enclosed areas to their natural wetland state, and reintegrating coastal areas with wetlands. These efforts aim to progressively enhance the extent and quality of natural wetland habitats [61].

4.3.2. Addressing Wetland Fragmentation

- It is crucial to establish ecological corridors between wetlands to maintain connectivity within wetland ecosystems. These corridors facilitate the movement and genetic exchange of wetland biopopulations, thereby promoting ecological resilience and biodiversity conservation [62].
- Addressing human-induced disruptions to wetland hydrology is essential. Remedial measures, such as installing controllable tidal gates and optimizing drainage networks, should be prioritized. These actions aim to stabilize and enhance the hydrological conditions necessary for sustainable wetland ecosystems.

For detailed recommendations and specific restoration strategies tailored to different locations, please refer to Figure 6, which provides an illustrative guide to restoration engineering solutions.

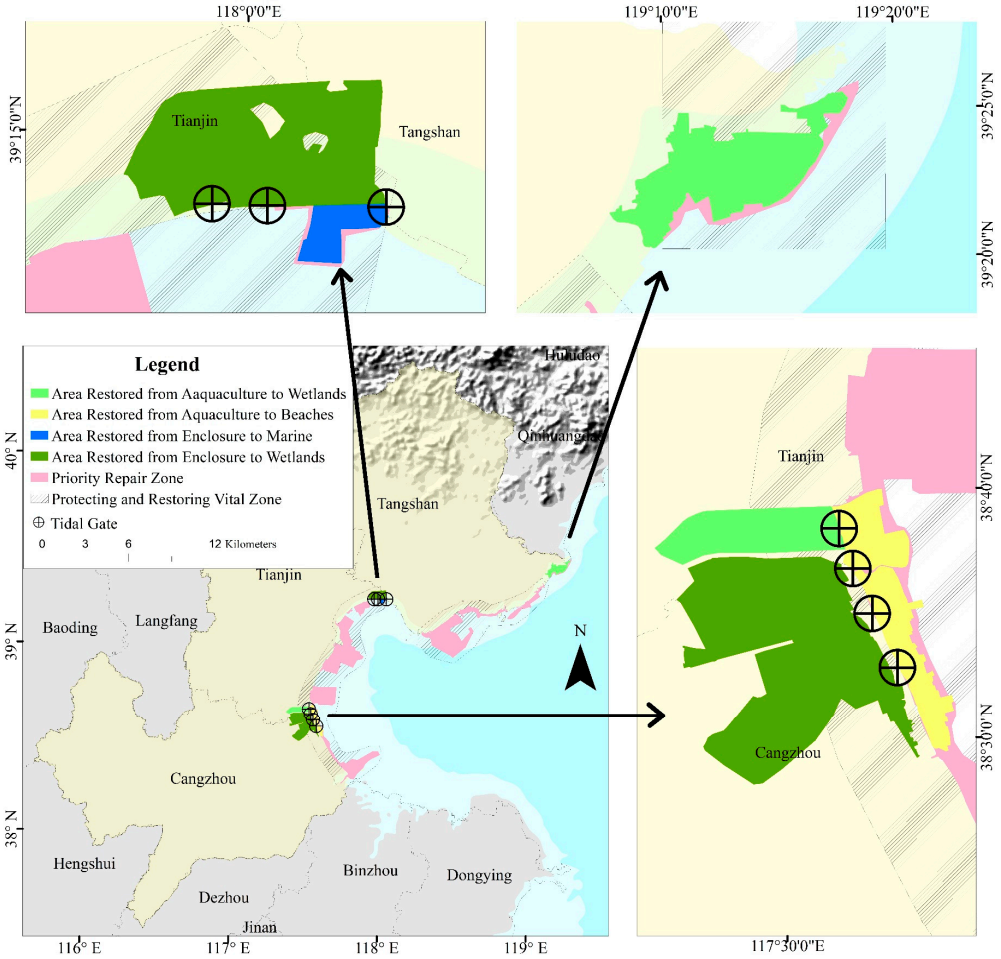

Figure 6. Schematic diagram of coastal wetland restoration locations and projects in the study area.

5. Conclusions

Based on comprehensive analyses utilizing remote sensing, topographic maps, and field survey data, this study investigates the dynamic changes and driving factors influencing the Tianjin–Hebei coastal wetlands from 1940 to 2020. The key conclusions are as follows:

- Overall, the coastal wetland area has shown a pattern of decrease, increase, and then a subsequent decrease, though it remains relatively extensive in the current period. Specifically, Tianjin and Tangshan have experienced fluctuating increases in wetland areas historically, with recent decades showing a decline. In contrast, Cangzhou has seen a fluctuating decrease in wetland areas.
- Coastal wetlands have undergone significant landscape changes, particularly with an increase in fragmentation. The primary change in wetland types is the conversion of wetlands into non-wetlands.
- In response to the observed changes and challenges in coastal wetlands over the past eight decades, we recommend the following: First, strengthen wetland protection policies and enforce strict regulations to prevent further degradation. Second, focus on restoring damaged wetlands and expanding natural wetland habitats. Establish ecological corridors to improve connectivity and support the migration of species.

These measures are essential for preserving coastal wetland ecosystems, protecting biodiversity, and promoting sustainable development.

Author Contributions: Conceptualization: F.W. (Fu Wang), F.W. (Feicui Wang); Methodology: F.W. (Feicui Wang), K.Z.; Investigation: F.W. (Fu Wang), P.Y., T.W., Y.H., L.Y.; Writing—original draft: F.W. (Feicui Wang); Writing—review and editing: F.W. (Fu Wang), F.W. (Feicui Wang). All authors have read and agreed to the published version of the manuscript.

Funding: This research was funded by NSFC (No. 42293261), China Geological Survey Program (DD20189506, DD20211301).

Data Availability Statement: The original contributions presented in the study are included in the article, any further inquiries, please email directly to the corresponding author.

Acknowledgments: We would like to thank Shi, P X, and Wen, M Z for their assistance in verifying the accuracy of the data and conducting field research for this article.

Conflicts of Interest: Author Zhu, K was employed by Tianjin Tian Ke Digital Innovation Science and Technology Co., Ltd. The remaining authors declare that the research was conducted in the absence of any commercial or financial relationships that could be construed as a potential conflict of interest.

References

1. Li, C.; Wang, F.; Yang, P.; Wang, F.C.; Hu, Y.Z.; Zhao, Y.L.; Tian, L.; Zhao, R. Assessment ecological risk of heavy metal caused by high-intensity land reclamation in Bohai Bay, changing trend analyzation and carbon storage assessment of China. *China Geol.* **2024**, *7*, 1–11. [CrossRef]
2. Bn, P.O.T. Ramsar Convention on Wetlands. Ramsar Fact Sheet 3 Wetlands: A Global Disappearing Act 2015. Available online: https://www.ramsar.org/sites/default/files/documents/library/factsheet3_global_disappearing_act_0.pdf (accessed on 16 March 2024).
3. Ye, S.; Pei, L.; He, L.; Xie, L.; Zhao, G.; Yuan, H.; Laws, E.A. Wetlands in China: Evolution, Carbon Sequestrations and Services, Threats, and Preservation/Restoration. *Water* **2022**, *14*, 1152. [CrossRef]
4. The State Forestry Administration of The Peoples's Republic of China. *China Wetlands Resource*; China Forestry Publishing House: Beijing, China, 2015.
5. Cui, B.; He, Q.; Gu, B.; Bai, J.; Liu, X. China's Coastal Wetlands: Understanding Environmental Changes and Human Impacts for Management and Conservation. *Wetlands* **2016**, *36*, 1–9. [CrossRef]
6. Ning, H.; Jiang, W.J.; Sheng, Y.Z.; Wang, K.L.; Chen, S.M.; Zhang, Z.; Liu, F.T. Comprehensive evaluation of nitrogen contamination in water ecosystems of the Miyun reservoir watershed, northern China: Distribution, source apportionment and risk assessment. *Environ. Geochem. Health* **2024**, *46*, 278. [CrossRef]
7. Jiang, W.J.; Meng, L.S.; Liu, F.T.; Sheng, Y.Z.; Chen, S.M.; Yang, J.L.; Mao, H.R.; Zhang, J.; Zhang, Z.; Ning, H. Distribution, source investigation, and risk assessment of topsoil heavy metals in areas with intensive anthropogenic activities using the positive matrix factorization (PMF) model coupled with self-organizing map (SOM). *Environ. Geochem. Health* **2023**, *45*, 6353–6370. [CrossRef]
8. Orimoloye, I.R.; Mazinyo, S.P.; Kalumba, A.M.; Nel, W.; Adigun, A.I.; Ololade, O.O. Wetland shift monitoring using remote sensing and GIS techniques: Landscape dynamics and its implications on Isimangaliso Wetland Park, South Africa. *Earth Sci. Inform.* **2019**, *12*, 553–563. [CrossRef]
9. Dang, A.T.; Kumar, L.; Reid, M.; Nguyen, H. Remote Sensing Approach for Monitoring Coastal Wetland in the Mekong Delta, Vietnam: Change Trends and Their Driving Forces. *Remote Sens.* **2021**, *13*, 3359. [CrossRef]
10. Zhu, J.F.; Zhou, Y.; Wang, S.X.; Wang, L.T.; Liu, W.L.; Li, H.Y.; Mei, J.J. Analysis of changes of Baiyangdian wetland from 1975 to 2018 based on remote sensing. *Natl. Remote Sens. Bull.* **2019**, *23*, 971–986. [CrossRef]
11. Couvillion, B.R.; Beck, H.; Schoolmaster, D.; Fischer, M. *Land Area Change in Coastal Louisiana (1932 to 2016)*; U.S. Geological Survey: Reston, VA, USA, 2017. [CrossRef]
12. White, E.E., Jr.; Ury, E.A.; Bernhardt, E.S.; Yang, X. Climate change driving widespread loss of coastal forested wetlands throughout the North American coastal plain. *Ecosystems* **2021**, *25*, 812–827. [CrossRef]
13. Bournazel, J.; Kumara, M.P.; Jayatissa, L.P.; Viergever, K.; Morel, V.; Huxham, M. The impacts of shrimp farming on land-use and carbon storage around Puttalam lagoon, Sri Lanka. *Ocean. Coast. Manag.* **2015**, *113*, 18–28. [CrossRef]
14. Tian, B.; Wu, W.; Yang, Z.; Zhou, Y. Drivers, trends, and potential impacts of long-term coastal reclamation in China from 1985 to 2010. *Estuar. Coast. Shelf Sci.* **2016**, *170*, 83–90. [CrossRef]
15. Cheng, M.; Huang, B.; Kong, L.; Ouyang, Z. Ecosystem spatial changes and driving forces in the Bohai coastal zone. *Int. J. Environ. Res. Public Health* **2019**, *16*, 536. [CrossRef] [PubMed]
16. Zhu, G.; Xie, Z.; Li, T.; Ma, Z.; Xu, X. Assessment ecological risk of heavy metal caused by high-intensity land reclamation in Bohai Bay, China. *PLoS ONE* **2017**, *12*, e0175627. [CrossRef]

17. Wei, F.; Han, G.X.; Zhang, J.P.; Li, Y.Z.; Zhao, J.M. Temporal and spatial dynamic evolution of coastal wetland under the action of sea reclamation in Bohai Rim during 1980–2015. *Chin. J. Ecol.* **2018**, *37*, 1527–1537. [CrossRef]
18. Hou, X.Y.; Hou, W.; Wu, T. Shape changes of major gulfs along the mainland of China since the early 1940s. *Acta Geogr. Sin.* **2016**, *71*, 118–129. [CrossRef]
19. Ding, Y.; Wei, H. Research of the influential factors on the simulation of storm surge in the Bohai Sea. *Open Mech. Eng. J.* **2014**, *8*, 151–156. [CrossRef]
20. Wang, R.B.; Zhou, W.; Li, F.L.; Wang, H.; Yang, G.Y.; Yao, Z.J.; Kuang, S.J. Tectonic subsidence and prospect of ground subsidence control in Tianjin area. *Hydrogeol. Eng. Geol.* **2003**, *5*, 12–17. [CrossRef]
21. McKee, M.; White, J.R.; Putnam-Duhon, L.A. Simulated storm surge effects on freshwater coastal wetland soil porewater salinity and extractable ammonium levels: Implications for marsh recovery after storm surge. *Estuar. Coast. Shelf Sci.* **2016**, *181*, 338–344. [CrossRef]
22. Wang, H.; Shang, Z.W.; Wang, F. On the muddy coast, western Bohai Bay, China. *Geol. Bull. China* **2010**, *29*, 641–649. Available online: http://dzhtb.cgs.cn/en/article/id/20100502 (accessed on 4 April 2024).
23. *GB/T 24708-2009*; Wetland Classification. National Forestry and Grassland Administration of China: Beijing, China, 2009.
24. NH, R.K. Study of fluctuations in surface area of Lake Haramaya using NDWI and MNDWI methods. *J. Geospat. Inf. Sci. Eng.* **2022**, *5*, 36–41. [CrossRef]
25. Chang, L.; Cheng, L.; Huang, C.; Qin, S.; Fu, C.; Li, S. Extracting urban water bodies from Landsat imagery based on mNDWI and HSV transformation. *Remote Sens.* **2022**, *14*, 5785. [CrossRef]
26. Wang, S.; Zhang, L.; Zhang, H.; Han, X.; Zhang, L. Spatial–temporal wetland landcover changes of poyang lake derived from Landsat and HJ-1A/B data in the dry season from 1973–2019. *Remote Sens.* **2020**, *12*, 1595. [CrossRef]
27. Liu, J.Y.; Wang, D.C.; Sun, R.H.; Wang, F.C.; Hu, B.X.; Chen, J.H.; Sun, Z.C. Study on spatial relevance of ecological-land loss based on change trajectory analysis method. Geographical Research. *Geogr. Res.* **2020**, *39*, 103–114. [CrossRef]
28. Huang, Y.; Wang, F.Y.; Cai, T.J.; Wang, D.C.; Wang, Q.Q.; Chen, W.G. Landscape pattern dynamic analysis based on change trajectory method in Bohai rim area. *J. Soil Water Conserv.* **2015**, *29*, 314–319. [CrossRef]
29. Zong, X.Y.; Gao, L.H.; Qiao, Y.L.; Lin, S. Study on dynamic changes of wetland landscape pattern in yellow river delta. *J. Geo-Inf. Sci.* **2009**, *11*, 91–97. [CrossRef]
30. Li, Y.Z.; Yu, J.B.; Han, G.X.; Wang, X.H.; Wang, Y.L.; Guan, B. Dynamic evolution of natural wetlands in Yellow River Delta and related driving factors. *Chin. J. Ecol.* **2011**, *30*, 1535–1541. Available online: https://www.cje.net.cn/CN/Y2011/V30/I07/1535 (accessed on 5 April 2024).
31. Bao, J.; Gao, S.; Ge, J. Dynamic land use and its policy in response to environmental and social-economic changes in China: A case study of the Jiangsu coast (1750–2015). *Land Use Policy* **2019**, *82*, 169–180. [CrossRef]
32. Wang, Q.; Liu, H.; Sui, J. Mariculture: Developments, present status and prospects. *Aquac. China Success Stories Mod. Trends* **2018**, 38–54. [CrossRef]
33. Bai, J.Y.; Sui, J.X. Requirement of rule of law for the marine ecological protection:an empirical study under the revision of the draft of the marine environment protection law. *J. Shandong Univ. Sci. Technol.* **2018**, *3*, 74–83. [CrossRef]
34. Li, A.H.; Bai, L.L.; Huang, H.J.; Yang, X.R.; Zhao, Z.N. Optimization and enhancement of flood-control reservoir layout and function in China in the new era. *China Water Resour.* **2023**, *14*, 8–10. [CrossRef]
35. Kundzewicz, Z.W.; Su, B.; Wang, Y.; Xia, J.; Huang, J.; Jiang, T. Flood risk and its reduction in China. *Adv. Water Resour.* **2019**, *130*, 37–45. [CrossRef]
36. Liu, J.; Zang, C.; Tian, S.; Liu, J.; Yang, H.; Jia, S.; You, L.; Liu, B.; Zhang, M. Water conservancy projects in China: Achievements, challenges and way forward. *Glob. Environ. Chang.* **2013**, *23*, 633–643. [CrossRef]
37. Liu, T.; Liu, L.; Luo, Y.; Lai, J. Simulation of groundwater evaporation and groundwater depth using SWAT in the irrigation district with shallow water table. *Environ. Earth Sci.* **2015**, *74*, 315–324. [CrossRef]
38. Li, D.; Tian, P.; Luo, Y.; Dong, B.; Cui, Y.; Khan, S. Importance of stopping groundwater irrigation for balancing agriculture and wetland ecosystem. *Ecol. Indic.* **2021**, *127*, 107747. [CrossRef]
39. Les Landes, A.A.; Aquilina, L.; De Ridder, J.; Longuevergne, L.; Pagé, C.; Goderniaux, P. Investigating the respective impacts of groundwater exploitation and climate change on wetland extension over 150 years. *J. Hydrol.* **2014**, *509*, 367–378. [CrossRef]
40. Duan, H.; Zhang, H.; Huang, Q.; Zhang, Y.; Hu, M.; Niu, Y.; Zhu, J. Characterization and environmental impact analysis of sea land reclamation activities in China. *Ocean Coast. Manag.* **2016**, *130*, 128–137. [CrossRef]
41. Masson-Delmotte, V.; Zhai, P.; Pirani, A.; Connors, S.L.; Péan, C.; Chen, Y.; Goldfarb, L.; Gomis, M.I.; Matthews, J.B.R.; Berger, S.; et al. Climate Change 2021: The Physical Science Basis. Contribution of Working Group I to the Sixth Assessment Report of the Intergovernmental Panel on Climate Change. 2021, Volume 2, p. 2391. Available online: https://www.ipcc.ch/report/ar6/wg1/downloads/report/IPCC_AR6_WGI_FrontMatter.pdf (accessed on 7 June 2024).
42. Ministry of Natural Resources of the People's Republic of China. China Natural Resources Bulletin 2023. Available online: https://gi.mnr.gov.cn/202402/P020240312701247258838.pdf (accessed on 17 June 2024).
43. Wang, F.; Wang, H.; Li, J.F.; Wang, F.C.; Tian, L.Z.; Yu, Q.; Huang, Z.Q.; Fang, J.; Hu, Y.Z.; Xiao, G.Q.; et al. Evolution and trending prediction of the Chinese mainland coasts since 20 ka BP: Implication for ecological protection and restoration. *Geol. China* **2023**, *50*, 61–83. [CrossRef]

44. Wang, F.; Li, J.F.; Shi, P.X.; Shang, Z.W.; Li, Y.; Wang, H. The impact of sea-level rise on the coast of Tianjin-Hebei, China. *China Geol.* **2019**, *2*, 26–39. [CrossRef]
45. Wang, F.; Hu, Y.Z.; Tian, L.Z.; Shi, P.X.; Li, J.F.; Chen, Y.S.; Li, Y.; Shang, Z.W.; Jiang, X.Y.; Yuan, H.F.; et al. Sea Level Change in Bohai Bay. *N. China Geol.* **2024**, *47*, 1–20. [CrossRef]
46. Li, J.F.; Kang, H.; Wang, H.; Pei, Y.D. Modern geological action and discussion of influence factors on the west coast of Bohai Bay, China. *Geol. Surv. Res.* **2007**, *30*, 295–301. [CrossRef]
47. Shi, P.X.; Wang, F.; Shang, Z.W.; Li, Y. The present situation and changing characteristics of the shorelines along Tianjin-Hebei coastal areas and proposal for protection. *Geol. Bull. China* **2016**, *35*, 1630–1637. [CrossRef]
48. Sheng, Y.; Baars, O.; Guo, D.; Whitham, J.; Srivastava, S.; Dong, H. Mineral-bound trace metals as cofactors for anaerobic biological nitrogen fixation. *Environ. Sci. Technol.* **2023**, *57*, 7206–7216. [CrossRef] [PubMed]
49. Gómez-Baggethun, E.; Tudor, M.; Doroftei, M.; Covaliov, S.; Năstase, A.; Onără, D.F.; Mierlă, M.; Marinov, M.; Doroșencu, A.-C.; Lupu, G.; et al. Gabriel Changes in ecosystem services from wetland loss and restoration: An ecosystem assessment of the Danube Delta (1960–2010). *Ecosyst. Serv.* **2019**, *39*, 100965. [CrossRef]
50. Jiang, M.; Chen, H.; Chen, Q.; Wu, H.; Chen, P. Wetland ecosystem integrity and its variation in an estuary using the EBLE index. *Ecol. Indic.* **2015**, *48*, 252–262. [CrossRef]
51. Ding, X.; Shan, X.; Chen, Y.; Li, M.; Li, J.; Jin, X. Variations in fish habitat fragmentation caused by marine reclamation activities in the Bohai coastal region, China. *Ocean Coast. Manag.* **2020**, *184*, 105038. [CrossRef]
52. Jackson, M.V.; Carrasco, L.R.; Choi, C.-Y.; Li, J.; Ma, Z.; Melville, D.S.; Mu, T.; Peng, H.-B.; Woodworth, B.K.; Yang, Z.; et al. Multiple habitat use by declining migratory birds necessitates joined-up conservation. *Ecol. Evol.* **2019**, *9*, 2505–2515. [CrossRef] [PubMed]
53. Kan, Z.; Chen, B.; Yu, W.; Chen, G.; Ma, Z.; Hu, W.; Liao, J.; Du, H. Forecasting land-cover change effects on waterbirds in Xiamen Bay, China: Determining prospective species winners and losers. *Mar. Environ. Res.* **2023**, *188*, 106003. [CrossRef]
54. Møller, A.P.; Laursen, K. Reversible effects of fertilizer use on population trends of waterbirds in Europe. *Biol. Conserv.* **2015**, *184*, 389–395. [CrossRef]
55. Alho, C.J.R. Environmental effects of hydropower reservoirs on wild mammals and freshwater turtles in Amazonia: A review. *Oecologia Aust.* **2011**, *15*, 593–604. [CrossRef]
56. Wang, D.C.; Wang, F.C.; Huang, Y.; Duan, X.W.; Liu, J.Y.; Hu, B.X.; Sun, Z.C.; Chen, J.H. Examining the effects of hydropower station construction on the surface temperature of the Jinsha River Dry-Hot Valley at different seasons. *Remote Sens.* **2018**, *10*, 600. [CrossRef]
57. Fuller, M.R.; Doyle, M.W.; Strayer, D.L. Causes and consequences of habitat fragmentation in river networks. *Ann. N. Y. Acad. Sci.* **2015**, *1355*, 31–51. [CrossRef] [PubMed]
58. Zedler, J.B.; Kercher, S. Wetland resources: Status, trends, ecosystem services, and restorability. *Annu. Rev. Environ. Resour.* **2005**, *30*, 39–74. [CrossRef]
59. Castello, M.; Poldini, L.; Altobelli, A. The aquatic and wetland vegetation of Lake Doberdò: An analysis for conservation value assessment of a disappearing lake of the Classical Karst (North East Italy). *Plant Sociol.* **2021**, *58*, 75–106. [CrossRef]
60. Zhang, H.; Jia, E.R.; Chen, S.; Fang, Y.X.; Dong, K.; Jia, W. Experience of Haikou wetlands conservation and restoration. *Environ. Sustain. Dev.* **2021**, *2*, 144–150.
61. Zhu, C.Y.; Li, J.S.; Li, A.L.; Shen, K.M.; Wang, P.P.; Yan, Z.C.; Yuan, L. Analysis of temporal and spatial changes of the Laoshan Bay shoreline and discussion on ecological restoration. *Mar. Geol. Front.* **2024**, *40*, 63–72. [CrossRef]
62. Zhuan, Q.; Yu, X.G.; Lin, Z.L.; Wen, R.; Zhang, J.W.; Long, Z.X. Assessment of Ecological Restoration Effect and Conservation Measures of Xinglin Bay in Xiamen. *Ocean. Dev. Manag.* **2021**, *38*, 91–98. [CrossRef]

Disclaimer/Publisher's Note: The statements, opinions and data contained in all publications are solely those of the individual author(s) and contributor(s) and not of MDPI and/or the editor(s). MDPI and/or the editor(s) disclaim responsibility for any injury to people or property resulting from any ideas, methods, instructions or products referred to in the content.

water

MDPI

Article

Biogeochemical Fe-Redox Cycling in Oligotrophic Deep-Sea Sediment

Di Zhan [1,2,3], Qingyin Xia [1,*], Gaoyuan Li [3], Xinyu Li [3], Yang Li [3], Dafu Hu [3], Jinglong Hu [3], Ziqi Zhou [4] and Yizhi Sheng [3]

[1] Beijing Research Institute of Chemical Engineering and Metallurgy, China National Nuclear Corporation, Beijing 101149, China; zd_12366@126.com
[2] School of Historical Culture and Tourism, Fuyang Normal University, Fuyang 236037, China
[3] State Key Laboratory of Biogeology and Environmental Geology, China University of Geosciences, Beijing 100083, China; ligy@cugb.edu.cn (G.L.); subluepikkka@163.com (X.L.); 59720@126.com (Y.L.); dafu_hu@126.com (D.H.); hujinglong123@gmail.com (J.H.); shengyz@cugb.edu.cn (Y.S.)
[4] UNSW Water Research Centre, School of Civil and Environmental Engineering, The University of New South Wales, Sydney, NSW 2052, Australia; ziqi.zhou2019@foxmail.com
* Correspondence: qingyin.xia@outlook.com; Tel.: +86-010-51674164

Abstract: Biogeochemical redox cycling of iron (Fe) essentially governs various geochemical processes in nature. However, the mechanistic underpinnings of Fe-redox cycling in deep-sea sediments remain poorly understood, due to the limited access to the deep-sea environment. Here, abyssal sediment collected from a depth of 5800 m in the Pacific Ocean was characterized for its elemental, mineralogical, and biological properties. The sedimentary environment was determined to be oligotrophic with limited nutrition, yet contained a considerable amount of trace elements. Fe-redox reactions in sediment progressed through an initial lag phase, followed by a fast Fe(II) reduction and an extended period of Fe(III) oxidation before achieving equilibrium after 58 days. The presence of an external H_2 electron donor significantly increased the extent of Fe(III) bio-reduction by 7.73% relative to an amendment-free control under high pressure of 58 MPa. A similar enhancement of 11.20% was observed following lactate amendment under atmospheric pressure. Fe(II) bio-oxidation occurred after 16 days' anaerobic culturing, coupled with nitrate reduction. During Fe bio-redox reactions, microbial community composition was significantly shaped by the presence/absence of an electron donor, while the hydrostatic pressure levels were the controlling factor. *Shewanella* spp. emerged as the primary Fe(III)-reducing microorganisms, and were stimulated by supplemented lactate. *Marinobacter hydrocarbonoclasticus* was the predominant Fe(II)-oxidizing microorganism across all conditions. Our findings illustrate continuous Fe-redox reactions occurring in the deep-sea environment, with coexisting Fe-redox microorganisms determining the oscillation of Fe valence states within the abyssal sediment.

Keywords: iron-redox reaction; abyssal sediment; microbial community; hydrostatic pressure; biogeochemical element cycling

1. Introduction

Iron (Fe) is the most abundant redox-active metal element in the Earth's crust. The biogeochemical redox cycle of Fe plays a critical role in various environmental processes, including the cycling of essential elements, carbon storage, transformation of contaminants, and ocean productivity [1–3]. Fe-redox cycling in the epigenetic natural environment has been widely investigated over the last few decades. Iron cycles between its reduced (Fe^{2+}) and oxidized (Fe^{3+}) states, driven by both biotic and abiotic reactions. In marine and terrestrial ecosystems, microorganisms mediate these redox processes, influencing nutrient availability and the fate of toxic metals [4]. Biologically, Fe is physiologically essential for nearly all living organisms. Fe(II) supplies the requisite chemical energy for metal-oxidizing

microorganisms, such as *Acidithiobacillus* or *Leptospirillum*, whereas Fe(III) functions as the electron acceptor for dissimilatory reduction in anaerobic environments [5,6].

Due to the difficulty in accessing deep-sea environments, little was known about Fe bio-redox reactions in deep-sea sediments until recently. Significant progress has been made in understanding these environments, including the ultradeep sea, due to the advancements in deep-sea exploration technology. However, much remains to be discovered [7–9]. Recent advances have demonstrated that Fe bio-redox cycling is active and prevalent in the anaerobic environments of deep sea, especially in oxygen minimum zones, coupled with organic carbon mineralization [10–12]. Despite the harsh environment of deep sea, characterized by the absence of light, extremely high hydrostatic pressure, low temperature, limited amount of organic matter, and low dissolved oxygen, a variety of microorganisms have been identified in abyssal sediments, dominated by bacteria and archaea [13,14], which significantly contribute to Fe-redox processes. Some species of *Shewanella* and *Geobacter* are known to transfer electrons from organics to Fe(III) through direct physical contact [15,16] or via nanowires [17,18]. Fe-oxidizing bacteria are also extensively distributed in deep-sea environments, such as *Marinobacter hydrocarbonoclasticus*, with dissolved oxygen or nitrate as electron acceptors [19]. In particular, nitrate concentration in the deep sea (16–43 μmol/kg) is generically higher than that at the epigenetic level (0–30 μmol/kg), making nitrate a dominant electron acceptor [20]. Genuine deep-sea sedimentary environments are generally complex and characterized by the coexistence of Fe(II), Fe(III), oxygen, and nitrate across diverse spatial and temporal scales [13]. Nitrate-reducing Fe(II)-oxidizing bacteria may have a symbiotic relationship with dissimilatory Fe(III)-reducing bacteria, facilitating Fe(III) oxide migration and Fe(II) regeneration [21]. However, the specific electron transfer mechanisms between Fe(III) and electron donors in abyssal sediment remain poorly understood. In particular, the long-term kinetics of Fe(III) reduction and Fe(II) oxidation in deep-sea sediments have not been thoroughly explored. Additionally, the impact of hydrostatic pressure on Fe-redox cycling and the corresponding microbial composition has not been sufficiently investigated.

The objective of this study was therefore to examine the biogeochemical cycling of Fe in the deep-sea environment. Abyssal sediments collected from a depth of 5800 m in the Pacific Ocean were characterized for elemental, mineralogical, and microbial compositions. The relationships between microorganisms, hydrostatic pressure. and electron donors/acceptors were statistically analyzed. The microbial functions related to Fe-redox properties were predicted based on FAPROTAX or BugBase, established databases. Our results provide novel insights into the Fe-redox reactions in nutrient-deficient abyssal environments, which are closely related to the global biogeochemical cycling of contaminants and essential elements.

2. Materials and Methods

2.1. Sample Collection

Sediment samples were collected from depths of 5800 m at 21.909° N, 130.141° E in the Pacific Ocean. A 30 cm-long undisturbed core was obtained using a box-type collector. To ensure sample freshness during repeated experiments, the sediments were divided into several equal parts and placed in airtight sterilized polyethylene containers. The samples were stored at 4 °C before use.

2.2. Bio-Redox Reactions of Fe in Abyssal Sediment

The artificial seawater medium was prepared as follows: 0.4 M NaCl, 27.6 mM Na_2SO_4, 7.65 mM NH_4Cl, 24.5 mM $MgCl_2{\cdot}6H_2O$, 10 mM $CaCl_2$, 2.29 mM $NaHCO_3$, 8.91 mM KCl, 50 μM KBr, 0.32 mM H_3BO_3, 0.15 mM $SrCl_2$, 71.4 μM NaF, 17.91 μM $FeSO_4{\cdot}7H_2O$, 7.72 μM $ZnSO_4{\cdot}5H_2O$, 9.15 μM $MnCl_2{\cdot}4H_2O$, 1.61 μM $Na_2MoO_4{\cdot}2H_2O$, 0.17 μM $Co(NO_3)_2{\cdot}6H_2O$, 0.32 μM $CuSO_4{\cdot}5H_2O$, 26.86 μM $Na_2EDTA{\cdot}2H_2O$, 40.93 nM D-biotin, 7.38 nM cobalamin, 296.50 nM thiamine, and 1 L ddH_2O.

The properties of abyssal sediment and its microbial composition can change due to a lack of pressure-holding technology. Hence, Fe reduction experiments were conducted under atmospheric pressure (as a mechanistic comparison to high hydrostatic pressure) or 58 MPa in the presence or absence of an external electron donor (H_2 or lactate), labeled as follows: H-Original (no external electron donor under high pressure), H-H_2, H-Lactate, A-Original (no external electron donor under atmospheric pressure), A-H_2, and A-Lactate. For the atmospheric experiments (A-), 100 mL of artificial seawater medium was added to a 200 mL glass container. To ensure anaerobic conditions, nitrogen or hydrogen was used to replace the air and the media were autoclaved at 121 °C for 20 min. After sterilization, a stock solution containing 0.5 g of abyssal sediments was added. Oxygen-free lactate was filtered into the medium through a sterilized filter (0.22 μm). Lactate (5 mM) or hydrogen (headspace) served as electron donors. For high-pressure experiments (H-), the systems were set up in custom-made high-strength polyethylene bags and placed in a high-pressure vessel. The cultures were maintained at 20 °C in the dark. Before use, all glassware was washed with neutral detergent and soaked in 1 M HNO_3 overnight. All cultures were prepared in duplicate due to the excellent reproducibility observed in preliminary triplicate experiments. Fe-redox experiments were performed more than 3 times each, exhibiting excellent reproducibility. Total Fe(II) and total Fe were determined at days 0, 5, 16, 20, 39, and 58.

The preparation for the Fe oxidation experiment was similar to that of the reduction experiment, with the exception that the hydrostatic pressure was a uniform 0.1 Mpa and $FeCl_2$ (1 mM) and $NaNO_3$ (1 mM) were used as the electron donor and acceptor, respectively. After autoclaving, an $FeCl_2$ stock solution was filtered through a sterilized filter (0.22 μm) into the medium. Abiotic controls were prepared to verify that Fe oxidation was driven by microbial activity. Total Fe(II) and total Fe were measured at days 0, 1, 3, 5, 7, 10, 17, 28, and 45. All cultures were prepared in duplicate.

2.3. Bioinformatic Analysis

2.3.1. DNA Extraction, 16S rRNA Gene Amplification, and High-Throughput Sequencing

DNAs were extracted from 0.25 g of sediment using the MoBio Power Soil DNA isolation kit (MoBio Laboratories, Carlsbad, CA, USA) according to the manufacture's protocol. The V4 hypervariable region of the prokaryotic 16S rRNA genes for both bacteria and archaea was amplified using the primer set 515F (5′-CAGCMGCCGCGGTAA-3′) and 806R (5′-GGACTACHVGGGTWTCTAAT-3′) with unique barcode sequences at both 5′ ends. PCR amplification was carried out in a 50 μL reaction system containing 5 μL 10× PCR buffer, 1.5 μL dNTP mixture (10 mM for each), 1.5 μL forward and reverse primers (10 μM), 0.5 μL Taq DNA Enzyme (TaKaRa), 2 μL of template DNA (5–30 ng), 1 μL of BSA, and 37 μL ddH_2O. The PCR program was as follows: 94 °C for 1 min, 30 cycles at 94 °C for 20 seconds, 57 °C for 25 seconds, and 68 °C for 45 seconds, and a final extension at 68 °C for 10 min. PCR products were purified by gel electrophoresis and quantified with a Qubit fluorimeter (Invitrogen, Carlsbad, CA). Equal molar amounts of DNA were pooled for library construction and sequencing on the Illumina Hiseq platform at Magigene Biotechnology Co., Ltd. (Guangzhou, China).

2.3.2. Data Processing and Statistical Analysis

The 16S rRNA gene sequences were analyzed using tools available on the BMKCloud platform (www.biocloud.net, accessed on 5 June 2024). The raw sequences were demultiplexed by barcode identification, with the maximum barcode error rate set at 1.5. Quality filtering of the raw data was performed using Trimmomatic (version 0.33) [22], with a sliding window size of 50 bp. Sequences were trimmed if the quality within the window fell below 20. Cutadapt (version 1.9.1) [23] was used to identify and remove primer sequences, with a maximum mismatch rate of 20% and a minimum coverage of 80%. USEARCH (version 10.0) [24] was employed to concatenate paired-end reads, and UCHIME (version 8.1) [25] was used to remove chimeras, resulting in high-quality sequences for further

analysis. For USEARCH, the minimum overlap length was set to 10 bps, with a required minimum similarity of 90% and a maximum of 5 mismatched bases. High-quality reads were used to generate operational taxonomic units (OTUs) at a 97% similarity level using UPARSE [26]. Taxonomic assignment for representative sequences was performed based on the Silva database (release 138).

The rarefaction, Shannon, and rank abundance curves were analyzed using QIIME2 [27]. The data of 6 groups were processed through principal component analysis (PCA) using R, without further grouping. To create a heatmap, the 80 most abundant genera were extracted and visualized using R. The values for the heatmap were normalized with the R scale function to compute Z-scores across different samples of the same species. Redundancy analysis (RDA) or canonical correspondence analysis (CCA) was chosen based on the decision curve analysis (DCA) results of species sample abundance, depending on the length of the first axis of the DCA. CCA was selected if this length exceeded 4.0; otherwise, RDA was used. RDA or CCA was performed using the Vegan (version 2.3) package of R. The functional composition was predicted using FAPROTAX [28], based on the evidence from published and cultured microorganisms. FAPROTAX annotation can greatly enhance understanding of biogeochemical cycles in environmental samples. The microbial phenotypes of each group were predicted using BugBase [29], and the results were normalized based on the predicted 16S copy numbers. For each sample in the biological dataset, the relative abundance of traits was estimated across a range of coverage thresholds (0 to 1, in increments of 0.01). The coverage threshold was determined with the highest variance among all samples for each feature, and the final organism level trait prediction table was generated, which included the relative abundance of predicted traits for each sample. The predicted phenotypes were aerobic, anaerobic, facultative anaerobic, Gram-positive, Gram-negative, biofilm forming, mobile element containing, oxygen utilization, and oxidative stress tolerance.

2.3.3. Data Submission and Accession Numbers

The full-length 16S rRNA gene sequences were deposited in the NCBI database and can be accessed under project ID PRJNA1141258.

2.4. Analytical Methods

2.4.1. Measurements of Total Fe(II), Total Fe and Nitrate

At preselected time points during Fe-redox reactions, a 0.2 mL sediment suspension was withdrawn from the experimental bottle or bag using a sterile syringe. As described earlier [30], the sediment suspension was mixed with 0.48 mL of 3.6 N H_2SO_4 in a dark tube, then 40 µL of 48% HF and 80 µL of 10% (w/v) 1,10-phenanthroline were added. The tubes were then heated to 100 °C and boiled for 30 min. After cooling, 0.4 mL of 5% (w/v) boric acid was added to the mixture. Following this, 0.1 mL of the sample was combined with 1 mL of 1% (w/v) Na citrate to develop color for 20 min. A UV-vis spectrophotometer (Thermo Fisher, Waltham, MA, USA) was utilized to measure the absorbance at 510 nm. To determine the concentration of total Fe, including both Fe(III) and Fe(II), a 0.1 mL sample was added to a 1 mL mixture of Na citrate (1% w/v) and hydroxylammonium chloride (10% w/v). All Fe(III) was reduced to Fe(II), and then the concentration of Fe(II) was measured again. Additionally, at least 1 mL sediment suspension was filtrated through a 0.2 µm nylon filter, and the nitrate concentrations of the filtrate were measured using ion chromatography (Thermo Fisher ICS 600) with an electrical conductivity detector.

2.4.2. X-ray Diffraction Analysis

Abyssal sediment samples were freeze-dried and crushed to powder below 300 mesh using an agate mortar. X-ray diffraction (XRD) pattern was obtained following a previously described protocol [31]. Briefly, an X-ray powder diffractometer (Rigaku Smart Lab X, Tokyo, Japan) was used, equipped with a Cu Kα radiation source, a rotating-anode generator, and power of 9000 W (200 kV, 45 mA). The samples were scanned from 3° to 70°

(2θ) in steps of 0.02° with 1 second per step. The mineralogical analysis was performed using MDI Jade software (Version 6.5).

2.4.3. Scanning Electron Microscopy Analysis

Scanning electron microscopy (SEM) was performed to examine mineral–microbe associations at the end of bio-reduction experiments. Samples were prepared following procedures described in our previous work [32]. Briefly, an aliquot of the sediment suspension was withdrawn from the experimental serum bottle, smeared onto a glass coverslip, and fixed using a mixture of 2.5% glutaraldehyde and 2% paraformaldehyde in phosphate-buffered saline (PBS). After fixation, gradient dehydration was performed with various proportions of ethanol and water. Afterwards, the samples were dried with a critical point dryer (CPD, Quorum K850) and Pt-coated with a Quorum SC7620 sputter coater. SEM (Zeiss Supra 55 SAPPHIRE) was used for morphological observation.

2.4.4. Major and Trace Element Analysis

Carbon (C), hydrogen (H), nitrogen (N), and sulfur (S) content were analyzed on decarbonated samples using an element analyzer (Vario Macro Cube, Elementar, Langenselbold, Germany). Other elements were determined at the Analytical Laboratory of Beijing Research Institute of Uranium Geology, China National Nuclear Corporation. For major elements (Si, Al, Fe, Mg, Ca, Na, K, Mn, Ti, P), samples were ground to 200 mesh and oven-dried overnight at 105 °C. Each sample of 2.0 g was weighed, ignited at 1100 °C in a platinum crucible, and reweighed to determine the loss on ignition (LOI). A 0.5 g (weight before ignition) ignited sample was mixed with 4.5 g $Li_2B_4O_7$–$LiBO_2$–LiF (4.5:1:0.4, wt%), fused in a platinum crucible at 1100 °C, and then pressed to create a flattened disk. The pressed discs were analyzed using an X-ray fluorescence spectrometer (XRF, PANalytical, Almelo, the Netherlands) at 25 kV with 144 mA emission current. Calibrations of accuracy and reproducibility were conducted using the GB/T 14506.14-2010 and GB/T 14506.28-2010 standards, with a standard deviation consistently below 5%. For trace element analysis, samples were crushed in an agate mortar and digested with HNO_3 and HF to obtain the sample solution. Trace element concentrations were determined using ICP mass spectrometry (NEXION 300D, PerkinElmer, Shelton, CT, USA) coupled with an ESI SC-2 DX4 auto-sampler (Elemental Scientific, Omaha, NE, USA). Samples were diluted (1:20 v:v) with a diluent consisting of 0.05% Triton X-100 and 1% HNO_3 in 18.2 MΩ·cm distilled deionized water. Calibrations for accuracy and reproducibility were conducted using the GB/T 14506.30-2010 standard, with a standard deviation consistently below 5%.

3. Results and Discussion

3.1. Characterization of the Abyssal Sediment

The sedimentary environment at 5800 m depth was carbon-deficient (0.22%, Table 1), significantly lower than the average carbon content (0.66%) in deep-sea sediments [33]. The C/N value in the sediment was slightly above 4, indicating the presence of chemoautotrophic microbial communities [34].

Substantial amounts of redox-active metals (e.g., Fe and Mn) were observed (Table 1), suggesting that the redox reactions may be prevalent at this depth. The high content of SiO_2, Al_2O_3, and Fe_2O_3 indicated the argillaceous features of abyssal sediment, which was confirmed by XRD analysis (Figure 1), showing the dominant mineralogical composition of quartz, muscovite, albite, and lizardite.

A variety of trace elements were detected in the abyssal sediment (Table 1), which were closely associated with the co-present minerals. Clay minerals of muscovite can adsorb trace elements through ion exchange [35–37], while Fe–Mn (hydr)oxides also play a role in scavenging trace elements [38,39]. Active Fe-redox regions in deep-sea sediment can accumulate various trace elements, which may serve as active centers for coenzymes and catalyze methane production and nitrogen fixation [40–42].

Table 1. Measures of carbon (C), hydrogen (H), nitrogen (N), sulfur (S), 11 major elements, and 44 trace elements in the abyssal sediment.

C, H, N, S (%)	C (%)	H (%)	N (%)	S (%)	C/N	C/H
	0.22	0.682	0.053	0.639	4.177	0.3238
Major elements (%)	SiO_2	Al_2O_3	Fe_2O_3	MgO	CaO	Na_2O
	49.11	14.05	9.78	4.69	2.91	4.49
	K_2O	MnO	TiO_2	P_2O_5	LOI	FeO
	2.07	1.2	0.759	0.356	10.28	0.36

Trace elements (μg/g)											
	Li	Be	Sc	V	Cr	Co	Ni	Cu	Zn	Ga	Rb
	45.2	1.52	24.2	171	90.6	72.1	168	331	149	17.5	61.1
	Sr	Y	Mo	Cd	In	Sb	Cs	Ba	La	Ce	Pr
	231	77.3	11.1	0.394	0.118	1.88	5.52	735	49	67	12.5
	Nd	Sm	Eu	Gd	Tb	Dy	Ho	Er	Tm	Yb	Lu
	55.5	12.4	3.28	10.2	2.39	14	2.89	7.55	1.28	7.72	1.05
	W	Re	Tl	Pb	Bi	Th	U	Nb	Ta	Zr	Hf
	3.44	0.006	1.79	35.5	0.638	7.73	1.5	10.8	1.11	129	3.75

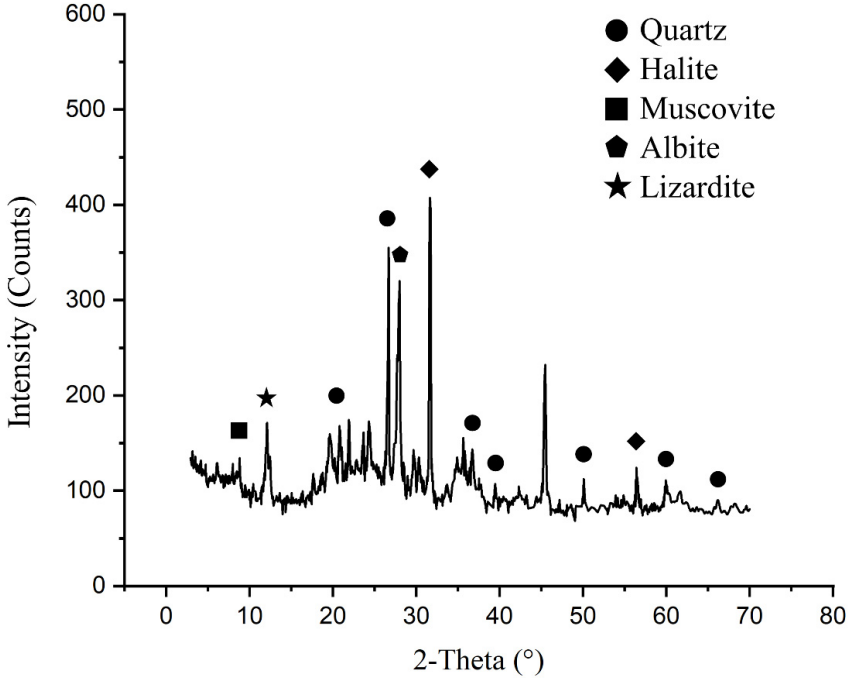

Figure 1. XRD pattern of the untreated abyssal sediment.

3.2. Fluctuation of Fe-Redox State in the Abyssal Sediment

Due to the presence of dissolved oxygen, the majority of Fe in shallow abyssal sediment existed as Fe(III) (t = 0 d, Figure 2). Bio-induced oscillation of Fe-redox states in the abyssal sediment was observed over 58 days' anaerobic culturing, regardless of the presence/absence of an external electron donor and environmental pressures (Figure 2).

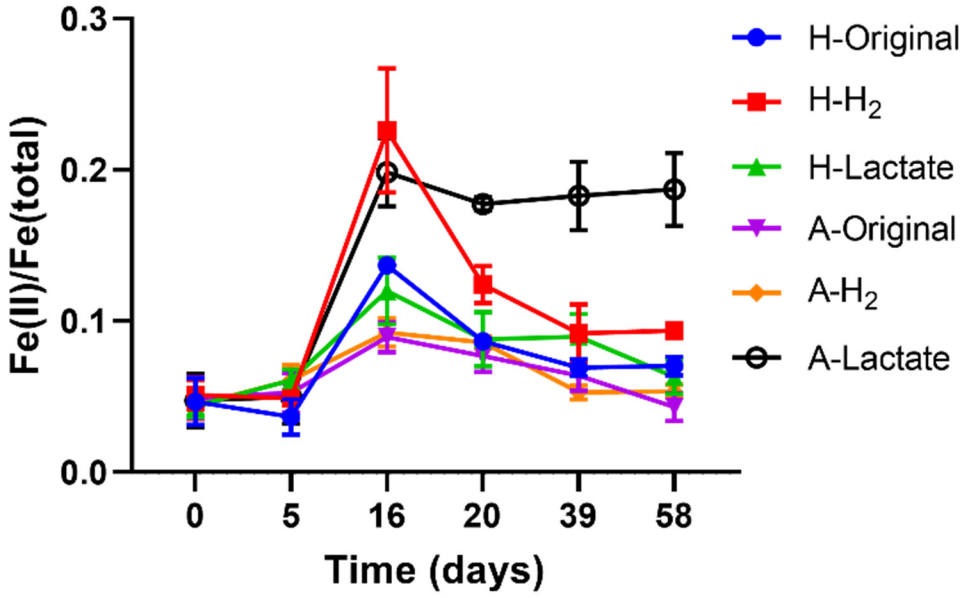

Figure 2. Fe-redox curves of the abyssal sediment over 58 days' anaerobic culturing under atmospheric pressure or 58 MPa in the presence or absence of an external electron donor (H_2 or lactate).

During the initial 5 days, bio-redox activity was low and Fe(II) concentration remained unchanged. From day 5 to 16, Fe reduction increased sharply. Under high pressure of 58 MPa (H-), Fe(III) reduction in the H_2-amended group (H-H_2) reached 17.74%, which was 11.84% and 7.73% higher than that in the lactate-amended group (5.9%, H-Lactate) and amendment-free original group (10.01%, H-Original), respectively. Under atmospheric pressure (A-), Fe(III) reduction in the lactate group (A-Lactate) reached 14.86%, 11.69%, and 11.2% higher than that in the H_2-amended group (3.17%, A-H_2) and original group (3.66%, A-Original).

These findings indicate a shift in the Fe-redox equilibrium toward Fe reduction during the first 16 days, which was kinetically affected by the presence or absence of external electron donors and environmental pressures. Even in the absence of external electron donors, biogenic Fe(II) increased from 3.67% to 13.68% (high pressure) and from 5.27% to 8.93% (atmospheric pressure), suggesting a spontaneous Fe reduction using *in situ* electron donors. However, external electron donors further accelerated the reduction processes (Figure 2).

Environmental pressures also had an impact on the Fe redox. Under atmospheric pressure, lactate significantly promoted Fe(III) reduction from 8.93% (A-Original) to 19.84% (A-Lactate), but high pressure diminished this effect (Figure 2). Previous studies have similarly reported that the Fe reduction efficiency of *Shewanella* spp. was inhibited by high hydrostatic pressure due to the lack of piezotolerance [43]. Our observations suggest that high pressure universally inhibits microbial growth, thereby suppressing Fe(III) reduction. In contrast to lactate, H_2 as an electron donor significantly enhanced Fe(III) reduction under high pressure (58 Mpa), increasing from 13.68% (H-Original) to 22.62% (H-H_2), while showing negligible effects under atmospheric pressure. This enhancement likely resulted from piezotolerant or piezophilic Fe-reducing bacteria utilizing H_2 as an electron donor [44]. This discovery aligns with the observed serpentinization in the 5800 m sample (Figure 1), wherein reactions between ultrabasic rock and water generate H_2, which acts as a bioenergy source [45].

All groups reached Fe(II) concentration peaks at day 16 and started an extended period of gradual Fe oxidation before achieving a redox equilibrium after 58 days, except for A-Lactate, in which Fe(II) concentration stabilized between 17.75% and 18.71%, possibly due to a sufficient supply of effective electron donors (Figure 2). Despite measurable Fe-redox reactions, most sediment-bound Fe remained inactive (Figure 2).

The validity of the Fe bio-oxidation process was confirmed through an independent Fe oxidation experiment supplemented with nitrate as the electron acceptor (Figure 3). Fe(II) decreased significantly from 0.829 mM to 0.108 mM within a 10-day period, coupled with a decrease in nitrate from 1.0 mM to 0.669 mM. The abiotic control maintained stable Fe(II) and nitrate concentrations, suggesting the absence of chemical oxidation of Fe(II) by nitrate under these conditions (Figure 3).

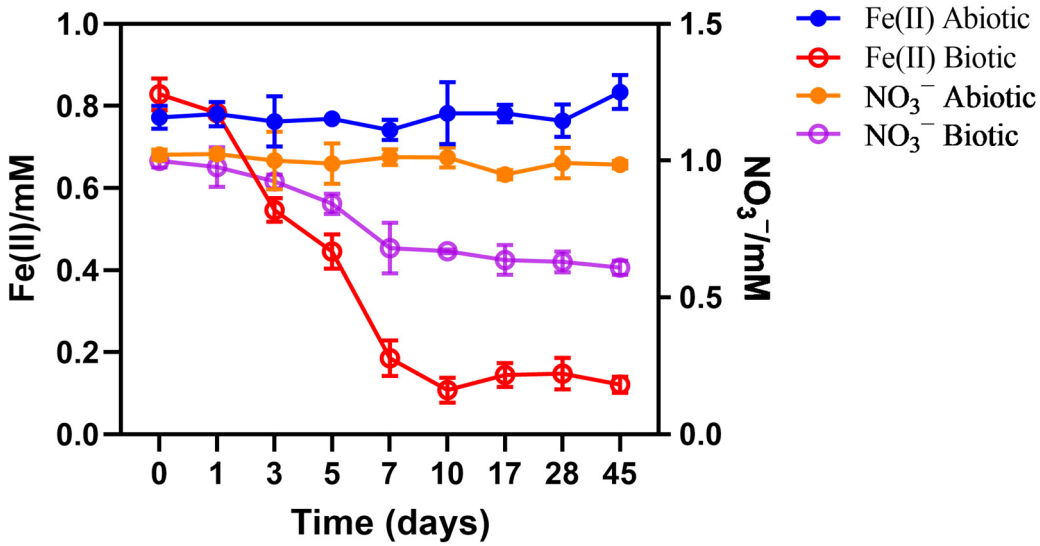

Figure 3. Nitrate-amended oxidation of the abyssal sediment over 45 days.

Oxidation of Fe(II) by nitrate or other oxidants is a frequently observed phenomenon in redox transition areas. The Fe(III) involved in dissimilatory reduction is typically generated through the microbial oxidation of Fe(II). This process is particularly prevalent in abyssal zones where organic carbon is limited, facilitating the growth of autotrophic organisms that rely on Fe(II) as an energy source and nitrate as an electron acceptor [46].

3.3. Pressure Controlling the Microbial Community Composition in Abyssal Sediment

A total of 525 operational taxonomic units (OTUs) was recognized within the six treated samples, with A-Original exhibiting the greatest OTU count (Figure 4a). Rarefaction and Shannon curves validated the sufficiency and dependability of the sampling and sequencing process (Figure S1). The introduction of external H_2 or lactate did not influence the diversity of the anaerobic system, as the OTU counts remained comparable to the original groups. Elevated pressure significantly reduced the microbial diversity. For instance, samples subjected to 0.1 MPa displayed a microbial diversity of over 150 OTUs, in contrast to samples under 58 MPa, which exhibited fewer than 78 OTUs (Figures 4a and S2). Despite the cumulative OTUs surpassing 500 across the samples, only 12 OTUs were shared (Figure 4b). This pattern was similarly evident at the genus level (Figure S3). These findings indicate that the addition of electron donors and the variations in pressure conditions significantly impacted the microbial compositions.

Principal component analysis (PCA, Figure 4c) and a clustering heatmap (Figure 4d) confirmed that environmental pressure primarily shaped the microbial community structures. PC1 explained 89% of the overall data variance, while PC2 accounted for 7.7%. The distinct separation of the three groups under atmospheric pressure and the three groups under 58 MPa along PC1 indicates a notable similarity within groups sharing the same pressure levels.

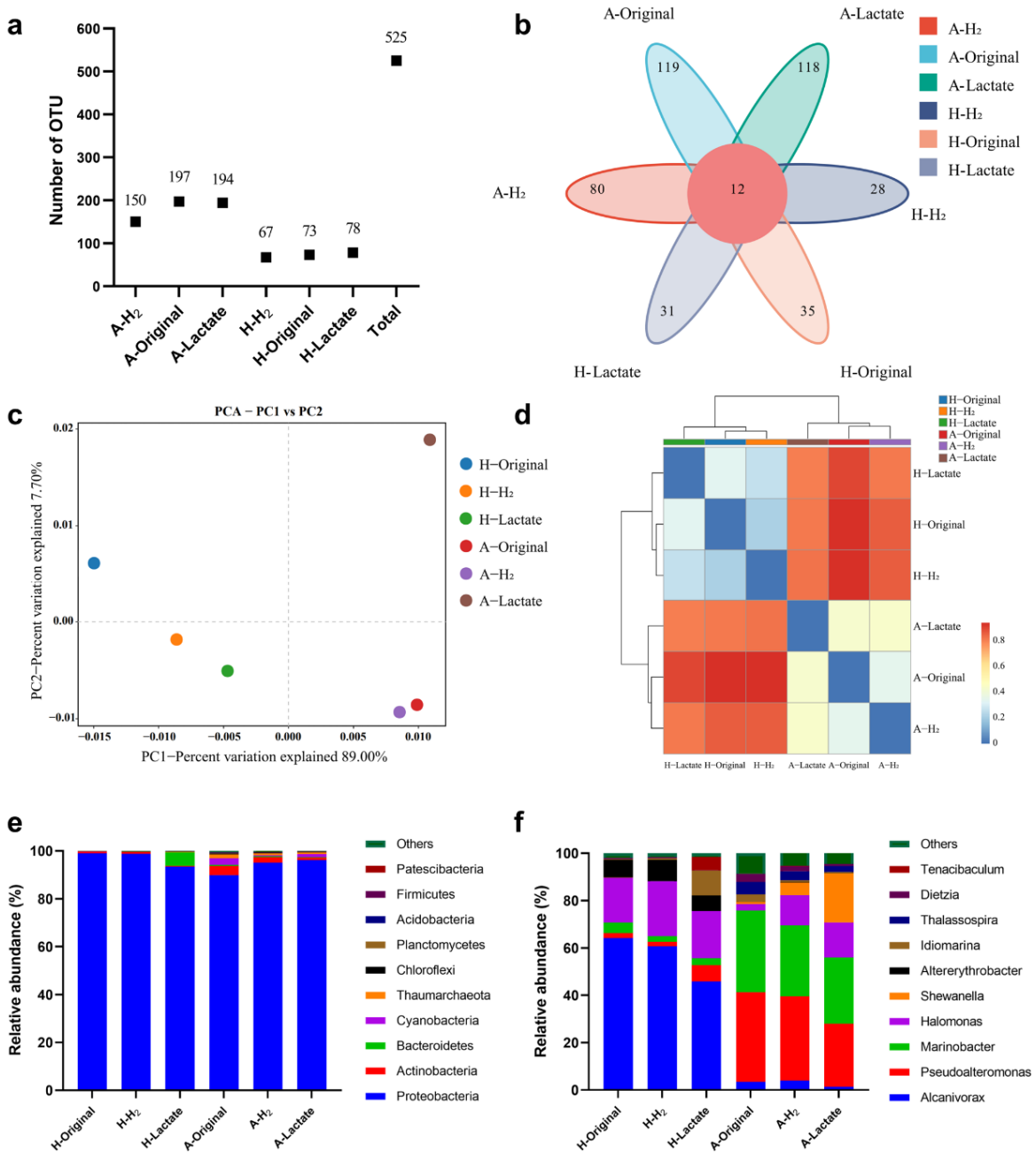

Figure 4. (**a**) OTU number and (**b**) corresponding distribution; (**c**) principal component analysis; (**d**) sample clustering; relative abundance of (**e**) phylum and (**f**) genus in the 6 treated abyssal sediment cultures.

Consistent with previous observations [47,48], Proteobacteria, especially Gammaproteobacteria and Alphaproteobacteria, were the most prevalent bacteria in the abyssal sediment cultures (Figure 4e). Proteobacteria demonstrate extensive phylogenetic diversity within the Bacteria domain, enabling numerous species to adapt and thrive in distinct ecological niches within the deep-sea sediment environment [49]. These Proteobacteria found in deep-sea sediments are commonly characterized as psychrophilic and chemolithoautotrophic, displaying a preference for cold temperatures, low nutrient availability, and high pressure typical of abyssal sediment environments [50]. Proteobacteria have been discovered thriving in deep-sea hydrothermal fields, showcasing their remarkable diversity and ability to thrive in extreme environments [51]. Their diverse metabolic capabilities enable Proteobacteria to harness various energy sources, including the oxidation of iron

and sulfur compounds abundant in deep-sea environments [52]. In comparison to other bacterial phyla, Proteobacteria have a higher representation in high-pressure environments, indicating that non-piezotolerant organisms are inhibited by high pressure, paving the way for piezotolerant Proteobacteria to flourish.

Bacteroidetes, a phylum with very low abundance across the treated sedimentary groups, revealed an interesting anomaly within the lactate group under 58 MPa (H-Lactate). In this unique case, Bacteroidetes accounted for a notable 5.72%. Further analysis unveiled that 98.6% of these Bacteroidetes were identified as *Tenacibaculum*, suggesting its piezophilic nature and preference for lactate as a carbon source. Notably, while *Tenacibaculum*'s metabolic activities indicate an affinity for lactate [53], its involvement in the oxidation or reduction of Fe remains unreported.

At the genus level, pressure was also the controlling factor for microbial community compositions. The microbial communities exhibited relatively similar characteristics across the three samples subjected to the same pressure conditions (Figure 4f), consistent with the findings of PCA and clustering analyses. Notably, *Alcanivorax* and *Halomonas* stood out as the predominant genera in the three high-pressure groups, with *Altereythrobacter*, *Pseudoalteromonas*, and *Marinobacter* also being prevalent. Conversely, under atmospheric conditions, *Marinobacter* and *Pseudoalteromonas* were the dominant genera, while the proportion of *Alcanivorax* was considerably lower.

The heatmap depicts the distribution of the primary genera among the six treated abyssal sediment samples (Figure 5), revealing two distinct microbial compositions based on varying levels of pressure. Under high pressure, H_2 or lactate had minimal impact on the microbial composition, except for *Pseudomonas*, *Idiomarina*, and *Tenacibaculum*, which displayed a significant positive relationship with lactate. Conversely, under atmospheric pressure, lactate and H_2 selectively enriched the presence of specific genera that were not originally abundant within the group. Genera such as *Shewanella*, *Phenylobacterium*, *Sphingobium*, *Escherichia_Shigella*, and *Lysinibacillus* had a strong positive correlation with lactate, while *Thermus*, unclassified *Woesearchaeales*, *Zunongwangia*, *Woeseia*, *Alteromonas*, *Roseovarius*, *Proteiniphilum*, *Arthrobacter*, *Hyphomicrobium*, *Methyloversatilis*, unclassified Thermoplasmata, *Bosea*, *Limnobacter*, *Brevundimonas*, unclassified *Vicinamibacterales*, *Sphingomonas*, *Acinetobacter*, *Blastococcus*, and *Candidatus Caldatribacterium* had a strong positive correlation with H_2. Additionally, *Methylophaga*, *Methylobacterium_Methylorubrum*, and *Sphingopyxia* showed a strong positive correlation with both H_2 and lactate.

The genera positively correlated with lactate were predominantly heterotrophic, utilizing various organic compounds like short-chain organic acids, ketones, aldehydes, or esters as carbon source [54–61]. Notably, *Lysinibacillus* and *Shewanella* were identified as potential participants in Fe(III) reduction [62–64]. On the other hand, the genera associated with H_2 were more diverse, including *Thermus*, *Alteromonas*, and *Sphingomonas* as potential Fe-reducing microorganisms [65–67], while *Methyloversatilis* was recognized as a potential Fe-oxidizing microorganism [68]. These microorganisms rely on simpler carbon and energy sources such as hydrogen and formate. Additionally, certain unidentified species of Thermoplasmata might function as potential Fe-oxidizing archaea or utilize hydrogen for energy production [69,70].

However, under atmospheric pressure, the majority of genera appeared to be more negatively correlated with H_2 or lactate (Table S1). Among the negatively enriched genera, the proportions of uncultured and unclassified species were high, as was the proportion of archaea, including uncultured archaeon_CRA7_0cm, *Candidatus Nitrosopumilus*, uncultured *Cenarchaeum* spp., uncultured euryarchaeote, *Candidatus Nitrosopelagicus*, and uncultured Thermoplasmatales archaeon. This suggests that the preferential enrichment of H_2 or lactate impaired symbiosis and microbial diversity in abyssal sediments, leading to a decrease in extremophilic archaea populations.

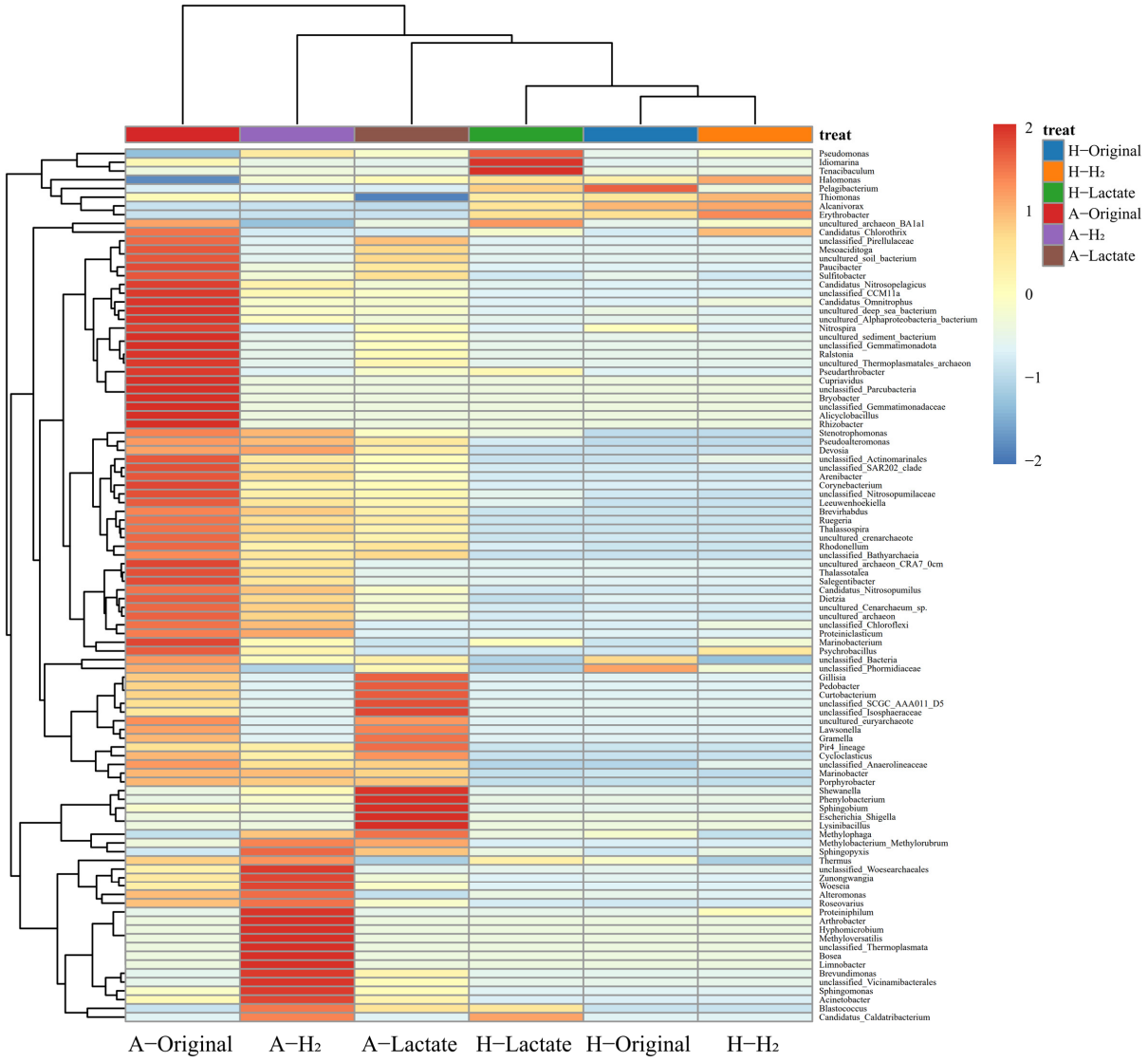

Figure 5. Correlation heatmap indicating major microbial composition across the 6 treated abyssal sediment samples.

3.4. The Dynamics between Microbial Community and Fe-Redox Fluctuation

Except for *Lysinibacillus*, *Thermus*, *Alteromonas*, and *Sphingomonas*, which exhibited a positive correlation with the supplied H_2 or lactate, *Shewanella*, *Thalassospira*, and *Thermodesulfovibrio* have been identified as potential iron-reducing bacteria (Table 2) [71,72]. *Thalassospira* demonstrated enhanced growth under atmospheric conditions compared to high-pressure environments, while the proportion of *Thermodesulfovibrio* remained consistently low across all cultivation systems (Table 2).

It is worth noting that the proportion of *Shewanella*, a genus capable of dissimilatory Fe reduction [73], varied significantly across the six treated abyssal sediments, influenced by both pressure levels and the availability of electron donors. The genus *Shewanella* encompasses more than 70 species, a few of which demonstrate a notable tolerance to high-pressure conditions [74]. Notably, in the present investigation, *Shewanella* was represented by three species: *Shewanella putrefaciens* (<0.02%), *Shewanella oneidensis* (<0.01%), and an unclassified *Shewanella* sp. (Table 2). The piezotolerance of *Shewanella putrefaciens* and *Shewanella oneidensis* is evident, while the unclassified *Shewanella* sp. was more prevalent under 0.1 MPa (Table 2). In general, most *Shewanella* spp. demonstrate a preference for atmospheric conditions, with even piezotolerant strains such as *Shewanella piezotolerans*

WP3 showing optimal growth under pressures below 20 MPa [74]. Additionally, the abundance of *Shewanella* was significantly correlated with the supply of electron donors.

Table 2. The proportions of Fe-reducing and Fe-oxidizing microorganisms (%).

	Genus/Species	H-Original	H-H_2	H-Lactate	A-Original	A-H_2	A-Lactate
Fe-reducing microorganisms	*Shewanella*	0.0637	0.0553	0.023	0.998	5.407	20.679
	S. putrefaciens	0	0.0164	0	0	0	0.00369
	S. oneidensis	0	0.00614	0.00628	0	0	0.00738
	Unclassified *S.* sp.	0.0637	0.0328	0.0167	0.998	5.407	20.668
	Thalassospira	0.00554	0.00615	0.00209	5.233	3.864	2.438
	Thermodesulfovibrio	0.00139	0	0	0	0	0
	Lysinibacillus	0	0.00205	0	0.00833	0	0.0148
	Thermus	0.00692	0.00205	0.0126	0.00625	0.00557	0.00123
	Alteromonas	0.166	0.191	0.149	0.281	0.443	0.0701
	Sphingomonas	0.00139	0.0123	0.00837	0.0167	0.0445	0.0184
Fe-oxidizing microorganisms	*Marinobacter*	4.46	2.356	2.99	34.458	29.995	28.034
	Uncultured *M.* sp.	0.370	0.154	0.234	1.013	0.665	0.873
	M. lacisalsi	0.032	0.047	0.015	1.215	0.846	0.216
	M. hydrocarbonc-lasticus	1.292	0.918	1.029	16.617	14.954	19.154
	Thiomonas	0.0263	0.0307	0.0293	0.0125	0.0111	0.00861
	Sulfolobus	0	0	0	0	0	0.00246
	Methyloversatilis	0	0	0	0.00208	0.420	0

Under atmospheric pressure, the amendment of lactate (A-Lactate) significantly increased the abundance of *Shewanella putrefaciens*, *Shewanella oneidensis*, and the unclassified *Shewanella* sp. compared to amendment-free original samples (A-Original) (Table 2), with notably elevated Fe(II) concentrations (A-Lactate: 19.84%) compared to the other experimental cohorts (A-Original: 8.93%, A-H_2: 9.25%, Figure 2). The supply of H_2 (A-H_2) also slightly promoted the growth of the unclassified *Shewanella* sp. compared to the original samples (A-Original) (Table 2). In contrast, under high pressure (58 MPa), *Shewanella putrefaciens* and *Shewanella oneidensis* exhibited enhanced growth in the presence of H_2 (H-H_2), aligning with the observations of water–rock interactions in ultrabasic rocks (serpentinization), as evidenced in the 5800 m sample (Figure 1). The abundance of *Shewanella* spp. correlated closely with Fe(II) levels (Table 2; Figure 2).

Hydrogen-utilizing Fe(III)-reducing microorganisms were expected to be prevalent in the H-H_2 group, coinciding with the peak concentration of Fe(II) observed during incubation (Figure 2). Contrary to expectations, microbial community analysis did not support this hypothesis, possibly due to a gradual decrease in the abundance of Fe(III)-reducing microorganisms during incubation (Figure 4f), while sampling was conducted at the end of incubation.

The four dominant Fe-oxidizing genera, including *Methyloversatilis*, which was positively correlated with H_2 amendment, were identified in the six treated abyssal sediment samples (Table 2). *Thiomonas* preferred high-pressure environments, whereas Fe-oxidizing archaea *Sulfolobus* were minimally present across all cultivation conditions. Certain species of *Marinobacter* have the capacity to oxidize Fe(II), such as *Marinobacter hydrocarbonoclasticus*, which utilizes Dps proteins for the oxidation of Fe(II) as a detoxification mechanism under anaerobic or oxygen-limited growth conditions [19]. The abundance of *Marinobacter hydrocarbonoclasticus* was observed to be relatively lower under high pressure (0.918–1.292%), but increased significantly when exposed to atmospheric conditions (14.953–19.154%), indicating a potential contribution to the enhanced Fe oxidation observed in later stages (Figure 2; Table 2).

Therefore, the presence of diverse microbial communities, especially Fe-redox microorganisms, contributed to the fluctuation observed in Fe-redox processes, which were further influenced by a range of environmental factors such as electron donor availability and ambient pressure levels.

The relationship between environmental factors (pressure, H_2, lactate) and microbial communities was examined via redundancy analysis (RDA), revealing a distinct separation

of the six treated abyssal sediment groups across four quadrants (Figure 6a). Notably, the two lactate groups (A-Lactate, H-Lactate) were distinctively situated in separate quadrants, whereas the original group and the H_2 group at the same pressure level were clustered together in another quadrant. This distribution pattern suggests that environmental pressure levels played a pivotal role in shaping the microbial composition with respect to lactate and H_2, as further confirmed by the elongation along the RDA1 axis. Notably, certain genera, such as *Alanivorax*, *Erythrobacter*, *Pelagibacterium*, and *Halomonas*, displayed positive correlations with pressure, while *Dietzia*, *Thalassospia*, *Pseudoalteromonas*, and *Marinobacter* exhibited negative associations, indicating varying degrees of resilience to the ambient pressure levels. This relationship was further confirmed by the correlation heatmap (Figure S4), illustrating the positive correlation of *Halomonas*, *Pelagibacterium*, *Thiomonas*, *Alcanivorax*, and *Erythrobacter* with pressure, and conversely the negative correlation of *Shewanella* and *Marinobacter* with pressure (Figure S4).

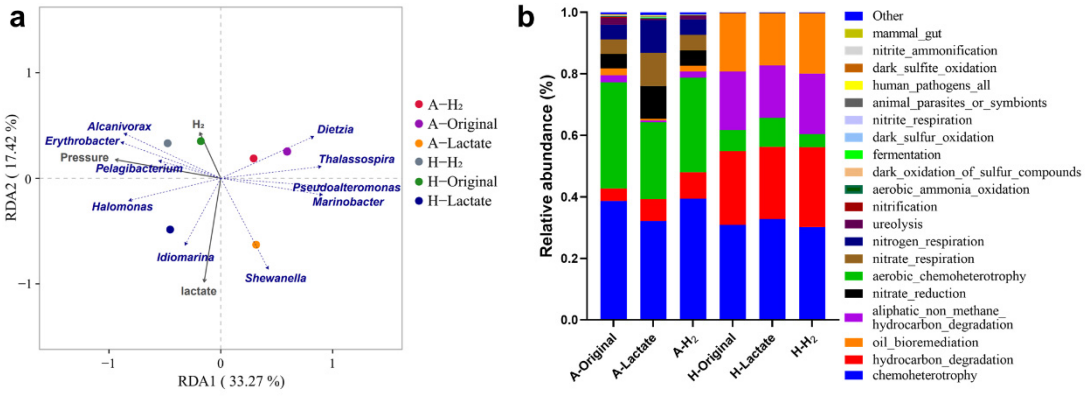

Figure 6. (**a**) Redundancy analysis (RDA) among the 6 treated abyssal sediment samples and environmental factors (pressure, H_2 and lactate) and (**b**) the community functional prediction based on the FAPROTAX database.

The functional diversity (Figure 6b) observed was closely correlated with the microbial diversity (Figure 4f), with atmospheric consortia exhibiting more comprehensive functions compared to the high-pressure microbial community. Under high-pressure conditions, the supplement of exogenous electron donors did not exert a notable influence on the metabolic traits of the microbial communities. Conversely, in atmospheric pressure settings, the amendment of lactate distinctly influenced the prevalence of specific metabolic pathways (Figure 6b and Figure S5). On one hand, lactate was previously observed to accelerate nitrate reduction [75], which explained the observed enhancement of nitrogen respiration, nitrate respiration, and nitrate reduction in A-Lactate compared to A-Original well (Figure 6b). On the other hand, high levels of lactate were reported to impede Fe(II) oxidation and nitrate reduction processes [76], which in turn supports the observation that Fe(II) concentrations in A-Lactate remained elevated compared to other experimental groups, where a decline of Fe(II) concentration was noted after day 16 (Figure 2).

The analysis revealed a general prevalence of aerobic microorganisms across six treated abyssal sediment samples (Figure 7a). Facultatively anaerobic microorganisms were found to make up approximately 22.70–29.12% of the atmospheric groups (A-, Figure 7c). Anaerobic microorganisms exhibited a notably low relative abundance, accounting for less than 0.05%, predominantly observed within the atmospheric groups (A-, Figure 7b). These findings coincide with the established knowledge that contemporary oceanic and shallow abyssal sediments typically harbor oxygen [77], thus supporting the proliferation of aerobic microorganisms. The findings suggest that piezotolerant microorganisms tend to be aerobic, whereas those adapted to low-pressure settings are often anaerobic. *Marinobacter* and *Pseudoalteromonas* are recognized as genera capable of withstanding stress, making the three atmospheric groups stress-tolerant (Figure 7d). Notably, a significant proportion of

microorganisms found in abyssal sediments were Gram-negative (Figure 7e). In contrast, Gram-positive microorganisms, predominantly represented by *Dietzia*, accounted for less than 5% of the total population and were primarily situated within the atmospheric groups (Figure 7f).

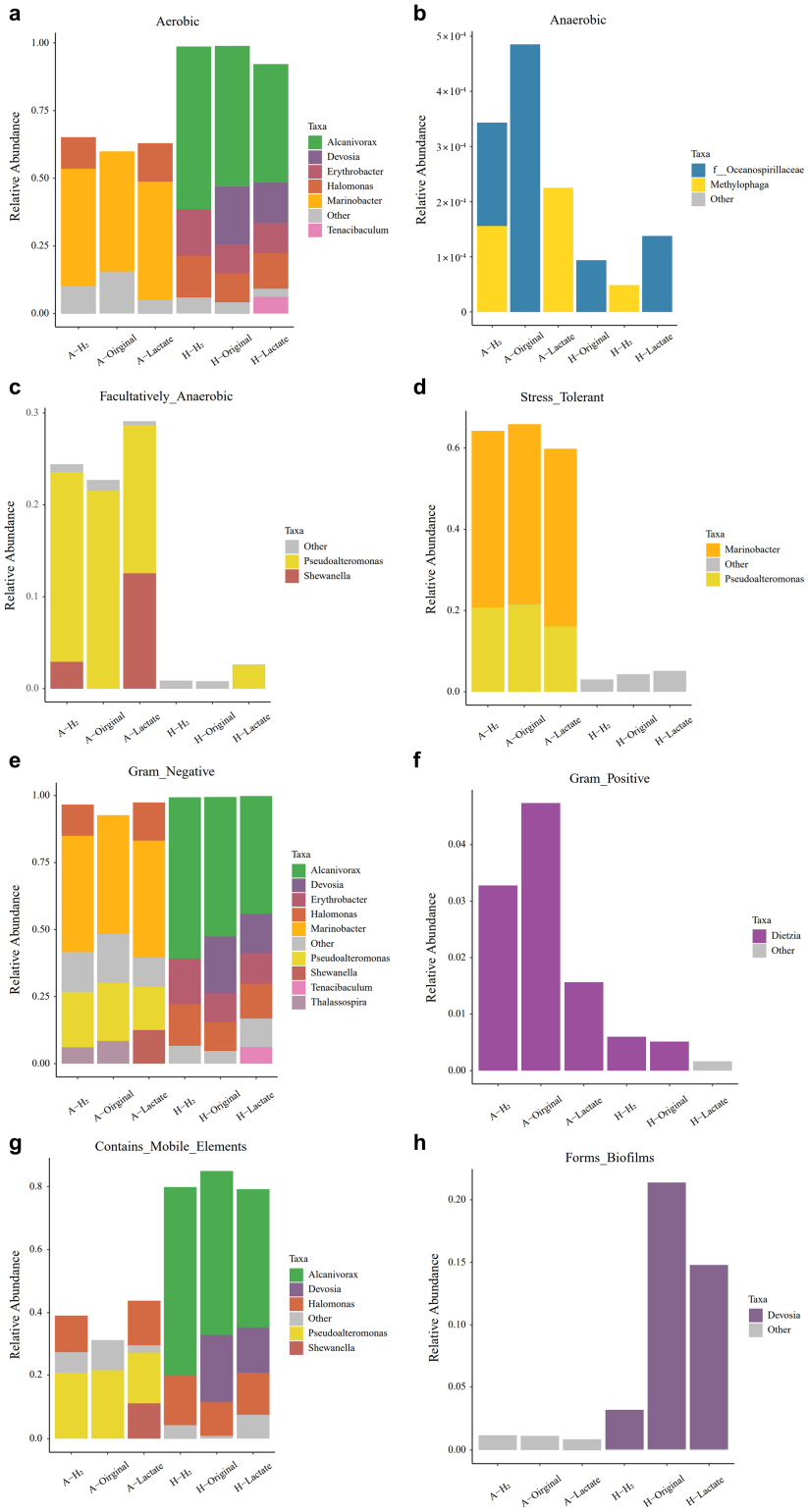

Figure 7. Phenotypic predictions of the dominant phyla within the 6 treated abyssal sediment samples based on BugBase: (**a**) aerobic, (**b**) anaerobic, (**c**) facultative anaerobic, (**d**) stress-tolerant, (**e**) Gram-negative, (**f**) Gram-positive, (**g**) containing mobile elements, and (**h**) forming biofilms.

Ocean microorganisms often possess flagella, aiding their migration towards favorable environments [78]. Flagellated microorganisms were identified to make up 79.19–84.91% of high-pressure groups (H-), while only 31.30–43.75% was observed in atmospheric pressure groups (A-) (Figure 7g). *Devosia*, found in all three high-pressure groups, exhibited biofilm formation capability, a feature less common in microorganisms from atmospheric pressure groups (Figure 7h). Biofilms, composed of numerous microbial cells, play a vital role in facilitating symbiotic relationships among different microorganisms [79]. This symbiosis is essential for deep-sea microorganisms to thrive under extreme conditions and drive various biogeochemical processes.

Abyssal sediments are composed of various Fe-redox microorganisms. *Shewanella* was identified as the predominant genus involved in dissimilatory Fe(III) reduction, constituting approximately 20.679% of the total biomass in the A-Lactate group. Scanning electron microscopy (SEM) images illustrated the direct interactions between microbial entities and phyllosilicate minerals within the abyssal sediments (Figure 8). Of particular interest were the microbial filaments that bridged cells and minerals, likely serving as microbial nanowires to facilitate extracellular electron transfer between the microbial community and iron-containing substances such as Fe(III) oxides. This intriguing phenomenon of microbial nanowires has been documented in the iron reduction mechanisms of both *Geobacter* spp. and *Shewanella* spp. [17,80].

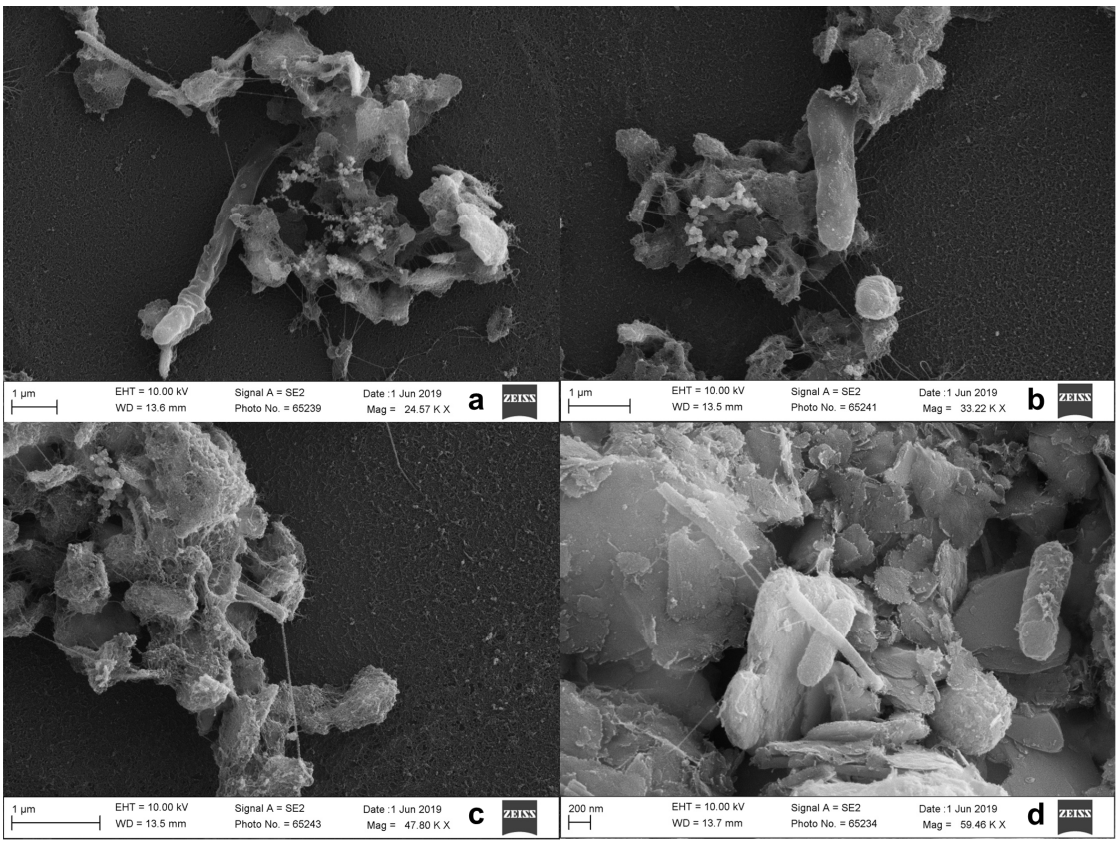

Figure 8. Scanning electron microscopic images of mineral–microbe interactions in A-Lactate.

4. Conclusions

The oligotrophic abyssal sediment experienced oscillations in Fe-redox states during anaerobic culturing, progressing through an initial lag phase, followed by a fast Fe reduction, and an extended period of gradual Fe oxidation before achieving equilibrium after 58 days. The supplement of external electron donors (H_2 or lactate) significantly enhanced the extent of Fe(III) bio-reduction: (1) 7.73% by H_2 under high pressure (58 MPa, H-H_2) and (2) 11.20% by lactate under atmospheric pressure (A-Lactate). Fe(II) bio-oxidation

occurred after 16 days' anaerobic culturing, coupled with nitrate reduction. Bacteria were the dominant microorganisms in the abyssal sediment. Microbial community composition was heavily influenced by the presence or absence of an electron donor and the level of hydrostatic pressure, with pressure being the dominant factor. Fe(III) reducing and Fe(II) oxidizing were abundant in the abyssal sediment. *Shewanella* spp. were identified as the major Fe(III)-reducing microorganisms, particularly with lactate supplemented (A-Lactate). However, high pressure significantly lowered the proportion of *Shewanella*. *Marinobacter hydrocarbonoclasticus* was the dominant Fe(II)-oxidizing microorganism in all conditions.

Supplementary Materials: The following supporting information can be downloaded at: https://www.mdpi.com/article/10.3390/w16192740/s1, Figure S1: Rarefaction and Shannon curves; Figure S2: Rank abundance curves; Figure S3: Changes in the number of total and shared microbial communities at genera; Figure S4: Correlation heatmap; Figure S5: Comparison of metabolic functions; Table S1: Microbial community at genera negatively correlated to electron donor.

Author Contributions: Conceptualization, D.Z.; data curation, G.L.; formal analysis, X.L.; funding acquisition, Q.X.; investigation, D.Z., X.L. and Z.Z.; methodology, D.Z., G.L. and D.H.; resources, Q.X.; software, J.H.; supervision, Q.X.; validation, D.Z. and Q.X.; visualization, G.L., Y.L. and Y.S.; writing—original draft, D.Z.; writing—review and editing, Q.X. All authors have read and agreed to the published version of the manuscript.

Funding: This research was funded by grants from the National Natural Science Foundation (NSFC-42407333), Young Elite Scientist Sponsorship Program by Bast (BYESS2024071), and Young Talents Sponsorship Program by CNNC (2024-58).

Data Availability Statement: The original contributions presented in the study are included in the article/Supplementary Material, further inquiries can be directed to the corresponding author.

Conflicts of Interest: The authors declare no conflict of interest.

References

1. Boyd, P.W.; Ellwood, M.J. The Biogeochemical Cycle of Iron in the Ocean. *Nat. Geosci.* **2010**, *3*, 675–682. [CrossRef]
2. Lu, J.; Yu, P.; Zhang, J.; Guo, Z.; Li, Y.; Wang, S.; Hu, Z. Biotic/Abiotic Transformation Mechanisms of Phenanthrene in Iron-Rich Constructed Wetland under Redox Fluctuation. *Water Res.* **2024**, *261*, 122033. [CrossRef] [PubMed]
3. Sheng, Y.; Baars, O.; Guo, D.; Whitham, J.; Srivastava, S.; Dong, H. Mineral-Bound Trace Metals as Cofactors for Anaerobic Biological Nitrogen Fixation. *Environ. Sci. Technol.* **2023**, *57*, 7206–7216. [CrossRef] [PubMed]
4. Dong, H.; Zeng, Q.; Sheng, Y.; Chen, C.; Yu, G.; Kappler, A. Coupled Iron Cycling and Organic Matter Transformation across Redox Interfaces. *Nat. Rev. Earth Environ.* **2023**, *4*, 659–673. [CrossRef]
5. He, H.; Zhang, C.-G.; Xia, J.-L.; Peng, A.-A.; Yang, Y.; Jiang, H.-C.; Zheng, L.; Ma, C.-Y.; Zhao, Y.-D.; Nie, Z.-Y.; et al. Investigation of Elemental Sulfur Speciation Transformation Mediated by Acidithiobacillus Ferrooxidans. *Curr. Microbiol.* **2009**, *58*, 300–307. [CrossRef]
6. Sheng, Y.; Dong, H.; Kukkadapu, R.K.; Ni, S.; Zeng, Q.; Hu, J.; Coffin, E.; Zhao, S.; Sommer, A.J.; McCarrick, R.M. Lignin-Enhanced Reduction of Structural Fe (III) in Nontronite: Dual Roles of Lignin as Electron Shuttle and Donor. *Geochim. Cosmochim. Acta* **2021**, *307*, 1–21. [CrossRef]
7. Danovaro, R.; Snelgrove, P.V.; Tyler, P. Challenging the Paradigms of Deep-Sea Ecology. *Trends Ecol. Evol.* **2014**, *29*, 465–475. [CrossRef]
8. Leng, D.; Shao, S.; Xie, Y.; Wang, H.; Liu, G. A Brief Review of Recent Progress on Deep Sea Mining Vehicle. *Ocean Eng.* **2021**, *228*, 108565. [CrossRef]
9. Zhou, R.; Bai, B.; Cai, G.; Chen, X. Thermo-Hydro-Mechanic-Chemical Coupling Model for Hydrate-Bearing Sediment within a Unified Granular Thermodynamic Theory. *Comput. Geotech.* **2024**, *167*, 106057. [CrossRef]
10. Kim, J.; Dong, H.; Yang, K.; Park, H.; Elliott, W.C.; Spivack, A.; Koo, T.; Kim, G.; Morono, Y.; Henkel, S.; et al. Naturally Occurring, Microbially Induced Smectite-to-Illite Reaction. *Geology* **2019**, *47*, 535–539. [CrossRef]
11. Sheng, Y.; Dong, H.; Coffin, E.; Myrold, D.; Kleber, M. The Important Role of Enzyme Adsorbing Capacity of Soil Minerals in Regulating β-Glucosidase Activity. *Geophys. Res. Lett.* **2022**, *49*, e2021GL097556. [CrossRef]
12. Gao, X.; Han, Z.; Zhao, Y.; Zhou, G.; Lyu, X.; Qi, Z.; Liu, F.; Tucker, M.E.; Steiner, M.; Han, C. Interaction of Microorganisms with Carbonates from the Micro to the Macro Scales during Sedimentation: Insights into the Early Stage of Biodegradation. *J. Environ. Manag.* **2024**, *356*, 120714. [CrossRef] [PubMed]
13. Roden, E.E. Microbial Iron-Redox Cycling in Subsurface Environments. *Biochem. Soc. Trans.* **2012**, *40*, 1249–1256. [CrossRef] [PubMed]

14. Hu, L.; Wang, Z.; Wang, Z.; Wang, L.; Fang, J.; Liu, R. Community Composition and Functional Characterization of Microorganisms in Surface Sediment of the New Britain Trench. *Curr. Microbiol.* **2024**, *81*, 282. [CrossRef] [PubMed]
15. Lovley, D.R. Dissimilatory metal reduction. *Annu. Rev. Microbiol.* **1993**, *47*, 263–290. [CrossRef]
16. Dong, H.; Coffin, E.S.; Sheng, Y.; Duley, M.L.; Khalifa, Y.M. Microbial Reduction of Fe(III) in Nontronite: Role of Biochar as a Redox Mediator. *Geochim. Cosmochim. Acta* **2023**, *345*, 102–116. [CrossRef]
17. Reguera, G.; McCarthy, K.D.; Mehta, T.; Nicoll, J.S.; Tuominen, M.T.; Lovley, D.R. Extracellular Electron Transfer via Microbial Nanowires. *Nature* **2005**, *435*, 1098–1101. [CrossRef]
18. Wang, Z.; Hu, Y.; Dong, Y.; Shi, L.; Jiang, Y. Enhancing Electrical Outputs of the Fuel Cells with *Geobacter Sulferreducens* by Overexpressing Nanowire Proteins. *Microb. Biotechnol.* **2023**, *16*, 534–545. [CrossRef]
19. Penas, D.; Pereira, A.S.; Tavares, P. Direct Evidence for Ferrous Ion Oxidation and Incorporation in the Absence of Oxidants by Dps from *Marinobacter hydrocarbonoclasticus*. *Angew. Chem.* **2019**, *131*, 1025–1030. [CrossRef]
20. Nagata, T.; Tamburini, C.; Arístegui, J.; Baltar, F.; Bochdansky, A.B.; Fonda-Umani, S.; Fukuda, H.; Gogou, A.; Hansell, D.A.; Hansman, R.L. Emerging Concepts on Microbial Processes in the Bathypelagic Ocean–Ecology, Biogeochemistry, and Genomics. *Deep Sea Res. Part II Top. Stud. Oceanogr.* **2010**, *57*, 1519–1536. [CrossRef]
21. Blöthe, M.; Roden, E.E. Composition and Activity of an Autotrophic Fe(II)-Oxidizing, Nitrate-Reducing Enrichment Culture. *Appl. Environ. Microbiol.* **2009**, *75*, 6937–6940. [CrossRef] [PubMed]
22. Bolger, A.M.; Lohse, M.; Usadel, B. Trimmomatic: A Flexible Trimmer for Illumina Sequence Data. *Bioinformatics* **2014**, *30*, 2114–2120. [CrossRef] [PubMed]
23. Martin, M. Cutadapt Removes Adapter Sequences from High-Throughput Sequencing Reads. *EMBnet J.* **2011**, *17*, 10–12. [CrossRef]
24. Edgar, R.C. Search and Clustering Orders of Magnitude Faster than BLAST. *Bioinformatics* **2010**, *26*, 2460–2461. [CrossRef]
25. Edgar, R.C.; Haas, B.J.; Clemente, J.C.; Quince, C.; Knight, R. UCHIME Improves Sensitivity and Speed of Chimera Detection. *Bioinformatics* **2011**, *27*, 2194–2200. [CrossRef]
26. Edgar, R.C. UPARSE: Highly Accurate OTU Sequences from Microbial Amplicon Reads. *Nat. Methods* **2013**, *10*, 996–998. [CrossRef]
27. Bolyen, E.; Rideout, J.R.; Dillon, M.R.; Bokulich, N.A.; Abnet, C.C.; Al-Ghalith, G.A.; Alexander, H.; Alm, E.J.; Arumugam, M.; Asnicar, F. Reproducible, Interactive, Scalable and Extensible Microbiome Data Science Using QIIME 2. *Nat. Biotechnol.* **2019**, *37*, 852–857. [CrossRef]
28. Louca, S.; Parfrey, L.W.; Doebeli, M. Decoupling Function and Taxonomy in the Global Ocean Microbiome. *Science* **2016**, *353*, 1272–1277. [CrossRef]
29. Ward, T.; Larson, J.; Meulemans, J.; Hillmann, B.; Lynch, J.; Sidiropoulos, D.; Spear, J.R.; Caporaso, G.; Blekhman, R.; Knight, R. BugBase Predicts Organism-Level Microbiome Phenotypes. *BioRxiv* **2017**, 133462. [CrossRef]
30. Xia, Q.; Zhang, L.; Dong, H.; Li, Z.; Zhang, Y.; Hu, J.; Chen, H.; Chen, Y. Bio-Weathering of a Uranium-Bearing Rhyolitic Rock from Xiangshan Uranium Deposit, Southeast China. *Geochim. Cosmochim. Acta* **2020**, *279*, 88–106. [CrossRef]
31. Xia, Q.; Chen, J.; Dong, H. Effects of Organic Ligands on the Antibacterial Activity of Reduced Iron-Containing Clay Minerals: Higher Extracellular Hydroxyl Radical Production Yet Lower Bactericidal Activity. *Environ. Sci. Technol.* **2023**, *57*, 6888–6897. [CrossRef]
32. Xia, Q.; Jin, Q.; Chen, Y.; Zhang, L.; Li, X.; He, S.; Guo, D.; Liu, J.; Dong, H. Combined Effects of Fe(III)-Bearing Nontronite and Organic Ligands on Biogenic U(IV) Oxidation. *Environ. Sci. Technol.* **2022**, *56*, 1983–1993. [CrossRef] [PubMed]
33. Parameswaran, N.K.; González, E.; Burwicz-Galerne, E.; Braack, M.; Wallmann, K. NN-TOC v1: Global Prediction of Total Organic Carbon in Marine Sediments Using Deep Neural Networks. *EGUsphere* **2024**. [CrossRef]
34. Debbarma, R.; Singh, S.K.; Waikhom, G.; Biswas, P.; Meena, D.K.; Choudhary, B.K. Chapter 12—Biofloc Technology: A Strategic Way to Waste Recycling in Aquaculture. In *Organic Farming*, 2nd ed.; Sarathchandran, M.U., Thomas, S., Meena, D.K., Eds.; Woodhead Publishing Series in Food Science, Technology and Nutrition; Woodhead Publishing: Cambridge, UK, 2023; pp. 395–419, ISBN 978-0-323-99145-2. [CrossRef]
35. Joshi, P.; Gorski, C.A. Anisotropic Morphological Changes in Goethite during Fe^{2+}-Catalyzed Recrystallization. *Environ. Sci. Technol.* **2016**, *50*, 7315–7324. [CrossRef] [PubMed]
36. Yang, M.; Liang, X.; Ma, L.; Huang, J.; He, H.; Zhu, J. Adsorption of REEs on Kaolinite and Halloysite: A Link to the REE Distribution on Clays in the Weathering Crust of Granite. *Chem. Geol.* **2019**, *525*, 210–217. [CrossRef]
37. Zhang, L.; Dong, H.; Li, R.; Liu, D.; Bian, L.; Chen, Y.; Pan, Z.; Boyanov, M.I.; Kemner, K.M.; Wen, J.; et al. Effect of Siderophore DFOB on U(VI) Adsorption to Clay Mineral and Its Subsequent Reduction by an Iron-Reducing Bacterium. *Environ. Sci. Technol.* **2022**, *56*, 12702–12712. [CrossRef]
38. Sheng, Y.; Hu, J.; Kukkadapu, R.; Guo, D.; Zeng, Q.; Dong, H. Inhibition of Extracellular Enzyme Activity by Reactive Oxygen Species upon Oxygenation of Reduced Iron-Bearing Minerals. *Environ. Sci. Technol.* **2023**, *57*, 3425–3433. [CrossRef]
39. Cui, S.; Wang, R.; Chen, Q.; Pugliese, L.; Wu, S. Geobatteries in Environmental Biogeochemistry: Electron Transfer and Utilization. *Environ. Sci. Ecotechnol.* **2024**, *22*, 100446. [CrossRef]
40. Dong, H.; Huang, L.; Zhao, L.; Zeng, Q.; Liu, X.; Sheng, Y.; Shi, L.; Wu, G.; Jiang, H.; Li, F. A Critical Review of Mineral–Microbe Interaction and Co-Evolution: Mechanisms and Applications. *Natl. Sci. Rev.* **2022**, *9*, nwac128. [CrossRef]

41. Ji, X.; Zhou, C.; Chen, L.; Li, Y.; Hua, T.; Li, Y.; Wang, C.; Jin, S.; Ding, H.; Lu, A. Reduction, Mineralization, and Magnetic Removal of Chromium from Soil by Using a Natural Mineral Composite. *Environ. Sci. Ecotechnol.* **2022**, *11*, 100181. [CrossRef]
42. Wang, H.; Bao, W.; Sarwar, M.T.; Tian, L.; Tang, A.; Yang, H. Mineral-Enhanced Manganese Ferrite with Multiple Enzyme-Mimicking Activities for Visual Detection of Disease Markers. *Inorg. Chem.* **2023**, *62*, 8418–8427. [CrossRef]
43. Liu, D.; Wang, F.; Dong, H.; Wang, H.; Zhao, L.; Huang, L.; Wu, L. Biological Reduction of Structural Fe (III) in Smectites by a Marine Bacterium at 0.1 and 20 MPa. *Chem. Geol.* **2016**, *438*, 1–10. [CrossRef]
44. Nixon, S.L.; Bonsall, E.; Cockell, C.S. Limitations of Microbial Iron Reduction under Extreme Conditions. *FEMS Microbiol. Rev.* **2022**, *46*, fuac033. [CrossRef] [PubMed]
45. Klein, F.; Bach, W.; McCollom, T.M. Compositional Controls on Hydrogen Generation during Serpentinization of Ultramafic Rocks. *Lithos* **2013**, *178*, 55–69. [CrossRef]
46. He, Y.; Zeng, X.; Xu, F.; Shao, Z. Diversity of Mixotrophic Neutrophilic Thiosulfate-and Iron-Oxidizing Bacteria from Deep-Sea Hydrothermal Vents. *Microorganisms* **2022**, *11*, 100. [CrossRef] [PubMed]
47. Zhang, J.; Chen, M.; Huang, J.; Guo, X.; Zhang, Y.; Liu, D.; Wu, R.; He, H.; Wang, J. Diversity of the Microbial Community and Cultivable Protease-Producing Bacteria in the Sediments of the Bohai Sea, Yellow Sea and South China Sea. *PLoS ONE* **2019**, *14*, e0215328. [CrossRef]
48. Hoshino, T.; Doi, H.; Uramoto, G.-I.; Wörmer, L.; Adhikari, R.R.; Xiao, N.; Morono, Y.; D'Hondt, S.; Hinrichs, K.-U.; Inagaki, F. Global Diversity of Microbial Communities in Marine Sediment. *Proc. Natl. Acad. Sci. USA* **2020**, *117*, 27587–27597. [CrossRef]
49. Sharma, V.; Vashishtha, A.; Jos, A.L.M.; Khosla, A.; Basu, N.; Yadav, R.; Bhatt, A.; Gulani, A.; Singh, P.; Lakhera, S.; et al. Phylogenomics of the Phylum Proteobacteria: Resolving the Complex Relationships. *Curr. Microbiol.* **2022**, *79*, 224. [CrossRef]
50. Cristóbal, H.A.; Benito, J.; Lovrich, G.A.; Abate, C.M. Phylogenentic and Enzymatic Characterization of Psychrophilic and Psychrotolerant Marine Bacteria Belong to γ-Proteobacteria Group Isolated from the Sub-Antarctic Beagle Channel, Argentina. *Folia Microbiol.* **2015**, *60*, 183–198. [CrossRef]
51. Takai, K.; Inagaki, F.; Nakagawa, S.; Hirayama, H.; Nunoura, T.; Sako, Y.; Nealson, K.H.; Horikoshi, K. Isolation and Phylogenetic Diversity of Members of Previously Uncultivated ε-Proteobacteria in Deep-Sea Hydrothermal Fields. *FEMS Microbiol. Lett.* **2003**, *218*, 167–174.
52. Edwards, K.J.; Rogers, D.R.; Wirsen, C.O.; McCollom, T.M. Isolation and Characterization of Novel Psychrophilic, Neutrophilic, Fe-Oxidizing, Chemolithoautotrophic α- and γ-*Proteobacteria* from the Deep Sea. *Appl. Environ. Microbiol.* **2003**, *69*, 2906–2913. [CrossRef] [PubMed]
53. Oh, Y.-S.; Kahng, H.-Y.; Lee, D.-H.; Lee, S.B. Tenacibaculum Jejuense Sp. Nov., Isolated from Coastal Seawater. *Int. J. Syst. Evol. Microbiol.* **2012**, *62*, 414–419. [CrossRef] [PubMed]
54. Urakami, T.; Komagata, K. Characterization of Species of Marine Methylotrophs of the Genus Methylophaga. *Int. J. Syst. Bacteriol.* **1987**, *37*, 402–406. [CrossRef]
55. Nataro, J.P.; Bopp, C.A.; Fields, P.I.; Kaper, J.B.; Strockbine, N.A. Escherichia, Shigella, and *Salmonella*. In *Manual of Clinical Microbiology*; Versalovic, J., Carroll, K.C., Funke, G., Jorgensen, J.H., Landry, M.L., Warnock, D.W., Eds.; Wiley: Hoboken, NJ, USA, 2011; pp. 603–626. ISBN 978-1-68367-411-5.
56. Roy, M.; Khara, P.; Basu, S.; Dutta, T.K. Catabolic Versatility of Sphingobium Sp. Strain PNB Capable of Degrading Structurally Diverse Aromatic Compounds. *J. Bioremed. Biodeg.* **2013**, *4*, 2. [CrossRef]
57. Jo, J.H.; Choi, G.-M.; Lee, S.-Y.; Im, W.-T. Phenylobacterium Aquaticum Sp. Nov., Isolated from the Reservoir of a Water Purifier. *Int. J. Syst. Evol. Microbiol.* **2016**, *66*, 3519–3523. [CrossRef] [PubMed]
58. Khan, I.U.; Hussain, F.; Habib, N.; Wadaan, M.A.M.; Ahmed, I.; Im, W.-T.; Hozzein, W.N.; Zhi, X.-Y.; Li, W.-J. Phenylobacterium Deserti Sp. Nov., Isolated from Desert Soil. *Int. J. Syst. Evol. Microbiol.* **2017**, *67*, 4722–4727. [CrossRef]
59. Green, P.N.; Ardley, J.K. Review of the Genus Methylobacterium and Closely Related Organisms: A Proposal That Some Methylobacterium Species Be Reclassified into a New Genus, Methylorubrum Gen. Nov. *Int. J. Syst. Evol. Microbiol.* **2018**, *68*, 2727–2748. [CrossRef]
60. Saratale, R.G.; Cho, S.K.; Saratale, G.D.; Ghodake, G.S.; Bharagava, R.N.; Kim, D.S.; Nair, S.; Shin, H.S. Efficient Bioconversion of Sugarcane Bagasse into Polyhydroxybutyrate (PHB) by Lysinibacillus Sp. and Its Characterization. *Bioresour. Technol.* **2021**, *324*, 124673. [CrossRef]
61. Sharma, M.; Khurana, H.; Singh, D.N.; Negi, R.K. The Genus Sphingopyxis: Systematics, Ecology, and Bioremediation Potential-A Review. *J. Environ. Manag.* **2021**, *280*, 111744. [CrossRef]
62. Gan, C.; Wu, R.; Luo, Y.; Song, J.; Luo, D.; Li, B.; Yang, Y.; Xu, M. Visualizing and Isolating Iron-Reducing Microorganisms at the Single-Cell Level. *Appl. Environ. Microbiol.* **2021**, *87*, e02192-20. [CrossRef]
63. Zhu, Y.; He, X.; Xu, J.; Fu, Z.; Wu, S.; Ni, J.; Hu, B. Insight into Efficient Removal of Cr(VI) by Magnetite Immobilized with *Lysinibacillus* Sp. JLT12: Mechanism and Performance. *Chemosphere* **2021**, *262*, 127901. [CrossRef] [PubMed]
64. Li, Y.; Liu, Y.; Guo, D.; Dong, H. Differential Degradation of Petroleum Hydrocarbons by Shewanella Putrefaciens under Aerobic and Anaerobic Conditions. *Front. Microbiol.* **2024**, *15*, 1389954. [CrossRef]
65. Fredrickson, J.K.; Balkwill, D.L.; Romine, M.F.; Shi, T. Ecology, Physiology, and Phylogeny of Deep Subsurface *Sphingomonas* sp. *J. Ind. Microbiol. Biotechnol.* **1999**, *23*, 273–283. [CrossRef] [PubMed]

66. Kieft, T.L.; Fredrickson, J.K.; Onstott, T.C.; Gorby, Y.A.; Kostandarithes, H.M.; Bailey, T.J.; Kennedy, D.W.; Li, S.W.; Plymale, A.E.; Spadoni, C.M.; et al. Dissimilatory Reduction of Fe(III) and Other Electron Acceptors by a Thermus Isolate. *Appl. Environ. Microbiol.* **1999**, *65*, 1214–1221. [CrossRef] [PubMed]
67. Lovley, D.R.; Phillips, E.J.P.; Lonergan, D.J. Hydrogen and Formate Oxidation Coupled to Dissimilatory Reduction of Iron or Manganese by Alteromonas Putrefaciens. *Appl. Environ. Microbiol.* **1989**, *55*, 700–706. [CrossRef]
68. Jakus, N.; Blackwell, N.; Straub, D.; Kappler, A.; Kleindienst, S. Presence of Fe(II) and Nitrate Shapes Aquifer-Originating Communities Leading to an Autotrophic Enrichment Dominated by an Fe(II)-Oxidizing *Gallionellaceae* sp. *FEMS Microbiol. Ecol.* **2021**, *97*, fiab145. [CrossRef]
69. Golyshina, O.V.; Kublanov, I.V.; Tran, H.; Korzhenkov, A.A.; Lünsdorf, H.; Nechitaylo, T.Y.; Gavrilov, S.N.; Toshchakov, S.V.; Golyshin, P.N. Biology of Archaea from a Novel Family Cuniculiplasmataceae (Thermoplasmata) Ubiquitous in Hyperacidic Environments. *Sci. Rep.* **2016**, *6*, 39034. [CrossRef]
70. Greening, C.; Cabotaje, P.R.; Alvarado, L.E.V.; Leung, P.M.; Land, H.; Rodrigues-Oliveira, T.; Ponce-Toledo, R.I.; Senger, M.; Klamke, M.A.; Milton, M.; et al. Minimal and Hybrid Hydrogenases Are Active from Archaea. *Cell* **2024**, *187*, 3357–3372.e19. [CrossRef]
71. Wu, J.; Wang, P.; Zhang, D.; Chen, S.; Sun, Y.; Wu, J. Catalysis of Oxygen Reduction Reaction by an Iron-Reducing Bacterium Isolated from Marine Corrosion Product Layers. *J. Electroanal. Chem.* **2016**, *774*, 83–87. [CrossRef]
72. Garber, A.I.; Nealson, K.H.; Okamoto, A.; McAllister, S.M.; Chan, C.S.; Barco, R.A.; Merino, N. FeGenie: A Comprehensive Tool for the Identification of Iron Genes and Iron Gene Neighborhoods in Genome and Metagenome Assemblies. *Front. Microbiol.* **2020**, *11*, 499513. [CrossRef]
73. Ross, D.E.; Ruebush, S.S.; Brantley, S.L.; Hartshorne, R.S.; Clarke, T.A.; Richardson, D.J.; Tien, M. Characterization of Protein-Protein Interactions Involved in Iron Reduction by *Shewanella Oneidensis* MR-1. *Appl. Environ. Microbiol.* **2007**, *73*, 5797–5808. [CrossRef] [PubMed]
74. Wang, F.; Wang, J.; Jian, H.; Zhang, B.; Li, S.; Wang, F.; Zeng, X.; Gao, L.; Bartlett, D.H.; Yu, J.; et al. Environmental Adaptation: Genomic Analysis of the Piezotolerant and Psychrotolerant Deep-Sea Iron Reducing Bacterium Shewanella Piezotolerans WP3. *PLoS ONE* **2008**, *3*, e1937. [CrossRef]
75. Akunna, J.C.; Bizeau, C.; Moletta, R. Nitrate and Nitrite Reductions with Anaerobic Sludge Using Various Carbon Sources: Glucose, Glycerol, Acetic Acid, Lactic Acid and Methanol. *Water Res.* **1993**, *27*, 1303–1312. [CrossRef]
76. Pang, Y.; Wang, J. Various Electron Donors for Biological Nitrate Removal: A Review. *Sci. Total Environ.* **2021**, *794*, 148699. [CrossRef]
77. Kendall, B.; Anbar, A.D.; Kappler, A.; Konhauser, K.O. The Global Iron Cycle. In *Fundamentals of Geobiology*; Knoll, A.H., Canfield, D.E., Konhauser, K.O., Eds.; Wiley: Hoboken, NJ, USA, 2012; pp. 65–92. ISBN 978-1-118-28081-2.
78. Eloe, E.A.; Lauro, F.M.; Vogel, R.F.; Bartlett, D.H. The Deep-Sea Bacterium Photobacterium Profundum SS9 Utilizes Separate Flagellar Systems for Swimming and Swarming under High-Pressure Conditions. *Appl. Environ. Microbiol.* **2008**, *74*, 6298–6305. [CrossRef]
79. Flemming, H.-C.; Wuertz, S. Bacteria and Archaea on Earth and Their Abundance in Biofilms. *Nat. Rev. Microbiol.* **2019**, *17*, 247–260. [CrossRef]
80. Gorby, Y.A.; Yanina, S.; McLean, J.S.; Rosso, K.M.; Moyles, D.; Dohnalkova, A.; Beveridge, T.J.; Chang, I.S.; Kim, B.H.; Kim, K.S.; et al. Electrically Conductive Bacterial Nanowires Produced by *Shewanella oneidensis* Strain MR-1 and Other Microorganisms. *Proc. Natl. Acad. Sci. USA* **2006**, *103*, 11358–11363. [CrossRef]

Disclaimer/Publisher's Note: The statements, opinions and data contained in all publications are solely those of the individual author(s) and contributor(s) and not of MDPI and/or the editor(s). MDPI and/or the editor(s) disclaim responsibility for any injury to people or property resulting from any ideas, methods, instructions or products referred to in the content.

MDPI AG
Grosspeteranlage 5
4052 Basel
Switzerland
Tel.: +41 61 683 77 34

Water Editorial Office
E-mail: water@mdpi.com
www.mdpi.com/journal/water

Disclaimer/Publisher's Note: The title and front matter of this reprint are at the discretion of the Guest Editors. The publisher is not responsible for their content or any associated concerns. The statements, opinions and data contained in all individual articles are solely those of the individual Editors and contributors and not of MDPI. MDPI disclaims responsibility for any injury to people or property resulting from any ideas, methods, instructions or products referred to in the content.

Academic Open
Access Publishing

mdpi.com

ISBN 978-3-7258-4346-6